The Genesis of Stars: From Giant Molecular Clouds to Star-Forming Cores

Inaugural-Dissertation
zur
Erlangung des Doktorgrades
der Mathematisch-Naturwissenschaftlichen Fakultät
der Universität zu Köln

vorgelegt von

Eduard Keilmann

aus Saryagatsch

angenommen im
Jahr 2025

Begutachtung:

Prof. Dr. Jürgen Stutzki
Prof. Dr. Andreas Schadschneider

"I've always looked upon myself as a physicist, learning new tricks by looking at nature. Space, the whole galaxy, the whole universe. I know no better place to find new physics."

Eugene N. Parker, Physicist

To my son, Nicolas

Abstract

Understanding how stars and planets form out of molecular clouds in galaxies is one of the central questions in modern astrophysics. Many unresolved questions relate to the formation and evolution of molecular clouds in galaxies, which are shaped by gravitational instabilities, spiral density waves, stellar feedback, magnetic fields, and turbulence within the interstellar medium (ISM). To enhance our understanding of these processes, it is necessary to investigate cloud- and star-formation on different spatial scales and with various observational tracers.

In this thesis, I thus investigate the galaxy M33 and star-forming regions in the Milky Way, using line emission data from atoms and molecules as well as dust continuum observations. Spectroscopic lines such as the far-infrared (FIR) fine-structure line of ionized carbon ([C II]) as well as rotational lines of the carbon monoxide molecule (CO) are essential to understand the dynamics and the heating and cooling processes in the ISM. My intention was to address some fundamental questions: What mechanisms drive the formation of molecular clouds? How do cloud properties vary across different galactic environments, such as central regions or spiral arms? Do cloud properties systematically differ between the Milky Way and other galaxies like M33? What mechanisms drive stellar feedback?

I have written several studies dealing with these topics as first and co-author that have been published in the renowned peer-review journal Astronomy & Astrophysics (A&A), resulting in this cumulative doctoral thesis in which I integrate the main papers. My work concentrates on the formation of molecular clouds, initial conditions conducive for star formation (SF), and the destruction of molecular clouds due to stellar feedback processes, such as stellar winds and radiation. Thus, this thesis encompasses work ranging from small-scale cloud formation (Draco), to large-scale Giant Molecular Clouds (GMCs) properties (M33), and back to small-scale stellar feedback processes and the destruction of the molecular cloud in RCW79. I first focus on the early cloud formation in Draco, then I briefly summarize the study on the compact H II region in RCW79 (H II refers to ionized hydrogen). Subsequently, I present the results regarding the large-scale questions with M33 and end with a summary on other work not presented in this thesis. Studies cited in this abstract refer to papers that I authored and co-authored.

The emission of ionized carbon ([C II]) provides insight into early cloud formation in the diffuse, high-latitude cloud Draco. This region high above the Galactic plane is exposed to a weak far-ultraviolet (FUV) field and the [C II] emission is interpreted as arising from shocks induced by atomic hydrogen (H I) colliding flows (Schneider et al., 2024) and not from photodissociation regions (PDRs). We find that Draco is on the verge of becoming a molecular cloud because CO emission was detected across the region. My contributions as third co-author include radiative transfer modeling of CO with RADEX and PDR

modeling, position-velocity (PV) cuts, and discussions of the results of this work. I am also involved in the follow-up paper studying the H I-to-H_2 (atomic-to-molecular hydrogen) transition (Schneider et al., in press).

The compact H II region S144 in RCW79 in the Milky Way presents an early stage of an expanding [C II] bubble, which is observed for the first time to be filled with ionized carbon emission. My first-author *Letter to the Editor*, published in A&A (Keilmann et al., 2025), presents a detailed analysis of S144. The ionization from an O7.5–9.5V/III star results in emission that forms a compact H II region (S144) inside the larger RCW79 bubble (a shell of [C II] emission). Inside this compact H II region another bubble of [C II] emission has formed (a bubble in a bubble). The associated [C II] shell of this small bubble in S144 has a slow expansion velocity, in contrast to what is found for more evolved H II regions (like the large shell of the entire RCW79 region itself or RCW120). The expansion dynamics of this [C II]-bubble align with a stellar wind model in a power-law density field, highlighting the crucial role of stellar winds in shaping the ISM. Furthermore, S144 in RCW79 exhibits a so-called [C II]-deficit, which refers to lowered [C II] emission compared to FIR emission. PV cuts and channel maps show a central emission dip within the bubble, partly due to [C II] self-absorption that is responsible for the [C II]-deficit. In order to quantify this deficit, I used radiative transfer equations to fit the hyperfine-structure (HFS) of the spectrum's double-peaked wings. With a two-layer multicomponent model, I determine a lower limit for the excitation temperature. The spectra are qualitatively modeled using SimLine, which supports the hypothesis that [C II] self-absorption contributes to the double-peak formation. The findings in this thesis demonstrate (i) the diagnostic potential of ionized carbon emission in tracing [C II] bubble dynamics and early cloud formation, and (ii) that the [C II]-deficit can be attributed to [C II] self-absorption under specific physical conditions. Another follow-up project, in which I take the lead, further analyzes the cloud evolution and PDR physics of RCW79.

The study on S144 in RCW79 used data obtained with the German REceiver for Astronomy at Terahertz Frequencies (GREAT) with Dr. Rolf Güsten as the initial Principal Investigator (PI) and Professor Dr. Jürgen Stutzki the subsequent PI built and developed in collaboration at the I. Physikalisches Institut at the University of Cologne and at Max-Planck Institute for Radio Astronomy (MPIfR), onboard the Stratospheric Observatory for Infrared Astronomy (SOFIA). SOFIA was a collaboration between NASA and Deutsches Zentrum für Luft- und Raumfahrt (DLR). As part of this team at the University of Cologne, I am a member of the *FEEDBACK* consortium, which provided me with GREAT data that were used in this thesis. These include several species such as the ionized carbon line [C II] at 158 μm, carbon monoxide CO, as well as complementary data from other observatories (e.g., APEX, Herschel, VLA) like atomic hydrogen H I and dust data.

For the galaxy M33, I conducted two first-author A&A publications focusing on the molecular cloud content and their properties. I prepared the data that have been used, and generated the molecular hydrogen (H_2) column density maps and related data, such as the dust absorption coefficient map, the column density probability distribution functions (N-PDFs), the CO-to-H_2 ($X_{\rm CO}$) conversion factor map, as well as performing all calculations, interpretation, and discussion of Paper I (Keilmann et al., 2024a). The $X_{\rm CO}$ conversion factor in M33 appears to be similar to or even slightly lower than the Galactic standard value, contradicting previous assumptions that correlate the factor only with metallicity (which refers to all elements heavier than helium). This finding of Paper I challenges oversimplified assumptions that attribute $X_{\rm CO}$ solely to metallicity effects. In

Paper II (Keilmann et al., 2024b), the H_2 column density maps were utilized to identify GMCs using a dendrogram-based machine learning technique and to examine their physical characteristics, such as mass, density, surface mass density, size, or elongation. These GMCs were compared to those in the Milky Way to comprehend their properties under varying conditions of different galaxies. Furthermore, the properties of M33 GMCs are analyzed to determine if they vary systematically with their galactic environments. A comparison of GMC properties in M33 and the Milky Way reveals both similarities and differences. Notably, both galaxies exhibit an upper limit on cloud sizes despite differing physical conditions such as mass, age, metallicity, and size. This similarity may be attributed to comparable galactic disk scale heights. In addition, M33 lacks the most massive clouds (above $\sim 10^6\,\mathrm{M}_\odot$), suggesting a strong dependence on gas density. This is also reflected by the findings on the different power-law mass spectra of both galaxies. Furthermore, the physical properties of the GMCs in M33 do not show significant dependence on different galactic environments, implying that large-scale galactic conditions do not play a dominant role in shaping the GMC properties. This finding raises the question of whether small-scale stellar feedback has a more substantial impact on molecular cloud properties. Another follow-up project (Keilmann et al., in prep.), in which I take the lead, further analyzes the magnetic fields and rotation of the detected GMCs in M33 described in Paper II alongside a deeper investigation of the N-PDFs and turbulence.

Further projects I was involved with but are not part of this thesis are as follows. The *Letter to the Editor* Bonne et al. (2023), published in A&A, demonstrated that the large shell of RCW79 is undergoing dispersal. I contributed with PV cuts, as well as with the discussion and interpretation of the findings. This letter closes the path from the initial cloud formation on a small scale (Draco, Schneider et al., 2024) and the investigation of the early phases in a young region influenced by a massive young star (Keilmann et al., 2025), to the large-scale conditions in GMCs (M33) that are conducive to star formation (Keilmann et al., 2024a,b), and the eventual destruction of a natal molecular cloud (Bonne et al., 2023).

Another project in which I am involved is a study (Dannhauer et al., submitted to A&A) of an unusually slowly expanding [C II] bubble (velocities $\lesssim 1.3\,\mathrm{km\,s^{-1}}$) in the Cygnus X region – termed “Diamond Ring.” The SOFIA [C II] and CO data are compared with dedicated simulations and reveal a presumably terminal stage of a formerly fast expanding bubble. I contributed with producing PV cuts, channel maps, and discussion as well as interpretation of the results of the paper and with writing and discussing an associated IRAM 30m telescope proposal to map the region in HCO^+ and HCN.

Furthermore, another paper is in preparation on a protoplanetary disk-like object (proplyd #7) in the Cygnus region, in which I am also involved. Two accompanying IRAM proposals for the 30m telescope and NOEMA (NOrthern Extended Millimetre Array) have been submitted and accepted to which I contributed.

During my Ph.D., I further gained experience in observations with the IRAM 30m telescope that was used to study NGC205. Additionally, two successful APEX proposals for which I am PI were accepted and observed: one in [C I] in M33 (ESO time, 109.23FN) and another in several CO lines in RCW79 (Max-Planck time, M-0113.F-9502A-2024). I gained a lot of experience in Python and the GILDAS software package, with which I developed and used many methods and models to analyze the data.

Contents

List of Figures

List of Tables

Chapter 1

Introduction

Star formation fundamentally drives the structure and evolution of galaxies. In the local universe, stars contain most matter and actively shape their host galaxies' morphology and dynamics. The significant role of stellar mass underscores the need to understand star formation and its impacts, making it a focal point in modern astrophysical research. Most stars form in molecular clouds (MCs) smaller than $\sim 50\,\mathrm{pc}$, whereas massive star clusters preferentially form in giant molecular clouds (GMCs) exceeding $\sim 50\,\mathrm{pc}$.

The interstellar medium (ISM) undergoes dynamic cycles that promote molecular cloud formation and subsequent star formation (SF). Gas accretes onto galactic disks, cools, and forms a neutral phase in the ISM. This diffuse gas gives rise to (giant) molecular clouds that develop into dense filaments, cores, and eventually due to gravitational collapse into stars. In particular, massive stars ($M \gtrsim 8\,\mathrm{M}_\odot$) subsequently affect the ISM through their stellar feedback mechanisms (radiation, mechanical winds, supernovae), altering its properties and enriching galaxies chemically over cosmic time.

Gravitational instabilities, spiral density waves, stellar feedback, magnetic fields, and turbulence actively drive the formation and evolution of MCs and their dense substructures in galaxies. Debate persists over whether the galactic environment, such as the central region or spiral arms and inter-arms, or stellar feedback more significantly influences the mechanisms of star formation.

Numerical simulations support a more recent scenario in which converging atomic hydrogen (H I) flows in the warm neutral medium quickly (less than a few $10^6\,\mathrm{yr}$) form molecular clouds (Vázquez-Semadeni et al., 2006; Heitsch and Hartmann, 2008) that consist of molecular hydrogen (H_2). Turbulence is essential, as it maintains large-scale cloud support and generates an inhomogeneous molecular cloud structure marked by significant density contrasts (Mac Low and Klessen, 2004). Although most density fluctuations are transient, energy dissipation and shocks form dense filaments (Neufeld and Dalgarno, 1989; Godard et al., 2019).

The heating-cooling balance influences gas thermodynamics, and magnetic fields likely regulate this balance on both large and small scales. Stellar feedback (radiation, wind, supernovae), shocks at different velocities, and cosmic-rays/X-rays drive key processes, while dust[1] and line emission at (sub)millimeter, far-, and mid-infrared wavelengths primarily cool the gas, making this wavelength range essential for studying processes in Galactic

---

[1] Interstellar dust is mainly composed of amorphous silicate grains, such as magnesium or iron, or carbon-based materials, such as amorphous carbon, graphite, or polycyclic aromatic hydrocarbons (PAHs).

and extragalactic cloud and star formation.

Understanding the physical mechanisms driving stellar feedback – and ultimately star and planet formation – is crucial for understanding the processes behind galactic evolution. Thus, it is necessary to combine local conditions that influence individual star formation with properties evident only on a global scale. Essential aspects include studying the ionized, atomic, and molecular phases of the interstellar medium, as well as its life cycle and thermal equilibrium. This entails analyzing the formation and evolution of molecular clouds and stars in large-scale systems (e.g., the M33 galaxy) and smaller-scale entities (e.g., Galactic clouds).

1.1 Tracer of the ISM

Big Bang nucleosynthesis formed atomic hydrogen H I (approximately 70% by mass) and helium (about 28%) which constitute the atomic matter in the universe. Stars have been synthesizing the remaining 2% of heavier elements like carbon (C), oxygen (O), and nitrogen (N) through nuclear fusion and supernovae, which were partly also formed during Big Bang. Hydrogen and helium remain the most abundant elements, while stellar nucleosynthesis makes carbon and oxygen most common among heavier elements (Bradt and Peters, 1950).

Molecular clouds consist mainly of hydrogen in its molecular form, H_2, which requires reliable measurements of mass, density, and size. However, detecting cool H_2 directly is challenging due to the molecule's symmetry, which results in no permanent dipole moment, and the high energy of the upper-level of its weakly-allowed rotational quadrupole transitions because of its small moment of inertia.

One method to ascertain the H_2 distribution within a galaxy is the observation of dust in the far-infrared (FIR) using instruments like the *Herschel* satellite, with which a total hydrogen column density map can be created through spectral energy distribution (SED) fitting to the observed fluxes. Subtracting the H I component from this total hydrogen column density map yields the H_2 distribution. I employed this method to obtain a H_2 column density map of M33 in Keilmann et al. (2024a).

Carbon monoxide (CO) and the CO-to-H_2 conversion factor X_{CO} provide a reliable tracer for mapping molecular hydrogen (Bolatto et al., 2013). Using CO and determining an X_{CO} factor map of M33 is another method used to obtain the H_2 content of M33 in Keilmann et al. (2024a). CO exhibits a strong dipole moment as an unsymmetrical molecule, and its rotational energy levels easily excite at low temperatures (up to several tens of Kelvin) and low critical densities (a few hundred to several thousand cm^{-3}) required for collisional excitation (Schinnerer and Leroy, 2024). Consequently, CO emits strongly in the millimeter and submillimeter wavelengths, serving as an excellent tracer for dense molecular clouds. Critical density determines the efficiency of CO emission. This parameter denotes the gas density at which collisional de-excitation equals spontaneous radiative decay for a transition. When the gas density falls below the critical density, collisional excitation becomes inefficient, reducing emission intensity while radiative processes yield sub-thermal emission. In contrast, when the gas density exceeds the critical density, collisional excitation dominates and thermalizes the emission, reflecting the local gas temperature (Bolatto et al., 2013). However, CO as a tracer for the molecular gas (H_2) photodissociates more quickly and easily than H_2, resulting in a small fraction of H_2 becoming untraceable with CO referred to as "CO-dark" (Grenier et al., 2005).

Dust effectively traces the ISM, molecular clouds, and star formation unbiased to CO-dark gas by absorbing stellar photons and re-emitting energy via the photoelectrical effect in the infrared (IR) to millimeter range. This process provides insight into radiation field intensity and star formation activity, and it enables estimates of column densities and masses (Grenier et al., 2005). Dust emission, when mixed with gas in the ISM, correlates with gas tracers such as CO and H I, which allows tracing atomic and molecular gases, including CO-dark gas undetectable by traditional means (see above). Dust also shields molecules from radiation, thereby supporting H_2 formation and star formation (Compiègne et al., 2010). Moreover, changes in dust properties in star-forming regions reveal physical conditions and processes within MCs (Ysard et al., 2019).

The ionized carbon fine-structure line [C II] at 158 μm and the neutral oxygen [O I] line at 63 μm are essential for studying the ISM because they dominate cooling in star-forming regions. They are discussed in more detail in Sect. 4.3. [C II] was central in the study of the Draco cloud (Schneider et al., 2024), in which I co-authored, and in my first-author letter Keilmann et al. (2025). Its application in astronomy advanced over time, especially in photodissociation regions (PDRs) where stellar radiation affects molecular clouds, and early studies recognized [C II]'s potential for tracing ISM processes (Dalgarno and McCray, 1972; Tielens and Hollenbach, 1985a). Early research in the 1970s identified the far-Infrared (FIR) [C II] line as the main cooling mechanism in the star-forming ISM (Dalgarno and McCray, 1972).[2]

Together, the [C II] and [O I] lines offer complementary insights into the ISM because they trace different temperature and density regimes, allowing us to disentangle the contributions of different gas phases and to study the complex interplay of radiation, chemistry, and dynamics in star-forming regions. These lines are essential for understanding the life cycle of molecular clouds and the processes that lead to star formation. The [C II] line, for instance, can account for up to 1% of the total FIR luminosity in galaxies, highlighting its significance in the cooling budget of the ISM (Stacey et al., 1991).

Observations reveal a so-called [C II]-deficit in bright PDRs, where [C II] emission shows a deficiency compared to FIR emission. In Keilmann et al. (2025), I also observe and analyze such a [C II]-deficit. Studies suggest various mechanisms to explain this phenomenon in both Galactic and extragalactic star-forming regions. In ultra-luminous IR galaxies, several processes are discussed that contribute to the deficit, such as high dust optical depth, increased ionization parameters (yielding C^{2+} or higher), metallicity variations, and intense radiation fields (Malhotra et al., 1997, 2001; Luhman et al., 2003; Lagache et al., 2018; Ebagezio et al., 2024). Under less extreme Galactic PDR conditions, alternative mechanisms are considered (Goicoechea et al., 2015; Pabst et al., 2021). In very dense regions, dust grain heating efficiency may increase, and [C II] might undergo collisional de-excitation. In addition, [C II] may saturate in some cases, allowing [O I] cooling to dominate in warm, dense PDRs.

However, in PDR regions with moderate gas and temperature conditions, these explanations are probably less valid. By studying the compact H II region S144 in RCW79, I found that local temperature and velocity gradients within the PDR likely cause the [C II]-deficit in S144, impacting line emission more significantly than external factors. Consequently, in Keilmann et al. (2025), I propose the self-absorption of the [C II] line as a potential cause of this deficit. This effect reduces the observed [C II] emission while the FIR continuum remains stable, thus causing a low [C II]/FIR ratio at high emission levels.

---

[2] The historical context is briefly highlighted in Sect. 4.4.1.

1.2 Molecular Cloud Formation, Evolution and Fragmentation

Molecular clouds are the birthplaces of star formation within galaxies, created through complex processes affected by multiple physical processes. The star formation efficiency (SFE) is determined by physical properties like mass, density, and temperature, as well as environmental influences such as metallicity and stellar feedback. The triggering of star formation and the disruption of molecular clouds across different galaxies depend on dynamics like shear forces, gravitational potentials, and galactic rotations or bars (Renaud et al., 2015) in large-scale environments, including spiral arms or central regions, combined with stellar feedback mechanisms like stellar winds or supernovae. This cycle is qualitatively shown in Fig. 1.1 (and in Fig. 1.2 as an example showing the M51 galaxy).

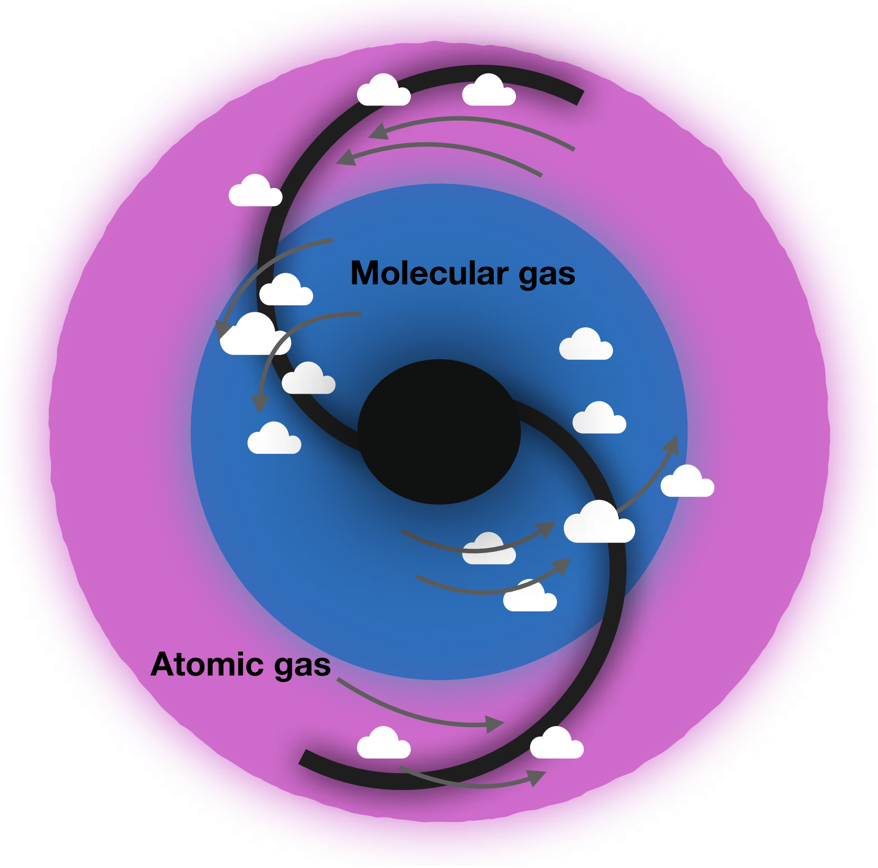

Figure 1.1: Assembly of GMCs within a galactic disk. Top-Down assembly: H_2 forms due to instabilities in compressed atomic gas layers, influenced by shocks like those from spiral density waves. These clouds last as long as H_2, equal to or shorter than the arm-crossing time, about 10 to 50 Myr. Bottom-Up assembly: GMCs arise from merging smaller H_2 clouds in galaxy spiral arms. Exiting the spiral's potential, GMCs fragment into smaller H_2 clouds, which then transit to the next spiral arm. The H_2 lifespan exceeds the clouds', lasting over 10^8 years. This figure draws on and is inspired by Koda et al. (2016).

However, the mechanism of mass accumulation in molecular clouds remains unresolved. Investigations have yet to determine the relative impacts of material flowing from high Galactic latitudes onto the disk's gravitational field, versus gas compression in spiral density waves, or expanding shells from supernovae-driven atomic hydrogen. Studying GMC properties in the Milky Way and M33 and their dependence on the galactic environment (central region, spiral arms, outskirts), as demonstrated in my first-author publication Keilmann et al. (2024a), can help shed light on these questions.

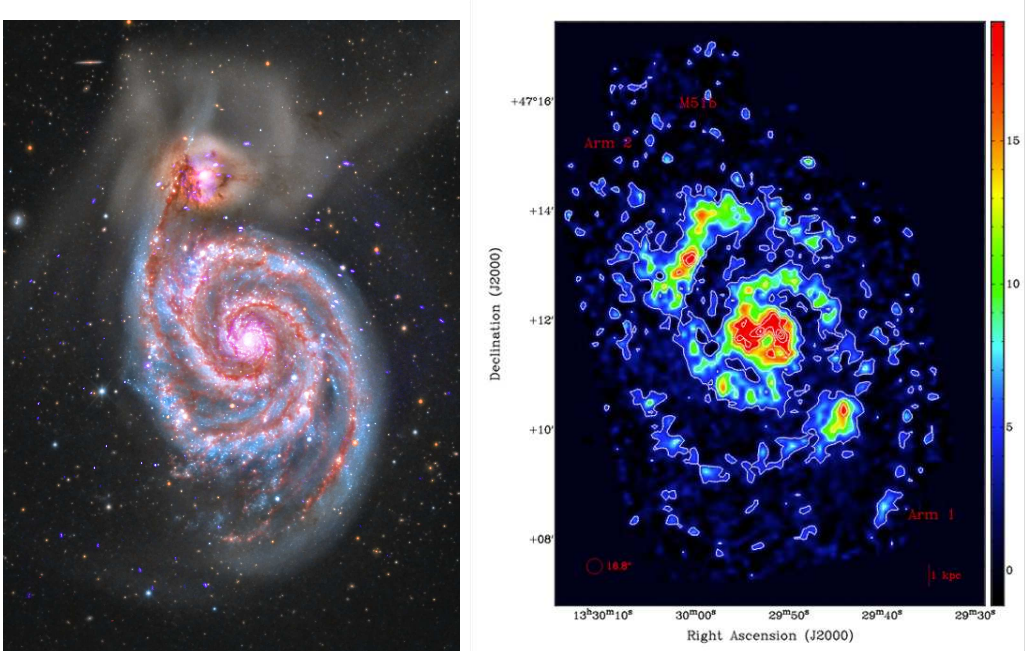

Figure 1.2: M51 galaxy in optical/X-ray/IR composite image and [C II] 158 μm emission. Left: The M51 galaxy with its nicely formed spiral arms in optical/X-ray/IR composite emission. Image credit: NASA/CXC/SAO; Optical: Detlef Hartmann; Infrared: NASA/JPL-Caltech. Right: The [C II] counterpart reflecting the M51 spiral's structure distribution (Pineda et al., 2020). Both images show that star-formation mostly takes place in the spiral arms and the galaxy's center.

Historical models viewed cloud formation, and hence the formation of H_2 gas, as a quasi-static process driven by gravitational infall that occurs over timescales up to 100 million years (Tielens and Hollenbach, 1985a; Sternberg and Dalgarno, 1989; Krumholz and McKee, 2005; Krumholz et al., 2008; Dobbs et al., 2014). This Top-Down approach, characterized by gravitational instabilities in the Galactic disk, generates GMCs through self-gravitating fragmentation, particularly in spiral arms with high gas surface densities (e.g., Elmegreen, 1979; Tubbs, 1980; Balbus and Cowie, 1985; Balbus, 1988). In this scenario, the clouds acquire masses that match the characteristic mass of these instabilities, often reaching several $10^6\,M_\odot$ (Wada et al., 2000; Shetty and Ostriker, 2008; Tasker and Tan, 2009; Dobbs et al., 2011; Hopkins et al., 2012; Kruijssen and Longmore, 2014).

However, observations of our Galaxy suggest that most clouds are actually less massive, frequently below $10^5\,M_\odot$ (e.g., Roman-Duval et al., 2010). This dynamical framework (Bottom-Up approach, see Fig. 1.1) posits that stellar feedback from newly formed stars disrupts gravitationally unstable gas before it fully collapses, resulting in lower-mass clouds (Reina-Campos and Kruijssen, 2017).

Several processes counteract gravitational collapse. Such processes are, for example, heat generated during gas contraction, along with turbulence and magnetic fields created by charged particles from cosmic-ray ionization and UV radiation of massive stars (including feedback from stellar winds or supernovae). Magnetic fields drive ambipolar diffusion that separates neutral particles (mainly hydrogen molecules) from plasma (ions and electrons). Without collisions with charged particles, these neutral particles would collapse under gravity; however, due to these collisions the interstellar magnetic field counteracts the collapse. In MCs with very low ionization, neutral particles rarely interact with charged particles; consequently, these particles fail to fully hinder their dynamical (instead of a free fall) collapse into a star (Lazarian et al., 2015).

The Jeans criterion (or Jeans instability) drives the fragmentation of MCs (Jeans, 1902). According to this criterion, a gas cloud becomes instable and collapses when its mass exceeds the Jeans mass or its size surpasses the Jeans length. The Jeans mass is proportional to

$$M_{\rm J} \propto \frac{c_s^3}{(G^3\rho_0)^{1/2}} \ , \tag{1.1}$$

where G is the gravitational constant, ρ_0 the gas density, and $c_s = \sqrt{\frac{k_{\rm B}T}{\mu m_{\rm H}}}$ the isothermal sound speed with $k_{\rm B}$ the Boltzmann constant, T the gas temperature, μ the mean molecular weight, and $m_{\rm H}$ the hydrogen mass. The Jeans length is proportional to

$$R_{\rm J} \propto \frac{c_s}{(G\rho_0)^{1/2}} \ . \tag{1.2}$$

The latter two are determined by the balance between gravitational forces and thermal pressure. Lower temperatures and higher densities favor cloud collapse. As the cloud contracts, its increasing density further reduces the Jeans length, promoting smaller regions to become gravitationally instable. This hierarchical fragmentation breaks the cloud into substructures that can subsequently collapse independently to form stars or stellar clusters. Turbulent density fluctuations create local regions that exceed the Jeans criterion, accelerating the formation of smaller-scale structures.

Turbulence, gravitational instability, and magnetic fields collectively shape filament formation. Turbulent motions may generate shocks that compress gas into dense sheets, which fragment due to gravitational instability into elongated structures. Magnetic fields may then channel and stabilize these structures, ultimately forming filaments. However, magnetic fields may also suppress or slow the cascade of turbulence to smaller scales, where it would dissipate, thereby reducing fragmentation.

Thus, turbulent mixing motions within the ISM significantly affect H_2 formation. These motions generate density fluctuations on both large and small scales, reducing H_2 formation timescales from tens of millions to a few million years (Glover and Mac Low, 2007; Bialy et al., 2017; Valdivia et al., 2016). Consequently, stellar feedback frequently disrupts star-forming clouds before they reach H_2 formation equilibrium (Mac Low and Glover, 2012).

The ISM exhibits highly turbulent behavior, characterized by a Reynolds number of approximately 10^6 (determined from (magneto-)hydrodynamical calculations).[3] Turbulence in molecular clouds requires continuous replenishment, as it decays within a crossing time without external driving forces. Despite its prevalence, the mechanisms driving interstellar turbulence remain unclear. Supernova explosions are an important source of turbulence in galaxies (Mac Low and Glover, 2012). Observed filament networks align qualitatively with magneto-hydrodynamic turbulence simulations in infalling gas (e.g.,

---

[3] Since the ISM is highly turbulent and complex, which would be enough to serve as a single Ph.D. thesis topic, I will not explore turbulence and a detailed description is not provided.

Padoan and Nordlund, 2011; Federrath and Klessen, 2013). Supersonic turbulence probably arises from mass accretion (Goldbaum et al., 2011). This aligns with observations linking filamentary structures to earlier large-scale atomic collisions (Walch et al., 2015; Seifried et al., 2017).

Early work by Larson (1981) laid the foundation that turbulence is a key factor in cloud support and fragmentation by exploring the role of turbulence in molecular clouds. Larson's subsequent studies emphasized the importance of thermal physics and cloud geometry in determining the stellar initial mass function (IMF), proposing that the Jeans mass at the transition from cooling to heating phases plays a critical role in cloud fragmentation (Larson, 2005). In particular, molecular line surveys have identified the Larson linewidth-size relations of $\sigma \propto R^{\epsilon}$ with ϵ roughly around 0.5 and the mass-size (which can also be based on dust observations) relations of $M \propto R^{\kappa}$ with κ roughly around 2 (e.g., Goldsmith et al., 1987; Heyer et al., 2004; Lombardi et al., 2010; Keilmann et al., 2024b), and a mass distribution for molecular clumps of the form of $\mathrm{d}N/\mathrm{dM} \sim M^{\alpha}$ with α roughly between 1.5 and 2.6 (Stutzki and Guesten, 1990; Kramer et al., 1998; Keilmann et al., 2024b). For instance, $\epsilon = 0.33$ characterizes a fractal, incompressible, non-magnetic fluid where the statistical flow properties remain scale-invariant, following Kolmogorov turbulence (Kolmogorov, 1941). In contrast, other turbulence models describe a supersonic, isothermal turbulent flow with $\epsilon = 0.5$ and $\alpha = 2$. Each model emphasizes different physical effects like turbulence-driven sources, magnetic fields, self-gravity, or thermal balance, and thus represents distinct physical scenarios. Such deviations from an idealized purely turbulent medium may alter scaling laws, which might explain why many molecular line studies have not detected a linewidth-size relation in molecular clumps (e.g., Loren, 1989; Simon et al., 2001; Schneider and Brooks, 2004; Schneider et al., 1998, and references therein).

Several studies have characterized the spatial structure of emission using power spectra relations. These revealed that clump mass spectra show scale-independent fragmentation of molecular clouds. Stutzki et al. (1998) contributed significantly by analyzing the clump mass spectra in molecular clouds, revealing a power-law distribution of clump masses. This work highlighted the self-similar nature of cloud structures on different scales (Schneider et al., 2011), suggesting that fragmentation processes are scale-independent (Kramer et al., 1998). Further advancements in observational techniques reveal cloud morphology and dynamics. High-resolution CO mapping enables detailed studies of cloud structure and confirms the presence of filamentary and clumpy substructures that are crucial for understanding the initial conditions of star formation (e.g., Schneider et al., 1998).

Remaining debate exists regarding the mechanisms that form molecular clouds and their embedded stars, as well as the impact of galactic environments. Small-scale factors (turbulence, magnetic fields, and stellar feedback) are considered to impact cloud fragmentation and structure, while large-scale dynamics (spiral density waves and galactic shear) govern the distribution and evolution of GMCs (Schinnerer and Leroy, 2024).

Large-scale instabilities driven by spiral density waves may shape cloud assembly and star formation. Gravitational collapse of dense regions illustrates a Top-Down approach, in which cloud formation spans tens of millions of years (see Fig. 1.1). This collapse is triggered by ISM instabilities from spiral density waves and stellar feedback (McKee and Ostriker, 2007; Dobbs et al., 2014; Renaud et al., 2015). The spiral arm's gravitational attraction may clusters molecular gas into large conglomerates that, when exposed to strong shear forces, disintegrate into smaller, elongated formations (La Vigne et al., 2006). As the wave travels through the disk, it may heat the gas by compression and shocks at the trailing edge of the spiral arms (Fujimoto, 1968; Roberts, 1969), resulting in dense molecular clouds where cooling processes become inevitable. Hence, spiral arms may exhibit higher star formation rates than less dense regions (Lord and Young, 1990; Silva-Villa and Larsen, 2012; Yu et al., 2021). However, studies report mixed findings on star formation efficiency, with some indicating higher efficiency in spiral arms and others finding comparable rates in spiral and interarm regions.

Shear may disrupt molecular clouds, thereby hindering star formation (Dobbs and Pringle, 2013; Meidt et al., 2015; Chevance et al., 2020; Bonne et al., 2023). Galactic dynamics and stellar feedback induce this shear. Chevance et al. (2022) suggested early stellar feedback prior to supernovae as key to cloud disruption. Dynamic scenarios propose that colliding clouds may form dense molecular structures (Haworth et al., 2015; Bisbas et al., 2017; Fukui et al., 2021).

Additionally, recent simulations and observations suggest that molecular cloud formation is a more dynamic process occurring on shorter timescales, up to 10 million years, due to mechanisms such as colliding flows and cloud–cloud collisions (Schneider et al., 2010, 2015b; Dobbs and Pringle, 2013). Additionally, Dobbs et al. (2020) and Schneider et al. (2023) noted that colliding atomic hydrogen flows can produce massive star-forming structures and studies such as Schneider et al. (2010) and Schneider et al. (2023) highlight that large-scale converging flows rapidly form dense molecular structures. Consequently, these dynamic processes accelerate molecular cloud formation compared to quasi-static model predictions. Moreover, Kobayashi et al. (2017) and Kobayashi et al. (2018) performed a semi-analytic model of cloud–cloud collisions that shows minimal impact on GMC growth in the Milky Way, except for clouds above 10^6 $M_\odot$, which can only contribute up to 50%. The Global Hierarchical Collapse (GHC) approach introduced by Vázquez-Semadeni et al. (2019, 2024) offers another novel perspective on cloud formation by involving hierarchical scale collapses that gather material from larger structures.

However, recent developments of sensitive, high spectral resolution instruments that are able to efficiently map large areas on the sky have enabled systematic studies of GMCs across various galactic environments, improving our understanding of their formation, evolution and destruction (Chevance et al., 2022). The detection of so far more than 300 molecules in the ISM has expanded our knowledge of the chemical complexity and physical conditions (temperature, density, dynamics) within (giant) molecular clouds (Guélin and Cernicharo, 2022). One such instrument is the German REceiver for Astronomy at Terahertz Frequencies (GREAT), which is a high-resolution spectrometer (Heyminck et al., 2012; Risacher et al., 2018; Duran et al., 2021) onboard the Stratospheric Observatory of Far-Infrared Astronomy (SOFIA). As a PI-instrument of the team in which I work, it was developed and built in collaboration of the University of Cologne and MPIfR in Bonn. The GREAT team supported open-time (OT) flights, handled observation preparation, execution of observations on SOFIA, and data reduction. In exchange, the GREAT team received guaranteed-time (GT) for more sophisticated observations that required detailed instrument knowledge.

Overall, the formation and evolution of molecular clouds in galaxies is a multifaceted process driven by gravitational instabilities, spiral density waves, stellar feedback, magnetic fields, and turbulence within the interstellar medium. These processes rank among the prominent subjects of modern astrophysics, explored through multi-wavelength observations and theoretical models, including simulations. Identifying the dominant processes – stellar feedback, shear, or cloud–cloud collisions – that regulate star formation is essential to understand the life cycles of molecular clouds and galaxy evolution (Kruijssen et al., 2019). Controversy persists over whether environmental conditions (e.g., central regions versus spiral arms) or stellar feedback mechanisms primarily govern star formation (Corbelli et al., 2017; Rey-Raposo et al., 2017; Kruijssen et al., 2019; Chevance et al., 2022; Liu et al., 2022; Choi et al., 2023).

Hence, an open question is whether these processes are universal across different galaxies, such as the Milky Way and M33, or whether they vary due to differences in metallicity, starburst activity, and other galactic properties. Variations in metallicity can affect cooling rates, dust content, and the efficiency of molecule formation, potentially leading to differences in cloud formation and star formation processes (Bolatto et al., 2013). Starburst galaxies show intense star formation rates; hence, they may exhibit different feedback mechanisms and timescales compared to more quiescent galaxies. Investigating these differences is crucial for a comprehensive understanding of molecular cloud formation and evolution in diverse galactic environments.

M33 is one such diverse galactic environment, differing from the Milky Way in terms of metallicity, mass, size, age, and other properties. In Keilmann et al. (2024a) and Keilmann et al. (2024b), I examined the physical properties of GMCs in M33, comparing them to those in the Milky Way, and explored these properties as a function of galactocentric radius and galactic environment in M33. My studies reveal that M33's galactic environments mainly do not influence cloud properties; and while some properties are similar to those of the Milky Way, others vary significantly, possibly due to differing galactic environments. However, most GMCs still appear to be insensitive to the galactic environment, suggesting that small-scale effects, such as stellar feedback, are more significant.

1.3 Stellar Feedback and its Impact

Stellar feedback refers to the mechanisms through which stars, especially massive ones, affect the ISM by emitting energy and ejecting matter that interacts with the surrounding medium. Key components of these mechanisms include radiative feedback, stellar winds and supernovae. Such feedback is essential for regulating star formation and shaping both the structure and evolution of galaxies. I investigated the driving mechanism of the bubble in the compact H II region in RCW79 by examining the stellar feedback from the ionizing source, with particular emphasis on the stellar wind (see Sect. 5.3.2).

Stellar feedback acts on multiple spatial scales. It ranges from small-scale (typically around one parsec) impact of protostellar outflows in molecular cores (e.g., Matzner and McKee, 2000; Bally, 2016; Offner and Chaban, 2017), to the creation of H II regions (a few to tens of parsec) by massive stars within their natal clouds (e.g., Rogers and Pittard, 2013a; Geen et al., 2015; Haid et al., 2018), and up to the influence of star clusters within galactic disks (e.g., Hennebelle and Iffrig, 2014; Gatto et al., 2017; Kim and Ostriker, 2017).

Stellar feedback enriches the ISM and regulates galactic evolution. Supernovae add heavy elements essential for forming planets and complex molecules, thereby influencing subsequent generations of stars and planetary systems (Tanabe et al., 2011). On larger scales, stellar feedback drives galactic winds and outflows that remove gas from galaxies, thereby controlling their growth (Somerville and Davé, 2015). However, according to Chevance et al. (2022), it is the early stages of stellar feedback that predominantly contribute to cloud dissipation within galaxies, prior to supernova events. This was also shown in Bonne et al. (2023) for RCW79, where I am involved as co-author.

Figure 1.3 impressively shows the presence of newly formed stars within the gas and

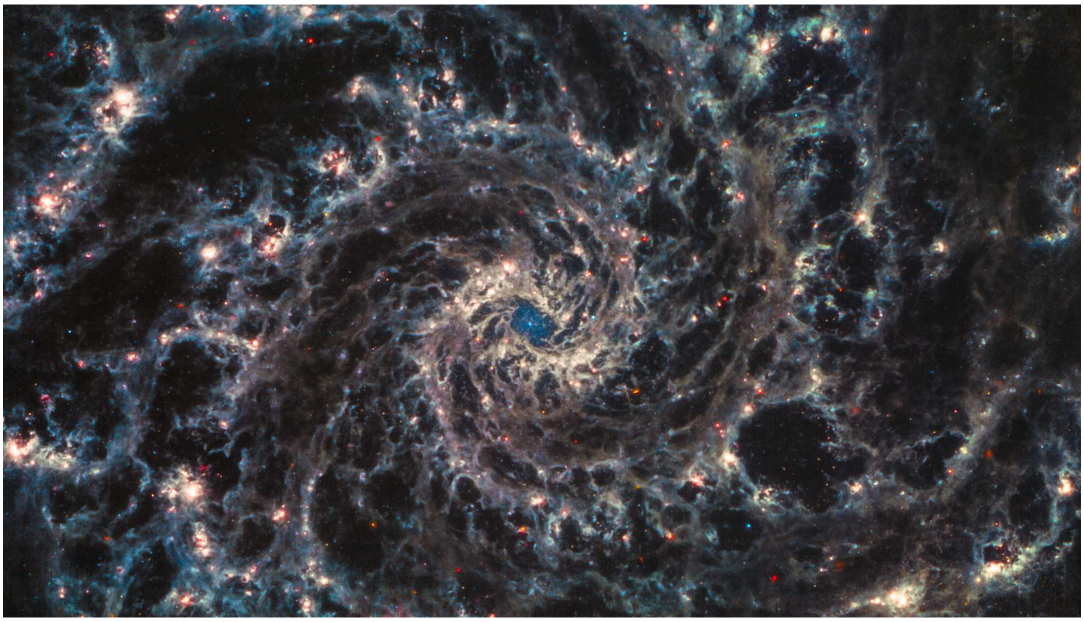

Figure 1.3: Composite image of NGC628 using JWST data. This high-resolution image shows the fine-structures and bubbles of NGC628 (M74), a spiral galaxy at a distance of 9.77 Mpc, influenced by the formation of young stars. MIRI data are shown at 21.0 μm (red), 11.3 μm (orange), 7.7 μm (cyan) and 10.0 μm (grayscale). Image credit: NASA/ESA/CSA/Judy Schmidt (CC BY 2.0).

dust spurs located between neighboring spiral arms that affect their environment, shaping bubbles across the entire disk of NGC628. It is a composite image of the James Webb Space Telescope (JWST) and its Mid-Infrared Instrument (MIRI), combining data at wavelengths of 21.0 μm (red), 11.3 μm (orange), 7.7 μm (cyan), and 10.0 μm (grayscale). The galactic center is surrounded by streams of luminous dust, while an exposed Nuclear Star Cluster (NSC) is distinctly visible at its center. The data also indicate the presence of newly formed stars.

Feedback mechanisms regulate the star formation rate by injecting energy into the ISM. As a result, star formation remains notably inefficient, as only a small fraction of a galaxy's gas mass converts into stellar mass over gravitational timescales (e.g., Kennicutt, 1998a; Krumholz and Tan, 2007; Evans et al., 2009; Barnes et al., 2017; Utomo et al., 2018; Kruijssen et al., 2019).

However, star formation in molecular clouds proceeds through positive stellar feedback. After molecular clouds form, stars emerge within dense substructures such as filaments and clumps/cores. Low-mass stars likely develop through filament fragmentation (Pineda et al., 2023), while massive stars form mostly as clusters in the center of hub-filament systems (Schneider et al., 2012; Peretto et al., 2013), in which massive dense cores and protostars compete for available gas (Bonnell and Bate, 2006). Intense far-ultraviolet (FUV) radiation with energies from 6 to 13.6 eV from OB-type stars ionizes the surrounding medium to create an H II region, and their radiation and winds clear out nearby material. One can gauge the radiation intensity by identifying the exciting stars and determining their stellar type, luminosity, temperature, and distance. As an H II region expands supersonically, a compressed layer of gas and dust accumulates between the ionization and shock fronts, often forming ring-like structures. This compressed ring fragments further, and the resulting dense clumps become gravitationally instable, thereby triggering new star formation (Elmegreen and Lada, 1977). This process is referred to as "collect-and-collapse" and represents "positive" stellar feedback. Figure 1.4 shows an RGB plot of RCW79. The PDR region is induced by the stellar feedback of a cluster of twelve O-type stars, which compresses the local ISM into a ring-like formation. Molecular gas traced by CO envelopes the [C II] ring, producing the characteristic layered structures typical of PDRs. [C II] emission can stem from gas in different physical conditions, including the H II region or the adjacent PDR (refer to Sect. 4.3).

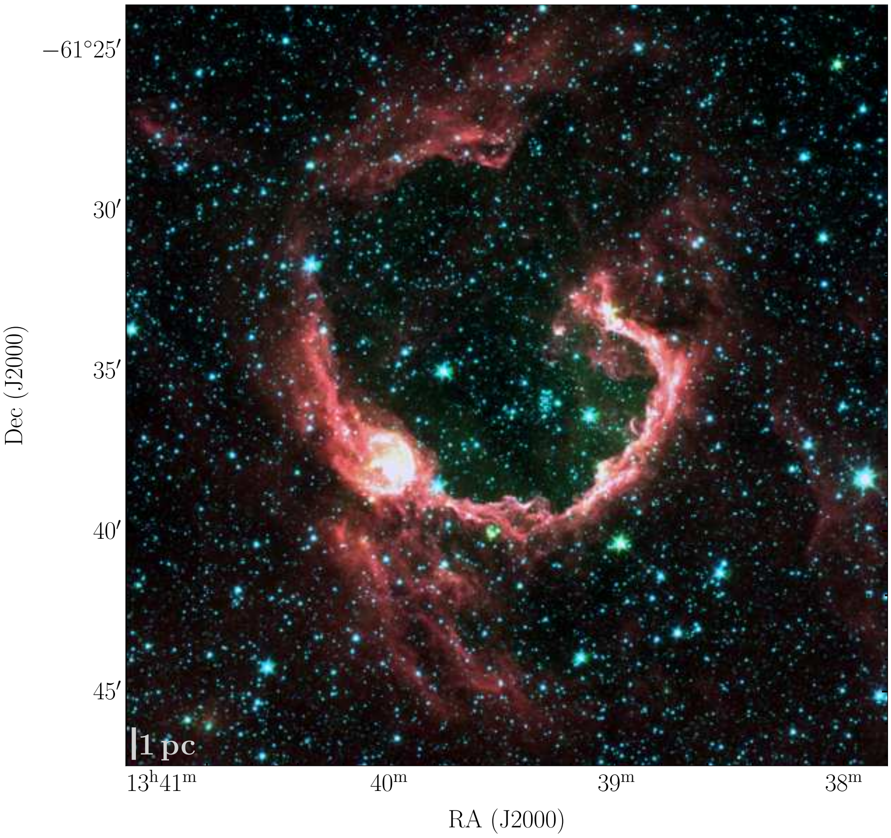

Figure 1.4: Composite image of three colors of RCW79. Spitzer data at 3.6 μm, 4.5 μm and 8 μm are shown in blue, green and red, respectively. The PDR region is nicely reflected in bright red emission, reflecting hot dust, mixed with atomic and molecular gas.

Multiple processes regulate star formation by either triggering or suppressing molecular cloud collapse. Turbulence and compression from stellar feedback, along with galactic shear effects (Chevance et al., 2020), can trigger molecular cloud collapse and lead to SF, while feedback can also dissipate clouds (e.g., Bonne et al., 2023). Magnetic fields resist gravitational collapse and influence gas dynamics, whereas turbulence fragments and reorganizes clouds. Moreover, surface mass density alongside ambipolar diffusion regulates the SFR (Roman-Duval et al., 2010). In clouds with low surface mass density, a high ionized fraction induced by the interstellar radiation field provides magnetic support that prevents collapse, maintaining a low star formation rate (SFR), whereas high surface mass density increases the SFR. Energetic radiation and strong stellar winds disrupt dense structures and hinder cloud collapse, illustrating negative stellar feedback (Matzner, 2002; Geen et al., 2016). Understanding the impact of stellar feedback on the evolution of molecular clouds, galaxies, and the universe remains an essential question in modern astrophysics.

The three main components of stellar feedback from massive stars are briefly laid out in the following sections (from which also PDRs emerge; see Sect. 4.3).

1.3.1 Stellar radiation

Radiation from massive stars significantly affects the interstellar medium (Kahn, 1954; Spitzer, 1978; Dyson et al., 1981). Stars emit Lyman continuum extreme-ultraviolet (EUV) photons with energies above 13.6 eV that initiate photo-ionization of nearby gas producing an H II region marked by an ionization front separating ionized from neutral gas. To maintain ionization, the photo-ionized gas requires a constant flow of ionizing photons, as it will otherwise revert to neutral hydrogen. Geometric dilution reduces the photon flux at the ionization front, a result of photons dispersing over expanding spherical shells as they travel radially from the star. The ionization front progresses if additional ionizing photons continue to arrive. The warmer photo-ionized gas ($\sim 10^4$ K) expands thermally against the cooler surrounding neutral gas ($10 - 1000$ K). This expansion decreases the density and recombination rates of the photo-ionized gas, allowing photons to reach further and the ionization front to move outward, thereby expanding the H II region. Consequently, a leading shock wave forms, accelerating and compacting nearby gas into a dense shell, which may be partially or completely neutral.

The FUV radiation of massive stars is able to photodissociate molecules in the ISM and ionize atoms such as carbon, creating so-called photodissociation regions. They are further described in Sect. 4.3.

1.3.2 Stellar wind

Eugene N. Parker introduced the first models of stellar wind in the late 1950s (Parker, 1958, 1960). Parker's work laid the foundation for understanding solar and stellar winds by proposing the concept of a continuous outflow of particles from the Sun, which was later extended to other stars. His model described how the solar wind is driven by the thermal pressure of the hot solar corona, leading to a supersonic flow of charged particles into space. This groundbreaking work provided a theoretical framework that has been expanded upon in subsequent decades to include various types of stellar wind, such as those from massive and evolved stars (Waldron, 1984).

Further early theoretical analyses by Avedisova (1972), Castor et al. (1975), and Weaver et al. (1977) advanced our understanding of adiabatic wind bubbles and their behavior under radiative cooling and ionizing radiation. Later, Capriotti and Kozminski (2001) investigated wind bubbles in photo-ionized H II regions, suggesting these bubbles play a secondary role to photo-ionization. Haid et al. (2018) confirmed this view through hydrodynamic simulations in a uniform medium, and Geen et al. (2020) further concluded that an efficiently cooling wind bubble can exist within a pre-existing photo-ionized region in a power-law density field.

Stellar winds, despite representing a small fraction of a star's energy, significantly influence interstellar bubble dynamics; and stellar wind bubbles that retain most of their energy can significantly drive the expansion of hot regions (over 10^6 K) around massive stars. Although stellar wind has often been regarded as minimal in the past, Pabst et al. (2019, 2020) demonstrated that stellar winds drive the Orion Veil Bubble. They detected the expanding shell with velocity-resolved [C II] observations, measuring an expansion velocity of $v \approx 13\,\mathrm{km\,s^{-1}}$. They concluded that the stellar wind's mechanical energy is efficiently transformed into the kinetic energy of the expanding bubble. These insights were enabled by the wide spatial coverage of the velocity-resolved [C II] data with instruments such as GREAT onboard SOFIA. Several studies then showed that stellar winds indeed drive the expansion of fast [C II] bubbles (e.g., Tiwari et al., 2021; Bonne et al., 2022; Beuther et al., 2022).

This unique discovery prompted questions about the significance and prevalence of stellar wind-driven bubbles, leading to multiple recent theoretical and simulation studies (Lancaster et al., 2021a,b; Pittard et al., 2021; Pittard, 2022; Geen and de Koter, 2022). Several other studies have identified significant effects of bubbles formed by stellar winds (e.g., Kabanovic et al., 2022), which are briefly described below.

Debate persists regarding whether these bubbles conserve the majority or the entirety of the stellar energy. Fierlinger et al. (2016) emphasize the importance of precisely resolving the contact discontinuity between the hot, less dense wind bubble and its denser surrounding shell to determine the energetics of the wind bubble.

Additional dynamic processes further influence wind bubble evolution. Fielding et al. (2020) and Tan et al. (2021) suggest that strong turbulence increases the wind bubble's cooling rate via turbulent mixing. Increased wind pressure raises the density of the shell surrounding the wind bubble, thereby trapping ionizing radiation more effectively.

The study of wind-radiation interactions has advanced with the integration of stellar winds into self-consistent (radiative-)(magneto-)hydrodynamic simulations for cloud-level star formation. Rogers and Pittard (2013b) examined stellar wind behavior in clustered O stars within irregular clouds, while Dale et al. (2014) used simulations to investigate the impact of winds on turbulent cloud star formation with photo-ionization. Building on these foundational studies, Wall et al. (2019), Wall et al. (2020), Decataldo et al. (2020), Geen et al. (2021), and Grudić et al. (2021) further incorporated stellar winds into their simulations. In addition, other studies analyzed wind from single sources or simple models (e.g., Gallegos-Garcia et al., 2020) and explored their effects on larger scales (e.g., Agertz et al., 2013; Gatto et al., 2017). The research group of Prof. Walch-Gassner at the University of Cologne also conducts such simulations.

Stellar wind simulations are considerably more computationally expensive than those involving solely photo-ionization due to their characteristic velocities and temperatures that impact simulation timesteps. While photo-ionized gas generally has a sound speed of about $10\,\mathrm{km\,s^{-1}}$ (Oort and Spitzer, 1955), stellar winds can reach velocities nearly 1% the speed of light (Groenewegen and Lamers, 1989; Lamers and Leitherer, 1993; Howarth et al., 1997; Massey et al., 2005). Thus, detailed studies are critical for exploring the parameter space of wind effects and to ensure simulations accurately reflect the interactions in a star-forming cloud.

One recent approach was developed by Lancaster et al. (2021a), who introduced a model suggesting that strong interface cooling from turbulent mixing drives bubble evolution via stellar winds. The authors propose that highly efficient cooling at the interface between the stellar wind and the surrounding medium reduces the injected energy by up to 99%. This energy loss results in a momentum-driven expansion ($p \propto t$). This differs from the energy-driven model by Weaver et al. (1977) ($E \propto t$) impacting gas dispersal in star-forming regions and thereby leading to lower expansion rates and sizes. However, another recent approach invokes a wind bubble around a star to describe the early evolution of the wind bubble expanding in a power-law density field (Geen and de Koter, 2022), which contains the Weaver model as a limit and which I use to describe the bubble dynamics in RCW79 (Sect. 5.3.2). Sect. 4.2 briefly describes this model alongside the classical "Weaver" model.

1.3.3 Supernovae

Supernovae (SNe) feedback shapes interstellar gas dynamics (e.g., McKee and Ostriker, 1977) and drives galaxy evolution (e.g., Larson, 1974). Core-collapse Type II SNe release immense energy (about 10^{51} erg), disrupting molecular clouds (White and Long, 1991), driving ISM turbulence (McCray and Snow, 1979), and fueling outflows and winds (Mathews and Baker, 1971). These explosions serve as major metal sources, notably contributing substantially to interstellar oxygen (Burbidge et al., 1957). Type Ia SNe also supply feedback energy and metal enrichment through thermonuclear processes (Kawata, 2001).

Uncertainties and evolving models continue to challenge our understanding of SN feedback. Key questions address determining which stars undergo SN events, the timing of these explosions, and the yields of energy, mass, and metals, as well as whether large-scale energy is kinetic or thermal. Historically, stars above $5 - 10\,\mathrm{M}_\odot$ were assumed to end as SNe, releasing about 10^{51} erg and contributing $7 - 100\,\mathrm{M}_\odot$ to the ISM (e.g., Katz, 1992). On a galactic level, uncertainties in the ISM energy dispersion exceeded those in stellar models (Naab and Ostriker, 2017; Rosdahl et al., 2017), leading to the assumption that the details of core-collapse SNe were secondary due to cooling and mixing uncertainties. However, recent studies (Keller and Kruijssen, 2022) and high-resolution simulations (Gutcke et al., 2021) reveal that the complexities of stellar evolution significantly affect galaxies.

GMC sizes might be regulated by supernovae or the galactic disk scale height (as I have discussed in my M33 papers). Supernovae concentrate H I gas into GMCs and set the maximum expansion scale of GMCs by linking it to potential supernova sizes, as proposed by Kobayashi et al. (2017) and Kobayashi et al. (2018). An alternate explanation suggests that GMC growth depends on the galactic gas disk scale height, h_z. GMCs smaller than h_z expand in three dimensions; once they approach h_z, vertical growth is hindered, limiting expansion to the two remaining dimensions and slowing overall growth. This constraint permits stellar feedback or galactic differential rotation to regulate cloud sizes.

In summary, many of the approaches, hypotheses, and models presented above remain unresolved and are subjects of ongoing debate. A key question concerns whether large-scale galactic environments or small-scale stellar feedback bear higher importance in shaping interstellar structures. Debates persist regarding the contributions and influence of stellar radiation and stellar wind and at which evolutionary stages their influence may shift. All these processes also affect cloud evolution and their dispersal – a claim frequently asserted but rarely quantified. One of the few observations that reveal cloud destruction is our study of [C II] in RCW79 (Bonne et al., 2023).

Since [C II] has proven to be an excellent tracer of both cloud formation and destruction, further observations of this important line are necessary. After the shutdown of SOFIA in 2022, the only available facilities include the NASA balloon project GUSTO (Galactic/Extragalactic ULDB Spectroscopic Terahertz Observatory), which conducted observations end of 2024, as well as planned missions such as the European balloon project "Co-PILOT" or NASA's balloon project ASTHROS (Astrophysics Stratospheric Telescope for High Spectral Resolution Observations at Submillimeter-wavelengths) and the NASA space-born satellite mission PRIMA (PRobe far-Infrared Mission for Astrophysics).

This thesis aims at identifying a number of key aspects of early cloud formation (Draco) and the roles of stellar feedback and large-scale galactic environments. By studying nearby galactic sources dominated by stellar feedback (RCW79) and extragalactic systems (M33), it aims to quantitatively understand the role of feedback and galaxy dynamics in shaping the local universe around us. In RCW79, I also investigated why the [C II] line shows a deficit in emission compared to FIR emission (the so-called [C II]-deficit). Thus, throughout my doctoral studies, I have contributed with small but essential pieces to this puzzle using and analyzing existing data that further expand our knowledge of these complex mechanisms. These include recent open questions such as:

- What mechanisms lead to the formation of molecular clouds?
- How do cloud properties differ as a function of galactic environment, such as the central region or spiral arms?
- Do cloud properties systematically differ between the Milky Way and other galaxies, such as M33 with e.g. lower metallicity?
- What is the driving mechanism of stellar feedback? Which has a greater impact on the surrounding interstellar medium, stellar winds or radiation?
- What could be the potential time dependence of these processes and their final evolution?
- What influences the cooling pathways of different tracers in the ISM?

With this in mind, the next chapters establish the theoretical background for this thesis (Chapter 2). Chapter 3 centers on the key principles of observational radio astronomy. I also present the most relevant observatories, which provided most of the data used in this thesis. Chapter 4 follows by exploring relevant astrophysical concepts and the objectives of the observations. Chapter 5 presents the results and the papers on which I have worked during this thesis. Finally, Chapter 6 provides a conclusion and outlines open questions along with possibilities for future observations.

Chapter 2

Theoretical and Observational Concepts

Studying how radiation interacts with matter is essential for two reasons when studying the interstellar medium. The radiation that reaches Earth provides our primary source of information about the universe beyond our solar system; understanding its generation sheds light on the materials that emit and absorb it along the line-of-sight (LOS). Analyzing the different physical processes that influence the density, temperature, composition, and velocity in interstellar space requires considering how atoms, molecules, and dust grains absorb and re-emit photons (Spitzer, 1978).

The subsequent sections lay out the theoretical background and concepts relevant to this thesis. A comprehensive understanding of the physical conditions of the interstellar medium requires grasping how photons interact with matter. After a short introduction of basic quantities, such as specific intensity and flux in Sect. 2.1, I cover some prerequisites of radiative transfer, such as energy transfer regarding atoms and molecules and Einstein coefficients (Sect. 2.1.2). The origins of the spectral line emissions are described in Sect. 2.1.3. In Sect. 2.1.4, I derive the radiative transfer equation, which explains particle interaction with the interstellar radiation field. Finally, Section 2.2 then discusses how observed line emissions can disclose the physical attributes of the ISM.

2.1 Radiation

The universe can be explored through the analysis of various tracers, such as cosmic rays,[1] neutrinos, gravitational waves, and photons. Galactic magnetic fields influence cosmic rays, which consist of charged particles, causing them to spiral along magnetic field lines and complicating the determination of their origin. Neutrinos rarely interact with other matter and are mainly relevant in nuclear interactions. For instance, neutrinos are important in measurements of the Sun, which helped to refine stellar models. Gravitational waves are very weak and relevant for particular events such as black hole mergers. Photons, in contrast, enable us to examine the full electromagnetic spectrum, making them ideal for studying the diverse processes occurring in the ISM. In what follows, I introduce the photon interaction with the ISM and briefly present the equation for the radiative transfer

---

[1] Cosmic rays are primarily composed of charged high-energy particles such as protons, electrons, and alpha particles (helium nuclei), produced in extreme environments where immense amounts of energy are available. These sources include for example supernovae, black holes, gamma-ray bursts, pulsars, and many other phenomena.

model (Spitzer, 1978). Firstly, I discuss Einstein coefficients, line profiles, and the splitting of spectral lines, followed by the radiative transfer equation and models for more complex conditions.

Radiation, in the form of electromagnetic waves, propagates in straight lines, referred to as rays, through space. We define the energy of a ray passing through an area $\mathrm{d}A$ perpendicular to the ray's direction, within a solid angle $\mathrm{d}\Omega$, over a time $\mathrm{d}t$, and within a frequency range $\mathrm{d}\nu$, as

$$\mathrm{d}E = I_\nu \,\mathrm{d}\Omega\,\mathrm{d}A\,\mathrm{d}t\,\mathrm{d}\nu \ [\mathrm{erg}]\ , \tag{2.1}$$

where I_ν denotes the specific intensity

$$I_\nu = \frac{\mathrm{d}E}{\mathrm{d}\Omega\,\mathrm{d}A\,\mathrm{d}t\,\mathrm{d}\nu}\ [\mathrm{erg\,s^{-1}\,cm^{-2}\,Hz^{-1}\,sr^{-1}}]\ . \tag{2.2}$$

Essentially, specific intensity is "per everything" and an intrinsic property of the source. Thus, it is a conserved quantity along the ray path. Given the speed of light c, the specific energy density u_ν is the energy in a volume with length $c\,\mathrm{d}t$ and area $\mathrm{d}A$.

$$\mathrm{d}E = u_\nu(\Omega)\,\mathrm{d}\Omega\,\mathrm{d}A\,c\,\mathrm{d}t\,\mathrm{d}\nu\ [\mathrm{erg}]\ . \tag{2.3}$$

Thus, with Eqs. 2.1 and 2.3, the specific energy density is

$$u_\nu(\Omega) = \frac{1}{c} I_\nu\ [\mathrm{erg\,cm^{-3}\,Hz^{-1}\,sr^{-1}}]\ . \tag{2.4}$$

With above equations, the mean intensity $\bar{\mathcal{J}}_\nu$ can be defined as

$$\bar{\mathcal{J}}_\nu = \frac{1}{4\pi}\int I_\nu\,\mathrm{d}\Omega\ [\mathrm{erg\,s^{-1}\,cm^{-2}\,Hz^{-1}\,sr^{-1}}]\ . \tag{2.5}$$

For an isotropic radiation field, I_ν is independent of angle, implying $I_\nu = \bar{\mathcal{J}}_\nu$.

The flux density is the specific intensity integrated over $\mathrm{d}\Omega$

$$F_\nu = \int I_\nu\,\mathrm{d}\Omega\ [\mathrm{erg\,s^{-1}\,cm^{-2}\,Hz^{-1}}]\ . \tag{2.6}$$

This quantity depends on the telescope and hence is different for each one.[2]

Integrating the flux density over frequency yields the flux

$$F = \int\int I_\nu\,\mathrm{d}\Omega\mathrm{d}\nu\ [\mathrm{erg\,s^{-1}\,cm^{-2}}]\ . \tag{2.7}$$

Moving a source twice as far reduces received power by a factor of 4 (inverse square law), yet the telescope's beam covers 4 times more area, balancing these effects and maintaining a conserved specific intensity.[3]

2.1.1 Planck function and Rayleigh-Jeans radiation temperature

Planck function The Planck spectrum describes the electromagnetic radiation emitted by a black body in thermal equilibrium. In such a state, the specific intensity above is given by the black body emission $B_\nu(T)$ at temperature T and frequency ν, as

$$I_\nu|_{\mathrm{LTE}} = B_\nu(T) = \frac{2h\nu^3}{c^2}\frac{1}{\mathrm{e}^{h\nu/k_\mathrm{B}T}-1}\ , \tag{2.8}$$

where k_B is the Boltzmann constant and LTE stands for local thermal equilibrium.

---

[2] Technically, the integral must include a $\cos\theta$, which is the angle between the surface's normal vector and the direction of the specific intensity's incidence. However, for small fields $\cos\theta \approx 1$.

[3] Neglecting cosmological distances in an expanding universe.

Rayleigh-Jeans brightness temperature The exponential term of the Planck function can be approximated for low frequencies $h\nu \ll k_\mathrm{B}T$ as

$$\mathrm{e}^{\frac{h\nu}{k_\mathrm{B}T}} \approx 1 + \frac{h\nu}{k_\mathrm{B}T} + \frac{1}{2}\left(\frac{h\nu}{k_\mathrm{B}T}\right)^2 . \tag{2.9}$$

In this approximation, the brightness temperature follows a linear relation in $h\nu/k_\mathrm{B}T$

$$B_\nu(T) \approx \frac{2h\nu^3}{c^2}\left(\left[1 + \frac{h\nu}{k_\mathrm{B}T} + \frac{1}{2}\left(\frac{h\nu}{k_\mathrm{B}T}\right)^2\right] - 1\right)^{-1} = \frac{2k_\mathrm{B}T\nu^2}{c^2}\left(1 + \frac{1}{2}\frac{h\nu}{k_\mathrm{B}T}\right)^{-1} \tag{2.10}$$

$$\approx \frac{2k_\mathrm{B}T\nu^2}{c^2}\left(1 - \frac{1}{2}\frac{h\nu}{k_\mathrm{B}T}\right) = \frac{2k_\mathrm{B}\nu^2}{c^2}\left(T - \frac{h\nu}{2k_\mathrm{B}}\right) . \tag{2.11}$$

Since only the first term depends on temperature T, the linear relation of radiation and temperature is

$$B_\nu(T) \approx \frac{2k_\mathrm{B}\nu^2}{c^2} T . \tag{2.12}$$

The brightness (radiation) temperature T can be expressed as

$$\mathcal{J}(T) = \frac{c^2}{2k_\mathrm{B}\nu^2} B_\nu(T) = \frac{c^2}{2k_\mathrm{B}\nu^2} I_\nu(T) \tag{2.13}$$

$$= T_0\left(\mathrm{e}^{T_0/T} - 1\right)^{-1} , \tag{2.14}$$

where $T_0 = h\nu/k_\mathrm{B}$ is the equivalent temperature of the transition at frequency ν. Finally, the brightness (radiation) temperature is given by

$$T_\mathrm{b} = \frac{c^2}{2k_\mathrm{B}\nu^2} I_\nu \, (= T_\mathrm{R}) . \tag{2.15}$$

This is known as the “Rayleigh-Jeans law” or the “Rayleigh-Jeans limit.” Equation 2.15 enables the calculation of the corresponding brightness (radiation) temperature T_b associated with a given intensity, which is universally true. In the Rayleigh-Jeans limit for the LTE case, the calculated temperature is particularly beneficial, as it corresponds to the excitation temperature of the observed transition line. Thus, the intensity is expressed as temperature.

We can estimate the regime within which the Rayleigh-Jeans limit holds by examining the third term in Eq. 2.9, which leads to

$$\frac{\nu}{[\mathrm{GHz}]} \ll 20.84\left(\frac{T}{[\mathrm{K}]}\right) . \tag{2.16}$$

2.1.2 Einstein coefficients and transition energy

Quantum mechanics assigns discrete energy states to an atom or molecule X, resulting in distinct energy levels. The Einstein coefficients quantify the probability of photon absorption or emission by an atom or molecule. The Einstein A coefficient relates to the rate of spontaneous light emission, while the Einstein B coefficients relate to the stimulated emission and absorption of light, respectively. These coefficients were introduced by Albert Einstein in 1916 (Einstein, 1916), considering isotropic radiation of frequency ν with a spectral energy density $\rho(\nu)$, and proposing three processes to occur in the formation of an atomic spectral line.

Spontaneous emission corresponds to an atom or molecule that is excited to its upper energy level u. It will transition back to its lower energy state l by emitting a photon with energy $E_{\rm ph} = h\nu$,

$$X_u \rightarrow X_l + h\nu \ . \tag{2.17}$$

This transition rate is characterized by the Einstein coefficient A_{ul}. The photon's energy corresponds to the difference in energy between the two energy states of the emitting particle.

$$h\nu = E_u - E_l \ . \tag{2.18}$$

The Einstein A coefficient characterizes the constant probability of spontaneous emission, describing an isolated particle in excited state u. Since the particle interacts with virtual photons of the zero-point fluctuations of the quantum vacuum field, the particle will eventually de-excite to a lower or ground state l, releasing excess energy as a photon. This emission process is independent of the ambient radiation field.

The Einstein B coefficients quantify the likelihood of stimulated radiative excitation and de-excitation. Specifically, the B_{lu} coefficient represents the probability that a particle in a lower state l is excited to an upper state u by photon absorption, described by

$$X_l + h\nu \rightarrow X_u \ . \tag{2.19}$$

This transition rate is characterized by the Einstein coefficient B_{lu}.

On the other hand, an already excited particle can be stimulated by an additional photon to transition from the upper state u to the lower level l

$$X_u + h\nu \rightarrow X_l + 2h\nu \ , \tag{2.20}$$

which is characterized by the Einstein coefficient B_{ul}.

Line profiles

The transition line with transition frequency $\nu_0 = (E_u - E_l)/h$ corresponds to an exact energy difference between two states. The observed transition exhibits a finite spectral linewidth due to the finite lifetime of the upper state and pressure broadening (both caused by Heisenberg's energy-time uncertainty principle). Additionally, Doppler broadening as a result of the thermal or turbulent motion of the emitters contributes to the width of the spectral line. The first two broadening effects (limited lifetime of upper state due to natural spontaneous decay and pressure broadening) are described by a Lorentz profile

$$\phi_L(\nu) = \frac{1}{\pi} \frac{w_L/2}{(\nu - \nu_0)^2 + (w_L/2)^2} \ . \tag{2.21}$$

Doppler broadening gives rise to a Gaussian line profile as a result of the thermal motion of particles in a gas moving with a range of velocities due to their temperature, which is

$$\sigma_{v,{\rm th}} = \sqrt{\frac{k_{\rm B}T}{m}} \ , \tag{2.22}$$

where $k_{\rm B}$ is the Boltzmann constant, T is the temperature, and m is the mass of the particle. $\sigma_{v,{\rm th}}$ is the velocity dispersion or standard deviation[4] of a Maxwell distribution.

---

[4] Sometimes the broadening is quantified by the Doppler parameter b, which includes a factor of 2 in the square root of Eq. 2.22, so that $b = \sqrt{2}\sigma$. The difference only arises depending on the convention used.

For typical [C II] gas temperatures of 100 to 200 K, the thermal line widths are 0.26 to $0.37\,\mathrm{km\,s^{-1}}$.

In the ISM, however, turbulent motion dominates the broadening mechanism, which generally also produces a Gaussian line shape

$$\phi_G(\nu) = \frac{2\sqrt{2\ln 2}}{w_G\sqrt{2\pi}}\,\mathrm{e}^{-4\ln 2\left(\frac{\nu-\nu_0}{w_G}\right)^2} \ . \tag{2.23}$$

Thermal and turbulent broadening arise from an ensemble of particles and add in quadrature. Turbulence-induced broadening is often ~ 5 to ~ 10 times larger than thermal broadening. Multiplying the standard deviation σ by $2\sqrt{2\ln 2}$ converts it to the full width at half maximum (FWHM) w_G, a measure more common in astrophysics. The transition frequency ν_0 defines the line peak position.

The prefactor in the above equation is the normalization factor, for which the normalized line profile integrates to 1 over all frequencies

$$\int_0^\infty \phi(\nu)\,\mathrm{d}\nu = 1 \ . \tag{2.24}$$

An emitted photon may be absorbed by an atom or molecule along its path, thereby exciting the absorbing particle to an upper energy level u. This process is the reverse of that described in Eq. 2.17. The absorption rate of photons by the ISM is proportional to the number of particles in the lower state n_l and the radiation field $\mathcal{J}_\nu$, which is weighted by the normalized line profile $\phi(\nu)$, and integrated over all frequencies ν. The mean line average intensity is then defined as

$$\mathcal{J}_\nu = \int_0^\infty \bar{\mathcal{J}}_\nu\,\phi(\nu)\,\mathrm{d}\nu \ , \tag{2.25}$$

where $\bar{\mathcal{J}}_\nu$ is defined as in Eq. 2.5 and is the specific intensity I_ν integrated over the source subtended by Ω,

$$\bar{\mathcal{J}}_\nu = \frac{1}{4\pi}\int_0^\infty I_\nu\,\mathrm{d}\Omega \ , \tag{2.26}$$

where I_ν is the Planck function B_ν (Eq. 2.8) in the thermalized case. The relative effectiveness of absorbing or emitting a photon with frequency ν is indicated by the normalized line shape.

Equations of Detailed Balance

An atom or molecule reaches statistical equilibrium when the rate at which a given energy level is populated is equal to the rate at which it is depopulated (Einstein, 1916; Griffiths, 2016). The condition of statistical equilibrium can be formulated as

$$n_i \sum_j R_{ij} = \sum_j n_j R_{ji} \ , \tag{2.27}$$

where R_{ij} and R_{ji} denote the transition rates between energy levels i and j, and n_i and n_j represent the corresponding particle number densities (Mangum and Shirley, 2015). By expressing these transition rates using Einstein coefficients along with the probabilities for excitation and de-excitation caused by collisions, denoted as C, the above equation can now be written as

$$n_i\left[\sum_j (n\,C_{ij} + B_{ij}\mathcal{J}_\nu) + \sum_{j<i} A_{ij}\right] = \sum_j n_j\,(n\,C_{ji} + B_{ji}\mathcal{J}_\nu) + \sum_{i<j} nA_{ji}\ . \tag{2.28}$$

For a two-level system, we define i as the lower energy state l and j as the upper energy state u. A transition from the lower to the upper sate, A_{lu}, violates energy conservation and is therefore set to zero.

The collision coefficient C denotes the probability of excitation and de-excitation of energy levels due to collisions, thereby accounting for particle interactions. Because the relation between the Einstein coefficients only includes radiative excitation, we consider only radiative processes. For a two-level system, we can then express Eq. 2.28 as

$$n_l B_{lu}\mathcal{J}_\nu = n_u(A_{ul} + B_{ul}\mathcal{J}_\nu)\ . \tag{2.29}$$

On the other hand, we know from statistical mechanics that in LTE the number of particles with energy E and temperature T is proportional to the Boltzmann factor $\exp(-E/k_\mathrm{B}T)$. Thus, the relative population of both states follows the Boltzmann distribution

$$\frac{n_l}{n_u} = \frac{g_l}{g_u}\frac{\mathrm{e}^{-E_l/k_\mathrm{B}T}}{\mathrm{e}^{-E_u/k_\mathrm{B}T}} = \frac{g_l}{g_u}\mathrm{e}^{\Delta E/k_\mathrm{B}T} = \frac{g_l}{g_u}\mathrm{e}^{h\nu_0/k_\mathrm{B}T}\ , \tag{2.30}$$

where $\Delta E = h(\nu_u - \nu_l) = h\nu_0$ represents the energy difference from the lower to the upper states, and g_l and g_u denote their statistical weights that account for the energy degeneracy of the quantum states. For a given ν_0, the temperature T that satisfies the Boltzmann distribution (Eq. 2.30) defines the excitation temperature T_ex for a population of particles via the Boltzmann factor. Equation 2.29 can then be written as

$$\mathcal{J}_\nu = \frac{A_{ul}}{\frac{g_l}{g_u}\mathrm{e}^{h\nu/k_\mathrm{B}T}B_{lu} - B_{ul}}\ . \tag{2.31}$$

The coefficients A_{ul}, B_{ul}, and B_{lu} describe the transitions between the lower and the upper states. In a thermally balanced medium, the mean line average intensity $\mathcal{J}_\nu$ is described by the Planck function $B_\nu(T)$. Hence, for Eq. 2.31 to be equal to the Planck function (Eq. 2.8), the Einstein coefficients must fulfill the Einstein relations

$$A_{ul} = \frac{2h\nu^3}{c^2}B_{ul} \quad \text{and} \tag{2.32}$$

$$g_l B_{lu} = g_u B_{ul}\ . \tag{2.33}$$

The two Einstein relations above, called equations of detailed balance, link the three Einstein coefficients, implying their interdependence; therefore, identifying one coefficient allows for the determination of all three. These relations capture the detailed balance relation between a microscopic process and its inverse, namely emission and absorption.

The latter equation confirms that the transition rate of stimulated emission and absorption is the same. This was an astonishing result in the 20th century and Albert Einstein had to "invent" stimulated emission in order to arrive at Planck's formula (Einstein, 1916; Griffiths, 2016). This led to the theoretical basis for masers and lasers. The Einstein B-coefficients are frequently defined in terms of the energy density $\rho(\nu)$ rather than $\mathcal{J}_\nu$ (Griffiths, 2016). This introduces a difference in the definitions by a factor of $c/(4\pi)$.

2.1.3 Spectral line splitting

Since this thesis relies on the only recent possible observations of the [C II] (hyper)fine-structure lines as a fundamentally important astrophysical line, I discuss in this section the fine- and hyperfine-structure lines of [^{12}C II] and [^{13}C II], respectively. In addition, as this thesis also makes use of the H I line and the rotational line of CO, I also discuss these lines.

Fine-structure lines are energy level splittings ($J = S + L$) caused by the interaction between the electron's spin S and its orbital angular momentum L (spin-orbit coupling) due to relativistic corrections, leading to closely spaced energy levels (Griffiths, 2016). When an atom interacts with light, the total angular momentum (including that carried by the photon) must be conserved. This conservation law restricts how the quantum numbers can change during a transition.

[C I] The fine-structure line [C I] arises from the splitting of the electronic ground state of neutral carbon due to spin-orbit coupling. Neutral carbon has the electronic ground-state configuration 1s^2 2s^2 2p^2 (of which only the electrons in 2p^2 are relevant in what follows), which corresponds to a triplet state ^3P due to the two unpaired electrons. The total spin $S = 1$ and orbital angular momentum $L = 1$ combine to produce a total electronic angular momentum J with three possible values: $J = 2$, $J = 1$, and $J = 0$. Consequently, the ground state splits into three fine-structure levels: $^3P_2$ (highest-energy level), $^3P_1$ (intermediate-energy level), and $^3P_0$ (lowest-energy level). The two commonly observed fine-structure transitions are $^3P_1 \rightarrow {}^3P_0$, which emits a photon with a wavelength of 609 μm, and $^3P_2 \rightarrow {}^3P_1$, which emits a photon with a wavelength of 370 μm. These transitions correspond to relatively low energy separations between levels, yielding temperatures of $\sim$24 K and $\sim$62 K, respectively. The [C I] lines trace neutral atomic carbon in the ISM, particularly in PDRs and molecular clouds. They contribute to the cooling of the ISM, especially in regions where carbon is not fully ionized or locked in CO molecules. The relative intensities of the [C I] lines provide information on the density, temperature, and excitation conditions of the emitting gas.

[C II] The electrons of singly ionized carbon ^{12}C$^+$ have the electronic configuration 1s^2 2s^2 2p^1. This configuration places the outermost electron in a 2p-orbital with an orbital angular momentum quantum number $l = 1$. Since there is only one electron in the 2p-orbital, the total orbital angular momentum of the ion is $L = 1$, which corresponds to a P-state. The single unpaired electron carries a spin angular momentum quantum number $S = 1/2$. Thus, singly ionized carbon has two fine-structure energy states, $^2P_{1/2}$ and $^2P_{3/2}$, which are the lower and higher energy levels, respectively. The observed [^{12}C II] fine-structure line corresponds to the transition $^2P_{3/2} \rightarrow {}^2P_{1/2}$, which emits a photon with a wavelength of 157.74 μm (rest frequency of 1900.5369 GHz). The energy separations between the levels correspond to a temperature of 91.25 K. Collisions with free electrons, atomic hydrogen, or molecular hydrogen in the ISM typically excite the electron. The critical density n_{cr} for thermal excitation depends on the temperature (Goldsmith et al., 2012) and is $\sim$10 cm^{-3} for electrons, $\sim$3000 cm^{-3} for H I, and $\sim$6100 cm^{-3} for H$_2$ at a temperature of 100 K. When de-excitation occurs, it emits a photon at 157.74 μm. The statistical weights for the [C II] fine-structure transition are $g_l = 2$ and $g_u = 4$. Carbon can also transition into higher ionization states (e.g., C^{2+} or C^{3+}) under extreme conditions, i.e., a high radiation field and high temperatures.

Hyperfine-structure lines are spectral lines that arise from transitions between energy levels split by the interaction between the nuclear magnetic moment and the electron's magnetic field. This splitting is much smaller than the fine-structure splitting. The quantum number $F = J + I$ refers to the total angular momentum of an atom or ion, which depends on the coupling between the nuclear spin I and the electronic angular momentum J.

[^{13}C II] The hyperfine-structure of the [^{13}C II] line arises from the interaction between the nuclear spin of the ^{13}C^{+} isotope $I = 1/2$ (because of the spin of the additional neutron) and the electronic angular momentum of the ionized carbon's fine-structure levels, $J = 3/2$ and $J = 1/2$. The additional nuclear spin gives the nucleus a magnetic dipole moment that interacts with the magnetic field generated by the electron. This interaction splits the fine-structure levels of the [C II] line into multiple hyperfine components. The $^2P_{3/2}$ level splits into two hyperfine sublevels ($F = 1$ and $F = 2$), while the $^2P_{1/2}$ level splits into two sublevels ($F = 0$ and $F = 1$). These splits yield three allowed hyperfine transitions – also denoted $F(2 \rightarrow 1)$, $F(1 \rightarrow 0)$, and $F(1 \rightarrow 1)$ – whose relative intensities derive from the dipole matrix elements. The strongest [^{13}C II] satellite lies close to the red-shifted wing of the [^{12}C II] line (see Table 2.1). Since turbulence increases the thermal line width by a factor of ∼5 to ∼10 (Sect. 2.1.2), a line width of ∼5 km s^{-1} is typical for [C II] and can therefore contaminate the F(2 → 1) satellite line emission. If contamination remains minor, fitting a Gaussian model to the wing emission can correct it. Alternatively, one may use only the two outer lines, which lie sufficiently far from the [^{12}C II] line, to determine, for instance, the optical depth of the [C II] line or isotopic ratios (although these account for only a smaller fraction of the total intensity as I have done in Keilmann et al. 2025). Table 2.1 details the relative line intensities and Doppler shifts of [^{13}C II] compared to the [^{12}C II] emission line and presents updated [^{13}C II] frequencies that were initially identified by Cooksy et al. (1986). The frequency differences are of the order of a few to 10 MHz and were identified with high S/N observations with SOFIA in Orion by Kabanovic et al., in preparation.

Table 2.1: [^{12}C II] fine-structure and [^{13}C II] hyperfine transition parameter.

Transition line	**Statistical weight**		**Frequency**	**Velocity offset**	**Relative intensity**
	g_u	g_l	ν [GHz]	$\Delta v_{\mathrm{F}\rightarrow\mathrm{F'}}$ [km s^{-1}]	$\Delta s_{\mathrm{F}\rightarrow\mathrm{F'}}$
[^{12}C II] ^{2}P$_{1/2}$ – ^{2}P$_{3/2}$	4	2	1900.5369	0	1
[^{13}C II] F(2 → 1)	5	3	1900.46526	+11.30	0.625
[^{13}C II] F(1 → 0)	3	1	1900.94976	−65.12	0.250
[^{13}C II] F(1 → 1)	3	3	1900.13966	+63.66	0.125

This table shows updated frequencies for [^{13}C II] (Kabanovic, in prep.), which were first determined by Cooksy et al. (1986), and the relative strengths of [^{13}C II] compared to [^{12}C II] (Ossenkopf et al., 2013).

H I The hyperfine-structure of the H I 21 cm line arises from the interaction between the proton's magnetic moment (nuclear spin) and the magnetic field produced by the electron's spin in a neutral hydrogen atom. The coupling of the proton spin ($I = 1/2$) and the electron spin ($S = 1/2$) splits the ground state of neutral hydrogen (1s) into two hyperfine levels. The two possible configurations are a parallel spin state with $F = 1$ (higher energy) and an antiparallel spin state with $F = 0$ (lower energy). The energy difference is extremely small, corresponding to a wavelength of 21 cm (frequency of 1420.405 MHz) and an equivalent temperature of 0.068 K. The H I 21 cm hyperfine transition has statistical weights of $g_l = 1$ and $g_u = 3$. A very low spontaneous emission rate ($A \sim 2.9 \times 10^{-15}\,\mathrm{s}^{-1}$) makes the transition highly forbidden, which results in an excited atom lifetime of about 11 Myr. However, hydrogen is the most abundant element in the universe, allowing us to observe this transition. The 21 cm line is an important tracer of neutral hydrogen in the ISM and is used to map the distribution and kinematics of H I in galaxies.

CO Carbon monoxide, as a diatomic asymmetric molecule, possesses a permanent electric dipole and exhibits additional rotational and vibrational energy levels unlike atoms. The rotational energy levels can be estimated as in Gordy and Cook (1984) via

$$E_J = hB_0\,J(J+1)\ , \tag{2.34}$$

where J denotes the total angular momentum and $B_0 = h/(8\pi I)$ represents the rigid rotor rotation constant with I the moment of inertia. For rotational linear molecules such as CO, the statistical weights are expressed as $g = 2J + 1$, where J is the angular momentum quantum number.

2.1.4 Radiative transfer

The radiative transfer equation describes energy transfer in form of electromagnetic radiation. Absorption, emission, and scattering processes affect radiation as it propagates through a medium. Absorption and emission of photons along the path s influence the frequency-dependent intensity I_ν of a light beam traveling through interstellar material, as illustrated in Fig. 2.1. Following (Spitzer, 1978), photons passing point r at time t have unique directions, represented by the unit vector k, and possess distinct frequencies ν. Neglecting polarization (which is not used throughout this work), an electromagnetic wave is fully described by its direction and frequency. Describing the radiation field requires specifying the energy based on these four variables. We define the specific intensity $I_\nu(k, r, t)$ such that $I_\nu\,\mathrm{d}\nu\mathrm{d}\omega\mathrm{d}A\,\mathrm{d}t$ represents the energy of photons, passing through area $\mathrm{d}A$, within the frequency range $\mathrm{d}\nu$ around ν, and with directions within the solid angle $\mathrm{d}\omega$ around k. The area $\mathrm{d}A$ is positioned at r and is perpendicular to the direction k.

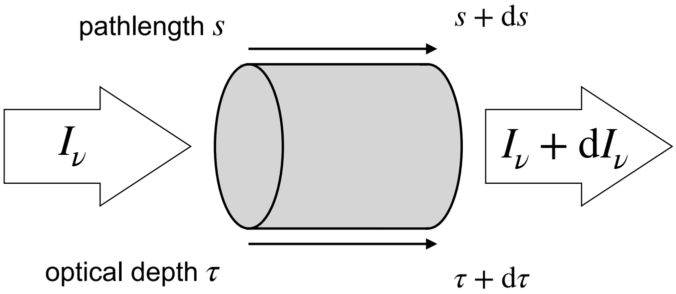

Figure 2.1: Radiative transfer sketch.

The radiative transfer equation describes the variation in I_ν due to interactions with matter. This equation is formulated by analyzing the energy flow entering and exiting a cylindrical section of length ds, using the absorption coefficient κ_ν and the emission coefficient j_ν. The emission coefficient $j_\nu(k, r, t)$, or emissivity, is such that $j_\nu \, \mathrm{d}V \mathrm{d}v \mathrm{d}\omega \, \mathrm{d}t$ represents the energy emitted from a volume element dV (equivalent to dsdA) during the intervals dv, dω and dt. Meanwhile, $\kappa_\nu I_\nu \, \mathrm{d}V \mathrm{d}v \mathrm{d}\omega \mathrm{d}t$ stands for the energy absorbed from a beam with specific intensity I_ν. The alteration in I_ν over a segment ds for a straight-line photon travel (Spitzer, 1978) is thus given by

$$\mathrm{d}I_\nu = -\kappa_\nu I_\nu \, \mathrm{d}s + j_\nu \, \mathrm{d}s \; . \tag{2.35}$$

The first term $-\kappa_\nu I_\nu \, \mathrm{d}s$ on the right-hand side of the equation accounts for the change in I_ν caused by absorption and stimulated emission, whereas the subsequent term $j_\nu \, \mathrm{d}s$ considers the effect of spontaneous emission.

The "optical depth" τ_ν is defined along the ray path back via the expression

$$\tau_\nu = -\kappa_\nu \, \mathrm{d}s \; . \tag{2.36}$$

Using the optical depth is more convenient than the path length s, as it can be used as the integrand in Eq. 2.42 (see below). Equation 2.35 becomes

$$\mathrm{d}I_\nu = -I_\nu \, \mathrm{d}\tau_\nu + S_\nu \, \mathrm{d}\tau_\nu \; , \tag{2.37}$$

with the "source function" S_ν defined as

$$S_\nu = \frac{j_\nu}{\kappa_\nu} \tag{2.38}$$

The "emissivity" j_ν and "absorption coefficient" κ_ν at the frequency ν can be described using Einstein coefficients alongside the number density of particles n in the relevant state (Mangum and Shirley, 2015). The emission coefficient j_ν is assumed to be distributed as the line profile function $\phi(\nu)$ (Eq. 2.23), analogous to absorption. The emissivity may be described as being proportional to the density of particles in the upper state n_u times the emission rate A_{ul}, with each photon carrying an energy of $h\nu$ leading to

$$j_\nu = \frac{h\nu}{4\pi} A_{ul} \, n_u \; , \tag{2.39}$$

where 4π accounts for isotropic radiation into all spatial directions. The absorption coefficient κ_ν naturally includes the Einstein absorption coefficient. However, stimulated emission (like absorption) is proportional to intensity and occurs simultaneously with absorption, making them indistinguishable. Thus, stimulated emission can also be treated as negative absorption. The absorption can be described as

$$\kappa_\nu = \frac{h\nu}{4\pi}(n_l B_{lu} - n_u B_{ul})\phi_\nu \tag{2.40}$$

$$= \frac{c^2}{8\pi\nu^2} \frac{g_u}{g_l} n_l A_{ul} \left(1 - \frac{g_l n_u}{g_u n_l}\right) \phi_\nu \; , \tag{2.41}$$

where h is the Planck constant and A and B the Einstein coefficients.

Multiplying Eq. 2.37 with $\mathrm{e}^{-\tau_\nu}$ and solving the resulting differential equation finally yields the radiative transfer equation in its integral form

$$I_\nu(\tau_\nu) = I_{\nu,0} \mathrm{e}^{-\tau_\nu} + \int_0^{\tau_\nu} \mathrm{e}^{-(\tau_\nu - \tau')} S_\nu(\tau') \, \mathrm{d}\tau' \; , \tag{2.42}$$

with the background intensity $I_{\nu,0} = I_\nu(\tau_\nu = 0)$ attenuated by the optical depth factor $\mathrm{e}^{-\tau_\nu}$. This is the formal solution of the radiative transfer Eq. 2.35. The intensity $I_\nu(\tau_\nu)$ can be interpreted as the sum of two contributions: matter along the pathway attenuates the initial intensity $I_{\nu,0}$ by a factor $\mathrm{e}^{-\tau_\nu}$, combined with the emission from the cloud $S_\nu\,\mathrm{d}\tau$, which is reduced by $\mathrm{e}^{-(\tau_\nu-\tau')}$ due to material in the column between the observer and the source.

For a very rough approximation, if a constant excitation temperature T_ex describes the population of energy levels in a homogeneous medium, then the source function S_ν can be represented using the Planck function $B_\nu(T_\mathrm{ex})$. This presumption enables the analytical integration of Eq. 2.42, resulting in

$$I_\nu(\tau_\nu) = I_{\nu,0}\mathrm{e}^{-\tau_\nu} + B_\nu(T_\mathrm{ex})\left(1 - \mathrm{e}^{-\tau_\nu}\right) . \tag{2.43}$$

As τ approaches 0, the equation reduces to $I_\nu(\tau_\nu) = I_{\nu,0}$, implying that radiation passing through a medium with low optical thickness retains its original intensity. In the limit where $\tau \rightarrow \infty$, the equation simply gets $I_\nu(\tau_\nu) = B_\nu(T_\mathrm{ex})$, which means that in an opaque medium, radiation is emitted solely by the medium itself. In summary, the medium is termed opaque or optically thick if the integral of $\mathrm{d}\tau_\nu$ along the path results in $\tau_\nu \gtrsim 1$ close to the line's transition frequency ν_0. On the other hand, the medium is considered optically thin or transparent for the line if $\tau_\nu < 1$ across all frequencies.

The background continuum intensity adds to the emission originating from the specific source being observed in a measurement of a spectral line. Thus, we subtract the background continuum intensity $I_{\nu,0}$ from the measured line intensity I_ν by

$$\begin{aligned}
\Delta I_\nu &= I_\nu - I_{\nu,0} && (2.44)\\
&= I_{\nu,0}\mathrm{e}^{-\tau_\nu} + B_\nu(T_\mathrm{ex})\left(1 - \mathrm{e}^{-\tau_\nu}\right) - I_{\nu,0} && (2.45)\\
&= \left(B_\nu(T_\mathrm{ex}) - B_\nu(T_\mathrm{bg})\right)\left(1 - \mathrm{e}^{-\tau_\nu}\right) . && (2.46)
\end{aligned}$$

The lower limit of the background temperature $T_\mathrm{bg} = 2.725\,\mathrm{K}$ is constrained by cosmic microwave background radiation. However, typical values in molecular clouds do not fall below ~ 10 to $\sim 15\,\mathrm{K}$ due to heating by cosmic rays.

However, in reality, optical depth and excitation temperature differ across different locations, making the above formal description overly simplistic. Therefore, numerical models such as RADEX (van der Tak et al., 2007) and SimLine (Ossenkopf et al., 2001) adopt distinct methods to address radiative equations under non-LTE conditions. Since I employed these during my Ph.D., they are detailed in the following sections.

2.1.5 Non-LTE radiative transfer

In the above section, we have discussed the radiative transfer equation in LTE. However, if T_ex is not constant and unknown, we only have the formal solution. Thus, in realistic scenarios under non-local thermal equilibrium (non-LTE) one needs to obtain T_ex, which is determined by the radiation field from all directions through the molecular cloud of the corresponding transition line. This radiation field is determined by the specific intensity, which must be determined at each position in the cloud by averaging I_ν from all other directions. This finally leads to coupled differential equations, which are solved numerically.

Several models address the radiative transfer equation under non-LTE conditions. In this section, I first concentrate on two relevant models, RADEX and SimLine. The subsequent section then describes the two-layer multicomponent model, which also solves the radiative transfer equation for non-LTE scenarios.

RADEX

RADEX is a tool for modeling the radiative transfer of molecular lines in astrophysical environments under non-LTE conditions (van der Tak et al., 2007). It is designed to handle the excitation and radiative transfer of molecular lines in interstellar clouds, where the assumption of LTE does not hold due to low densities.

RADEX solves the statistical equilibrium equations for molecular level populations, considering collisional and radiative processes. The fundamental equation for statistical equilibrium is

$$\sum_{j \neq i} n_j P_{ji} = n_i \sum_{j \neq i} P_{ij} \ , \tag{2.47}$$

where n_i and n_j are the populations of energy levels i and j, respectively. P_{ij} and P_{ji} are the transition probabilities from level i to j and vice versa, including collisional and radiative components. The radiative transfer equation in RADEX is given by

$$\frac{dI_\nu}{ds} = -\kappa_\nu I_\nu + j_\nu \ , \tag{2.48}$$

where I_ν is the specific intensity at frequency ν, κ_ν the absorption coefficient and j_ν the emission coefficient.

RADEX uses the escape probability formalism to approximate radiative transfer, which simplifies the treatment of line trapping effects in optically thick media. The escape probability β is a key parameter in RADEX, representing the probability that a photon escapes the medium without being absorbed. It modifies the radiative transition rates and is defined for different geometries, such as

- Slab Geometry: $\beta = \frac{1-\mathrm{e}^{-\tau}}{\tau}$
- Spherical Geometry: $\beta = \frac{1-\mathrm{e}^{-\tau}}{\tau}\left(\frac{1+\tau}{2}\right)$

where τ is the optical depth.

RADEX provides the level populations, line intensities, and optical depths for specified molecular transitions, allowing for the interpretation of observed spectra in terms of physical conditions such as density and temperature.

SimLine

SimLine is a 1D radiative transfer code designed to simulate molecular line emissions in astrophysical environments (Ossenkopf et al., 2001). The code is particularly focused on handling complex geometries and velocity fields, which makes it suitable for studying interstellar clouds and star-forming regions. It also includes H II regions and different density and temperature profiles, configured as a series of individual shells. The code solves the radiative transfer equations, allowing for the treatment of non-LTE conditions. SimLine is capable of modeling both spherical and cylindrical geometries and can incorporate arbitrary velocity fields, which are essential to accurately simulate the dynamics of molecular clouds.

The fundamental equation solved by SimLine is the radiative transfer Eq. 2.48 as in the case of RADEX. It solves the statistical equilibrium equations (Eq. 2.47) for molecular level populations, using a Monte Carlo method to simulate the propagation of photons through the medium, accounting for absorption, emission and scattering processes.

The Two-Layer Multicomponent Model

The two-layer multicomponent radiative transfer model is yet another approach for solving the radiative transfer equations. It consists of two gas layers and separates the warm-emitting background material from the cold-absorbing layer and solves the radiative transfer equations for multiple velocity components spread across these two layers. Initially, Guevara et al. (2020) introduced the model (with foundational concepts from Urs Graf). Subsequently, Kabanovic et al. (2022) refined it to address multiple optically thick overlapped velocity components observed in several transition lines simultaneously, while I have written a code producing the same results that focuses on computational methods and usability. In this section, I provide a brief overview of this advanced two-layer model.

A sequence of sums over a collection of line transition frequencies allows parallel solving of the radiative transfer equation for multiple transition lines with frequency ν,

$$\begin{aligned} T_{\mathrm{mb}}(v) = \left[\mathcal{J}_\nu(T_{\mathrm{ex,bg}})\left(1-\mathrm{e}^{-\sum_{i_{\mathrm{bg}}}\tau_{i_{\mathrm{bg}}}(v)}\right)\right]\mathrm{e}^{-\sum_{i_{\mathrm{fg}}}\tau_{i_{\mathrm{fg}}}(v)} + \\ \mathcal{J}_\nu(T_{\mathrm{ex,fg}})\left(1-\mathrm{e}^{-\sum_{i_{\mathrm{fg}}}\tau_{i_{\mathrm{fg}}}(v)}\right) . \end{aligned} \tag{2.49}$$

To achieve this, each line must be distinct in velocity space; hence, the line shift Δv must significantly exceed the line width w. This allows simultaneous modeling for isotopes such as ^{12}CO and ^{13}CO. In scenarios where two lines overlap, such as [^{12}C II] and [^{13}C II] F$(2-1)$, applying a unified line shape approximation with a common transition frequency $\nu_{[\mathrm{C\,II}]} \approx \nu_{[^{12}\mathrm{C\,II}]} \approx \nu_{[^{13}\mathrm{C\,II}]}$ circumvents the problem.

The equivalent brightness temperature of a black body emission at a temperature T_{ex} can be expressed as

$$\mathcal{J}_\nu(T_{\mathrm{ex},i}) = \frac{T_0}{\mathrm{e}^{T_0/T_{\mathrm{ex}}}-1} , \tag{2.50}$$

where $T_0 = h\nu/k_B$ is the equivalent temperature of the transition and ν is the transition frequency. The optical depth of each component is assumed to be Gaussian

$$\tau(v) = \tau_0\,\mathrm{e}^{-4\ln 2\,\left(\frac{v-v_0}{w}\right)^2} , \tag{2.51}$$

where v_0 is the central local standard of rest (LSR) velocity of each component. The line width w of each component is expressed in FWHM. In a two-level system like [C II], the optical depth for each Gaussian component can be expressed in terms of the excitation temperature T_{ex} and the column density N (Kabanovic et al., 2022), leading to

$$\tau(v) = \Phi(v)\,N\frac{c^3}{8\pi\nu^3}\frac{g_u}{g_l}A_{ul}\frac{1-\mathrm{e}^{-T_0/T_{\mathrm{ex}}}}{1+\frac{g_u}{g_l}\mathrm{e}^{-T_0/T_{\mathrm{ex}}}} , \tag{2.52}$$

where $\Phi(v)$ is the combined line profile of each component i, which can be written as

$$\Phi(v) = \phi_i(v) + \sum_{\mathrm{F}\to\mathrm{F}'} s_{\mathrm{F}\to\mathrm{F}'}\phi_i(v-\Delta v_{\mathrm{F}\to\mathrm{F}'}) . \tag{2.53}$$

Here, $s_{\mathrm{F}\to\mathrm{F}'}$ is the relative intensity of each line. In the case of ^{13}CO, the relative intensity is equal to 1 and for [^{13}C II] refer to the relative line strengths listed in Table 2.1. $v_{\mathrm{F}\to\mathrm{F}'}$ is the line velocity offset from the main isotope. $\phi_i(v)$ in the above equation is the normalized Gaussian line profile of each component i and expressed as

$$\phi_i(v) = \frac{2\sqrt{\ln 2}}{w_i\sqrt{\pi}}\,\mathrm{e}^{-4\ln 2\left(\frac{v-v_{0,i}}{w_i}\right)^2} , \tag{2.54}$$

which is analogue to Eq. 2.23, where the factor $4\ln 2$ converts from the standard deviation σ_i to the FWHM w_i. Integration over the normalized line profile yields 1. Hence, the peak optical depth τ_0 for each Gaussian component can be written as (Keilmann et al., 2025)

$$\tau_0 = N\frac{c^3}{8\pi\nu^3}\frac{g_u}{g_l}A_{ul}\frac{1-\mathrm{e}^{-T_0/T_\mathrm{ex}}}{1+\frac{g_u}{g_l}\mathrm{e}^{-T_0/T_\mathrm{ex}}}\frac{2\sqrt{2\ln 2}}{w\sqrt{2\pi}}\ . \tag{2.55}$$

The [C II] fine-structure transition has a rest frequency of $\nu = 1900.5369\,\mathrm{GHz}$, an Einstein coefficient for spontaneous emission $A_{ul} = 2.29\cdot 10^{-6}\,\mathrm{s}^{-1}$ (Wiese and Fuhr, 2007), and an equivalent upper level temperature of $T_0 = h\nu/k_\mathrm{B} = 91.25\,\mathrm{K}$. The statistical weights of the transition energy levels are $g_u = 4$ and $g_l = 2$. Equation 2.55 is useful when the calculation considers only the line's peak position.

The physical characteristics of the background layer can be determined from an optically thin line that does not have self-absorption issues. Thus, to describe [C II], the weaker hyperfine transition lines of [^{13}C II] can be utilized; refer to Guevara et al. (2020) for more details. Parameters like LSR velocity, line width and number of components are easily derived from the observed line. However, optical depth and excitation temperature are interdependent; thus, for example, the excitation temperature must be fixed from the data, which leaves the optical depth as a free fit parameter. Assuming that the warm emitting background partially penetrates the cold absorbing layer (Kabanovic et al., 2022; Keilmann et al., 2025), we can calculate the excitation temperature as

$$T_\mathrm{ex} = \frac{T_0}{\ln\left(\frac{T_0}{T_{[\mathrm{C\,II}],\mathrm{peak}}}\left(1-\mathrm{e}^{-\tau_0}\right)+1\right)}\ . \tag{2.56}$$

At the [C II] emission peak, the optical depth can be determined from the observed ratio of [C II] to [^{13}C II] via

$$\frac{T_{[^{12}\mathrm{C\,II}]}(v)}{T_{[^{13}\mathrm{C\,II}]}(v)} = \frac{1-\mathrm{e}^{-\tau(v)}}{\tau(v)/\alpha} = \frac{1-\mathrm{e}^{\tau(v)}}{\tau(v)}\alpha\ , \tag{2.57}$$

with the local carbon abundance ratio α and assuming $\tau_{[^{13}\mathrm{C\,II}]} = \tau_{[^{12}\mathrm{C\,II}]}/\alpha$ (refer to Sect. 2.2.1).

During this doctoral thesis, I have (re-)written and refined the two-layer model's code base regarding computational methods to improve efficiency, stability, and usability.

2.2 Physical Properties of the Interstellar Medium

This section briefly describes the column density system and modeling of dust, which are crucial to interpret observational measurements.

2.2.1 Column densities

The column density of gas (atomic and/or molecular) is an essential physical quantity because it provides a measure of the amount of material along a line-of-sight, integrated over the depth of the medium. It is directly accessible via observations, in contrast to a property such as the density, which requires an assumption of the geometry. It directly relates to observable quantities, such as absorption and emission lines or dust extinction, and allows us to estimate the total mass of gas or dust in different environments in the ISM.

In addition, it provides information on the physical conditions of these regions, including temperature, pressure, and ionization states. In the context of SF, column density maps help identify dense regions within molecular clouds that are likely star-forming sites. It is also useful in radiative transfer calculations, which affects the optical depth and the dynamics of emission and absorption processes.

The column density N is given by the integral of the number density of particles n per unit length s along the line-of-sight

$$N = \int n \, \mathrm{d}s \ . \tag{2.58}$$

As the path length and number density are not directly measurable, we instead utilize the optical depth and attenuation coefficient. For atomic and molecular line transitions, these can be expressed in terms of the Einstein coefficients and the energy levels' population of interstellar particles, which is constrained by the gas temperature

$$\begin{align} \tau_\nu &= \int \kappa_\nu \, \mathrm{d}s \tag{2.59} \\ &= \frac{c^2}{8\pi\nu^2} \frac{g_u}{g_l} \phi_\nu A_{ul} \int n_l \left(1 - \frac{g_l n_u}{g_u n_l}\right) \mathrm{d}s \tag{2.60} \\ &= \frac{c^2}{8\pi\nu^2} \left(\mathrm{e}^{T_0/T_\mathrm{ex}} - 1\right) A_{ul} \phi_\nu N_u \ . \tag{2.61} \end{align}$$

The equation associates optical depth with the total number of particles along the line-of-sight in either the lower or upper state. Assuming LTE conditions, the column density of the particles in state i can be connected to the total column density N for a specific excitation temperature by

$$\frac{N}{N_i} = \frac{Q}{g_i} \mathrm{e}^{E_i/(k_\mathrm{B} T_\mathrm{ex})} \ , \tag{2.62}$$

where Q represents the partition function, defined such that the total column density N_i summed over all possible states i equals the total column number density

$$N = \sum_i N_i \ . \tag{2.63}$$

The partition function Q for a single T_ex (LTE) can be written as

$$Q = \sum_i g_i \, \mathrm{e}^{-\frac{E_i}{k_\mathrm{B} T_\mathrm{ex}}} \tag{2.64}$$

by combining the equations 2.62 and 2.63. The ionized carbon line [^{12}C II] and hydrogen line H I energy levels can be represented as a two-level system, for which the partition function is

$$Q_{\uparrow\downarrow} = g_l \, \mathrm{e}^{-\frac{E_l}{k_\mathrm{B} T_\mathrm{ex}}} + g_u \, \mathrm{e}^{-\frac{E_u}{k_\mathrm{B} T_\mathrm{ex}}} \ . \tag{2.65}$$

From Eq. 2.61 using Equations 2.62 and 2.65, the temperature-dependent conversion factor between the optical depth and the column number density can be written as

$$\tau_{\nu,\uparrow\downarrow} = N_{\uparrow\downarrow} \frac{c^2}{8\pi\nu^2} \frac{g_u}{g_l} A_{ul} \phi_\nu \frac{1 - \mathrm{e}^{T_0/T_\mathrm{ex}}}{1 + \frac{g_u}{g_l} \mathrm{e}^{-T_0/T_\mathrm{ex}}} \ , \tag{2.66}$$

which is valid for a two-level system. It is more convenient to work in velocity space, for which the transformation is given by the Doppler shift $\mathrm{d}\nu = (\nu/c)\,\mathrm{d}v$. The reason is that in velocity space different tracers with different individual rest frequencies are represented on one common scale. The line profile in the above equation can be eliminated by integrating over the velocity, leading to the column density of a two-level system

$$N_{\uparrow\downarrow} = \frac{8\pi\nu^3}{c^3}\frac{g_l}{g_u}\frac{1}{A_{ul}}\frac{1+\frac{g_u}{g_l}\mathrm{e}^{-T_0/T_{\mathrm{ex}}}}{1-\mathrm{e}^{T_0/T_{\mathrm{ex}}}}\int \tau_{\uparrow\downarrow}(v)\,\mathrm{d}v\ . \tag{2.67}$$

In the optically thin case, the radiative transfer equation can be written as

$$T_{\mathrm{mb}} = f(\mathcal{J}_\nu(T_{\mathrm{ex}}) - \mathcal{J}_\nu(T_{\mathrm{bg}}))\tau\ \ , \tag{2.68}$$

where f is the beam filling factor, which refers to the fact that an unresolved source may not fully fill the beam, and hence the emission is diluted over the beam size. Equation 2.67 can then be written in a more convenient form as

$$N_{\uparrow\downarrow} = \frac{8\pi\nu^3}{c^3}\frac{g_l}{g_u}\frac{1}{A_{ul}}\frac{1+\frac{g_u}{g_l}\mathrm{e}^{-T_0/T_{\mathrm{ex}}}}{1-\mathrm{e}^{T_0/T_{\mathrm{ex}}}}\frac{\int T_{\mathrm{mb}}(v)\,\mathrm{d}v}{f(\mathcal{J}_\nu(T_{\mathrm{ex}}) - \mathcal{J}_\nu(T_{\mathrm{bg}}))}\ . \tag{2.69}$$

This equation enables the direct determination of the column number density from the measured integrated intensity. Note that the calculated column density represents a lower limit, as accounting for neglected optical depth will result in a higher value.

A more convenient access to the optical depth avoids using excitation temperature and column number density. These parameters are, in general, not easily accessible. However, under the assumption of a homogeneous medium, we can determine the optical depth from the intensity ratio between two isotopes (Ossenkopf et al., 2013) via

$$\frac{T_{\mathrm{mb},^{12}\mathrm{C}}(v)}{T_{\mathrm{mb},^{13}\mathrm{C}}(v)} = \frac{\mathcal{J}_{^{12}\mathrm{C}}(T_{\mathrm{ex}})}{\mathcal{J}_{^{13}\mathrm{C}}(T_{\mathrm{ex}})}\left(\frac{1-\mathrm{e}^{-\tau(v)}}{1-\mathrm{e}^{-\tau(v)/\alpha}}\right) \tag{2.70}$$

$$\approx \frac{1-\mathrm{e}^{-\tau(v)}}{1-\left(1-\frac{\tau(v)}{\alpha}\right)} \tag{2.71}$$

$$= \frac{1-\mathrm{e}^{-\tau(v)}}{\tau(v)}\alpha\ , \tag{2.72}$$

where α is the local abundance ratio of the isotopes and $\tau(v) \ll \alpha$, as well as assuming optically thin [^{13}C II] emission and same excitation temperatures of [^{12}C II] and [^{13}C II]. These relations are also valid for the molecular transitions of ^{12}CO and ^{13}CO.

2.2.2 [C I] line emission

Under LTE conditions, the column density of neutral carbon (Gerin et al., 1998) is

$$N = 1.9\times 10^{15}\int \mathrm{d}v\, T_{\mathrm{mb}} Q(T_{\mathrm{kin}})\mathrm{e}^{\frac{E_1}{k_{\mathrm{B}}T_{\mathrm{kin}}}}\ [\mathrm{cm}^{-2}]\ . \tag{2.73}$$

The partition function is given by $Q(T) = 1 + 3\mathrm{e}^{-E_1/k_{\mathrm{B}}T} + 5\mathrm{e}^{-E_2/k_{\mathrm{B}}T}$, where the carbon atom energy levels are $E_1/k = 23.6\,\mathrm{K}$ and $E_2/k = 62.5\,\mathrm{K}$, with the integrated intensity measured in $\mathrm{K\,km\,s^{-1}}$ and T_{kin} representing the kinetic temperature of the carbon gas.

2.2.3 H I line emission

For a given velocity-resolved optical depth and temperature of the cold hydrogen cloud, we can derive the hydrogen column density. Taking into account that for any possible excitation temperature $T_{\mathrm{ex}} \gg T_0$, we can simplify Eq. 2.67 (Rohlfs and Wilson, 1996) to

$$N_{\mathrm{H}} = \frac{8\pi\nu^3}{c^3}\frac{1}{A_{ul}}\frac{T_{\mathrm{ex}}}{T_0}\left(1+\frac{g_l}{g_u}\right)\int \tau(v)\,\mathrm{d}v \tag{2.74}$$

$$= 1.823\times 10^{18}[\mathrm{cm}^{-2}]\frac{T_{\mathrm{ex}}}{[\mathrm{K}]}\int\frac{\tau(v)\,\mathrm{d}v}{[\mathrm{km\,s}^{-1}]}\ . \tag{2.75}$$

2.2.4 CO line emission and X_{CO} conversion factor

For the CO molecule, the column density can be determined by beginning with Eq. 2.61. This requires calculating the conversion factor from the column density of the excited state N_u to the total column density of the rotational transitions N_{rot}. The molecular partition function for diatomic linear molecules is approximated (Mangum and Shirley, 2015) as

$$Q_{\mathrm{rot}} = \sum_{J=0}^{\infty}(2J+1)\mathrm{e}^{-\frac{E_J}{k_{\mathrm{B}}T}} \approx \frac{k_{\mathrm{B}}T}{hB_0}+\frac{1}{3}\ , \tag{2.76}$$

where B_0 is the rotational constant of the molecule. The relationship between optical depth and column density can be expressed through

$$\tau_{\nu,\mathrm{rot}} = N_{\mathrm{rot}}g_u A_{ul}\frac{c^2}{8\pi\nu^2}\frac{\mathrm{e}^{-\frac{E_J}{k_{\mathrm{B}}T_{\mathrm{ex}}}}}{\left(\frac{k_{\mathrm{B}}T_{\mathrm{ex}}}{hB_0}+\frac{1}{3}\right)}\left(\mathrm{e}^{\frac{T_0}{T_{\mathrm{ex}}}}-1\right)\phi_\nu\ . \tag{2.77}$$

In the context of a dipole transition, the Einstein coefficient A_{ul} for spontaneous emission can be expressed in terms of the electric dipole moment μ_{lu} (Wilson et al., 2009), which leads to

$$A_{ul} = \frac{64\pi^4\nu^3}{3hc^3}|\mu_{ul}|^2\ , \tag{2.78}$$

where the dipole matrix element $|\mu_{ul}|$ can be expressed as

$$|\mu_{ul}|^2 = \mu^2 S = \frac{J_u}{2J_u+1}\ , \tag{2.79}$$

with μ^2 the permanent electric dipole moment of the molecule and the line strength $S = J/(2J+1)$, which is valid for linear molecular transitions $J \rightarrow J-1$ (Mangum and Shirley, 2015). With the rotational degeneracy $g_J = 2J_u + 1$ and the equivalent temperature of the upper energy state $T_u = E_u/k_{\mathrm{B}}$, the column density can be written as

$$N_{\mathrm{rot}} = \frac{3h}{8\pi^3 J_u\mu^2}\left(\frac{k_{\mathrm{B}}T}{hB_0}+\frac{1}{3}\right)\mathrm{e}^{\frac{T_u}{T_{\mathrm{ex}}}}\left(\mathrm{e}^{\frac{T_0}{T_{\mathrm{ex}}}}-1\right)\int\tau_{\mathrm{rot}}(v)\,\mathrm{d}v\ . \tag{2.80}$$

The above equation was transformed from frequency space to velocity space and integrated on both sides following Mangum and Shirley (2015). In the optically thin case, the above equation simplifies to

$$N_{\mathrm{rot}} = \frac{3h}{8\pi^3 J_u\mu^2}\left(\frac{k_{\mathrm{B}}T}{hB_0}+\frac{1}{3}\right)\mathrm{e}^{\frac{T_u}{T_{\mathrm{ex}}}}\left(\mathrm{e}^{\frac{T_0}{T_{\mathrm{ex}}}}-1\right)\frac{\int T_{\mathrm{mb}}\,\mathrm{d}v}{f(\mathcal{J}\nu(T_{\mathrm{ex}})-\mathcal{J}_\nu(T_{\mathrm{bg}}))}\ . \tag{2.81}$$

The X_{CO} conversion factor is a crucial and often used parameter to estimate the column density of molecular hydrogen H_2 from the observed intensity of CO emission lines, specifically the $^{12}\mathrm{CO}(J = 1 \rightarrow 0)$ transition. This factor is essential for understanding the mass and distribution of molecular gas in galaxies, as CO is the most accessible tracer of H_2 due to its strong emission and its widespread presence in molecular clouds.

The X_{CO} factor is defined as the ratio of the H_2 column density $N_{\mathrm{H_2}}$ to the integrated intensity of the CO line W_{CO}

$$X_{\mathrm{CO}} = \frac{N_{\mathrm{H_2}}}{W_{\mathrm{CO}}} \ , \tag{2.82}$$

where $N_{\mathrm{H_2}}$ is the column density of molecular hydrogen, typically expressed in units of $\mathrm{cm^{-2}}$ and W_{CO} the integrated intensity of the CO line, expressed in $\mathrm{K\,km\,s^{-1}}$. The X_{CO} factor is thus expressed in units of $\mathrm{cm^{-2}\,(K\,km\,s^{-1})^{-1}}$.

2.2.5 Dust emission

Dust emission is crucial to understanding the ISM and the processes within it. These processes relate to cooling, SED fits to estimate H_2 masses unbiased to CO-dark gas, or total IR emission. Two important parameters in the description of dust are the emissivity index β and the dust absorption coefficient κ_0.

The optical depth $\tau_{\nu,\mathrm{d}}$ of dust at frequency ν can be described as

$$\tau_{\nu,\mathrm{d}} = \kappa_\nu \Sigma_{\mathrm{d}} \ . \tag{2.83}$$

In this equation κ_ν is the dust absorption (opacity) at frequency ν and Σ_{d} the dust surface density.

For a simple consideration, one can assume that the optical depth of dust should decrease with decreasing frequency with a power-law dependency of -2. The dust absorption coefficient κ_ν is often represented as

$$\kappa_\nu = \kappa_0 \left(\frac{\nu}{\nu_0}\right)^{\beta} \ , \tag{2.84}$$

where κ_0 is the dust absorption coefficient at a reference frequency ν_0 and β is the emissivity index. The parameter β is then allowed to vary around a value of 2 to account for different conditions in complex interactions that cause dust emission.

The emissivity index β quantifies how the dust emissivity changes with frequency and exhibits significant variation across different environments. Although often assumed to be constant, studies show that it can vary substantially with environmental conditions and dust properties. For instance, measurements in the starless core TMC-1C reveal that β is close to 2, a typical value of interstellar dust (Schnee et al., 2010). In the Galactic plane, β ranges from about 1.54 in diffuse regions to 1.66 in denser areas, correlating with the presence of molecular gas (Planck Collaboration et al., 2014). This variation indicates that dust composition and temperature influence β, and that β correlates with molecular clouds, reaching values above 2 in M33 (Tabatabaei et al., 2014).

The dust absorption coefficient κ_0 measures how much light dust grains absorb at a given wavelength. It plays a crucial role in determining dust mass and understanding dust emission. Studies show that κ_0 varies with temperature and composition. For example, studies on interstellar silicate dust analogs show that κ_0 decreases with temperature and that its spectral shape is complex, not following a single power-law (Coupeaud et al., 2011).

This complexity requires detailed models that account for temperature and compositional variations to accurately interpret observational data (Demyk et al., 2017). A value of the dust absorption coefficient is often used from Hildebrand (1983). However, that study determined the value for only one cloud in the Milky Way. Thus, for Paper I on M33, I calibrated κ_0 using the generated hydrogen column density and H I data. For the resulting gaps in the map, I assumed a non-changing κ_0 between the atomic and molecular phases (see Keilmann et al. (2024a) for further details).

In summary, both β and κ_0 are essential for dust modeling and their variability must be considered to improve the accuracy of models used in astrophysics.

Chapter 3

Radio Astronomy Observation

In radio astronomy, the concept of antenna temperature helps to understand the sensitivity and performance of radio telescopes. It measures the power received by an antenna from a source in terms of the equivalent temperature of a resistor that would produce the same power. This parameter characterizes the noise performance of radio telescopes and depends on factors such as antenna design and the surrounding environment (Marr et al., 2020).

Understanding and optimizing antenna temperatures is vital to enhance the sensitivity and accuracy of radio astronomical observations. Section 3.1 presents concepts on antenna temperature and its relation to the main beam temperature, which is the essential quantity used in this thesis. Sections 3.2 and 3.3 describe the necessary observational methods, while Sect. 3.4 introduces the radiometer equation, a fundamental relation regarding noise that is critical for observations. The subsequent sections briefly present the telescopes, including the GREAT instrument onboard SOFIA (essential for the FEEDBACK program), and important programs relevant to this thesis, such as FEEDBACK and HerM33es, which provided the data used in this doctoral research.

3.1 Antenna Temperature and Efficiencies

Equation 2.15 establishes a linear link between the intensity of an astronomical source and its radiation temperature T_b (T_R). However, telescope antenna pattern $P_n(\theta, \phi)$ influences the observed intensity. For ground-based telescopes, atmospheric attenuation also affects the signal. The relationship between the emitting source's radiation temperature and the observed antenna temperature is given by (Kutner and Ulich, 1981)

$$T_\mathrm{A} = T_\mathrm{b} \left(\frac{\int\int_{\Omega_s} P_n(\theta - \theta', \phi - \phi')\, \psi(\theta', \phi')\, \mathrm{d}\Omega'}{\int\int_{4\pi} P_n(\theta, \phi)\, \mathrm{d}\Omega} \right) \mathrm{e}^{-\tau_a A} \ , \tag{3.1}$$

where $P_n(\theta, \phi) = P_n(\theta, \phi)/P_\mathrm{max}$ is the normalized antenna pattern, T_b averaged over the source brightness distribution ψ (ranging from zero to one), Ω_s is the source solid angle, τ_a is the optical depth of the atmosphere, and $A \sim 1/\sin(\epsilon)$ is the air mass, depending on elevation ϵ.

Equation 3.1 shows that determining the brightness (or radiation) temperature from the observed antenna temperature requires knowledge of the source structure and antenna pattern. To express these with quantities accessible by direct measurements, we divide

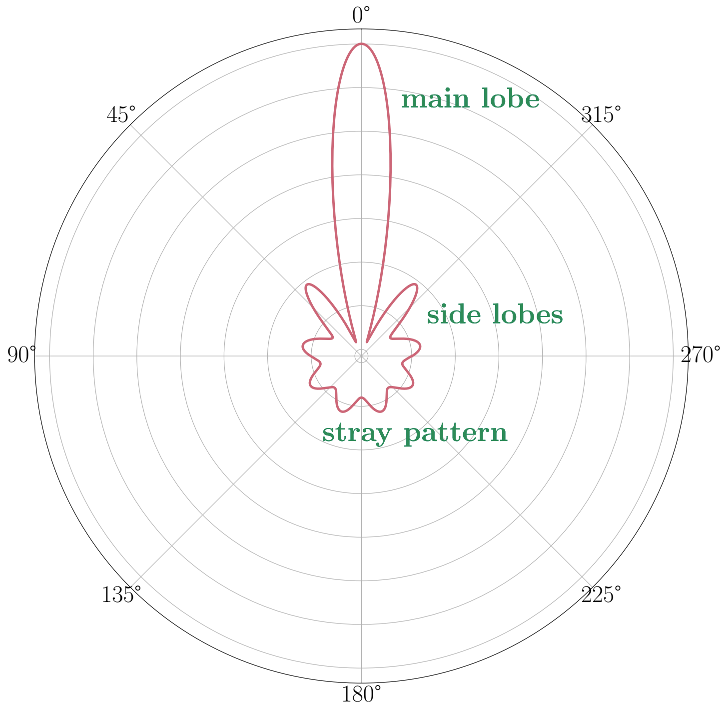

Figure 3.1: Schematic illustration of an antenna pattern in polar coordinates. The top section displays the sensitivity of the forward half, covering the main beam and side lobes, while the bottom section illustrates the sensitivity of the rear side, including the stray pattern.

the telescope pattern, illustrated in Fig. 3.1, into two parts: (i) the forward section, which includes the main beam and side lobes, and (ii) the rear side containing the stray pattern.

Defining the solid angle Ω_{mb} to encompass the diffraction pattern's main lobe allows us to calculate the coupling efficiency η_c, indicating antenna-source coupling within the solid angle Ω_s

$$\eta_c = \frac{\iint_{\Omega_s} P_n(\theta-\theta', \phi-\phi')\, \psi(\theta', \phi')\, \mathrm{d}\Omega'}{\iint_{\Omega_{\mathrm{mb}}} P_n(\theta, \phi)\, \mathrm{d}\Omega} \; . \tag{3.2}$$

When the source is resolved (fills the beam), the antenna temperature equals the radiation temperature of the source $T_{\mathrm{A}} = T_{\mathrm{b}}$. If the source is smaller than the main beam, we need to take into account that the source is unresolved and the observed intensity is smaller. Therefore, we define the corrected source intensity, known as the main beam temperature, as

$$T_{\mathrm{mb}} = \eta_c \, T_{\mathrm{b}} \; . \tag{3.3}$$

Without knowing the structure of the source, T_{mb} is the best approach to the actual radiation (brightness) temperature of the emitting source.

The relationship between source-corrected intensity and antenna temperature adjusted for atmospheric attenuation is given by

$$T'_{\mathrm{A}} = T_{\mathrm{A}} \mathrm{e}^{\tau_a A} \; . \tag{3.4}$$

We can find an expression for the main beam efficiency η_{mb} by combining Eqs. 3.1, 3.2, and 3.3, which leads to

$$T'_{\mathrm{A}} = T_{\mathrm{mb}} \underbrace{\left(\frac{\int\!\!\int_{\Omega_{\mathrm{mb}}} P_n(\theta, \phi)\, \mathrm{d}\Omega}{\int\!\!\int_{4\pi} P_n(\theta, \phi)\, \mathrm{d}\Omega} \right)}_{=:\eta_{\mathrm{mb}}} \ . \tag{3.5}$$

The main beam efficiency indicates the portion of power captured in the main lobe relative to the overall detected power. Therefore, the connection between the main beam temperature and antenna temperature is compactly expressed as

$$T_{\mathrm{mb}} = \frac{T'_{\mathrm{A}}}{\eta_{\mathrm{mb}}} \ . \tag{3.6}$$

In the mm/sub-mm range, a frequent calibration method is the chopper wheel (Wilson et al., 2009), used for determining the forward beam brightness temperature

$$T^*_{\mathrm{A}} = \frac{T'_{\mathrm{A}}}{\eta_{\mathrm{f}}} \ , \tag{3.7}$$

where the forward efficiency is

$$\eta_{\mathrm{f}} = \frac{\int\!\!\int_{2\pi} P_n(\theta, \phi)\, \mathrm{d}\Omega}{\int\!\!\int_{4\pi} P_n(\theta, \phi)\, \mathrm{d}\Omega} \ . \tag{3.8}$$

Forward efficiency is the fraction of power in the half-sphere facing forward relative to the total detected power. The forward beam brightness temperature T^*_{A}, known as the corrected antenna temperature, relates to the main beam temperature as follows

$$T^*_{\mathrm{A}}\, \eta_{\mathrm{f}} = T_{\mathrm{mb}}\, \eta_{\mathrm{mb}} \ . \tag{3.9}$$

The radiative transfer Eq. 2.46 can now be rewritten using the main beam temperature, which leads to

$$T_{\mathrm{mb}} = \eta_c [\mathcal{J}_\nu(T_{\mathrm{ex}}) - \mathcal{J}_\nu(T_{\mathrm{bg}})](1 - \mathrm{e}^{-\tau_\nu}) \ . \tag{3.10}$$

The coupling efficiency η_c in the above equation ranges from 0 to 1, and is also known as the filling factor f and is already used in Sect. 2.2.1. It indicates the portion of the area occupied by the emitting source relative to the telescope's main beam. Even extended sources larger than the beam, such as molecular clouds, may have a filling factor less than one because of their clumpy structure. Note that if a significant part of the power from an extended source appears in the side lobes (see Fig. 3.1), it can cause unwanted contributions to the measurements.

3.2 Receiver Calibration

Radio telescopes require careful calibration to ensure that the signals recorded truly represent the astronomical sources rather than artifacts of the instrument or the environment.

Receivers output a voltage or digital counts[1] that must be converted into physical units such as brightness temperature (Kelvin). This is achieved by calibrating the relationship between the measured signal and a known temperature or power scale.

The system power P_{sys} is the receiver output, which is the sum of the power received from the atmospheric emission P_{A} and the power from the receiver noise P_{rec}

$$P_{\text{sys}} = P_{\text{A}} + P_{\text{rec}} \ . \tag{3.11}$$

The measured system power relates to system temperature through the gain factor g as

$$P_{\text{sys}} = gT_{\text{sys}} \ , \tag{3.12}$$

where the system temperature T_{sys} is the sum of the antenna temperature T_{A}, which measures the flux from the source, the actual power received due to the sky (source plus atmosphere) and the receiver (T_{rec}). Thus, the system temperature is the sum of

$$\begin{aligned} T_{\text{sys}} &= T_{\text{A}} + T_{\text{atm}} + T_{\text{rec}} && (3.13)\\ &= T_{\text{A,sky}} + T_{\text{rec}} \ , && (3.14) \end{aligned}$$

where $T_{\text{A,sky}}$ accounts for the source and atmosphere. This leads to

$$P_{\text{sys}} = g(T_{\text{A,sky}} + T_{\text{rec}}) \tag{3.15}$$

The gain factor g is the conversion factor that relates the input signal (e.g., counts per Kelvin) to the output "counts" recorded by the receiver.

The two unknowns, receiver temperature and gain factor, must be determined by measuring system power of two radiation sources with two known different temperatures

$$\begin{aligned} P_{\text{hot}} &= g(T_{\text{hot}} + T_{\text{rec}}) \quad \text{and} && (3.16)\\ P_{\text{cold}} &= g(T_{\text{cold}} + T_{\text{rec}}) \ . && (3.17) \end{aligned}$$

This is called "Hot-Cold-Load." To remain within the dynamic receiver's range, the ambient temperature T_{amb} is used as the "Hot-Load," where T_{hot} is measured using an absorber in the radiation path to the detector. For T_{cold}, a much colder source is used, such as liquid nitrogen. The gain factor g can now be expressed as a function of measured power and temperature by subtracting Eq. 3.17 from Eq. 3.16, which leads to

$$g = \frac{P_{\text{hot}} - P_{\text{cold}}}{T_{\text{hot}} - T_{\text{cold}}} \ . \tag{3.18}$$

The receiver noise temperature is given by

$$T_{\text{rec}} = \frac{T_{\text{hot}} - YT_{\text{cold}}}{Y - 1} \ , \tag{3.19}$$

---

[1] In a radio telescope, the incoming electromagnetic signal is first converted into an electrical (analog) signal. This analog signal is then sampled and digitized by an analog-to-digital converter (ADC) or digital Fast-Fourier-Transform (FFT) spectrometer. ADC and FFT (and, for example, amplifier gains) produce "counts," which are essentially quantized representations of the signal's amplitude or power. That is, "counts" are the raw digital numbers produced by the detector system that represent the intensity or power of the incoming radio signal. These numbers are in arbitrary units that depend on the electronics (amplifiers, converters, etc.) in the receiver.

by making use of the Y-factor, which is the ratio of

$$Y = \frac{P_{\text{hot}}}{P_{\text{cold}}} \,. \tag{3.20}$$

While ideally the gain would be constant, it can vary over time because of environmental factors or instrumental drifts. These drifts are changes in receiver performance over time due to temperature changes, aging components, or minor fluctuations in power supplies or electronic circuits; and lead to variations in gain, system noise temperature, or baseline offset. Thus, depending on those factors, the receiver requires calibration over time.

The antenna temperature depends also on the atmospheric temperature. Placing the observatory at a higher altitude minimizes the atmospheric contribution and significantly reduces the measurement noise. According to the radiometer equation (Eq. 3.23), noise is inversely proportional to the square root of the integration time τ for a fixed bandwidth $\Delta\nu$. Therefore, doubling the integration time reduces the noise by a factor of $1/\sqrt{2}$.

3.3 Observing Modes

Most ground-based and air-borne radio-astronomical observations are carried out as difference measurements by comparing an ON-source position with an OFF-source position, which is devoid of any source emissions, to eliminate variations in receiver noise (see Sect. 3.4), gain, and offset. These variations may occur due to temperature instabilities, mechanical load changes, or aging of the components; and cause an instrumental "drift" with a characteristic drift spectrum of the system. While noise is characterized by fluctuations maintaining a constant average value across all timescales and instances, drifts consist of fluctuations that change the average value at various timescales, specifically over an interval of particular duration at different time instances. These drifts can become significant quickly, affecting how frequently an OFF-source reference measurement is needed to correct for the drifts. This frequency depends on the drift rate of the receiver. Or in other words, due to the limited stability of the detector/receiver system, "referencing" is required on timescales faster than the characteristic stability time of the system. Furthermore, when high sensitivity is required to measure weak signals, the drift's relative strength to the signal determines the necessity of frequent reference measurements.

Besides receiver drifts, atmospheric fluctuations also introduce noise changes. Similar to receiver drifts, the frequency of reference measurements is influenced by the rapidity and intensity of these atmospheric changes, as well as the required measurement precision.

Each reference measurement reduces the available ON-source observing time, and the telescope's switching time between ON- and OFF-source measurements may further decreases the effective observing time. Consequently, observing modes are tailored based on the source and precision requirements. Although different observatories may use varying terminology and combinations, in the following I will outline some basic modes, such as beam-switching, frequency-switching, and On-The-Fly (OTF) mapping (Emerson and Graeve, 1988; Wilson et al., 2013; Thompson et al., 2017).

Position-switching (also total power mode or "nodding") physically moves the whole telescope between the target ON position and an OFF reference position. While slower than beam-switching or chopping (see below), this mode also provides a reference measurement for background and instrumental effects. The OFF-source measurement is subtracted from the ON-source measurement to account for fluctuations. Position-switching also comes with disadvantages, such as requiring precise and rapid movement of telescope components, which can be mechanically challenging.

(Chopped) Beam-switching is an observing mode that switches the telescope's beam between the target source and a nearby reference position. This means that the secondary mirror is wobbling by alternating its angle several times per second, or a chopper wheel (or a combination of both) is used to minimize the impact of short-term fluctuations in atmospheric emission and instrumental noise. The telescope's beam alternates between the ON-source position – point the beam at the target source and record the signal for a specified integration time t_{on} – and a nearby OFF-source position – point the beam at a reference position offset from the target (usually a few beam widths away) and record the signal for an integration time t_{off} – at a high frequency. The difference between the ON and OFF signals removes atmospheric and instrumental fluctuations via

$$S_{\mathrm{BS}} = S_{\mathrm{ON}} - S_{\mathrm{OFF}} \ . \tag{3.21}$$

Beam-switching improves sensitivity canceling out atmospheric fluctuations and is particularly useful for detecting weak continuum sources.

However, beam-switching also comes with disadvantages such as that the OFF position must be close to the ON position, limiting the choice of reference positions and allowing one to only observe sources that are not extended. Standing waves can arise due to varying optical path lengths resulting from the secondary mirror's differing positions. Furthermore, another offset spectrum is possible, as the secondary mirror may not always illuminate the receiver in the changing positions in the same way.

To mitigate the latter two disadvantages, a dual-beam mode is used, in which both problems cancel out in the two beam-switching phases. The beam switches from ON to an OFF1 position and afterwards from another OFF2 position back to the ON position. Chop-nod-switching is such a dual-beam mode and is a combination of chopped beam-switching and nodding. With "chop," one divides the two positions on the sky into "beam A" and "beam B." Using nodding, one can then observe a sequence A-B-B-A, obtaining particularly smooth baselines.

Frequency-switching is an observing technique that rapidly alternates the observing frequency between the target line frequency and a nearby offset frequency. The local oscillator (LO) frequency shifts back and forth between the line frequency f_{line} and an offset frequency $f_{\mathrm{line}} + \Delta f$. Spectra are recorded at both frequencies during the same integration time. The difference between the spectra at the two frequencies and the difference between these spectra is calculated to remove instrumental baselines and continuum emission

$$S_{\mathrm{FS}} = S(f_{\mathrm{line}}) - S(f_{\mathrm{line}} + \Delta f) \ . \tag{3.22}$$

All time is spent ON-source, which increases observing efficiency compared to beam- and position-switching. However, the shifted line may appear in the offset frequency, causing confusion, and the frequency shift Δf must remain small to avoid moving out of the receiver bandpass. The bandpass must remain flat across the relevant frequency range; otherwise, it may lead to problematic baselines of the spectra. In addition, the lines to be observed should not be too broad in order to avoid overlap. Thus, observations of galaxies or the Galactic center are excluded with line widths of up to a few $100\,\mathrm{km\,s^{-1}}$.

On-The-Fly (OTF) mapping is an efficient observing mode for creating large-area maps of the sky. In OTF mapping, the telescope continuously scans across the target area instead of observing discrete points. The telescope moves smoothly along predefined paths at a constant speed, while data are sampled continuously at high rates (oversampling) to ensure adequate spatial sampling according to the Nyquist theorem.[2] The integration time per sample is kept short enough to ensure that the telescope's movement during one sample does not exceed a small fraction of its beam size. The collected data are then gridded onto a regular spatial grid using convolution kernels, such as Gaussian functions, to produce the final map.

The advantages of OTF mapping include maximizing ON-source time, avoiding dead time by eliminating the overhead of moving between discrete pointings (from ON- to OFF-source), which was performed in a mode prior to OTF called raster mapping and has dead time between ON-source measurements. OTF provides consistent sensitivity across the mapped area and enables high-speed mapping suitable for surveying large regions of the sky. However, OTF mapping requires careful calibration due to the continuous changes in telescope position and system gain. This observing mode is commonly applied in mapping molecular clouds, large-scale structures and conducting surveys of the Galactic plane or extragalactic fields where spatial context is essential.

3.4 The Radiometer Equation

The radiometer equation in radio astronomy fundamentally describes the sensitivity of an instrument. It determines the minimum detectable signal, or noise level, of a radiometer system. The noise temperature of an antenna system is a combination of thermal noise from the antenna itself and noise from the surrounding environment, including the atmosphere and cosmic background. Advanced methods have been developed to estimate antenna noise temperature rapidly, taking into account the geometric parameters of reflector dishes, which are commonly used in radio astronomy (de Villiers, 2016).

The noise equals $T_{\mathrm{sys}}/\sqrt{N}$, where N denotes the number of independent signal samples. With a receiver bandwidth of $\Delta\nu$, the signal remains statistically independent over a time interval of $1/\Delta\nu$, so that $N = \tau\Delta\nu$. Here, τ is the integration time. This finally results in the radiometer equation expressed as the uncertainty or standard error (root mean square, rms) σ_{rms} of the measurement given by

$$\sigma_{\mathrm{rms}} = \frac{T_{\mathrm{sys}}}{\sqrt{\tau\Delta\nu}} \ , \tag{3.23}$$

where σ_{rms} is also referred to as ΔT_{sys}. This "derivation" is based on plausibility arguments, relying on statistical processes that follow Gaussian statistics. A rigorous derivation based on original references (e.g., Johnson, 1928; Dicke, 1946; Oliver, 1965) and fundamental statistical concepts can be found in Hunter and Kimberk (2015).

Relating the radiometer equation to the signal, leads to the signal-to-noise (S/N) ratio

$$\frac{\mathrm{Signal}}{\mathrm{Noise}} = \frac{T_{\mathrm{A}}}{\sigma_{\mathrm{rms}}} = \frac{T_{\mathrm{A}}}{T_{\mathrm{sys}}}\sqrt{\tau\Delta\nu} \ . \tag{3.24}$$

---

[2] The Nyquist theorem states that to accurately reconstruct a continuous signal from its samples without any loss of information (and to avoid aliasing), one must sample the signal at a rate that is at least twice the highest frequency present in the signal.

Radiometer equation for OTF mapping When observing astronomical sources, a simple question arises: Is it possible to optimize the S/N ratio by minimizing the time spent in the OFF position? For an observing mode, in which a single OFF position measurement is used for N ON mapping positions, and neglecting the dead time of the telescope to switch between ON- and OFF-source, we have

$$\sigma_{\mathrm{rms,ON}} = \frac{T_{\mathrm{sys}}}{\sqrt{\tau_{\mathrm{ON}}\Delta\nu}} \quad \text{and} \tag{3.25}$$

$$\sigma_{\mathrm{rms,OFF}} = \frac{T_{\mathrm{sys}}}{\sqrt{\tau_{\mathrm{OFF}}\Delta\nu}} \ , \tag{3.26}$$

with an ON-source integration time of τ_{ON} and an OFF-source integration time of $\tau_{\mathrm{OFF}} = a\,\tau_{\mathrm{ON}}$. Since both expressions are statistically independent (error propagation), they add in quadrature, which leads to

$$\sigma_{\mathrm{rms,ON-OFF}} = \sqrt{(\sigma_{\mathrm{rms,ON}})^2 + (-\sigma_{\mathrm{rms,OFF}})^2} \tag{3.27}$$

$$= \frac{T_{\mathrm{sys}}}{\sqrt{\tau_{\mathrm{ON}}\Delta\nu}}\sqrt{1+\frac{1}{a}} \ . \tag{3.28}$$

Hence, the signal-to-noise is given by

$$\mathrm{S/N} = \frac{T_{\mathrm{A}}}{\sigma_{\mathrm{rms,ON-OFF}}} = \frac{T_{\mathrm{A}}}{T_{\mathrm{sys}}}\sqrt{\tau_{\mathrm{ON}}\Delta\nu}\sqrt{1+\frac{1}{a}} \ . \tag{3.29}$$

To find the best S/N for each mapping position for a given total observing time ($N\,\tau_{\mathrm{ON}} + \tau_{\mathrm{OFF}} = \tau_{\mathrm{total}} = \mathrm{const.}$), one can show that $a = \sqrt{N}$. This result also remains valid for raster mapping (although this derivation does not account for loosing time additionally due to switching between ON-source and OFF-source). It also follows that, for single-point observations, identical integration times are needed for both the ON and the OFF positions.

3.5 SOFIA

SOFIA was an airborne observatory that combined advanced design with high-altitude operation to explore the universe in infrared to submillimeter wavelengths. The airplane was a specially modified Boeing 747SP equipped with a 2.7 m telescope, which has an effective aperture of 2.5 m (Fig. 3.2). This airborne observatory is a collaborative effort between NASA and the German Aerospace Center (DLR) and was designed to explore the universe through infrared to submillimeter wavelengths, which are largely inaccessible to ground-based telescopes due to atmospheric interference. SOFIA operated in the stratosphere at altitudes ranging from 11.6 to 13.7 km, thus above the majority of the Earth's absorbing atmospheric layers. This allowed the observatory to cover the mid- to far-infrared wavelength range in continuum and line observations.

An advantage of using an aircraft-based observatory over a space-based one is the flexibility to switch, maintain and upgrade instruments between flights. Throughout its operational period, SOFIA carried multiple cutting-edge receivers including FORCAST, EXES, HAWC+, FIFI-LS and GREAT. The instruments on SOFIA could also be adjusted during observations as they were accessible in the cabin along with the science team. The distinctive mobility of SOFIA allowed us to perform observations that were not possible from ground-based observatories or spacecraft, such as planetary occultations.

Figure 3.2: NASA's Stratospheric Observatory for Infrared Astronomy 747SP aircraft flies over Southern California's high desert with the large door of its 2.5 m German-built telescope open. Image Credit: NASA/Jim Ross

3.5.1 GREAT receiver

The German REceiver for Astronomy at Terahertz Frequencies (GREAT) is a multi-pixel spectrometer (Heyminck et al., 2012; Risacher et al., 2018; Duran et al., 2021) onboard SOFIA. GREAT was designed in a collaboration between the Max Planck Institute for Radio Astronomy (MPIfR) and the I. Physikalisches Institut at the University of Cologne (KOSMA), alongside the Max Planck Institute for Solar System Research and the DLR Institute of Planetary Research. As a PI instrument, GREAT also supported Open Time observations in a collaborative mode.

The data used in this thesis were obtained with the instrument operating in two distinct configurations, 4GREAT and upGREAT. The upGREAT setup used two channels: the low-frequency array (LFA) and the high-frequency array (HFA). The LFA comprises two hexagonal arrays with 7 pixels per polarization, operating within a $1.83 - 2.07$ THz frequency range, enabling observations of [C II] and [O I] at 145 μm. Both spectral lines can be detected simultaneously with one line in each polarization. Each [C II] frequency pixel had a beam size of $14.1''$. The HFA featured a 7-pixel hexagonal array in single polarization to observe the [O I] 63 μm line with a beam size of $6.3''$. LFA and HFA were capable of simultaneous observations, addressing up to six essential ISM cooling lines concurrently.

The 4GREAT configuration used a single pixel with four channels, spanning frequencies of $91 - 635$, $890 - 1090$, $1240 - 1525$, and $2490 - 2590$ GHz (Duran et al., 2021). This frequency coverage provides access to the high-J rotational transitions of CO.

3.5.2 SOFIA Legacy Program FEEDBACK

The SOFIA legacy program's FEEDBACK primary objective is to study how stellar feedback from massive stars influences the surrounding interstellar medium. Specifically, FEEDBACK aims to elucidate the radiative coupling of PDR gas to FUV photons, measure the energy input into the ISM from stellar winds and radiation, and determine radiative heating efficiencies. The notable strength of FEEDBACK lies in its observation of 11 galactic high-mass star formation regions in [C II] at 158 μm and [O I] at 63 μm simultaneously, enabling comparisons across regions with varying physical conditions and providing a larger dataset for extragalactic research comparisons.

The principal investigators are Prof. Dr. Alexander Tielens from the University of Maryland and Dr. Nicola Schneider from the University of Cologne. A consortium of around 30 experts from various international institutions collaborated on this project. The program received approximately 100 hours of observing time, beginning in 2019 (Program number 07_0077). It completed 77% of the proposed area before the SOFIA program ended in September 2022.

Table 3.1: Overview of the 11 FEEDBACK sources Schneider et al. (2020).

Region	**RA** (1)	**Dec** (2)	**D_{HD}** (3)	**FUV** (4)	**Spectral type** (5)
Cygnus X	20 : 38 : 20.22	+42 : 24 : 18.29	1.40	290	~ 50 O, 3 WR
M16	18 : 18 : 35.69	−13 : 43 : 30.98	1.74	300	1 O4, ~ 10 late O
M17	18 : 20 : 43.16	−16 : 06 : 14.87	1.98	1295	2 O4, ~ 10 late O
NGC6334	17 : 20 : 14.07	−35 : 55 : 05.18	1.30	580	5 O5 − 8, 8 B
NGC7538	23 : 13 : 46.41	+61 : 31 : 42.01	2.65	904	1 O3
RCW49	10 : 24 : 11.57	−57 : 46 : 42.50	4.21	555	2 WR, 12 early O
RCW79	13 : 40 : 05.86	−61 : 42 : 36.94	3.90	140	2 O4, ~ 10 late O
RCW120	17 : 12 : 22.82	−38 : 26 : 51.61	1.68	375	1 O8
RCW36	08 : 59 : 26.81	−43 : 44 : 14.06	0.95	413	1 O8, B-cluster
W40	18 : 31 : 28.58	−02 : 07 : 35.39	0.26	237	1 O, 2 B
W43	18 : 48 : 01.04	−01 : 58 : 22.27	5.49	741	OB, WR-cluster

(1, 2) Central coordinates of the observed [C II] maps. (3) Distance to the regions in kpc, (4) Average FUV-field in Habing units [G_0], derived from 70 μm and 160 μm Herschel FIR-flux maps (Schneider et al., 2016). (5) Dominant stars and their spectral types.

Table 3.1 provides a catalog of the observed sources, detailing their central coordinates, distance, average FUV field and the related stellar cluster. These star formation regions were selected to cover a wide range of physical conditions in terms of excitation, geometry, and star-formation activity etc. For instance, RCW79 features a cluster of twelve O-type stars near the center of its roughly spherical H II region (Sect. 5.3), and hosts a young compact H II region, which was studied in Keilmann et al. (2025). Cygnus X, on the other hand, contains several massive star clusters with over 160 OB stars for the most influential one, exhibiting a complex spatial arrangement.

To cover the 11 targets, the high observing speed of the OTF array mapping was used. The LFA has a beam size of around 14″ (depending on the line observed) and is primarily used for fully sampled maps of both lines, while the HFA array has a smaller beam size of 6.3″ for the [O I] 63 μm line. However, the HFA's small array size would require significant time to cover all target areas in the "classical" mode. Thus, an alternative approach was used to optimize speed. Each tile was covered four times using OTF array mapping, with LFA as the leading array. Initial coverage comprises two perpendicular scan directions, resulting in a fully sampled [C II] map with sufficient pixel redundancy. To fill gaps in the [O I] map, two extra coverages were performed with an array shift of $(-362'', -362'')$. This method improved the S/N of the [C II] map, allowing access to weak [^{13}C II] lines and enabling a continuous, nearly beam-sampled [O I] map.

Atmospheric and instrumental instabilities may influence the spectral baseline. In certain cases, conventionally subtracting a polynomial fit from the baseline does not suffice. To achieve optimum data quality, an approach based on Principal Component Analysis (PCA) was used. Briefly, PCA identifies the "eigen spectra" of the observations that capture most of the emission-free OFF-spectrum variability and subtracts these components to eliminate systematic variations from the ON-spectra, resulting in a flat baseline. This method was used to reduce the [C II] data of RCW79, further details on PCA can be found in Schneider et al. (2023).

Among the aims for the FEEDBACK observations of the 11 high-mass star formation regions 3.1 was to measure the various feedback mechanisms from stellar winds and stellar radiation. Although the energy from stellar winds is only a small portion compared to that from stellar radiation, Luisi et al. (2021) and Bonne et al. (2022) demonstrated that stellar wind energy can be efficiently transformed into the kinetic energy of the expanding bubble. However, Keilmann et al. (2025) demonstrated that, in the case of the early compact H II region in RCW79, stellar radiation can significantly contribute to the energy input into the surrounding matter.

3.6 Herschel Observatory

The Herschel Space Observatory, established by the European Space Agency (ESA), operated from 2009 to 2013. It was the largest space-borne (mirror diameter 3.5 m) infrared telescope until the James Webb Space Telescope (diameter 6.5 m) launched in 2021. It featured several instruments, the Photodetecting Array Camera and Spectrometer (PACS), the Spectral and Photometric Imaging Receiver (SPIRE), and the Herschel-Heterodyne Instrument for the Far-Infrared (HIFI), observing continuum and spectral lines in the far-IR and submillimeter wavelength range ($55 - 672\,\mu$m).

The dust data observed using PACS and SPIRE in photometric mode were crucial for my studies in all papers that are part of this thesis.

3.6.1 HerM33es Program

The Herschel M33 Extended Survey (HerM33es) Open Time Key Program observed the Local Group galaxy M33 with PACS and SPIRE (Kramer et al., 2010) to map its dust spectral energy distribution and study the properties of the ISM. The program allocated 191.9 hours of observational time with Dr. Carsten Kramer as the PI. One objective was to observe the far-IR emission from the nearby spiral galaxy M33 to investigate the physical properties of its ionized, atomic, and molecular ISM, its life cycle, and thermal balance, while also establishing a reference point for interpreting phenomena in other galaxies.

M33 is an ideal target for this study because it actively forms stars, is observed mainly face-on with an inclination of 56° (Regan and Vogel, 1994), and has been extensively studied across radio, optical, and X-ray wavelengths. Its proximity at a distance of 847 kpc (Karachentsev et al., 2004) allows us to resolve giant molecular clouds and complexes (exceeding $\sim 50\,\mathrm{pc}$) in Herschel observations and individual clouds (up to $\sim 50\,\mathrm{pc}$) using interferometers such as ALMA.

Employing data from this program, I first investigated the physical properties of dust in M33 by analyzing its far-IR emission. I constructed maps of dust temperature, the X_{CO} conversion factor, and hydrogen column density using the unique wavelength coverage (160, 250, 350, and $500\,\mu\mathrm{m}$) provided by Herschel. Then I performed a census of the molecular cloud population that I detected in M33 in dust and CO and compared the cloud properties to Milky Way clouds. For that, I used the publicly available data from an IRAM Large Program (Gratier et al., 2010; Druard et al., 2014) that was designed to map M33 with the multi-beam receiver HERA at the 30m telescope in the CO$(2-1)$ line transition (see below).

3.7 IRAM 30m

The Institute for Radio Astronomy in the Millimeter (IRAM) operates two of the most advanced radio astronomy facilities in the world. One is the Northern Extended Millimetre Array (NOEMA) in the french Alps, an interferometer that consists of an array of 12 individual 15-meter antennas. The other one is the IRAM 30m single-dish telescope with a diameter of 30 m, located in Spain's Sierra Nevada, to observe astronomical objects in the (sub)millimeter range. It ranks among the world's largest and most sensitive millimeter wavelength telescopes.

3.8 APEX

The Atacama Pathfinder Experiment (APEX) is a 12 m diameter radio telescope. It was developed by the Max Planck Institute for Radio Astronomy (MPIfR), the European Southern Observatory (ESO), and the Swedish Onsala Space Observatory (OSO) near the radio interferometer Atacama Large Millimeter Array (ALMA). Located in the Chilean Atacama Desert at 5064 m above sea level, this site is ideal for submillimeter observations because its dry air limits water vapor absorption.

This thesis benefited from APEX, which provided CO data at several transition lines.

Chapter 4

Astrophysical Concepts and Objectives of Observations

Throughout my Ph.D., I utilized various pre-existing techniques – such as Dendrograms with `astrodendro` (Rosolowsky et al., 2008), or the radiative transfer models `RADEX` (van der Tak et al., 2007), and `SimLine` (Ossenkopf et al., 2001) (see Sect. 2.1.5) – alongside methods that I have developed independently. These include a modified and improved approach to generate H_2 column density maps (Palmeirim et al., 2013) and fitting of the radiative transfer equations for [C II] line profiles on observational data to determine the missing [C II] flux caused by self-absorption. I also implemented additional methods such as N-PDF construction and fitting, among others, too numerous to detail comprehensively in this thesis. I have developed and written these data analysis methods in Python, which are also used by other members of the FEEDBACK consortium.

In this chapter, I first briefly describe the astrophysical concepts of stellar radiative and wind feedback (Sects. 4.1 and 4.2), followed by a description of PDRs (Sect. 4.3), and important ingredients of PDRs, such as [C II] and CO (Sects. 4.4 and 4.5). Next, I present the selected sources and their data sets in Sect. 4.6, followed by the tools used to analyze the data presented in Sect. 4.7. Lastly, I describe the methods that I have developed to determine the missing [C II] flux by fitting [C II] line profiles to observational data due to self-absorption using radiative transfer equations.

4.1 Stellar Radiative Feedback

Radiative feedback from stars fundamentally affects the dynamics and evolution of the ISM and star formation. Massive stars, with their high luminosities and energetic radiation, inject energy and momentum into their environment. Understanding radiative feedback is essential for constructing accurate galaxy evolution models, interpreting observations of star-forming regions, and understanding the ISM life cycle (Osterbrock and Ferland, 2006; Murray and Rahman, 2010; Krumholz, 2014).

Radiative feedback encompasses several mechanisms by which stellar radiation interacts with the surrounding gas and dust. UV photons ionize neutral hydrogen, creating ionized H II regions and heating the gas to form Strömgren spheres. They can also dissociate molecular hydrogen, affecting the chemistry and cooling of the gas. Dust grains absorb stellar radiation, heat up, and re-emit in the infrared, influencing the ISM's thermal balance. Momentum transfer from photons to gas and dust grains can drive outflows and impact the dynamics of the ISM.

4.1.1 Strömgren sphere

The radiative feedback of hot stars ionizes hydrogen gas, leading to the formation of Strömgren spheres (Strömgren, 1939). The Strömgren radius R_S reaches equilibrium when the star's ionizing photon emission rate Q_H is balanced by the recombination rates in the ionized gas, ensuring that the number of ionizing photons equals the number of recombinations. Here, n_e and n_p denote the number densities of electrons and protons, respectively, which are approximately equal in a fully ionized hydrogen region ($n_e \approx n_p$). Thus, the Strömgren radius R_s is given by

$$R_\mathrm{S} = \left(\frac{3Q_\mathrm{H}}{4\pi n_e n_p \alpha_\mathrm{B}} \right)^{1/3} . \tag{4.1}$$

The Strömgren sphere represents the initial size of the ionized region prior to hydrodynamic expansion.

The injected total momentum of the ionizing radiation with an escape fraction equal to zero can be described as

$$\dot{p}_\mathrm{ion,th} = 4k_\mathrm{B}\, T \sqrt{\frac{3\pi\, Q_i r_\mathrm{IF}}{\alpha_\mathrm{B}}} , \tag{4.2}$$

where k_B is the Boltzmann constant, T the temperature, r_IF the radius of the ionization front, and α_B the hydrogen recombination coefficient. These equations describe the size and dynamics of the ionized regions around massive stars, shaping the interstellar medium and influencing star formation processes.

In environments with uniform densities similar to star-forming molecular clouds, solutions generally predict that the ionization front initially propagates rapidly outwards during the gas's recombination time. In this phase, ionizing photons fail to reach the ionization front, leading the H II region to attain a state of photo-ionization equilibrium, wherein the recombination rate equals the star's ionizing photon emission rate. The recombination time in dense molecular cloud gas is much shorter than the lifespan of massive stars, which emit large amounts of ionizing radiation. Once photo-ionization equilibrium is established, the H II region mainly expands due to thermal expansion at velocities below the sound speed in the ionized gas.

As the ionization front progresses into regions of lower gas density, such as the edges of a molecular cloud, it accelerates because diffuse gas absorbs ionizing photons less efficiently than dense material within the cloud. In such an inhomogeneous medium, the H II region shifts from photo-ionization equilibrium, causing the front to move outwards at supersonic speeds. This evolution is termed "champagne" flow, a concept introduced by Tenorio-Tagle (1979), who modeled the transition from a dense cloud to the surrounding diffuse medium using a density step function.

4.2 Stellar Wind Feedback

A variety of models have been formulated to characterize stellar wind. A recent approach by Lancaster et al. (2021a) introduces a model for bubble evolution driven by stellar winds that emphasizes strong interface cooling from turbulent mixing. The authors propose that highly efficient cooling at the interface between the stellar wind and the surrounding medium reduces the injected energy by up to 99%, making the expansion momentum-driven ($p \propto t$) due to this energy loss. This differs from the energy-driven model by Weaver et al. (1977) ($E \propto t$), which impacts gas dispersal in star-forming regions and thereby leads to lower expansion rates and sizes.

Another recent approach invokes a wind bubble around a star to describe the early evolution of the wind bubble expanding in a power-law density field (Geen and de Koter, 2022). The following sections briefly lay out the description of the classical model for a uniform gas distribution (Weaver et al., 1977) and the more contemporary model based on a power-law distribution (Geen and de Koter, 2022).

4.2.1 Stellar wind in a uniform distribution

The classical analysis of the structure and evolution of a bubble created by a constant-luminosity wind in a uniform medium was outlined by Weaver et al. (1977) (also see Avedisova 1972, Castor et al. 1975, and McCray and Kafatos 1987). This section focuses on the pressure-driven (PD) phase, which is generally considered as the most influential during the wind-blown bubble's evolution in a star-forming cloud influenced by a single massive star or cluster. During this phase, the wind injects energy that accumulates in the hot, overpressured gas within the expanding bubble relative to the surrounding cloud. As it expands, the bubble accelerates and compresses the ambient medium into a dense shell around the low-density interior. When the bubble's expansion becomes supersonic relative to the ambient gas (typical for cold gas in GMCs), the supersonic motion shocks the

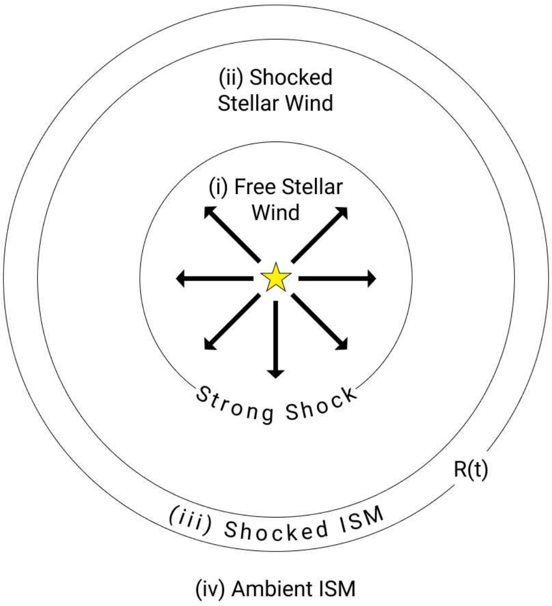

Figure 4.1: Schematic illustration showing the expanding bubble's structure driven by winds. This classical model by Weaver et al. (1977) shows a pressure-driven bubble with uniform cooling at the shock front.

ambient gas to high temperatures, which then rapidly cools to form a dense shell around the hot bubble. According to Weaver et al. (1977), the solution comprises four regions: (i) free hypersonic wind; (ii) shocked stellar wind; (iii) shocked, cooled shell of interstellar gas; (iv) ambient interstellar gas. This structure is presented schematically in Fig. 4.1.

Assuming all thermal energy from the leading shock is radiated away and the bubble's interior stays non-radiative, the similarity solution for the bubble radius is

$$R = R_{\mathrm{W}}(t) \equiv \left(\frac{125}{154\,\pi}\right)^{1/5} \left(\frac{\mathcal{L}_{\mathrm{W}} t^3}{\bar{\rho}}\right)^{1/5} , \tag{4.3}$$

where $\mathcal{L}_{\mathrm{W}}$ represents wind luminosity (i.e. the mechanical power of the material ejected by the star), $\bar{\rho}$ denotes the background mass density and t is time. The subscript "W" refers to the Weaver solution. The pressure within the shocked stellar wind changes as

$$P = P_{\mathrm{W}}(t) \equiv \frac{5}{22\,\pi} \left(\frac{125}{154\,\pi}\right)^{-3/5} \left(\frac{\mathcal{L}_{\mathrm{W}}^2 \bar{\rho}^3}{t^4}\right)^{1/5} . \tag{4.4}$$

In the PD bubble solution, the shell's radial momentum is determined by

$$p_r = p_{\mathrm{W}}(t) \equiv \frac{4\pi}{5} \left(\frac{125}{154\,\pi}\right)^{4/5} (\mathcal{L}_{\mathrm{W}}^4 \bar{\rho} t^7)^{1/5} , \tag{4.5}$$

About 45% of the total wind energy $\mathcal{L}_{\mathrm{W}} t^7$ emitted by time t is stored as thermal energy within the bubble

$$E_{\mathrm{th,W}} = \frac{3}{2} P_{\mathrm{W}} V_{\mathrm{W}} = \frac{5}{11} \mathcal{L}_{\mathrm{W}} t , \tag{4.6}$$

where V_{W} represents the bubble's volume. Concurrently, only 19% is converted into the kinetic energy of the swept-up shell

$$E_{\mathrm{kin,W}} = \frac{1}{2} M_{\mathrm{sh}} \left(\frac{\mathrm{d}R_{\mathrm{W}}}{\mathrm{d}t}\right)^2 = \frac{15}{77} \mathcal{L}_{\mathrm{W}} t , \tag{4.7}$$

for which $M_{\mathrm{sh}} = 4\pi\bar{\rho}R^3/3$ assumes that all the swept-up gas is concentrated in the shell (where M_{sh} denotes the mass contained in the shell). The remaining $\sim 35\%$ of the wind energy is assumed to be radiated away from the ISM gas that was shocked and then efficiently cooled at high density as it was swept into the progressing front of the bubble. Notably, in the simplest PD bubble model, radiative cooling occurs only for the post-shock, swept-up ISM gas. However, Weaver et al. (1977) also discusses late-stage evolution when the bubble's interior cools sufficiently to become radiative.

4.2.2 Stellar wind in a power-law density distribution

The Weaver model describes the growth of an adiabatic wind bubble in a uniform medium with a surrounding shell of swept-up interstellar gas. A recent and more general approach, which contains the Weaver model as a limit, offers a solution for a wind bubble expanding into a power-law density distribution (Geen and de Koter, 2022) and aligns more closely with observational data on how stellar winds shape bubbles.

The dense medium initially traps ionizing radiation, creating a thin photo-ionized layer inside the dense neutral shell swept up around the wind bubble. Stellar winds, injected at high velocity, heat the bubble's interior to high temperatures. Weaver et al. (1977) describes this wind bubble's internal structure as featuring a central "free-streaming" area where the wind material travels supersonically until it shocks the gas, raising temperatures exceeding 10^6 K. Collisional ionization occurs within the wind bubble's interior. Hence, the star's ionizing radiation flux remains largely depleted until it encounters the wind bubble's dense shell's inner edge at r_w, where it begins to photo-ionize the gas. This thin photo-ionized shell attains a temperature around 10^4 K, determined by the equilibrium of cooling and heating of the gas.

In the absence of radiation pressure, the region maintains a uniform density sustained solely by thermal pressure. Introducing radiation pressure creates an internal pressure difference due to the larger surface area at greater radii and the presence of dust. A cold, dense neutral shell forms from material accumulated by the wind bubble; when this shell overflows, its neutral component vanishes, allowing ionizing radiation to penetrate the neutral power-law density field beyond.

This picture corresponds to the steeper power-law density fields observed near young massive stars. According to Geen and de Koter (2022), a fiducial density field is typical around very young massive stars in star-forming cores that have just ended the protostellar phase and is known as a "singular isothermal sphere" with a power-law index of −2.

The model presented by Geen and de Koter (2022) permits a wind bubble to be fully confined by dense gas along specific sightlines, resembling a cavity or an outflow confined to a small solid angle around the star. In this model, the wind bubble subtends a solid angle Ω, approaching 4π as it expands isotropically into a uniform density field. A spherically symmetric power-law density distribution that describes cold, neutral gas enveloping a young massive star is given by

$$n(R) = n_0 (R/R_0)^{-\omega} \ , \tag{4.8}$$

where $n(R)$ represents the hydrogen number density at a distance R, n_0 denotes the density at a reference radius R_0 and ω is the exponent of the power-law. A value of $\omega = 0$ corresponds to a uniform density field, while $\omega = 2$ characterizes a singular isothermal sphere.

The thermal energy E_b in the shocked gas within the wind bubble is given by

$$E_b = \frac{3}{2}\frac{\Omega}{3} R_w^3 P_w \ , \tag{4.9}$$

where Ω represents the solid angle subtended by the wind bubble, R_w denotes the radius of the wind bubble, and P_w signifies the pressure exerted by the wind bubble on the shell's interior. Geen and de Koter (2022) find

$$E_b = \left(\frac{5-\omega}{11-\omega}\right) \mathcal{L}_w t \ , \tag{4.10}$$

where t represents the time since the onset of the wind.

Solving these equations, assuming that $R_w \propto t^B$, where B represents a power-law index, yields

$$R_w(\omega, t) = (A_w(\omega, \Omega) \mathcal{L}_w \rho_0^{-1} R_0^{-\omega} t^3)^{1/(5-\omega)} \ , \tag{4.11}$$

where

$$A_w(\omega, \Omega) = \frac{4\pi}{\Omega} \frac{(1-\omega/3)(1-\omega/5)^3}{(1-2\omega/7)(1-\omega/11)} \frac{250}{308\pi} \ . \tag{4.12}$$

For a parameter set of $\Omega = 4\pi$ and $\omega = 0$, this becomes the "Weaver" solution (Eq. 21 of Weaver et al., 1977). Given $\omega = 2$ and $\Omega = 4\pi$, the preceding Eq. 4.11 transforms into

$$R_{\omega=2}(t) = 13.9\,\mathrm{pc} \left(\frac{\mathcal{L}_w}{10^{36}\,\mathrm{erg/s}}\right)^{1/3} \left(\frac{n_0}{1000\,\mathrm{cm}^{-3}}\right)^{-1/3} \times \left(\frac{t}{1\,\mathrm{Myr}}\right) \ , \tag{4.13}$$

with a constant expansion velocity of

$$v_{\omega=2}(t) = 13.5\,\mathrm{km\,s^{-1}} \left(\frac{\mathcal{L}_w}{10^{36}\,\mathrm{erg/s}}\right)^{1/3} \left(\frac{n_0}{1000\,\mathrm{cm^{-3}}}\right)^{-1/3} . \tag{4.14}$$

This solution particularly applies to near young massive stars (e.g., Lee and Hennebelle, 2018; Geen and de Koter, 2022) and is used in the analysis of the stellar feedback in the compact H II region in RCW79 (refer to Sect. 5.3.2). Further outward, where the sharp density profile merges with the cloud background, the solution likely shifts to a Weaver-like state or becomes disrupted by cloud clumping and turbulence.

In summary, stellar feedback in the form of radiation and wind has a strong impact on the surrounding molecular cloud, regardless of which model is considered. The compressed neutral gas shell may fragment and initiate new star formation ("collect-and-collapse" scenario by Elmegreen and Lada 1977), or the cloud may instead disperse (Dale et al., 2012). Which of the processes dominates depends on many factors such as initial mass of the cloud, geometry, spectral type of the exciting star(s), etc.

4.3 Photo-Dissociation Regions

Intense stellar Far-UV radiation interacts with nearby atomic and molecular gas that photodissociates molecules, thereby creating regions known as photodissociation regions (PDRs).These regions typically occur around OB-type stars that release a significant number of energetic photons in the 6 to 13.6 eV range, thereby influencing the cloud's structure, thermal balance, and chemistry (Tielens and Hollenbach, 1985a). Accordingly, PDRs are also sometimes called photon-dominated regions (Sternberg and Dalgarno, 1995).

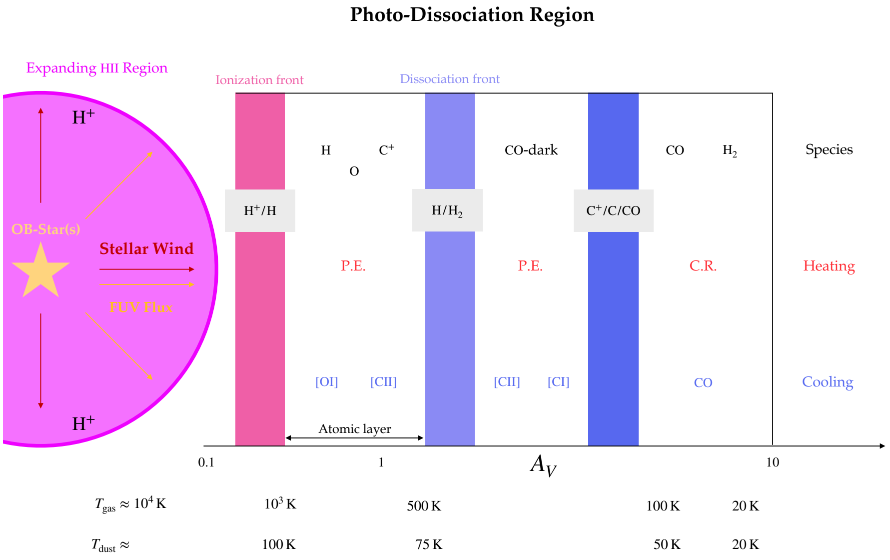

Figure 4.2: Schematic illustration of a plane-parallel PDR. The primary heating mechanisms are colored red. At the PDR surface, P.E. prevails, whereas C.R. ionization dominates deeper within the cloud. The main cooling lines for each PDR layer appear in blue. Note that the exact values of A_V vary with the G_0/n ratio; a lower G_0/n or a reduced UV field shifts the hydrogen and carbon transitions to lower A_V. This illustration is based on Goicoechea et al. (2016) and Wolfire et al. (2022).

Photons with energies greater than 13.6 eV ionize hydrogen, forming an H II region around the star and separating the fully ionized gas from the dense molecular gas. The PDR lies between the hot ($T \sim 10^4$ K) ionized region and the molecular phase and features a layered structure that contrasts with the sharp boundary of an H II region, as illustrated for a simple, homogeneous plane-parallel PDR model in Fig. 4.2. Carbon has an ionization potential of 11.3 eV. Absorption of all photons with energies $\geqslant 13.6$ eV leaves atoms with higher ionization potentials, such as oxygen and nitrogen, in a neutral state. Nonetheless, these hot ionized H II regions exhibit low visual extinctions ($A_V < 0.1$).

Near the surface of the PDR, the photoelectric effect heats hydrogen gas to $100-1000$ K by releasing electrons that collide with hydrogen atoms. This process, also known as photoelectric heating (P.E.), transfers surplus energy from electrons released by grains and polycyclic aromatic hydrocarbons (PAHs) to the surrounding environment (Tielens and Hollenbach, 1985a). Cooling, predominantly through fine-structure line emissions of [C II] 158 μm, [O I] 63 μm and high-J rotational transitions in CO, offsets this heating. As a result, distinct profiles and layers of CO, C, and C^+ emerge, each exhibiting different temperatures and densities (see Fig. 4.2), thereby regulating the energy budget. The abundance of C^+ decreases deeper into the cloud as a result of the competition between C^+ recombining into C or CO and C being photo-ionized into C^+. Consequently, the CO/C/C^+ transition is crucial to define the energy balance and line intensities of PDRs.

The low ionization potential of C^+ makes it abundant in H II regions and on UV-illuminated surfaces of atomic and molecular clouds. It is produced through the photo-ionization of carbon

$$\mathrm{C} + h\nu \rightarrow \mathrm{C}^+ + \mathrm{e}^- \ . \tag{4.15}$$

The dominant reactions for C^+ destruction are radiative recombination into C with free electrons near the ionization front,

$$\mathrm{C}^+ + \mathrm{e}^- \rightarrow \mathrm{C} + h\nu \ . \tag{4.16}$$

Further inside, radiative association with H_2 (Röllig et al., 2006) becomes important, forming CH or CH_2, which then reacts with O to produce CO,

$$\mathrm{C}^+ + \mathrm{H}_2 \rightarrow \mathrm{CH}^+/\mathrm{CH}_2^+ + h\nu \ . \tag{4.17}$$

Neutral carbon plays an important role in molecular chemistry by undergoing simultaneous formation and destruction, which is essential for synthesizing molecules such as CO. It forms via the re-ionization of C^+ (see Eq. 4.16), as well as charge exchange with sulfur S, and CO photodissociation (Röllig and Ossenkopf, 2013),

$$\mathrm{C}^+ + \mathrm{S} \rightarrow \mathrm{C} + \mathrm{S}^+ \ , \tag{4.18}$$
$$\mathrm{CO} + h\nu \rightarrow \mathrm{C} + \mathrm{O} \ . \tag{4.19}$$

As one progresses deeper into the cloud, the FUV intensity decreases and subsequently reduces the photodissociation of molecules, which leaves a molecular layer. Within the range of $A_V \sim 0.1 - 0.8$ (refer to Schneider et al. 2022 and references therein), we observe the H I-to-H_2 transition zone. Further into the cloud at $A_V \sim 2 - 4$, neutral carbon C and CO emerge through a series of ion-neutral interactions. The specific A_V values depend on the ratio of the radiation field to density, G_0/n. Hence, a lower G_0/n or simply a weaker UV field shifts the hydrogen and carbon transitions to lower A_V values (Wolfire et al., 2022).

Gas in regions where hydrogen becomes molecular but CO remains undetectable are referred to as "CO-dark" H_2 gas (Grenier et al., 2005; Wolfire et al., 2010). Metallicity, which refers to the abundance of elements heavier than hydrogen and helium, has a substantial impact on molecular clouds: At lower metallicity, there is less dust that leads to reduced dust shielding and self-shielding of UV radiation; as a result, FUV radiation can penetrate deeper into the cloud, dissociate CO, and create a larger layer of emitting ionized carbon around a smaller, CO-rich core (Tielens and Hollenbach, 1985a,b; Poglitsch et al., 1995; Stark et al., 1997; Wilson, 1997; Bolatto et al., 2013). This effect is amplified as the decrease in CO abundance further weakens CO self-shielding. H_2 also undergoes photodissociation through absorption of Lyman-Werner band photons. However, it can form substantial column densities to self-shield at moderate extinction (A_V) within the C^+ emitting region, thus becoming a significant mass reservoir. Consequently, a large molecular hydrogen reservoir exists outside the CO-emitting region, the CO-dark H_2 gas (Röllig et al., 2006; Wolfire et al., 2010; Madden et al., 2020; Schneider et al., 2023). Deeper within the cloud, the temperatures decline to around $T \sim 10\,\mathrm{K}$ and the gas remains molecular. Cosmic-ray ionization (C.R.) primarily heats the gas, and cooling mainly occurs through low-J rotational transitions of CO molecules.

4.3.1 Numerical models

The balance between UV photodissociation and atomic hydrogen recombination on grain surfaces regulates the atomic-to-molecular transition in the ISM (Tielens and Hollenbach, 1985a; Hollenbach et al., 1991; Sternberg and Dalgarno, 1995; Kaufman et al., 1999; Le Petit et al., 2006). Numerical models require iterative solutions to achieve a balance between the formation and destruction of chemical species (Federman et al., 1979), with local temperature affecting reaction rates. These models incorporate cooling via spectral line emissions and heating from photoelectric effects and cosmic rays (Sternberg, 1988; Krumholz et al., 2008; Krumholz, 2014; Bialy and Sternberg, 2016; Bialy et al., 2017).

Astrochemical ISM models originating from the 1950s (Bates and Spitzer, 1951) have evolved to include detailed processes, particularly molecular hydrogen formation on grain surfaces (Tielens and Hagen, 1982; Garrod, 2013). Early PDR models aimed to explain fine-structure emission in low-density gas (Melnick et al., 1979; Stacey et al., 1983; Glassgold and Langer, 1974, 1975; Black and Dalgarno, 1977; de Jong et al., 1980), while later models focused on higher-density scenarios (Tielens and Hollenbach, 1985a; Sternberg and Dalgarno, 1989). Notable modern models include tools like the PDR Toolbox (Kaufman et al., 1999; Kaufman et al., 2006; Pound and Wolfire, 2023), which provides computed model grids, and the Meudon PDR code (Le Petit et al., 2006), a plane-parallel model emphasizing radiative processes and chemical reactions.

Figure 4.2 illustrates a plane-parallel PDR. However, in reality, radiation penetrates from various directions, heating and photodissociating the gas from all sides. This leads to a clumpy distribution of the gas. Observations that molecular clouds are clumpy, porous, or fractal have historically driven this model geometry (e.g., Stutzki et al., 1988). More accurate modeling of this scenario has led to the clumpy PDR model KOSMA-τ (Röllig et al., 2006; Röllig and Ossenkopf-Okada, 2022), which has been developed at the University of Cologne – in the group where I work on my Ph.D. – in collaboration with Tel Aviv University. The KOSMA-τ model has been used in numerous publications (e.g., Gierens et al., 1992; Stoerzer et al., 1996; Ossenkopf et al., 2013; Schneider et al., 2018), and is continuously improved. It also forms an integral part of the PDR toolbox (see above).

In summary, given that the rotational energy levels of CO transitions are easily excited at low densities and temperatures (Schinnerer and Leroy, 2024), CO serves as an excellent tracer for dense molecular clouds. H I mainly occupies the interstellar regions that lie between these dense clouds, whereas [C II] can originate from both the illuminated surfaces of molecular clouds and cold atomic gas flows.

4.4 The [C II] Line

As one of the strongest cooling lines (Tielens and Hollenbach, 1985a) in the ISM and an excellent indicator of gas dynamics (Pabst et al., 2019; Luisi et al., 2021; Kabanovic et al., 2022), the [C II] line primarily traces the interface between ionized and molecular gas in PDRs. It is particularly effective in regions with moderate UV radiation fields, where it can originate from both ionized and neutral gas phases (Mookerjea et al., 2011). Moreover, the [C II] emission is often used to estimate the SFR in galaxies, although its effectiveness can vary with metallicity and the presence of diffuse ionized gas (De Looze et al., 2014).

The [C II] line effectively traces gas at densities between approximately $10\,\mathrm{cm}^{-3}$ (collisions with electrons in H II regions) and up to $10^4\,\mathrm{cm}^{-3}$ (collisions with atomic and molecular hydrogen) and varying temperatures of a few hundred Kelvin (in PDRs), making it particularly useful in low-density environments where the [O I] $63\,\mu$m line may be less effective (Goldsmith et al., 2012). In contrast, the [O I] line serves as a key tracer of denser, warm gas in PDRs and is frequently employed to study the physical conditions in star-forming regions. It is especially sensitive to high-density environments (typically above $10^4\,\mathrm{cm}^{-3}$) and high temperatures of up to a few 100 K and provides insights into heating processes within molecular clouds (Leurini et al., 2015). Additionally, [O I] emission is typically associated with regions of active star formation and can probe the dynamics of outflows and jets in these environments (Contursi et al., 2013; Schneider et al., 2018).

4.4.1 [C II] History

The first calculations predicted the [C II] transition wavelength to be approximately at $156\,\mu$m (Schaefer and Klemm, 1970). Later, Russell et al. (1980) detected it after receiving a precise estimate via private communication, reporting the detection in M42 and NGC2024 at $174.4 \pm 0.4\,\mu$m. A discovery that led to the modeling of heating and cooling mechanisms as well as photodissociation chemistry in H II–molecular cloud interfaces (de Jong et al., 1980). This effort condensed into the “standard” Tielens and Hollenbach (1985a) photodissociation region model (refer to Sect. 4.3). The past four decades have affirmed [C II] emission in PDRs as a tracer of active star formation in the ISM from the Milky Way far to galaxies at high redshift and thus throughout the universe’s age (Stutzki et al., 2023).

Cooksy et al. (1986) confirmed the [C II] wavelength and reported the frequencies of three [^{13}C II] hyperfine satellites, which are crucial for measuring [C II] optical depth. Observing the FIR spectral range of the [C II] line remains challenging due to the Earth’s atmosphere being significantly opaque at $158\,\mu$m, requiring airborne or space observatories, and by technological constraints. Advances in continuum detector materials and Fabry-Perot meshes for spectral resolution have led to a series of improved direct detection experiments starting with the Lear-Jet and KAO (Kuiper Airborne Observatory) facilities to the BICE balloon experiment, ISO satellite mission (1995-1998), PACS on the Herschel Space Observatory (2009-2013), and FIFI-LS on SOFIA (2013-2022). Similarly, high-resolution heterodyne spectrometers, as initiated by early KAO work (Betz and Zmuidzinas, 1984), have reduced receiver temperatures by two orders of magnitude and increased observing speed by four orders (see radiometer equation in Sect. 3.4). The advent of these advanced observational technologies and SOFIA (Young et al., 2012) have enabled extensive mapping of [C II] emissions, providing insights into the kinematics of star-forming regions and the impact of stellar feedback on the ISM. Furthermore, the GREAT (Heyminck et al., 2012) and upGREAT (Risacher et al., 2016) heterodyne array receivers have further enhanced the resolution and sensitivity of [C II] observations, allowing for detailed studies of molecular clouds and their interactions with radiation sources. Only recently the [C II] line was shown to trace the CO-dark gas (Schneider et al., 2023). This was the first time C^+ was detected in low-density ($\sim 100\,\mathrm{cm}^{-3}$) atomic gas with colliding flows that form molecular clouds (as predicted in simulations Clark et al., 2019).

Other early observations of spectrally resolved [C II] emission in M42 (Boreiko et al., 1988) revealed that [C II] can be optically thick, after its first detection in NGC2024 and M42 by Russell et al. (1980). Many observations with (up)GREAT onboard SOFIA further confirmed that the [C II] line is generally optically thick in regions such as M43, the Horsehead Nebula, Monoceros R2, and M17-SW (Guevara et al., 2020). In their study, Guevara et al. (2020) implemented the two-layer multicomponent model to fit radiative transfer equations to the [C II] spectra, successfully separating the warm emitting layer from the underlying cold absorbing gas. Their analysis revealed that a significant portion of ionized carbon resides within a cold absorbing layer; however, the origin of the substantial column densities of cold ionized carbon remains not fully understood.

4.5 X_{CO} Conversion Factor

The X_{CO} conversion factor (CO-to-H_2) is crucial for estimating the total mass of molecular gas within galaxies, which is essential for understanding star formation processes, galactic evolution, and comparing molecular gas content across various galactic environments. Precise determination of X_{CO} is crucial for minimizing uncertainties in estimates of molecular gas mass. Achieving this precision requires careful calibration using independent measurements, such as dust emission, as shown in Keilmann et al. (2024a). Insight into how X_{CO} depends on environmental conditions can refine models of molecular cloud formation and evolution, especially in diverse galactic settings.

The typical Milky Way value of X_{CO} is approximately $2 \times 10^{20}\,\mathrm{cm}^{-2}\,(\mathrm{K\,km\,s}^{-1})^{-1}$. However, this value varies significantly with environmental conditions such as metallicity, radiation field, and the dynamical state of the molecular clouds (Bolatto et al., 2013). In low-metallicity environments, such as dwarf galaxies or M33, X_{CO} may be higher due to reduced CO abundance relative to H_2. However, the X_{CO} conversion factor may be skewed due to its strong dependence on factors like metallicity, dust content, and the interstellar radiation field (Bolatto et al., 2013), causing it to fluctuate with environmental changes. As demonstrated by Ramambason et al. (2024) and Keilmann et al. (2024a), the conversion factor for such galaxies can remain low and exhibit significant local variation.

4.6 Selection of Sources

Throughout this thesis, I studied various regions (Galactic and extragalactic sources), each with specific objectives. This section provides a brief overview of these sources and the goals behind their study.

4.6.1 Draco

We analyzed the H I-H_2 transition by selecting the Draco intermediate-velocity cloud (IVC), a region with a weak UV field at the onset of molecular cloud formation. High-latitude IVCs, which are part of the Milky Way's H I halo, originate from either a galactic fountain process or extragalactic gas infall and typically contain molecular gas with detectable CO emission. Some IVCs also exhibit high-velocity cloud (HVC) components (mainly atomic) alongside local velocity gas (LVC) that contains both atomic and molecular material. In addition to Draco, we examined another IVC (Spider) and low-density clouds at local velocities (Polaris and Musca). These conditions allow us to study the highly dynamic processes of early molecular cloud formation in UV-weak, low-density environments.

Datasets The study used [C II] and CO data obtained with PI-programs on SOFIA and at the IRAM 30m telescope, respectively. It was complemented with archival data, i.e., H I 21 cm observations from the Dominion Radio Astrophysical Observatory (DRAO) and the Green-Bank-Telescope (GBT) data along with all-sky H I data from the Effelsberg-Bonn H I survey (EBHIS) and dust data from Herschel.

4.6.2 M33

M33 is a flocculant Sc-type spiral galaxy located nearby (847 kpc, Karachentsev et al., 2004) with an inclination angle of 56°. Its proximity enables good spatial resolution with minimal line-of-sight confusion, making it an excellent extragalactic target. Since M33 is in a different evolutionary stage than the Milky Way – with less mass and metallicity, for instance – it provides a great opportunity not only to investigate molecular cloud properties within its galactic environment, but also to study systematic differences of molecular cloud properties depending on different environments (the Milky Way and M33). This helps to understand how cloud properties (and hence star formation) change as a function of environment.

Datasets I was provided the variable emissivity index β map along with the corresponding dust temperature data from Tabatabaei et al. (2014) and used the Herschel archival dust data (PACS and SPIRE), the IRAM 30m CO$(2-1)$, and the VLA H I data.

4.6.3 RCW79

RCW79 constitutes one of the eleven FEEDBACK sources and is characterized by an H II region created by a cluster of twelve O-type stars. It shows a large expanding shell traced by [C II] emission, making it an ideal site to study stellar feedback mechanisms, with expansion velocities reaching up to 25 km s^{-1}. In the southeastern part of the large-scale shell, a compact H II region has formed around an O star that directly ionizes the surrounding medium via stellar radiation and wind; here, the expansion velocity in this area is considerably lower than in typical H II regions explored by the FEEDBACK program, and is only around 2.6 km s^{-1}. RCW79 also shows a [C II]-deficit, which arises in the compact H II region, thus providing a suitable site to investigate the infamous [C II]-deficit accounting for different ISM cooling processes between the dust FIR continuum and the [C II] cooling pathways. In Bonne et al. (2023), we have demonstrated that the molecular cloud is eroded by stellar feedback.

Datasets For RCW79, FEEDBACK data of [O I] and [C II] obtained with SOFIA, and my PI data from APEX (^{12}CO and ^{13}CO $6 \rightarrow 5$ and C^{18}O $3 \rightarrow 2$) were used. In addition, I used archival data, i.e., FIR flux maps from Herschel, radio continuum (843 MHz), Spitzer, and WISE.

4.7 Tools for Data Analysis

This section provides a brief description and a selection of tools and methods that I have used and developed during this thesis, such as Dendrograms, N-PDFs, or the automatic detection of signal peaks used to analyze the data. I also describe the method to determine the missing [C II] flux by fitting [C II] line profiles to observational data due to self-absorption using radiative transfer equations.

4.7.1 Generating the high-resolution N_{H_2} map

Hydrogen column density maps in Galactic and extragalactic studies are commonly constructed by fitting the SED to Herschel flux densities measured between 160 and 500 μm (see Fig. 4.3 for an example plot). The method fits the dust temperature T_d, β, and the surface density Σ using a one-component graybody model (modified Planck function) on a pixel-by-pixel basis. The graybody function takes the form $I_\nu = \kappa_\nu B_\nu(T_\mathrm{d})\Sigma$, where I_ν denotes the surface brightness at frequency ν and κ_ν represents the dust opacity per unit (dust+gas) mass (refer to Sect. 2.2.5). The method calculates the surface density as $\Sigma = \mu_m \, m_\mathrm{H} \, N_\mathrm{H}$, with $\mu_m = 1.36$ as the mean molecular weight and the total hydrogen column density N_H defined as $N_\mathrm{H} = N_\mathrm{HI} + 2 \times N_{\mathrm{H}_2}$, accounting for the proton number. In this conventional approach, it is essential to first smooth all flux maps to match the 36″ angular resolution of the 500 μm map, which serves as the lowest common resolution for the final map (e.g., André et al., 2010).

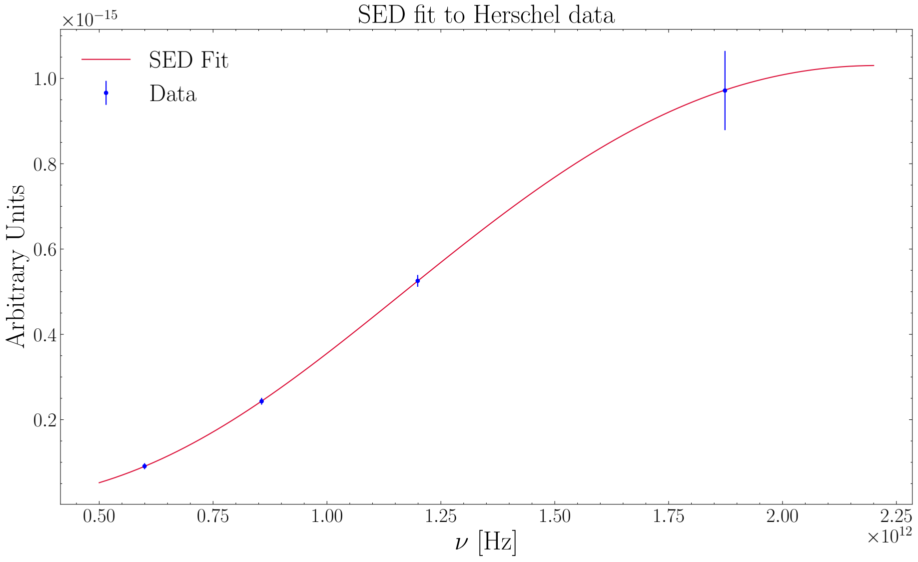

Figure 4.3: Example SED fit to 4-band Herschel data. The data points correspond to the wavelengths (frequencies) of 160 μm (1.874 THz), 250 μm (1.199 THz), 350 μm (0.857 THz), and 500 μm (0.6 THz), respectively.

While the above mentioned method is simple, it suffers from a lower angular resolution of the final map. An alternative and more advanced technique attains a column density map with a higher angular resolution at 18.2″. Proposed by Palmeirim et al. (2013), it relies on a multi-scale decomposition of the flux maps and had not yet been applied to extragalactic data. In Keilmann et al. (2024a), I made the first effort to utilize a method similar but adjusted to that of Palmeirim et al. (2013) and describe the application to extragalactic data. In the following, I present a description of this method aimed at providing a more intuitive access.

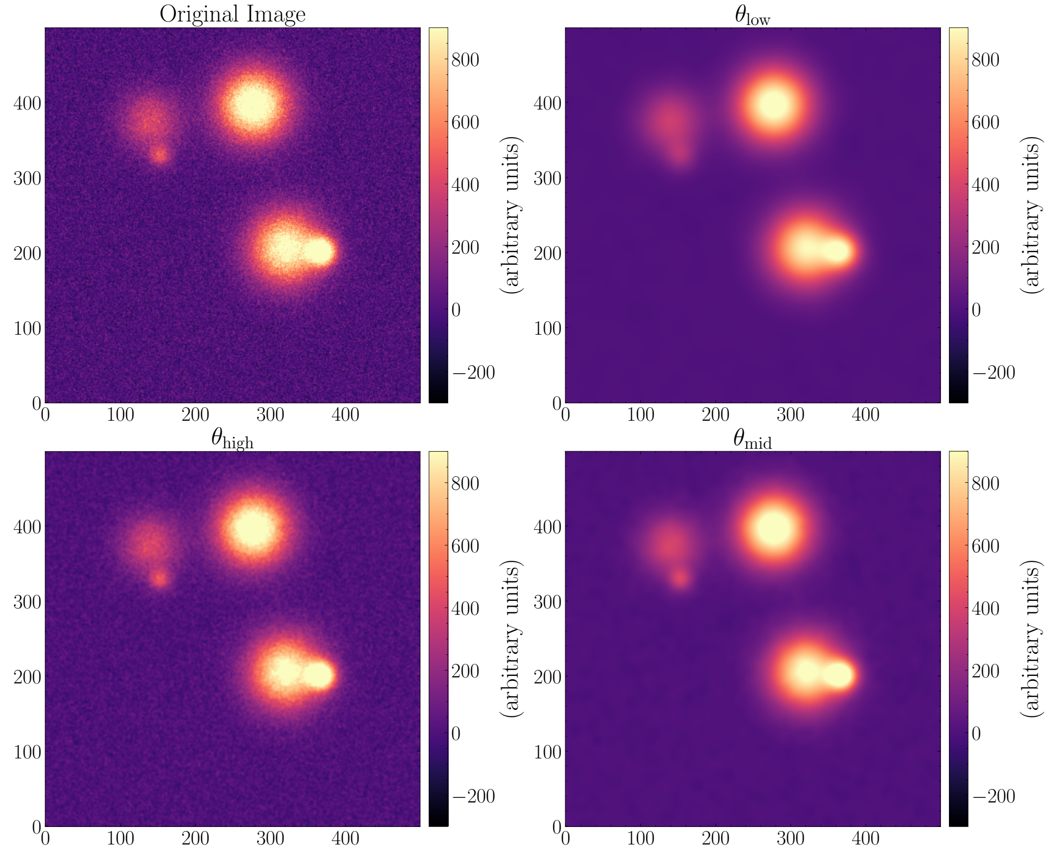

Figure 4.4: Synthetic GMC Sources with synthetic noise. The upper left panel shows a synthetic GMC distribution, which serves as an intrinsic gas distribution. The lower left depicts a smoothed version with an Gaussian filter with 1σ and serves a the “high-resolution” distribution we want to achieve (corresponds to 18.2″ from the SPIRE 250 μm observations). The lower right shows the correspondingly smoothed version with intermediate resolution (5σ Gaussian kernel and SPIRE 250 μm). The upper right panel shows the distribution with the lowest resolution (10σ Gaussian kernel and SPIRE 500 μm). All images have arbitrary units and a pixel grid of 500 times 500 pixels. All values for all convolution kernels do not reflect any smoothing in the published papers, but shall illustrate the idea behind this approach.

Spatial decomposition

Imaging maps can be regarded as a combination of emissions on various spatial scales (e.g., Starck et al., 2004). Consequently, efforts have been made to characterize the ISM as either a two-component system composed of a diffuse, self-similar fractal component and a coherent filamentary component (Robitaille et al., 2019), or as a multi-fractal system (Elia et al., 2018; Yahia et al., 2021). To generate a high-resolution column density map, one must reverse this procedure by assembling a map from high-resolution sub-maps that preserve individual spatial scales through SED fits at different wavelengths. A concise description of this method can be found in Palmeirim et al. (2013) or Keilmann et al. (2024a). In the following, I outline the method additionally in a more illustrative way.

The method put forward by Palmeirim et al. (2013) constructs a column density map at an 18.2″ resolution using the SPIRE 250 μm data. The method smooths the gas surface density distribution to the SPIRE 250 μm resolution and represents it as a combination of three components

$$\Sigma_{250} = \Sigma_{500} + (\Sigma_{350} - \Sigma_{500}) + (\Sigma_{250} - \Sigma_{350}) \ , \tag{4.20}$$

where Σ_{500}, Σ_{350}, and Σ_{250} denote smoothed versions of the intrinsic gas surface density distribution Σ obtained by convolving with the respective SPIRE beams B_{xyz} at Σ_{500}, Σ_{350}, and Σ_{250}, respectively. Specifically, the distribution smooths to the SPIRE 500 μm resolution as $\Sigma_{500} = \Sigma * B_{500}$, while $\Sigma_{350} = \Sigma * B_{350}$ and $\Sigma_{250} = \Sigma * B_{250}$ follow analogously, where $*$ commonly denotes convolution. The concept of Eq. 4.20 rests on the fact that for any telescope used to observe the intrinsic gas distribution, the outcome is always a convolved version of Σ. Even telescopes with extremely high angular resolution only provide a convolved representation. Thus, each representation should consistently reflect the same intrinsic gas distribution on the sky, except for resolution and other aspects of physical processes, such as varying optical thickness of dust at distinct wavelengths, or because different wavelengths represent different physical processes.

I also provide an illustrative explanation of the procedure and depict its process using synthetic images in arbitrary units (a.u.) that I have created. Figure 4.4 presents synthetic gas distributions similar to observed GMCs. The top left panel indicates Σ, while the other three remaining images are smoothed versions at coarser resolutions with Gaussian convolution kernels of 1, 5, and 10σ.[1] These images correspond to Σ_{500}, Σ_{350}, and Σ_{250}. The "Original Image" was produced with a noise level of 100 a.u. and a background level of 0 a.u. To represent GMCs, the "signal" is modeled with a Gaussian distribution whose peaks can reach 1000 a.u. (generated randomly with a uniform distribution) and a standard deviation σ randomly between 1 and 3 to represent the signal (GMC) size. Subsequently, three smoothed versions were produced using the aforementioned parameters; they serve as comparison representations for the SPIRE 250, 350, and 500 μm observations but do not reflect the same physical resolutions.

This means that the first term in Eq. 4.20 refers to the surface density distribution smoothed to the resolution of the SPIRE 500 μm data. The method computes Σ_{500} by smoothing the 160, 250, and 350 μm maps to the 500 μm resolution (36.3″) and fitting the data with a graybody model. Prior to this, the Herschel images were reprojected onto a common grid. An optically thin graybody function (see above) fits the SEDs from Herschel bands between 160 μm and 500 μm on a pixel-by-pixel basis (four SED data points per pixel), which yields the best-fit $\Sigma_{500}(x, y)$ and $T_{\mathrm{d},500}(x, y)$ for each (x, y) pixel.

Analogously, the method computes Σ_{350} by smoothing the 160 μm and 250 μm maps to match the 350 μm band's resolution (24.9″) and applying a pixel-by-pixel SED graybody fit to the 3 band data, excluding 500 μm. It then constructs Σ_{250} by smoothing the 160 μm

---

[1] I use the standard deviation σ of a Gaussian instead of the FHWM for illustration purposes, yet this does not affect the results.

map to the resolution of the 250 μm band ($18.2''$) and then performing a graybody fit to the 2 band data.

Thus, to obtain Σ_{250}, the original method of Palmeirim et al. (2013) used SED fits to derive the temperature for Σ_{500} and Σ_{350}, fixing it via the 250 μm/160 μm (color) flux ratio for Σ_{250}. I opted for an alternate method, employing the temperature map from Tabatabaei et al. (2014) (which was kindly provided) for Σ_{250}. The reason is that the flux ratio approach caused irregular column density values in the outskirts of M33 where noise dominates. As both wavelengths (160 μm and 250 μm) are in the Rayleigh-Jeans limit and close in value, they approximately cancel out the dust temperature in the calculation of the flux ratio, making it insensitive to the dust temperature and causing irregular numbers. Furthermore, computational numerical methods avoid dividing small values, which can cause numerical instability and yield potential meaningless high values; in the noise regime of M33's outskirts, very small numbers led to such instabilities.

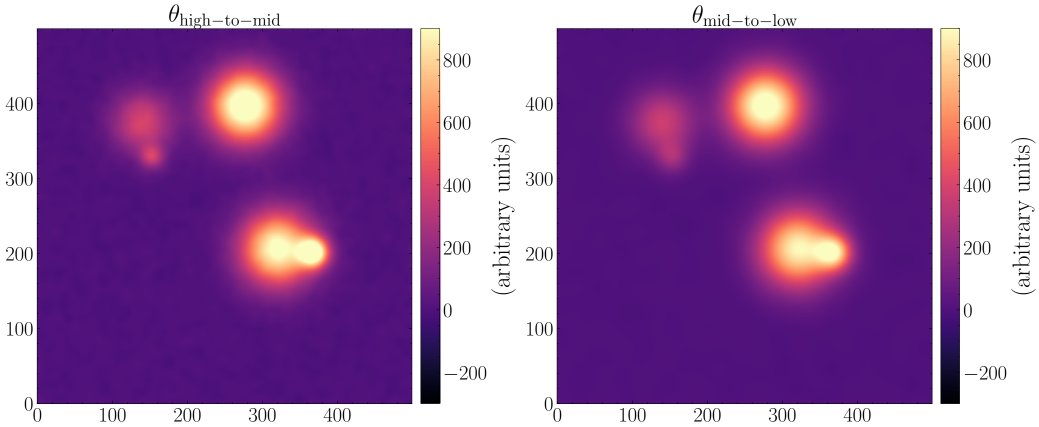

Figure 4.5: Synthetic GMC sources of the convolved images in terms B and A. The left panel shows the high resolution image smoothed to the intermediate resolution. The right panel shows the intermediate resolution to the lowest resolution. All panels have again arbitrary units and a pixel grid of 500 times 500. All values for all convolution kernels do not reflect any smoothing in the published papers, but shall illustrate the idea behind this approach.

The second term of Eq. 4.20 computes $\Sigma_{350} - \Sigma_{350} * G_{500\_350}$, where G_{500_350} is a circular Gaussian with a full width at half maximum (FWHM) of $\sqrt{(36.3'')^2 - (24.9'')^2} \approx 26.4''$. The SPIRE beam at 500 μm is a smoothed version of the beam at 350 μm, thus $B_{500} = B_{350} * G_{500\_350}$. This term adds spatial information accessible at 350 μm but not at 500 μm. Thus, by subtracting $\Sigma_{350} * G_{500\_350}$ the information from low-spatial frequency is removed. Figure 4.5 shows the corresponding smoothed version of the synthetic data with a convolution kernel of $\sqrt{5^2 - 1^2}$ in the left panel.

Analogously, the third term in Eq. 4.20 is expressed as $\Sigma_{250} - \Sigma_{250} * G_{350\_250}$, where G_{350_250} represents a circular Gaussian Σ_{500} and adds information on spatial scales observable at wavelengths $\leqslant 250\,\mu$m. Figure 4.5 shows the corresponding smoothed version of the synthetic data with convolution kernel of $\sqrt{10^2 - 5^2}$ in the right panel.

Let us break this down. Figure 4.4 shows synthetic gas distributions similar to observed GMCs, where the upper left panel represents Σ, and the remaining three images represent smoothed versions at a coarser resolution with a Gaussian beam of 1, 5, and 10σ. The latter three refer to Σ_{250}, Σ_{350}, and Σ_{500}, respectively. We cannot achieve the original

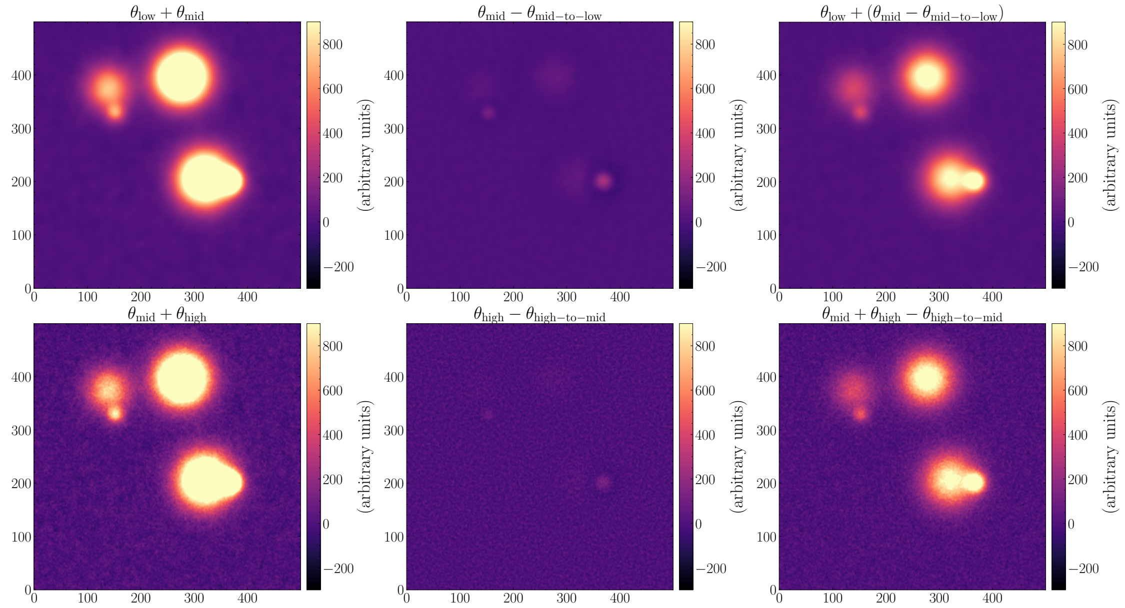

Figure 4.6: Synthetic GMC sources of images from intermediate steps. Left column: The panels show the summation of lowest and intermediate resolution images as well as the intermediate and highest resolution. Middle column: The panels show the intermediate steps B and A of convolution with the corresponding kernel and subtraction, respectively. Right column: The panels show the result of adding the images of the middle column to the images at the same corresponding resolutions. All panels have again arbitrary units and a pixel grid of 500 times 500. All values for all convolution kernels do not reflect any smoothing in the published papers, but shall illustrate the idea behind this approach.

distribution called “Original image” as explained above. Hence, the goal is to achieve an image at a resolution of the SPIRE 250 μm data, which corresponds to the synthetic data named $\theta_{\rm high}$. Based on the above explanations, Eq. 4.20 can be written as

$$\Sigma_{\rm high} = \Sigma_{500} + \underbrace{(\Sigma_{350} - \Sigma_{350} * G_{500\_350})}_{=:B=\theta_{\rm mid}-\theta_{\rm mid-to-low}} + \underbrace{(\Sigma_{250} - \Sigma_{250} * G_{350\_250})}_{=:A=:\theta_{\rm high}-\theta_{\rm high-to-mid}} , \tag{4.21}$$

where the resulting “intermediate” images are denoted shortly with B and A. The synthetic images corresponding to $\Sigma_{350} * G_{500\_350}$ and $\Sigma_{250} * G_{350\_250}$ are shown in Fig. 4.5. By close comparison, it becomes obvious that each of them represents the next coarse resolution. These images contain the low-spatial frequency of the corresponding image with higher resolution and will be subtracted from the corresponding images at the same resolution.

In order to get a grasp of how this method removes low-spatial frequency information by subtraction of the corresponding images, let us take a closer look at Fig. 4.6. The upper row represents the term denoted as B, while the lower row represents the term A in Eq. 4.21. If we only add Σ_{500} and Σ_{350}, then this results in obviously overestimated values (left column of Fig. 4.6). The middle column of Fig. 4.6 shows the resulting images of B and A. The smoothed image $\Sigma_{350} * G_{500\_350}$ in B contains only the lower spatial frequency information compared to Σ_{350} alone. Thus, subtracting the smoothed version from Σ_{350} results in an image with net high-spatial frequency information. Therefore, the next step is to add this to the Σ_{500} image. Hence, we added high-spatial frequency

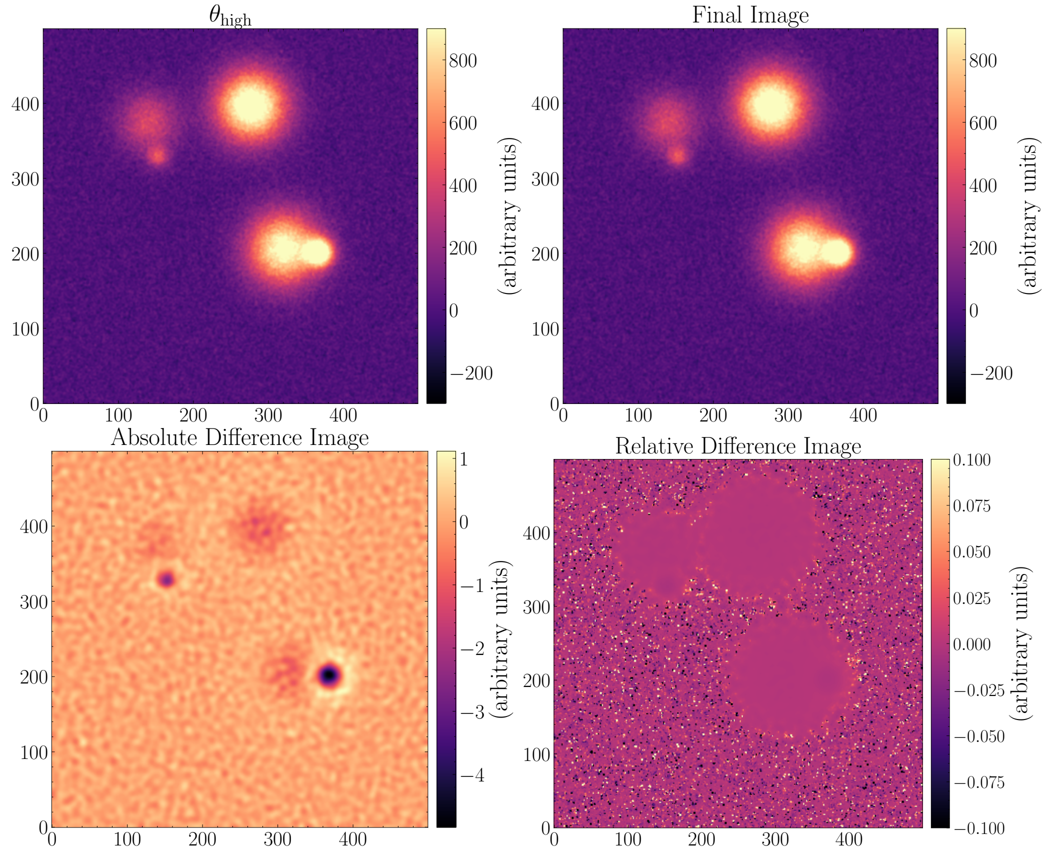

Figure 4.7: Synthetic GMC sources of expected to final image and difference maps. The upper left panel shows once more the high-resolution image we want to achieve. The upper right panel shows the final image, when the whole procedure has been calculated. The bottom panels show the absolute and relative difference maps of the images in the upper panels. All panels have again arbitrary units and a pixel grid of 500 times 500. All values for all convolution kernels do not reflect any smoothing in the published papers, but shall illustrate the idea behind this approach.

information to Σ_{500} and low-spatial frequency information was removed via $\Sigma_{350} * G_{500\_350}$. The term A analogously adds high-spatial frequency information that is only accessible to the observations with higher resolutions. Or in other words, $\Sigma_{350} * G_{500\_350}$ removes low-spatial frequency information from the sum of Σ_{500} and Σ_{350}, leaving the sum with higher spatial frequency information. $\Sigma_{250} * G_{350\_250}$ does the same in term A. The darker rings in the middle column of Fig. 4.6 nicely illustrate how beam dilution in lower-resolution images enlarges the appearance of synthetic GMCs. In these regions the image with higher resolution has basically less intensity because there is less "gas," which effectively reflects that these images contain higher spatial frequency information.

The final image generated using Eq. 4.21 is shown in Fig. 4.7 (upper right) alongside the ideal representation $\theta_{\rm high}$ (upper left); the two maps look very akin by eye-inspection. The lower panels display the absolute difference (Final Image − $\theta_{\rm high}$) and relative difference ([Final Image − $\theta_{\rm high}$]/$\theta_{\rm high}$) maps, respectively. The absolute difference map indicates that the final assembled image exhibits slightly reduced peak values (darker regions at the individual synthetic GMC peaks). Nonetheless, the drop is less than 0.3% compared to the peak values. On the other hand, the difference map shows that the final assembled image shows increased values in the noise regime. Considering the relative difference map reveals that the final constructed map barely differs from the θ_{high} image's values in areas where the images contain synthetic signals (the GMCs). However, outside the synthetic GMCs, the noisy discrepancies become evident but remain minimal. This underscores the efficacy of this multi-scale decomposition approach.

4.7.2 Source extraction

Over decades, continuum and line observations have revealed that (giant) molecular clouds possess complex velocity structures and non-spherical geometries. Simulations further demonstrate that clouds and the stars within them form out of interacting flows of gas that build filaments and hub-filaments. Stellar feedback, magnetic fields, and galactic shear forces further shape clouds, making it oversimplified to define molecular clouds as self-consistent entities with clear borders. However, it remains necessary to develop methods that identify and characterize these entities – whether entire clouds in a galaxy or clumps and cores within a cloud – to analyze and quantify their properties. For example, changes in cloud properties under varying environmental conditions reveal insights into their dynamics and influence on cloud formation and evolution. For that, many algorithms have been developed in the last decades, based on different assumptions and simplifications. These include GAUSSCLUMPS (Stutzki and Guesten, 1990), ClumpFind (Williams et al., 1994), CPROPS (Rosolowsky and Leroy, 2006), and Dendrograms (Rosolowsky et al., 2008), or FilFinder (Koch and Rosolowsky, 2015). Some approaches presume an inherent cloud morphology, such as GAUSSCLUMPS which assumes Gaussian shapes, or FilFinder which explicitly identifies filaments. In contrast, other approaches, such as Dendrograms, do not assume a predefined morphology, allowing it to detect any kind of shape. A more detailed comparison of different methods is found in Men'shchikov et al. (2012). During this thesis, I explored GAUSSCLUMPS and Dendrograms.

Stutzki and Guesten (1990) developed GAUSSCLUMPS for analyzing 3D position-velocity data cubes in molecular line studies of molecular clouds. The algorithm fits a Gaussian profile to the brightest peak using a least-squares method while ensuring the position and amplitude remain close to the image maximum. After subtracting the fitted Gaussian from the image, it generates a residual image and identifies the next brightest peak for another fit. This iterative process continues until either the total intensity of all subtracted clumps matches the integrated intensity of the original image, or no significant peaks remain.

To apply GAUSSCLUMPS to the IRAM 30m CO$(2-1)$ map and the dust-derived H_2 map of M33 in order to identify individual molecular clouds, I added a spectral dimension (a single slice set to $1\,\mathrm{km\,s^{-1}}$) to the FITS files, since both maps only have spatial information and no velocity axis. I performed this adjustment because the GAUSSCLUMPS code that is implemented in the GILDAS (Grenoble Image and Line Data Analysis Software/Continuum and Line Analysis Single-dish Software) software package[2] requires 3D cubes with both spatial and spectral dimensions. I tested GAUSSCLUMPS on both maps, but the algorithm did not succeed in reliably extracting all clouds. This shortfall likely stems from two factors. First, adding an additional slice for the spectral dimension (which I have constantly set to $1\,\mathrm{km\,s^{-1}}$) may cause some issues in detecting the sources; since I am not in control of the code, I can only speculate on this possible issue. Second, the dust-derived H_2 map of M33 contains regions where pixels with proper values only resemble an

---

[2] `https://www.iram.fr/IRAMFR/GILDAS`

unordered, granular distribution, causing GAUSSCLUMPS – designed to find Gaussian shapes – to fail in fitting the data. However, since the detection of GMCs performed better for the CO map showing a smoother distribution of CO emission, this is a possible explanation.

Nevertheless, in Keilmann et al. (2024b) I use Dendrograms, which is briefly introduced in the following.[3]

Dendrograms

Dendrograms (Rosolowsky et al., 2008) identify hierarchical structures in astronomical data using a clustering approach. This approach is an unsupervised machine learning algorithm that finds a specific solution based on three initial conditions:

- Minimum significance: Determines whether a peak intensity of one identified structure is significantly different compared to the peak intensity of another possible structure.
- Minimum value: Sets a lower intensity threshold for all identified structures, excluding data below this value.
- Minimum pixel number: Sets a minimum pixel number as a threshold for structures in 2D or 3D data sets that each identified structure must fulfill.

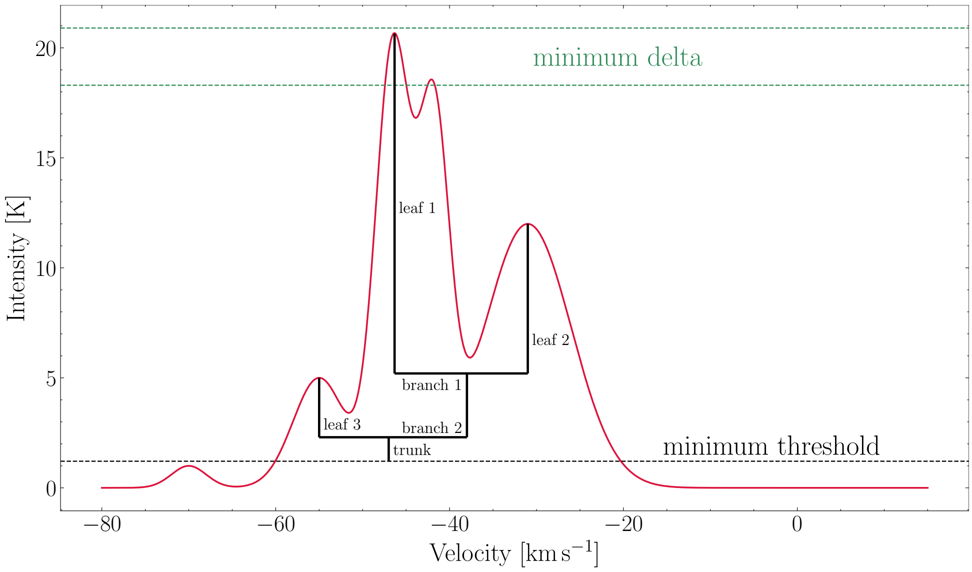

Figure 4.8: Sample spectrum illustrating Dendrogram parameters.

Figure 4.8 schematically represents the algorithm. The method hierarchically identifies local intensity peaks as clusters. The largest structure encompassing all sub-structures is termed the *trunk*, defined by the minimum given value. Structures above the trunk that contain sub-structures are called *branches*, whereas structures without further sub-structures are designated *leaves*, each exceeding the minimum significance. The local minimum of a branch distinguishes two leaves (Fig. 4.8).

---

[3] FilFinder was excluded since our resolution does not allow to reliably detect the relatively small widths of filaments. This becomes possible with facilities such as ALMA.

I examined various thresholds and, as demonstrated in Appendix D, the specific value only marginally impacts the outcomes, which remain stable for the M33 maps. A minimum detection limit of 3σ or higher is reasonable, while the minimum number of pixels for structure identification depends on the beam size θ and the pixel size $\theta_{\rm RA}\,\theta_{\rm Dec}$. A structure is considered significant if it covers at least 1.2 times the main beam area. I also explored different values (refer to Appendix D). The minimum pixel number for the area is derived by

$$N_{\rm pix,min} = \frac{3\pi}{4}\frac{\theta^2}{\theta_{\rm RA}\,\theta_{\rm Dec}}\ , \tag{4.22}$$

which enables the calculation of the mass for a specific structure, for example, a GMC.

4.7.3 Probability distribution functions of column density (N-PDFs)

The study of star formation rates, efficiencies, and timescales is connected to the complex gas distribution and energy in galaxies. ISM observations reveal self-similar structures that span from kiloparsec large galactic scales to much smaller sub-parsec scales within molecular clouds (e.g., Goldsmith et al., 2008; Schneider et al., 2013; Stutz and Kainulainen, 2015; Pety et al., 2017; Sawada et al., 2018; Sun et al., 2020; Leroy et al., 2021). Studies on the density structure and gas energetics across these scales lead to canonical relations such as the Kennicutt-Schmidt (KS) relation (Schmidt, 1959; Kennicutt, 1998b). Early studies showed that the decomposition of intensity distributions into clumps yields power-law relations for clump number and size versus mass (Heithausen et al., 1998), consistent with a fractal clump distribution (Stutzki et al., 1998). Turbulent internal cloud motion predominantly induces the likely largely random internal structure of molecular clouds (Stutzki et al., 1998). Although observations from both Galactic and extragalactic regions offer insights into these scales, linking small-scale cloud structures with larger galactic distributions remains challenging. Moreover, earlier diagnostics (e.g., velocity dispersion, clump mass functions) struggled to statistically separate turbulent from collapsing gas or to capture the hierarchical structure of clouds (Spilker et al., 2021).

Column density probability distribution functions (N-PDFs) are commonly used and simple statistical tools. They are directly deduced from observations, in contrast to the volume density (ρ)-PDFs, which require knowledge about the line-of-sight extent of the cloud. N-PDFs describe the overall distribution of column densities and enable a unified analysis of the turbulent and gravitational processes that drive molecular cloud evolution and star formation (Klessen et al., 2000; Federrath et al., 2008).

Typically, N-PDFs show a log-normal distribution at low column densities – indicative of supersonic turbulence (Klessen et al., 2000; Federrath et al., 2008; Federrath and Klessen, 2013) – and develop a power-law tail at higher densities, commonly attributed to self-gravity (Girichidis et al., 2014; Chen et al., 2018; Schneider et al., 2022). N-PDFs are the most important statistical measures for star formation theories (Hennebelle and Falgarone, 2012; Padoan et al., 2014; Burkhart and Mocz, 2019) and facilitate direct comparisons between simulations and observations (Brunt, 2015; Spilker et al., 2021).

However, exact shapes of N-PDFs (whether log-normal, power-law, or both) remain a subject of debate. Galactic studies predominantly use N-PDFs, and questions persist as to whether they follow a log-normal, power-law, or combined distribution (Kainulainen et al., 2009; Csengeri et al., 2016; Schneider et al., 2015b, 2022).

Environmental factors significantly shape the form of N-PDFs, affecting both the log-normal and power-law components. Turbulence, gravity, magnetic fields, and external pressures each contribute to the evolution of a cloud's density structure. Turbulence drives primarily the log-normal component of N-PDFs. In isothermal environments dominated by turbulence, the log-normal shape of an N-PDF reflects random, chaotic density fluctuations (e.g., Passot and Vázquez-Semadeni, 1998; Klessen et al., 2000; Federrath et al., 2008; Burkhart and Lazarian, 2012). The width of this log-normal distribution correlates with the Mach number $\mathcal{M}$, with higher turbulence producing broader distributions (Chen et al., 2018). As $\mathcal{M}$ quantifies compressibility in a velocity field, high values indicate strong compressibility, leading to significant local density increases.

In a log-normal ρ-PDF, the sonic Mach number $\mathcal{M}$ quantifies turbulence by relating to the standard deviation σ_ρ through

$$\sigma_\rho^2 = \ln\left(1 + b^2\mathcal{M}^2\right) . \tag{4.23}$$

The forcing parameter b relates to the relative amount of stirring versus compression in the turbulence and varies with the kinetic energy injection – $b \approx 1/3$ for solenoidal and $b = 1$ for compressive forcing (Federrath et al., 2008). When considering magnetic fields, the density variance also depends on the thermal pressure p_{th} to magnetic pressure p_{mag} ratio, which is given by

$$\beta = \frac{p_{\mathrm{th}}}{p_{\mathrm{mag}}} = 2\frac{c_s^2}{v_{\mathrm{A}}^2} , \tag{4.24}$$

where c_s is the sound speed and v_{A} is the Alfénic velocity. The Alfénic velocity represents the speed at which magnetic disturbances, known as Alfvén waves, propagate through a magnetized plasma and is given by $v_{\mathrm{A}} = B/\sqrt{\mu_0\rho}$, where B is the magnetic flux density strength, μ_0 the permeability of free space, and ρ the density of the plasma. If B is proportional to $\rho^{1/2}$ (Molina et al., 2012), then the density variance is

$$\sigma_{\rho,\mathrm{mag}}^2 = \ln\left(1 + b^2\mathcal{M}^2\frac{\beta}{\beta+1}\right) . \tag{4.25}$$

In column density N-PDFs, Burkhart and Lazarian (2012) established a relation described by

$$\sigma_N^2 = 0.11\,\ln\left(1 + b^2\mathcal{M}^2\right) . \tag{4.26}$$

Assuming a similar scaling for magnetized cases, the variance can then be expressed as

$$\sigma_{N,\mathrm{mag}}^2 = 0.11\,\ln\left(1 + b^2\mathcal{M}^2\,\frac{\beta}{\beta+1}\right) . \tag{4.27}$$

The sonic Mach number $\mathcal{M}_{\mathrm{H\,I}}$ for H I, for example, can lastly be described by

$$\mathcal{M}_{\mathrm{H\,I}} = \frac{\sqrt{3}}{c_s}\sqrt{\frac{\Delta v_{\mathrm{HI}}^2}{8\ln 2} - \frac{k_{\mathrm{B}}\,T}{m_{\mathrm{H}}}} , \tag{4.28}$$

where the isothermal sound speed c_s is given by

$$c_s = \sqrt{\frac{k_{\mathrm{B}}T}{\mu\,m_{\mathrm{H}}}} , \tag{4.29}$$

using the hydrogen mass m_{H}, Boltzmann constant k_{B}, and the mean molecular weight μ.

Gravity, magnetic fields, and external pressures actively shape the power-law tail of N-PDFs. Gravity induces the power-law tail, indicating gravitational collapse and the formation of dense cores and stars; its slope reveals the strength of gravitational forces within a cloud (Vázquez-Semadeni and García, 2001; Stutz and Kainulainen, 2015; Spilker et al., 2021; Schneider et al., 2013, 2015b). Magnetic fields provide additional support against gravitational collapse, and strong fields can suppress the formation of a power-law tail, preserving a log-normal shape even in dense regions – potentially delaying or preventing star formation (Burkhart et al., 2015). External pressures from nearby supernovae or expanding H II regions compress molecular clouds, enhancing the power-law tail by promoting collapse while potentially broadening the log-normal component through increased turbulence (Tremblin et al., 2014; Spilker et al., 2021).

N-PDF shapes and characteristics vary across molecular cloud types, reflecting diverse physical conditions and evolutionary stages (Schneider et al. 2022 presents N-PDFs for the various cloud types):

- Quiescent Clouds: In non-star-forming clouds, N-PDFs typically exhibit a log-normal distribution, indicative of turbulence-dominated environments where supersonic turbulence drives density fluctuations. This form suggests an early evolutionary stage with minimal gravitational influence and may not be actively forming stars, though such clouds may evolve into star-forming regions if external compression or gravitational instability increases (Chen et al., 2018).

- Star-Forming Clouds: In active star-forming regions, N-PDFs often develop a power-law tail at higher column densities, which indicates gravitational collapse and the formation of dense cores that precede star formation. This tail reflects the significant role of self-gravity in shaping cloud structure and indicates where gravity overcomes turbulence. The steepness and extent of the power-law tail can provide information about the intensity and scale of future star formation activity (Vázquez-Semadeni and García, 2001).

- High-Mass Star-Forming Regions: In regions that form high-mass stars, a second power-law tail is sometimes observed (Schneider et al., 2015a). This second tail can be flatter or steeper and reflects the intense gravitational forces and higher densities needed for massive star formation. Stellar feedback and magnetic fields, however, can also produce this second power-law tail.

Analyzing the N-PDFs of various clouds helps infer their evolutionary states and the likelihood of near-future star formation. This predictive capability makes N-PDFs a valuable tool to understand the life cycle of molecular clouds and the conditions that lead to star formation (Syed et al., 2020; Spilker et al., 2021; Schneider et al., 2022).

However, extragalactic studies often reveal log-normal distributions (Hughes et al., 2013; Druard et al., 2014), in contrast to the mixed results found in the Milky Way. Reconciling these differences requires comparative studies between Galactic and extragalactic observations. In addition, in extragalactic studies, a power-law tail may not be identified due to resolution limits. Line-of-sight effects further add challenges in the interpretation of the N-PDF shapes. In Keilmann et al. (2024b), I analyze and describe N-PDFs in M33. Future studies using even higher resolution data from facilities such as ALMA will help to better understand N-PDF in external galaxies.

4.7.4 Determining missing [C II] flux

In the compact H II region in RCW79, the [C II] spectra around the ionizing O7.5–O9.5V/III star display double-peak features. Assuming that self-absorption causes the emission dip, the method I have developed and described below determines the missing flux by fitting radiative transfer equations to the observed spectra of any source. The process is implemented in Python and reflects how significantly the peaks stand out from its surroundings.

First, I implemented the [C II] fine- and [^{13}C II] hyper-fine-structure line profiles using the parameters listed in Table 2.1. To account for varying abundances of [C II] and [^{13}C II], I had to incorporate the abundance ratio α (see Eq. 2.57). Because Eq. 2.56 shows that $T_{\rm ex}$ and τ are interdependent, one of these two parameters must be fixed during fitting; here, $T_{\rm ex}$ is fixed, while τ remains a free fit parameter.

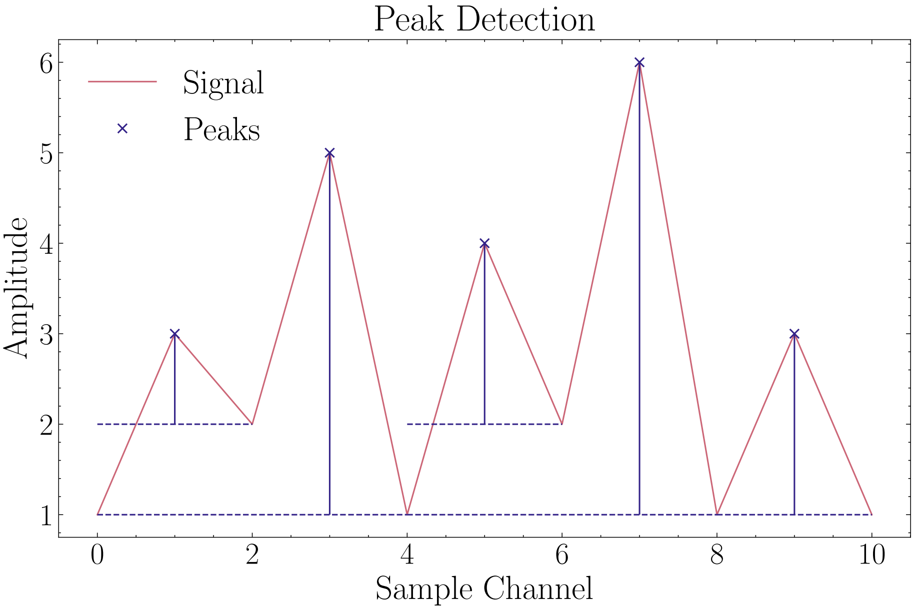

Figure 4.9: Sample spectrum illustrating peak detection.

Second, assuming in general that the dip in between the double peaks arises from missing flux (neglecting what the cause of this missing flux is at this step), we need to exclude the velocity range between the two peaks during the fit. As the positions in velocity vary from spectra to spectra (i.e., position to position), it is essential to automatically and reliably detect these double peaks to ensure the method's practicality. Therefore, several requirements are applied to the spectra to be reliably identified as a double peak spectrum.

Lower and upper velocity limits constrain the range where the two peaks are generally expected. Within this defined range, the rms noise of the individual spectrum is determined. If a spectrum's peak intensity does not exceed a predetermined threshold, the entire spectrum will be excluded from the fitting process. Otherwise, the next steps assess whether a peak is sufficiently significant by measuring how prominently the signal rises from its baseline. To do this, my code calculates the vertical distance between the peak and the lowest contour line that encloses it without any higher peaks. In other words, it determines the minimum vertical drop required to reach a higher peak or the signal boundary to be classified as a peak (see Fig. 4.9).

Calculating the peak significance: the step-by-step procedure

- identify the peak
- locate the local maximum (peak) in the signal

- find left and right bases
- left base: Move left from the peak until the signal rises to a higher point or reaches the left end of the spectrum
- record the minimum value encountered
- right base: Move right from the peak until the signal rises to a higher point or reaches the right end of the spectrum
- record the minimum value encountered
- determine the reference level: The higher of the left and right base values is the reference level
- calculate significance: significance = peak height − reference level

If this *significance* criterion is met for a second peak, the emission dip between the two peaks remains sufficiently shallow to classify the spectrum as double-peaked at the designated significance level (in Kelvin). Figure 4.9 shows an example spectrum with the lowest contour line that encircles a detected peak, where the dashed horizontal lines represent the individual contours.

The method applies further criteria to parameterize the identified peaks. The range to be excluded from the fitting is additionally expanded by a certain value, which is allowed by the code to be adjusted. This ensures that only the likely unaffected wings are considered during the fit, as the detected peaks may already show lower intensity due to self-absorption or other effects. Hence, this approach more reliably fits the actual line without the influence of (self-)absorption. All of these parameters remain adjustable, providing maximum flexibility across different sources.

Once the above requirements are met, the code subtracts either a single-component baseline (for cases such as continuum emission) or a two-component baseline to account for high-velocity gas from a superordinate shell, as observed in RCW79.

However, since [^{13}C II] is not detected at every position in RCW79, the code is further designed to adapt by precisely restricting the fitting range to the outer wings of the blue- and red-shifted peaks. This restriction enables the user to qualitatively assess the reliability of the fit when the modeled [^{13}C II] lines remain consistent with the noise level; that is, their intensities do not exceed the noise level of the measured data and hence give more control to the user in cases where [^{13}C II] is not detected.

Once the channels (or velocity indices) of the spectrum have been selected for fitting, the code automatically determines the initial guesses for the fit. For the amplitude, it uses the maximum value of the observed spectrum as the default guess (which can be scaled upward if desired). The code calculates the initial peak position as $(v_{\text{blue-shifted peak,0}} + v_{\text{red-shifted peak,0}})/2$ and the initial line width as $(v_{\text{red-shifted peak,0}} - v_{\text{blue-shifted peak,0}})/4$.

Chapter 5

Results

This chapter provides an overview of the publications that I worked on during my doctoral studies and of which I am first author and co-author, and outlines my specific contributions. After summarizing each paper, I integrate it into this thesis.

I start with a paper on the Galactic cloud Draco, where I am the third co-author. I subsequently present my two papers on M33, for which I am the first author, and end with a paper on the Galactic source S144 in RCW79, where I am also the first author and which is a *Letter to the Editor*. The first three papers and the letter article are all peer-reviewed and published in Astronomy & Astrophysics (A&A), one of the highest impact journals worldwide for astronomical publications.

5.1 First detection of the [C II] line in the intermediate-velocity cloud Draco

In Schneider et al. (2024), we report the first detection of the [C II] 158 μm line in the high-latitude, intermediate-velocity cloud (IVC) Draco. IVCs, which form part of the Milky Way's halo, can originate from Galactic processes (gas from the Galactic plane is expelled but falls back due to the disk's high gravitational potential) or extragalactic gas infall. These clouds are cold and diffuse, lacking exposure to a significant UV field. In this study, we used the upGREAT spectroscopic receiver on SOFIA to observe the Draco and Spider IVCs. Data were obtained during both guaranteed and open times with N. Schneider as PI. Alongside, we used archival data from quiescent clouds, specifically Musca and Polaris, which are no IVCs and also exhibit minor to no star-formation activity. We also employed complementary CO data obtained from the IRAM 30m telescope through PI proposals and archival resources.

We detected the [C II] line at intermediate velocities in Draco at four out of five positions, but not at local or high velocities. The two observed positions in the Spider IVC show no [C II] emission in any of the velocity ranges. The findings suggest that shocks heat the gas, triggering [C II] emission and early molecular cloud formation, and that these shocks are likely induced by the fast motion of the Draco cloud toward the Galactic plane and subsequent cloud collisions. The absence of [C II] emission in Spider and other low-density clouds supports the idea that dynamic processes are necessary for excitation in UV-faint regions (Schneider et al., 2024).

The objective of this study is to explore molecular cloud formation by focusing on the transition from atomic H I to H_2 gas in the ISM – a process that remains difficult to observe due to the selective formation of CO molecules, which makes H_2 gas "CO-dark." The formation of H_2 and CO depends on the local interstellar radiation field and self-shielding efficiencies. Photoelectric heating, dust cooling, and collisionally excited FIR emission regulate the gas's thermal state, resulting in a multiphase ISM. In contrast to the bright [C II] lines in massive star-forming regions, which are straightforward to observe and map over large areas, detecting the [C II] line in the low-density and cool environment of Draco proved challenging. Only single pointings were possible to perform, and long integration times were necessary to succeed in this first detection.

Remarkably, we detected [C II] emission in Draco but not in the other clouds (Spider, Polaris, Musca), suggesting that dynamics and cloud interactions influence [C II] excitation. This seems likely because the Draco cloud is "falling" with significant velocity toward the Galactic plane. Our determination of the FUV field revealed discrepancies among different methods, and we propose that shock heating may serve as a mechanism for dust heating. The PDR modeling that I have performed and cross-checked indicates that the observed [C II] and CO lines can be explained by a low FUV field, while shock modeling supports the measured [C II] intensities. We acknowledge that the PDR model's requirement for a very low UV field is not fully supported by independent FUV field determinations. Overall, these results underscore the importance of dynamics in driving the evolution of interstellar clouds.

The study combined archival data with new observations to analyze the physical characteristics of the clouds. We determined the FUV field using several methods, including translating 160 μm flux from Herschel into FUV emission, and employing a continuous model of the OB star distribution. The PDR modeling that I performed was used to fit line intensities and ratios, which established the most likely values for the density and the FUV field.

Since part of the Draco cloud is molecular and our intention was also to study the H I-to-H_2 transition, a crucial part of the study was to investigate the excitation conditions of the denser H_2 gas. For that, I performed RADEX non-LTE line analysis calculations using different CO rotational transitions and isotopologues to determine the physical properties of this gas phase. I wrote most of the text and contributed figures to the "Non-LTE line analysis with RADEX" section (Sect. 5.3) in the paper. Furthermore, my contributions extend to discussions that carefully interpreted the results of the PDR, RADEX, and shock modeling, leading to the interpretation that shocks likely trigger [C II] emission and drive early cloud formation in Draco through collisions of H I clouds. Lastly, I contributed to discussions on the surprisingly strong 160 μm emission attributed to FUV radiation. From 160 μm emission it is typically inferred that the presence of small, warm dust grains are heated by an external source, yet no OB star is identified near the Draco cloud.

A&A, 686, A109 (2024)
https://doi.org/10.1051/0004-6361/202348349

Astronomy & Astrophysics

First detection of the [CII] 158 μm line in the intermediate-velocity cloud Draco

Nicola Schneider[1], Volker Ossenkopf-Okada[1], Eduard Keilmann[1], Markus Röllig[2,1], Slawa Kabanovic[1], Lars Bonne[3], Timea Csengeri[4], Bernd Klein[5,6], Robert Simon[1], and Fernando Comerón[7]

[1] I. Physikalisches Institut, Universität zu Köln, Zülpicher Str. 77, 50937 Köln, Germany
e-mail: `nschneid@ph1.uni-koeln.de`
[2] Physikalischer Verein, Gesellschaft für Bildung und Wissenschaft, Robert-Mayer-Str. 2, 60325 Frankfurt, Germany
[3] SOFIA Science Center, NASA Ames Research Center, Moffett Field, CA 94 045, USA
[4] Laboratoire d'Astrophysique de Bordeaux, Université de Bordeaux, CNRS, B18N, 33615 Pessac, France
[5] Max-Planck Institut für Radioastronomie, Auf dem Hügel 69, 53121 Bonn, Germany
[6] University of Applied Sciences Bonn-Rhein-Sieg, Grantham-Allee 20, 53757 Sankt Augustin, Germany
[7] European Southern Observatory, Karl-Schwarzschild-Str. 2, 85748 Garching, Germany

Received 23 October 2023 / Accepted 7 March 2024

ABSTRACT

High-latitude intermediate-velocity clouds (IVCs) are part of the Milky Way's H I halo and originate from either a galactic fountain process or extragalactic gas infall. They are partly molecular and can most of the time be identified in CO. Some of these regions also exhibit high-velocity cloud gas, which is mostly atomic, and gas at local velocities (LVCs), which is partly atomic and partly molecular. We conducted a study on the IVCs Draco and Spider, both were exposed to a very weak UV field, using the spectroscopic receiver upGREAT on the Stratospheric Observatory for Infrared Astronomy (SOFIA). The 158 μm fine-structure line of ionized carbon ([C II]) was observed, and the results are as follows: In Draco, the [C II] line was detected at intermediate velocities (but not at local or high velocities) in four out of five positions. No [C II] emission was found at any velocity in the two observed positions in Spider. To understand the excitation conditions of the gas in Draco, we analyzed complementary CO and H I data as well as dust column density and temperature maps from *Herschel*. The observed [C II] intensities suggest the presence of shocks in Draco that heat the gas and subsequently emit in the [C II] cooling line. These shocks are likely caused by the fast cloud's motion toward the Galactic plane that is accompanied by collisions between H I clouds. The nondetection of [C II] in the Spider IVC and LVC as well as in other low-density clouds at local velocities that we present in this paper (Polaris and Musca) supports the idea that highly dynamic processes are necessary for [C II] excitation in UV-faint low-density regions.

Key words. ISM: clouds – evolution – ISM: general – ISM: molecules – photon-dominated region (PDR) – ISM: structure

1. Introduction

The formation of molecular clouds is commonly defined as the transition of atomic to molecular hydrogen in the interstellar medium (ISM). In steady-state and chemical equilibrium models (Tielens & Hollenbach 1985; van Dishoeck & Black 1988; Sternberg & Dalgarno 1989; Krumholz et al. 2008), the formation of H_2 depends mostly on the local radiation field (dissociation of H_2 by photons in the Lyman-Werner bands versus H_2 formation on dust grains) and H_2 shielding efficiencies. In a more dynamic scenario, H_2 formation is also governed by turbulent mixing motions in the ISM (Glover & Mac Low 2007; Bialy et al. 2017) that cause large- and small-scale density fluctuations. In these dynamical models of molecular cloud formation, H_2 formation happens in shock-compressed layers in converging H I flows in the warm neutral medium (Walder & Folini 1998; Klessen et al. 2000; Heitsch et al. 2006; Vázquez-Semadeni et al. 2006; Dobbs 2008; Clark et al. 2012). This dynamic, turbulent scenario reduces the H_2 formation times from a few 10 Myr to a few Megayears (Glover & Mac Low 2007; Valdivia et al. 2016). The flows are driven by the complex interplay between gravity and stellar feedback effects. Additionally, they are influenced by the thermodynamic response of the multiphase ISM. However, the observation of these large-scale flows presents a challenge due to the selective nature of CO molecule formation. Notably, CO only becomes apparent at the shocked stagnation points within the broader turbulent flow, making the H I and H_2 gas "CO-dark". In a recent study by Schneider et al. (2023), it was demonstrated that the 158 μm line of ionized carbon (see below) can effectively characterize this component and unveil high-velocity H I flows within the Cygnus X region.

The formation of H_2 and CO critically depends on the local interstellar radiation field[1] and self-shielding efficiencies. In plane-parallel photodissociation region (PDR) models for low-column density[2], the transition typically takes place at values of $A_{\mathrm{eff,V}} \approx 0.3$ for H_2 (Röllig et al. 2007; Glover et al. 2010; Sternberg et al. 2014; Bisbas et al. 2019; Schneider et al. 2022). We note that the model $A_{\mathrm{eff,V}}$ is the local visual extinction at each point in the cloud and not directly comparable to the A_V that is an average along the line of sight (Seifried et al. 2022). This is

---

[1] We express the far ultraviolet (FUV) field in units of Habing G_o (Habing 1968) or Draine χ (Draine 1978), with $\chi = 1.71\ G_o$.

[2] We used the conversion $N(H) = 1.87\ A_V\ 10^{21}\ \mathrm{cm^{-2}\ mag^{-1}}$ and $N(H_2) = 0.94\ A_V\ 10^{21}\ \mathrm{cm^{-2}\ mag^{-1}}$ (Bohlin et al. 1978) with the total hydrogen column density N(H) and the molecular hydrogen column density $N(H_2)$ and the visual extinction A_V.

why it is difficult to observationally trace the H I-to-H_2 transition, though it has been the subject of a number of observational studies using various tracers (Imara & Burkhart 2016).

The thermal state of the gas is mostly regulated by photoelectric heating and cooling through dust and collisionally excited emission from far-infrared (FIR) molecular and atomic fine-structure lines. Nevertheless, cooling rates exhibit only a weak dependence on temperature for $T < 10^4$ K. Consequently, the cooling process driven by atomic fine-structure lines (primarily the [C II] 158 μm line) induces a thermal instability, giving rise to a multiphase ISM (Field et al. 1969; Wolfire et al. 1995). This multiphase ISM includes a volume-filling warm neutral gas (referred to as the H I WNM) characterized by temperatures around $T \sim 8000$ K and densities of $n \sim 1$ cm^{-3} in pressure equilibrium with the cold neutral medium (CNM) exhibiting temperatures of approximately $T \sim$ 30–100 K and densities of $n \sim$ 50–100 cm^{-3} within the atomic phase. The ISM also encompasses H_2 gas with temperatures typically below 30 K and densities n exceeding a few hundred cm^{-3}. Observing gas in these thermally unstable conditions poses a considerable challenge.

One tracer for the gas conditions in very different physical environments is the [C II] 158 μm line. It serves as a cooling line for gas over a large range of temperatures, typically $T \sim 100$ K, and densities, typically above a few 10^3 cm^{-3}, in PDRs (Hollenbach et al. 1991; Ossenkopf et al. 2013) and at much lower temperatures (around 20 K) in CO-dark but H_2-rich regions (Wolfire et al. 2010; Schneider et al. 2023) and can also arise from the warm ionized medium and from diffuse atomic gas at lower densities (Pineda et al. 2013; Beuther et al. 2014; Kabanovic et al. 2022). The transition from ionized carbon (C^+) to CO occurs deeper in the cloud, typically at $A_{\rm eff,V} \sim 1$ (Lee et al. 1996; Visser et al. 2009; Glover et al. 2010; Seifried et al. 2020). Here, the photodissociation of CO by FUV photons dominates over the production reaction (Wolfire et al. 2010; Clark et al. 2012; Glover et al. 2015). The [C II] 158 μm line is easy to excite thermally by collisions with electrons and atomic and molecular hydrogen. The critical density, defined by the collisional de-excitation rate being equal to the effective spontaneous decay rate, depends on the temperature. It is 9 cm^{-3}, 3×10^3 cm^{-3}, and 6.1×10^3 cm^{-3} for collisions with e^-, H, and H_2, respectively, for gas temperatures $\lesssim$100 K (Goldsmith et al. 2012). In diffuse gas, the excitation temperature of [C II], which can go down to less than 20 K (Kabanovic et al. 2022), is notably lower than the kinetic temperature because the densities are too low to produce a collisional excitation rate comparable to the spontaneous decay rate (Goldsmith et al. 2012). In addition, the [C II] line can also serve as a cooling line in low to moderate velocity C-type shocks with a low incident UV field (Lesaffre et al. 2013). The authors developed models of low-UV irradiated low and moderate (up to 40 km s^{-1}) C- and J-type shocks and compared the results with observations. They concluded that [C II] is a good tracer for the dissipation of kinetic and magnetic energy in weakly shielded gas where it is the dominant carbon species.

While there is an increasing number of studies focusing on [C II] emission in bright PDRs, [C II] studies of diffuse, translucent, and low-column density clouds[3], are relatively scarce. In a work conducted by Goldsmith et al. (2018), a limited number of diffuse interstellar clouds were observed using H I absorption features measured against a background quasar. This approach allowed for the sampling of the entire line of sight through the Galaxy. The researchers concluded that photoelectric heating stands out as the predominant heating mechanism for these clouds, with the [C II] line being the principal cooling line.

In this study, we present novel observational findings pertaining to [C II] and CO emissions within the Draco and Spider high-latitude diffuse clouds. We utilized archival [C II] and CO data concerning the quiescent Polaris cloud and the low-density Musca molecular cloud. All of these clouds are subject to a low-incident UV field, which is, depending on the method used to infer the UV radiation field, between ∼1.5 to ∼10 G_o. The [C II] emission line has been exclusively detected in the intermediate-velocity cloud Draco, with no detection observed at local velocities in the Spider, Polaris, and Musca clouds. A comprehensive comparison of the physical characteristics across these distinct clouds was conducted using models of PDR emission, shocks, and non-LTE (Local Thermodynamic Equilibrium) conditions, leading to an argument in favor of shock excitation as the most plausible rationale for the presence of [C II] within the Draco cloud. This deduction is based on the cloud's high-velocity descent toward the Galactic plane and its interaction between H I clouds. Consequently, this highlights the significance of dynamics in influencing the chemical evolution within interstellar clouds.

We start with a description of the sources (Sect. 2) and the observations (Sect. 3). The observations are presented in Sect. 4 and analyzed in Sect. 5. Section 6 provides a discussion of the results, and Sect. 7 presents a summary of the paper.

2. The observational cloud sample

Draco and Spider are both part of the interstellar cirrus, associated with diffuse H I clouds (Heiles & Habing 1974). Draco constitutes a relatively isolated feature, containing gas concentrated within local, intermediate, and high-velocity clouds, referred to as LVC, IVC, and HVC, respectively. The distances to the IVC and LVC were established to be within the range of 463–618 pc by Gladders et al. (1998) through the utilization of sodium doublet absorption. In a recent study, Zucker et al. (2020) employed *Gaia* DR2 parallax measurements to deduce a distance of 481±50 pc, a value we will adopt in this paper. Spider and Polaris are situated within the North Celestial H I Loop (Meyerdierks et al. 1991). Using *Gaia* data, Zucker et al. (2020) determined distances ranging from 341 to 472 pc (with uncertainties between 10 and 40 pc) for three locations close to the Polaris cloud. It is important to note that these locations are distant from the area of the [C II] observation, which primarily focuses on the brightest region evident in dust and CO emissions. An additional *Gaia*-based study by Yan et al. (2019) reports a distance of 489 pc. These distances surpass earlier estimates. Heithausen & Thaddeus (1990) discussed various potential distances to Polaris and proposed an upper limit of 240 pc, while Falgarone et al. (2009) employed a distance of 150 pc. In order to maintain consistency with our prior work on dust column density probability distribution functions (Schneider et al. 2022), the results of which will be employed herein, we opt for adopting a distance of 489 pc. For Spider, Zucker et al. (2020) determined a value of 369±18 pc (we will use here) for the distance which places this region further away than earlier estimated of around 100 pc (de Vries et al. 1987). Musca is located in the southern Chamaleon-Musca cloud complex. Distances between 140 and 225 pc are reported (Franco 1991; Knude & Hog 1998;

---

[3] Clouds with $A_V < 1$, A_V = 1–5, and $A_V > 5$ are typically called diffuse, translucent, and low-column density or dark clouds (Barriault et al. 2010a) respectively.

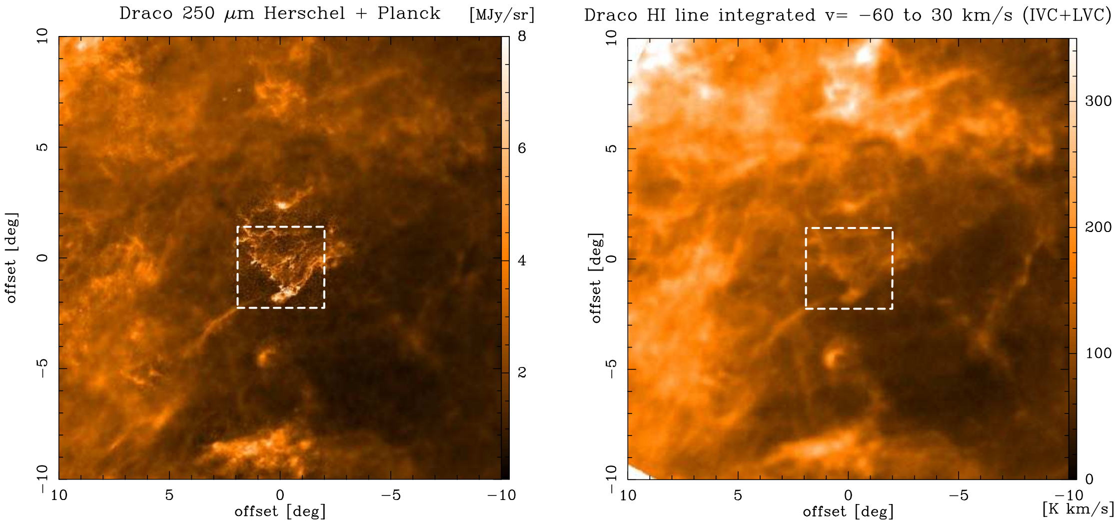

Fig. 1. FIR and H I maps of Draco. Left: combined *Herschel* and *Planck* 250 μm map of the Draco cloud and its environment. The offsets in degrees correspond to the center position of RA(2000) = $16^h47^m57^s$, Dec(2000) = 61°45′16″ ($l = 91.829$, $b = 38.156$). The angular resolution of the *Herschel* map (in the image center) is 36″ and the one of the *Planck* map is ~5′. The white dashed square indicates the area for which we show the dust column density map. Right: velocity integrated H I map from the Effelsberg H I survey (EBHIS) at 10′ resolution. The velocity range covers the IVC and LVC. Maps of the other velocity ranges are shown in Appendix A.

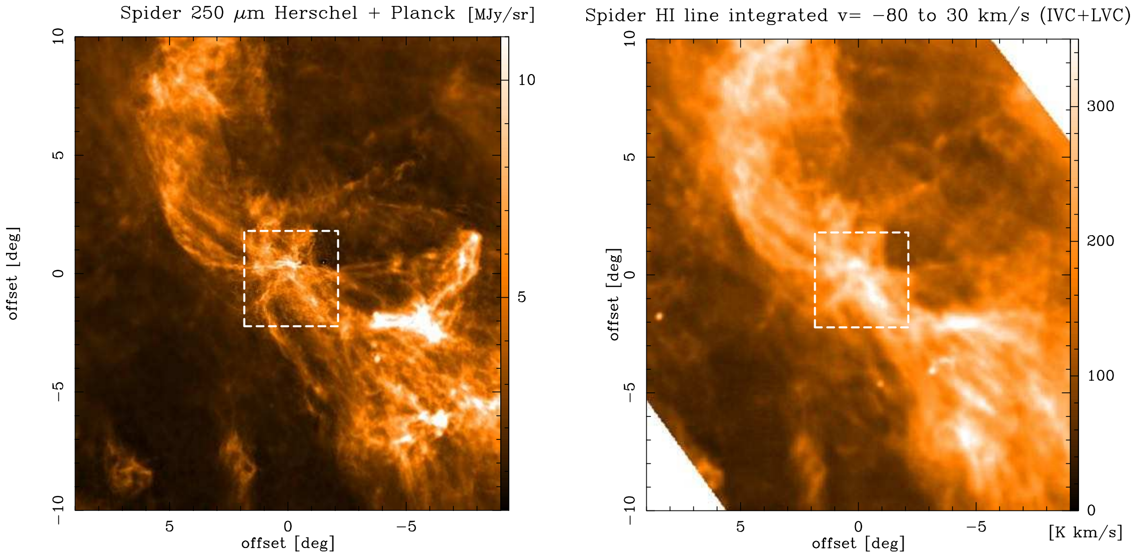

Fig. 2. Same as Fig. 1 but for Spider. The offsets correspond to the center position of RA(2000) = $10^h37^m58^s$, Dec(2000) = 72°59′42″ ($l = 135.200$, $b = 40.800$).

Bonne et al. 2020b). We here adopt a value of 150 pc to be consistent with Schneider et al. (2022). It is not straightforward to give an error range of this value, see Appendix A in Bonne et al. (2020b). The reddening of stars due to cloud material starts at 90 pc and reaches its peak at ≈180 pc. It is, however, difficult to assess at which distance the gas of the Musca filament is located.

Figure 1 provides an overview of the *Herschel* 250 μm map of Draco, outlined by a white dashed square, situated within a larger scale *Planck* map at the same wavelength (left panel). Additionally, the right panel depicts H I emission across the intermediate and low velocity range spanning from −60 to 30 km s^{-1}. Notably, the velocity structure within the H I data becomes even more intricate when dissecting the velocity ranges. Refer to Fig. A.1 for a depiction of faint gas emission at local velocities ranging between −10 and 30 km s^{-1}, a prominent component representing intermediate velocities spanning from −30 to −10 km s^{-1}, and focused emission at high velocities ranging from −200 to −100 km s^{-1}. Figure 2 shows the combined *Herschel* and *Planck* 250 μm map for the Spider region where distinct LVC (−10 to 30 km s^{-1}) and IVC (−80 to −10 km s^{-1}) components are observable, although no HVC is apparent. It is important to highlight that Draco stands out as the only region dominated by H I emission of the IVC, whereas Spider solely exhibits a weak IVC component. Furthermore, Polaris and Musca exclusively feature gas at local velocities, derived from CO observations, which correspond to H I emission velocities of −3.7 km s^{-1} and 3 km s^{-1}, respectively.

Draco (IVC G091.0+38.0, MBM41) is located at $b = 38.4°$ at a height of around 298 pc above the Galactic plane, considering a distance of 481 pc. There are no OB stars in the immediate environment, but there is noteworthy 160 μm flux in the *Herschel* map. Emission at 70 μm is at the noise level. Assuming that the dust is only heated by external FUV radiation of stars, the 160 μm flux can be translated into a FUV field (see Sect. 5.1) and we derive a field of 3.6 G_o averaged over the 4 positions (the average FUV field is 1.6 G_o from a census of the stars).

It has been recognized for quite some time (Mebold et al. 1985) that the IVC descends toward the Galactic plane with a significant velocity and experiences deceleration due to its interaction with the surrounding warm neutral medium. Notably, observations have revealed high FIR emissivities and elevated CO abundances (Herbstmeier et al. 1993), which were interpreted as arising from a direct interaction with the HVC. This high-velocity gas could originate from the infall of extragalactic material. However, recent H I surveys (Westmeier 2018) have identified a velocity gap between the IVC and the HVC in Draco (Fig. B.1), rendering a collision scenario less plausible. Furthermore, the Draco region prominently exhibits emissions at intermediate velocities. A proposed explanation for Draco's origin involves a Galactic fountain process, where material from the Galactic disk is lifted above the plane and subsequently returns at high velocities to the disk (as elaborated in Lenz et al. 2015 and references therein). For a more comprehensive discourse on the underlying physics and potential sources of IVCs, readers are encouraged to explore Putman et al. (2012), Röhser et al. (2014, 2016a,b), Kerp et al. (2016), and the accompanying references.

By investigating probability distribution functions of H I (N_{HI}-PDF) and of *Herschel* derived total hydrogen column density (N-PDFs), Schneider et al. (2022) showed that the N-PDF of Draco has the form of a double-log-normal. The authors propose that one log-normal arises from atomic gas and the other one from molecular gas. The H I-to-H_2 transition is defined where the two log-normal dust N-PDFs have equal contributions and takes place at $A_V = 0.33$ (N(H) = 6.2×10^{20} cm^{-2}). Importantly, the absence of a power-law tail in the distribution implies that self-gravity does not currently play a significant role in the region. Nevertheless, certain regions within Draco have exhibited detections of [C I], CO, and other molecules with critical densities exceeding 10^3 cm^{-3} (Mebold et al. 1985; Herbstmeier et al. 1993) and are thus mostly molecular. Furthermore, Miville-Deschênes et al. (2017), utilizing *Herschel* dust observations, inferred that the molecular gas primarily comprises small (~0.1 pc), dense (n ~1000 cm^{-3}), and cold (T ~ 10–20 K) clumps. Despite the presence of such molecular structures, no indications of active star formation have been observed within the cloud, as evidenced by the lack of detected pre- or proto-stellar cores.

In contrast to Draco, the Spider region has received significantly less attention. Barriault et al. (2010a,b) presented maps of H I, OH, and CO emission and concluded that around 20% of the gas exists in the molecular phase. CO, serving as a tracer of CO-bright H_2, is found where two H I velocity components merge into one component or where there is a velocity shear. Barriault et al. (2010b) derived an upper limit for the volume density of 2×10^3 cm^{-3}. The *Herschel* dust and Effelsberg H I emission distributions, shown in in Fig. 2, support qualitatively this idea because the densest parts of the Spider cloud are located in the center of various flows. As already pointed out, in contrast to Draco, H I emission in Spider is dominated by the LVC and not the IVC (see Fig. A.2) and has no HVC component. Similarly to Draco, we derive the FUV field from the 160 μm flux, assuming radiative excitation, yielding a maximum value of 2.9 G_o.

The Polaris flare exhibits abundant extended, diffuse emission previously observed through IRAS at 100 μm (Low et al. 1984), and now unveiled in large detail using *Herschel* (Miville-Deschênes et al. 2010). The most densely concentrated region, MCLD 123.5+24.9, referred to as the 'saxophone', has been scrutinized across various CO lines (Heithausen & Thaddeus 1990; Falgarone et al. 1998), as well as in [C I] (Bensch et al. 2003), housing a handful of prestellar cores. The peak column density at the core positions ranges from 6 to 13 × 10^{21} cm^{-2} (Ward-Thompson et al. 2010). The density at this position, which coincides with our [C II] position, is derived to be between 2 and 5×10^4 cm^{-3} from CO, HCN, and *Herschel* FIR data (Grossmann & Heithausen 1992; Heithausen et al. 1995; Ward-Thompson et al. 2010). The incident FUV field at the cloud's location was estimated to be approximately one G_o (Bensch et al. 2003). By leveraging the methodology that converts the 160 μm flux to a FUV field, we ascertain a field strength of around ~1.5 G_o at the precise coordinates of the [C II] observation site. In an earlier investigation, Heithausen & Thaddeus (1990) approximated that roughly 40% of the hydrogen in the Polaris flare is molecular. Consequently, it follows that this cloud is more advanced in its evolutionary stage compared to Draco and Spider, supported by its N-PDF (Schneider et al. 2013, 2022).

Musca is located in the south, embedded in the extended Chameleon complex. It presents itself as a prominent filamentary structure extending over 6 pc, as illustrated in previous works (Kainulainen et al. 2009, 2016; Cox et al. 2016), yet exhibits minimal star-formation activity. Notably, a sole protostar has been identified in the northernmost part of the filament, while the cloud remains relatively unaffected by protostellar feedback. The external FUV field is approximated to be 3.4 G_o as an upper limit (without considering extinction), as deduced from an analysis of neighboring stars (Bonne et al. 2020b,a). Alternative estimates place the FUV field at 5.8 G_o based on the 160 μm flux and roughly 10 G_o according to the Musca map featured in Xia et al. (2022). Within the dense crest region, peak column densities surpass those observed in Polaris, reaching $N \sim 10^{22}$ cm^{-2} (Cox et al. 2016) at the position of the protostar. In all other locations, the column densities are smaller than 8 × 10^{21} cm^{-2} and the (column)-densities are also notably lower at the exact location of the [C II] observation. The volume density at this position is at least 7×10^3 cm^{-3}, based on CO and [C I] observations presented in Bonne et al. (2020a). They performed a non-LTE analysis of the observed tracers and obtained this density for the warm gas layer slightly outside of the denser (up to 10^4 cm^{-3}) Musca ridge.

3. Observations

3.1. SOFIA

Draco was observed during Cycle-5, both within guaranteed time and open time allocations, under the program number 05_0208, with N. Schneider as the principal investigator (PI). A total of five positions were targeted for observation, with their coordinates provided in Table 1, and their locations given in Fig. 3. These observations took place over the course of three flights utilizing the Stratospheric Observatory for Infrared Astronomy (SOFIA), operating from Palmdale, California. Among the selected positions, two were situated at peaks in dust column density in the southern region, designated as Nose 1 and Nose 2. These locations had previously exhibited detections of CO (refer to Fig. 4 for our CO spectra) and other molecular lines. Additionally, two positions were chosen within the eastern region, labeled as Front 1 and Front 2. It is noteworthy that all these positions display prominent H I emission within the IVC and LVC velocity ranges. In contrast, the position denoted as IVC is positioned farther away from the regions of high column density.

Table 1. Observational parameters for the [C II] data.

Cloud	α_{J2000}	δ_{J2000}	rms [K]	S/N
Draco				
Draco Front 1	$16^h58^m18^s$	61°30′10″	0.0445	3.4
Draco Front 2	$16^h50^m54^s$	60°54′37″	0.0270	3.2
Draco Nose 1	$16^h49^m06^s$	59°55′58″	0.0251	4.4
Draco Nose 2	$16^h46^m29^s$	60°19′31″	0.0344	4.7
Draco IVC	$16^h32^m13^s$	61°39′10″	0.0487	–
Spider				
Spider 1	$10^h40^m59^s$	73°22′21″	0.0445	–
Spider 2	$10^h33^m58^s$	73°56′12″	0.0647	–
Polaris	$01^h59^m32^s$	87°39′41″	0.0317	–
Musca	$12^h24^m41.6^s$	−71°46′41″	0.0278	–

Notes. The coordinates specify the positions of each setting of the seven-pixel [C II] array. For the rms determination, the seven positions from the single array were averaged and resampled to a velocity resolution of 0.6 km s^{-1}. The signal-to-noise ratio (S/N; peak main beam brightness temperature over rms in one channel) is given in the last column if the [C II] line was detected.

This position is exclusively discernible within the IVC and HVC velocity range.

The Front 1 position was observed on November 8, 2016, using the GREAT instrument (Heyminck et al. 2012). The 7-pixel GREAT/LFA array was tuned to the [C II] 158 μm line, and the single-pixel L1 channel was tuned to the [N II] 1.461 THz line. This observation was repeated, and another position (Nose 1) was added on February 3, 2017, employing upGREAT (Risacher et al. 2018). The 2 × 7 pixels LFA array was again tuned to the [C II] 158 μm line, and the L1 channel on the [N II] 1.461 THz line. Three further positions (Nose 2, Front 2, and IVC) were observed on February 14, 15, 16, and 17, 2017, in the same upGREAT/LFA setup, but tuning the L1 channel to the CO 11→10 line at 1.1 THz. All observations were carried out in total power mode, and different emission-free positions with offsets of typically 10′–15′ to the center positions were used. The total observing time for each position (ON+OFF) was typically one hour. Beam efficiencies used in this paper were determined using Mars as a calibrator for each pixel; the average is 0.64 for the LFA and 0.65 for L1. Third-order spectral baselines were applied to the LFA/L1 spectra and then averaged with a fixed velocity axis and 1/rms^2 weighting, smoothed to a channel width of 0.6 km s^{-1}. The main beam sizes are 19″ at 1.1 THz, 17″ at 1.4 THz, and 14.1″ at 158 μm, respectively.

Spider was observed during Cycle-6 under the program number 06_0153 (PI N. Schneider). The observations were carried out on May 23, 2018, from Palmdale, California, using upGREAT on SOFIA. The upGREAT/LFA array (2 × 7 pixels) was tuned to the [C II] 158 μm line, and the HFA array (7 pixels) was tuned to the [O I] 63 μm line. Two pointings were performed in total power mode, centering on positions Spider 1 at RA(2000) = $10^h40^m59^s$, Dec(2000) = 73°22′21″, and Spider 2 at RA(2000) = $10^h33^m58^s$ (Fig. 5), Dec(2000) = 73°56′12″. The reference positions were located at an offset of 15′ east of the center positions. Spider 1 is identical with 'S3' in Barriault et al. (2010a) and represents the peak of IR emission at 100 μm. Spider 2 coincides with position 'S6' in Barriault et al. (2010a) and has peak emission in the atomic phase. The total observing time for each position (ON+OFF) was typically one hour. The determination of beam efficiencies was accomplished by utilizing Mars as a calibrator for each pixel. The calculated averages are 0.64 for the Low-Frequency Array (LFA) and 0.66 for the High-Frequency Array (HFA). For the LFA/HFA spectra, baseline corrections of the first and third orders were applied. The corrected spectra were then subjected to averaging, employing a fixed velocity axis and a weighting scheme of 1/rms^2. Further refinement was achieved by smoothing to a channel width of 0.6 km s^{-1}. The physical dimensions of the main beams are 6.3″ at a wavelength of 63 μm and 14.1″ at 158 μm, respectively.

We also use archival [C II] data from a SOFIA PI-program on Polaris (Cycle-5, 75_0020 PI W. Reach) and Musca (Cycle-6, 06_0177, PI S. Bontemps).

In the Polaris flare a single position-switch pointing at RA(2000) = $01^h59^m32.0^s$, Dec(2000) = 87°39′41.0″ was performed 2017 June 14 from Palmdale, California, in the LFA/HFA configuration with the [C II] 158 μm line and the [O I] 63 μm line, respectively. The reduced data on a main beam brightness temperature scale were taken from the SOFIA archive[4]. The position corresponds to the 'core 4' position in Ward-Thompson et al. (2010) within the MCLD 123.5+24.9 region.

Musca was observed 2018 June from Christchurch, New Zealand. A single pointing in position-switch at RA(2000) = $12^h24^m41.6^s$, Dec(2000) = −71°46′41.0″ was carried out in the same [C II] and [O I] configuration as for Polaris. The total duration of the observations was 70 min. No line was detected in [C II] or [O I] in the individual array spectra (see Fig. A.1 in Bonne et al. 2020b).

3.2. (Sub)Millimeter line data

For Draco and Spider, we utilized unpublished CO data acquired at the IRAM 30 m telescope in 2017 and 2018 for two projects (002-17, led by PI: Q. Salome; 003-18, led by PI: J. Kerp).

In August 2017, we conducted small-scale maps in the ^{12}CO and ^{13}CO 1→0 and 2→1 lines, centered on the five SOFIA positions in Draco, employing the EMIR E090 and E230 receivers in frequency-switching mode. In this study, we leveraged ^{13}CO 2→1 observations from all positions and all CO data for the Front 2 and Nose 2 positions from this program, as they were excluded from the 2018 observing campaign. All data were smoothed to a velocity resolution of 0.5 km s^{-1} for the 1→0 line observations and 0.25 km s^{-1} for the 2→1 line to match the 2018 observations.

In July 2018, the observation focus shifted to other regions in Draco. Nevertheless, we conducted small-scale maps around the Front 1 position (110″×110″) and the Nose 1 position (400″ × 400″). For Spider, a map of dimensions 140″ × 140″ was obtained around the Spider 1 position, while Spider 2 involved a single extended integration. All observations were performed in total power mode with a reference position situated 33′ east of the map center. We used the EMIR E090 and E230 receivers in parallel, tuned to the ^{12}CO 1→0 and 2→1 lines at 115.271 GHz and 230.538 GHz, respectively, ensuring that the ^{13}CO 1→0 line fell within the bandpass. As the backend, we utilized the Fourier Transform Spectrometer (FTS) in a configuration that yielded velocity resolutions of 0.51 and 0.53 km s^{-1} for the ^{12}CO and ^{13}CO 1→0 data, and 0.25 km s^{-1} for the ^{12}CO 2→1 data. The beamsize of the CO 2→1 data is 11″ and of the CO 1→0 data 22″. In this study, we incorporated all CO data

---

[4] `https://irsa.ipac.caltech.edu/applications/sofia`

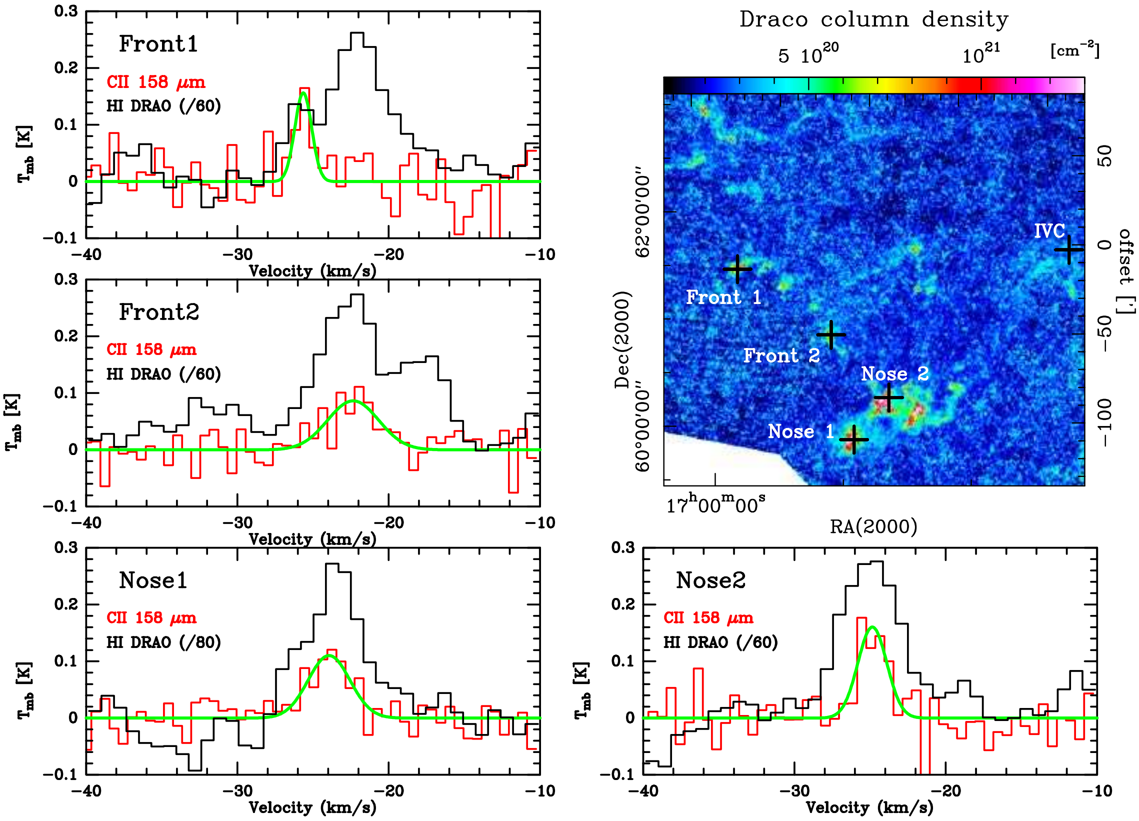

Fig. 3. Spectra and column density map of Draco. Right panel: *Herschel* hydrogen column density map derived from dust in color in which the observed [C II] positions are indicated with black crosses. In the panels around, spectra of the [C II] 158 µm line and the H I 21 cm line (DRAO), both at ∼1′ resolution, are displayed. We note that the H I line was reduced for better visibility. The green curve indicates a single Gaussian fit to the [C II] line.

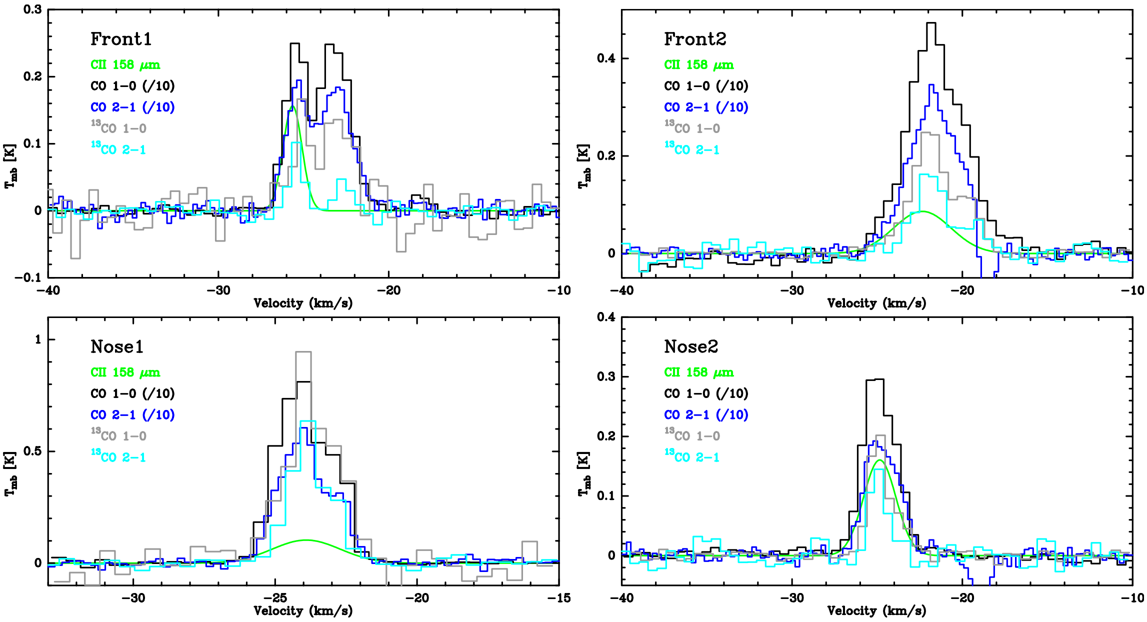

Fig. 4. Spectra of [C II] and CO emission at the 4 positions. For better visibility of the [C II] spectra, only the Gaussian fit is shown (in green) and the ^{12}CO line intensities were reduced by a factor of 10.

from the Front 1, Nose 1, and IVC positions, as well as the CO data from Spider, which was not covered in 2017. The Front 1 and Nose 1 positions were also observed in 2017, and the spectra exhibit consistent line positions and intensities. All data are

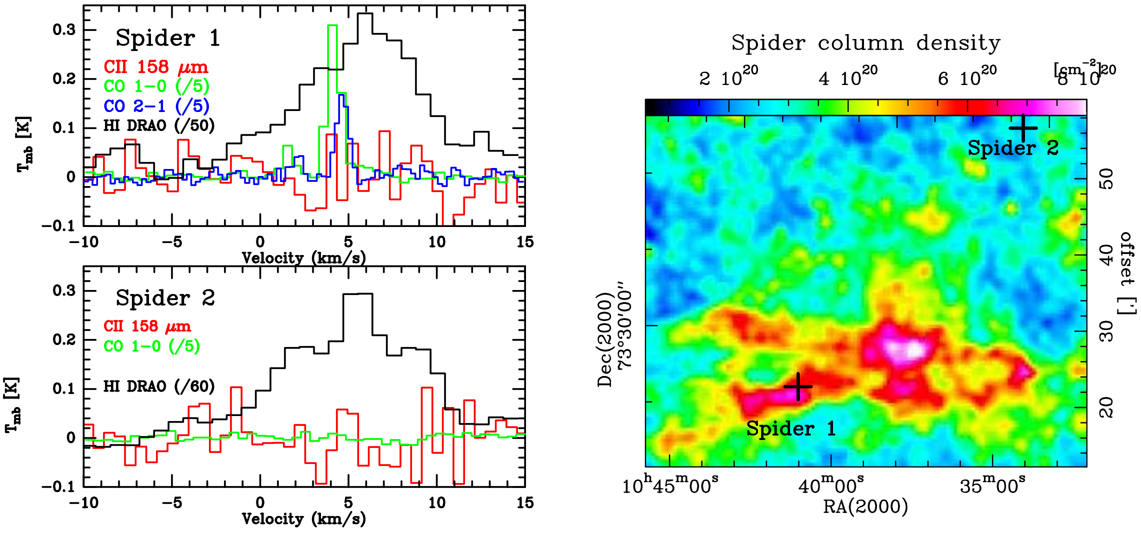

Fig. 5. Spectra and column density map of Spider. Right panel: *Herschel* hydrogen column density map derived from dust in color in which the observed [C ii] positions are indicated with black crosses. Left panels: Spectra of the [C ii] 158 μm, CO, and H i (DRAO) lines, all at ∼1′ resolution. We note that some line intensities were reduced for better visibility.

presented on a main beam brightness temperature scale (using main beam efficiencies[5] of 0.78 at 115 GHz and 0.59 at 230 GHz).

For Polaris, we use data from the IRAM key-project “Small-scale structure of pre-star forming regions” (PIs E. Falgarone, J. Stutzki). The data were made available via the Centre de données astronomique Strasbourg (CDS). We here only employ spatially smoothed isotopomeric CO 2→1 and 1→0 spectra extracted for the [C ii] position (the maps are all large enough to allow for smoothing to 70″). For more details on the observations see Falgarone et al. (1998). For Musca, we use CO data presented in Bonne et al. (2020b,a) that stem from various CO observing runs at the APEX telescope. For technical details we refer to the relevant papers given above. In order to allow for a comparison to the array-averaged [C ii] data, we smoothed all CO spectra for all sources to a beam of 70″.

For one position in Draco (Nose 1), we use integrated intensities of the 1→0 line of atomic carbon ([C i]) at 490 GHz, given in Table 1 in Heithausen et al. (2001) that stem from observations performed with the *Heinrich-Hertz* telescope (HHT) located on Mount Graham in Arizona. Four positions in Draco were covered, with one observations (0″,0″) very close to our Nose 1 position and the others in steps of 30″ offset in *x*-direction. The beamsize of the HHT at 490 GHz is 16″ and thus smaller than what we use here to compare line intensities and ratios (70″). However, the [C i] line intensity does not change significantly over the range of 0 to 90″ so that we can assume to first order a beam filling of unity. This will be important for the PDR modeling.

3.3. Complementary data sets

We use publicly available[6] observations of the H i 21 cm line (1420 MHz) for the Draco and Spider regions from the DRAO Synthesis Telescope and the Green Bank Telescope (GBT; Blagrave et al. 2017). The data have an angular resolution of 1′ and a velocity resolution of 1.32 km s^{-1} for a channel spacing of 0.824 km s^{-1} and comprise a total velocity range of −103 to 33 km s^{-1} for Draco and −164 to 44 km s^{-1} for Spider.

Additionally, we make use of the all-sky H i data from the Effelsberg-Bonn HI survey (Winkel et al. 2016) at an angular resolution of ∼10′. The EBHIS survey[7] is a joined project of the AIfA and the MPIfR to image the neutral hydrogen content of the Milky Way galaxy and trace extragalactic sources. The spectra have a channel width of 1.3 km s^{-1}, the rms noise is less than 90 mK, and the data is corrected for stray radiation (Röhser et al. 2014). We obtained fits data cubes from the CDS.

4. Results

4.1. Draco

Figure 3 displays the total hydrogen column density map at 36″ of Draco, derived from *Herschel* dust flux maps (Schneider et al. 2022). The positions observed in [C ii] with SOFIA and CO with the IRAM 30 m telescope are indicated. The [C ii] spectra, averaged over the entire array for each position, resulting in an effective angular resolution of 70″, are shown in the surrounding panels, along with H i spectra from the DRAO survey. Figure 4 presents the [C ii] spectra alongside various CO isotopologues and transitions (^{12}CO and ^{13}CO 1→0 and 2→1), all at an angular resolution of 70″. The IVC position is not displayed due to the absence of a [C ii] detection. Table 2 provides the observed [C ii] main beam brightness temperature, line position and width, and line-integrated intensity resulting from a single Gaussian line fit. Additionally, it includes the total hydrogen column density and dust temperature from *Herschel*, both measured within a 70″ beam. Table 3 lists the main beam brightness temperatures, line positions and widths, and line-integrated temperatures for the ^{12}CO and ^{13}CO 2→1 and 1→0 lines, derived from Gaussian fits with two components. The [C ii] line was detected at a level of 0.1–0.2 K, corresponding to a S/N of 3–5 (Table 1), within velocities ranging from −22 to −26 km s^{-1} at four out of the

---

[5] `http://www.iram.es/IRAMES/mainWiki/Iram30mEfficiencies`

[6] `http://www.cita.utoronto.ca/DHIGLS`

[7] `https://astro.uni-bonn.de/~jkerp/index.php?page=EBHISproject`.

Table 2. Physical parameters of Draco for the five observed positions.

Position	[C II] $T_{\rm mb}$ [K]	[C II] v [km s^{-1}]	[C II] $FWHM$ [km s^{-1}]	[C II] I [K km s^{-1}]	N(H) [10^{20} cm^{-2}]	T_d [K]	FUV 160 µm [G$_\circ$]	FUV stars [G$_\circ$]
Front 1	0.16	−25.6	1.32	0.22	8.48	13.4	3.7	$1.55^{1.59}_{1.51}$
Front 2	0.09	−22.4	4.03	0.37	5.80	13.8	3.1	$1.56^{1.60}_{1.52}$
Nose 1	0.11	−23.9	3.26	0.38	12.70	13.1	4.3	$1.57^{1.61}_{1.52}$
Nose 2	0.16	−24.9	2.02	0.36	13.17	12.9	3.2	$1.57^{1.61}_{1.53}$
IVC	–	–	–	–	3.21	13.3	2.2	$1.58^{1.61}_{1.54}$

Notes. The name of the position is given in the first column, followed by the [C II] main beam brightness temperature, line velocity, FWHM, and line integrated intensity. These values were determined from a single Gaussian line fit. Columns 6 and 7 give the hydrogen column density and temperature from *Herschel*. Column 8 displays the FUV field in Habing units, determined from the 160 µm flux, and Col. 9 the one from the census of the stars (Sect. 5.1). The FUV values are given for the heliocentric distance D of the source. The upper and lower values indicate the field considering the uncertainty in the distances (D+ΔD and D-ΔD).

Table 3. Draco's CO line parameters determined from a Gaussian line fit with two velocity components.

	^{13}CO 1→0				^{12}CO 1→0				^{13}CO 2→1				^{12}CO 2→1			
	$T_{\rm mb}$ [K]	v $[\frac{\rm km}{\rm s}]$	Δv $[\frac{\rm km}{\rm s}]$	I $[\frac{\rm Kkm}{\rm s}]$	$T_{\rm mb}$ [K]	v $[\frac{\rm km}{\rm s}]$	Δv $[\frac{\rm km}{\rm s}]$	I $[\frac{\rm Kkm}{\rm s}]$	$T_{\rm mb}$ [K]	v $[\frac{\rm km}{\rm s}]$	Δv $[\frac{\rm km}{\rm s}]$	I $[\frac{\rm Kkm}{\rm s}]$	$T_{\rm mb}$ [K]	v $[\frac{\rm km}{\rm s}]$	Δv $[\frac{\rm km}{\rm s}]$	I $[\frac{\rm Kkm}{\rm s}]$
Front 1 a	0.16	−25.1	1.01	0.17	2.44	−25.4	1.43	3.72	0.10	−25.4	0.91	0.10	1.75	−25.4	1.54	2.87
Front 1 b	0.14	−22.9	2.31	0.35	2.52	−23.1	2.15	5.77	0.05	−22.7	1.09	0.06	1.82	−23.1	2.28	4.42
−29.5,−20	$I_{\rm int}$ = 0.54 K km s^{-1}				$I_{\rm int}$ = 9.5 K km s^{-1}				$I_{\rm int}$ = 0.14 K km s^{-1}				$I_{\rm int}$ = 7.3 K km s^{-1}			
Front 2 a	0.24	−22.0	2.33	0.60	3.73	−21.8	3.47	13.78	0.16	−21.9	2.09	0.36	3.14	−22.1	2.72	9.09
Front 2 b	0.10	−19.5	1.39	0.15	0.90	−20.3	4.23	4.04	0.06	−19.2	1.34	0.09	1.53	−20.2	1.39	2.26
−27,−18	$I_{\rm int}$ = 0.82 K km s^{-1}				$I_{\rm int}$ = 18.0 K km s^{-1}				$I_{\rm int}$ = 0.47 K km s^{-1}				$I_{\rm int}$ = 11.1 K km s^{-1}			
Nose 1 a	0.85	−24.0	1.50	1.35	8.22	−24.2	1.80	15.78	0.61	−24.0	1.33	0.87	5.69	−24.1	1.81	11.00
Nose 1 b	0.38	−22.6	0.96	0.39	3.71	−22.7	0.78	3.07	0.24	−22.6	0.53	0.14	2.25	−22.6	0.76	1.82
−27,−20	$I_{\rm int}$ = 1.78 K km s^{-1}				$I_{\rm int}$ = 19.0 K km s^{-1}				$I_{\rm int}$ = 1.04 K km s^{-1}				$I_{\rm int}$ = 12.9 K km s^{-1}			
Nose 2 a	0.21	−25.0	1.17	0.26	3.02	−25.2	1.74	5.60	0.14	−25.1	0.94	0.14	1.92	−24.9	2.27	4.63
Nose 2 b	0.06	−23.6	1.27	0.08	1.22	−23.8	1.32	1.71	0.04	−24.3	1.42	0.06	0.36	−23.3	2.81	1.08
−28,−20	$I_{\rm int}$ = 0.35 K km s^{-1}				$I_{\rm int}$ = 7.6 K km s^{-1}				$I_{\rm int}$ = 0.18 K km s^{-1}				$I_{\rm int}$ = 4.9 K km s^{-1}			

Notes. $I_{\rm int}$ gives the line integrated intensity in the total velocity range in km s^{-1} indicated in the first column. The typical errors for the fitting are 0.2–0.5 K km s−1 for the line integrated intensity in ^{12}CO, 0.01 to 0.08 K km s^{-1} for ^{13}CO, ~0.06 km s^{-1} for the line position and ~0.05 km s^{-1} for the line width for all CO lines, respectively.

five positions. Only the IVC position did not exhibit a [C II] line above the noise threshold. Neither the [N II] nor the [O I] line or the CO 11→10 line were detected at any position.

While the CO and H I spectra exhibit a complex line shape characterized by at least two distinct components, the [C II] line corresponds to one of these velocity components (Front 1a at −25.6 km s^{-1}, Front 2a at −22.4 km s^{-1}), Nose 1 at −23.9 km s^{-1}, and Nose 2 at −24.9 km s^{-1}). The −22 km s^{-1} component is evident in both CO and H I spectra for both Front 1 and Front 2 positions. However, the Front 2 position displays an additional component ranging from −18 to −20 km s^{-1} in both H I and CO spectra. In contrast, no significant velocity difference is discernible between the two nose positions. Overall, the H I line exhibits larger width compared to the [C II] and CO lines. The distinct components of the CO lines are unmistakably distinct velocity features and are not attributed to self-absorption effects. This assertion is supported by the observation that the optically thin ^{13}CO lines present the same two-component line profile.

4.2. Spider

Figure 5 presents a map of the total hydrogen column density in Spider at a resolution of 36″, utilizing *Herschel* dust observations. This methodology is the same as the one employed for Draco, as described in Schneider et al. (2022). The plot identifies the positions observed for [C II] using SOFIA and for CO using the IRAM 30 m telescope. The left panels display the CO and H I DRAO spectra, while Table 4 provides a summary of observations from SOFIA, *Herschel*, and IRAM 30 m. No emission in CO or [C II] within the IVC or LVC velocity ranges is detected at the Spider 2 position. The column density is notably low, measuring 2.4 × 10^{20} cm^{-2} (within a ∼1′ beam). In Spider 1, narrow ^{12}CO 1→0 and 2→1 lines in the LVC were observed. A prominent velocity component at 4.2 km s^{-1} is evident, with a corresponding main beam brightness of $T_{\rm mb}$ = 1.6 K for ^{12}CO 1→0, along with a weaker component at 1.6 km s^{-1} with $T_{\rm mb}$ = 0.3 K for ^{12}CO 1→0. It is worth noting that the emission between ∼1 and 4 km s^{-1} corresponds to just one component

Table 4. Spider observational [C II] and CO data.

	CII	^{12}CO 1→0				^{12}CO 2→1				N(H)	T_d
	I $[\frac{\text{Kkm}}{\text{s}}]$	T_{mb} [K]	v $[\frac{\text{km}}{\text{s}}]$	Δv $[\frac{\text{km}}{\text{s}}]$	I $[\frac{\text{Kkm}}{\text{s}}]$	T_{mb} [K]	v $[\frac{\text{km}}{\text{s}}]$	Δv $[\frac{\text{km}}{\text{s}}]$	I $[\frac{\text{Kkm}}{\text{s}}]$	$[10^{20}$ cm$^{-2}]$	[K]
Spider 1 a	<0.06	1.57	4.18	0.92	1.54	0.85	4.67	0.81	0.73	6.30	17.7
Spider 1 b	<0.06	0.31	1.59	0.77	0.26	0.22	2.12	0.65	0.16	6.30	17.7
Spider 2	<0.06	–	–	–	–	–	–	–	–	2.4	16.8

Notes. The CO line parameters were determined from a Gaussian line fit with two components. The error (for both CO lines) of the line integrated intensity is 0.035 K km s^{-1} and 0.025 km s^{-1} for the linewidth. There was no CO detection at the Spider 2 position. The last two columns give the hydrogen column density and temperature.

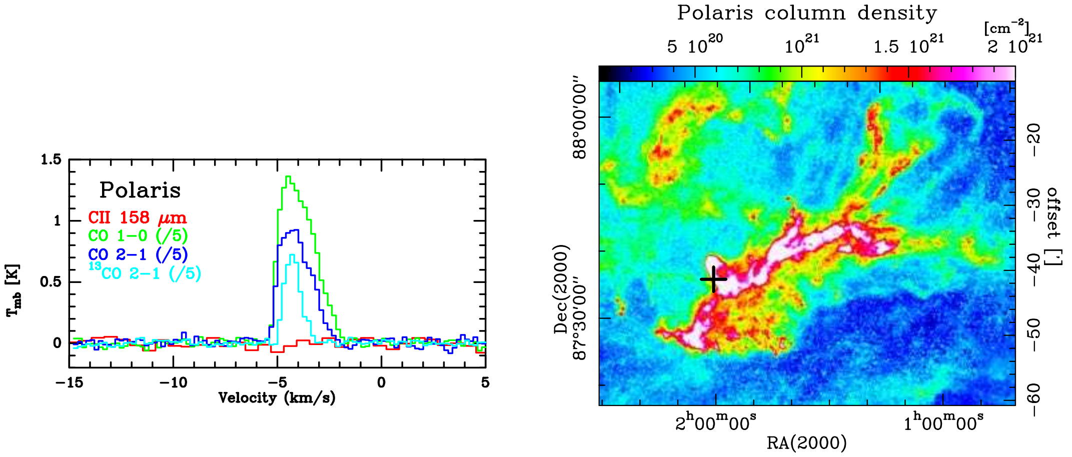

Fig. 6. Spectra and column density map of Polaris. Right panel: cutout of the *Herschel* hydrogen column density map derived from dust of Polaris in color in which the observed [C II] position indicated with black crosses. Left panel: spectra of the [C II] 158 µm and CO lines, all at ∼1′ resolution. We note that some line intensities were reduced for better visibility.

of the broader LVC H I line, which spans significantly wider velocities (refer to Fig. A.2). The *Herschel* data yields a column density value of N(H) = 6.3 × 10^{20} cm^{-2} at the Spider 1 position. This aligns with a peak in IR excess emission, where Barriault et al. (2010a) derived a column density of N(H) = 4.05 × 10^{20} cm^{-2}. The authors highlight that this excess suggests a potential decrease in the quantity of small grains and/or a possible reduction in the temperature of larger grains (Abergel et al. 1996). Such conditions may provide a favorable environment for H_2 formation, as a lower temperature is conducive to this process.

4.3. Polaris and Musca

Figures 6 and 7 display the *Herschel* total hydrogen column density maps from dust for Polaris and Musca (Schneider et al. 2022), respectively, with the observed [C II] position indicated. The left panels show various CO lines, all at a resolution of 70″, to indicate the velocity of the molecular gas. For Polaris, the bulk emission of the cloud is traced by the ^{13}CO 2→1 line at $v \approx -4.5$ km s^{-1}. The ^{12}CO 2→1 and 1→0 lines have an additional component at lower velocities around −3 km s^{-1}. These velocity features are present throughout the Polaris region and were studied in detail by Hily-Blant & Falgarone (2009). They concluded that the occurrence of these two velocity components is a signature of intermittency in turbulent molecular gas.

In the case of Musca, the main velocity component occurs at $v \approx 3$ km s^{-1}, while the ^{12}CO line shows an additional component around 2.5 km s^{-1}. This emission feature was interpreted by Bonne et al. (2020b) as being caused by the dissipation of turbulence in a low-velocity shock. The [C II] line was not detected above the noise limit. The physical properties of both regions are summarized in Table 5.

5. Analysis

In the following, we will determine the FUV field in the sources using different methods (Sect. 5.1), and then derive the physical properties of the gas in the PDR with the help of a PDR model (Sect. 5.2), a non-LTE radiative transfer code (Sect. 5.3), and a shock model (Sect. 5.4). The objective of this exercise is to distinguish which heating mechanism is responsible for the emission of the [C II] and CO lines.

5.1. Determination of the FUV field

For the determination of the FUV field, we employed several approaches we summarize in the following.

Firstly, we translated the observed 160 µm flux into an FUV field, assuming that only radiation from stars is responsible for heating the dust, which is then fully re-radiated at FIR wavelengths. The FUV field was estimated using the correlation (Kramer et al. 2008; Roccatagliata et al. 2013; Schneider et al. 2016): $F_{\text{FUV}}[G_\circ] = (4\pi/1.6)\, I_{\text{FIR}} \times 1000$ where the 160 µm intensity I_{FIR} is given in units of 10^{-17} erg cm^{-2} s^{-1} sr^{-1}.

Secondly, we used the continuous model proposed by Parravano et al. (2003) to estimate the FUV field impinging on

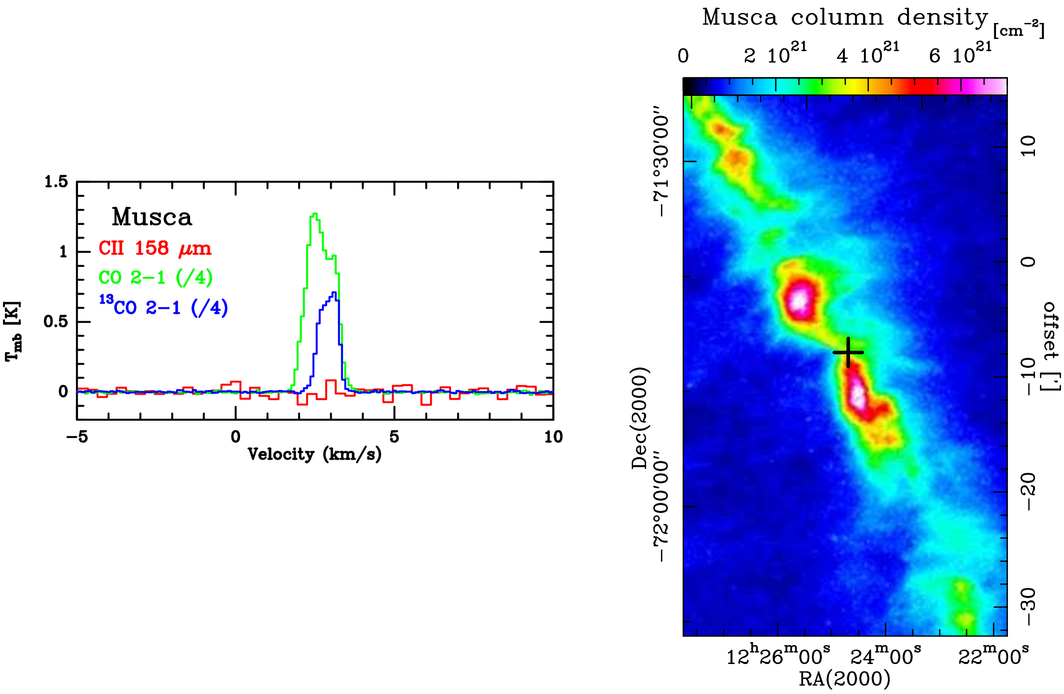

Fig. 7. Spectra and column density map of Musca. Right panel: cutout of the *Herschel* hydrogen column density map derived from dust of Musca in color in which the observed [C II] position indicated with black crosses. Left panel: spectra of the [C II] 158 μm and CO lines, all at ∼1′ resolution. We note that some line intensities were reduced for better visibility.

Table 5. Polaris and Musca observational [C II] and CO data.

	CII	^{12}CO 1→0				^{12}CO 2→1				N(H)	T_d
	I	$T_{\rm mb}$	v	Δv	I	$T_{\rm mb}$	v	Δv	I		
	$[\frac{\rm km}{\rm s}]$	[K]	$[\frac{\rm km}{\rm s}]$	$[\frac{\rm km}{\rm s}]$	$[\frac{\rm Kkm}{\rm s}]$	[K]	$[\frac{\rm km}{\rm s}]$	$[\frac{\rm km}{\rm s}]$	$[\frac{\rm Kkm}{\rm s}]$	[10^{20} cm^{-2}]	[K]
Polaris	<0.03	5.46	−4.06	1.92	11.1	3.82	−4.16	1.75	7.1	32.2	13.8
Musca	<0.03	-	-	-	-	5.11	2.65	1.02	5.58	34.3	14.0

Notes. The CO line parameters were determined from a single Gaussian line fit. The error of the line integrated intensity is 0.09 K km s^{-1} for Polaris and 0.01 K km s^{-1} for Musca, respectively. The error for the linewidth is 0.017 km s^{-1} for Polaris and 0.002 km s^{-1} for Musca, respectively. There is no high angular resolution CO 1→0 data for Musca available. The last two columns give the dust column density and temperature.

Table 6. Distance and FUV field.

Source	$D^{(a)}$ [pc]	$z^{(b)}$ [pc]	FUV from 160 μm [G$_\circ$]	FUV from stars [G$_\circ$]
Draco	481 ± 50	298	3.6$^{(c)}$	1.6
Spider	369 ± 18	240	2.9	1.6
Polaris	489 ± 10	206	1.5	1.3
Musca	150	24	5.8	1.4$^{(d)}$

Notes. FUV field determined at the positions where [C II] was observed with different methods. $^{(a)}$Distance from the sun according to the values given in Sect. 2. $^{(b)}$Approximate height above the Galactic plane. $^{(c)}$Average value of the 4 positions in Draco where [C II] was detected. $^{(d)}$Note that Bonne et al. (2020b) derived a field of 3.4 G$_\circ$ for Musca also from a census of the stars but without considering extinction and assuming a 2D geometry, that is, all stars in the plane of the sky at the Musca distance.

our sources. They assumed a statistically homogeneous distribution of OB stars in the Galactic plane with a scale height of 85 pc for the OB stars and typical dust properties for the FUV absorption and scattering (see below). Despite the local and temporal variations of these properties, they showed that the model reproduces the typical radiation field in the solar neighbourhood with a median value of about 1.6 G$_\circ$. We treated the distribution of the OB stars as a continuous UV source and used the same properties for the dust ($\kappa_{\rm absorption,FUV}$ = 8.0 × 10^{-22} cm^2/H-atom, $\kappa_{\rm scattering,FUV}$ = 7.5 × 10^{-22} cm^2/H-atom, mean scattering angle $g \gtrsim 0.75$ (Appendix B from Parravano et al. 2003) and the vertical gas density distribution (see their Eq. (22) and also our Eq. (4)) of the ISM[8] to compute the flux above the Galactic plane. In this one-dimensional configuration no geometrical dilution occurs but only dust extinction and scattering. The effective optical depth for the FUV radiation is then $\tau_{\rm FUV} = N({\rm H}) \times [\kappa_{\rm absorption,FUV} + (1-R)\kappa_{\rm scattering,FUV}]$, where $0.9 < R < 1$ depending on the number of scattering events. That means that practically only absorption acts as an effective extinction. For Musca falling within the disk of OB stars, the intensity is then only slightly smaller than in the Galactic midplane, but even for the highest latitude cloud, Draco, the radiation field is only

---

[8] Newer numbers for the vertically integrated column from Marasco et al. (2017) are only higher by 6%.

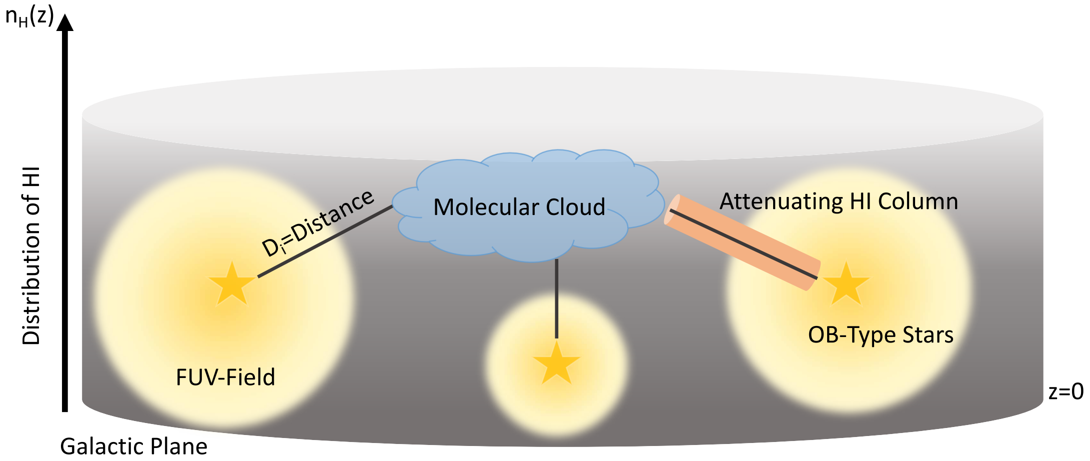

Fig. 8. Schematic illustration of the method to derive the FUV field at each source. The gray cylinder indicates the hydrogen distribution with respect to the galactic height z. The yellow stars indicate the 3D stellar distribution in the Milky Way. The solid black lines originating from the stars indicate the distance from the star to the source. The yellow halo around the star illustrates the FUV field generated by each star. The orange cylinder placed along the path between the star and the source shows schematically the hydrogen column which attenuates the FUV field.

reduced by a factor of 0.8 due to the extinction by the dust column above the Galactic plane of $N(\mathrm{H}) = 2.6 \times 10^{20}$ cm^{-2}. In such a continuous model, all our clouds thus experience an external radiation field between 1.2 and 1.6 G$_\circ$.

In a third approach we dropped the assumption of a homogeneous stellar distribution since a molecular cloud located in the vicinity to an OB-cluster can experience a higher FUV field than the one typical for the solar neighborhood. Thus, we compiled a stellar census from *Gaia* DR3 and compared to the information in SIMBAD, the astronomical database in Strasbourg[9] and utilized the distances provided in the Introduction (also mostly *Gaia* based). Since the data base in *Gaia* DR3 is much larger than the one in SIMBAD, we finally only used the stellar census from *Gaia*. We note, however, a discrepancy we found for one star in Draco that was declared as a B-star in SIMBAD via the original HD star catalog (see compilation in Cannon & Pickering 1993). In the more recent Apogee survey, Jönsson et al. (2020) determined a reliable temperature fit of 6800 K, which puts it at a spectral type F2V. This is in agreement with the *Gaia* parallax, with sets its distance to 300 pc, which is actually not the one considered for Draco (480 pc following Zucker et al. 2020). We checked in addition the Apogee spectrum and it shows that the metallicity is subsolar. In summary, everything agrees with the star being an old F2V star at a distance of 300 pc. The FUV field was then calculated by taking all stars into account from the latest *Gaia* DR3 release (Creevey et al. 2023; Gaia Collaboration 2023), which provides the necessary information such as the stellar position, distance, temperature and luminosity. Since most stars are not hot enough to contribute significantly to the FUV field, we only considered stars with a effective temperature T_{eff} above 10 000 K, thus all spectral types O and B, resulting in 1 192 351 stars[10]. This number is a lower limit since highly embedded stars were not detected. However, such embedded stars do not contribute significantly to the FUV field at our sources since their radiation is extinct in all directions. On the other hand, there can be a substantial column between the star and the observed cloud and therefore a direction dependent extinction. However, the sources of this study all lie within a radius of 0.5 kpc, see Table 6, and it is therefore unlikely that the source is exposed to a radiation field of an undetected stellar cluster. The temperature information of each star is provided by the GSP-Phot (General Stellar Parametrizer from photometry) module[11] and the corresponding luminosity information was taken from the FLAME (Final Luminosity Age Mass Estimator) module. If the stellar luminosity was not provided by FLAME we used the stellar radius and temperature, provided by GSP-Phot to derive the (bolometric) luminosity L:

$$\frac{L}{L_\odot} = \left(\frac{R}{R_\odot}\right)^2 \left(\frac{T_{\mathrm{eff}}}{T_{\mathrm{eff},\odot}}\right)^4 , \tag{1}$$

with the effective temperature of the Sun $T_{\mathrm{eff},\odot} = 5772$ K, the solar radius $R_\odot$ and solar luminosity $L_\odot$. The distance to each star was derived from the parallax information. However, if the parallax error is large, more than half of the parallax, we used instead the distance provided by the GSP-Phot module.

We determined the FUV luminosity by assuming that the spectral radiance of each star can be approximated by a black-body curve. The *Planck* function was integrated over the FUV range spanning from 910 to 2066 Å, corresponding to a photon energy range of 6–13.6 eV. The FUV luminosity is then defined through the ratio of the spectral radiance in the FUV range and the entirety of the black-body spectrum:

$$L_{\mathrm{FUV}} = \frac{\pi \int_{\lambda_{910}}^{\lambda_{2066}} B(\lambda, T)\, \mathrm{d}\lambda}{\sigma T^4} L , \tag{2}$$

with the Stefan-Boltzmann constant σ. The superposition of the stellar FUV flux of all stars considered gives the FUV field at every point in the map:

$$F_{\mathrm{FUV}} = \sum_i \frac{L_{\mathrm{FUV,i}}}{4\pi D_i^2} e^{-\tau_{\mathrm{FUV,i}}} , \tag{3}$$

where D_i represents the distance from the source to each star. The FUV optical depth is defined as described above and the

---

[9] http://simbad.cds.unistra.fr/simbad

[10] We initially also considered cooler supergiants ($T_{\mathrm{eff}} < 10\,000$ K) with a radius larger than 30 $R_\odot$ because they have large luminosities but found that their contribution to the overall radiation field is small.

[11] See https://gea.esac.esa.int/archive/documentation/GDR3 for the *Gaia* DR3 manual.

attenuating column N_H is calculated for each star individually, based on its position with respect to the source. This differs from the continuous model, where the column is simply determined by galactic height of the source. Thus, the hydrogen density $n_H(z)$ (Eq. (22) in Parravano et al. 2003) integrated along the path connecting each star at the galactic height z_i with the source at the galactic height z_s results in the hydrogen column density:

$$\begin{aligned} N_{\rm H,i}(z_s, z_i, D_i) &= \frac{D_i}{z_s - z_i} \int_{z_i}^{z_s} n_{\rm H}(z)\,{\rm d}z \\ &= \frac{D_i}{z_s - z_i} \int_{z_i}^{z_s} 0.566 \left[0.69 \exp\left(-\frac{z}{127\,{\rm pc}}\right)^2 \right. \\ &\quad + 0.189 \exp\left(-\frac{z}{318\,{\rm pc}}\right)^2 \\ &\quad \left. + 0.113 \exp\left(-\frac{|z|}{403\,{\rm pc}}\right) {\rm d}z \right] {\rm cm}^{-2}\,. \end{aligned} \quad (4)$$

Equation (4) is valid for $z_i \neq z_s$, for $z_i = z_s$ the equation simplifies to $N_{\rm H,i} = D_i n_{\rm H}(z_i)$ (with the distance in cm). While *Gaia* DR3 data allow for a more sophisticated 3D treatment of the extinction (Zucker et al. 2022), this goes beyond the scope of this paper. Thus, for the sake of comparison with the previous approach given by Parravano et al. (2003) we use the above Eq. (4). The method is schematically illustrated in Fig. 8. The resulting values for the FUV field are around 1.3−1.6 $G_\circ$ and given in Table 6. They are similar to the ones estimated with the second method and again close to the typical value in the solar neighborhood. When sticking to this approximation of the interstellar extinction, we can only quantify the change of values considering the error of the distance (Table 2 for Draco, the variation is very small for the other sources and thus not given) but note that a larger error is introduced by the uncertain detailed n(H) distribution in the galaxy.

As a fourth method, we compared our numbers to a study conducted by Xia et al. (2022). This study derived the FUV field through the fitting of a spectral energy distribution (SED) to the *Herschel* fluxes. Furthermore, a dust radiative transfer analysis was performed using the DUSTY code (Nenkova et al. 2000). The results are presented for a selection of sources, which includes Polaris and Musca. Moreover, the empirical correlation $\log(G_o) = (0.62 \pm 0.12) \log(N(H_2)[{\rm cm}^{-2}]) - (11.56 \pm 2.87)$ was given in Xia et al. (2022) to derive the FUV field. In order to estimate a value for the molecular hydrogen column density in Draco, we used the N-PDF presented in Schneider et al. (2022). This N-PDF consists of two lognormals with one peak at A_V = 0.4 that we attribute to molecular hydrogen (Schneider et al. 2022). With that value of the column density, we obtained a field of 15.7 G_o from the correlation given in Xia et al. (2022). For Spider, we adopted a value of 7.3×10^{19} cm^{-2} for the molecular hydrogen column density N(H_2), cited in Barriault et al. (2010a), and derived a field of 6 G_o.

Table 6 summarizes the values for the 160 µm flux and the FUV field for all sources at the observed positions. There is obviously a discrepancy between the values derived from the *Herschel* fluxes and the census of the stars. We will come back to this point in the discussion.

5.2. PDR modeling of line emission

For modeling the observed [C II], CO and [C I] intensities and ratios, we used the KOSMA-τ 1D spherical model (Röllig & Ossenkopf-Okada 2022) with an isotropic radiation field. The model results are included in the PDR toolbox[12] (Pound & Wolfire 2023) that also delivers results from a plane-parallel PDR model, the Wolfire-Kaufman models from 2006 and 2020 (see references in Pound & Wolfire 2023). The toolbox presents the models as grids of model predictions for the intensity or intensity ratio as a function of the hydrogen nucleus density n and the radiation field strength FUV. Here, we stick to the KOSMA-τ model because this represents a finite configuration that we can adjust to the geometry of the sources while the plane-parallel models adopted a fixed PDR depth of A_v = 7, too high for the sources in our study.

Table 7. Density and FUV field from the PDR model.

Source	n(H) [cm^{-3}]	FUV [G$_\circ$]	χ^2
Draco F1	311 ± 1	0.23 ± 0.0008	4.4 10^{-4}
Draco F2	370 ± 85	0.17 ± 0.05	2.91
Draco N1	636 ± 18	0.23 ± 0.005	0.15
Draco N2	272 ± 78	0.17 ± 0.04	6.65
Spider	293 ± 297	0.16 ± 0.02	116
Polaris	3838 ± 52	0.35 ± 0.004	7.3 10^{-3}

The KOSMA-τ model solves the radiative transfer equation with chemical balance and thermal equilibrium for a clumpy PDR exposed to a variable FUV radiation field and cosmic rays according to the typical primary ionization rate of 2×10^{-16} s^{-1}. The model that we used assumes a dust composition that produces a reddening parameter $R_V = 3.1$, where R_V is the ratio of visual extinction A_V to reddening $E(B - V)$, typical for diffuse clouds (model 7 from Weingartner & Draine 2001). It assumes a spherical cloud configuration with a radial density profile approximating a critical Bonnor-Ebert sphere with a constant central density and a power law density decay in the outer 80% of the radius. Models are characterized by clump mass, density at the surface, and impinging FUV field. From the simple geometry the average density is 1.92 times the density at the surface and we get a fixed relation between clump mass, $M_{\rm clump}$, density at the surface, n, and average column density

$$\langle N \rangle = 1.25 \times 10^{20} {\rm cm}^{-2} \frac{M_{\rm clump}/M_\odot}{\pi (r_{\rm clump}/{\rm pc})^2} \quad (5)$$

with

$$r_{\rm clump} = 40.5{\rm pc} \left(\frac{M_{\rm clump}/M_\odot}{4\pi/3 \times 1.92 \times n/{\rm cm}^{-3}} \right)^{1/3} \quad (6)$$

combining to a fixed relation between column density and density at the surface

$$\frac{n}{{\rm cm}^{-3}} = \left(\frac{\langle N \rangle}{1.348 \times 10^{19} {\rm cm}^{-2}} \right)^{3/2} \Bigg/ \sqrt{\frac{M_{\rm clump}}{M_\odot}}. \quad (7)$$

From Eq. (7) we obtained for a column density of 10^{21} cm^{-2} (average value for the 4 positions in Draco) a density at the surface of 2020 cm^{-3} when using a clump mass of 0.1 $M_\odot$ or 640 cm^{-3} for a clump mass of 1 $M_\odot$. This is the density range we expect to be seen in the PDR modeling of the observed lines.

We show here the line intensities and ratios of [C II], CO and [C I] emission and fit the line ratios to obtain the most likely

---

[12] `https://dustem.astro.umd.edu`

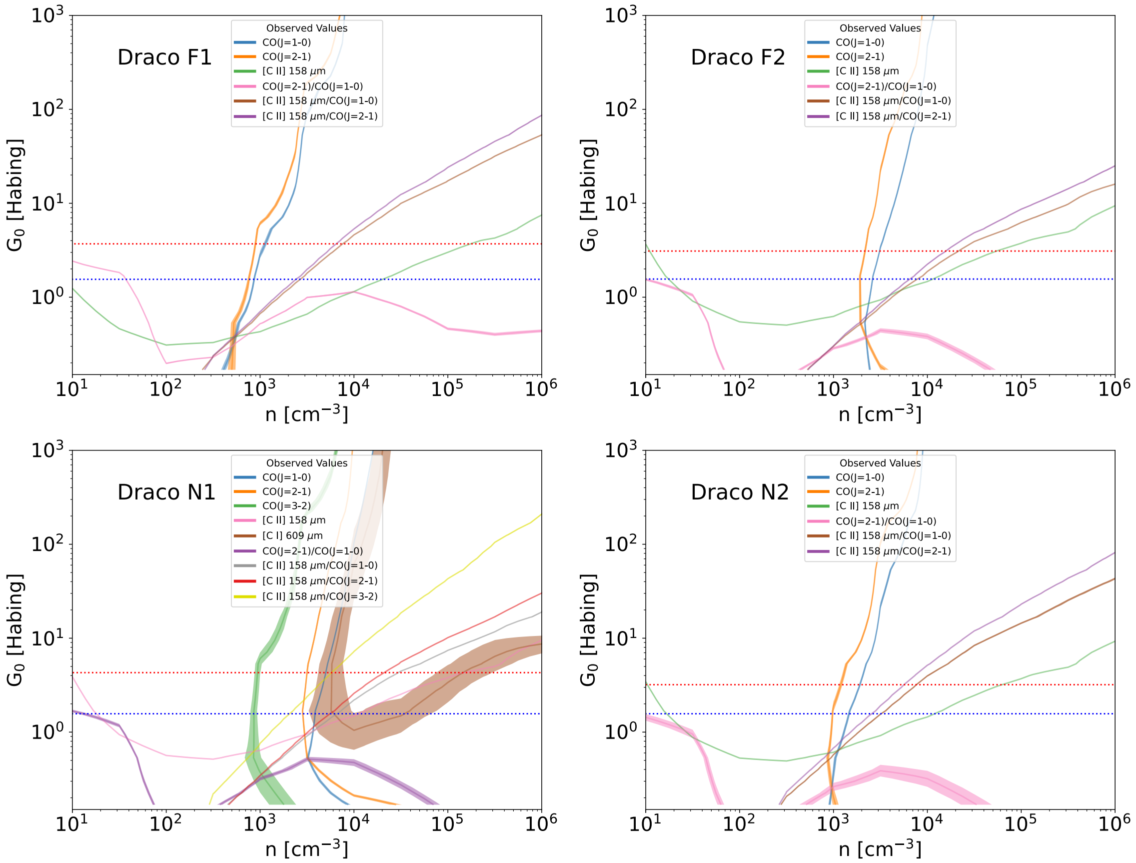

Fig. 9. PDR modeling results for Draco. Parameter space of hydrogen surface density n and FUV field calculated from the KOSMA-τ model for 0.1 $M_{\odot}$ clumps taken from the PDR toolbox for the Draco Front 1 and Front 2 (left) positions and the Nose 1 and Nose 2 (right) positions. The isocontours at different colors show the observed line integrated intensities or ratios, including the rms noise. The estimated FUV field for each source from the 160 μm flux is indicated by a red dashed line. The FUV field from the census of the stars is given as a dashed blue line.

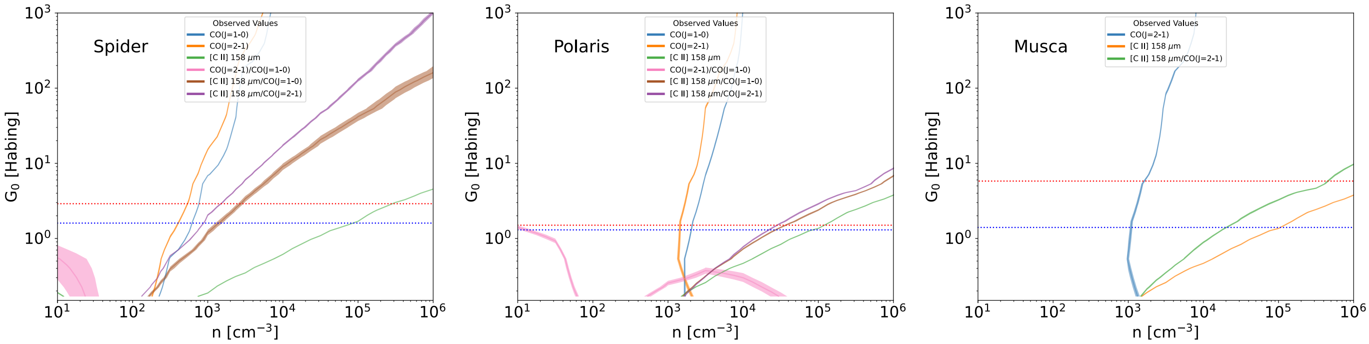

Fig. 10. PDR modeling results for Spider, Polaris, and Musca. Parameter space of hydrogen density n and FUV field calculated from the KOSMA-τ model taken from the PDR toolbox for the Spider 1 position (left, 0.1 $M_{\odot}$ clumps), the Polaris single pointing (middle, 1 $M_{\odot}$ clumps), and the Musca single pointing (right, 0.1 $M_{\odot}$ clumps). The isocontours at different colors show the observed line integrated intensities or ratios, including the rms noise. The estimated FUV field for each source from the 160 μm flux is indicated by a red dashed line. The FUV field from the census of the stars is given as a dashed blue line.

value for density and FUV field. We only use the velocity components that correspond to the velocity of the [C II] line (for example -25 km s^{-1} for Draco Front 1a and -22 km s^{-1} for Draco Front 2a, respectively). However, each source has a different set of lines available so that a comparison is difficult. We emphasize that the CO lines are very sensitive to the assumed total depth of the cloud. The [C II] intensity and the surface temperature trace surface properties while the CO emission only arises from the layers deeper in the cloud where CO can form. It is a simplified approach to consider a single density only and not a density distribution. A surface tracer like [C II] traces somewhat thinner material than the molecular lines. However, Fig. 9 shows that this has no significant impact on our results. The curves for the [C II] intensity have a very shallow density dependence. Because of the low critical density of the [C II] transition, a shift in density has little effect on the [C II] luminosity and consequently our fit results do not depend on the density of the [C II] emitting material.

KOSMA-τ provides models for different clump masses integrating over that mass. Using the *Herschel* total hydrogen column densities with a beamsize of 70″ they are all well below 1 $M_\odot$, except for Polaris with a value of ∼1 $M_\odot$. Specifically, we determine a mass of 0.21 $M_\odot$, 0.14 $M_\odot$, 0.31 $M_\odot$, and 0.32 $M_\odot$ for the Draco F1, F2, N1, and N2 positions, 0.09 $M_\odot$ for Spider, 0.08 $M_\odot$ for Musca, and 0.8 $M_\odot$ for Polaris. For simplicity, and because these models are directly available in the open access PDR toolbox and all results can thus easily be verified, we used pre-calculated models with $M = 0.1$ $M_\odot$ for Draco, Spider, and Musca and with $M = 1$ $M_\odot$ for Polaris. Note that using models with $M = 0.3$ $M_\odot$ (Röllig, Ossenkopf, priv. comm.) do not significantly change the results. With the higher mass the solution for the absolute intensities of the CO and [C I] lines shift by about a factor of two to lower densities while the [C II] intensity and the ratios remain almost unchanged.

Figures 9 and 10 display the results of the PDR model in a parameter space of FUV field and hydrogen density for all sources. The observed lines and line ratios are presented as isocontours, along with their associated errors. It should be noted that for [C II] in Spider, Polaris, and Musca, only the noise level is available, effectively serving as an upper limit. We show in Fig. C.1 the full model results for [C II] emission for masses M = 0.1 $M_\odot$ and M = 1 $M_\odot$ and in Fig. C.2 the model result (as an example) for CO 2→1. In terms of representing the FUV field, a dashed red horizontal line corresponds to the field determined through the translation of the 160 μm fluxes, while a blue line signifies the field established via the stellar census. Notably, data from Xia et al. (2022), which tend to be higher than other values, are omitted. This omission does not alter the interpretation of the PDR modeling.

A solution for the density and FUV field from the PDR plots is defined by a common crossing point of all lines. Because the absolute line intensities depend on geometrical details like beam dilution effects, line ratios are more reliable. We thus used the line ratios in the LineRatioFit method in the PDR toolbox to determine the most likely values of total hydrogen density density and FUV field including errors and χ^2. These values are listed in Table 7.

For the Front1 position, the observations align with a very low FUV field of around 0.4 G$_\circ$ and densities of approximately 500 cm^{-3} by eye-inspection of Fig. 9. The FUV field and the density from the fit are lower, that is, 0.23 G$_\circ$ and 311 cm^{-3}.

For the Front 2 position, the [C II] line crosses the CO intensities for a density of ∼2 × 10^3 cm^{-3} at an UV field of 1 G$_\circ$. The CO 2→1/1→0 ratio points toward a lower UV field of around 0.4 G$_\circ$. The fitted values are much lower with a FUV field of 0.17 G$_\circ$ and a density of 370 cm^{-3}.

For the Nose 1 position, we also consider the CO 3→2 line intensity (Heithausen, priv. comm.) and the [C II]/CO 3→2 and CO 3→2/2→1 line ratios and the [C I] line intensity. We derived the latter by averaging over the 4 positions observed in Draco close to the Nose 1 position (Heithausen et al. 2001) and arrive to a value of 4.3 × 10^{-7} erg s^{-1} sr^{-1} cm^{-2}. The CO 3→2/2→1 ratio falls essentially outside the parameter space (very low FUV field and densities) and is not visible in the plot. On the other hand, the [C II]/CO 3→2 ratio, the [C I] line, and the CO 2→1 and 1→0 intensities could align for densities of approximately 3 × 10^3 cm^{-3} for a low FUV field of around 1–2 G$_\circ$. Fitting only the line ratios, however, leads to a lower FUV field of 0.23 G$_\circ$ and a density of 636 cm^{-3}.

For the Nose 2 position, the individual CO line intensities intersect with the [C II] line at densities around 10^3 cm^{-3} at an UV field of around 0.6 G$_\circ$. In contrast, the line ratio fitting leads to a much smaller density of 272 cm $^{-3}$ and a FUV field of 0.17 G$_\circ$. It is mostly the CO(2→1)/(1→0) ratio that leads to these low values.

Figure 10 displays the PDR modeling results for Spider, Polaris, and Musca. Note that the [C II] value is only the noise level and that there are fewer complementary lines. The FUV field needs to be around 0.1 G$_\circ$ for Polaris to explain the observed lines and ratios and then yields a density of 2 × 10^3 cm^{-3}. The line ratio fitting gives a higher value of 3838 cm $^{-3}$ for the density but a lower value of 0.35 G$_\circ$ for the FUV field. The same mismatch was already noticed by Bensch et al. (2003) when analysing [CI] observations of Polaris. They proposed some kind of preshielding of the gas to explain the low FUV field. For Musca, it is very difficult to make any definitive statements since we only have two line intensities and no ratios. However, the tendency is that the FUV field is very low (<0.1 G$_\circ$) and the density is around 10^3 cm^{-3}.

Summarizing, it becomes obvious that the line ratio fitting in the PDR model always arrives to a very low FUV field (<0.35 G$_\circ$) for all sources, which is neither supported by the FUV field determined from the 160 μm flux by us and by Xia et al. (2022) nor by the theoretical prediction of 1.2–1.6 G$_\circ$ we obtained using the procedure outlined in Parravano et al. (2003) or the census of the stars. The densities are also lower than in the case where we also consider line intensities.

5.3. Non-LTE line analysis with RADEX

The PDR modeling provided results for observations of warm surface gas tracers such as [C II] and [C I] as well as CO lines for the cooler interior of the gas clump. We used RADEX (van der Tak et al. 2007) to determine the physical properties of the cooler, molecular gas. We investigated whether the observed ^{13}CO 1→0, 2→1 and ^{12}CO 1→0 and 2→1 lines and their ratios can be reproduced with this non-LTE molecular radiative transfer code. We excluded the [C II] line since it is not possible to determine independently the density, temperature and column density only from one line intensity. In other words, the determination of the [C II] column density is possible, but not independent of the line brightness and vice versa.

RADEX computes the line intensities as a function of temperature, H$_2$ density (assuming that H$_2$ is the main collision partner) and the column density of the species for the configuration of an isothermal homogeneous medium with a given velocity dispersion in the simplified shape of a uniform sphere. Using an ^{12}CO/^{13}CO abundance ratio of 70 (Langer & Penzias 1990) and a total carbon abundance of X(C)/X(H) = 2.34 × 10^{-4} (Simón-Díaz & Stasińska 2011) we translated the column densities of ^{13}CO and CO into minimum hydrogen column densities by assuming all carbon is in CO.

To estimate the velocity dispersion of the molecular gas we used the mean of the line width of the two ^{13}CO lines observed. For all calculations, we only used the CO velocity component (Table 3) that corresponds to the [C II] velocity component. For example, the Front 1 position only has a velocity component for [C II] at −25.6 km s^{-1} (Table 2), while the CO lines have two components (Table 3). We thus used only the Front 1a velocity component at −25.1 km with a mean velocity dispersion of 0.96 km s^{-1} in the RADEX fit.

We display the results for RADEX in two different ways, either using the line intensities or the ratios. The line fit for the intensities computed a three dimensional χ^2 distribution in the space of the parameters. The minimum gives the numerically best solution. This is visualized in Figs. 11 and 12 for the

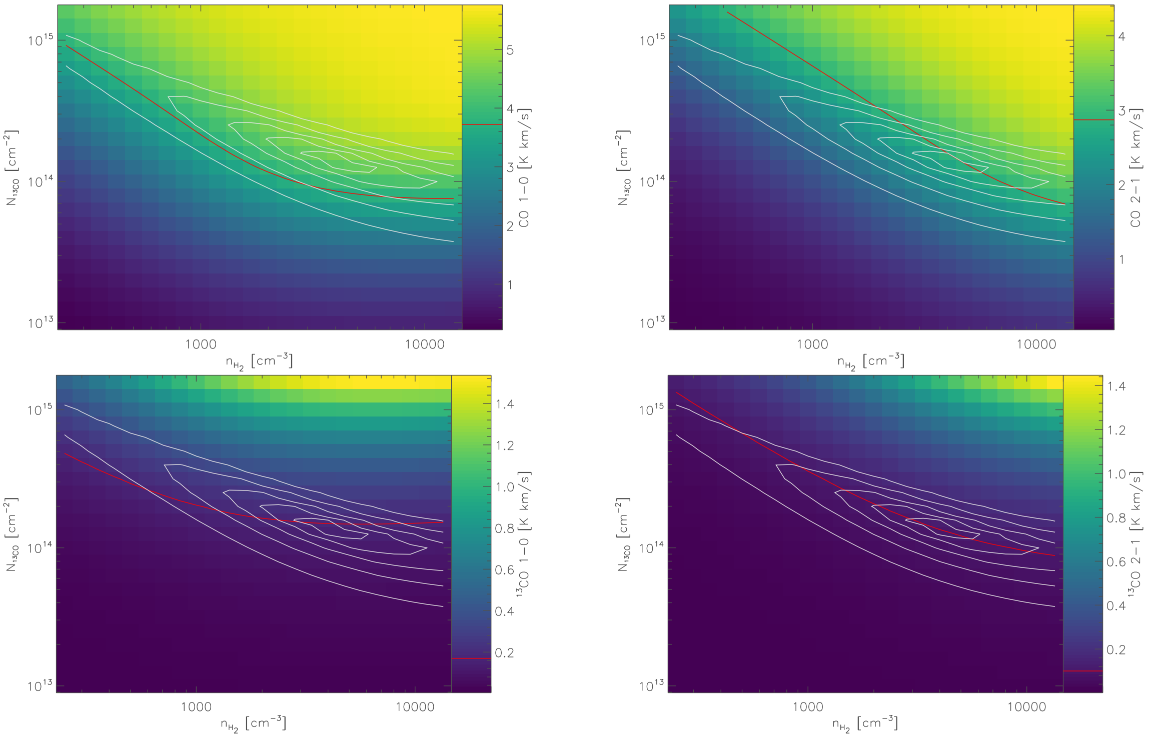

Fig. 11. Visualization of the RADEX fit to the four CO and ^{13} CO lines at the F1 position in Draco. Each plot shows a constant temperature cut through the three dimensional distribution of line intensities and χ^2 values. The kinetic temperature of the χ^2 minimum, that is, 9 K (see Table 8) was used. The colors in the plot show the integrated line intensities for the four lines, the observed value is marked by a red line. The gray contours give χ^2 values of 8, 16, 32, 64, and 128. As the χ^2 distribution is a global property, those contours are the same in all four subplots.

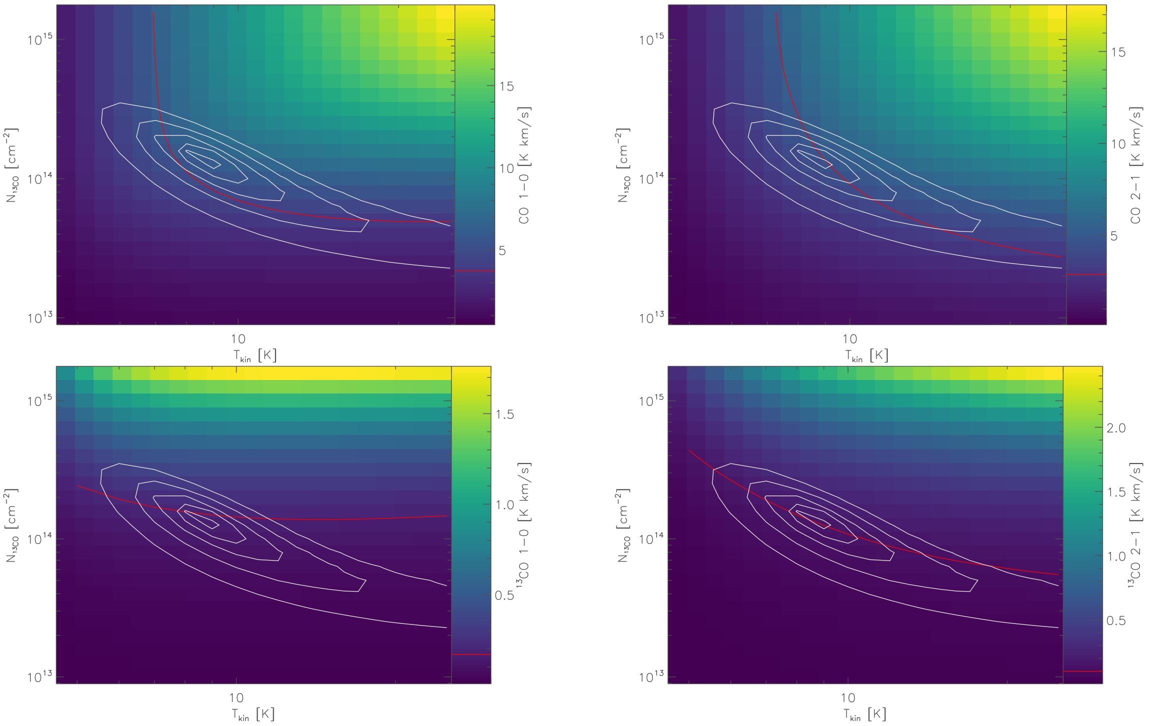

Fig. 12. Same as Fig. 11 but for a cut at the constant density of the χ^2 minimum of 4.9×10^3 cm^{-3} (see Table 8).

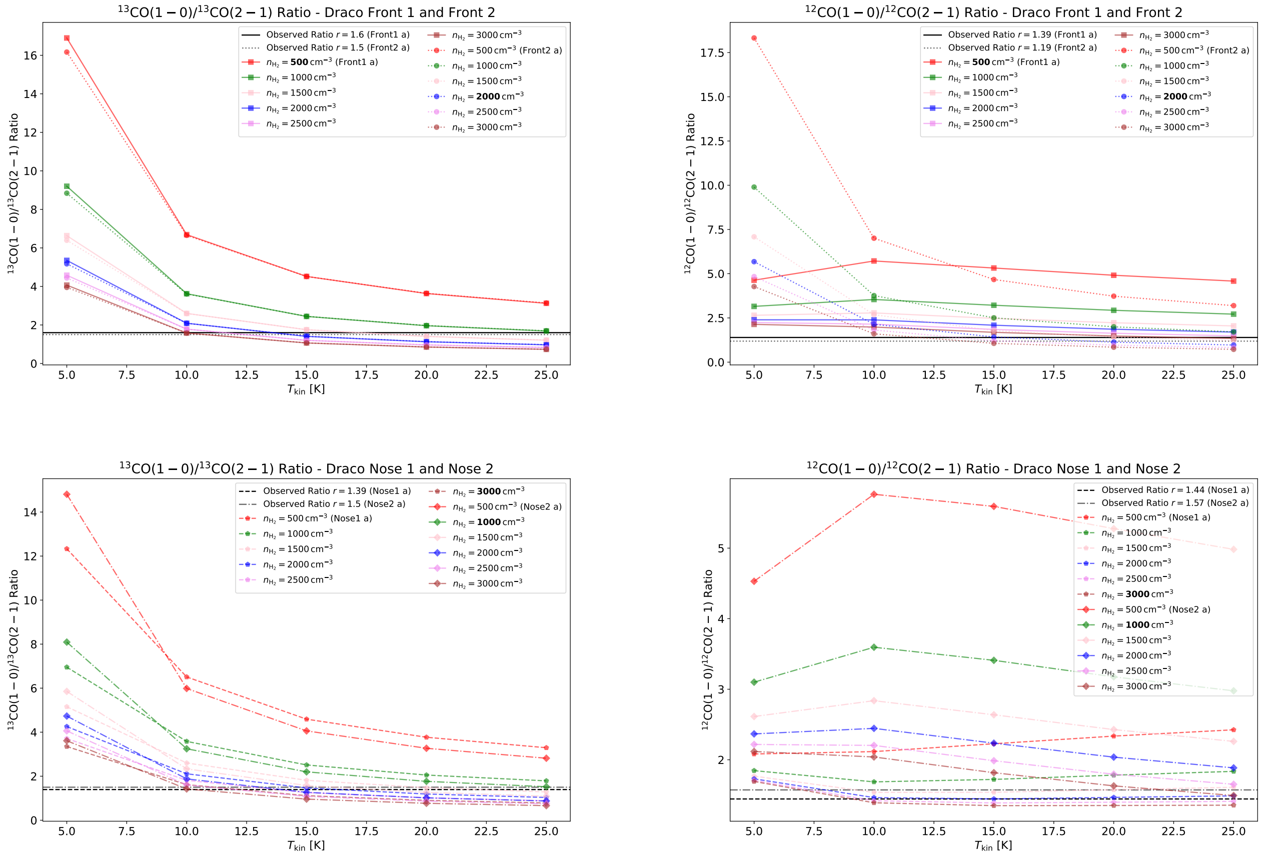

Fig. 13. RADEX results for the ^{13}CO 1→0/2→1 and ^{12}CO 1→0/2→1 brightness ratios as a function of density and temperature for the Draco front and nose positions. The observed ratios are shown as a solid and dashed black line. The density obtained with PDR modeling is marked in bold.

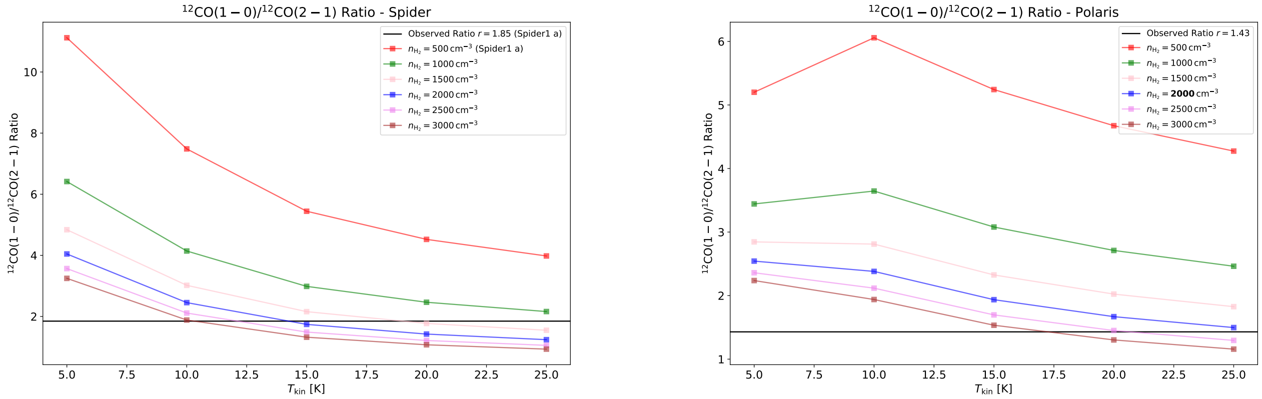

Fig. 14. RADEX results for the ^{12}CO 1→0/2→1 brightness ratios as a function of density and temperature for the Spider 1a position (left panel) and the Polaris positions (right panel). The observed ratios are shown as a solid and dashed black line. The density obtained with PDR modeling is marked in bold.

data from the F1 position in Draco. The figures show perpendicular cuts through the 3D cube of column density, density and temperature at the location of the χ^2 minimum. Each plot shows the integrated intensity of one of the four CO and ^{13}CO lines in colors and the global χ^2 distribution. The observed values are marked by a red line. From the crossing of the intensity isocontours it is obvious that the density is best constrained by the combination of the CO 2→1 and the ^{13}CO 1→0 lines but that the fit overpredicts the intensity of the CO 1→0 line. The kinetic gas temperature is well constrained by the combination of the CO lines and the ^{13}CO 1→0 line. The column density is also well constrained by the total intensities.

The best fit parameters for all four positions in Draco are given in Table 8. The corresponding plots for the other three positions are very similar to Figs. 11 and 12, this is why we omit showing all positions. The intensities just have to be shifted according to the values given in Table 3. The minimum χ^2 values fall between 4 and 13, which indicates a reasonable but imperfect fit by this model with one degree of freedom, based on four observed line intensities and three model parameters. The assumption of a homogeneous medium is obviously an oversimplification but the parameters are quite well constrained. It is interesting that the column density of gas traced by the CO isotopologues falls significantly below the column density

Table 8. Parameters of the minima of the RADEX fits to all four measured intensities in Draco.

Position	$T_{\rm kin}$ [K]	$n_{\rm H_2}$ [10^3 cm^{-3}]	$N_{\rm ^{13}CO}$ [10^{14} cm^{-2}]	$N_{\rm H,mol}$ [10^{20} cm^{-2}]	χ^2
F1	9.03	4.92	1.30	0.39	3.94
F2	13.7	1.65	4.92	1.47	4.41
N1	15.9	1.97	9.94	2.97	12.1
N2	11.1	3.56	2.04	0.61	12.9

measured through the dust emission (Table 2). This is partially due to the fact that the RADEX fit considers only one velocity component but in particular for the F1 and the N2 positions the difference is so large that it indicates a large fraction of atomic or CO-dark molecular material that is not traceable through CO. This is in agreement with the estimate from Schneider et al. (2022) that identified only 11% of the gas mass is molecular.

Unfortunately, we cannot perform the same RADEX fit for the other clouds where no ^{13}CO data are available as a three-dimensional problem cannot be constrained from two measured values only.

For a more intuitive visualization we also plot the RADEX output brightness ratios of ^{13}CO 1→0/2→1 and ^{12}CO 1→0/2→1 as a function of temperature and H_2 density in Fig. 13 for the Draco positions. Here, the column densities were determined in the classical way from the ^{13}CO 1→0 line integrated intensity using an excitation temperature $T_{\rm ex}$ that was determined from the ^{12}CO 1→0 line peak brightness, assuming optically thick emission (Mangum & Shirley 2015). The upper panels show the results for the Front 1 and Front 2 positions, the lower ones for the two nose positions. The model ratios for Draco are compared to the observed ones (indicated as a solid black and dashed line) and have the advantage that the ratios are independent of beam filling to first order. We can start from the PDR modeling densities to compare our ratios with the RADEX results. For that, we use the upper limits from the PDR modeling obtained by eye inspection of the observed line intensities and ratios. With the PDR model density of 500 cm^{-3} for Front 1 we obtain no solution at all. The density must be at least 3×10^3 cm^{-3} at a temperature of around 10 K. Note that from Table 8, we derive a density of 4.9×10^3 cm^{-3} at a temperature of 9 K. The Front 2 position can be reproduced by the upper limit PDR model with a density of 2×10^3 cm^{-3} (note that the density from the line ratio fitting is only 370 cm^{-3}) and leads to a consistent temperature of 15 K for both, ^{13}CO and ^{12}CO line ratios. This also fits with our values from Table 8 with the most likely density of 1.65×10^3 cm^{-3} at a temperature of 14 K. The Nose 1 position has the highest PDR model density of 3×10^3 cm^{-3} (but only 636 cm^{-3} from the line ratio fitting) that would give a low temperature of 10 K, again for both, ^{13}CO and ^{12}CO line ratios. From RADEX, we obtain slightly smaller densities of around 2×10^3 cm^{-3} at a temperature of 16 K. For the Nose 2 position, it is more difficult to obtain a fully coherent output from the analysis: a PDR model density of 10^3 cm^{-3} requires a temperature of 25 K for ^{13}CO. But the RADEX ^{12}CO line ratio is much higher (around 3) at this temperature (and also for lower temperatures) than the observed one of 1.57. Only high densities of around at least 3×10^3 cm^{-3} make the observed ^{12}CO line ratio fitting with low temperatures of around 10 K.

Note that PDR model densities are by no means the 'exact' values. They only give an estimate of the density in case of a very low FUV field and we observe a discrepancy between the densities and FUV field determined from line intensities and ratios and from line ratios alone. For the optical depths, we derived values below 1 for temperatures above 5 K for the ^{13}CO lines. For the ^{12}CO lines the values range between the optical thin case with $\tau \lesssim 0.3$ for Front 1 and the optical thick case with mostly $\tau > 1$ for the Front 2 position over all temperatures. In both nose positions the opacity lies above 1 throughout the whole parameter range of temperatures.

Summarising, we have a parameter space of possible solutions for all positions from the RADEX model alone. The densities are between 1650 and 4900 cm^{-3} at a temperature of 9–16 K (Table 8). Overall, these values align mostly with the ones of Miville-Deschênes et al. (2017) who found molecular clumps in Draco at a temperature of 10 K and an average density of $\sim 10^3$ cm^{-3} (note that the density of individual molecular clumps is sometimes higher). The dust temperatures in Draco are low (around 13 K, see Table 2), so that in case the dust and gas is well mixed, the low gas temperatures are consistent.

Figure 14 displays the RADEX results for the ^{12}CO 1→0/2→1 ratio in Spider and Polaris since only these lines are available. We omit Musca because we only have the ^{12}CO 2→1 line brightness. It is noteworthy that for Spider, the ^{12}CO 1→0 line is optically thin with values between ~0.2 and ~0.5 for a temperature range of 10–20 K and the ^{12}CO 2→1 line is optically thick with values above 1 for the whole parameter space, whereas for Polaris, the optical depth is mostly above 1 for both ^{12}CO lines. This discrepancy renders the interpretation of the results somewhat less reliable. The PDR modeling for Spider did not yield reasonable density estimates, even for very low FUV fields (outside the model's range). We anticipate that the densities and temperatures are low in this relatively diffuse region with a substantial atomic contribution. Assuming the curve with the lowest density for the CO clump in Spider that would fit with our observations ($n = 1.5 \times 10^3$ cm^{-3}) yields a temperature of 20 K. Interestingly, the dust temperature in Spider is also approximately this value (~18 K), slightly higher than in all other sources. For Polaris, the PDR modeling provides a density of $\sim 2 \times 10^3$ cm^{-3} and even 3838 cm^{-3} from the line ratio fit for a very low FUV field. The observed ^{12}CO ratio then fits well with a temperature of around 25 K. However, it is important to note that the ^{12}CO lines in Polaris are optically thick. Hence, we propose that the resulting possible temperature and density range is approximately 10–25 K at densities of around 2–3 × 10^3 cm^{-3}.

5.4. Shock modeling of line emission in Draco

For modeling a potential shock-origin of the [C II] emission, we utilized the Paris-Durham shock code[13]. Our objective was not to conduct an exhaustive modeling but rather to assess whether the observed quantities can be preliminary explained by shocks. The pre-calculated model grids[14] were employed for this purpose. The shock models are executed using shock code version

---

[13] `https://ism.obspm.fr/shock.html`

[14] `https://app.ism.obspm.fr/ismdb`

1.1.0, revision 115, and encompass C-type shocks at moderate velocities (<100 km s^{-1}), or J-type shocks at low velocities (<30 km s^{-1}), both propagating in weakly magnetized environments. The shocks are implemented as propagating through a layer of gas and dust, manifested as stationary, plane-parallel, multifluid shock waves, in environments with or without external UV radiation. The parameters that are parameterized include the shock velocity (2–90 km s^{-1}), initial density of the preshock medium (100–10^8 cm^{-3}), intensity of the UV radiation field (0–1700 G$_\circ$), cosmic ray ionization rate (10^{-17}–10^{-15} s^{-1}/H_2), and the magnetic field strength, expressed in terms of β and ranging from 0.1 to 10. β defines the initial transverse magnetic field strength in µG and is equal to $\beta \times \sqrt{n(H)[\mathrm{cm}^{-3}]}$. The fractional abundance of PAHs is fixed at 10^{-8}, and the chemistry incorporates 140 species through a chemical network involving about 3000 reactions. Surface reactions, adsorption, and desorption processes are not considered except for H_2 formation. For further elaboration, refer to Gusdorf et al. (2008), Lesaffre et al. (2013), Goddard et al. (2019), Lehmann et al. (2020, 2022) and the references therein.

The code generates output containing the thermodynamic and chemical structure of the shock, including temperature, fluid velocities, abundances, column density profiles, and line intensities of H_2 as well as several ionized or neutral atoms. We utilized this output to analyze [C II] line intensities and the total hydrogen column density, N(H), in comparison with Draco observations. Specifically, we applied the observed [C II] line intensities and *Herschel* hydrogen column density values from Table 2 to positions Draco Front 1 and 2, and Nose 1 and 2. The [C II] intensities at the Front 1, Front 2, Nose 1, and Nose 2 positions are 1.55, 2.60, 2.67, and 2.53, respectively, measured in units of 10^{-6} erg s^{-1} sr^{-1} cm^2. For our model, we fixed the radiation field at 1.7 G$_\circ$ (note that available values are 0.17, 1.7, 17, ... G$_\circ$) and the preshock density at n = 100 cm^{-3} which is the lowest possible density to select. We tried also higher densities but could not find a match between the shock model results and the observations. We thus used a preshock gas of 100 cm^{-3}, though the preshock density can indeed be lower. However, densities lower than 1000 cm^{-3} are a reasonable assumption since the density of the densest molecular clumps currently found in Draco is between 1000 and 4900 cm^{-3} (Sects. 5.2 and 5.3 and Miville-Deschênes et al. 2017). We then explored variations in other parameters, such as the cosmic ray rate, β, and shock speed, within reasonable ranges. Different cosmic ray rates (10^{-15}, 10^{-16}, and 10^{-17} s^{-1}/H_2) have limited impact on the [C II] intensity and H column density. We choosed 10^{-16} s^{-1}/H_2 as it is suggested as the average value for the diffuse ISM in the Milky Way (Dalgarno 2006; Indriolo & McCall 2012). The magnetic field strength, characterized by low values of β (0.1, 0.3), results in diminished [C II] intensities and H column densities. Higher values of β (3, 10) produce larger hydrogen column densities, but these values do not align well with the [C II] emission. In summary, our analysis provides insights into the impact of various parameters on the [C II] emission and hydrogen column density, revealing the influence of factors such as the radiation field, density, cosmic ray rate, and magnetic field strength in the Draco region.

The best match between model values and observations is found for the Front 1 position, with a shock velocity of 20 km s^{-1}, preshock density n = 100 cm^{-3}, and β = 1. The model predicts a [C II] intensity of 1.63×10^{-6} erg s^{-1} sr^{-1} cm^2 at a total hydrogen column density of 3.73×10^{20} cm^{-2}. It is important to note that the column density is calculated for a single layer, representing a lower limit. When comparing all Draco positions, the [C II] intensity is roughly consistent across all of them. Running models with different preshock densities would probably better match the observed intensities, but this is for the moment out of the scope of this paper. The hydrogen column density is approximately four times higher than the model's predicted values for the nose positions. However, this discrepancy could be attributed to the limitations of the single layer model. It is evident that higher shock speeds are not feasible. Beyond a threshold of v = 25 km s^{-1}, the [C II] intensity experiences a significant drop. J-type shocks prove ineffective, while only C-type shocks with velocities ≤20 km s^{-1} yield reasonable results. Nonetheless, reducing the velocities further leads to a decline in the [C II] intensity.

Table 9. Summary of physical parameters.

Source	I_{CII} [K km s^{-1}]	F_{160} [MJy sr^{-1}]	FUV [G$_\circ$]	N(H) [10^{20} cm^{-2}]	n [10^3 cm^{-3}]
Draco$^{(a)}$	0.3325	44	3.6	10.0	3.0
Spider	<0.06	38	2.9	6.3	2.0$^{(b)}$
Polaris	<0.03	18	1.5	32.2	20–50$^{(c)}$
Musca	<0.03	61	5.8	34.3	7.0$^{(d)}$

Notes. Comparison between the [C II] intensity (Col. 2), the 160 µm flux (Col. 3), the FUV field from the 160 µm flux (Col. 4), the total hydrogen column density (Col. 5), and the volume density (Col. 6) for the observed sources. $^{(a)}$Average value from the 4 positions observed in Draco. $^{(b)}$From Barriault et al. (2010b). $^{(c)}$From Grossmann & Heithausen (1992); Heithausen et al. (1995); Ward-Thompson et al. (2010). $^{(d)}$From Bonne et al. (2020b).

6. Discussion

The main result of this study is that the [C II] 158 µm line was detected at several positions in the Draco cloud, but not in any of the other quiescent clouds (Spider, Polaris, Musca), even though these regions have similar column and volume densities, 160 µm fluxes, and FUV fields (see Table 9). We note that the volume densities are similar for all sources (a few 10^3 cm^{-3}), only Polaris has a higher density of 2–5×10^4 cm^{-3} and should thus emit even stronger in [C II] than Draco because subthermal, optically thin [C II] intensities scale with n^2 (Goldsmith et al. 2012). As we explained in Sect. 5.2, though the density of the gas is higher in the interior of a molecular clump than at the surface, we can consider similar densities for the CO and [C II] emitting gas because the [C II] line shows a very weak dependency on the density.

It is important to emphasize that the accurate derivation of the FUV field is a critical point. As discussed in Sect. 5.1, different methods yield variations in the estimated FUV field. A census of Galactic OB-stars and a continuous approximation (Parravano et al. 2003) using the distribution and birthrates of OB stars in the Milky Way from McKee & Williams (1997) and considering the extinction toward our sources, yields values between 1.2 and 1.6 G$_\circ$. On the other hand, the calculation based on the 160 µm flux and a dust model (Xia et al. 2022) results in larger values (at least a few G$_\circ$) when assuming that the dust is only heated through the FUV radiation.

We checked if the FUV field determined from the 160 µm emission may be underestimated because the wavelength range below 160 µm is not taken into account. This is not the case. There is nearly no or only weak 70 µm emission visible in the

Herschel maps of all sources and only very weak 12 µm emission (Meisner & Finkbeiner 2014). There is also no overestimation of the 160 µm flux due to the contribution of cold thermal dust emission from the molecular cloud. It is thus difficult to understand why the 160 µm fluxes are so high in all sources if it is not an external FUV field that heats the dust.

When looking for alternative mechanisms for the heating of the dust we can quickly exclude cosmic rays. At a typical cosmic ray ionization rate of 2×10^{-16} s^{-1} and heating efficiencies below 10 eV per ionization event (Glassgold et al. 2012) the cosmic ray heating rate falls more than three orders of magnitude below the UV heating rate at one Habing field so that even an enhanced cosmic ray rate is probably insufficient to explain the observed dust heating. Instead shock heating from cloud collisions can in principle inject enough energies. For example, with a rather low hydrogen gas density of 500 cm^{-3} (Front 1 position in Draco), a kinetic temperature of 100 K, and relative velocities of 20 km s^{-1}, like the difference between the IVC and LVC in Draco, the thermalization time, $\tau_{\rm therm}$ is at maximum 30 years when assuming perfectly elastic collisions (Sauder 1967). Inelastic contributions may shorten this. The compressive heating from the shock, $\Gamma = n \times m_{\rm H}/2 \times v_{\rm shock}^2/\tau_{\rm therm}$ is then more than four orders of magnitude above the UV heating rate at one Habing field. Higher densities would even increase Γ. Although the details of the shock physics may modify this rate relative to the idealized value, the order of magnitude estimate shows that shock heating at our conditions could easily feed enough energy into the dust to explain the enhanced 160 µm emission. Note that referring to Lehmann et al. (2020, 2022) up to 10–30% of shock energy can be irradiated away in LyAlpha (which then can be absorbed and reemitted by the dust, potentially resulting in an increase of the 160 µm emission; see also Bonne et al. 2022). This, however, requires shock velocities around 30 km s^{-1}. Nevertheless, lower velocity shocks may still have a measurable impact.

The 'cloud collision' in Draco that can give an explanation to the increased 160 µm emission and the [C II] emission can be seen as an interaction of the atomic/molecular IVC with mostly atomic gas (the LVC) while the Draco cloud moves through the ISM. Notably, local gas within the velocity range of −10 to 30 km s^{-1} contributes to these interactions, while the high-velocity gas (−200 to −100 km s^{-1}) remains excluded from this process (refer to Figs. A.1 and B.1). Figure 3 presents a clear representation of the complex velocity structure of H I in Draco, with a minimum of two components observed between approximately −16 and −30 km s^{-1}. At the forefront, the two positions in Draco distinctly exhibit two H I components, out of which only one corresponds to the [C II] line, situated around −26 and −24 km s^{-1} for the Front 1 and Front 2 positions, respectively. The Nose 1 and Nose 2 H I spectra are more complex and do not show clearly two components. This is not surprising because the gas is here mostly molecular and denser. Conversely to Draco, the other sources primarily exhibit inconspicuous dynamics. Musca stands out as having more pronounced dynamics due to filament formation (Bonne et al. 2020b,a). The dissipation of turbulence through the emergence of dense structures results in low-velocity shocks that elevate both gas and dust temperatures and may thus also explain the rather high 160 µm flux. However, it is noteworthy that no detection of [C II] occurred in Musca. Spider and Polaris have lower 160 µm fluxes compared to Draco and Musca, but the emission is mostly at local velocities and does not seem to involve cloud collisions.

The PDR modeling indicates that the [C II] and CO lines can only be accounted for by a significantly small UV field, much smaller than 1 G$_\circ$. Among the positions studied, only Draco Nose 1, Nose 2, and Front 2 positions exhibit some compatibility with a model where CO emission originates from the inside of high-density (1–3 × 10^3 cm^{-3}), cold (T ∼ 10–20 K) molecular clumps. The CO emission is then a result of thermal excitation within the dense gas clumps, which likely possess a limited filling factor. [C II] may then arise from the PDR surfaces at those densities but it can also stem from a mostly atomic interclump component. As for the Draco Front 1 position, as well as Polaris and Musca, their [C II] and CO line emissions (and the corresponding upper limits) are reconcilable with a PDR model featuring very low FUV fields, less than 0.2 G$_\circ$, coupled with densities around 10^3 cm^{-3}. Only the Front 1 positions falls out of this with its density of only 500 cm^{-3}. The Spider position cannot be modeled with very low FUV intensities. RADEX modeling of the observed CO line ratios in all sources determines mostly higher densities than estimated from the PDR modeling (except of the low densities for the Draco Front 1 position), but we cannot make a statement about [C II]. The puzzling result is still why the [C II] line was observed in Draco and not in all other quiescent sources. The only differences between Draco on one hand, and Spider, Polaris, and Musca on the other hand, is the higher dynamics of Draco because of a possible cloud interaction. An approach of shock modeling applied to the [C II] emission in Draco reveals that the observed intensities are compatible with conditions akin to a preshock density of 100 cm^3 and a shock velocity of 20 km s^{-1}. The shock velocity is not very high which may explain why the [C II] line widths (between 1.3 km s^{-1} for Front 1 and 4 km s^{-1} for Front 2) are not very broad and not significantly larger than the ones of CO.

In consideration of these findings, it is plausible that Draco contains dense, cold, molecular clumps that are enveloped by a diffuse atomic phase (≃10–100 cm^{-3}, $T > 50$ K), serving as the source of the [C II] emission. This emission, in turn, acts as a cooling line to dissipate kinetic energy stemming from interactions between H I clouds or as the IVC descends onto the galactic disk. In such a scenario, the primary factor driving this process is the ram pressure exerted on the cloud by the escalating halo density, as stated by Desert et al. (1990).

7. Summary

The [C II] 158 µm line was observed with SOFIA at selected positions in the quiescent clouds Draco, Spider, Polaris, and Musca. Emission on a level of ∼0.2 to 0.4 K km s^{-1} ($S/N \sim 4$) of the [C II] line was only detected in four positions in the Draco cloud, and CO lines (^{12}CO and ^{13}CO 1→0, 2→1) were observed with the IRAM 30 m and APEX and mostly detected in all sources. The flux at 160 µm is rather high in all sources (18 MJy sr^{-1} for Polaris; 44 MJy sr^{-1} for Draco; up to 61 MJy sr^{-1} for Musca), while the FUV field is very low. Converting the 160 µm flux gave values of 1.5–6 G$_\circ$, while the FUV field from a stellar census is around 1.3–1.6 G$_\circ$. A theoretical determination considering the distribution of OB stars in the galaxy and extinction yielded a value of 1.2–1.6 G$_\circ$. The PDR modeling ([C II], [C I], and CO) and RADEX modeling (CO) can partly explain the observed emission arising from clumps with a density of a few 10^3 cm^{-3} at a temperature of 10–20 K in Draco. The PDR model, however, requires a very low UV field, much lower than 1 G$_\circ$, which is not provided by the different methods of our FUV field determinations. For Draco, heating by collisions of H I clouds could explain the high level of the 160 µm flux and the [C II] emission, which is reproduced by a shock model with a preshock density of 100 cm^{-3} and a C-shock with a velocity of 20 km s^{-1}. We propose that the shock arises from the interaction of the H I clouds associated with Draco.

Acknowledgements. This study was based on observations made with the NASA/DLR Stratospheric Observatory for Infrared Astronomy (SOFIA). SOFIA is jointly operated by the Universities Space Research Association Inc. (USRA), under NASA contract NNA17BF53C, and the Deutsches SOFIA Institut (DSI), under DLR contract 50 OK 0901 to the University of Stuttgart. upGREAT is a development by the MPIfR and the KOSMA/University Cologne, in cooperation with the DLR Institut für Optische Sensorsysteme. N.S. acknowledges support from the FEEDBACK-plus project that is supported by the BMWI via DLR, Projekt Number 50OR2217. S.K. acknowledges support by the BMWI via DLR, project number 50OR2311. This work is supported by the Collaborative Research Center 1601 (SFB 1601 sub-project A6 and B2) funded by the Deutsche Forschungsgemeinschaft (DFG, German Research Foundation) – 500700252.

References

Abergel, A., Boulanger, F., Delouis, J. M., Dudziak, G., & Steindling, S. 1996, A&A, 309, 245
Barriault, L., Joncas, G., Falgarone, E., et al. 2010a, MNRAS, 406, 2713
Barriault, L., Joncas, G., Lockman, F. J., & Martin, P. G. 2010b, MNRAS, 407, 2645
Bensch, F., Leuenhagen, U., Stutzki, J., & Schieder, R. 2003, ApJ, 591, 1013
Beuther, H., Ragan, S. E., Ossenkopf, V., et al. 2014, A&A, 571, A53
Bialy, S., Burkhart, B., & Sternberg, A. 2017, ApJ, 843, 92
Bisbas, T. G., Schruba, A., & van Dishoeck, E. F. 2019, MNRAS, 485, 3097
Blagrave, K., Martin, P. G., Joncas, G., et al. 2017, ApJ, 834, 126
Bohlin, R. C., Savage, B. D., & Drake, J. F. 1978, ApJ, 224, 132
Bonne, L., Bontemps, S., Schneider, N., et al. 2020a, A&A, 644, A27
Bonne, L., Schneider, N., Bontemps, S., et al. 2020b, A&A, 641, A17
Bonne, L., Peretto, N., Duarte-Cabral, A., et al. 2022, A&A, 665, A22
Cannon, A. J., & Pickering, E. C. 1993, VizieR Online Data Catalog: III/135A
Clark, P. C., Glover, S. C. O., Klessen, R. S., & Bonnell, I. A. 2012, MNRAS, 424, 2599
Cox, N. L. J., Arzoumanian, D., André, P., et al. 2016, A&A, 590, A110
Creevey, O. L., Sordo, R., Pailler, F., et al. 2023, A&A, 674, A26
Dalgarno, A. 2006, Proc. Natl. Acad. Sci., 103, 12269
Desert, F. X., Bazell, D., & Blitz, L. 1990, ApJ, 355, L51
de Vries, H. W., Heithausen, A., & Thaddeus, P. 1987, ApJ, 319, 723
Dobbs, C. L. 2008, MNRAS, 391, 844
Draine, B. T. 1978, ApJS, 36, 595
Falgarone, E., Panis, J. F., Heithausen, A., et al. 1998, A&A, 331, 669
Falgarone, E., Pety, J., & Hily-Blant, P. 2009, A&A, 507, 355
Field, G. B., Goldsmith, D. W., & Habing, H. J. 1969, ApJ, 155, L149
Franco, G. A. P. 1991, A&A, 251, 581
Gaia Collaboration (Drimmel, R. et al.) 2023, A&A, 674, A37
Gladders, M. D., Clarke, T. E., Burns, C. R., et al. 1998, ApJ, 507, L161
Glassgold, A. E., Galli, D., & Padovani, M. 2012, ApJ, 756, 157
Glover, S. C. O., & Mac Low, M.-M. 2007, ApJ, 659, 1317
Glover, S. C. O., Federrath, C., Mac Low, M. M., & Klessen, R. S. 2010, MNRAS, 404, 2
Glover, S. C. O., Clark, P. C., Micic, M., & Molina, F. 2015, MNRAS, 448, 1607
Goddard, C. R., Nakariakov, V. M., & Pascoe, D. J. 2019, A&A, 624, L4
Goldsmith, P. F., Langer, W. D., Pineda, J. L., & Velusamy, T. 2012, ApJS, 203, 13
Goldsmith, P. F., Pineda, J. L., Neufeld, D. A., et al. 2018, ApJ, 856, 96
Grossmann, V., & Heithausen, A. 1992, A&A, 264, 195
Gusdorf, A., Cabrit, S., Flower, D. R., & Pineau Des Forêts, G. 2008, A&A, 482, 809
Habing, H. J. 1968, Bull. Astron. Inst. Netherlands, 19, 421
Heiles, C., & Habing, H. J. 1974, A&AS, 14, 1
Heithausen, A., & Thaddeus, P. 1990, ApJ, 353, L49
Heithausen, A., Corneliussen, U., & Grossmann, V. 1995, A&A, 301, 941
Heithausen, A., Weiß, A., Kerp, J., & Fritz, T. 2001, ApJ, 561, 238
Heitsch, F., Slyz, A. D., Devriendt, J. E. G., Hartmann, L. W., & Burkert, A. 2006, ApJ, 648, 1052
Herbstmeier, U., Heithausen, A., & Mebold, U. 1993, A&A, 272, 514
Heyminck, S., Graf, U. U., Güsten, R., et al. 2012, A&A, 542, L1
Hily-Blant, P., & Falgarone, E. 2009, A&A, 500, L29
Hollenbach, D. J., Takahashi, T., & Tielens, A. G. G. M. 1991, ApJ, 377, 192
Imara, N., & Burkhart, B. 2016, ApJ, 829, 102
Indriolo, N., & McCall, B. J. 2012, ApJ, 745, 91
Jönsson, H., Holtzman, J. A., Allende Prieto, C., et al. 2020, AJ, 160, 120
Kabanovic, S., Schneider, N., Ossenkopf-Okada, V., et al. 2022, A&A, 659, A36
Kainulainen, J., Beuther, H., Henning, T., & Plume, R. 2009, A&A, 508, L35
Kainulainen, J., Hacar, A., Alves, J., et al. 2016, A&A, 586, A27
Kerp, J., Lenz, D., & Röhser, T. 2016, A&A, 589, A123
Klessen, R. S., Heitsch, F., & Mac Low, M.-M. 2000, ApJ, 535, 887
Knude, J., & Hog, E. 1998, A&A, 338, 897
Kramer, C., Cubick, M., Röllig, M., et al. 2008, A&A, 477, 547
Krumholz, M. R., McKee, C. F., & Tumlinson, J. 2008, ApJ, 689, 865
Langer, W. D., & Penzias, A. A. 1990, ApJ, 357, 477
Lee, H. H., Herbst, E., Pineau des Forets, G., Roueff, E., & Le Bourlot, J. 1996, A&A, 311, 690
Lehmann, A., Godard, B., Pineau des Forêts, G., & Falgarone, E. 2020, A&A, 643, A101
Lehmann, A., Godard, B., Pineau des Forêts, G., Vidal-García, A., & Falgarone, E. 2022, A&A, 658, A165
Lenz, D., Kerp, J., Flöer, L., et al. 2015, A&A, 573, A83
Lesaffre, P., Pineau des Forêts, G., Godard, B., et al. 2013, A&A, 550, A106
Low, F. J., Beintema, D. A., Gautier, T. N., et al. 1984, ApJ, 278, L19
Mangum, J. G., & Shirley, Y. L. 2015, PASP, 127, 266
Marasco, A., Fraternali, F., van der Hulst, J. M., & Oosterloo, T. 2017, A&A, 607, A106
McKee, C. F., & Williams, J. P. 1997, ApJ, 476, 144
Mebold, U., Cernicharo, J., Velden, L., et al. 1985, A&A, 151, 427
Meisner, A. M., & Finkbeiner, D. P. 2014, ApJ, 781, 5
Meyerdierks, H., Heithausen, A., & Reif, K. 1991, A&A, 245, 247
Miville-Deschênes, M. A., Martin, P. G., Abergel, A., et al. 2010, A&A, 518, L104
Miville-Deschênes, M. A., Salomé, Q., Martin, P. G., et al. 2017, A&A, 599, A109
Nenkova, M., Ivezić, Ž., & Elitzur, M. 2000, ASP Conf. Ser., 196, 77
Ossenkopf, V., Röllig, M., Neufeld, D. A., et al. 2013, A&A, 550, A57
Parravano, A., Hollenbach, D. J., & McKee, C. F. 2003, ApJ, 584, 797
Pineda, J. L., Langer, W. D., Velusamy, T., & Goldsmith, P. F. 2013, A&A, 554, A103
Pound, M. W., & Wolfire, M. G. 2023, AJ, 165, 25
Putman, M. E., Peek, J. E. G., & Joung, M. R. 2012, ARA&A, 50, 491
Risacher, C., Güsten, R., Stutzki, J., et al. 2018, J. Astron. Instrum., 7, 1840014
Roccatagliata, V., Preibisch, T., Ratzka, T., & Gaczkowski, B. 2013, A&A, 554, A6
Röhser, T., Kerp, J., Winkel, B., Boulanger, F., & Lagache, G. 2014, A&A, 564, A71
Röhser, T., Kerp, J., Ben Bekhti, N., & Winkel, B. 2016a, A&A, 592, A142
Röhser, T., Kerp, J., Lenz, D., & Winkel, B. 2016b, A&A, 596, A94
Röllig, M., & Ossenkopf-Okada, V. 2022, A&A, 664, A67
Röllig, M., Abel, N. P., Bell, T., et al. 2007, A&A, 467, 187
Sauder, W. C. 1967, J. Res. Natl. Bureau Standards A. Phys. Chem., 72A, 91
Schneider, N., André, P., Könyves, V., et al. 2013, ApJ, 766, L17
Schneider, N., Bontemps, S., Motte, F., et al. 2016, A&A, 591, A40
Schneider, N., Ossenkopf-Okada, V., Clarke, S., et al. 2022, A&A, 666, A165
Schneider, N., Bonne, L., Bontemps, S., et al. 2023, Nat. Astron., 7, 546
Seifried, D., Haid, S., Walch, S., Borchert, E. M. A., & Bisbas, T. G. 2020, MNRAS, 492, 1465
Seifried, D., Beuther, H., Walch, S., et al. 2022, MNRAS, 512, 4765
Simón-Díaz, S. & Stasińska, G. 2011, A&A, 526, A48
Sternberg, A., & Dalgarno, A. 1989, ApJ, 338, 197
Sternberg, A., Le Petit, F., Roueff, E., & Le Bourlot, J. 2014, ApJ, 790, 10
Tielens, A. G. G. M., & Hollenbach, D. 1985, ApJ, 291, 722
Valdivia, V., Hennebelle, P., Gérin, M., & Lesaffre, P. 2016, A&A, 587, A76
van der Tak, F. F. S., Black, J. H., Schöier, F. L., Jansen, D. J., & van Dishoeck, E. F. 2007, A&A, 468, 627
van Dishoeck, E. F. & Black, J. H. 1988, ApJ, 334, 771
Vázquez-Semadeni, E., Ryu, D., Passot, T., González, R. F., & Gazol, A. 2006, ApJ, 643, 245
Visser, R., van Dishoeck, E. F., & Black, J. H. 2009, A&A, 503, 323
Walder, R., & Folini, D. 1998, A&A, 330, L21
Ward-Thompson, D., Kirk, J. M., André, P., et al. 2010, A&A, 518, L92
Weingartner, J. C., & Draine, B. T. 2001, ApJ, 548, 296
Westmeier, T. 2018, MNRAS, 474, 289
Winkel, B., Kerp, J., Flöer, L., et al. 2016, A&A, 585, A41
Wolfire, M. G., Hollenbach, D., McKee, C. F., Tielens, A. G. G. M., & Bakes, E. L. O. 1995, ApJ, 443, 152
Wolfire, M. G., Hollenbach, D., & McKee, C. F. 2010, ApJ, 716, 1191
Xia, J., Tang, N., Zhi, Q., et al. 2022, Res. Astron. Astrophys., 22, 085017
Yan, Q.-Z., Zhang, B., Xu, Y., et al. 2019, A&A, 624, A6
Zucker, C., Speagle, J. S., Schlafly, E. F., et al. 2020, A&A, 633, A51
Zucker, C., Goodman, A. A., Alves, J., et al. 2022, Nature, 601, 334

Appendix A: Velocity integrated HI maps of Draco and Spider

Figures A.1 and A.2 show the column density contributions of the different velocity components to the total column density in Draco and Spider derived from the H I observations. They should be compared to the dust column densities in Figs. 4 and 5. Comparing the morphology we can assign the individual velocity components to the analyzed dust maps. For Draco we find a clear correspondence of the dust column with the IVC (−30 to −10 km s^{-1}, for Spider to the local velocity component (−10 to 30 km s^{-1}).

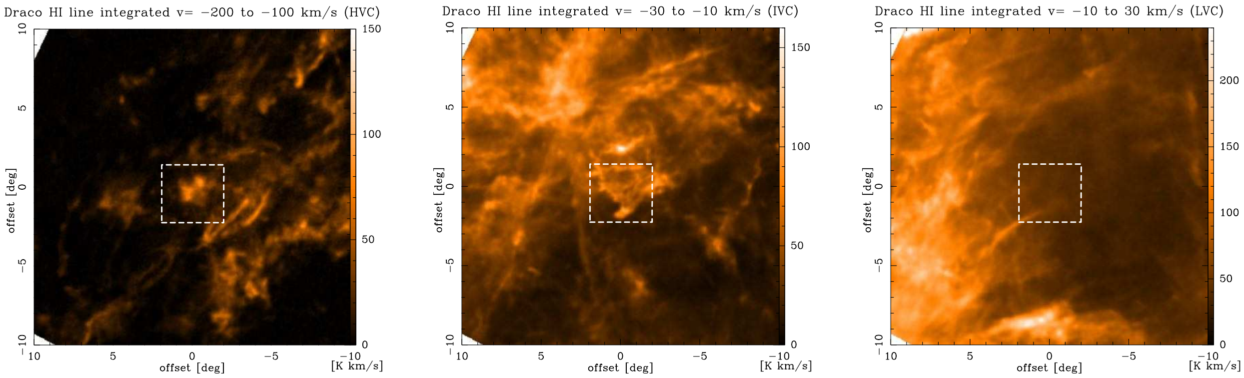

Fig. A.1. Velocity integrated H I maps of the Draco region from the EBHIS survey. The panels show the H I line integrated emission over all velocity ranges, covering the HVC (left, v=-200 to -100 km s^{-1}), the IVC (middle, v=-30 to -10 km s^{-1}), and the LVC (right, -10 to 30 km s^{-1}. For better comparison, the scale in K kms^{-1} was kept constant.

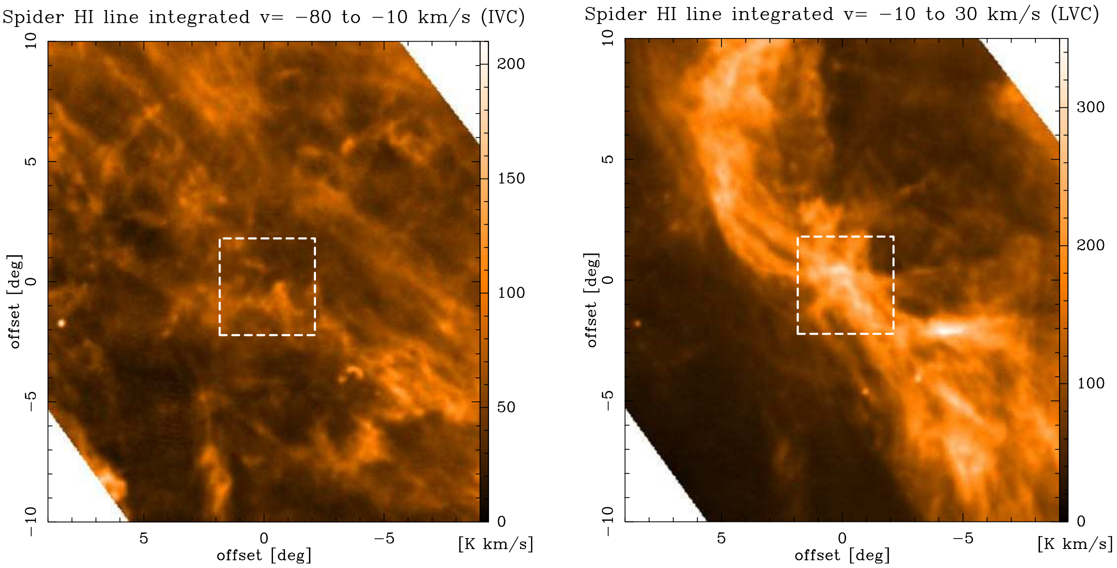

Fig. A.2. Velocity integrated H I maps of the Spider region from the EBHIS survey. The panels show the H I line integrated emission over all velocity ranges, covering the IVC (left, v=−80 to −10 km s^{-1}), and the LVC (right, −10 to 30 km s^{-1}).

Appendix B: Position-velocity cut for Draco

Figure B.1 displays a position-velocity cut in Draco at constant declination of 62 deg in the H I line emission on a logarithmic scale. The LVC, IVC, and HVC, respectively, are indicated in the plot. While LVC and IVC are closely connected in velocity space, there is no velocity bridge between the HVC and LVC/IVC.

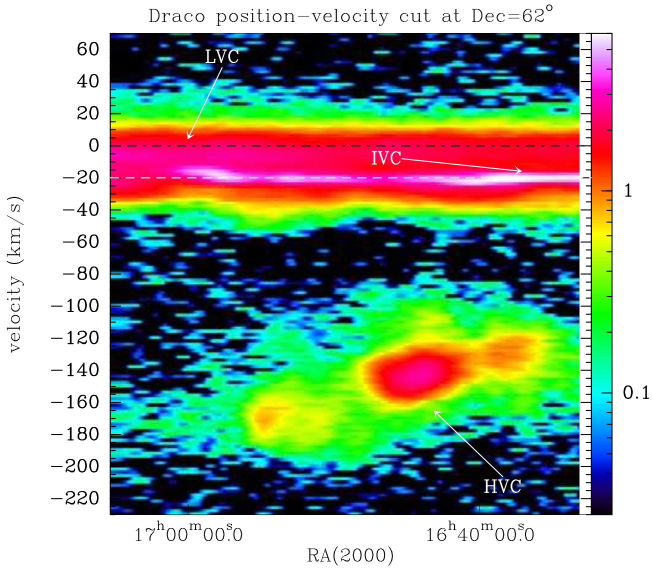

Fig. B.1. Postion-velocity cut in Draco at a constant declination of 62 deg in the H I line emission. The full velocity range comprising the LVC, IVC, and HVC is shown and indicated in the plot. There is no clear velocity bridge between the HVC and LVC.

Appendix C: PDR toolbox results for [C II] emission

Figure C.1 displays the calculated parameter range of density and UV field from the KOSMA-τ model for [C II] 158 μm emission for masses of M = 0.1 $M_\odot$ and M = 1 $M_\odot$ in units of erg cm^{-2} s^{-1} sr^{-1}. Figure C.2 displays as one example (M = 0.1 $M_\odot$) such a plot for ^{12}CO 2→1. Since the [C II] observations in Polaris, Musca, and Spider only represent the noise level, these figures illustrate in which direction the density and UV field goes in case of higher/lower [C II] limits.

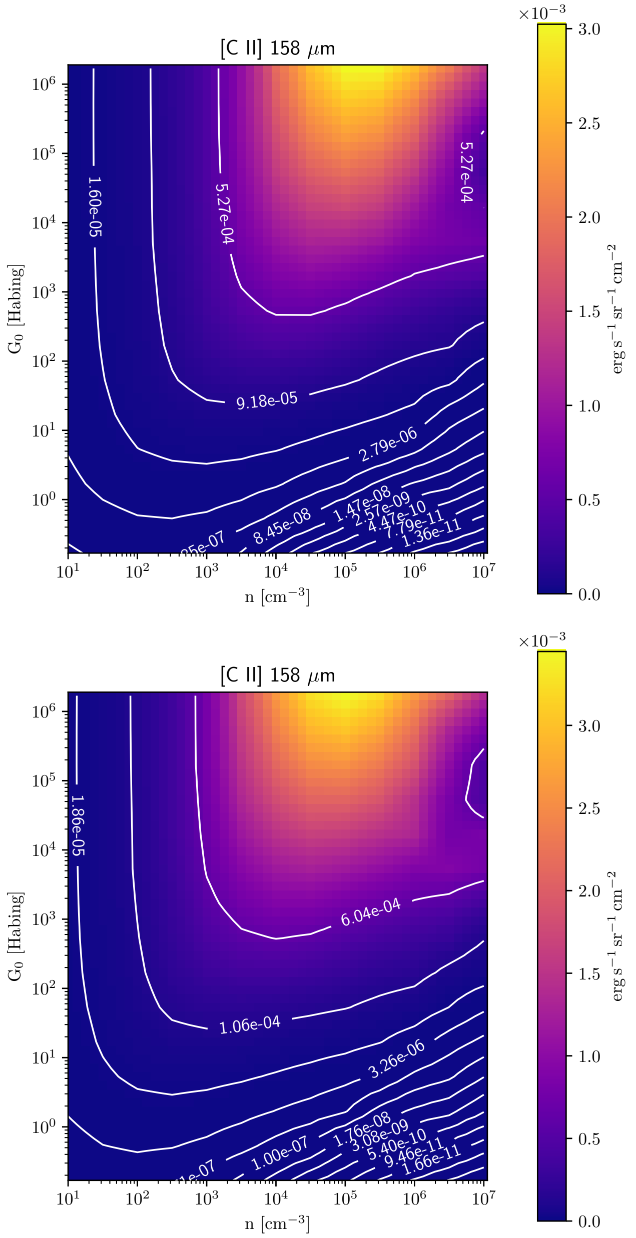

Fig. C.1. PDR toolbox predictions for the density and FUV field from [C II] 158 μm emission in erg cm^{-2} s^{-1} sr^{-1} using the KOSMA-τ model. The model using a mass of M = 0.1 $M_\odot$ (Draco, Spider, Musca) is shown in the top panel, the one with M = 1 $M_\odot$ (Polaris) in the lower panel.

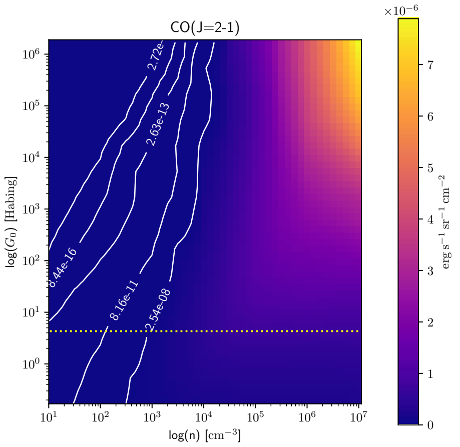

Fig. C.2. PDR toolbox predictions for density and FUV field from CO(2→1) emission in erg cm^{-2} s^{-1} sr^{-1} using the KOSMA-τ model with the model using a mass of M = 0.1 M$_\odot$.

5.2 M33

M33 is classified as a flocculent Sc-type spiral galaxy (Fig. 5.1) located at a distance of 847 kpc (Karachentsev et al., 2004) with an inclination near 56° (Regan and Vogel, 1994). It hosts numerous large star-forming regions. I generated maps that achieve an angular resolution of 18.2″, which corresponds to about 75 pc that is comparable to typical GMC or Giant Molecular Association (GMA) sizes in the Milky Way (Nguyen-Luong et al., 2016). At this resolution, we can resolve individual GMCs in 2D images (spectrally resolved maps were not used). Recent interferometric studies (Peltonen et al., 2023; Muraoka et al., 2023) achieve resolutions below 50 pc but are excluded here due to our focus on large GMCs. Neon and oxygen abundance measurements in H II regions reveal that metallicity in M33 varies from Milky Way-like levels to lower values (see Magrini et al. 2010), with an average of half the solar standard value (Gratier et al., 2012; Druard et al., 2014; Corbelli et al., 2019; Kramer et al., 2020). The total mass of M33, including gas and stars ($\sim 10^{11}\,\mathrm{M}_{\odot}$), is about 10% of the mass of the Milky Way (van der Marel et al., 2012; Patel et al., 2018).

Figure 5.1: Optical image of M33. Image credit: NOAO/AURA/NSF/T.A.Rector

Extensive observations have investigated M33's molecular gas and dust properties using the IRAM 30m telescope, the Plateau de Bure Interferometer (see Gratier et al. 2010 for a compilation of CO surveys with other telescopes), and *Herschel* for FIR to sub-mm continuum data. These studies have examined dust properties (Boquien et al., 2011; Xilouris et al., 2012; Tabatabaei et al., 2014; Relaño et al., 2016, 2018), star-formation rates (Gardan et al., 2007; Verley et al., 2010a; Boquien et al., 2010, 2015), the X-factor (Braine et al., 2010a,b), individual sources (Braine et al., 2012b,a; Gratier et al., 2012), dense gas properties (Buchbender et al., 2013), CO$(2-1)$ mapping (Gratier et al., 2010; Druard et al., 2014), gas cooling via FIR lines (Kramer et al., 2020), H II regions (Relaño et al., 2013), and 250 μm dust sources (Verley et al., 2010b).

Our objective in studying M33 is to compare the properties of molecular clouds in the Milky Way with those in an external spiral galaxy that differs in mass and metallicity but lacks extreme conditions (e.g., active galactic nuclei, starbursts). It is of great interest to explore whether the formation and evolution of molecular clouds and stars are governed by the same processes and to what extent environmental properties impact them.

To achieve these goals, we required improved hydrogen column density datasets for M33 as a basis for studying its molecular cloud population. Thus, I produced such higher-quality maps (the methods are described in Paper I and with a more intuitive/illustrative access in Sect. 4.7.1), which were subsequently used in Paper II for scientific exploration.

5.2.1 High-resolution N_{H_2} map of M33 (Paper I; Keilmann et al., 2024a)

The dust-derived H_2 column density (N_{H_2}) maps of M33 (~ 75 pc) that I construct via two methods enable a detailed study of disruptive processes in individual GMCs. The two methods refer to a simple approach using only the SPIRE 250 μm map and all relevant parameters and a more sophisticated approach, including an SED fit to the four Herschel maps from 160 to 500 μm. With these column density maps, I investigate the characteristics and potential variations of GMCs across large-scale environments, linking cloud-level dynamics with the galactic context. Consequently, I performed a comprehensive statistical study of GMCs in various dynamical environments in Paper II (Keilmann et al., 2024b). I strengthened the determination of the H_2 column density maps for Methods I and II by employing the variable emissivity index β map from F. Tabatabaei (Tabatabaei et al., 2014) and performed a new calibration of the dust opacity κ_0 based on the SPIRE 250 μm, VLA H I, and IRAM 30m CO$(2-1)$ maps, which is the first entire map of κ_0 for M33.

However, the κ_0 map exhibited gaps from the chosen calibration method and I had to find a way to fill these gaps in a meaningful way, for which I have used a machine learning algorithm. I performed consistency checks for the provided variable β map and the variable κ_0 map produced by myself.

I also calculated a first X_{CO} conversion factor map for M33 for both methods and found drastic variations in each across the galactic disk, which questions a commonly and frequently used solely single value in the literature. I analyzed their substantial variations and condensed the X_{CO} factor into a single representative value, revealing that none of the three methods yielded an "overall" value twice the Galactic standard value – $2 \times 10^{20}\,\mathrm{cm}^{-2}/(\mathrm{K\,km\,s}^{-1})$ – as frequently used in the literature; instead, they produced a value slightly lower than that. These results further imply that one cannot infer the overall X_{CO} value solely from the half-solar metallicity of M33, and they highlight substantial spatial variation consistent with the observed wide spread of metallicity in M33, and questions the common assumption that X_{CO} can be inferred solely from the half-solar metallicity of M33. I also discussed how the significant variation of X_{CO} aligns with the observed variations in the metallicity of M33, which show consistency.

After that, I have reviewed all the steps and results of my work because the procedures became quite complex. I analyzed all the different outcomes that I have obtained so far with the final maps to justify them, including not only analyzing the column density maps and the β and κ_0 maps, but also the dust temperature maps of all different approaches. I also calculated the H_2 column density from CO under LTE and with constant conversion factors (the standard Galactic value and twice this value, which is frequently used in the literature) and compared these with the resulting maps using the $X_{\rm CO}$ conversion factor maps that I have derived.

In the published version of this study, I use H I data from Gratier et al. (2010) without short-spacing corrections. However, in the subsequent Paper II (Keilmann et al., 2024b), I used updated H I data with short-spacing corrections by Koch et al. (2018) and I have regenerated all relevant maps. I explore their impact in Appendix C and confirm that the results remain substantially unchanged.

My remaining work and contributions to Paper I are as follows. I took the lead in this study. I have gathered all relevant maps (Herschel maps from 160 to 500 μm, IRAM 30m CO$(2-1)$, and VLA H I data) and pre-processed them through unit conversions (e.g., to MJy sr^{-1} for the Herschel maps), subtracting the average contribution from the Galactic emission in regions beyond the galaxy, and converting the CO and H I maps to main beam temperature and column density scales, respectively. I then constructed high-resolution H_2 column density maps via two the methods (single Herschel wavelength calculation versus SED fit with four Herschel bands) as described in Keilmann et al. (2024a), including all SED fits.

Initially, I followed the approach of Palmeirim et al. (2013), but this method caused issues in the outskirts of M33. At that time, I also used four distinct regions of the emissivity index β, which approximately resembled the gradient of β determined by Tabatabaei et al. (2014). However, to solve the problem on the outskirts of M33, I was provided the β and corresponding dust temperature map from Tabatabaei et al. (2007). With these maps, I was able to adjust the original method. I also calibrated a variable κ_0, using SPIRE 250 μm, H I, and CO maps (see Keilmann et al. 2024a), and derived the basic equation incorporating the dust-to-gas ratio (DGR), which thereby improves the original method.

I further compared and analyzed the final maps of Method I against those of Method II and both against the CO map. I constructed N-PDFs to explore the column density distribution, which were challenging to interpret in an extragalactic context. Additionally, I compared the high-resolution column density maps with those produced from different data and methods, which typically did not achieve the same high-spatial resolution as the maps that I have produced.

I led all discussions with the co-authors and incorporated their helpful comments and suggestions. We also discussed the interpretation of the results and I gained and learned valuable insights from my colleagues.

In addition to small things such as calculating the Pearson and Spearman correlation coefficients, I have written the entire paper. Of course, I have received helpful comments and feedback from the co-authors on my drafts, who also made minor edits to the manuscript. All of this improved the paper.

A&A, 688, A171 (2024)
https://doi.org/10.1051/0004-6361/202349027

Astronomy & Astrophysics

Molecular cloud matching in CO and dust in M33

I. High-resolution hydrogen column density maps from *Herschel*

Eduard Keilmann[1,⋆], Christof Buchbender[1], Volker Ossenkopf-Okada[1], Nicola Schneider[1], Slawa Kabanovic[1], Jürgen Stutzki[1], Robert Simon[1], Dominik Riechers[1], Fatemeh Tabatabaei[2,3], and Frank Bigiel[4]

[1] I. Physikalisches Institut, Universität zu Köln, Zülpicher Straße 77, 50937 Köln, Germany
[2] School of Astronomy, Institute for Research in Fundamental Sciences (IPM), PO Box 19395-5531, Tehran, Iran
[3] Max-Planck-Institut für Astronomie, Königstuhl 17, 69117 Heidelberg, Germany
[4] Argelander-Institut für Astronomie, Universität Bonn, Auf dem Hügel 71, 53121 Bonn, Germany

Received 19 December 2023 / Accepted 22 April 2024

ABSTRACT

This study is aimed to contribute to a more comprehensive understanding of the molecular hydrogen distribution in the galaxy M33 by introducing novel methods for generating high angular resolution (18.2″, equivalent to 75 pc for a distance of 847 kpc) column density maps of molecular hydrogen (N_{H_2}). M33 is a local group galaxy that has been observed with *Herschel* in the far-infrared (FIR) wavelength range from 70 to 500 µm. Previous studies have presented total hydrogen column density maps (N_H), using these FIR data (partly combined with mid-IR maps), employing various methods. We first performed a spectral energy distribution (SED) fit to the 160, 250, 350, and 500 µm continuum data obtain N_H, using a technique similar to one previously reported in the literature. We also use a second method which involves translating only the 250 µm map into a N_H map at the same angular resolution of 18.2″. An N_{H_2} map via each method is then obtained by subtracting the H I component. Distinguishing our study from previous ones, we adopt a more versatile approach by considering a variable emissivity index, β, and dust absorption coefficient, κ_0. This choice enables us to construct a κ_0 map, thereby enhancing the depth and accuracy of our investigation of the hydrogen column density. We address the inherent biases and challenges within both methods (which give similar results) and compare them with existing maps available in the literature. Moreover, we calculate a map of the carbon monoxide CO(1 − 0)-to-molecular hydrogen (H$_2$) conversion factor (X_{CO} factor), which shows a strong dispersion around an average value of 1.8×10^{20} cm^{-2}/(K km s^{-1}) throughout the disk. We obtain column density probability distribution functions (*N*-PDFs) from the N_H, N_{H_2}, and N_{HI} maps and discuss their shape, consisting of several log-normal and power-law tail components.

Key words. methods: analytical – dust, extinction – ISM: general – ISM: structure – galaxies: ISM – Local Group

1. Introduction

Column density maps obtained from dust observations in the mid and far-infrared (MIR-FIR) to submillimetre wavelengths are valuable indicators of a galaxy's total hydrogen content. Spectral energy distribution (SED) fits to the flux maps acquired through *Herschel* provide a commonly used measure of the total hydrogen column density, expressed as $N_H = N_{HI} + 2 \times N_{H_2}$. This method of analysis assumes the absence of an ionised gas contribution. Subtracting an H I column density map from the map of N_H allows us to construct a map of the total molecular gas, as done in Braine et al. (2010b) for the Triangulum galaxy M33 (cf. see their Fig. 4). However, high angular resolution dust maps are limited in availability, making comprehensive maps exceedingly valuable. The HerM33es Key Project provides the required data sets for M33, namely, full continuum mapping using *Herschel* (Kramer et al. 2010). It also delivers a ^{12}CO(2 − 1) map via an IRAM 30m Large Program (Druard et al. 2014).

M33 is an Sc-type spiral galaxy at a distance of 847 kpc (Karachentsev et al. 2004). Its proximity and inclination angle of ∼56° (Regan & Vogel 1994) allow for resolving individual giant molecular clouds (GMCs). 18.2″ correspond to ∼75 pc at the distance cited, which is the size of large cloud complexes in the Milky Way (Nguyen-Luong et al. 2016). In optical and infrared images, M33 displays a spiral structure, containing numerous distinct, massive star-forming regions alongside a diffuse extended component. The metallicity of M33 has been determined using various methods, mostly relying on measurements of neon and oxygen abundances in H II regions (Willner & Nelson-Patel 2002; Crockett et al. 2006; Magrini et al. 2009). These studies show a large scatter in absolute values of the metallicity (ranging from values comparable to the Milky Way to lower ones), but consistently suggest that it varies with galactocentric radius. The largest sample of H II regions in M33 is presented by Rosolowsky et al. (2008), Relaño et al. (2016). They also find that the metallicity is a function of galactocentric radius. The overall average metallicity they derive is approximately half of the Milky Way value and is frequently cited in the literature. Despite its relatively modest mass, which is only about 10% of that of the Milky Way, M33 serves as a crucial link between objects with lower metallicity and more irregular structures such as the Large Magellanic Cloud, as well as more evolved spiral galaxies such as the Milky Way.

⋆ Corresponding author; `keilmann@ph1.uni-koeln.de`

Several dust column density maps (and from that N_H maps) have been derived for M33 using mostly SED fits to FIR data from *Herschel* (Braine et al. 2010b; Tabatabaei et al. 2014; Relaño et al. 2018; Clark et al. 2021, 2023). However, each map has been created with different assumptions on the absorption coefficient $\kappa_{0,\mathrm{dust}}$, the emissivity index β and the dust-to-gas ratio (DGR). For example, Braine et al. (2010b) derived a column density map with a variable absorption coefficient, κ_0, in the dust opacity law, but with a fixed emissivity index, β. Tabatabaei et al. (2014) obtained a map of β and dust surface densities that were shown for both the cold and warm gas components. Other studies such as Clark et al. (2021) employed a fixed DGR and a broken emissivity law with a modified blackbody.

The approach presented here is novel because we use a variable dust emissivity index, β, and a spatial map of the absorption coefficient, $\kappa_{0,\mathrm{DGR}}$, in which the DGR is intrinsically included. For that purpose, we employ the map of β indices given by Tabatabaei et al. (2014) as well as their temperature map of the cold dust component, obtained from a two-component model with a constant $\kappa_{0,\mathrm{dust}}$ for the dust.

It is one objective of this paper to confront the different methods used to obtain hydrogen column density maps with each other and discuss their individual biases. With the β and $\kappa_{0,\mathrm{DGR}}$ maps, we then perform an SED fit to the *Herschel* data (method I) and convert the 250 µm *Herschel* map (method II) to obtain the total hydrogen column density map. From these maps, we then subtract the H I component to derive the H_2 column density maps.

Another way of obtaining a map of molecular hydrogen is to use observations of CO. The H_2 molecule is difficult to observe directly, primarily due to its low moment of inertia and consequently high rotational energy, which requires high temperatures to excite rotational transitions, and its lack of a dipole moment. As a surrogate for H_2, the second most abundant molecule, CO, is commonly used to trace H_2. The low-J rotational transitions of CO serve as effective tracers for the cold regions of molecular clouds. This is due to their low excitation temperatures (up to a few tens of Kelvin) and low critical densities (typically below $10^3\,\mathrm{cm}^{-3}$) for collisional excitation. Consequently, the mass of molecular gas in interstellar clouds is typically determined by employing a CO-to-H_2 conversion factor, denoted as X_{CO}, which scales the observed CO line intensities I_{CO} to molecular hydrogen column densities N_{H_2} (Bloemen et al. 1986; Israel 1997; Bolatto et al. 2013; Borchert et al. 2022). The relationship is expressed as: $N_{H_2} = X_{\mathrm{CO}} \times I_{\mathrm{CO}}$. For the Milky Way, the so-called 'X_{CO} factor' is approximately $2 \times 10^{20}\,\mathrm{cm}^{-2}/(\mathrm{K\,km\,s}^{-1})$, showing an increase from the centre to the outer disk (Sodroski et al. 1995; Bolatto et al. 2013; Veltchev et al. 2018). While studying galaxies in the local universe and at higher redshifts, CO observations are commonly employed to investigate individual cloud masses (Leroy et al. 2011; Bigiel et al. 2011; Cormier et al. 2014; Tacconi et al. 2018). However, the X_{CO} factor exhibits significant variations due to differing metallicities. In environments with low metallicity, the X_{CO} factor is expected to be higher than the standard value, which is attributed to a lower GDR (Leroy et al. 2013). However, this is challenged by a recent study of Ramambason et al. (2023), Chiang et al. (2024) that shows a very large variation of the X_{CO} factor in nearby dwarf galaxies and by den Brok et al. (2023) who showed a variation of the X_{CO} factor across the M101 galaxy.

The influence of far-ultraviolet (FUV) photons from massive stars also has an impact on the abundance of CO and the other carbon derivatives. In regions with lower metallicity, the FUV photons reach deeper into molecular clouds. These photons photodissociate CO and ionise carbon, leading to the creation of C^+. Consequently, a larger C^+-emitting envelope surrounds a more compact CO core in such environments. Simultaneously, H_2 photodissociates upon absorbing Lyman-Werner band photons. In denser regions, H_2 can become optically thick, thereby self-shielding from photodissociation. As a consequence, a substantial reservoir of molecular hydrogen exists beyond the CO-emitting region. This region is often referred to as CO-dark H_2 gas (Röllig et al. 2006; Wolfire et al. 2010; Pineda et al. 2013, 2014). Models (Clark et al. 2019b) predict that ionised and neutral carbon can serve as mass tracers for this CO-dark molecular gas (for a more in-depth discussion, we refer to Madden et al. 2020).

M33 has been extensively studied in CO and other molecular lines with the IRAM 30m telescope and the Plateau de Bure Interferometre (see Gratier et al. 2010 for a compilation of CO surveys with other telescopes) and with *Herschel* in the FIR to submm continuum. These studies focus on the dust properties (Boquien et al. 2011; Xilouris et al. 2012; Tabatabaei et al. 2014; Relaño et al. 2016, 2018), the star-formation rate (Gardan et al. 2007; Verley et al. 2010a; Boquien et al. 2010, 2015), the X_{CO} factor (Braine et al. 2010a,b), individual sources (Braine et al. 2012b,a; Gratier et al. 2012), the dense gas properties (Buchbender et al. 2013), the CO(2 − 1) mapping (Gratier et al. 2010; Druard et al. 2014), the gas cooling via FIR lines (Kramer et al. 2020), the properties of H II regions (Relaño et al. 2013), and on the 250 µm dust sources (Verley et al. 2010b).

In this paper, we produce high angular resolution (18.2″) N_H and N_{H_2} maps with two methods. We start with a description of the available data sets (Sect. 2) and continue with an outline of the methods (Sect. 3), including a discussion of the assumptions and shortcomings of the procedures. Section 4 shows the column density probability distribution functions (N-PDFs), presents and compares the dust-derived H_2 column density maps and the one obtained from CO and shows a map of the X_{CO} factor. In Sect. 5, we put our column density maps into context with others available in the literature. Section 6 summarises the paper.

2. Data

2.1. *Herschel* data

We utilise the FIR *Herschel* imaging data between 160 and 500 µm, which were observed in the framework of the *Herschel* Key Project HerM33es[1] (Kramer et al. 2010; Boquien et al. 2010, 2011; Xilouris et al. 2012; Tabatabaei et al. 2014). The shorter wavelength maps at 70 and 100 µm are omitted because we focus on the cold gas, characterised by dust temperatures typically below 20–30 K, which exhibits an SED peak around 250 µm. We thus use the PACS flux map at 160 µm, featuring an angular resolution of approximately 11″ and the SPIRE flux maps at 250 µm, 350 µm, and 500 µm, with angular resolutions of approximately 18″, 25″, and 36″, respectively. For the PACS maps, we employ the JScanam data products, obtained using the Scanamorphos algorithm (Roussel 2013), which have previously been used by HerM33es for earlier versions of the PACS maps. The data used for the analysis are from level 2.5 archives, processed with a calibration tree update beyond the calibration used for the original HerM33es maps. For SPIRE, we use data directly from the *Herschel* science archive that uses HIPE v14 photometric calibrations. The data have been reduced with the

---

[1] PACS observation ID: 1638302627, SPIRE observation ID: 1638304642

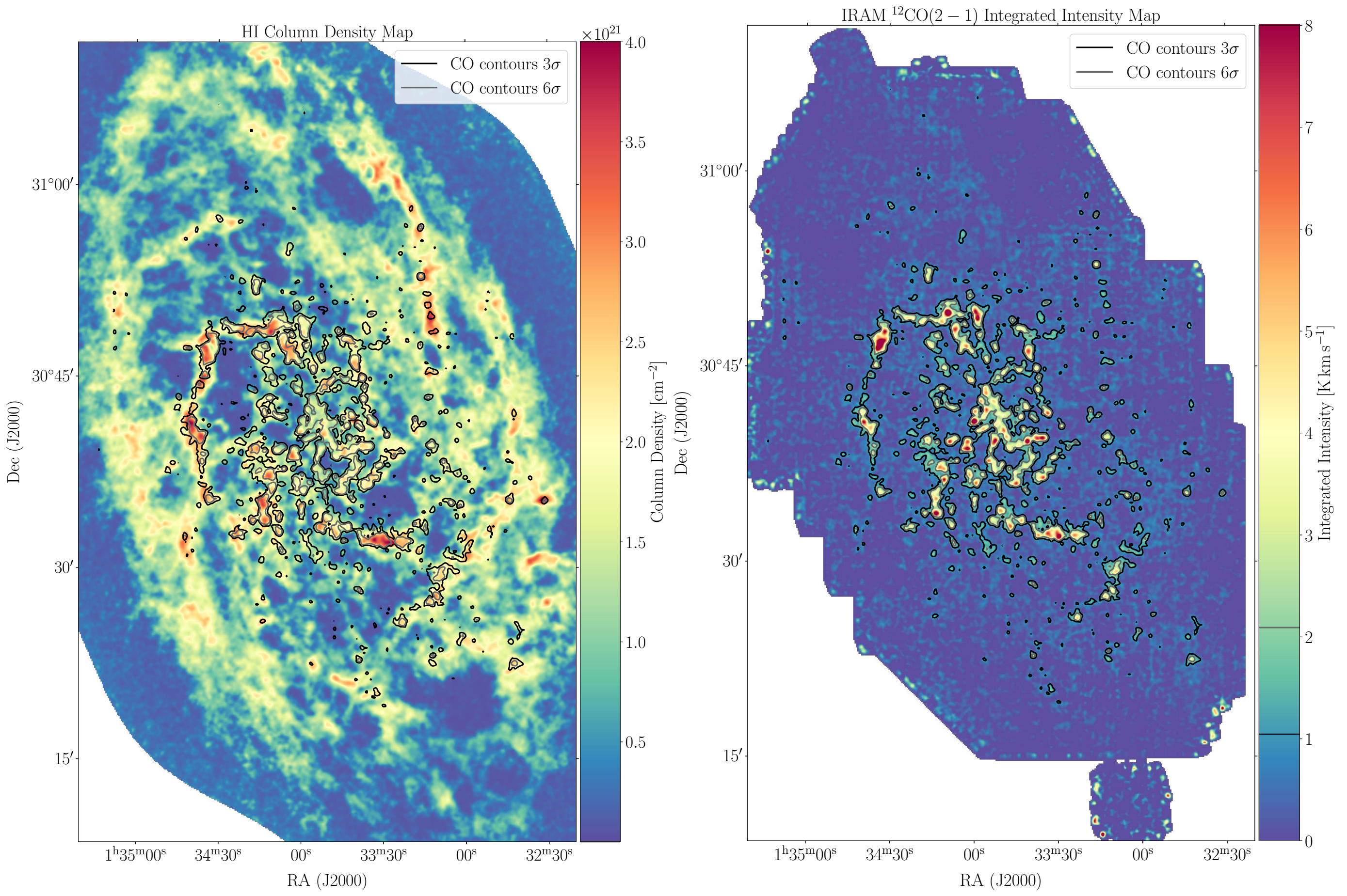

Fig. 1. $N_{\rm H\,I}$ and CO line-integrated intensity map. Left: H I column density map determined from VLA H I observations (Gratier et al. 2010). Right: IRAM 30 m CO(2 − 1) line integrated intensity map of M33 (Druard et al. 2014). The lines in the colour bar mark the 3σ and 6σ values of CO emission. Both maps are smoothed to a resolution of 18.2″ and re-gridded to a pixel size of 6″. CO contours at 3 and 6σ are overlaid on both maps.

relative gains of the SPIRE bolometers optimised to detect extended emission, using the beam area values provided in HIPE v15. As with all SPIRE final data products, all maps have been produced using the SPIRE de-striper to eliminate artefacts arising from instrumental drift. All flux maps used in this paper are shown in their native resolution in Fig. A.1. For a detailed overview of the *Herschel* data products, we refer to the publications of the HerM33es team and Clark et al. (2021).

2.2. VLA H I integrated intensity data

In order to extract only the H_2 gas from the total hydrogen column density map we derive from the *Herschel* data, it is required to remove the atomic hydrogen contribution. For that, we employed an H I map observed with the VLA at a resolution of 12″ (Gratier et al. 2010). This H I map recovers ∼90% of the flux detected by Putman et al. (2009) using the *Arecibo Observatory*.

We smoothed the VLA map to an angular resolution of 18.2″ using a Gaussian kernel, re-gridded the map and then transformed the integrated intensity to column density (Rohlfs & Wilson 1996) assuming warm, optically thin emission with:

$$N_{{\rm H}\,I} = 1.823\times10^{18}\,{\rm cm}^{-2}\int T_{\rm mb}\,{\rm d}v\,, \tag{1}$$

in which $T_{\rm mb}$ is the main beam brightness temperature in (K) and dv the velocity range in (km s^{-1}). This H I column density map is shown in the left panel of Fig. 1 with CO contour lines overlaid. Regions of peak emission are associated with the GMCs in the spiral arms, but there is also significant, more diffuse emission in the region between the arms. The mean noise of the map is $\sim 2\times10^{20}$ cm^{-2}.

2.3. IRAM 30 m telescope ^{12}CO(2 − 1) data

M33 has been observed in the ^{12}CO(2 − 1) line[2] with the HERA multibeam dual-polarisation receiver in the on-the-fly mapping mode within the IRAM Large Program “The complete CO(2 − 1) map of M33” (see Gratier et al. 2010; Druard et al. 2014). We obtained the CO data cube and the line integrated map from the IRAM repository. This data cube has an angular resolution of 12″ and a spectral resolution of 2.6 km s^{-1}, with a mean rms noise of 20.33 mK per velocity channel (Druard et al. 2014). In order to compare with the dust map, we smoothed the line integrated map to 18.2″ resolution using a Gaussian kernel. We here only use the line integrated CO intensity map for which we determined an rms noise of 0.35 K km s^{-1}, corresponding to $3\sigma = 1.046$ K km s^{-1}, from the smoothed 18.2″ map. The temperature scale of the archive data is in antenna temperatures and has been converted into main beam brightness temperatures using a forward efficiency of $F_{\rm eff} = 0.92$ and a beam efficiency of $B_{\rm eff} = 0.56$ (Druard et al. 2014). The final CO map is shown in the right panel of Fig. 1.

---

[2] From now on only denoted as CO(2 − 1).

3. Hydrogen column density maps from *Herschel* flux maps

This section first gives a derivation of the basic equations to obtain the total hydrogen column density, N_H, which is essential for both methods discussed in the following, as well as the properties of the dust emissivity index and absorption coefficient. The subsequent subsections describe the two methods deriving high-resolution (high-res) column density maps at 18.2″ from the *Herschel* flux maps and how the H_2 maps are produced[3].

3.1. Derivation of N_H

The flux density of the continuum emission, F_ν, is related to the Planck law, $B_\nu(T_\mathrm{d})$, and optical depth, τ_ν, via:

$$F_\nu = B_\nu(T_\mathrm{d})[1 - e^{-\tau_\nu}]\,\Omega\,, \tag{2}$$

with the Planck law

$$B_\nu(T_\mathrm{d}) = \frac{2h\nu^3}{c^2}\frac{1}{\mathrm{e}^{\frac{h\nu}{k_\mathrm{B}T_\mathrm{d}}} - 1}\,. \tag{3}$$

Herewith, ν represents the frequency, T_d denotes the dust temperature (free or fixed; see below), and Ω represents the solid angle of the source. For a low optical depth, which can generally be assumed for dust, $\tau_\nu \ll 1$, we can approximate the above expression by

$$F_\nu \approx \tau_\nu B_\nu(T_\mathrm{d})\,\Omega\,. \tag{4}$$

Since the specific intensity is given by $I_\nu = F_\nu/\Omega$ and

$$\tau_\nu = \frac{\kappa_\mathrm{d}(\nu)\cdot M_\mathrm{d}}{D^2\Omega}\,, \tag{5}$$

where M_d is the dust mass, $\kappa_\mathrm{d}(\nu)$ is the dust opacity or the extinction cross-section per dust mass (the subscript d stands for the dust), and D^2 is the distance squared to M33, the specific intensity, I_ν, is then:

$$I_\nu = \frac{\kappa_\mathrm{d}(\nu)\cdot M_\mathrm{d}}{D^2\Omega}B_\nu(T_\mathrm{d})\,. \tag{6}$$

Introducing the dust-to-gas ratio (DGR), we can rewrite the last equation as

$$I_\nu = \frac{\kappa_\mathrm{d}(\nu)\cdot \mathrm{DGR}\cdot M_\mathrm{d}}{D^2\Omega\,\mathrm{DGR}}B_\nu(T_\mathrm{d}). \tag{7}$$

Defining $\kappa_\mathrm{g}(\nu) := \kappa_\mathrm{d}(\nu)\cdot\mathrm{DGR}$, where the subscript g stands for gas, as well as $M_\mathrm{gas} := M_\mathrm{d}/\mathrm{DGR}$ leads to

$$I_\nu = \frac{\kappa_\mathrm{g}(\nu)\cdot M_\mathrm{gas}}{D^2\Omega}B_\nu(T_\mathrm{d})\,. \tag{8}$$

Here, $\kappa_\mathrm{g}(\nu)$ is the dust opacity per unit mass (total mass of gas and dust). The number of gas particles, N_g, multiplied by the mean molecular weight, μ_m, and the hydrogen mass, m_H, yields the gas mass, M_gas, the column density, N_H, can be related to the number of particles by $N_\mathrm{H} = N_\mathrm{g}/(D^2\Omega)$, so that the specific intensity can eventually be written as:

$$I_\nu = \kappa_\mathrm{g}(\nu)\,\mu_m\,m_\mathrm{H}\,N_\mathrm{H}\,B_\nu(T_\mathrm{d})\,. \tag{9}$$

Assuming a power-law frequency-dependent $\kappa_\mathrm{g}(\nu)$ (Juvela et al. 2015b), we can write the above equation as:

$$I_\nu = \kappa_{0,\mathrm{DGR}}(\lambda/250\,\mu\mathrm{m})^{-\beta}\,\mu_m\,m_\mathrm{H}\,N_\mathrm{H}\,B_\nu(T_\mathrm{d})\,, \tag{10}$$

where a dust opacity law similar to Krügel & Siebenmorgen (1994) has been used with

$$\kappa_\mathrm{g}(\nu) = \kappa_{0,\mathrm{DGR}} \times (\lambda/250\,\mu\mathrm{m})^{-\beta}\,. \tag{11}$$

Here, $\kappa_{0,\mathrm{DGR}}$ is the absorption coefficient in units of $(\mathrm{cm}^2/\mathrm{g})$ with the DGR inherently included, which will be described in Sect. 3.2, and β is the emissivity index. We will denote $\kappa_{0,\mathrm{DGR}}$ simply as κ_0 from now on. The hydrogen column density N_H is calculated from the surface density $\Sigma = \mu_m\,m_\mathrm{H}\,N_\mathrm{H}$, with a mean molecular weight of $\mu_m = 1.36$, and $N_\mathrm{H} = N_\mathrm{HI} + 2\times N_{\mathrm{H}_2}$. Re-arranging for the column density, N_H, the above expression finally gives

$$N_\mathrm{H} = \frac{I_\nu}{\kappa_0(\lambda/250\,\mu\mathrm{m})^{-\beta}\,\mu_m\,m_\mathrm{H}\,B_\nu(T_\mathrm{d})}\,. \tag{12}$$

The values of the parameters in the dust opacity law, κ_0 and β, are crucial but their spatial variation is difficult to determine correctly. We devote Sect. 3.2 to a more detailed discussion. Note that the DGR is contained within κ_0 in this notation.

We note that other studies often express $\kappa_0(\lambda/250\,\mu\mathrm{m})^{-\beta}\,\mu_m\,m_\mathrm{H} = \sigma_\mathrm{H}$ as the cross-section per H-atom, denoted as σ_H, which writes Eq. (12) equivalently to

$$N_\mathrm{H} = \frac{I_\nu}{\sigma_\mathrm{H}\,B_\nu(T_\mathrm{d})}\,. \tag{13}$$

3.2. The dust absorption coefficient, κ_0, and emissivity index, β

A crucial point for SED fitting (described in Sect. 3.4) and the calculation of the column density is the choice of the dust absorption coefficient, κ_0, and the dust emissivity index, β. The resolution of 18.2″ (equivalent to 75 pc) of our final hydrogen column density maps samples a mixture of dust and gas properties. The derived values of parameters such as β, κ_0, or T_d thus are intensity-weighted averages over the equivalent resolved beam area along the lines of sight. Different physical processes such as grain-grain collisions, condensation of molecules onto grains or shattering can affect the grain properties and, as such, the value of the emissivity index. The grain properties will vary within each beam, and the beam-averaged properties will also vary with the galactic environment, including factors such as star formation efficiency, metallicity, turbulence, and so on. Thus, the value of β is most likely not constant over a full galaxy, but rather depends on grain size, structure, distribution and chemical composition. A detailed discussion of the fundamentals is provided by Ossenkopf & Henning (1994). Observational constraints for Milky Way clumps are summarised by Juvela et al. (2015a,b). For particles small compared to the wavelength and non-changing optical constants, β would take the value of 1 from absorption in the Rayleigh limit (Krügel 2003). However, for any real material, this must break down at long wavelengths due to the integrability of the Kramers-Kronig relation for the optical constants. Ossenkopf & Henning (1994) showed that this leads to $\beta = 2$ for the bulk absorption in the millimetre regime and beyond, but shallower spectra with $\beta = 1\ldots 2$ were discussed for large coagulated grains in the wavelength range covered by *Herschel*. The range for β derived from observations lies between 1 and 2.5 (Chapin et al. 2011; Casey et al. 2011;

---

[3] All final data products are publicly available at the Centre de Données astronomiques de Strasbourg (CDS).

Boselli et al. 2012). Boselli et al. (2012) found that $\beta \lesssim 1.5$ provides a better fit for metal-poor, low surface brightness galaxies.

For M33, dust properties have been extensively studied (Boquien et al. 2011; Xilouris et al. 2012; Tabatabaei et al. 2014; Relaño et al. 2016, 2018). While Xilouris et al. (2012) assumed $\beta = 1.5$ for M33, Tabatabaei et al. (2014) derived a variable emissivity index for the cold dust component, which decreases along the galactocentric radius from $\beta = 2$ in the centre to $\beta = 1.3$ in the outer disk. This might reflect the complexity of the grain properties in more detail. Tabatabaei et al. (2014) applied a two-component modified blackbody fit to the SED using *Spitzer* and *Herschel* data ranging from 70 to 500 µm. The two-component model was solved for the dust temperature, β parameter and dust surface density.

With the emissivity index (Fig. B.2) and dust temperature map (Fig. B.3) from Tabatabaei et al. (2014) which we use here, the corresponding κ_0 in the dust opacity law (Eq. (10)) will also vary pixel-by-pixel. The dust emission cross-section per H-atom, σ_H, can be related to the optical depth, τ_ν, and total column density by (see Sect. 3.1, Eq. (13)):

$$\tau_\nu = \sigma_\mathrm{H} N_\mathrm{H} = I_{250\,\mu\mathrm{m}} / B_\nu(T_\mathrm{d}) \,, \tag{14}$$

where $I_{250\,\mu\mathrm{m}}$ is the specific intensity of the SPIRE 250 µm map and σ_H is given in Eq. (13).

Considering only regions with no or low CO emission allows us to avoid any assumptions on the CO-to-H$_2$ conversion factor X_CO. We therefore exclude regions above the 2σ level of the CO emission for the calculation of κ_0 pixel-by-pixel, suggesting that the total hydrogen column density N_H is dominated by the atomic hydrogen column density $N_\mathrm{H\,I}$. Using the relation $\kappa_0(\lambda/250\,\mu\mathrm{m})^{-\beta}\,\mu_m\, m_\mathrm{H} = \sigma_\mathrm{H}$, Eq. (14) can then be re-arranged as follows:

$$\kappa_0 \approx \frac{I_{250\,\mu\mathrm{m}}}{(\lambda/250\,\mu\mathrm{m})^{-\beta}\,\mu_m\, m_\mathrm{H}\, N_\mathrm{H\,I} B_\nu(T_\mathrm{d})} \,, \tag{15}$$

which simplifies to

$$\kappa_0 \approx \frac{I_{250\,\mu\mathrm{m}}}{\mu_m\, m_\mathrm{H}\, N_\mathrm{H\,I} B_\nu(T_\mathrm{d})} \,. \tag{16}$$

With this approach, we get some cavities in the κ_0 map, where the CO emission exceeds its 2σ level (Fig. B.1). To fill these void regions, the machine learning interpolation technique *KNNImputer* from the scikit-learn Python package is employed (Pedregosa et al. 2011), as explained in Appendix B. The resulting κ_0 map, which incorporates the interpolated values, is displayed in Fig. 2.

At the edges of the galaxy, the κ_0 values fall below $0.02\,\mathrm{cm}^2\,g^{-1}$, while in some regions around the two main spiral arms, very high values are reached (red in the colour scale of Fig. 2) due to low H I column densities. From these regions, some interpolated values of κ_0 within the cavities in Fig. B.1 yield excessively high values in the molecular phase, resulting in negligible H$_2$ column density in a few areas, such as the southern central part of M33. This occurs where the H I column density rapidly decreases, causing an exceptionally high value of κ_0 (see Eq. (16)). This sharp transition in H I column density corresponds to a fast drop to the noise level of H I column density. Hence, our interpolation assigns very high values of κ_0 to areas where the CO emission exceeds the 2σ level. This is due to our assumption of a non-changing κ_0 and a lack of additional information on how κ_0 should behave.

However, since we know that H$_2$ must exist in these regions, we conclude that these κ_0 values are too high. Testing with different values of κ_0 manually reveals that a range of approximately 0.03 to $0.04\,\mathrm{cm}^2\,g^{-1}$ provides a lower limit for the H$_2$ column density. To set the excessively high values of κ_0 in a few regions to lower values, we calculate the median of the interpolated values after a first interpolation with *KNNImputer*. The median is $\sim 0.04\,\mathrm{cm}^2\,g^{-1}$ and is, hence, consistent with the lower limit for the H$_2$ column density as determined above. The median gives a robust estimate of the interpolated κ_0 values within the molecular phase, while the mean value is too sensitive to outliers (the excessively high values of κ_0). Subsequently, where the edges of the cavities (at the CO 2σ emission) exceed this median of $0.04\,\mathrm{cm}^2\,g^{-1}$, we set $\kappa_0 = 0.04\,\mathrm{cm}^2\,g^{-1}$ for those pixels. The interpolated values from the first interpolation are then discarded and re-interpolated with these updated κ_0 values at the edges of the cavities at the CO 2σ level. So, only those pixels at the edges of the cavities (at the CO 2σ level) are updated to the median value, where κ_0 was higher than the median after the first interpolation. And then a second interpolation has been applied with these updated pixels.

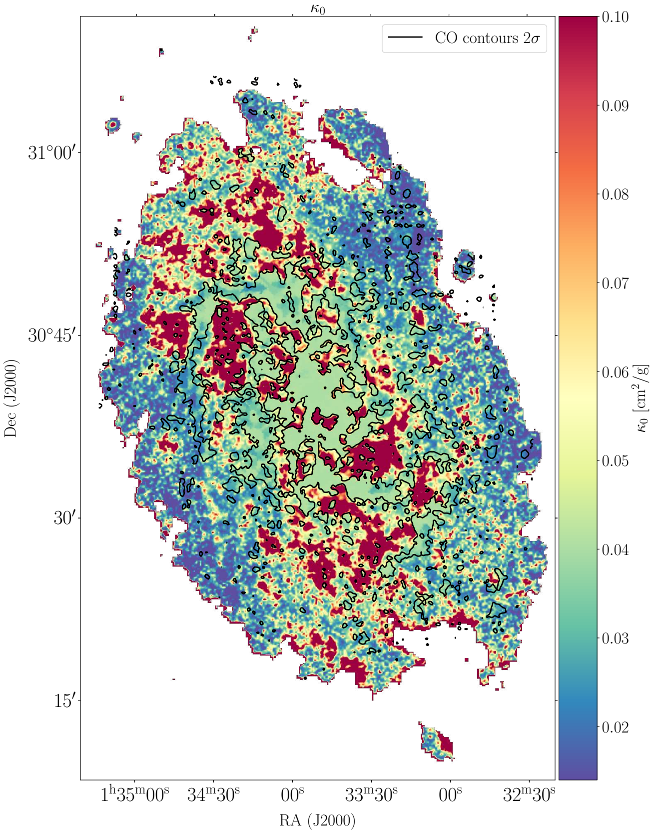

Fig. 2. κ_0 map obtained as described in Sect. 3.2. Note that the DGR is included in the notation of κ_0. CO contours at the 2σ level are overlaid on the map.

This approach results in a more uniformly distributed κ_0 within the molecular phase (or where CO exceeds the 2σ level), especially in the central part of the disk, aligning with our assumption of a constant κ_0, as no further information on the behaviour of κ_0 is available. One might argue for the adoption of a constant κ_0 across the entire interpolated region, since we 'update' the values to the median. However, such an approach would lead to the loss of information in regions that fall below the median, as exactly these values contribute to the calculation of the median. Furthermore, since we lack any information on a lower limit for κ_0, we have no additional justification for a universal update of κ_0 throughout the region.

Previous studies often suffered from assumptions on the X_{CO} factor, a fixed dust-absorption coefficient or from utilising a constant DGR. Our map intrinsically captures the overall trends on galactic scales, such as potential variations in the DGR or dependencies on the galactocentric radius. This is achieved by providing all relevant information on a pixel-by-pixel basis, thereby rendering the computation of κ_0 for each pixel. As a result, the determination of the X_{CO} factor remains unaffected by assumptions, allowing its evaluation while accounting for variations across the galactocentric radius. We note that the success of the interpolation technique relies on the assumption that the dust properties do not change significantly between the atomic and molecular phases. Further investigations are needed to confirm its applicability in specific cases.

With the method described above, we generate new high-resolution column density maps of M33, specifically focusing on the cold gas. However, accurately determining the final uncertainty of the map is challenging due to the involvement of multiple factors of uncertainty. Sources of uncertainty are introduced by the provided emissivity index map generated as discussed in Tabatabaei et al. (2014) and the calculated κ_0 map determined from the emissivity index and the VLA H I map. A fixed $\kappa_0 = 0.038\,\mathrm{cm}^2\,g^{-1}$ determined as the mean value above the 2σ CO regions and increased by 20% alters the mean column density by a factor of less than ~2 and ~2.5, respectively, whereas increasing β by 20% does not change the mean by more than a factor of ~0.8. Thus, we consider our generated column density map to be robust.

For any future reference, we will adopt the following terminology. With 'inter-main spiral regions', we refer to the area roughly inside the white dashed ellipses with a galactocentric distance of roughly 4 kpc in Fig. 3, excluding the two main spiral arms defined by the 3σ CO contours and the centre. Using the terms 'outer region' or 'outskirts' of M33, we specifically indicate the region roughly outside of those ellipses. We note that the white dashed ellipses are used solely to illustrate our terms and do not represent any physical means.

3.3. Preparation of the maps

Before running the code implemented to generate the high-resolution map, we applied a mask to the uneven edges of the original *Herschel* maps, which exhibit higher noise due to the scanning pattern of the telescope. The data obtained from the archive are absolutely calibrated, incorporating the necessary Planck-offset corrections for the SPIRE observations. They encompass emissions originating from the Milky Way. Consequently, we derived the average contribution from Galactic emissions in regions beyond the galaxy and subsequently subtracted the values thus determined from the maps (refer to Table A.1 in Appendix A for an overview of the background root-mean-square (rms) values). This procedure aligns with the methodology employed by the HerM33es consortium (Xilouris et al. 2012). The intensity units for all maps have been converted to MJy sr^{-1}. Subsequently, we reproject and re-grid all maps to the central coordinates and grid pattern of 6″ of the SPIRE 250 µm map. The ensuing algorithm, outlined below, has then been applied to these reprocessed maps.

3.4. Method I: Dust column density map from SED fits to *Herschel* maps

This method requires several steps, which are described in the following sub-subsections.

3.4.1. Spatial decomposition

The conventional approach employed to generate column density maps from *Herschel* observations, primarily applied to Galactic data, involves fitting the dust temperature, T_{d}, as well as β and the surface density, Σ, via a one-component greybody function (modified Planck function) pixel-by-pixel to the SED derived from the flux densities within the wavelength range of 160 to 500 µm. To allow for this, all flux maps are subject to smoothing, aligning them with the 500 µm map's resolution of 36″, which serves as the lowest common resolution for the fitting process. Consequently, the resultant map adopts this resolution (e.g. André et al. 2010). An alternative technique for obtaining a higher angular resolution column density map at 18.2″, introduced by Palmeirim et al. (2013), is based on a multi-scale decomposition of the flux maps and has not yet been employed for extragalactic observations.

Imaging maps can be considered a superposition of emissions at many different spatial scales (e.g., Starck et al. 2004). For this reason, attempts have been made to describe the interstellar medium (ISM) as a two-component system, consisting of a more diffuse self-similar fractal component and a coherent, filamentary component (Robitaille et al. 2019), or as a multifractal system (Elia et al. 2018; Yahia et al. 2021). Methods to separate these structures are often based on wavelet, ridgelet and curvelet transforms. To create a high-resolution column density map, one must reverse this approach and construct a map from higher resolution sub-maps that still contain individual spatial scales, involving SED fits at different wavelengths. In the following, we outline the method presented in Appendix A of Palmeirim et al. (2013).

The high angular resolution (high-res from now on) map of the gas surface density distribution Σ_{high} at 18.2″ is given by:

$$\Sigma_{\mathrm{high}} = \Sigma_{500} + (\Sigma_{350} - \Sigma_{350} * G_{500\_350}) + (\Sigma_{250} - \Sigma_{250} * G_{350\_250}), \tag{17}$$

where Σ_{500}, Σ_{350}, and Σ_{250} are the gas surface density distributions[4] at the angular resolution of their corresponding *Herschel* bands, i.e. 36.3″, 24.9″, and 18.2″, respectively, and $G_{\lambda_c\_\lambda_o}$ are the Gaussian kernels of width $\sqrt{{\theta_c}^2 - {\theta_o}^2}$ for the convolution, commonly denoted as $*$. The beam at the required resolution is specified by θ_c and the beam at the original resolution by θ_o so that the widths are

$$G_{500\_350}\ \sqrt{36.3^2\ -\ 24.9^2} \quad \text{and} \tag{18}$$

$$G_{350\_250}\ \sqrt{24.9^2\ -\ 18.2^2}\,. \tag{19}$$

The surface density maps are obtained with the following procedure:

- Σ_{500} is calculated by smoothing the 160, 250, and 350 µm maps to the resolution of the 500 µm band (36.3″) and then performing a greybody fit (see below) to the band 4 data.
- Σ_{350} is obtained by smoothing the 160 µm and 250 µm maps to the resolution of the 350 µm band (24.9″) and then performing a greybody fit to the band 3 data.
- Σ_{250} is made by smoothing the 160 µm map to the resolution of the 250 µm band (18.2″) and then performing a greybody fit to the band 2 data.

All maps are re-gridded onto the same raster of 6″ after the smoothing process. In the original method by

---

[4] We utilise *Herschel* dust data, incorporating an intrinsically included DGR in κ_0, thereby obtaining instantaneously gas surface densities.

Palmeirim et al. (2013), the temperature was obtained from the colours in the SED fits of Σ_{500} and Σ_{350}, while it was fixed using the 250/160 µm flux ratio for Σ_{250}. Here, we adopt a slightly different approach, using the temperature map provided in Tabatabaei et al. (2014) to determine Σ_{250} (Fig. B.3). This choice is motivated by the presence of stronger noise features in the flux ratio map at the outskirts of the galaxy compared to the method utilising the temperature map from Tabatabaei et al. (2014). Being consistent with the β and κ_0 values for the dust provides another advantage. Nonetheless, we determined the colour temperature map using the flux ratio applying Brent's method[5] within the scipy package 'brentq' and compared with the results employing the temperature map of Tabatabaei et al. (2014). The differences in the final column density maps are small, especially in the central regions of the galaxy and within the spiral arms. The temperature map from Tabatabaei et al. (2014) has an angular resolution of 36″ and represents the cold component of the dust (as shown in the left panel of their Fig. 9). The authors conducted a two-component modified blackbody fit using *Herschel* wavelengths of 70, 100, 160, 250, 350, and 500 µm with distinct cold and warm dust components. The temperature maps obtained from the SED fitting are presented in Fig. C.1. We revisit this fitting procedure in Sect. 4.

The final map of the gas surface density distribution, denoted as Σ_{high}, achieved at a (high) resolution of 18.2″, is determined by Eq. (17). This equation entails the summation of the intermediary outcomes stemming from all preceding stages. In practical terms, this signifies that the process commences with the map derived from 500 µm measurements. Subsequently, the information lost during the smoothing process to transition from the resolution of the 350 µm map to that of the 500 µm map is reintegrated. Following this, the spatial information of the data lost due to the smoothing procedure when transitioning from the resolution of the 250 µm map to that of the 350 µm map is incorporated in a similar way.

The angular resolution for both the provided β map (Fig. B.2) and the corresponding dust temperature map (Fig. B.3) is 36″. We did not observe any broad variations in β and T_{d} over a few beam sizes across the map, suggesting that our final hydrogen column density map at a resolution of 18.2″ is unlikely to be significantly affected by the lower resolution input maps. Furthermore, considering Eq. (17), it is evident that the primary contribution to the final hydrogen column density map of method I arises from the SPIRE 250 µm map. In this context, β does not play a role, since the reference wavelength of κ_0 is determined at 250 µm. Our approach is notably more sophisticated than using a constant value for β over the entire galaxy, as is often done in the literature (e.g. Braine et al. 2010b). The uncertainty in the final dust column density map is estimated to be around 20%, following the arguments given in Könyves et al. (2015), which discuss in detail the various error contributions for maps produced using the Palmeirim et al. (2013) method. It is likely that our error is reduced due to our approach of not utilising fixed β and κ_0 values, although we do maintain a cautious estimate of 20%.

3.4.2. SED fit to the data

A pixel-by-pixel greybody (also expressed as modified blackbody) function fit is performed using Eq. (10). Assuming optically thin emission, the frequency dependent surface brightness I_ν is given by the Planck function, $B_\nu(T_{\text{d}})$, the surface density, Σ, and the dust opacity, $\kappa_{\text{g}}(\nu)$, per unit mass (total mass of gas and dust). Each SED data point fit was weighted by $1/\sigma^2$, where σ corresponds to the calibration errors relevant for the *Herschel* bands. We assume an error of 20% of the intensity in the 160 µm and 10% for the SPIRE bands. These values are motivated by Galactic studies (Könyves et al. 2015) and are larger than those given in a recent work of Clark et al. (2021) who also fit *Herschel* flux maps of M33 to obtain column densities.

To perform the SED fits, we use the absorption coefficient and emissivity index maps as shown in Figs. 2 and B.2 at each computational step with the respective wavelengths to obtain Σ_{500}, Σ_{350} and Σ_{250}. Integrating these maps into Eq. (17) and performing the convolution then gives the high-res map, as shown in the left panel of Fig. 3. Subtracting the H I component from this map produces the H_2 column density map displayed in the left panel of Fig. 4. We note that the formal χ^2 values from the fitting procedure are very low. We also checked the SED fit itself by eye at a number of randomly selected positions in the map and found no noteworthy outliers for the four wavelength data points.

Fitting β with a variable κ_0 would result in different values for β. However, we avoid using the possibly wrong assumption of a fixed DGR. Instead, we establish the dependency of this parameter on galactocentric radius intrinsically[6], which is integrated into our definition of κ_0 (see Sect. 3.1). Given that β is correlated with star forming molecular gas (Tabatabaei et al. 2014), this correlation should still be maintained with a variable κ_0. We therefore compare the above mentioned SED fits with the hydrogen column density maps with another fit over a small region around NGC 604, where we set β as a free fitting parameter while employing our variable κ_0. This reproduces approximately the β map determined in Tabatabaei et al. (2014) (see Fig. D.1). The region covers both the atomic and molecular phases, with differences in β mostly below 0.2. The highest differences are located in the atomic phase, where our column density maps of molecular hydrogen are not affected anyway. However, the main drivers for the differences presumably arise from employing a one-component over a two-component modified blackbody fit, which includes a larger dataset. Additionally, different fitting parameters cause a non-unique solution for β. Nevertheless, as our simple fit reproduces approximately the same β values, we consider our approach to be self-consistent, despite the fact that the β map has been determined with a constant κ_0.

3.5. Method II: Column density map from SPIRE 250 µm

The SPIRE 250 µm flux density map allows for the determination of the total hydrogen column density using Eq. (12) at an identical angular resolution of 18.2″ as in method I. This approach offers a simpler and more straightforward calculation and can be compared to the high-res map obtained with method I described in Sect. 3.4 and thus serves as a consistency check.

As for method I, we use the information of the β and κ_0 maps at each pixel as described in Sect. 3.2 as well as the dust temperature map at each pixel from Tabatabaei et al. (2014), as shown in Fig. B.3. The resulting total hydrogen column density map is presented in Fig. 3 (right). Estimating the error of the dust column density map obtained with method II is not straightforward. Due to the utilisation of only one single band, the formal

---

[5] Brent's method (Brent 1973) is an iterative approach for determining a root, combining the bisection method, the secant method, and the inverse quadratic interpolation. From the combination of these techniques, Brent's method has a faster convergence rate and greater robustness compared to using each individual method alone.

[6] Thus, the variability of DGR must be considered in addition to the variability of κ_0.

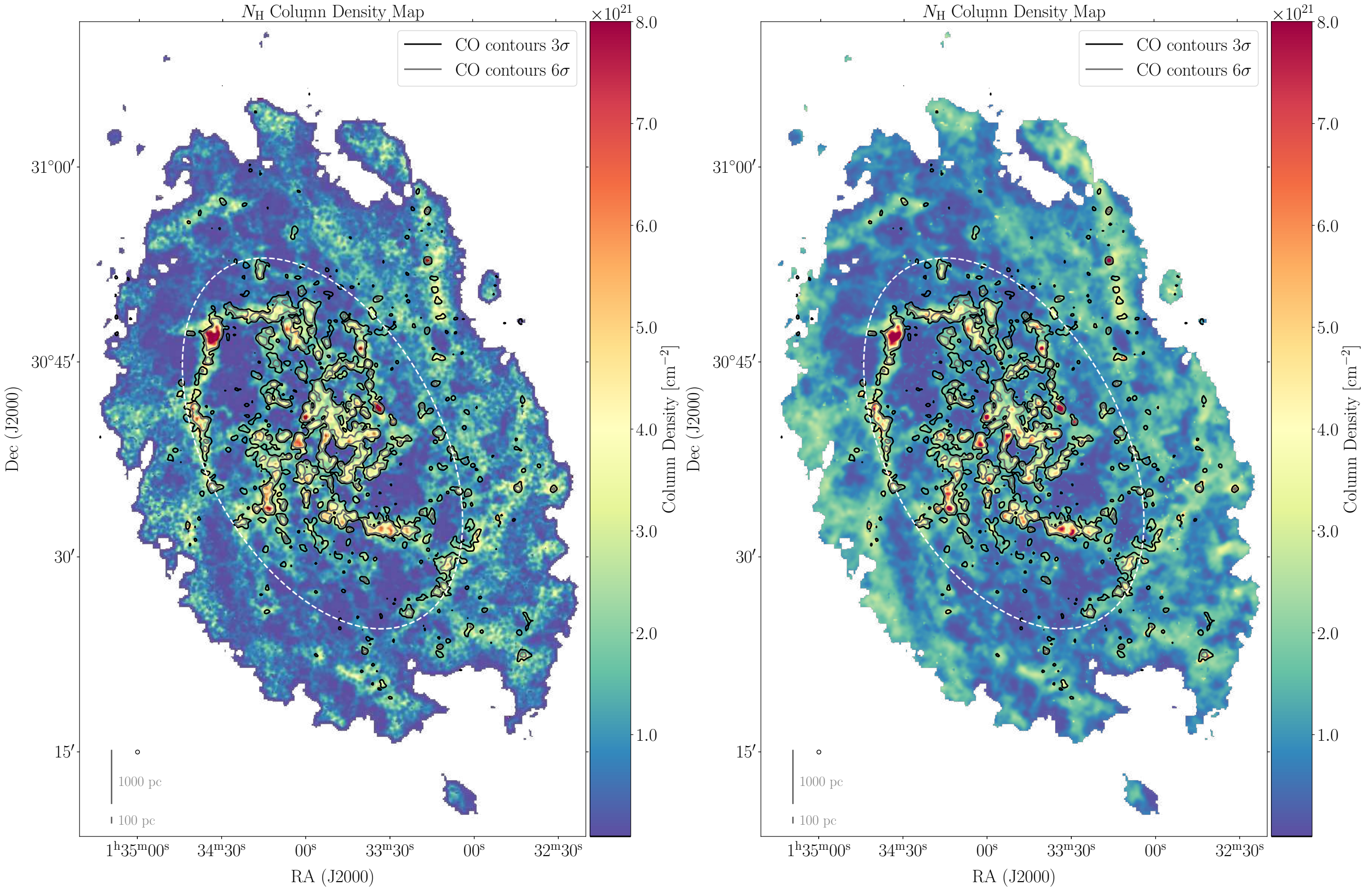

Fig. 3. Total hydrogen column density maps obtained via methods I and II. Left: high resolution N_H total gas column density map obtained from the *Herschel* maps of M33 at 18.2″ angular resolution using the β map from Tabatabaei et al. (2014) with method I. Right: total gas column density map N_H obtained from the *Herschel* SPIRE 250 µm map of M33 with method II at the same spatial resolution of 18.2″, indicated by the circle in the lower left corner. CO contours (as of Fig. 1) are overlaid in both maps. The white dashed ellipses mark roughly the regions we refer to as 'inter-main spiral' region or "outskirts".

error introduced by the flux uncertainty is low. However, relying solely on one wavelength is inherently less reliable compared to a full SED fit across multiple wavelengths. Therefore, we can only presume that the uncertainty associated with the resulting N_H map is of 30%.

Finally, we also subtract the H I column density (as for our high-res map obtained with method I) to arrive at an estimate of the molecular hydrogen column density shown in Fig. 4. Once more, determining a total error of the N_{H_2} maps obtained using methods I and II is challenging. Here, the H I observations introduce an additional uncertainty. Nevertheless, the conversion of the line-integrated H I intensity into the H I column density incurs a small error. Consequently, we can conclude that our final H_2 column density maps are accurate up to 20% for method I and 30% for method II.

4. Results and analysis

In this section, we start by presenting the probability distribution functions of the total hydrogen column density (*N*-PDFs) together with the H I *N*-PDF (Sect. 4.1). We then discuss the dust column density maps generated with both methods (Sect. 4.2) and compare them with the CO line-integrated map (Sect. 4.3). We finish by displaying and discussing the X_{CO} factor map (Sect. 4.5).

4.1. Hydrogen column density PDFs

Generally, *N*-PDFs or density (ρ) PDFs are a powerful tool to describe the ISM and investigate its properties. They form the basis of star-formation theories (e.g. Padoan & Nordlund 2002; Hennebelle & Chabrier 2008; Federrath & Klessen 2012) and are commonly employed in dust and line observations for Galactic and extragalactic sources (e.g. Kainulainen et al. 2009; Froebrich & Rowles 2010; Hughes et al. 2013; Lombardi et al. 2015; Schneider et al. 2022). Simulations and theory showed that supersonic isothermal turbulence results in a log-normal distribution for the ρ- and *N*-PDF and self-gravity introduces a power-law tail (PLT) in the distribution at high densities (e.g. Vazquez-Semadeni 1994; Federrath et al. 2008; Kritsuk et al. 2011; Ballesteros-Paredes et al. 2011; Girichidis et al. 2014; Jaupart & Chabrier 2020).

We construct *N*-PDFs for the total hydrogen column density maps shown in Fig. 3 (with blue error bars calculated using Poisson statistics Schneider et al. 2015), for the dust-derived molecular hydrogen column density maps (Fig. 4), as well as for the CO map converted into N_{H_2} with the derived X_{CO} factor maps shown in Sect. 4.5.1 for the H I column density map (Fig. 1, left). In order to compare identical regions in the *N*-PDFs, we construct the *N*-PDFs considering only those pixels, which exhibit non-blanked values in Fig. 4. Figure 5 displays these *N*-PDFs in grey for the total hydrogen column density

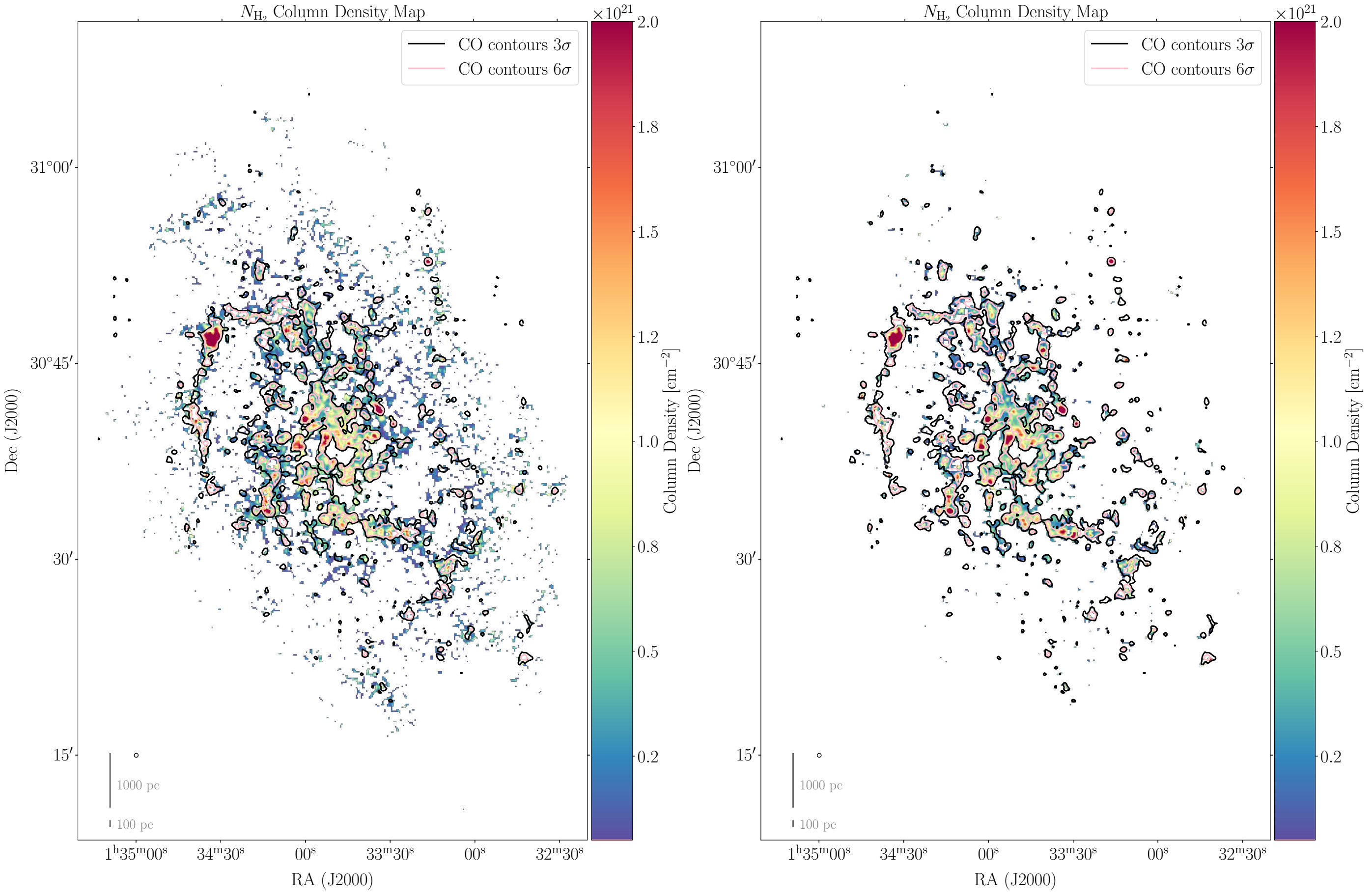

Fig. 4. Molecular hydrogen column density maps obtained via methods I and II. Left: high-res H_2 column density map derived using all *Herschel* dust data employing method I with CO contours above the 3 and 6 σ level of the CO map shown in Fig. 1. Right: H_2 column density map derived from SPIRE 250 µm map with method II. The circle to the lower left represents the resolution of 18.2″.

along with the dust-derived molecular hydrogen (in pink), the CO-to-N_{H_2} (in blue and denoted as $N_{H_2(CO)}$) and the atomic hydrogen N_{HI}-PDF (in green). Given that higher column density values result in smaller number statistics, and considering the limited resolution equivalent to 75 pc, we have beam-diluted column density values, leading to a plateau above ~2×10^{22} cm^{-2} for the N-PDFs. Consequently, we opt to exclude these values from the analysis. A further increase in angular resolution would likely distinguish smaller areas, potentially preserving the power-law tail towards higher values (Schneider et al. 2015; Ossenkopf-Okada et al. 2016).

Figure 5 suggests, by comparing the total (grey) and atomic (green) N-PDFs, that the majority of the column density is in the atomic phase, as the PDFs cover similar column density ranges. The $N_{\rm H\,I}$-PDF shows a sharp decrease towards higher column densities. Both peaks of the N_{H_2}-PDF and $N_{\rm H\,I}$-PDF are consistent with the peak of the total N-PDF, as adding the two peaks coincides with the total N-PDF peak. For values exceeding the H I column density (around 4×10^{21} cm^{-2}), Fig. 5 indicates that these higher column densities are covered by the total N-PDF as well as the N_{H_2} maps (derived from dust and CO). This suggests the presence of CO-bright molecular hydrogen. However, the border to CO-dark H_2 gas cannot be determined from the N-PDFs. Both molecular PDFs exhibit a broader width compared to the H I and total column density PDFs, while the dust-derived N_{H_2}-PDF has the broadest width. This broadness may suggest the presence of CO-dark gas. Consistently, the derived $N_{H_2(CO)}$-PDF has a less broad width. The broad width of the dust-derived N_{H_2}-PDF also arises from subtracting H I from the total hydrogen column density, a phenomenon generally expected and discussed in Ossenkopf-Okada et al. (2016). In this study, 'contamination' of atomic and molecular gas along the line-of-sight was investigated, showing that a simple subtraction of a constant screen is a valid approach for galactic molecular clouds to correct for this effect, although it leads to broader PDFs and a shift of the peak column density to lower values. In the case of M33, the situation is more complex because in many sightlines multiple clouds may overlap within the beam. Note that this does not lead to several peaks in the PDF (Ossenkopf-Okada et al. 2016), but to a broader PDF distribution.

Considering the constructed N-PDFs for the whole region, as described in Appendix E and shown in Fig. E.1, discloses a different error tail for the N-PDFs from methods I and II. For both methods, the N-PDF shapes above ~10^{20} cm^{-2}, approximately the noise level of the map, are very similar. Below this value, a slight shoulder is visible, followed by a noise slope towards lower values for method I, which is absent for method II. This difference is likely due to the conversion via method II of the 250 µm map, which involves a conservative, possibly overly high, subtraction of the background emission, leading to the absence of a noise slope for low column densities. In method I, the impact of the background subtraction is less evident because here an SED fit is performed and the maps are subtracted to obtain a final high-res map. As highlighted in Palmeirim et al. (2013),

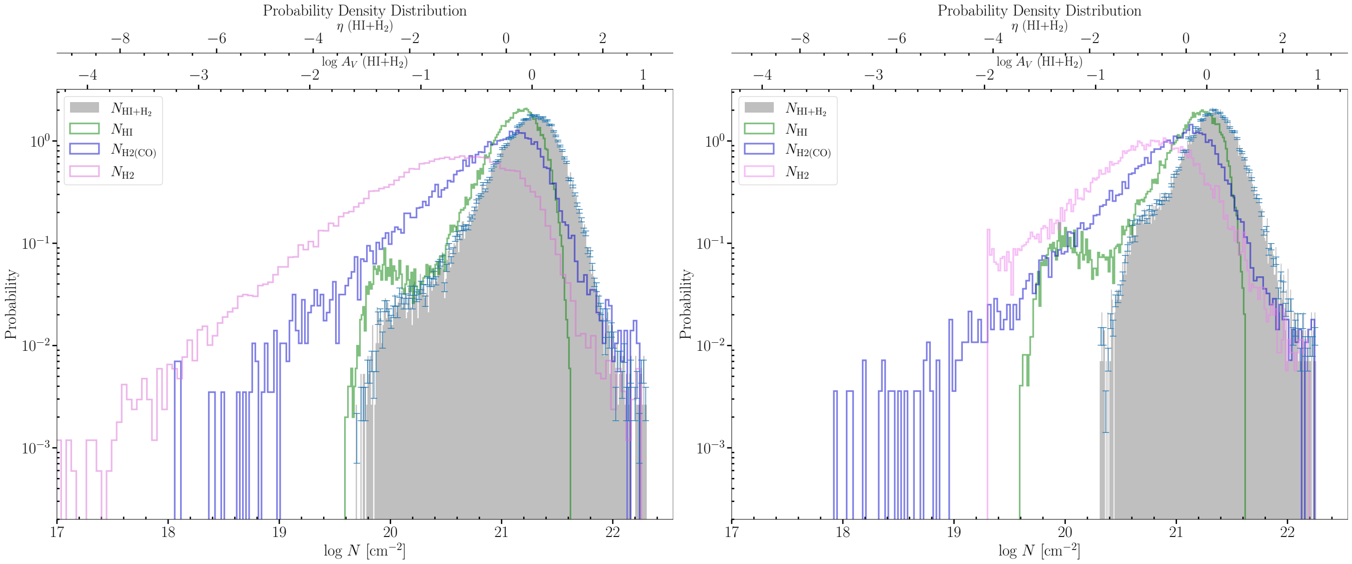

Fig. 5. *N*-PDFs obtained from the various column density maps. Left: *N*-PDF of the high-res N_H column density map derived using all *Herschel* dust data employing method I only for non-blanked pixels of Fig. 4. Right: *N*-PDF of the N_H column density map derived with method II for the same non-blanked pixels of Fig. 4. The green lines show the *N*-PDF of H I. Here, η is defined by $\eta = \ln \frac{N}{\langle N \rangle}$, where *N* is the column density and $\langle N \rangle$ the mean column density.

the noise in this final map is slightly increased. However, due to this missing error tail from method II, we also see in the N_{H_2}-PDF in Fig. 5 (right and pink) a sharp decline towards lower column density.

In both *N*-PDFs, we observe an excess at high column densities, typically above 10^{22} cm^{-2}. These data points in the context of the statistical analysis of the *N*-PDF exhibit significant uncertainty due to limited statistics and primarily stem from the most massive GMCs in M33. However, at such high column densities, we anticipate the onset of gravitational collapse of the whole GMC, or within larger clumps contained within them. In such cases, a PLT is expected to emerge, a phenomenon frequently observed in Milky Way studies (e.g. Lombardi et al. 2015; Stutz & Kainulainen 2015; Schneider et al. 2015, 2022), which links the PLT to self-gravity.

4.2. Comparison of dust-derived N_H and N_{H_2} maps

In the following subsections, we compare the N_H maps and subsequently the N_{H_2} maps derived with methods I and II.

4.2.1. Comparison of the N_H maps

Figure 3 displays the total column density map ($N_H = N_{HI} + 2 \times N_{H_2}$) derived using both methods I and II. Values exceeding the maximum threshold of 2.02×10^{22} cm^{-2} and 1.81×10^{22} cm^{-2} for methods I and II, respectively, are blanked. The GMC NGC604, the brightest region in M33, located at RA(2000) = $1^h34^m40^s$, Dec(2000) = 30°48′, was selected for this threshold. The mean column densities in both datasets are similar, with values of 1.06×10^{22} cm^{-2} and 1.23×10^{22} cm^{-2} for the N_H maps of methods I and II, respectively. Across the entire disk, the N_H maps shown in Fig. 3 exhibit a very similar morphology concerning the definition of the spiral arms, though method I produces slightly higher column densities in the spiral arms. Since dust has a lower optical depth at higher wavelengths, such as 500 µm, method I can potentially increase column density, as it gathers more information from dust emission than method II, which only uses the SPIRE map at 250 µm. Differences are primarily observed in the extent and smoothness of the diffuse inter-main spiral arm regions and the outer regions. method II appears to depict broader regions of gas in these areas of M33, while the map of method I exhibits higher local peaks, resulting in a more granular gas distribution. This discrepancy is most likely attributed to the implementation of the β parameter, which exhibits similar small-scale structures (as shown in Fig. B.2) and has a more pronounced impact on the final column density map for method I compared to method II, owing to differences in methodology (see Sect. 4.2.2). However, evaluating the authenticity of the small-scale structure is not straightforward. Additionally, we observe that in both N_H maps, the gas within the western outer region of the galaxy (dashed grey ellipse in Fig. 6) reaches higher column densities compared to the eastern half of M33.

However, it is evident from the vast literature of CO maps of M33 that the galaxy comprises numerous GMCs and smaller molecular clouds, leading to the expectation of a rather non-uniform distribution, which is indeed reflected in the map produced using method I. Figure 6 displays the similarity between the N_H maps obtained with methods I and II in a difference map. In the vicinity of the CO 3σ contours, method I tends to exhibit higher column densities. This transfers further into higher column densities concentrated within smaller regions in the outskirts and inter-main spiral regions, with a more rapid decline toward the edges of a GMC.

Those ‘peaks’ in the total hydrogen column density map obtained with method I can locally attain values of up to approximately 5×10^{21} cm^{-2}. This observation aligns with what can be inferred from Fig. 3, where the map derived using method II presents a more uniform and smooth gas distribution, covering a broader area with lower “peak” values. The majority of the difference map shows values close to zero, indicating very similar N_H maps.

4.2.2. Comparison of the N_{H_2} maps

Upon subtracting the H I column density from both N_H maps, as shown in Fig. 4, the spiral arms in the N_{H_2} maps become even

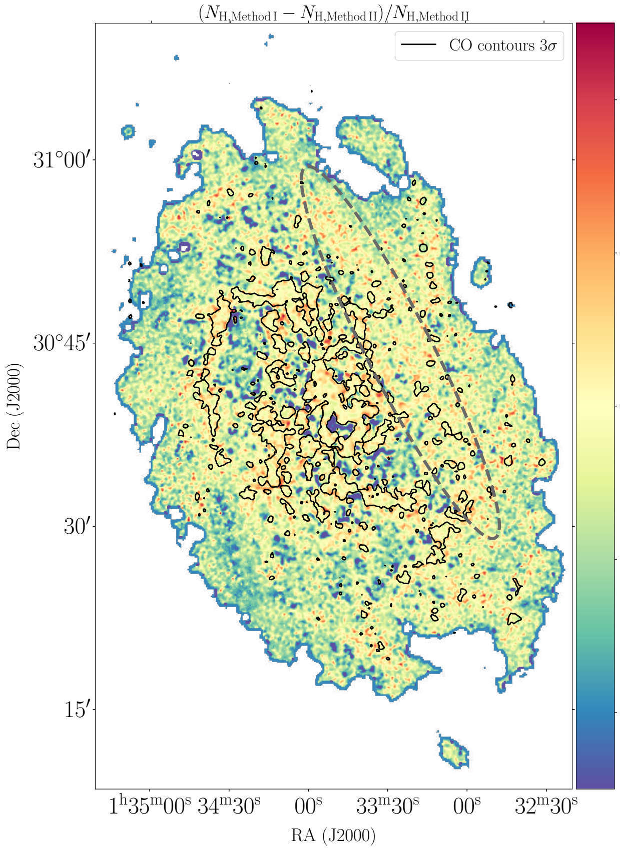

Fig. 6. $(N_{\rm H,Method\,I} - N_{\rm H,Method\,II})/N_{\rm H,Method\,II}$ difference map of the dust-derived total column density maps. The grey ellipse roughly delineates the area of enhanced emission observed in the western half of M33, as depicted in Figs. 3 (left) and 4 (left), in contrast to the eastern half.

more distinct, as expected when GMCs form in the gravitational potential of the spiral arms from more diffuse H I gas. However, the diffuse gas (region outside the CO 3σ level) is only evident in the map obtained with method I. As for the $N_{\rm H_2}$ maps, they have mean values of 2.95×10^{20} cm^{-2} for method I and 3.10×10^{20} cm^{-2} for method II.

While the morphology and overall magnitude of the $N_{\rm H_2}$ maps generated within both methods are quite similar, the most significant contrast once again arises in the inter-main spiral and outer regions (see Fig. 4). In method II, the gas in the inter-main spiral region primarily results in a smoothly distributed gas pattern. In contrast, the map produced by method I reveals a more granular gas distribution, with higher local peaks in these inter-main spiral regions. These peaks reach values of approximately $N_{\rm H_2} \approx 3 \times 10^{20}$ cm^{-2}. The reason for this discrepancy lies in the role of the parameter β. In method II, κ_0 is determined at 250 µm, so that the fraction in Eq. (12) is always 1. However, in method I, the situation is different. Here, all four bands spanning from 160 µm to 500 µm are utilised, leading to a fraction different from 1 in three out of four cases. Consequently, the value of β in the exponent significantly influences the resulting map. The maps produced by method I closely follow the morphology of the β emissivity index map in Fig. B.2 and contain additional information. As therefore β, which correlates with star formation and molecular gas Tabatabaei et al. (2014), is the main parameter causing this difference of molecular hydrogen gas seen in the dust-derived map of method I but not in the map of method II (which is unaffected by β) or CO, we tentatively attribute this partly to CO-dark gas.

4.2.3. Discussion of caveats and used methods

However, there is a caveat in our assumptions. We utilise the CO 2σ level to determine our dust absorption coefficient. Within this level, there is evidently CO emission spread across the entire disk of M33. As a result, the final dust absorption is overestimated, leading to a slight underestimation and hence a lower limit of the hydrogen column density (cf. Eq. (16)). Thus, there are a few regions, especially in the northern part of M33, where no $N_{\rm H_2}$ is left within CO regions above 2σ. With an $X_{\rm CO}$ factor of 1.8×10^{20} cm^{-2}/(K km s^{-1}) (see below) and the CO 2σ level, the H$_2$ column density can reach values up to $\sim 1.3 \times 10^{20}$ cm^{-2} in regions equal to and below the CO 2σ level. This is consistent with the mean column densities in the map for these regions, which fall below the specified threshold. Thus, we attribute this emission to originate from a non-changing κ_0 which is introduced by the assumption. Furthermore, even including CO emission would still lack information regarding contributions from CO-dark H$_2$ gas, which also plays a role in Eq. (16). Thus, trying to be as unbiased as possible regarding the CO emission and its CO-dark H$_2$ gas problem, suggests our approach is reasonable to use in this regard. We note that for our determination of the dust absorption coefficient κ_0, it is essential for the dust and gas to be well mixed. While this condition is certainly met in denser regions of molecular gas, it becomes less certain in the predominantly atomic phase.

Lastly, method II relies solely on information from a single *Herschel* map, while method I incorporates data from all four *Herschel* bands spanning from 160 µm to 500 µm, thus providing a more comprehensive dataset, particularly concerning cold GMCs. Furthermore, as the flux maps at wavelengths above 250 µm exhibit a lower dust optical depth, gaining more information from the dust emission, the column densities obtained with method I are more comprehensive. Furthermore, it encompasses additional information not only originating from the use of the various *Herschel* maps, but also from the β map. Method I is more elaborate to apply, but serves as a valuable tool for generating column density maps. Notably, it covers the information from the emissivity index to a greater extent compared to method II. Method II is a useful choice when only a single map is available and still produces satisfactory and comparable results. This method can be applied to any *Herschel* flux map; here we select 250 µm because it provides the best compromise between high angular resolution and detection of the cold gas component. Since the *N*-PDF of method I exhibits a noise tail, which is generally expected and absent in the *N*-PDF derived from method II, we consider method I to be the preferred option over method II, whenever the required data are available.

4.3. Comparison of the $N_{\rm H_2}$ maps to the CO map

Comparing the dust-derived $N_{\rm H_2}$ maps in Fig 4 with the CO line-integrated intensity map shown in Fig. 1 (right), all maps exhibit similar features with the spiral arms in both tracers. However, there are distinct differences. The emission of $N_{\rm H_2}$ is more prominent in the inter-main spiral regions and extends further outward, whereas the emission of CO tends to be more concentrated locally in the inner regions within the main spiral arms. The extended column density observed in the $N_{\rm H_2}$ maps may originate from CO-dark H$_2$ gas, particularly near GMCs or in the outskirts of the galaxy, where the total hydrogen column densities are relatively lower. This is particularly true for the $N_{\rm H_2}$ map derived using method I. A significant large-scale correlation between CO emission and H$_2$ column densities exists (see Fig. 4 and the CO contour levels). However, this correlation does not hold consistently at smaller scales for cases of higher CO emission and both dust-derived N_{H_2} from methods I and II. This discrepancy is observed in various regions of the disk.

Since we utilise CO$(2-1)$ data, characterised by a higher critical density of $n_{crit} = 1.1 \times 10^4\,cm^{-3}$ compared to CO$(1-0)$ with a critical density of $n_{crit} = 2.2 \times 10^3\,cm^{-3}$ (both at 20 K, Teng et al. 2022), a smaller region of CO$(2-1)$ emission is excited. Therefore, detected GMCs may have smaller envelopes and a larger proportion of gas could be falsely attributed to CO-dark gas. However, this potential concern is likely mitigated by smoothing the CO line-integrated map to lower resolution, effectively addressing this limitation.

For data points above 3σ in CO, the Spearman coefficients are $\rho_S = 0.4$ and $\rho_S = 0.49$ for methods I and II, respectively. In contrast, the Pearson correlation yields slightly higher coefficients of $\rho_P = 0.5$ and $\rho_P = 0.56$ for methods I and II, respectively[7]. Both correlation coefficients show a positive but only moderate correlation. One possible explanation could be a too high κ_0 value in the molecular phase, leading to an underestimation of the H_2 column density. This suggests that the assumption of a uniform κ_0 in both the atomic and molecular phases may be invalid in these regions, where the assumption treats κ_0 as independent of density. This observation is also reflected in the *Herschel* maps presented in Fig. A.1, which display a better overall correlation between dust and CO emission, but a weaker correlation (to a smaller extent) in few regions between regions of high dust and high CO emission. In both cases, the coefficients show a positive and higher, but still only moderate correlation[8]. This disparity could potentially account for the lower correlation of especially higher CO emission with the molecular hydrogen column density derived from dust in some regions.

In summary, there are signs suggesting the potential existence of CO-dark H_2 gas. Nonetheless, additional research is necessary to enhance our comprehension of the relationship and dynamics between CO and the dust tracers within M33. In Sect. 5 the results will be compared with the work of Braine et al. (2010b), who used a similar method to derive gas masses from the dust in M33.

4.4. The assumption of a non-changing κ_0

The composition of dust, and hence the dust absorption coefficient, varies significantly with volume density. Environmental conditions influence the extent to which various elements deplete from the gas phase onto dust grains (Jenkins & Wallerstein 2017; Roman-Duval et al. 2021, 2022). Additionally, studies by Hirashita & Kobayashi (2013) and Aoyama et al. (2020) have revealed that the size distribution of dust grains is also affected by density. While theoretical models (Ossenkopf & Henning 1994; Jones 2018) propose an increasing dust opacity (κ) with density, empirical evidence from Clark et al. (2019a) suggests the opposite in nearby galaxies. They observed a decrease in κ with surface density, following a power-law index of -0.4. In a recent investigation by Clark et al. (2023), they presented compelling evidence for a changing κ following a power-law index of -0.4 with surface density in M33. Other studies (Bianchi et al. 2019, 2022) have indicated that the dust surface brightness per unit gas surface density increases with higher ISM surface densities and higher molecular-to-atomic gas ratios. A similar trend is observed for the dust luminosity per unit gas mass, implying that dust shows reduced emissivity in denser environments.

Thus, considering the correlation between the dust-derived hydrogen column density maps and the *Herschel* maps in comparison to the CO emission, it is reasonable to conclude that the assumption of a constant κ_0 is valid only to a first-order approximation. However, since we lack the means to independently determine the column density before calculating κ_0 in the molecular phase or vice versa, we cannot introduce a model that adjusts κ_0 according to the density. Therefore, it is reasonable to consider our κ_0 as a conservative estimate, representing a lower limit. In Clark et al. (2023), the variation in the dust-to-hydrogen ratio, attributed to a changing κ based on density, spans a range of approximately 2.5. Consequently, scaling κ_0 with 2.5 in regions where CO exceeds 2σ leads to a column density showing a stronger correlation with CO emission. However, this approach does not account for a power-law relationship with density and can only provide a rough upper limit representation.

Other potential factors contributing to the observed variations could arise from variations in dust temperature. Lower dust temperature could lead to lower H_2 column density and vice versa. However, as illustrated in Figs. B.3 and C.1, the shift in dust temperature from the dominant H I phase, where CO is below its 2σ level, to the molecular phase, where CO is above its 2σ threshold, is negligible. The β parameter may also contribute to explaining the variations with density. As shown in Tabatabaei et al. (2014), β correlates with star formation and the molecular phase; therefore, it may also change between the atomic and molecular phases. As depicted in Fig. B.2, the parameter β does not follow a strong, distinct pattern or shift in its value between the atomic and molecular phases (CO emission at the 2σ level). Its values fluctuate, being both low and high within the spiral arms, as well as in the regions between them and in the outer disk. In addition, β does not play a role in the map obtained with method II, as the reference wavelength in $\kappa_g(\nu)$ matches the wavelength of the SPIRE map used for method II. Since we still observe very similar variations in the dust-derived hydrogen column density map obtained via method II to CO emission, we can exclude β as the cause of these variations.

4.5. The X_{CO} conversion factor

The X_{CO} factor depends on several factors, including the ambient radiation field, metallicity, dust content and the evolutionary state of the galaxy in terms of star formation (cf. e.g. Bolatto et al. 2013). Notably, Offner et al. (2014) derived strong fluctuations in X_{CO} depending on the ambient FUV flux. In regions with high FUV fields, CO can be readily photo-dissociated, making it a poor tracer for H_2 (Kaufman et al. 1999; Kramer et al. 2004). Moreover, Israel (1997) suggested a linear correlation between X_{CO} and the total infrared (TIR) luminosity, L_{TIR}, over a wavelength range from 1 µm to 1 mm.

---

[7] The Spearman correlation coefficient, which is applicable to any monotonic relationship (linear and non-linear) and data that do not necessarily need to be normally distributed, is more robust against outliers than the Pearson correlation coefficient. Since the Spearman correlation coefficient works well for both linear and non-linear relations, it therefore does not distinguish between them. In contrast, the Pearson correlation requires normally distributed data with a strict linear relation.

[8] For data points above 3σ in CO, the Spearman coefficients are 0.61, 0.66, 0.65, and 0.60 for the PACS 160 µm and SPIRE 250 µm, 350 µm, 500 µm maps, respectively. In contrast, the Pearson correlation yields slightly higher coefficients of 0.66, 0.72, 0.71, and 0.64 for the PACS 160 µm and SPIRE 250 µm, 350 µm, 500 µm maps, respectively.

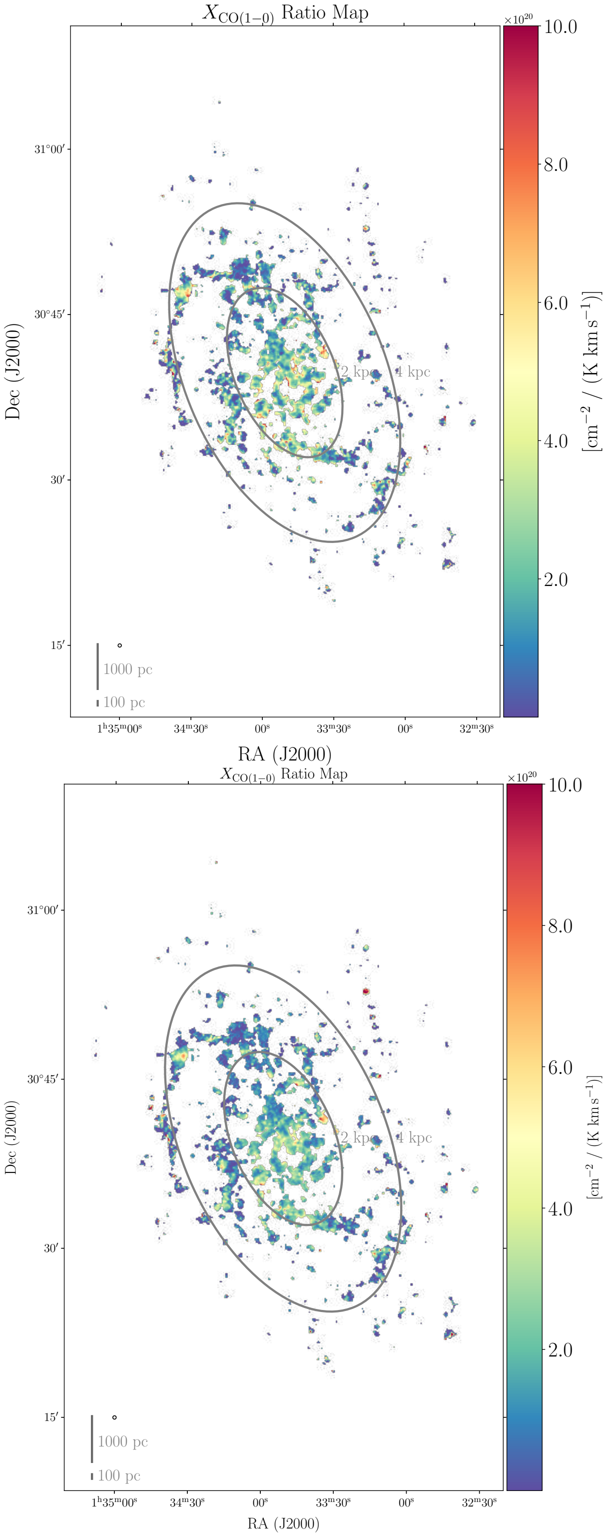

Fig. 7. X_{CO} factor (ratio) maps of methods I and II. Determined as the dust-derived H_2 column density over CO intensity determined at each position in both maps of M33 at 18.2″ and scaled with the CO($\frac{2-1}{1-0}$) ratio to the CO($1-0$) intensity of method I (top) and method II (bottom). The two ellipses correspond to an equivalent circular radius of 2 and 4 kpc.

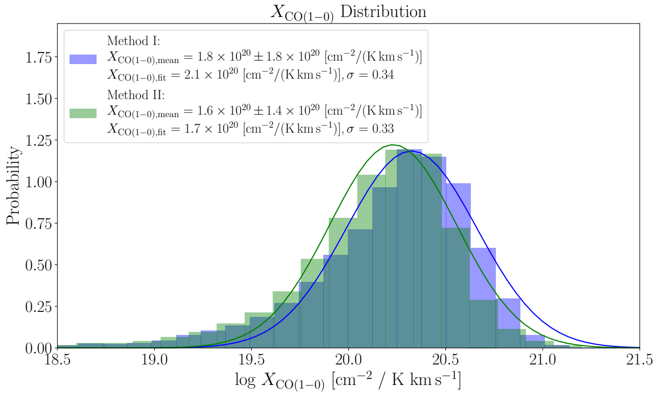

Fig. 8. Distribution of the X_{CO} conversion factor from methods I and II in blue and green, respectively. The $X_{CO(1-0)}$ conversion factors of Fig. 7 and their standard deviations are given in the panel. A log-normal Gaussian fit is shown in the corresponding colours for methods I and II.

4.5.1. Determination of the X_{CO} factor (ratio) map

With both a dust-derived H_2 column density map and a CO integrated intensity map at our disposal, we can create an X_{CO} factor (or ratio) map. This process involves dividing the values on a pixel-by-pixel basis in the dust-derived H_2 column density maps by their corresponding values in the line-integrated CO($1-0$) map. We apply a scaling factor of 0.8 based on the average CO($2-1$)/CO($1-0$) line ratio as discussed in (Druard et al. 2014) in order to obtain the CO($1-0$) map[9]. This ratio typically ranges between ~0.5 and ~1.5.

The resulting X_{CO} factor maps are visualised in Fig. 7. Both X_{CO} maps trace the primary spiral arms of M33. The lowest values are around 10^{19} cm^{-2}/(K km s^{-1}) in the outer region, whereas the highest values are found in NGC604 and parts of the southern spiral arm, exceeding 10^{21} cm^{-2}/(K km s^{-1}). This observation is expected, as the lower CO emissions in the outer regions are predominantly optically thin, while the GMCs are optically thick, resulting in higher values.

Figure 7 also reveals distinct spatial variations of the X_{CO} values within M33 in the two maps created via methods I and II. Although this variation is very large, a variability is expected, as the CO-to-H_2 ratio naturally varies across the ISM of any galaxy which has been emphasised by Bolatto et al. (2013) and in recent studies (Ramambason et al. 2023; Chiang et al. 2024) as well.

In order to compare to the X_{CO} values given for M33 in the literature, we derived an X_{CO} value from a binned histogram. Additionally, we performed scatter plots and a radial line profile (in Appendix F) to systematically explore the potential radial dependence of X_{CO}.

4.5.2. Analysis of the derived X_{CO} factor

Histogram analysis. Figure 8 displays the histogram of the X_{CO} conversion factor for all pixels exceeding the 3σ threshold of the data, as seen in the ratio maps in Fig. 7. Both distributions exhibit a slightly skewed Gaussian profile when viewed on a logarithmic scale. The standard deviation is large and close to the mean values for both methods, see Fig. 8. We performed a log-normal fit resulting in similar values of 2.1×10^{20} cm^{-2}/(K km s^{-1}) and 1.7×10^{20} cm^{-2}/(K km s^{-1}) for methods I and II, respectively.

Scatter plot analysis. The scatter plot analysis is presented in Fig. 9, exclusively for data points where CO emission exceeds

---

[9] The background is that the virial theorem was originally applied to determine total mass from the velocity dispersion of a cloud and correlated to the integrated ^{12}CO line intensity (Bolatto et al. 2013) to obtain X_{CO}. This approach was suitable even for the optically thick case of CO lines.

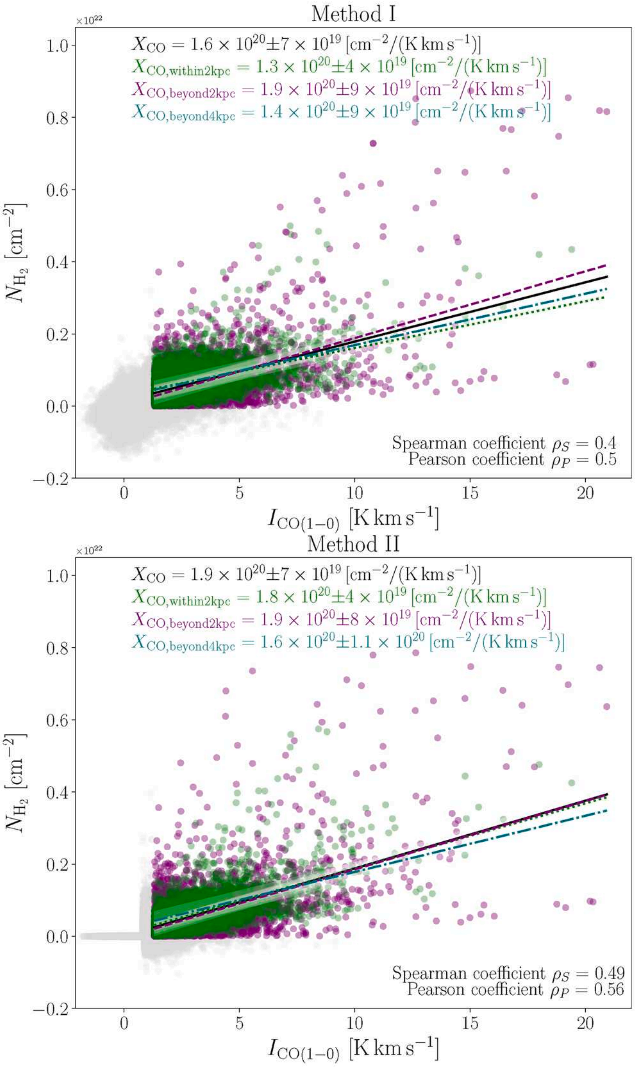

Fig. 9. Scatter plots of the dust-derived column density and CO(1 − 0) intensity determined for both maps of M33 at 18.2″. Grey data points correspond to those excluded in the fit. Top: scatter plot of method I. Bottom: scatter plot of method II. The estimated error of each individual data point is conservatively estimated to be 30%.

the 3σ threshold. Data points within a galactocentric radius of 2 kpc are coloured in green and those beyond 2 kpc in purple. The ellipses outlining the data points used in the fit are presented in Fig. 7.

A linear fit to all data points yields values of $(1.6 \pm 0.7) \times 10^{20}$ cm^{-2}/(K km s^{-1}) and $(1.9 \pm 0.7) \times 10^{20}$ cm^{-2}/(K km s^{-1}) for methods I and II, respectively. In the central region, relatively low values of $1.3(\pm0.4)-1.8(\pm0.4)\times10^{20}$ cm^{-2}/(K km s^{-1}) from both methods are obtained for a galactocentric radius within 2 kpc. Focusing solely on the outermost points (beyond 4 kpc) provides values around $1.4(\pm0.9)-1.6(\pm1.1) \times 10^{20}$ cm^{-2}/(K km s^{-1}). These numbers do not result in a clear dependence of the $X_{\rm CO}$ on the galactocentric radius.

The scatter is large and both correlation coefficients of Pearson and Spearman only yield moderate correlations for methods I and II (see Fig. 9). Especially, higher CO emission does not consistently correlate with an increased H_2 column density (see also Sect. 4.3).

4.5.3. Discussion of the $X_{\rm CO}$ factor

For simplicity, a single $X_{\rm CO}$ factor is commonly employed in the literature. Previous studies (Gratier et al. 2010; Druard et al. 2014) have utilised a constant conversion factor of $X_{\rm CO(1-0)} = 4 \times 10^{20}$ cm^{-2}/(K km s^{-1}) for M33, which is twice the value employed for the Milky Way. This choice is based on the assumption that M33 possesses half the solar metallicity and that all other factors affecting the conversion factor such as the ambient radiation field or the optical depth of the CO emission lines, are similar to those of the Milky Way.

M33's $X_{\rm CO}$ relation to the Galactic value. However, when calculating the mean value of our $X_{\rm CO}$ maps and conducting log-normal fitting, as well as a scatter plot analysis, we observe a contradiction to this assumption. The mean values appear to be below the Galactic value, and the scatter of the $X_{\rm CO}$ values is within the same order as the mean values. Our findings are consistent with those of Ramambason et al. (2023), who noted that low-metallicity galaxies can display $X_{\rm CO}$ factors as low as the Galactic value, coupled with an increasing dispersion of the conversion factor as metallicity decreases. Our results suggest a complex connection between the conversion factor and associated physical properties.

Braine et al. (2010b) determined an overall factor of $X_{\rm CO(1-0)} = 2.1 \times 10^{20}$ cm^{-2}/(K km s^{-1}) through a scatter plot analysis of dust column density and CO line intensity[10], revealing also a value close to the Galactic value. While they as well find a lowered $X_{\rm CO}$ value within 2 kpc of $X_{\rm CO(1-0)} = 1.5 \times 10^{20}$ cm^{-2}/(K km s^{-1}), their value beyond 2 kpc is higher with a value of $X_{\rm CO(1-0)} = 2.9 \times 10^{20}$ cm^{-2}/(K km s^{-1}). They argue that different regions within the galaxy, particularly the inner and outer areas, may exhibit distinct conversion factor values. Our results support this finding with regard to the scatter plot analysis (see Fig. 9). Figure 7 reveals lower values in the outskirts in comparison to the central region of M33.

This spatial variation does align with the expected relationship between the ambient radiation field and the $X_{\rm CO}$ value (Bolatto et al. 2013), as the central region experiences a more intense radiation field in contrast to the outer regions along the galactocentric radius. A possible explanation is an increased optical depth of the CO emission towards the centre, as the optically thin CO emission correlates more effectively with H_2 column density. This is supported by Druard et al. (2014), who observed broader line profiles of CO when successively approaching the centre.

Connection between enhanced metallicity and the $X_{\rm CO}$ factor in the south. A large scatter in metallicity in M33 has been reported, which is unexplained by abundance uncertainties (Magrini et al. 2010). The peak in metallicity has been identified in the southern region of M33. Since the $X_{\rm CO}$ factor is expected to decrease with increasing metallicity, we should observe lowered $X_{\rm CO}$ values in the southern region, assuming no substantial variations in other influencing factors of $X_{\rm CO}$, such as the ambient radiation field. However, our observations do not indicate a significantly lower $X_{\rm CO}$ factor in this area. We derive a mean value of 1.60×10^{20} cm^{-2}/(K km s^{-1}) for the northern part and 1.96×10^{20} cm^{-2}/(K km s^{-1}) for the southern part, respectively, using method I. For method II, these values are slightly

---

[10] Braine et al. (2010b) use a line ratio of CO$(\frac{2-1}{1-0})$ = 0.7 as determined in Gratier et al. (2010), who used the incomplete CO map from the IRAM Large Program. We use, however, the determined line ratio of CO$(\frac{2-1}{1-0})$ = 0.8 by Druard et al. (2014), who employed the full CO map of M33.

lower, at $1.43 \times 10^{20}\,\mathrm{cm^{-2}/(K\,km\,s^{-1})}$ for the northern part and $1.68 \times 10^{20}\,\mathrm{cm^{-2}/(K\,km\,s^{-1})}$ for the southern part, respectively. Although the values in the southern region are marginally higher, they still fall within the broad standard variation, thereby lacking the statistical power to account for the observed small difference or a systematic increase in metallicity in the southern region.

While the variability of the X_{CO} factor in general can be attributed to fluctuations in metallicity within M33, variations in dust content and star formation rates also play a role (Bolatto et al. 2013). Moreover, the X_{CO} factor is further influenced by the ambient radiation field. For instance, if we consider a scenario where all other factors remain constant but the radiation field decreases with increasing galactocentric radius, the X_{CO} factor would be expected to decrease correspondingly. Nevertheless, the intricate interplay of these processes, as discussed earlier, results in a complex relationship where all factors concurrently influence the X_{CO} factor. Investigating and differentiating the individual contributions of these processes to the observed variations in the X_{CO} factor are beyond the scope of this study.

Caveats of the methods and consequences of the results. While the scatter fit in Fig. 9 shows a potential correlation between CO emission and H_2 column density, the log-normal fit and histogram presented in Fig. 8 illustrate the distribution of the previously computed X_{CO} factor and the frequency of different values. Moreover, the radial profile in Appendix F is constructed by averaging the data points within a distance of 100 pc along the galactocentric radius. Each of those bins exhibit a higher scatter in the X_{CO} values compared to all the pixels in the X_{CO} maps. Furthermore, their contribution on the overall average decreases as the galactocentric radius increases, given that they consist of a significantly smaller number of data points in comparison to the entire dataset. This helps elucidate the difference in the results obtained from the methods used to determine the X_{CO} factor.

We emphasise that the range of the X_{CO} factor (Fig. 8) is broad. For all methods used to calculate the X_{CO} factor, the standard deviation is close to the determined mean value, indicating a substantial and wide variation of this parameter. Consequently, assuming a constant X_{CO} factor, as is often practised in other studies, can lead to results that differ by an order of magnitude and are insufficient for ensuring reliable outcomes.

5. Discussion and comparison of the H_2 column density maps with other studies

In this section, we present our results for the construction of hydrogen column density maps of M33 with the two different methods presented above in context with other studies such as those of Braine et al. (2010b), Tabatabaei et al. (2014), Gratier et al. (2017), Clark et al. (2021). An overview of the parameters used and their characteristics is provided in Table 1.

Braine et al. (2010b) made no assumptions regarding the X_{CO} factor and a variable dust absorption coefficient κ_0 (along with a variable dust-to-gas ratio) is determined similar to our approach. However, they only employ a fixed emissivity index β throughout the whole disk and a fixed κ_0 inside the galactocentric radius of 4 kpc, while in our case, κ_0 and β vary on a pixel-by-pixel basis throughout the disk. The molecular hydrogen column density map of Braine et al. (2010b) has a lower angular resolution (approximately 40″) due to the application of the simple canonical SED fit to all *Herschel* flux maps. It is also worth noting that the CO map used by Braine et al. (2010b) was incomplete and covers an area of approximately 2/3 of the final map of Druard et al. (2014) used here.

The primary focus of the study by Tabatabaei et al. (2014) lies on the emissivity index. For this purpose, the absolute value of the column density is not considered, and hence, they use a fixed dust absorption coefficient that does not bias the fitting of the emissivity index β.

Gratier et al. (2017) employed an H I dataset from Gratier et al. (2010) to derive the dust absorption coefficient in a manner similar to Braine et al. (2010b) and our present study for the purpose of calculating the total column density of hydrogen. They also utilised the same IRAM CO(2 − 1) map as we did for this purpose. However, the emissivity index β is only used with a radial dependence, rather than on a pixel-by-pixel basis. They solved for an X_{CO} factor and a gas-to-dust ratio (GDR) in their analysis of the molecular content, presenting radial trends. The angular resolution of their maps is approximately 25″ or about 100 pc, due to the utilisation of a canonical one-component modified blackbody SED fit.

Clark et al. (2021) employed a broken-emissivity modified blackbody model to account for the sub-millimetre excess, which arises relative to a canonical $\beta = 2$ at longer wavelengths in the Rayleigh-Jeans regime, specifically around the 500 µm Herschel data point. They determined different values of β for this purpose. However, this variation in β only affects the data points where the sub-millimetre excess is modelled and is not on a pixel-by-pixel basis. They note that the sub-millimetre excess for M33 is relatively small (Clark et al. 2021). For the dust-derived column density map of atomic hydrogen, they used a fixed dust absorption coefficient, with the value determined for the Large Magellanic Cloud. Additionally, they applied a fixed X_{CO} factor using the Galactic value. Both atomic and molecular phases were combined to produce a total surface density map, but this approach does not account for CO-dark H_2 gas. The resulting map has the same resolution as the Herschel 500 µm map, approximately 40″ or about 150 pc.

Despite of the differences in the calculation of column densities, all final maps as listed in Table 1 agree to within the same order of magnitude. In comparison to other studies, our methods have the advantage that the hydrogen column density maps are determined on a pixel-by-pixel basis, providing the highest angular resolution among them.

6. Conclusion and summary

We have generated dust-derived hydrogen column density maps using *Herschel* flux data of M33 with two methods. Method I follows the procedure outlined by Palmeirim et al. (2013) and employs an SED fit to the 160 µm to 500 µm data. It benefits from combining additional *Herschel* data at longer wavelengths, where the dust typically has lower optical depths. Method II transforms the 250 µm SPIRE map into a hydrogen column density. For both maps we incorporated the emissivity index β map and a temperature map of the cold dust component from Tabatabaei et al. (2014). With the H I map of Gratier et al. (2010) in addition, we calculated a variable κ_0 map on a pixel-by-pixel basis, thereby providing all parameters of the dust opacity law for each pixel. This approach circumvents the need for assumptions regarding the X_{CO} factor, dust-to-gas ratio (such as constant values for both) or the dependency on the galactocentric radius. The variability and dependencies of these factors are intrinsically encompassed through our computation of κ_0 and the utilisation of the provided β map. We note that the DGR is inherently included in our definition of κ_0. Subsequently,

Table 1. Parameters used to calculate column or surface densities of molecular hydrogen in several studies of M33.

Study	κ_0	β	DGR	X_{CO} factor	Resolution
Braine et al. (2010b)	Pixel-by-pixel[13]	Fixed	Pixel-by-pixel	Pixel-by-pixel	40″
Tabatabaei et al. (2014)	Fixed	Pixel-by-pixel	Fixed	–	40″
Gratier et al. (2017)	Pixel-by-pixel	Only radially	Only radially	Only radially	25″
Clark et al. (2021)	Fixed	Fixed	Fixed	Fixed	40″
This study	Pixel-by-pixel	Pixel-by-pixel	Pixel-by-pixel	Pixel-by-pixel	18.2″

Notes. The other studies either employed fixed parameters values or implemented them only partially on a pixel-by-pixel basis. Furthermore, these studies attained a relatively coarser spatial resolution.

we subtracted the H I contribution from the two N_H maps by transforming the VLA H I integrated intensity map to an H I column density map to create maps of molecular gas column densities, N_{H_2}.

Our column density maps of total and molecular hydrogen are consistent in the order of magnitude compared to other studies (Braine et al. 2010b; Gratier et al. 2017; Clark et al. 2021). Overall, the results obtained from method II confirm those derived by employing method I. Nevertheless, the results obtained using method I demonstrate a rise in H_2 column densities, manifesting as granular gas distributions in M33's intermain spiral and outer regions, which we cautiously propose may stem partially from CO-dark gas. Both methods display comparable hydrogen column density N-PDFs. We tentatively fit log-normal distributions at low column densities and a power-law tail at high column densities, which may indicate gravitational collapse of the dense gas in the GMCs. The high-column density part of the total hydrogen N-PDF likely arises from CO-bright H_2 gas, since the molecular N-PDFs from dust and CO cover the same range. The parts of CO-dark gas in the N-PDFs cannot be determined. We caution that the interpretation of extragalatic N-PDFs is challenging due to the sampling of many molecular clouds along the line-of-sight[14].

Furthermore, our investigation of the X_{CO} factor leads to consistent results falling within the standard deviation for each method. Remarkably, the X_{CO} factor is about half as large as the value observed in the Milky Way when considering the result from the scatter fit. This stands in contrast to prior assumptions claiming that the X_{CO} factor should be twice that of the Galactic value (Druard et al. 2014; Gratier et al. 2017). Notably, the dispersion of the X_{CO} factor can extend beyond one order of magnitude, rendering the assumption of a constant X_{CO} factor even more questionable.

To conclude, we demonstrate the robustness and applicability of method I in producing reliable results using extragalactic data, enabling us to present a previously unachieved and unprecedented N_H and N_{H_2} map of M33 with a remarkably improved angular resolution of 18.2″. This map reflects the dependency on important influencing factors such as the dust-to-gas ratio, dust opacity law, and the X_{CO} factor on a pixel-by-pixel basis. In a follow-up paper (in prep.), we apply Dendrograms on this column density map of method I to extract cloud structures. This will enable us to derive and explore various physical properties of these clouds, including number density, mass, size, mass-size relation, and mass spectra. By comparing our findings with existing Milky Way data, we aspire to provide a more comprehensive understanding of cloud properties and dynamics across diverse environments.

Data availability

All final data products are available at the CDS via anonymous ftp to `cdsarc.cds.unistra.fr` (`130.79.128.5`) or via `https://cdsarc.cds.unistra.fr/viz-bin/cat/J/A+A/688/A171`

Acknowledgements. E.K. and N.S. acknowledge support from the FEEDBACK-plus project that is supported by the BMWI via DLR, Project Number 50OR2217. E.K. acknowledges support by the BMWI via DLR, project number 50OK2101. S.K. acknowledges support from the Orion-Legacy project that is supported by the BMWI via DLR, project number 50OR2311. This work was supported by the Collaborative Research Center 1601 (SFB 1601 sub-projects A6 and B2) funded by the Deutsche Forschungsgemeinschaft (DFG, German Research Foundation) – 500700252.

References

André, P., Men'shchikov, A., Bontemps, S., et al. 2010, A&A, 518, L102
Aoyama, S., Hirashita, H., & Nagamine, K. 2020, MNRAS, 491, 3844
Ballesteros-Paredes, J., Vázquez-Semadeni, E., Gazol, A., et al. 2011, MNRAS, 416, 1436
Bianchi, S., Casasola, V., Baes, M., et al. 2019, A&A, 631, A102
Bianchi, S., Casasola, V., Corbelli, E., et al. 2022, A&A, 664, A187
Bigiel, F., Leroy, A. K., Walter, F., et al. 2011, ApJ, 730, L13
Bloemen, J. B. G. M., Strong, A. W., Mayer-Hasselwander, H. A., et al. 1986, A&A, 154, 25
Bohlin, R. C., Savage, B. D., & Drake, J. F. 1978, ApJ, 224, 132
Bolatto, A. D., Wolfire, M., & Leroy, A. K. 2013, ARA&A, 51, 207
Boquien, M., Calzetti, D., Kramer, C., et al. 2010, A&A, 518, L70
Boquien, M., Calzetti, D., Combes, F., et al. 2011, AJ, 142, 111
Boquien, M., Calzetti, D., Aalto, S., et al. 2015, A&A, 578, A8
Borchert, E. M. A., Walch, S., Seifried, D., et al. 2022, MNRAS, 510, 753
Boselli, A., Ciesla, L., Cortese, L., et al. 2012, A&A, 540, A54
Braine, J., Gratier, P., Kramer, C., et al. 2010a, A&A, 520, A107
Braine, J., Gratier, P., Kramer, C., et al. 2010b, A&A, 518, L69
Braine, J., Gratier, P., Contreras, Y., Schuster, K. F., & Brouillet, N. 2012a, A&A, 548, A52
Braine, J., Gratier, P., Kramer, C., et al. 2012b, A&A, 544, A55
Brent, R. P. 1973, Algorithms for Minimization without Derivatives (Englewood Cliffs: Prentice-Hall)
Buchbender, C., Kramer, C., Gonzalez-Garcia, M., et al. 2013, A&A, 549, A17
Casey, C. M., Chapman, S. C., Smail, I., et al. 2011, MNRAS, 411, 2739
Chapin, E. L., Chapman, S. C., Coppin, K. E., et al. 2011, MNRAS, 411, 505
Chiang, I.-D., Sandstrom, K. M., Chastenet, J., et al. 2024, ApJ, 964, 18
Clark, C. J. R., De Vis, P., Baes, M., et al. 2019a, MNRAS, 489, 5256
Clark, P. C., Glover, S. C. O., Ragan, S. E., & Duarte-Cabral, A. 2019b, MNRAS, 486, 4622
Clark, C. J. R., Roman-Duval, J. C., Gordon, K. D., Bot, C., & Smith, M. W. L. 2021, ApJ, 921, 35
Clark, C. J. R., Roman-Duval, J. C., Gordon, K. D., et al. 2023, ApJ, 946, 42
Cormier, D., Madden, S. C., Lebouteiller, V., et al. 2014, A&A, 564, A121
Crockett, N. R., Garnett, D. R., Massey, P., & Jacoby, G. 2006, ApJ, 637, 741
den Brok, J. S., Bigiel, F., Chastenet, J., et al. 2023, A&A, 676, A93
Druard, C., Braine, J., Schuster, K. F., et al. 2014, A&A, 567, A118

---

[13] Only beyond a galactocentric radius of 4 kpc.

[14] The line-of-sight effects depend on the inclination, which is 56° for M33.

Elia, D., Strafella, F., Dib, S., et al. 2018, MNRAS, 481, 509
Federrath, C., & Klessen, R. S. 2012, ApJ, 761, 156
Federrath, C., Klessen, R. S., & Schmidt, W. 2008, ApJ, 688, L79
Froebrich, D., & Rowles, J. 2010, MNRAS, 406, 1350
Gardan, E., Braine, J., Schuster, K. F., Brouillet, N., & Sievers, A. 2007, A&A, 473, 91
Girichidis, P., Konstandin, L., Whitworth, A. P., & Klessen, R. S. 2014, ApJ, 781, 91
Gratier, P., Braine, J., Rodriguez-Fernandez, N. J., et al. 2010, A&A, 522, A3
Gratier, P., Braine, J., Rodriguez-Fernandez, N. J., et al. 2012, A&A, 542, A108
Gratier, P., Braine, J., Schuster, K., et al. 2017, A&A, 600, A27
Hennebelle, P., & Chabrier, G. 2008, ApJ, 684, 395
Hirashita, H., & Kobayashi, H. 2013, Earth Planets Space, 65, 1083
Hughes, A., Meidt, S. E., Colombo, D., et al. 2013, ApJ, 779, 46
Israel, F. P. 1997, A&A, 328, 471
Jaupart, E., & Chabrier, G. 2020, ApJ, 903, L2
Jenkins, E. B., & Wallerstein, G. 2017, ApJ, 838, 85
Jones, A. P. 2018, arXiv e-prints [arXiv:1804.10628]
Juvela, M., Demyk, K., Doi, Y., et al. 2015a, A&A, 584, A94
Juvela, M., Ristorcelli, I., Marshall, D. J., et al. 2015b, A&A, 584, A93
Kainulainen, J., Beuther, H., Henning, T., & Plume, R. 2009, A&A, 508, L35
Karachentsev, I. D., Karachentseva, V. E., Huchtmeier, W. K., & Makarov, D. I. 2004, AJ, 127, 2031
Kaufman, M. J., Wolfire, M. G., Hollenbach, D. J., & Luhman, M. L. 1999, ApJ, 527, 795
Könyves, V., André, P., Men'shchikov, A., et al. 2015, A&A, 584, A91
Kramer, C., Jakob, H., Mookerjea, B., et al. 2004, A&A, 424, 887
Kramer, C., Buchbender, C., Xilouris, E. M., et al. 2010, A&A, 518, L67
Kramer, C., Nikola, T., Anderl, S., et al. 2020, A&A, 639, A61
Kritsuk, A. G., Norman, M. L., & Wagner, R. 2011, ApJ, 727, L20
Krügel, E. 2003, The physics of Interstellar Dust (Bristol, UK: The Institute of Physics)
Krügel, E., & Siebenmorgen, R. 1994, A&A, 288, 929
Larson, R. B. 1969, MNRAS, 145, 271
Leroy, A. K., Bolatto, A., Gordon, K., et al. 2011, ApJ, 737, 12
Leroy, A. K., Walter, F., Sandstrom, K., et al. 2013, AJ, 146, 19
Lombardi, M., Alves, J., & Lada, C. J. 2015, A&A, 576, L1
Madden, S. C., Cormier, D., Hony, S., et al. 2020, A&A, 643, A141
Magrini, L., Stanghellini, L., & Villaver, E. 2009, ApJ, 696, 729
Magrini, L., Stanghellini, L., Corbelli, E., Galli, D., & Villaver, E. 2010, A&A, 512, A63
Nguyen-Luong, Q., Nguyen, H. V. V., Motte, F., et al. 2016, ApJ, 833, 23
Offner, S. S. R., Bisbas, T. G., Bell, T. A., & Viti, S. 2014, MNRAS, 440, L81
Ossenkopf, V., & Henning, T. 1994, A&A, 291, 943
Ossenkopf-Okada, V., Csengeri, T., Schneider, N., Federrath, C., & Klessen, R. S. 2016, A&A, 590, A104
Padoan, P., & Nordlund, Å. 2002, ApJ, 576, 870
Palmeirim, P., André, P., Kirk, J., et al. 2013, A&A, 550, A38
Pedregosa, F., Varoquaux, G., Gramfort, A., et al. 2011, J. Mach. Learn. Res., 12, 2825
Pineda, J. L., Langer, W. D., Velusamy, T., & Goldsmith, P. F. 2013, A&A, 554, A103
Pineda, J. L., Langer, W. D., & Goldsmith, P. F. 2014, A&A, 570, A121
Putman, M. E., Peek, J. E. G., Muratov, A., et al. 2009, ApJ, 703, 1486
Ramambason, L., Lebouteiller, V., Madden, S. C., et al. 2023, A&A, 681, A14
Regan, M. W., & Vogel, S. N. 1994, ApJ, 434, 536
Relaño, M., Verley, S., Pérez, I., et al. 2013, A&A, 552, A140
Relaño, M., Kennicutt, R., Lisenfeld, U., et al. 2016, A&A, 595, A43
Relaño, M., De Looze, I., Kennicutt, R. C., et al. 2018, A&A, 613, A43
Robitaille, J. F., Motte, F., Schneider, N., Elia, D., & Bontemps, S. 2019, A&A, 628, A33
Rohlfs, K., & Wilson, T. L. 1996, Tools of Radio Astronomy (Springer Berlin, Heidelberg)
Röllig, M., Ossenkopf, V., Jeyakumar, S., Stutzki, J., & Sternberg, A. 2006, A&A, 451, 917
Roman-Duval, J., Jenkins, E. B., Tchernyshyov, K., et al. 2021, ApJ, 910, 95
Roman-Duval, J., Jenkins, E. B., Tchernyshyov, K., et al. 2022, ApJ, 928, 90
Rosolowsky, E. W., Pineda, J. E., Kauffmann, J., & Goodman, A. A. 2008, ApJ, 679, 1338
Roussel, H. 2013, PASP, 125, 1126
Sandstrom, K. M., Leroy, A. K., Walter, F., et al. 2013, ApJ, 777, 5
Schneider, N., Csengeri, T., Klessen, R. S., et al. 2015, A&A, 578, A29
Schneider, N., Ossenkopf-Okada, V., Clarke, S., et al. 2022, A&A, 666, A165
Sodroski, T. J., Odegard, N., Dwek, E., et al. 1995, ApJ, 452, 262
Spilker, A., Kainulainen, J., & Orkisz, J. 2021, A&A, 653, A63
Starck, J. L., Aghanim, N., & Forni, O. 2004, A&A, 416, 9
Stutz, A. M., & Kainulainen, J. 2015, A&A, 577, L6
Tabatabaei, F. S., Braine, J., Xilouris, E. M., et al. 2014, A&A, 561, A95
Tacconi, L. J., Genzel, R., Saintonge, A., et al. 2018, ApJ, 853, 179
Teng, Y.-H., Sandstrom, K. M., Sun, J., et al. 2022, ApJ, 925, 72
Vazquez-Semadeni, E. 1994, ApJ, 423, 681
Veltchev, T. V., Ossenkopf-Okada, V., Stanchev, O., et al. 2018, MNRAS, 475, 2215
Verley, S., Corbelli, E., Giovanardi, C., & Hunt, L. K. 2010a, A&A, 510, A64
Verley, S., Relaño, M., Kramer, C., et al. 2010b, A&A, 518, L68
Whitworth, A., & Summers, D. 1985, MNRAS, 214, 1
Willner, S. P., & Nelson-Patel, K. 2002, ApJ, 568, 679
Wolfire, M. G., Hollenbach, D., & McKee, C. F. 2010, ApJ, 716, 1191
Xilouris, E. M., Tabatabaei, F. S., Boquien, M., et al. 2012, A&A, 543, A74
Yahia, H., Schneider, N., Bontemps, S., et al. 2021, A&A, 649, A33

Appendix A: Background Correction for *Herschel* Fluxes and *Herschel* Flux Maps

Table A.1 shows the mean, rms, minimum and maximum intensity of the background for the *Herschel* dust maps at wavelength 160 µm, 250 µm, 350 µm and 500 µm. The mean values have been subtracted from each corresponding dust map prior to processing into the high-res column density map. Figure A.1 shows these *Herschel* maps at their original resolution in MJy sr^{-1}. We note the different scales in the colour bars for the 160 µm map compared to the other maps.

Table A.1. Basic statistics of the *Herschel* dust maps.

Map	mean	rms	min	max
160 μm (PACS)	−0.126	7.081	−53.004	125.930
250 µm (SPIRE)	3.357	0.856	0.319	31.099
350 µm (SPIRE)	2.337	0.460	0.847	8.992
500 µm (SPIRE)	1.101	0.225	0.262	2.512

Notes. Mean, rms, and minimum and maximum intensity of the background of the *Herschel* dust maps. The mean values have been subtracted from the dust intensity maps before further processing to produce high-res column density maps. All values are given in MJy sr^{-1}.

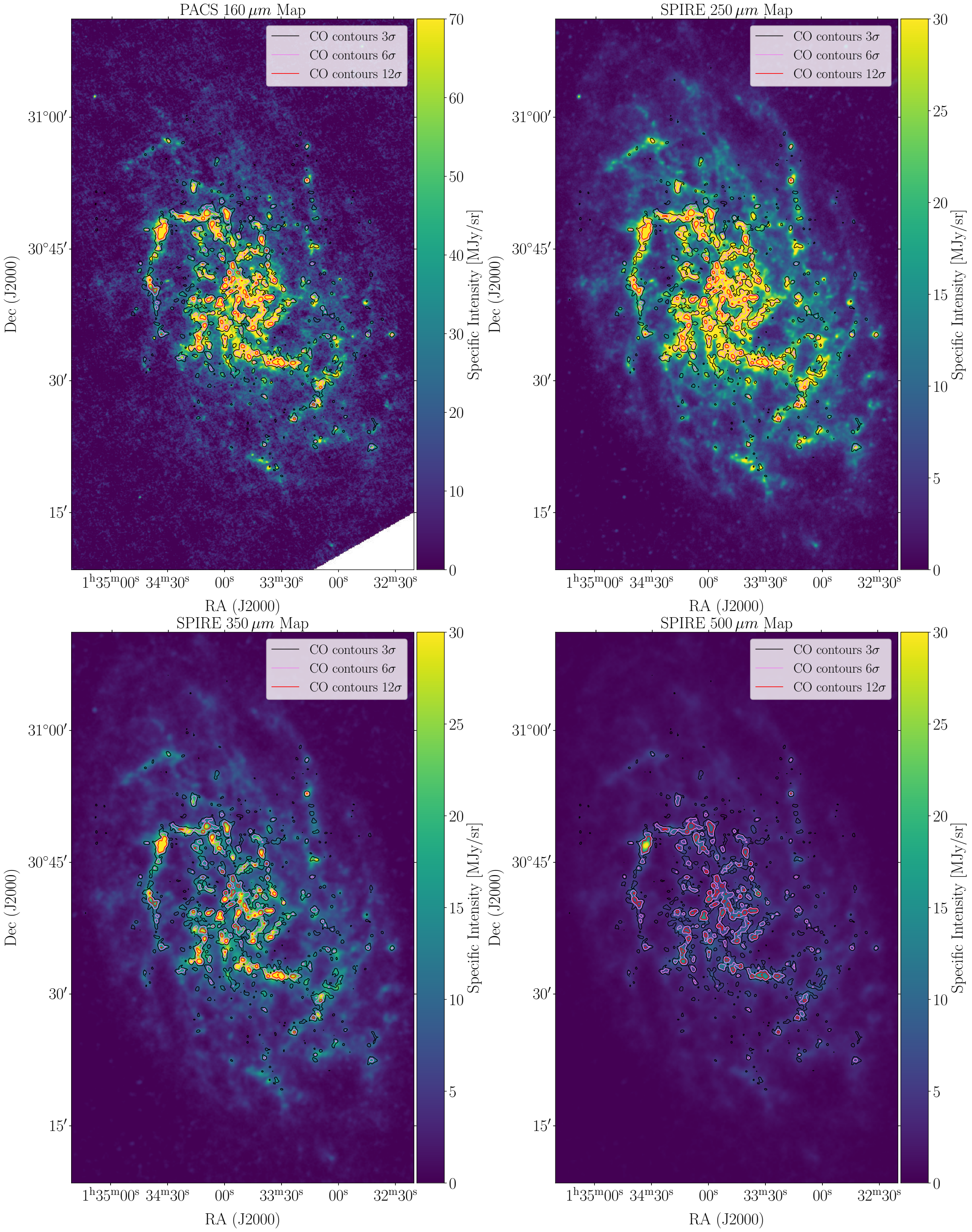

Fig. A.1. *Herschel* flux maps in MJy sr^{-1} at the four observing wavelengths with overlaid CO contours at 3σ, 6σ, and 12σ.

Appendix B: κ_0 map before filling and complementary maps

KNNImputer uses data from *k*-Nearest neighbouring pixels for computing their mean and substituting missing values with this information. It employs the Euclidean distance metric to assess the proximity of neighbouring data points, assigning equal importance to each. Assuming that there are no significant variations in the dust characteristics between the atomic and molecular phases of hydrogen, the *KNNImputer* method fills the gaps in the κ_0 map by considering $k = 5$ pixels located at the boundaries of the cavities depicted in Fig. B.1, where the CO emission reaches the 2σ threshold. For comparison, the κ_0 map before filling with *KNNImputer* is shown in Fig. B.1. The β and temperature maps of Tabatabaei et al. (2014) used to determine the κ_0 map are shown in Figs. B.2 and B.3

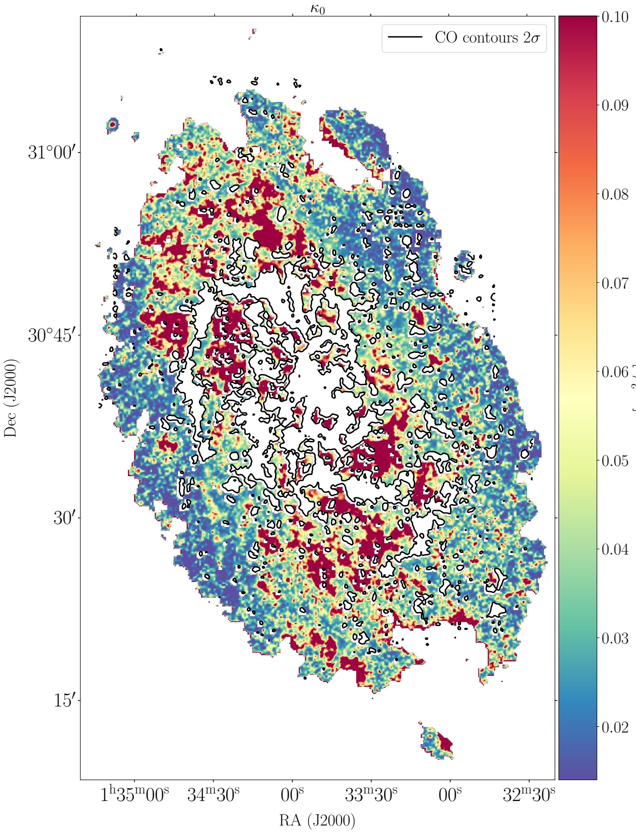

Fig. B.1. κ_0 map obtained as described in Sect. 3.2 before filling holes with *KNNImputer*.

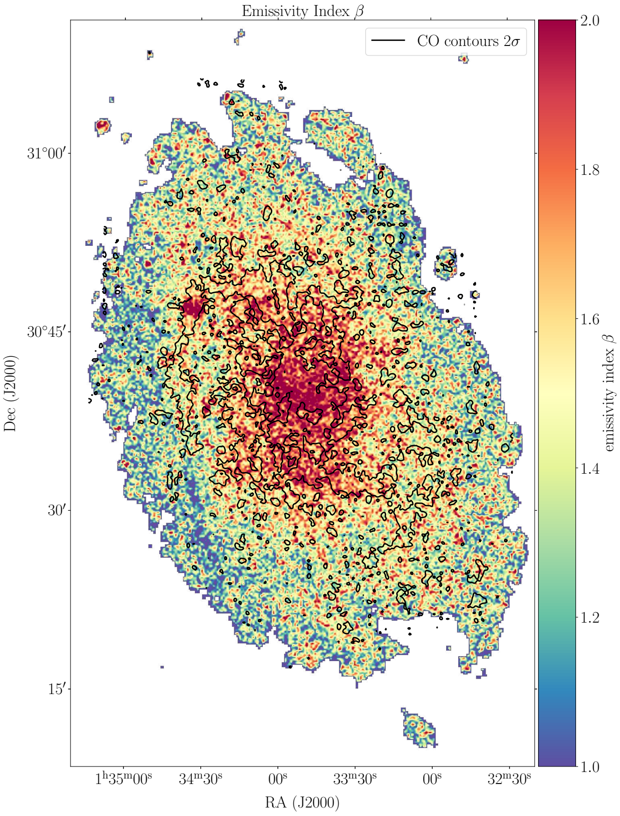

Fig. B.2. Emissivity index β map from Tabatabaei et al. (2014). CO contours at the 2σ level are overlaid on the map.

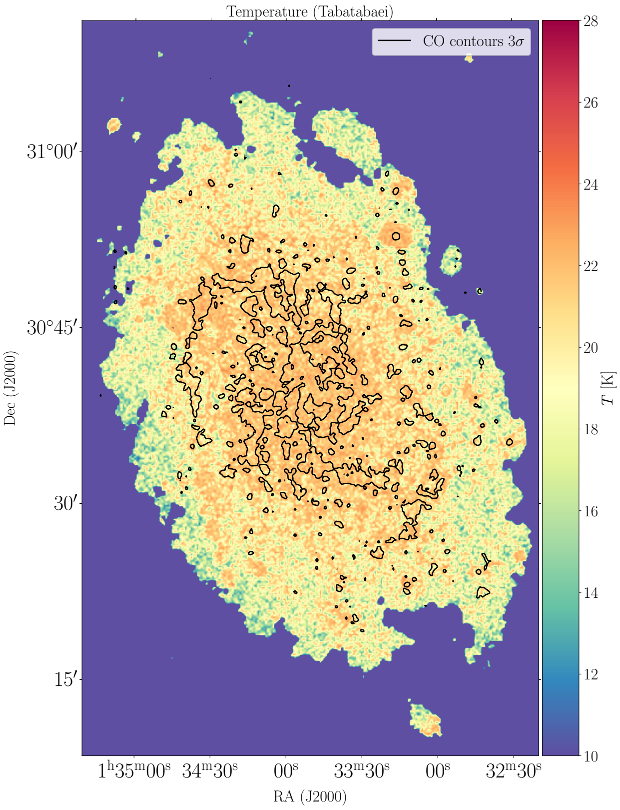

Fig. B.3. Temperature map obtained by Tabatabaei et al. (2014) used in both methods and in the determination of κ_0.

Appendix C: Temperature maps

Two temperature maps at the corresponding resolution of the SPIRE 350 µm and 500 µm maps are obtained from the SED fits, which are shown in Fig. C.1. The colour temperature obtained using the flux ratio at the corresponding resolution of the SPIRE 250 µm map was not used because using this map yields a column density map with higher noise in the outskirts of the galaxy. The requirements to use the flux ratio are anyway not fulfilled, since both wavelengths are in the Rayleigh-Jeans limit, where the dust temperature T_d will tend to cancel out due to $B_\nu(T_\mathrm{d}) \propto T_\mathrm{d}$. Additionally, the dust temperature should be uniform in the source and observations with two different frequencies should measure the same object. When the source is extended compared to the telescope beam and the observations have different spatial resolutions (as in our case), it is not trivial to fulfil this requirement.

Although the requirements for determining the colour ratio are not fully met, the result is remarkably good, as can be seen in Fig. C.1, bottom left. However, higher noise features are still produced in the outskirts when using this map. We therefore decided to use the temperature map provided by Tabatabaei et al. (2014) shown in Fig. B.3.

All temperature maps show a gradient declining from the centre to the outskirts of the disk. While the colour temperature map obtained with the flux ratio shows the highest temperatures and an unsmooth, bumpy distribution (due to the not fully met requirements), the two temperature maps obtained with the SED fits show a much smoother distribution with lower higher temperatures in the centre. The temperature map obtained at the corresponding resolution of the SPIRE 350 µm map has higher local values compared to the map at 500 µm. Comparing these to the map from Tabatabaei et al. (2014) shown in Fig. B.3, the latter has a similar gradient. The main difference is that the higher values spread over a larger area, whereas the local maxima are lower compared to especially the map at the corresponding 350 µm. However, all maps exhibit a mean value of around ~ 20 K.

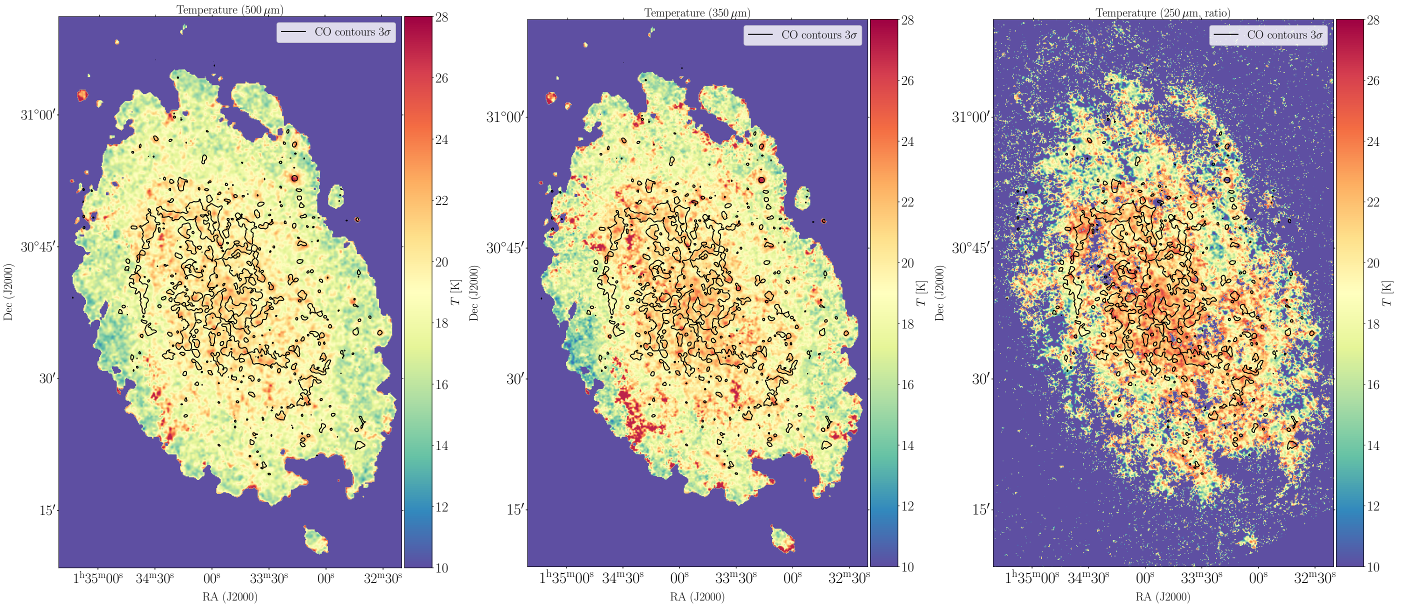

Fig. C.1. Temperature maps obtained and used within both methods. *Left*: Temperature map at 500 µm obtained with method I. *Middle*: Temperature map at 350 µm obtained with method I. *Right*: Colour temperature map at 250 µm obtained with method I using the flux ratio of SPIRE 250 µm and PACS 160 µm. Note, this map was not used.

Appendix D: Consistency of the emissivity index

To demonstrate that using a variable κ_0 will not cause inconsistencies when employing a variable β map, which has been determined with a constant κ_0, we present in Fig. D.1 a simple fit of β with our variable κ_0 map and compare it with the β map used by Tabatabaei et al. (2014), as described in Sect. 3. The fitted region around NGC604, shown in Fig. D.1, includes areas of both the atomic and molecular phases. Most differences, especially in the molecular phase, which is most important for the follow-up paper, are small.

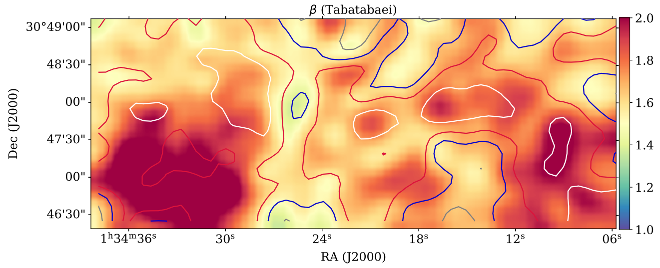

Fig. D.1. β map obtained by Tabatabaei et al. (2014) around NGC604 including areas of atomic and molecular phases. The contour lines represent the differences between our additional fit and the one of Tabatabaei et al. (2014), with values of −0.1, 0, 0.1 and 0.2 shown in white, red, blue and grey, respectively.

Appendix E: Hydrogen column density PDFs

We construct N-PDFs for the whole total hydrogen column density maps shown in Fig. 3. Figure E.1 displays these N-PDFs in grey (with blue error bars calculated using Poisson statistics Schneider et al. 2015) along with the atomic hydrogen N_{HI}-PDF (green) derived from the map in Fig. 1. For the same reasons as pointed out in Sect. 4.1, we opt to exclude values above $\sim 2 \times 10^{22}\,\mathrm{cm}^{-2}$ for the N-PDFs.

The H I PDF exhibits a sharp decrease in the PDF shape for both low and high column densities. At high column densities, we enter a regime in which atomic hydrogen transitions to the molecular phase, explaining the edge observed in the shape. At low column densities, the cutoff limit of values in the map leads to a steep decrease in the PDF. The noise level of this map is approximately $2 \times 10^{20}\,\mathrm{cm}^{-2}$, which may partially account for the bump in the PDF. Additionally, we speculate that H I self-absorption (HISA) could contribute to the dip in the N_{HI}-PDF around $4 \times 10^{20}\,\mathrm{cm}^{-2}$. However, this cannot be verified with the current datasets.

We fit the N-PDFs from method I with a combination of two log-normal and a PLT in the low and high density regime, similar to Spilker et al. (2021) with:

$$f(A_{\mathrm{V}}) = \begin{cases} \left(\frac{A_{\mathrm{V}}}{x_0}\right)^{-\alpha_1} \cdot \left(\frac{a_1}{\sigma_1\sqrt{2\pi}x_0} \exp\left(\frac{-(\ln(x_0)-\mu_1)^2}{2\sigma_1^2}\right)\right) & \text{if } A_{\mathrm{V}} \le x_0, \\ \frac{a_1}{\sigma_1\sqrt{2\pi}A_{\mathrm{V}}} \exp\left(\frac{-(\ln(A_{\mathrm{V}})-\mu_1)^2}{2\sigma_1^2}\right) + & \text{if } A_{\mathrm{V}} > x_0 \text{ and} \\ \qquad \frac{a_2}{\sigma_2\sqrt{2\pi}A_{\mathrm{V}}} \exp\left(\frac{-(\ln(A_{\mathrm{V}})-\mu_2)^2}{2\sigma_2^2}\right) & \quad A_{\mathrm{V}} < x_1, \\ \left(\frac{A_{\mathrm{V}}}{x_0}\right)^{-\alpha_2} \cdot \left(\frac{a_2}{\sigma_2\sqrt{2\pi}x_1} \exp\left(\frac{-(\ln(x_1)-\mu_2)^2}{2\sigma_2^2}\right)\right) & \text{if } A_{\mathrm{V}} \ge x_1, \end{cases} \tag{E.1}$$

where the visual extinction A_{V} is related to the total hydrogen column density by $N_{\mathrm{H}} = A_{\mathrm{V}} \cdot 1.87 \times 10^{21}\,\mathrm{cm}^{-2}\,\mathrm{mag}^{-1}$ (Bohlin et al. 1978). The coefficients a_1 and a_2 represent the normalisation factors of both log-normal distributions. x_0 is the first transition point from the noise slope at low column density to the log-normal regime. x_1 is the second transition point indicating the change from the log-normal regime to the power-law regime at high column density. Both transition points have been fitted as well. $\sigma_{1,2}$ are the widths of the first and second log-normal and $\mu_{1,2}$ their respective peaks. Since the shape of the N-PDF obtained with method II does not allow us to utilise the model given in Eq. E.1, we skip the first part of Eq. E.1 for values below the first transition x_0 and start with a log-normal instead.

Figure E.1 displays the results of the fitting process. The solid red line represents the entire fit, while the dashed red lines represent the log-normals. The peaks and widths of these log-normals are presented in the small panel, along with the slope α of the high-density PLT that was fitted. The slope m characterises the low-density error tail and has a value of 1.1 for method I. It is worth noting that the fit for method II is purely formal due to the absence of a portion of the noise. A value of around 1 for the noise slope, as per Ossenkopf-Okada et al. (2016), suggests that low column densities are primarily influenced by noise. When the noise level decreases, the slope increases. In any case, noise contributes to the broadening of the N-PDF, resulting in a width of $\sigma = 0.4$ for the first log-normal for both methods. The peak of the first log-normal is $2 \times 10^{20}\,\mathrm{cm}^{-2}$ for method I and $6 \times 10^{20}\,\mathrm{cm}^{-2}$ for method II. This finding is roughly consistent with the excess in the gas distribution observed in the inter-main spiral and outer regions of M33, as depicted in Fig. 4 (left). The first peak of the N_{H}-PDF of method I approximately corresponds to the first peak of the N_{HI}-PDF, while for method II, the N_{H}-PDF is found at higher column densities and corresponds more to the dip in the N_{HI}-PDF. However, it is important to note that the fit of the N-PDF for method II presents challenges due to the inadequate description of the low column density range, resulting in an excess at the intersection of the error slope and the first log-normal. Another caveat of method II is the difficulty in distinguishing the transition of the first log-normal fit to the PLT tail. Due to the relatively high peak at $6 \times 10^{20}\,\mathrm{cm}^{-2}$ and the large width of $\sigma = 0.4$, the transition between both can potentially occur over a wide range, leading to increased uncertainty in determining the slope of the PLT in method II.

The peaks of the second log-normal exhibit the same value of $1 \times 10^{21}\,\mathrm{cm}^{-2}$ and a width of $\sigma = 0.3$ and $\sigma = 0.2$ for methods I and II, respectively. Interpreting the N-PDFs of extragalactic data is different from Galactic data. In the Galactic context, the correlation between the peaks in H I and the total hydrogen PDF in principle suggest that the first log-normal in the N-PDF predominantly comprises atomic gas. Conversely, the second log-normal would likely originate from molecular gas. This behaviour has previously been observed in a diffuse cloud in the Milky Way (Schneider et al. 2022). However, as mentioned in Sect. 4.1, it is essential to compare corresponding regions of the maps. Thus, the excess in the total N-PDF (see Fig. E.1) at higher column densities surpassing the highest values of the N_{HI}-PDF can be attributed to molecular gas, similar to the approach used in Fig. 5.

As at high column densities, gravitational collapse of entire GMC or clumps within them, expect to form PLTs, we tentatively conduct a fitting procedure to determine the slope at the high column density regime, obtaining values of $\alpha = -1.8$ and $\alpha = -2.6$ for methods I and II, respectively. These values align with expectations for the gravitational collapse of an isothermal spherical density distribution, as described by Larson (1969) and Whitworth & Summers (1985). We note, however, that these

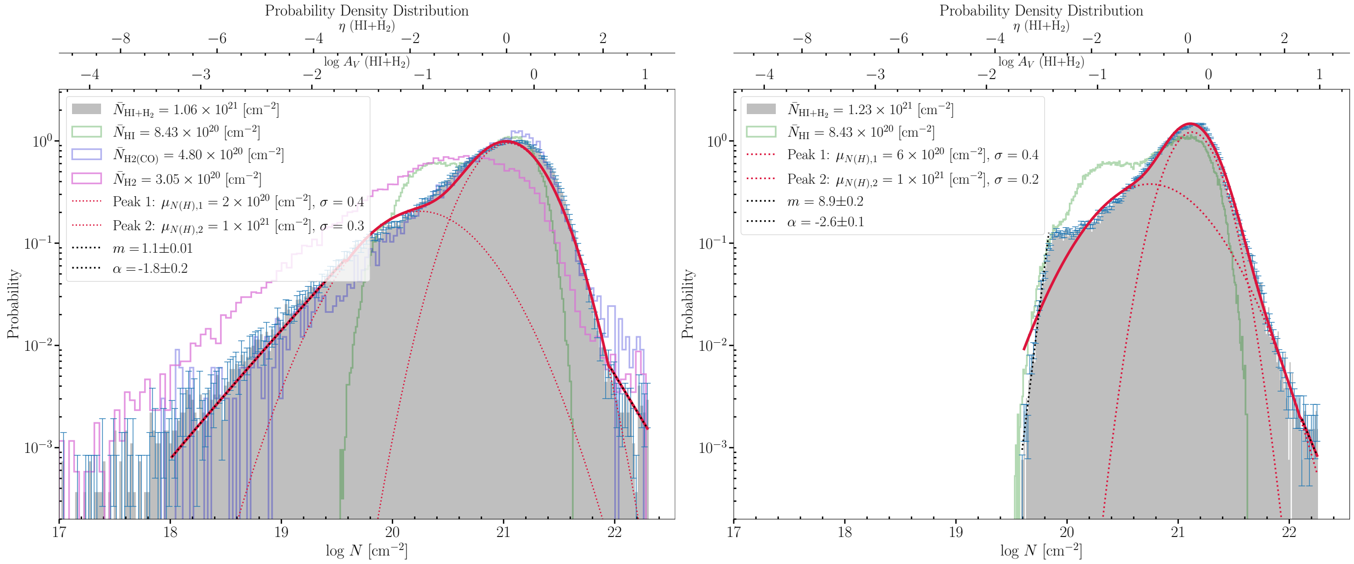

Fig. E.1. *N*-PDFs obtained from the various column density maps. Left: *N*-PDF of the high-res $N_{\rm H}$ column density map derived using all *Herschel* dust data employing method I. Right: *N*-PDF of the $N_{\rm H}$ column density map derived with method II. In solid red and dotted lines, the two-component log-normal fit is shown, whereas the power-law fits regimes are depicted in black dotted lines. The green lines show the *N*-PDF of H I. Here, *m* refers to the slope of the error tail for low column density, while α denotes the slope of the power-law tail for higher column densities. η is defined by $\eta = \ln \frac{N}{\langle N \rangle}$, where *N* is the column density and $\langle N \rangle$ the mean column density. μ and σ refer to the peak and width of the fitted log-normals, respectively. See Appendix E for more details.

findings are very preliminary and more data with higher resolution and a broader dynamic range are essential to provide a robust justification for these results.

Appendix F: The radial profile of the $X_{\rm CO}$ factor

The radial profile of the $X_{\rm CO}$ factor is given in Fig. F.1 and shows a relatively flat dependency for both $X_{\rm CO}$ maps. Each data point corresponds to a bin of 100 pc. The mean value has been calculated for each bin, and the colour indicates the standard deviation of the bin. The error bars represent the standard error $\sigma/\sqrt{N}$, where σ denotes the standard deviation and *N* the samples number. Only one error bar is displayed for each method, as the overall error bars remain relatively similar, hence being representative, and including all of them might distract from the focus on the radial profile. While the overall uncertainty is already substantial when taking all data into account, it increases further as fewer data points are utilised per 100 pc bin, demonstrating a substantial spread in the values within each bin. A visual inspection of Fig. 7 suggests an increase in the $X_{\rm CO}$ factor towards the centre, which is also indicated by a quantitative analysis of the radial profile revealing a slight decrease relative to values at ~ 2 kpc and being flat until ~ 4 kpc. Beyond ~ 4 kpc the profile separates between the two methods. Method I shows a decrease, while method II shows an increase. However, the scatter beyond ~ 4 kpc becomes even larger due to fewer data points, which corresponds to the extent of the main spiral arms (see Fig. 7).

Discussion of the radial profile

In a study by Sandstrom et al. (2013), the radial profile of the $X_{\rm CO}$ conversion factor has been examined in a sample of 26 nearby galaxies, excluding M33. Their analysis revealed that many galaxies exhibit a decreased $X_{\rm CO}$ factor by a factor of approximately 2 towards the centre, while maintaining a consistently flat dependency on the galactocentric radius. Some galaxies show no decrease towards the centre, but rather a slight increase, which we see in M33 as well.

Despite the large scatter of $X_{\rm CO}$ across the galactocentric radius (as shown in Fig. F.1), it is tentatively inferred that the radial dependence of $X_{\rm CO}$ in M33 is also flat, which is consistent with the conclusions drawn by Sandstrom et al. (2013). The low correlation coefficients of approximately −0.3 for both Spearman and Pearson correlation coefficients indicate a weak correlation, thus providing further support for this conclusion. In our data, obtained using method I, there is an increase beyond ~ 4 kpc, while for the data obtained via method II, there is a decrease. Both trends coincide with an increase in uncertainty due to fewer data points beyond ~ 4 kpc (see Fig. 7). Considering the large uncertainty, the radial trend still remains relatively flat.

However, the decline with galactocentric radius could be due to CO turning optically thin in the outskirts of the galaxy but given the high uncertainty from the few data points and a drop of merely ~ 20% this is not significant. It will certainly not affect any global properties in M33 so that we consider the radial profile of the $X_{\rm CO}$ factor rather as predominantly flat. The absence of a pronounced decrease towards the centre might be attributed to an augmented optical depth of the CO emission, as previously mentioned. The used line ratio of 0.8 is only an average and may bias the radial profile we observe, as it varies across the disk of M33 (Druard et al. 2014). However, there is no radial trend in the variation of this ratio, cancelling out rather large-scale effects along the galactocentric radius. Also of crucial importance is the disparity in critical density between CO(1 − 0) and CO(2 − 1), implying possible variations in the extent of the clouds (as previously mentioned). However, this effect is potentially mitigated by smoothing the CO data to reduce it to a lower resolution.

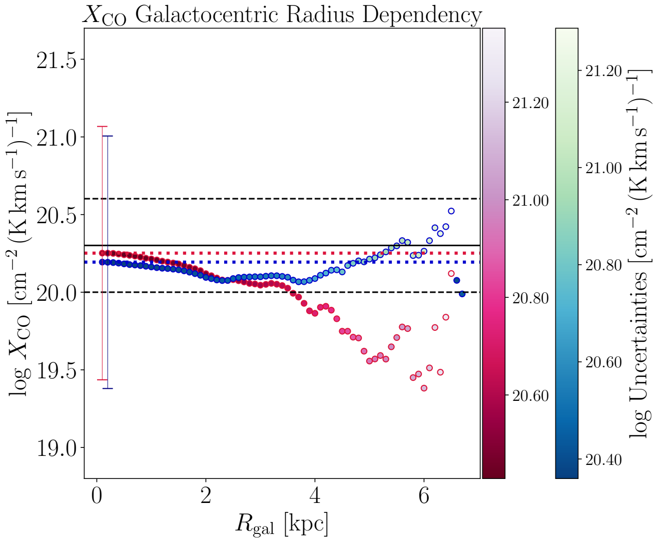

Fig. F.1. Radial profile of the $X_{\rm CO}$ factor as a function of the galactocentric radius in bins of 100 pc. Reddish data points refer to the $X_{\rm CO}$ factor obtained with method I, while the green to bluish represent $X_{\rm CO}$ obtained with method II. The uncertainty of each bin is given by the colour scale and the error bars represent the standard error ($\sigma/\sqrt{N}$). Red and blue dotted lines refer to the mean $X_{\rm CO}$ obtained using methods I and II, respectively. The solid black line shows the Galactic value, while the two black dotted lines show 2.5 times the Galactic value, respectively.

5.2.2 Physical properties of GMCs and their statistics in M33 (Paper II; Keilmann et al., 2024b)

In Keilmann et al. (2024b), I examine how the physical attributes of GMCs in M33 and the Milky Way vary across different large-scale galactic contexts, such as spiral arms or the central region, systematically uncovering the impact of the galaxy morphology on initial star formation conditions. Observations at "cloud-scales" (Schinnerer and Leroy, 2024), spanning $50 - 100$ pc, correspond to the dimensions of GMCs or GMAs, which can extend up to several hundred parsecs (Nguyen-Luong et al., 2016). This research mainly targets Molecular Cloud Complexes (MCCs) and "mini-starburst" GMCs characterized by an increased star formation rate. However, statistical analysis faces challenges in identifying the location of GMCs/GMAs within the Galactic environment (Rosolowsky et al., 2003; Colombo et al., 2022; Schinnerer and Leroy, 2024). Performing such an analysis only for one galaxy also lacks the possibility of studying the impact of other properties of galactic environments, such as metallicity.

The purpose of this study is to examine and contrast the properties of GMCs using N_{H_2} maps derived from both dust and CO data, while accounting for the galactocentric radius and environmental conditions within M33. Additionally, I seek to determine a GMC mass spectrum and compare the results with Milky Way studies by Nguyen-Luong et al. (2016) and Rice et al. (2016), as well as with findings of the PHANGS survey (Leroy et al., 2021), which is a large survey investigating galaxy formation and evolution.

The GMC properties of M33 and the Milky Way reveal both similarities and differences. Notably, M33 lacks very massive clouds (those exceeding approximately $\sim 10^6\,\mathrm{M}_\odot$) that are present in the Milky Way. This may be explained by supernovae that sweep up gas mass and thereby regulate maximum GMC masses. Another compelling result is that both galaxies, however, show GMCs with maximum sizes around ~ 150 pc. This similarity might be attributed to the regulation by the galactic disk scale height, which is indeed comparable in both galaxies.

I analyzed all physical properties in dependence on the galactocentric radius by properly accounting for the orientation of M33 on the sky (inclination, phase angle). The analysis has also been extended in dependence on the galactic environments of M33 (central region, spiral arms, and the remaining outskirt). To achieve this, I had to construct different masks. I also had to fit the spiral arms. In the literature, an approach is usually used that requires one to mask the data to allow the fit of the spiral arms to converge. However, these approaches only worked when I heavily masked the data. This questioned the whole approach in my opinion, as I had substantial influence on the final result depending on how I chose to mask. Therefore, I pursued another approach and developed a log-spiral fit, which yielded more reliable results with less manual intervention. However, an analysis of the final map that I have produced (see Appendix E) revealed that the exact definition of the spiral arm mask boundaries does not significantly affect the overall statistical results, thereby strengthening the findings reported in Keilmann et al. (2024b).

The dependence of GMC properties with the galactocentric radius and the galactic environment of M33 are as follows. The vast majority of the clouds do not depend on the galactocentric radius (except for a few clouds of some properties). Similarly, the majority of GMCs do not strongly depend on the galactic environment. This may imply that the vast majority of the clouds are not significantly influenced by galactic conditions and opens up a space for dedicated research on possibilities of whether small-scale effects of stellar feedback play a more dominant role in shaping cloud properties.

However, considering the findings of Schneider et al. (2024), which indicate that the transition from atomic H I to H_2 is likely driven by the gravitational potential of the Galactic plane – an example of large-scale effects – the claim presented in this paper (Keilmann et al., 2024b) is very compelling to further analyze and may require a statistical approach for a first glance to disentangle the underlying mechanisms. One possible distinct difference is probably that Draco is a low-density cloud, while the resolution and sensitivity of this study (Keilmann et al., 2024b) are probably limited to observe and study such clouds.

I determined and analyzed key statistical relations, such as the mass-size relation of all datasets (the dust- and CO-derived datasets as well as for the datasets of the other studies that I compared to). I determined and analyzed the power-law mass spectra for all identified GMCs in M33.

In response to the referee's request for this article, I redid the entire analysis of Paper I using H I data with short-spacing corrections to demonstrate that the results remain basically unchanged (see Appendix C).

I also produced complementary cumulative distributions and power-law mass spectra for the different galactic environments and performed a parameter study to confirm that the chosen dendrogram parameters yield robust and consistent results (see Appendix D).

My remaining work and contributions to the follow-up paper on M33 are as follows. I again took the lead by performing the Dendrogram analysis on all maps (both dust- and CO-derived H_2 column density maps). I calculated all reported physical properties for the identified GMCs and analyzed their distribution. Additionally, I computed all relevant parameters from other studies on M33 and the Milky Way for comparison (which were not reported by the studies themselves). These other studies employed partly different data and methods, which also had coarser spatial resolutions compared to the final maps that I generated.

Appendices D and E demonstrate the robustness of the chosen Dendrogram parameters and the definitions of the galactic environments that I determined for this study.

The paper does not mention my extensive use of GAUSSCLUMPS (as implemented in GILDAS) to analyze various maps that I have produced. This approach was unsuccessful, primarily due to the insufficiently large coherent emission in the outer galaxy regions that GAUSSCLUMPS could have approximated using a Gaussian profile.

I led all discussions regarding the progress and interpretation of this study. Once again, I have learned a lot from the co-authors. Of course, I also read the relevant literature for this study and, again, basically wrote the entire article. The co-authors provided helpful comments and feedback and minor edits that further improved the manuscript.

A&A, 692, A226 (2024)
https://doi.org/10.1051/0004-6361/202451451

Astronomy & Astrophysics

Molecular cloud matching in CO and dust in M33

II. Physical properties of giant molecular clouds

Eduard Keilmann[1,⋆], Slawa Kabanovic[1], Nicola Schneider[1], Volker Ossenkopf-Okada[1], Jürgen Stutzki[1], Masato I. N. Kobayashi[1], Robert Simon[1], Christof Buchbender[1], Dominik Riechers[1], Frank Bigiel[2], and Fatemeh Tabatabaei[3,4]

[1] I. Physikalisches Institut, Universität zu Köln, Zülpicher Straße 77, 50937 Köln, Germany
[2] Argelander-Institut für Astronomie, Universität Bonn, Auf dem Hügel 71, 53121 Bonn, Germany
[3] School of Astronomy, Institute for Research in Fundamental Sciences (IPM), PO Box 19395-5531, Tehran, Iran
[4] Max-Planck-Institut für Astronomie, Königstuhl 17, 69117 Heidelberg, Germany

Received 10 July 2024 / Accepted 6 November 2024

ABSTRACT

Understanding the physical properties such as mass, size, and surface mass density of giant molecular clouds or associations (GMCs/GMAs) in galaxies is crucial for gaining deeper insights into the molecular cloud and star formation (SF) processes. We determine these quantities for the Local Group flocculent spiral galaxy M33 using H*erschel* dust and archival ^{12}CO(2 − 1) data from the IRAM 30 m telescope, and compare them to GMC/GMA properties of the Milky Way derived from CO literature data. For M33, we apply the Dendrogram algorithm on a novel 2D dust-derived $N_{\mathrm{H_2}}$ map at an angular resolution of 18.2″ and on the ^{12}CO(2 − 1) data and employ an X_{CO} factor map instead of a constant value. Dust and CO-derived values are similar, with mean radii of ~58 pc for the dust and ~68 pc for CO, respectively. However, the largest GMAs have a radius of around 150 pc, similar to what was found in the Milky Way and other galaxies, suggesting a physical process that limits the size of GMAs. The less massive and smaller M33 galaxy also hosts less massive and lower-density GMCs compared to the Milky Way by an order of magnitude. Notably, the most massive (>a few 10^6 $M_\odot$) GMC population observed in the Milky Way is mainly missing in M33. The mean surface mass density of M33 is significantly smaller than that of the Milky Way and this is attributed to higher column densities of the largest GMCs in the Milky Way, despite similar GMC areas. We find no systematic gradients in physical properties with the galactocentric radius in M33. However, surface mass densities and masses are higher near the center, implying increased SF activity. In both galaxies, the central region contains ~30% of the total molecular mass. The index of the power-law spectrum of the GMC masses across the entire disk of M33 is $\alpha = 2.3 \pm 0.1$ and $\alpha = 1.9 \pm 0.1$ for dust- and CO-derived data, respectively. We conclude that GMC properties in M33 and the Milky Way are largely similar, though M33 lacks high-mass GMCs, for which there is no straightforward explanation. Additionally, GMC properties are only weakly dependent on the galactic environment, with stellar feedback playing a role that needs further investigation.

Key words. dust, extinction – ISM: structure – Galaxy: general – galaxies: ISM – Local Group – galaxies: star formation

1. Introduction

Molecular clouds (MCs) are the birthplaces of stars in galaxies and their formation is a complex process influenced by various physical mechanisms. One key process is the gravitational collapse of dense regions within the interstellar medium (ISM) of galaxies. These regions often arise from instabilities within the ISM, which are triggered by processes such as spiral density waves and stellar feedback (McKee & Ostriker 2007; Dobbs et al. 2014; Renaud et al. 2015). Spiral density waves in galaxies like the Milky Way are mediated by gravitational interactions between stars, gas, and dark matter in the galactic disk. As these waves propagate through the disk, they compress and shock the gas along the trailing edge of a spiral arm (Fujimoto 1968; Roberts 1969), leading to the formation of dense MCs. These clouds serve as sites for star formation (SF) due to their high density and low temperatures. Consequently, spiral arms are expected to exhibit a higher star formation efficiency (SFE) than less dense galaxy regions (Lord & Young 1990; Silva-Villa & Larsen 2012; Yu et al. 2021). Indeed, a greater number of young stars are found in the spiral arms, suggesting a higher star formation rate (SFR) in these areas (Bigiel et al. 2008; Schinnerer et al. 2013). However, the rise in the SFR in spiral arms may simply result from higher surface densities, with the spiral's gravitational potential restructuring and concentrating the gas rather than influencing SF directly. Elmegreen & Elmegreen (1986) and Querejeta et al. (2024) found no increase in the SFR in galaxies with strong spiral patterns. If this is true in general, the SFE should remain constant regardless of the galaxy, as various studies have noted (Moore et al. 2012; Ragan et al. 2016; Urquhart et al. 2021; Querejeta et al. 2021).

Stellar feedback –in the form of stellar winds, supernova explosions, and radiation pressure from massive stars– also plays a significant role in the formation, evolution, and lifetimes of MCs. These processes inject energy and momentum into the ISM, creating turbulence and disrupting the equilibrium of the gas. The compression and turbulence induced by stellar feedback, as well as the shear induced by galactic dynamics

---

[⋆] Corresponding author; `keilmann@ph1.uni-koeln.de`

(Chevance et al. 2020), can trigger the collapse of MCs, initiating the formation of new stars. However, stellar feedback can also lead to the destruction of MCs (e.g., Bonne et al. 2023). Chevance et al. (2022) suggested that the main causes of cloud destruction in galaxies are early stellar feedback mechanisms, which take place prior to supernova explosions. It is still a matter of debate as to whether SF is more influenced by the environment – for example, central regions versus spiral arms – or by stellar feedback mechanisms (Corbelli et al. 2017; Rey-Raposo et al. 2017; Kruijssen et al. 2019; Chevance et al. 2022; Liu et al. 2022; Choi et al. 2023). Additionally, other factors such as magnetic fields and turbulence within the ISM can influence the formation and evolution of MCs; magnetic fields provide support against gravitational collapse and can regulate the dynamics of the gas, while turbulence contributes to the fragmentation and structure of MCs.

Linking the physical properties of giant molecular clouds (GMCs) in different large-scale galactic environments, such as spiral arms versus central regions, allows the systematic exploration of how the morphology of a galaxy impacts initial SF conditions. Observations on "cloud scales" (Schinnerer & Leroy 2024) of 50−100 pc match the sizes of GMCs or giant molecular associations (GMAs), which are up to a few hundred parsecs in size (Nguyen-Luong et al. 2016, NL16 hereafter). The present study focuses mainly on what these latter authors refer to as molecular cloud associations (MCCs) and "mini-starburst" GMCs with an elevated SFR.

Molecular clouds consist mostly of molecular hydrogen H_2; however, it is difficult to detect cool H_2 directly due to its symmetry and small moment of inertia. One approach to determining the H_2 distribution in a galaxy is to employ observations of dust in the far-infrared (FIR) – for example using the *Herschel* satellite – and to derive a total hydrogen column density map from a spectral energy distribution (SED) fit to the fluxes. The H_2 distribution is then obtained by subtracting the H I component. H_2 maps can also be obtained using carbon monoxide (CO), the second-most abundant molecule, and applying the CO-to-H_2 conversion factor, $X_{\rm CO}$ (Bolatto et al. 2013). The low-J rotational transitions of CO are established as a good tracer of the cold regions of MCs because these lines have low excitation temperatures (up to a few 10 K) and low critical densities (a few 100 $\rm cm^{-3}$ up to a few 10^3 $\rm cm^{-3}$) for collisional excitation.

However, metallicity significantly affects MCs. Lower metallicity leads to less dust and therefore less dust shielding and self-shielding of ultraviolet (UV) radiation. Thus, the far-UV field can penetrate deeper into MCs, photo-dissociating CO, and leaving a larger envelope of emitting ionized carbon (C^+) around a smaller CO-rich core (Poglitsch et al. 1995; Stark et al. 1997; Wilson 1997; Bolatto et al. 2013). This is intensified by reduced CO self-shielding due to lower CO abundance. H_2 also photodissociates via absorption of Lyman-Werner band photons but achieves sufficient column densities to become self-shielded at moderate extinctions ($A_{\rm V}$) within C^+-emitting gas and thus can become a significant mass reservoir. Hence, there exists a substantial molecular hydrogen reservoir outside the CO-emitting area that is referred to as CO-dark H_2 gas (Röllig et al. 2006; Wolfire et al. 2010). This must be taken into account when comparing the mass estimates of dust and CO, as done in this study.

M33, classified as a flocculent Sc-type spiral galaxy, lies at a distance of 847 kpc (Karachentsev et al. 2004), has an inclination of ~56° (Regan & Vogel 1994), and contains numerous massive SF regions. Our 18.2″ angular resolution corresponds to ~75 pc, which is the size of GMCs or GMAs in the Milky Way (NL16), allowing us to resolve individual GMCs on a 2D image. Recent interferometric observations (Peltonen et al. 2023; Muraoka et al. 2023) have even higher resolution, resolving <50 pc scales, but are not discussed here because we focus on large GMCs. The metallicity of M33 was measured using neon and oxygen abundances in H II regions (Willner & Nelson-Patel 2002; Crockett et al. 2006; Rosolowsky & Simon 2008; Magrini et al. 2010) and varies widely, ranging from values comparable to the Milky Way to lower ones (see discussion and references in Magrini et al. 2010). However, the average metallicity is approximately half solar, which is frequently cited in the literature (Gratier et al. 2012; Druard et al. 2014; Corbelli et al. 2019; Kramer et al. 2020), and the total mass (gas and stars) of M33 is $\sim 10^{11}$ $\rm M_\odot$, roughly 10% of the Milky Way mass (van der Marel et al. 2012; Patel et al. 2018).

The objective of the present paper is to analyze and compare GMC properties based on dust- and CO-derived $N_{\rm H_2}$ maps, considering the galactocentric radius and environment within M33. We also aim to establish a GMC mass spectrum and compare our findings with Milky Way studies from NL16, Rice et al. (2016) and PHANGS (Leroy et al. 2021), a survey studying galaxy formation and evolution.

The paper is organized as follows. Section 2 summarizes the data and methods for producing H_2 maps at 18.2″ resolution presented by Keilmann et al. (2024, Paper I hereafter). Section 3 introduces the Dendrograms algorithm (Rosolowsky et al. 2008) and presents the extraction results. The equations for determining MC properties (mass, size, density, pressure, etc.) are given in Sect. 4. These results are presented in Sect. 5, where we also compare with Milky Way studies. Section 6 discusses cloud mass distributions and properties with respect to the galactic radius and environment. Section 7 summarizes the paper.

2. Data and methods

In Paper I, we presented two techniques using FIR H*erschel* data to produce a total hydrogen column density map of M33. The first procedure (Method I) consists of a multiwavelength SED fit and is briefly summarized in the following. A more detailed description of this method can be found in Paper I. The second approach (Method II) mainly served as a consistency check because it uses only the SPIRE 250 µm data to obtain the $N_{\rm H_2}$ map and does not account for the variable emissivity index β of the dust. Therefore, we only use the $N_{\rm H_2}$ map derived from Method I for the current study.

We make use of H I data acquired by Koch et al. (2018). The primary benefit of these data lies in the short-spacing corrections, which are absent in the H I data from Gratier et al. (2010) and which were utilized to generate the κ_0 map and final column density maps in Paper I. The incorporation of the H I data from Koch et al. (2018) for this present study has not resulted in any significant changes to the generated maps, especially in the molecular phase of the maps. In these areas, both H I maps are equal to within ~10%. The deviation increases in the diffuse region of M33 beyond the molecular regions, where GMCs are not detected anyway. All findings and conclusions of the initial Paper I remain unchanged. The updated data products are available at the CDS.

2.1. Herschel dust data

For Method I, we use the level 2.5 archive data at 160, 250, 350 and 500 µm from the Herschel Key Project

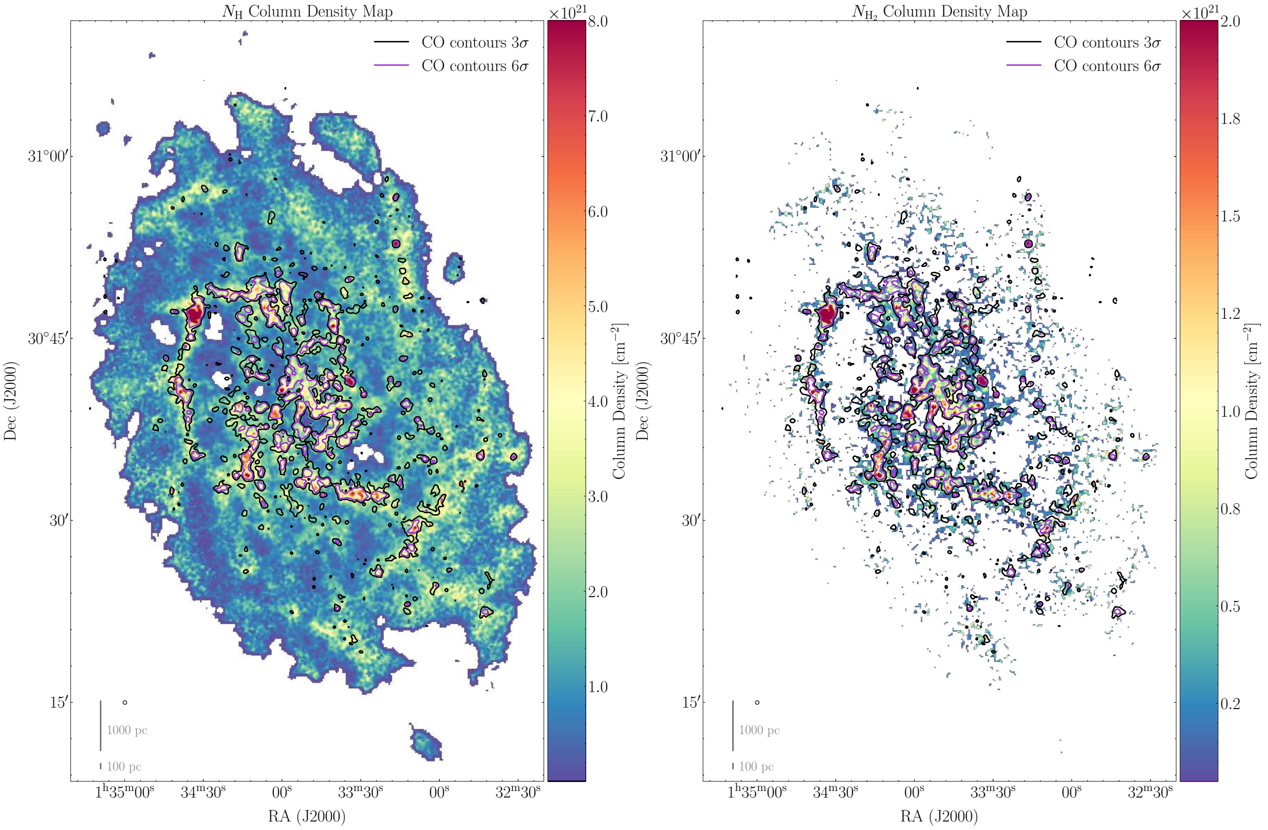

Fig. 1. Total and molecular hydrogen column density maps. Left: High-resolution N(H) total gas column density map obtained from the *Herschel* flux maps of M33 with 18.2″ angular resolution (indicated by the circle in the lower left corner) using the β map from Tabatabaei et al. (2014). Values below and above a minimum and maximum threshold (10^{18} cm^{-2} and 10^{22} cm^{-2}, respectively) are blanked. Right: High-resolution H_2 column density map derived from the total N(H) map by subtracting the H I component. In both maps, the CO contour levels 3 and 6σ of the CO map (Fig. A.1 in Appendix A) are shown.

HerM33es[1] (Kramer et al. 2010). All maps are in units of MJy sr^{-1} and reprojected to a grid of 6″.

Method I involved several steps. First, we performed spatial decomposition using a modified Planck function to fit the dust temperature and surface density, Σ, to the SED derived from flux densities within the 160 to 500 µm range. We then applied Eq. (17) from Paper I,

$$\Sigma_{\rm high} = \Sigma_{500} + (\Sigma_{350} - \Sigma_{350} * G_{500\_350}) + (\Sigma_{250} - \Sigma_{250} * G_{350\_250}) \ , \quad (1)$$

to generate a high-resolution map of gas surface density $\Sigma_{\rm high}$ at a resolution of 18.2″. This equation combines surface density distributions at 250 µm, 350 µm and 500 µm, convolved with a Gaussian kernel to the respective resolutions[2] in Eq. (1). $G_{\lambda_c\_\lambda_o}$ are the Gaussian kernels of width $\sqrt{{\theta_c}^2 - {\theta_o}^2}$ for the convolution, commonly denoted as $*$. The beam at the required resolution is specified by θ_c and the beam at the original resolution by θ_o, while the index $\lambda_c\_\lambda_o$ denotes the corresponding wavelengths. SED fitting was conducted for each map using a pixel-by-pixel modified blackbody function with the specific intensity given by Eq. (10) in Paper I with

$$I_\nu = \kappa_{0,\rm DGR}(\lambda/250\,\mu\rm m)^{-\beta}\, \mu_m\, m_{\rm H}\, N_{\rm H}\, B_\nu(T_d) \ , \quad (2)$$

assuming optically thin emission. The mean molecular weight is indicated as μ_m, $m_{\rm H}$ is the mass of the hydrogen atom, $N_{\rm H}$ the total hydrogen column density and $B_\nu(T_d)$ the Planck function. A dust opacity law similar to Krügel & Siebenmorgen (1994) has been used with

$$\kappa_g(\nu) = \kappa_{0,\rm DGR} \times (\lambda/250\,\mu\rm m)^{-\beta} \ . \quad (3)$$

The dust-to-gas ratio (DGR) is inherently included in our definition of the dust absorption coefficient in units of (cm^2/g), which we denote hereafter simply as κ_0, and β is the emissivity index determined by Tabatabaei et al. (2014). We use this β map alongside the dust temperature of the cold component that are given in Figs. 8 and 9, respectively, in Tabatabaei et al. (2014). We derived the dust absorption coefficient κ_0 pixel-by-pixel using Eq. (15) in Paper I. Further details on the determination of κ_0 and β, including interpolation techniques, are described in Section 3.2 of Paper I. Our approach avoids assumptions regarding the $X_{\rm CO}$ factor or DGR, allowing for a more accurate evaluation of these factors.

Following our application of this technique to M33, we obtained a total column density map of the galaxy with a spatial resolution of ~75 pc or an angular resolution of 18.2″ (Fig. 1, left). From this map, we derived a molecular gas column density map (Fig. 1, right) by subtracting H I data from the VLA (Koch et al. 2018). The H I data at 12″ angular resolution have been smoothed to 18.2″ and then transformed to column density using Eq. (1) in Paper I, based on Rohlfs & Wilson (1996). The total H_2 gas mass (Fig. 1, right) is 1.6×10^8 $M_\odot$.

---

[1] `http://archives.esac.esa.int/hsa/whsa/` (PACS observation ID: 1638302627, SPIRE observation ID: 1638304642). The SPIRE data reduction was optimized for extended emission.

[2] The angular resolutions are 18.2″, 24.9″ and 36.3″ for 250 µm, 350 µm and 500 µm, respectively.

2.2. *IRAM* 30 *m telescope* ^{12}CO(2 − 1) *data*

M33 was observed using the HERA multibeam dual-polarization receiver in the On-The-Fly mapping mode, targeting the ^{12}CO(2 − 1) line. The observations were conducted as part of the IRAM 30 m Large Program titled "The complete CO(2 − 1) map of M33" (Gratier et al. 2010; Druard et al. 2014). The CO line-integrated map has been acquired from the IRAM repository. The archive data have been converted from antenna temperature scale to main beam brightness temperature using a forward efficiency of $F_{\mathrm{eff}} = 0.92$ and a beam efficiency of $B_{\mathrm{eff}} = 0.56$ (Druard et al. 2014). We calculated an rms noise level of 0.35 K km s^{-1}, equivalent to $3\sigma = 1.046$ K km s^{-1}, for the smoothed map with a resolution of 18.2″ (Fig. A.1 in Appendix A). We only utilize the IRAM 30 m line-integrated intensity map of CO, since we do not have velocity information from the dust-derived data. Moreover, due to the inclination of 56°, M33 appears mostly face-on, resulting in small line of sight effects. Hence, employing only the line-integrated CO data is justified and serves as a meaningful comparison with the dust-derived data.

2.3. *The* X_{CO} *conversion factor map*

Using dust-derived N_{H_2} data and IRAM CO data, we computed the X_{CO} conversion factor map by dividing the N_{H_2} map by the CO(2 − 1) map, scaled to CO(1 − 0) with a line ratio of CO(2 − 1)/CO(1 − 0) = 0.8 (Druard et al. 2014). This generates a pixel-by-pixel X_{CO} map, avoiding a uniform value across the galaxy, as often used in the literature (Gratier et al. 2012; Druard et al. 2014; Clark et al. 2023; Muraoka et al. 2023). The X_{CO} map, based on the dust-derived N_{H_2} map, is thus influenced by assumptions in the dust-derived results. Figure B.1 shows the X_{CO} map outlining the main spiral arms of M33. Minimum values in the outer area are about 10^{19} cm^{-2}/(K km s^{-1}), with maxima in the northern and southern spiral arms exceeding 10^{21} cm^{-2}/(K km s^{-1}).

To compare the X_{CO} values to those reported in the literature for M33, we calculated a single X_{CO} value in Paper I using a simple mean and a binned histogram with a log-normal fit. We also conducted scatter plots and a radial line profile to investigate radial dependency. All methods show considerable variability in X_{CO} with no significant correlation with galactocentric radius. However, the simple mean, log-normal fit and scatter plot indicate values approximately at or below the Galactic X_{CO}, between 1.6×10^{20} cm^{-2}/(K km s^{-1}) and 2.1×10^{20} cm^{-2}/(K km s^{-1}). Despite the diversity, this spread is expected due to natural fluctuations in the CO-to-H$_2$ ratio across the interstellar medium, as noted by Bolatto et al. (2013) and recent studies (Ramambason et al. 2024; Chiang et al. 2024).

3. Identification of coherent structures

To derive physical quantities such as sizes, densities, and masses and to compare structures in H$_2$ column density maps derived from H*erschel* with CO data from the IRAM 30 m, we need to identify coherent structures in the 2D maps.

The ISM of a galaxy is a complex multi-phase environment, from hot, tenuous atomic gas to cold, dense molecular gas. The simplest approach defines MCs as entities with well-defined borders (Elmegreen 1985) but complex substructure consisting of clumps and filaments (e.g., Stutzki & Guesten 1990; Schneider et al. 2011; Pineda et al. 2023). Extraction algorithms separate dense gas into distinct clouds/clumps, often using velocity information from spectral line observations for statistical analysis. Various methods identify point sources, clumps, clouds and filaments in the Milky Way (Stutzki & Guesten 1990; Williams et al. 1995; Rosolowsky & Leroy 2006; Rosolowsky et al. 2008; Henshaw et al. 2019; Li et al. 2020; Men'shchikov 2021). Li et al. (2020) concluded that GAUSSCLUMPS (Stutzki & Guesten 1990) and Dendrograms (Rosolowsky et al. 2008) perform best in extracting clumps in synthetic data cubes, including noise.

Molecular clouds were extracted from the CO spectral data cube of the IRAM 30 m telescope at original angular resolution by Gratier et al. (2012) and Corbelli et al. (2017) using the CPROPS algorithm (Rosolowsky & Leroy 2006). CPROPS assumes contiguous, bordered emission of clouds by an isosurface in brightness temperature above a threshold, applying moment measurements to derive size, line width and flux from the position-position-velocity data cube. In our study, we employed Dendrograms for extracting GMCs.

3.1. *The Dendrograms method and initial values for M33*

The Dendrogram algorithm works intrinsically in two and three dimensions. The algorithm searches for the highest value in the map and systematically collects all other data points with lower values as long as three conditions are fulfilled. The first condition is the minimum difference (`min_delta`) in intensity between two identified peaks, which must be satisfied to consider those as two different structures. This retaining level of two structures is set to 1σ of the rms noise of the maps. We also have tested different values of `min_delta`, ranging from 1σ to 5σ. The second parameter is the minimum level (`min_value`) that a structure must have in order to be considered as a coherent clump/cloud. We explored levels from 3σ to 5σ and ultimately chose to set the threshold above the 3σ level of the rms noise, which is $\sim 6.5 \times 10^{19}$ cm^{-2} for the dust-derived N_{H_2} and ∼0.35 K km s^{-1} for the line-integrated CO map (Gratier et al. 2010; Druard et al. 2014; Keilmann et al. 2024). Our investigations did not reveal notable variations in the final identification of structures, indicating that the Dendrogram results are not substantially influenced by the selection of these two input parameters when applied to our data. The last parameter defines the minimum number of pixels to be considered as a structure (`min_npix`), which is related to the width of the structure when we assume circular geometry. This parameter is given by the actual number of pixels, which fit into the full width at half maximum (FWHM) beam width multiplied by 1.2 and corresponds to ∼11 pixels to ensure that the MCs are well resolved. We also experimented with factors of 1, 1.5 and 3 (see below). Obviously, a factor of 1 tends to find more smaller structures around the beam size and a factor of 3 "blurs" clouds into fewer but larger structures. We choose a factor of 1.2 as the best compromise to obtain reliable cloud statistics (see also Schneider & Brooks 2004; Kramer et al. 1998). The extraction of sources has then been applied to the dust-derived N_{H_2} map and to the line-integrated CO(2 − 1) map, for which the final properties of the detected GMCs have been derived using the X_{CO} factor map from Paper I. We investigate the influence of varying Dendrogram parameters in Appendix C.

Dendrograms distinguish between so called leaves and branches. Branches contain substructures like other branches or leaves, while leaves only consist of themselves. As the distance to M33 is 847 kpc (Karachentsev et al. 2004) and the angular resolution is 18.2″, the minimum resolved convolved structure that we can identify has a size of 75 pc. This corresponds roughly to the size of GMCs (and small GMAs) in

Table 1. GMC properties derived from the Dendrogram leaves in dust.

x [″]	y [″]	A [10^4 pc^2]	R [pc]	M [10^5 M$_\odot$]	n [cm^{-3}]	Σ [M$_\odot$ pc^{-2}]	T_d [K]	AR
305	−308	0.23	27	2.4	42	104	20.4	4.69
−70	−17	0.23	27	1.6	28	70	20.7	2.16
554	432	12.49	199	78.6	3	63	22.0	1.20
284	−171	0.23	27	1.3	23	56	21.0	1.44
304	−357	1.69	73	8.9	8	53	21.0	1.50
−856	1040	0.23	27	1.2	21	53	19.9	1.71
614	50	1.44	68	7.3	8	51	19.4	1.80
652	156	0.29	30	1.5	19	51	22.0	2.21
−121	−97	0.29	30	1.5	18	50	21.7	2.30
−194	−20	0.96	55	4.6	9	48	22.0	1.52

Notes. The table is ordered according to surface mass density and gives the properties of the first ten clouds. The offsets, x and y, are calculated regarding the center position of M33 of RA(2000) = $01^\mathrm{h}33^\mathrm{m}50.62^\mathrm{s}$ and Dec.(2000) = 30°39′46.45″. R is the radius, M the mass, n the density, Σ the surface mass density, T_d the dust temperature and AR the aspect ratio of each GMC. See Sect. 4 for details on the calculation of the listed quantities. The full table is provided in electronic form at the CDS.

Table 2. GMC properties derived from the Dendrogram leaves in CO.

x [″]	y [″]	A [10^4 pc^2]	R [pc]	X_CO $\left[\frac{10^{20}}{\mathrm{cm^2\,K\,km\,s^{-1}}}\right]$	L_CO [10^4 K km s^{-1} pc^2]	M [10^5 M$_\odot$]	n [cm^{-3}]	Σ [M$_\odot$ pc^{-2}]	T_d [K]	AR
92	406	4.47	119	0.2	10.3	47.8	10	107	22.0	1.30
−18	7	0.35	33	2.5	4.4	2.1	20	61	22.0	3.01
95	457	0.96	55	0.7	3.6	5.5	11	57	21.0	1.35
330	−122	1.81	76	5.5	5.4	10.1	8	56	21.4	1.65
455	−39	3.51	106	0.6	7.2	18.0	5	51	19.6	1.78
483	−93	0.35	33	0.5	1.2	1.8	17	51	19.6	1.02
301	−290	0.78	50	2.0	5.5	3.8	11	49	21.3	2.24
112	−223	0.71	48	2.2	5.4	3.4	11	48	21.7	1.34
−17	289	0.53	41	1.3	3.4	2.5	12	46	21.6	2.36
399	758	1.38	66	0.8	5.3	5.7	7	41	21.8	1.25

Notes. The table is ordered after surface mass density and gives the properties of the first ten clouds. The offsets, x and y, are calculated with respect to the center position of M33 of RA(2000) = $01^\mathrm{h}33^\mathrm{m}50.62^\mathrm{s}$ and Dec(2000) = 30°39′46.45″. See Sect. 4 for details on the calculation of the listed quantities. The full table is provided in electronic form at the CDS.

the Milky Way (Roman-Duval et al. 2010; Hughes et al. 2013; Nguyen-Luong et al. 2016; Spilker et al. 2022). We mostly concentrate on leaves in our analysis since they best represent a single GMC/GMA. However, leaves do not capture all the emission. Branches, which contain leaves and comprise larger areas, represent the more diffuse, extended H_2 emission that we define as “inter-cloud” medium. An example is the crowded center of M33, where separating individual clouds can become challenging. Branches also include emission just around individual, well-separated GMCs. We refer to this surrounding structure as the “envelope”. We note that this does not constitute an H I envelope. An example of this is the GMC NGC 604 in the northeast spiral arm, where the smaller leave structure is embedded in the larger branch. Unless stated otherwise, branches refer to dust, as CO branches show a relationship similar to dust branches as leaves do.

3.2. Dendrogram extraction of GMCs in the CO and dust-derived N_{H_2} maps

In the following sections, we discuss the morphology of detected GMCs, NGC 604 and the differing numbers of detected GMCs in dust and CO. We focus on leaf structures only because they represent mostly the GMC/GMA population. Tables 1 and 2 list the main cloud parameters for the first 10 clouds ordered by their surface mass density. See Sect. 4 for details on the calculation of the quantities listed in the tables. The tables show no one-to-one correlation between dust- and CO-derived GMCs. For example, NGC 604 is one single GMC in the dust-derived map, but in CO it splits into two smaller structures. This discrepancy arises because structures identified in both tracers differ in size and mass.

We focus on the distribution statistics in Sect. 5. A summary of the mean values is given in Table 3. The similarity in this table, especially in masses, is because the structures are well identified as leaves in both tracers (see Sect. 3.2). The CO-derived H_2 column density is lower, evident in the central branch masses, where the CO-derived mass is ~70% of the dust-derived mass. This similarity extends to many parameters, such as radius and densities. Their average values are comparable, varying by less than a factor of 2.

3.2.1. Morphological description

Figure 2 displays the 326 leaf (red) and 142 branch (green) structures identified in the dust-derived N_{H_2} map (left panel) and the

199 leaf (blue) and 94 branch (green) structures in the CO(2 − 1) map (right panel). To provide a clearer overview, we only show the lowest level of branch extraction, which may include other branches (and leaves). The overlay of CO and dust-derived structures on the $X_{\rm CO}$ map (Fig. 3) shows a similar morphology for both tracers. However, the dust emission identifies more structures beyond the spiral arms and central region. 199 structures in the CO map are more locally concentrated, with fewer structures between spiral arms or in M33's outer regions compared to the dust-derived map.

Furthermore, especially the central region in the dust-derived map shows substantial H_2 column density between the identified leaves. The emission distribution contained in branches focuses in the crowded center region of M33, where many GMCs/GMAs potentially overlap along the line of sight, leading to a rather homogeneous plateau of emission. This line of sight effect can be one reason why it is not possible to separate dust emission into smaller leaf structures. However, Koch et al. (2019) employed a Gaussian decomposition on the full spectral CO line cube of the IRAM 30 m data and found that only ∼10% of the CO spectra show multiple components. This finding does not conclusively rule out the possibility that there are several clouds along the line of sight, but overall this effect is probably less important than for other galaxies. It is also plausible that the crowded emission in the center seen in dust constitutes an inter-cloud H_2 medium, similar to what is found in the Milky Way. We note that the flocculent morphology of M33 already points toward an important gas reservoir between the GMCs. However, another explanation is that the inter-cloud gas is warmer and tends to decrease the CO brightness of the low-J lines, which requires future observations of CO(3 − 2) or CO(4 − 3) line emission. In any case, this more widespread gas reservoir in the center contains a significant mass. While dust-derived leaves collectively hold 8.3×10^7 M$_\odot$ in total, branches excluding leaves contain 3.1×10^7 M$_\odot$ of the H_2 gas mass. Especially in the central region of M33, the leaves contain 2.6×10^7 M$_\odot$, while the branches in the center comprise 1.5×10^7 M$_\odot$.

The CO emission map (Fig. 2, right) shows less homogeneous material in branches than the dust-derived map and reveals that the CO leaves are typically surrounded by a more extended envelope. This finding supports the one of Rosolowsky & Simon (2008), who propose that around 90% of the diffuse emission to within 100 pc of a GMC arises from a population of small, unresolved MCs. However, the CO sensitivity might be too low to detect CO-dark gas or CO might be easily dissociated in the center. Additionally, the H_2 emission from dust can be overestimated due to the complex map production process and the subtraction of a VLA H I map, which has its own detection limits. The dust map might still contain H I, as CO-faint column densities are low (0.5 to 1×10^{21} cm^{-2}), close to the atomic-to-molecular hydrogen transition level. The CO-identified leaf structures have a total mass of 4.2×10^7 M$_\odot$, with branches holding 2.1×10^7 M$_\odot$ (50% of the mass compared to leaves; 37% in the dust-derived map). In the center, the leaves contain 1.7×10^7 M$_\odot$ and branches 1.1×10^7 M$_\odot$ (64% of leaves' mass; 57% in dust-derived map).

3.2.2. The GMA NGC 604

The SF region NGC 604 stands out with the highest mass and largest area, forming a single structure on the dust-derived $N_{\rm H_2}$ map but several GMCs on the CO map (Fig. 2), similar to the findings of Williams et al. (2019). The discrepancy may arise from the greater extent of the GMC in dust compared to CO, as the 3σ CO signal shows a narrower north-south ridge (see Fig. 2). Another explanation could be CO-dark gas in the enveloping gas, with dust emission reaching 2×10^{20} cm^{-2}, conducive to CO formation. This and the limited spatial resolution probably explain the divergence of NGC 604 from the majority of the GMC population in this study.

Table 3. Average cloud properties derived with Dendrograms.

	Dust-derived	CO
Clouds	326	199
$\bar{R}$ [pc]	58 ± 13	68 ± 21
$\bar{n}$ [cm^{-3}]	5.2 ± 1.5	3.0 ± 1.1
$\bar{M}$ [M$_\odot$]	(2.8 ± 0.9) × 10^5	(2.9 ± 0.9) × 10^5
$\bar{\Sigma}$ [M$_\odot$ pc^{-2}]	22 ± 5	16 ± 6

Notes. $\bar{R}$, $\bar{n}$, $\bar{M}$, and $\bar{\Sigma}$ are the average values for the area, radius, beam-averaged column density, and number density as well as mass and surface mass density, determined from the leaves extraction from the dust-derived and CO maps, respectively.

However, Relaño et al. (2013) (and references therein) reported that NGC 604 is not a single H II region, but comprised of a few compact knots and filamentary structures joining the different knots. The whole complex has a radius of 280 pc and forms the second most luminous H II regions association in the Local Group, surpassed only by 30 Doradus in the LMC.

Observations of the Atacama Large Millimeter/submillimeter Array (ALMA) in ^{12}CO(2 − 1) and ^{13}CO(1 − 0) (Muraoka et al. 2020; Phiri et al. 2021; Peltonen et al. 2023) at an angular resolution of 0.44″ × 0.27″ (1.8 pc × 1.1 pc) (Muraoka et al. 2020) and 3.2″ × 2.4″ (13 pc × 10 pc) (Phiri et al. 2021) confirm that NGC 604 constitutes multiple individual molecular clouds.

3.2.3. Caveats regarding dust- and CO-derived GMCs

Some GMCs are identified only in the CO dataset, while others appear only in the dust-derived dataset. Dust-only detections may indicate CO-dark H_2 gas or may be due to smaller CO(2 − 1) envelopes given its higher critical density compared to CO(1 − 0) (Schinnerer & Leroy 2024). Regions seen only in CO may reflect underestimated molecular hydrogen column densities, possibly from overestimated κ_0 values derived from molecular hydrogen regions, casting doubts on the assumption of a constant κ_0 between atomic and molecular phases.

Furthermore, κ_0 may be overestimated as it requires regions with CO emission below 2σ, hence assuming no CO emission. This leads to a bias due to generally low CO emission in the disk (see Eq. (16) in Paper I). The IRAM CO map might show structures from noise fluctuations. Raising the detection threshold to 5σ can address this potential issue, but this approach also leads to similar detections when consistently increasing the threshold for dust-derived data. The uncertainty in H_2 detection and the prevalent use of the 3σ threshold for CO and dust data make it challenging to conclusively ascertain the origin of these structures.

Increased noise in the dust-derived $N_{\rm H_2}$ map may cause structures experience a quasi "beam-diluted" effect and to blend into the background due to too low $N_{\rm H_2}$ (not fulfilling `min_value`) or failing the minimum size condition (`min_npix`) to be identified. This aligns with the observation of low column densities in both dust-derived and CO-derived $N_{\rm H_2}$ maps. Figure 3 supports this,

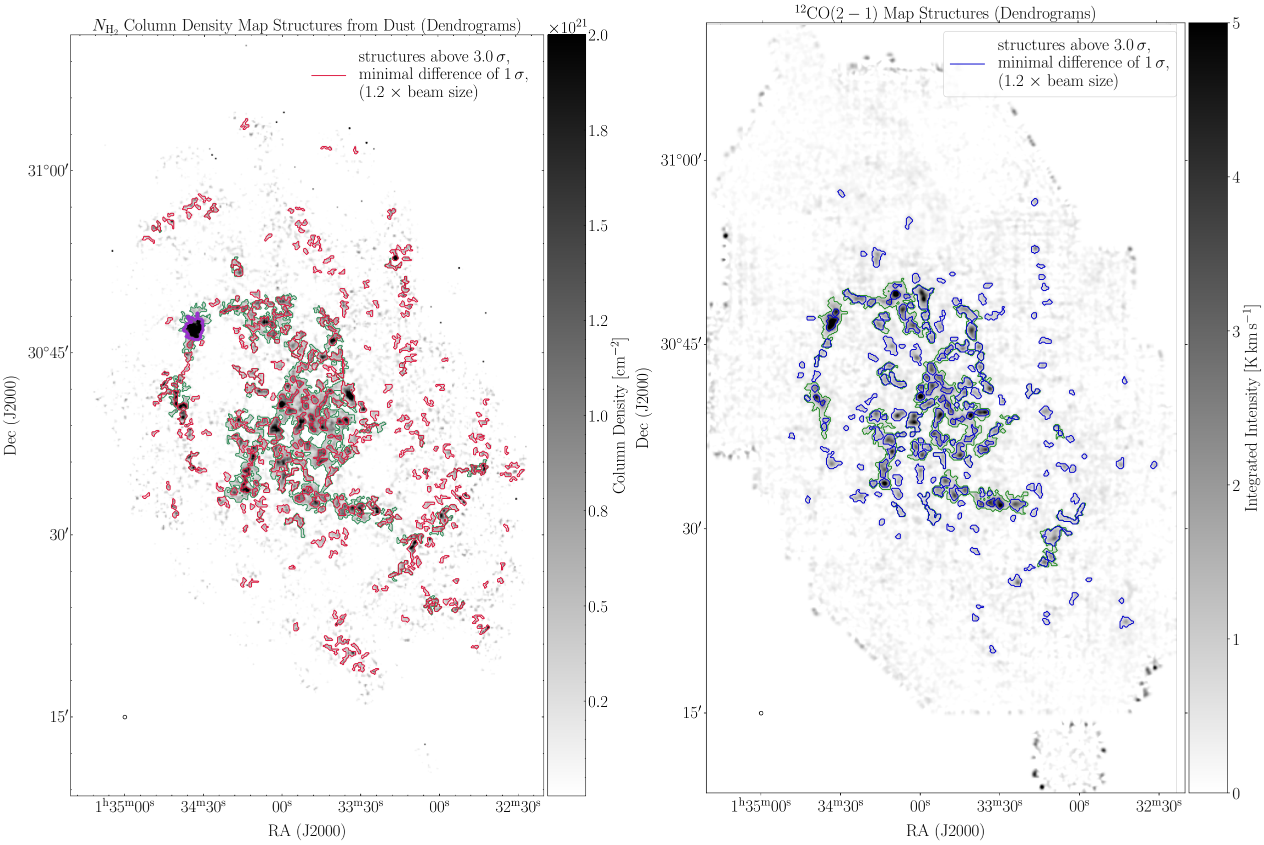

Fig. 2. Dendrogram source extraction from the $N_{\rm H_2}$ and CO maps. Left: GMC detections outlined by the lowest level branches in the dust-derived $N_{\rm H_2}$ map (green contours) and 326 leaf structures (red contours). NGC 604 is marked with a thick pink contour. Right: GMC detections identifying 199 leaf structures in the line-integrated CO(2 − 1) map (blue contours) and similar to the dust map, the branches (green contours). The small circle in the lower left corner of both figures shows the beam size of 18.2″.

showing that structures detected only in the CO-derived $N_{\rm H_2}$ data have the lowest $X_{\rm CO}$ factor. The presence of CO-dark gas and a non-changing κ_0 in both the atomic and molecular phases may explain the greater number of GMCs in the dust-derived data.

4. Determination of physical cloud properties

For each identified structure, we compute several parameters such as the area A in pc^2, the equivalent radius R in pc, the column density N in cm^{-2}, the (beam-averaged) number density n in cm^{-3} and the mass M in M$_\odot$ along with pressure $P/k_{\rm B}$ in cm^{-3} K. The shape of the identified structures is described by the aspect ratio (AR), that is, the ratio between major and minor axes of the GMC. The following section outlines the methodologies employed to compute these quantities.

To calculate A, the area of each pixel of the identified GMC is summed and scaled by the squared distance, D^2, to M33. This pixel size is denoted $A_{\rm pixel} = {\rm d}\theta_{\rm ra} \cdot {\rm d}\theta_{\rm dec} \cdot D^2$, where ${\rm d}\theta_{\rm ra}$ and ${\rm d}\theta_{\rm dec}$ represent the angular size of a pixel in radians. Dendrograms provides information on the location of the identified structure, which serves as a mask for the original dataset. This allows for the calculation of the number of pixels associated with a structure.

The radius R is determined as the equivalent radius of a circle with the area A of the Dendrogram structure, $A = \pi R^2$. The radius of each structure is de-convolved by $R'_i = \sqrt{R^2_{{\rm GMC},i} - R^2_{\rm beam}}$, where $R_{{\rm GMC},i}$ represents the radius of the i-th structure and $R_{\rm beam}$ corresponds to the beam size.

To calculate the column density of H$_2$ of a structure using CO(2 − 1) data, scaled to CO(1 − 0) using the line ratio of 0.8 (Druard et al. 2014), we consider all pixels from the $X_{\rm CO}$ factor map that belong to a detected structure in the line-integrated CO intensity map. We then multiply the corresponding $X_{\rm CO}$ values with the line-integrated intensities of this map on a pixel-by-pixel basis. This approach provides a more precise estimate compared to using a constant $X_{\rm CO}$ factor for the entire galaxy, and allows us to uncover intriguing variations in the distribution of GMCs within M33, which is further explored and discussed in Sect. 5. Additionally, to obtain an average $X_{\rm CO}$ value for each structure, we divided the dust-derived H$_2$ column density by the corresponding CO line-integrated intensity on a pixel-by-pixel basis. These $X_{\rm CO}$ values for each structure are presented in Table 2 (as discussed in Sect. 5).

To determine the masses of GMCs using the molecular hydrogen column densities obtained from Dendrograms (both from CO and dust), the pixel size $A_{\rm pixel} = {\rm d}\theta_{\rm ra} \cdot {\rm d}\theta_{\rm dec} \cdot D^2$ is multiplied by $N({\rm H_2})_j$. Here, j represents the index of a pixel within an identified structure. This is finally multiplied by the hydrogen mass, $m_{\rm H}$, and the mean molecular weight, μ,

$$M_{\rm GMC} = A_{\rm pixel} \cdot \sum_i N({\rm H_2})_j \cdot m_{\rm H} \cdot \mu \, , \tag{4}$$

with $\mu = 2.8$ (Kauffmann et al. 2008) to account for Helium (He) and metals.

To calculate the average number density n of a GMC consisting of H$_2$, we assume a spherical configuration and use the mass and the equivalent radius obtained above. The average density n

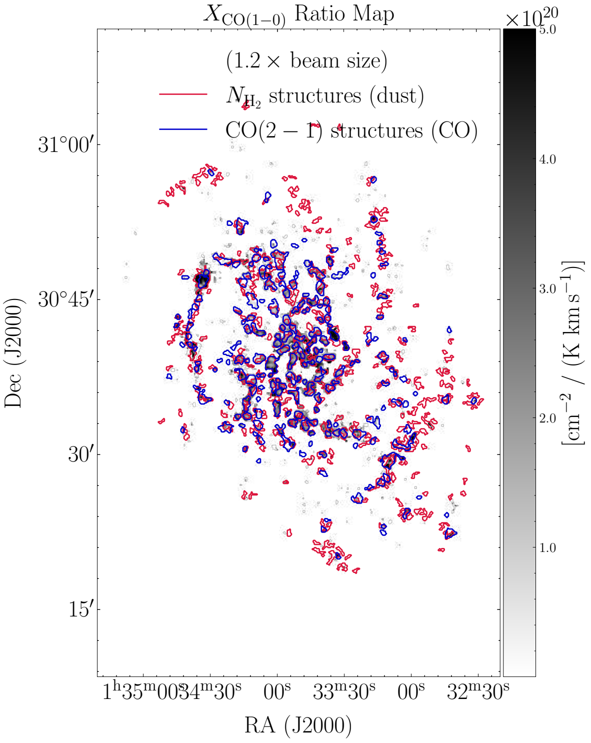

Fig. 3. Structures identified using Dendrograms on CO and dust-derived maps superimposed on the X_{CO} map. The structures found in the dust-derived N_{H_2} (red) and in the CO map (blue) are mapped onto the X_{CO} factor (ratio) map, which represents the dust-derived H_2 column density over CO intensity from Paper I.

is then determined as

$$\frac{n(H_2 + He)}{cm^{-3}} = 14.6\,\frac{M}{M_\odot}\cdot\left(\frac{4\pi}{3}\frac{R'^3}{pc^3}\right)^{-1}, \tag{5}$$

where M represents the mass of the cloud in solar masses and R' denotes the de-convolved equivalent radius of the cloud in parsecs[3]. Since our spatial resolution is 75 pc, the density can only reflect a beam-averaged density derived by dividing the (beam-averaged) column density by the (beam) size. The detected GMC will be composed of smaller substructures with much higher local densities. We note that, due to the critical density, the density of the clouds should be in the order of 10^3 cm^{-3} for the low-J CO transitions to be sufficiently excited.

The surface mass density Σ of the GMCs is determined via

$$\frac{\Sigma_{GMC}}{M_\odot\,pc^{-2}} = \left(\frac{M}{M_\odot}\right)\left(\frac{A}{pc^2}\right)^{-1}. \tag{6}$$

The elongation of detected GMCs is quantified by their column density-weighted aspect ratio of semi-major to semi-minor axis.

Finally, the CO luminosity, L_{CO}, is calculated as

$$\frac{L_{CO}}{K\,km\,s^{-1}\,pc^2} = \frac{D^2}{pc^2}\left(\frac{\pi}{180\cdot 3600}\right)^2 \sum_i I_{int.}\,d\theta_{ra}d\theta_{dec}, \tag{7}$$

where D represents the distance to M33 in parsecs, $d\theta_{ra}$ and $d\theta_{dec}$ are the spatial dimensions of a pixel given in radian and the integrated intensity $I_{int.}$ in units of K km s^{-1}. Hence, we sum over all pixels of a GMC, multiply each pixel by the size of a pixel, scale it by the distance and convert it to units of radians. The resulting L_{CO} therefore describes the integrated emission inside a GMC summed over its entire area.

It is formally possible to calculate the gas pressure within the GMCs, P, using the equation

$$\frac{P/k_B}{cm^{-3}\,K} = \frac{n\,\mu}{cm^{-3}}\,\frac{T}{K}, \tag{8}$$

where k_B is the Boltzmann constant, n the number density of Eq. (5) and T the "mass-weighted" dust temperature. We note, however, that the latter is only the cold component of the dust temperature (Fig. 9 (left) of Tabatabaei et al. 2014), which has also been used to produce the column density maps in Paper I. The dust temperature is around 20 K, which corresponds to a similar gas temperature only when gas and dust are thermally well coupled by collisions (Goldsmith 2001; Goicoechea et al. 2016), which is the case in cool, dense regions. In less dense regions, gas and dust temperatures can differ significantly due to the inefficiency of collisional energy transfer. We thus expect a difference between the inner regions within a GMC, with typical temperatures of around 10–20 K, and the inter-cloud gas, which can be significantly higher, corresponding to gas temperatures of >100 K. In addition, there is possible unresolved substructure in the beam and the density is rather low because of the beam-averaging. Thus, it is not surprising that our pressure results in lower values compared to Hughes et al. (2013), Sun et al. (2020a) and Sun et al. (2020b). The latter two use velocity-resolved CO data from which they obtain higher pressures. The pressure values we derive are therefore only valid for the cool, molecular GMCs and we do not go into great detail in our interpretation.

5. Dendrogram analysis and comparison with the Milky Way

In this section, we discuss the distributions of the key physical cloud properties from the Dendrogram leaves extraction of the dust-derived N_{H_2} and CO maps individually (Sects. 5.1 and 5.2). We compare our results with the Milky Way GMC statistics from Rice et al. (2016) and NL16 that rely on the Columbia (CfA) ^{12}CO(1 – 0) survey (Cohen et al. 1986; Dame et al. 2001), which provides the most comprehensive Milky Way GMC catalog. NL16 derived the cloud properties by eye inspection of line-integrated CO maps and focuses on large ($R \gtrsim 50$ pc) and massive ($M \gtrsim 10^6$ M$_\odot$) MCCs. Those MCCs with a SFR larger than 1 M$_\odot$ yr^{-1} kpc^{-2} are called "mini-starbursts", an example is the W43 region. However, what we find in M33 are more MCCs without a high SFR (Corbelli et al. 2017), though the SFR densities of MCCs are comparable with the SFR of super giant H II regions in M33 (Miura et al. 2014). Rice et al. (2016) performed a Dendrogram analysis on the velocity-resolved CO data and also included smaller (<50 pc) and lighter MCs, down to a limit of a few 10^4 M$_\odot$, which are beyond our resolutions. Since there are other CO surveys of the Milky Way with extensive datasets, we also partly compare our findings with those. Nevertheless, these studies mainly detect smaller molecular clouds, posing a challenge in making meaningful comparisons with the GMCs we can resolve. For a comprehensive overview of the current CO surveys of regions in the Milky Way, see Park et al. (2023). The most relevant studies utilize data from the Galactic Ring Survey (GRS); see Simon et al. (2001) and Roman-Duval et al. (2010) and cloud compilations presented in (e.g., Kramer et al. 1998; Schneider & Brooks 2004; Su et al. 2019).

We also compare our results with Dobbs et al. (2019), who studied molecular clouds in a simulation of a M33-type galaxy

---

[3] The prefactor 14.6 is derived by multiplying the solar mass, dividing by μ and the hydrogen mass and converting pc^3 to cm^3. Depending on constants and rounding, the prefactor can vary; Roman-Duval et al. (2010) determined 15.1 using rounded values.

and from the same IRAM CO data of M33 we use. Their models, based on Smooth Particle Hydrodynamic (SPH) codes SPHNG (Bate et al. 1995) and GASOLINE2 (Wadsley et al. 2017), are detailed in Dobbs et al. (2018). They used Friends-of-Friends (FoF) and CPROPS algorithms to determine cloud properties of the simulations.

For completeness and to compare with other studies, Appendix D shows and discusses the ^{12}CO(1 − 0) luminosity of M33.

5.1. GMC radii

The calculated mean of the beam-deconvolved cloud equivalent radius reveal a similar overall distribution and mean values of around 58 ± 13 pc and 68 ± 21 pc for dust- and CO-derived GMCs, respectively. The largest structure observed from dust data (NGC 604) exhibits the most notable difference, featuring a radius of approximately 200 pc. For completeness, we report that the branches have a mean radius of 354 ± 152 pc.

For comparison, Gratier et al. (2012) and Corbelli et al. (2017) found mean radii of 42±13 pc and 45±12 pc, respectively, from the IRAM CO map using CPROPS. These sizes are smaller compared to our findings, primarily due to the higher spatial resolution of 12″ of the unsmoothed IRAM CO map they used. Williams et al. (2019) report a median GMC size of 105 pc for their identified GMCs in M33, while we derived a mean value for this catalog of 116 ± 29 pc. They identified with Dendrogram the clouds in the SPIRE 250 μm map at 18″ resolution and then performed an SED fit on the averaged flux values of 160, 250, 450 and 850 μm within one identified structure and determined the cloud mass with a fitted DGR and $X_{\rm CO}$ factor. They find an $X_{\rm CO}$ value of ∼6×10^{20} cm^{-2}/(K km s^{-1}) by fixing the dust absorption coefficient κ_0 and emissivity index β and bin the GMCs at 500 pc. A DGR and $X_{\rm CO}$ factor are radially determined via scatter analysis fitting both parameters simultaneously, resulting in possibly degenerate values since different combinations can lead to the same result (their Eq. (6)). They subtracted an H I map without short-spacing from Gratier et al. (2012). A source extraction was also performed on the higher resolution (13″) 450 μm map, reporting a similar size distribution of the clouds.

Rice et al. (2016) has the most complete GMC catalog of the Milky Way, with mean radii of 34 ± 6 pc. Since the subset of NL16 only concentrates on large and massive clouds, the mean value is higher around 90 ± 20 pc (see Table 3 and Fig. 4). Despite this, the trend of the distribution closely mirrors the patterns observed in the M33 data derived from dust and CO data for larger GMCs. There appears to be a size limit of around 150 pc for the largest GMCs/GMAs, in the Milky Way as well as in M33, though both galaxies are different in terms of size, mass and age. Interestingly, Dobbs et al. (2019) find a similar threshold in their simulations of M33 and their cloud extractions of the IRAM CO data set (their Fig. 4). The three distributions exhibit a comparable decline in both the shape and the number of structures as they increase in size. We further do not clearly detect Giant Molecular Filaments (GMFs), which can reach lengths of up to 200 pc in the Milky Way (Wang et al. 2020). However, some of our GMCs have an elongated geometry and aspect ratios larger than 3 so that they formally fit to the definition of GMFs. We come back to this point in Sect. 6.2.5.

A potential mechanism that explains the growth of GMCs in alignment with the results can be attributed to supernovae. Kobayashi et al. (2017) and Kobayashi et al. (2018) show that H I gas is an important mass reservoir for growing GMCs and they show that supernovae can accumulate the H I gas to molecular clouds. In this case, the GMC growth is assumed to depend on the maximum potential sizes of supernovae remnants. Hence, most GMCs are predicted to show sizes of ≲100 pc, with a few exceptions of up to 150 to 200 pc. Another potential explanation is that GMC growth depends on the galactic gas disk scale height, h_z. When a GMC is smaller than h_z, it can grow in all three dimensions. Once it reaches the size of h_z, its ability to grow in the vertical direction will drop. Only the two remaining directions allow the GMCs to expand, but this slows their growth, giving time for stellar feedback or other mechanisms to destroy and regulate cloud sizes. The gas scale height of the galactic disk in the Milky Way ranges from 300 to 400 pc (Carroll & Ostlie 2007). M33 shows a comparable scale height of 320 ± 80 pc (Berkhuijsen et al. 2013). Therefore, this rationale could account for the analogous shape and upper size limit of the largest GMCs in both galaxies. We note, however, that Koch et al. (2019) determined a CO/H I line width ratio of around 0.7 and suggest that M33 has a marginal thick molecular disk and not a thin disk dominated by GMCs and a thicker diffuse molecular disk as seen for the Milky Way and other more massive spirals.

However, we caution that the GMCs identified in M33 potentially have line of sight effects due to limited resolution, the inclination and the increased thickness of the central region, which can blend distinct GMCs into a larger structure that is not one coherent GMA. In addition, as mentioned in Rice et al. (2016), the mass obtained for some GMCs can be inaccurate by up to an order of magnitude due to challenges of reliably determining the correct distances.

5.2. GMC masses and densities

Figure 4 (bottom row) shows the mass and average density distributions of H_2 derived from dust and CO. The black dashed line represents the minimum mass selection used in NL16. The average number density for the binned data set (Fig. 4 bottom right) and the individual clouds (Tables 1 and 2) are low, typically below 30 cm^{-3} for both tracers. The mean of the average densities are similar, with values of n = 5.2 ± 1.5 cm^{-3} for dust-derived and n = 3.0 ± 1.1 cm^{-3} for CO-derived GMCs. Our maps have a spatial resolution of 75 pc, and therefore the identified structures are likely composed of smaller substructures with higher local densities. The densities of GMCs in the Milky Way (29.1 ± 8.0 cm^{-3}) have been calculated using the same methodology, based on the data presented in Table 1 of NL16. The branches have a low average density of 1.1 ± 0.4 cm^{-3}, which is reasonable given that they span larger areas than the leaves and incorporate a significant amount of inter-cloud and envelope material, both of which are expected to have lower densities.

The mass distributions in M33 (Fig. 4, bottom left) show no significant differences between CO and dust for our study. The maximum GMC mass from CO is ≈5×10^6 M$_\odot$, whereas for dust it is NGC 604 with ≈8×10^6 M$_\odot$. We note that there are only a few GMCs in M33 above 10^6 M$_\odot$ in both tracers. The mean values derived from the dust data are very similar, with M = $(2.8 \pm 0.9) \times 10^5$ M$_\odot$ compared to $M = (2.9 \pm 0.9) \times 10^5$ M$_\odot$ for CO. The branches have a mean mass of $M = (1.3 \pm 0.2) \times 10^7$ M$_\odot$.

NL16 selected only Milky Way GMCs/GMAs with masses of larger than around 10^6 M$_\odot$, and thus it is not surprising that the distribution contains only GMCs in this mass range (GMCs with lower masses are not absent but were not included in the survey). Notably, M33 lacks a significant high-mass GMC population. The procedure for mass determination is the same for

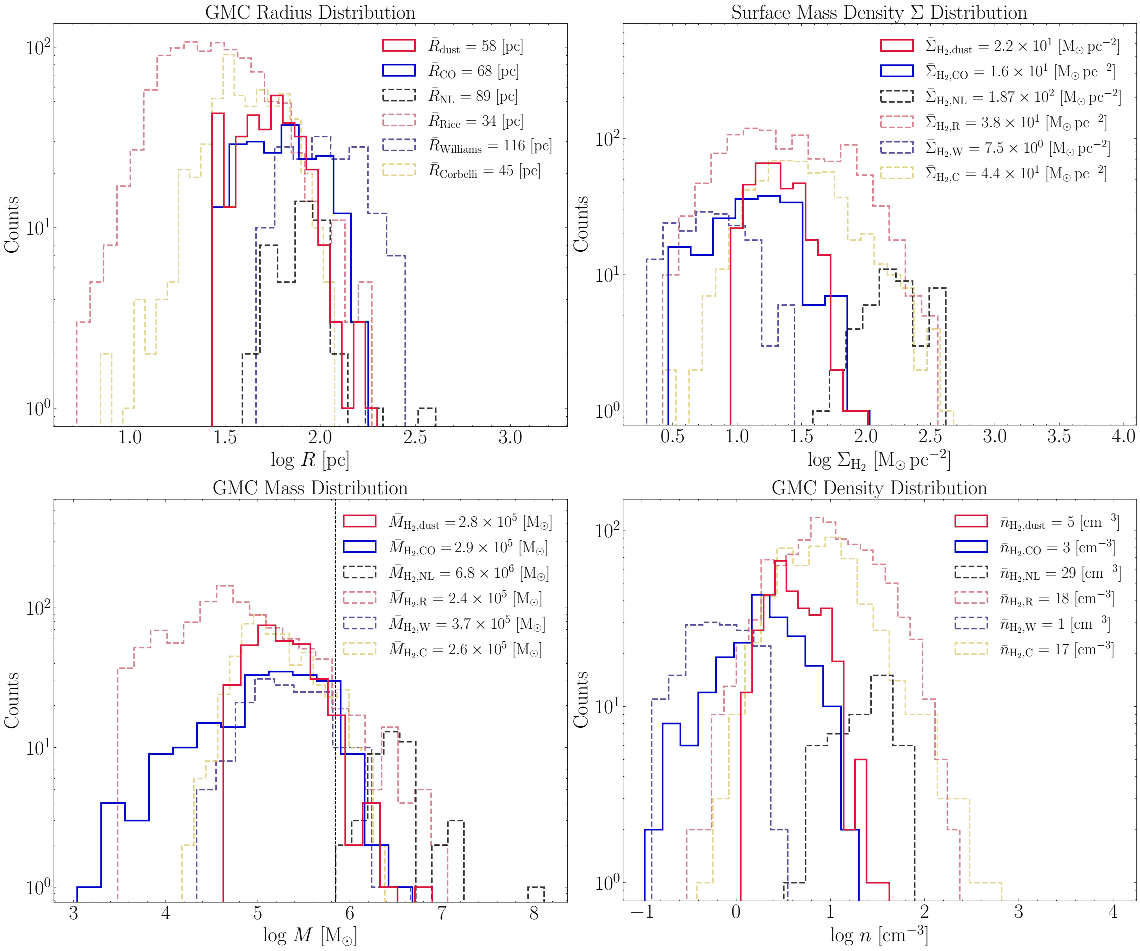

Fig. 4. Distributions of GMC properties from our study and the literature. The panels show histograms of radius (top left), surface mass density (top right), mass (bottom left) and beam-averaged number density (bottom right) derived from H_2 data from dust (solid red) and CO (solid blue) from this study. The dashed purple and golden lines display the distributions obtained for M33 from dust (Williams et al. 2019) and CO (Corbelli et al. 2017), respectively. The dashed black and light red lines give the distributions for the Milky Way studies of NL16 and Rice et al. (2016), respectively. The vertical black dashed line in the mass distribution signifies the minimum mass limit of the selected structures in the Milky Way by NL16.

our study and that for NL16: for CO, the line-integrated intensity was used to derive the CO column density and then finally the mass using an $X_{\rm CO}$ factor; and for the dust, the $N_{\rm H_2}$ column density was derived from an SED fit. Interestingly, the lack of significant high-mass GMCs in M33 also becomes evident by comparing with the comprehensive Rice et al. (2016) Milky Way catalog, which arises from a velocity-based identification of GMCs from CO data, which in addition shows a mean mass similar to our results of $(2.4 \pm 1.0) \times 10^5\ M_\odot$. The difference in mass thus stems from the lower overall CO luminosity and hydrogen column density in M33.

The H_2 gas mass in the center of M33 (see Fig. F.1 for an outline of the center) is ~25% of the total dust-derived H_2 mass and amounts to $4.3 \times 10^7\ M_\odot$. This is an order of magnitude lower than the central molecular zone (CMZ) of the Milky Way ($\sim 1.3 \times 10^8\ M_\odot$). We note that the overall mass of M33 is one order of magnitude lower than that of the Milky Way. The total H_2 mass of the Milky Way is suggested to be 1.4 times higher than the values found in earlier studies (Sun et al. 2021). Applied to the results reported in García et al. (2014), this leads to a total H_2 mass of $4.2 \times 10^8\ M_\odot$. Consequently, the proportion of the CMZ of the Milky Way to this mass is ~30%.

The Milky Way also shows higher number densities, with a mean density of about $30 \pm 11\ {\rm cm}^{-3}$ and $18 \pm 6\ {\rm cm}^{-3}$ for the dataset presented in NL16 and Rice et al. (2016), respectively. Mean values from dust and CO data are roughly five times smaller than those in the Milky Way datasets (and not one order of magnitude). According to the mass-size relation discussed in Sect. 5.3, the density decreases with size. This might explain why mean densities do not show the same trend like GMC masses, central region mass or total H_2 mass of M33, all of which are consistently an order of magnitude lower compared to those of the Milky Way.

Williams et al. (2019), using dust data, found in M33 GMC masses shifted to higher values averaging to ranges from $(3.7 \pm 1.4) \times 10^5\ M_\odot$ and low mean number densities of $1 \pm 0.4\ {\rm cm}^{-3}$, while the average cloud mass in Gratier et al. (2012) from CO data is $(2.4 \pm 0.9) \times 10^5\ M_\odot$ with a mean density of $30 \pm 7\ {\rm cm}^{-3}$. Corbelli et al. (2017) find similar results using the same data at the same angular resolution with $(2.6 \pm 1.1) \times 10^5\ M_\odot$ and $17 \pm 5\ {\rm cm}^{-3}$. The masses match our findings, but the higher number densities are due to detecting smaller structures. This may result from the 12″ resolution of the unsmoothed CO data and a different cloud extraction method (CPROPS).

The effects of limited resolution of our data do not cause non-detections of GMCs with similar masses and densities in M33 compared to the Milky Way. Using a larger beam would inaccurately merge smaller structures into fewer larger structures, consequently inflating the overall mass. The dissimilarity in mass between M33 and the Milky Way, with M33 having only around 10% of the mass of the Milky Way, probably originates from variations in the sizes and evolutionary stages of the galaxies. The diameter of M33 is approximately two-thirds the size of the Milky Way. NL16 used a dataset with an angular resolution of 8.′8, translating into a spatial resolution of ∼60 pc for the most distant GMCs in the Milky Way. For these distant GMCs, our spatial resolution is similar.

By considering sweeping the H I medium by supernovae as we discussed in Sect. 5.1, the typical maximum mass is limited by the gas scale height so that $n_{\rm ISM} \cdot h_z^3$, where $n_{\rm ISM}$ is the volume density of the ISM and h_z is the galactic gas disk scale height. The gas disk scale heights of both galaxies are similar, as discussed above. Thus, the remaining factor influencing the mass growth may be attributed to the density of galaxies. Given that the Milky Way has a higher H_2 density and total mass (from which a greater column density and ultimately a higher number density can be expected), we anticipate that the Milky Way will show higher densities. Therefore, we propose this mechanism as a possible driver. Meanwhile, Kobayashi et al. (2017) and Kobayashi et al. (2018) performed a semi-analytic theory to investigate the impact of cloud-cloud collisions. They show that, even in the Milky Way galaxy, cloud-cloud collisions have a minor impact on GMC growth and are only effective to clouds more massive than $10^6\,{\rm M}_\odot$. We therefore suspect that cloud-cloud collisions are mostly ineffective for M33.

5.3. Mass–size relations

Figure 5 illustrates Larson's (Larson 1981) relationship between mass and size for data derived from dust and CO. For dust-derived GMCs the slope is 1.8 ± 0.1, while it is 2.2 ± 0.2 for CO-derived GMCs. In the simulations of M33, Dobbs et al. (2019) also found a clear mass-size relation in the observations and simulations. However, they did not quantify the slope of this relation so that we extracted the data points from their Fig. 4 and fitted a linear function with a slope of 1.4 ± 0.1. This estimation carries a significant level of uncertainty, attributed to manual data extraction and the overlapping of numerous data points, preventing clear individual identification. As previously noted in Dobbs et al. (2019), the larger GMCs appear too extended, also compared to the GMCs we identified, leading to a less steep slope.

A slope of about 1.6 (Lombardi et al. 2010; Kauffmann et al. 2010) in the mass-size relation suggests the presence of substructures within individual clouds, while a slope of around 2.4 was identified for GMCs in the GRS Galactic plane survey (Roman-Duval et al. 2010). NL16 determined a slope of 1.9 for GMCs and a slope of 2.2 for MCCs. Given that the third Larson relation indicates a power-law connection between mass and size, represented as $M \propto R^\kappa$, with a typical power-law exponent usually around 2, it suggests similar gas surface mass densities for all GMCs. Furthermore, in line with assumptions for a spherical object, the mass can be linked to the size by $M \sim n/R^3 \sim N/R^2$, leading to $M \sim R^2$. This finding aligns well with observations that incorporate a column density threshold (see Schneider & Brooks 2004 and references therein).

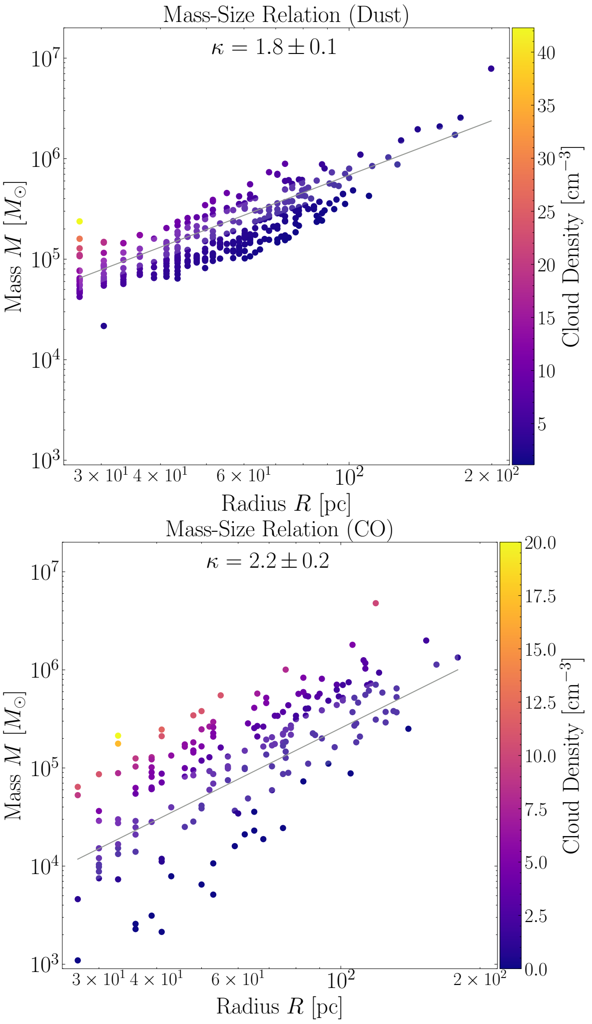

Fig. 5. Mass–size relation of the identified GMCs. *Top*: Mass–size Larson relation for GMCs derived from dust. *Bottom*: Mass–size Larson relation for GMCs derived from CO data. The various colors indicate the average density of individual clouds. The panel displays the slope κ and its corresponding error.

5.4. GMC surface mass densities

Comparing cloud masses and sizes across studies can be unreliable due to differing GMC definitions and boundary settings. Resolution limits may also cause undetected clouds or beam smearing. The concept of cloud surface densities inherently considers the cloud size per definition, $\Sigma_{\rm GMC} = M/A$, thereby mitigating the impact of varying resolutions across studies. However, complete resolution uniformity is not achieved for instance when the galaxy is not perfectly face-on, as some large clouds may still merge into one single larger cloud when the beam size is large, resulting in a higher surface mass density. Conversely, smaller clouds, if sufficiently spaced from others, may get smeared within the beam, causing dilution and a decrease in surface mass density. This can be mitigated by excluding too small structures, which we do by only accepting structures 1.2 times the beam size. Nonetheless, comparing surface mass densities can facilitate a less biased evaluation of clouds occupying similar spatial areas.

In Fig. 4, we compare the GMC surface mass densities. For Milky Way GMCs (NL16), the mean value of $187 \pm 51\,{\rm M}_\odot\,{\rm pc}^2$ is approximately one order of magnitude higher than our dust-derived ($22 \pm 5\,{\rm M}_\odot\,{\rm pc}^2$) and CO-derived values ($16 \pm 6\,{\rm M}_\odot\,{\rm pc}^2$) in M33. Whereas compared to the more complete cloud catalog obtained by Rice et al. (2016), the mean value is $38 \pm 14\,{\rm M}_\odot\,{\rm pc}^2$, approaching similar high surface densities at the higher end of the spectrum as the clouds presented in NL16. Branches show consistent mean surface mass densities of 19 ± 5 $\mathrm{M}_\odot$ pc^2.

For comparison, Hughes et al. (2013) report a gas surface mass density for M33 of 46 ± 20 $\mathrm{M}_\odot$ pc^2 using CO(1 − 0) data published by Rosolowsky et al. (2007). This value is roughly a factor of 2 higher than our results. Corbelli et al. (2017) similarly find 44 ± 15 $\mathrm{M}_\odot$ pc^2. Although they identify smaller GMCs with the CO data at 12″ angular resolution, they still find similar masses, resulting in higher surface mass densities. The fact that they find surface mass densities about twice as high as our data are likely attributed to their application of a X_{CO} value twice that of the Galactic standard value. However, this has been disputed in Paper I, which finds an average value nearly identical to the Galactic one. Gratier et al. (2012) find similar values for these properties for the same reasons. The data of Williams et al. (2019) exhibit the lowest mean surface mass densities of all with 7.5 ± 2.5 $\mathrm{M}_\odot$ pc^2 which is probably due to the large sizes of the GMCs. Roman-Duval et al. (2010) find for their Milky Way data a median surface mass density of 144 ± 20 $\mathrm{M}_\odot$ pc^2. Although the mass-size relations indicate a comparable surface mass density, there is an observed dissimilarity in the distribution shapes, with mean values varying by a factor of approximately one order of magnitude between M33 and the Milky Way. It should be noted that this finding aligns with the GMC masses we find in M33 being approximately an order of magnitude lower compared to the Milky Way GMCs and with the total masses of the two galaxies found by other studies mentioned above. We note that in the simulations of Dobbs (2008) the GMCs are more massive in galaxies with stronger spiral shocks or higher surface densities.

Increased SF activity and higher pressures correlate with increased molecular gas surface mass densities (Heyer et al. 2004; Lehnert et al. 2015; Wang et al. 2017; Krumholz et al. 2018). The difference between our results and the subset in NL16 is most likely due to manual selection of GMCs, involving a threshold applied to their masses. However, considering the Rice et al. (2016) Milky Way catalog reveals a similar range of especially high surface mass densities between both galaxies. Given the smaller mean sizes and higher masses of this catalog compared to our results, both mass and size lead to increased surface mass densities by a factor of ∼2. However, Corbelli et al. (2017) find a distribution similar to the GMCs in the Rice et al. (2016) catalog. We attribute this to the higher spatial resolution of the observations by Corbelli et al. (2017), which yield smaller GMC sizes relative to ours, although they still report mean masses comparable to ours probably due to the use of an X_{CO} value twice the Galactic standard value.

5.5. Power-law mass spectra

We aim to determine the mass spectrum of GMCs in M33 identified via dust and CO, which may relate to cluster and star mass functions (Kennicutt & Evans 2012, and references therein). Differences in the mass spectrum across regions might reflect variations in the processes that govern the formation, evolution and destruction of clouds (Rosolowsky 2005; Colombo et al. 2014). The mass spectrum typically conforms to a power-law probability distribution. To determine the power-law exponent α and its standard error ($\sigma/\sqrt{N}$) we first linearize the function

$$p(x) \propto x^{-\alpha}, \tag{9}$$

and then employ a least-squares approach to fit a linear slope to the data.

Figure 6 shows the distributions with an index determined to be $\alpha = 2.32 \pm 0.10$ for the dust-derived and $\alpha = 1.87 \pm 0.08$ for the CO-derived mass spectrum. The steeper slope of the dust-derived data indicates a larger number of less massive structures. This result is somewhat unexpected, because the low angular resolution of our data would have moreover suggested that many smaller molecular clouds along the line of sight would be artificially grouped into larger complexes, resulting in a flatter slope. Dobbs et al. (2019) reported $\alpha = 1.59$, using the CPROPS algorithm to identify clouds in M33 from the IRAM CO data. For the data of Corbelli et al. (2017), using the same data and extraction method, a curved pattern with an index of 1.6 has been identified. For the results reported in Gratier et al. (2012), using IRAM CO data as well as CPROPS, we determine a single power-law of $\alpha = 2.12 \pm 0.08$. We note that in the simulations of Dobbs et al. (2019), the spread in α is large, between 1.66 and 2.27 (with an uncertainty of 0.2) and depends on the simulation (SPHNG or GASOLINE2) and the identification algorithm (FoF or CPROPS). Williams et al. (2019) find a higher slope of 2.83. Their result suggests a poorer ability of M33 to form massive clouds. Rosolowsky (2005) report a similarly steep mass spectrum slope of 2.9 ± 0.4, which may be biased by only sampling the high-mass end of the mass spectrum where the slope tends to be steeper.

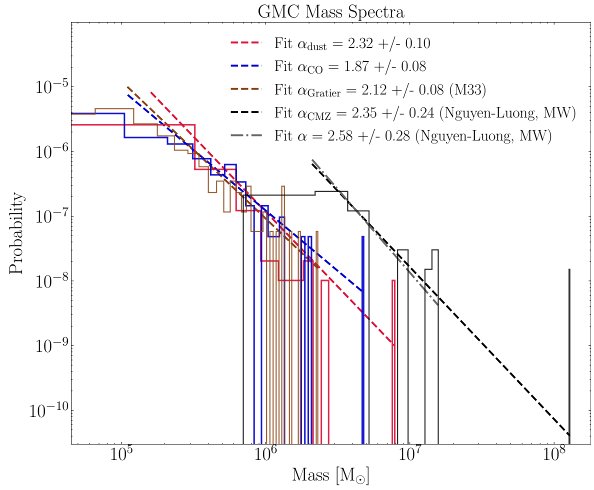

Fig. 6. Power-law mass spectra of detected GMCs from dust-derived data (red) and CO (blue) as well as from NL16 (Milky Way, black). In black, the fit is performed with all listed structures in NL16, while the light gray dotted-dashed line shows the fit, where the CMZ of the Milky Way is excluded.

For the power-law index of Milky Way clouds, including the CMZ, we determine $\alpha = 2.35 \pm 0.24$ using the data presented in NL16. Excluding the CMZ results in an exponent of $\alpha = 2.58 \pm 0.28$. We note that this comparison relies solely on the 44 structures manually selected by NL16 for structures more massive than 0.7 × 10^6 $\mathrm{M}_\odot$, which could introduce a potential bias and an undetected systematic error. For the results reported in Roman-Duval et al. (2010), we derive $\alpha = 1.61 \pm 0.03$ (not shown in the figure) for the Milky Way CO data from the Galactic Ring Survey. These findings are in alignment with Rice et al. (2016), who found a slope of 1.6 ± 0.1 for their entire catalog. For the outer Galaxy, they reported a higher slope of 2.2 ± 0.1, whereas for the inner Galaxy, the slope remained at 1.6 ± 0.1. Similarly, Fujita et al. (2023) found generally higher slopes, yet they show a consistent pattern with an index of $\alpha = 2.30 \pm 0.11$ derived from ^{12}CO data for distances below 8.15 kpc and $\alpha = 2.51 \pm 0.14$ for distances less than 16.3 kpc. The power-law indices found in several other studies of the

Milky Way, all using CO data, typically range between 1.6 and 2 (Kramer et al. 1998; Simon et al. 2001; Schneider & Brooks 2004; Roman-Duval et al. 2010).

The efficiency of cloud formation has been associated with various processes. As discussed in Williams et al. (2019), the influence on the GMC population of the spiral density wave amplitude (e.g., Shu et al. 1972) can be excluded to explain the tentatively higher slopes in M33 due to modeling efforts, which indicate that the spiral arms of M33 are likely due to gravitational instabilities (Dobbs et al. 2018). The interstellar gas pressure might also be influential (Elmegreen 1996; Blitz & Rosolowsky 2006). Kasparova & Zasov (2008) report increased interstellar pressure compared to the Milky Way, potentially leading to the formation of more massive clouds. Thus, interstellar pressure may not be the primary cause of a potential inefficient cloud formation. This contrasts with findings by Blitz & Rosolowsky (2006) and Sun et al. (2018), indicating M33 lies within a lower pressure regime. This scenario aligns with the upper cloud mass limit being influenced by interstellar pressure. Another factor could be the role of metallicity in the transformation of H I-to-H_2 (Krumholz et al. 2008; Kobayashi et al. 2023). If M33 indeed has subsolar metallicity, this conversion would be less efficient, resulting in similarly inefficient cloud formation. However, the determined metallicity of M33 shows a very high dispersion (Willner & Nelson-Patel 2002; Crockett et al. 2006; Rosolowsky & Simon 2008; Magrini et al. 2010). Furthermore, it is proposed that merging H I clouds could form H_2 (e.g., Heitsch et al. 2005), suggesting that larger H I velocity dispersions could lead to more massive clouds. In M33, however, the average H I velocity dispersion is around 13 km s^{-1} with minimal radial variation (Corbelli et al. 2018). This is consistent with the velocity dispersion of 11 nearby galaxies of ~10 km s^{-1} presented in Tamburro et al. (2009). Typical velocity dispersions measured for the Milky Way are in the same range (Malhotra 1995; Marasco et al. 2017). Another potential mechanism remains within supernovae. The power-law index may be considered to represent the balance between GMC mass-growth and destruction by massive stars (Kobayashi et al. 2017, 2018). The supernova frequency per unit volume varies across the galactic disk and the expansion of supernovae remnants compresses the ISM initiating the transition of H I-to-H_2 (Kobayashi et al. 2020, 2022). In this case, the power-law slopes of the GMC mass functions are determined by the balance between the transition rate from H I-to-H_2 and the destruction rate by stellar feedback from massive stars, mainly radiative feedback (Kobayashi et al. 2017). Additional mechanisms like shear may also set the maximum mass and lifetimes (Jeffreson & Kruijssen 2018), especially in a region where the shear rate is high and the orbital speed is fast (e.g., the outer regions of the CMZ in case of the Milky Way galaxy). We cannot determine which of these mechanisms primarily drive the potentially inefficient cloud formation in M33, as suggested by some of the findings discussed above.

In summary, the power-law index α shows a large spread for both M33 (1.6 to 2.9) and the Milky Way (1.6 to 2.5), due to differences in datasets and methods. Despite errors, there is no significant variance between M33 and the Milky Way, except for a slight tendency for higher values in M33. Both exhibit self-similarity from molecular clouds (~50 pc) to larger GMAs, suggesting similar physical mechanisms for massive GMCs in both galaxies and a limit in sizes and masses despite their high difference in mass. Given the values in the existing literature, it is difficult to determine whether the cloud mass distribution in M33 is significantly different from that in other large spirals within our Local Group.

6. Trends with galactocentric radius and galactic environment in M33

Molecular clouds do not possess a perfectly spherical shape. Instead, their morphology is often influenced by complex processes such as merging or turbulent flows (e.g., Vazquez-Semadeni et al. 1995; Heitsch et al. 2006; Clark et al. 2019; Schneider et al. 2023) or cloud-cloud collisions (Casoli & Combes 1982; Fukui et al. 2021), leading to irregular shapes characterized by clumps and filaments. Variations in cloud properties under different environmental conditions within a galaxy offer valuable insight into the factors shaping cloud formation and evolution (e.g., Sun et al. 2020b).

The molecular gas, for example, forms huge associations as a result of the gravitational attraction of the spiral arm. As the gas exits the spiral arms and experiences significant shear forces, it breaks apart and reverts to smaller elongated structures (La Vigne et al. 2006). Numerous observational and computational studies emphasize the presence of filamentary structures in the areas between the arms (Ragan et al. 2014; Duarte-Cabral & Dobbs 2016, 2017) and the presence of high-mass structures within the spiral arms (Dobbs et al. 2011; Miyamoto et al. 2014). Apart from structure variations, metallicity gradients within a galaxy can also lead to variations in the physical properties of the molecular cloud. We thus examine in the following sections the physical properties of the GMCs in M33 as a function of the galactocentric radius and the galactic environment of M33.

6.1. Trends with galactocentric radius

Figures 7 and 8 display the mass, average density, surface mass density, radius as well as aspect ratio and dust temperature as a function of the galactocentric radius. The relationship between GMC properties and galactocentric radius has also been examined by Gratier et al. (2012), Corbelli et al. (2017) and Braine et al. (2018). A comprehensive discussion of specific properties can be found in Appendix E.

In summary, the parameters show only a weak (for high-Σ GMCs) or non-existing (for low-Σ GMCs) trend with the distance from the galaxy's center, raising the question whether SF is influenced by the galactocentric radius. Only GMCs with the highest surface mass densities (above 40 $M_\odot$ pc^2) show a tendency to have higher values for density and Σ in the center of M33. This finding is similar to what is observed in the Milky Way. In both galaxies, self-gravity and cloud-cloud collisions become more important for these high-Σ GMCs in the respective CMZ.

In the following section, we discuss the more significant trends we observe for different regions (center, spiral arms, outskirts) in M33, as a radial dependence on the galactocentric radius does not entirely unveil systematic differences in the galactic environments.

6.2. Trends with galactic environment

It is not yet clear whether SF is more efficient in particular regions of galaxies and to which extent the SFR and SFE are linked to the physical properties of the GMC population. Observations and simulations indicate that GMCs are concentrated in spiral arms, often with regular spacing, which can be explained when GMCs are formed by gravitational instabilities (Elmegreen 1990; Kim & Ostriker 2002). On the other hand, GMCs can also form by agglomeration of smaller clouds or merging of flows (see references above). A higher

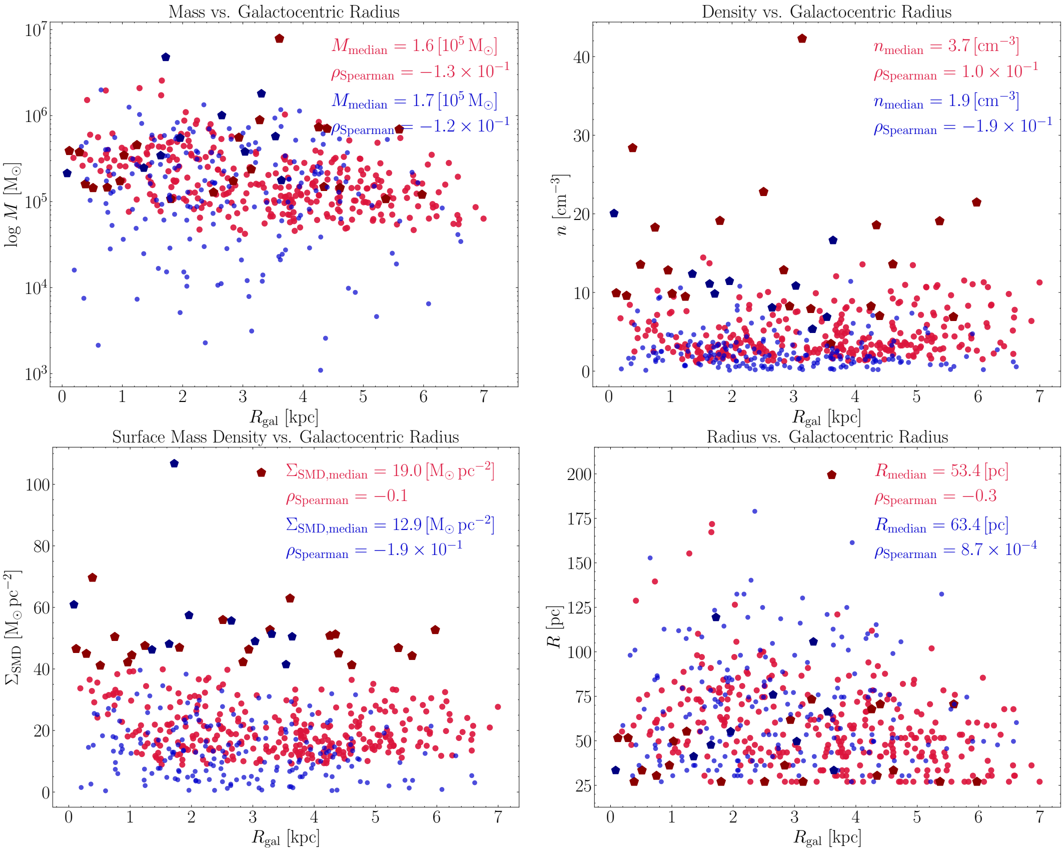

Fig. 7. Mass, average density, surface mass density, and radius of the identified GMCs along the galactocentric radius. The dust-derived GMCs are shown in red, whereas the CO-derived GMCs are represented in blue. The bigger dark red and blue data points mark the GMCs that have a surface mass density exceeding 40 $M_\odot$ pc^2.

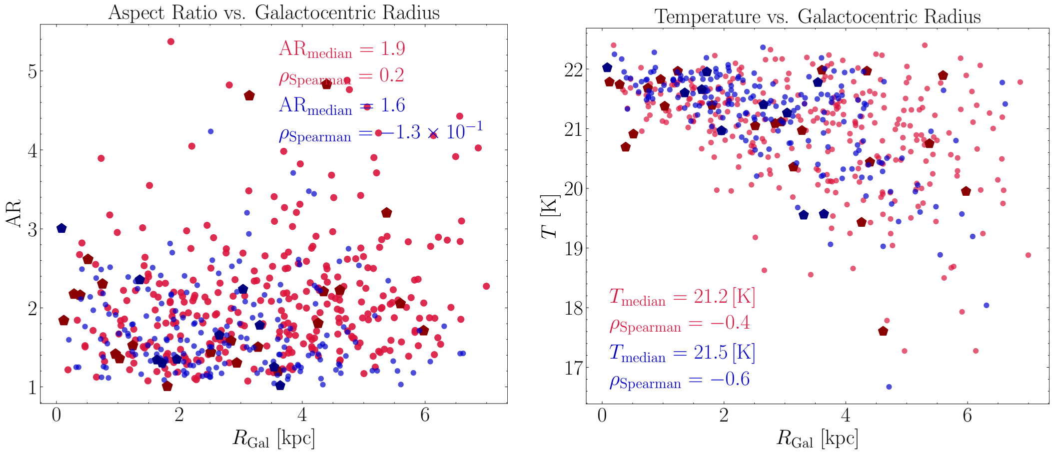

Fig. 8. Aspect ratio and temperature from dust and CO-derived data along the galactocentric radius. The bigger dark red and blue data points mark the GMCs that have a surface mass density exceeding 40 $M_\odot$ pc^2.

SFR can then be just a by-product of the higher material reservoir in the spiral arms. While some studies (Koda et al. 2009; Pettitt et al. 2020; Colombo et al. 2022) report variations between their spiral arms and inter-arm populations, others (Duarte-Cabral & Dobbs 2016; Querejeta et al. 2021) find no discernible differences in the overall properties of the cloud population.

In this section, we systematically investigate if there are variations in the physical properties of the GMC population in certain regions of M33. For that, we use our dust-derived column density map and split the galaxy by eye-view into a central region, the two main spiral arms and the outskirts (Fig. F.1). The two main spiral arms are approximated to extend to a galactocentric radius of roughly 4 kpc, whereas the central area of M33 can roughly be described as an equivalent circle with a galactocentric radius of around 1.3 kpc. The outskirts are considered to be the remaining area of M33's disk[4]. To determine the spiral

---

[4] Since the inter-arms are faint and challenging to distinguish from the surrounding diffuse gas, we refer to this area as the "outskirts" or outer region. We emphasize that this mask is not meant to be considered as a precise delimitation.

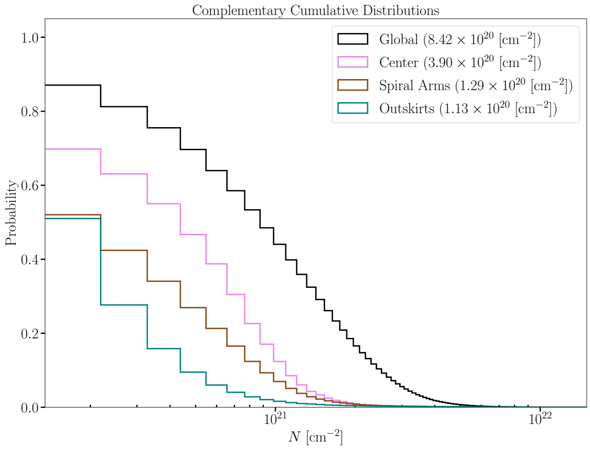

Fig. 9. Complementary cumulative N_{H_2} distributions of the entire galaxy (based on dust-derived data) and the three galactic environments. We note that these distributions are solely based on pixels and are not connected to GMCs.

arm structure more quantitatively, we additionally employ a similar approach as in Querejeta et al. (2021) and model the spiral arms with a log-spiral function and perform a fit to this model. Details of this procedure and the results are given in Appendix F and in Fig. F.1. The visually estimated borders of the spiral arms already capture the fitted log-spirals very well. We therefore continue to use the masks presented in Fig. F.1 to study the spiral arms and outskirts.

6.2.1. Column density complementary cumulative distributions

Querejeta et al. (2021) reported increased gas surface densities closer to the central regions of galaxies by analyzing the CO$(2-1)$ data obtained from the PHANGS-ALMA survey (Leroy et al. 2021). We confirm this finding for M33 using our dust-derived high-resolution N_{H_2} map (Fig. 9), which shows the complementary cumulative distributions of the entire disk of M33 and the three defined environments[5]. The complementary cumulative distribution function provides the likelihood that an observation from a sample exceeds a certain value on the x-axis. It becomes evident that the central region exhibits column densities throughout the spectrum higher than those of the spiral arms and outer regions. The spiral arms and the outskirts display comparable levels of low N_{H_2} below approximately 2×10^{20} cm^{-2}. Beyond this threshold, the spiral arms diverge, maintaining higher column density values. This finding aligns with the results reported in Leroy et al. (2021). The median value for the central region (provided in the panel for all distributions) is roughly three to 3.5 times higher than for the other two regions. Furthermore, the central region shows the steepest slope among all distributions, while the spiral arms and outer regions demonstrate a shallower slope towards higher column densities.

6.2.2. GMC properties in different environments

The distributions of GMC properties (mass, average density, surface mass density, radius and aspect ratio) are shown in Fig. 10 as a function of galactic environment. The global distribution of the entire disk of M33 is shown in red on the left for comparison. GMCs located in the center are represented in violet, those in the two main spiral arms are in brown and those in the outskirts, excluding the center and the two main spiral arms, are depicted in turquoise. The median is displayed as a straight line within the boxes in beige.

Most of the properties show a weak variation for the median values in different environments. Only the central region of M33 exhibits larger masses and surface mass densities of the GMCs compared to the regions in the remaining disk (see also Sect. 6.1, where we have already observed this trend). Overall, the GMCs in the center are denser, those in the spiral arms are larger, while those in the outskirts are more elongated. Generally, the GMC populations in the spiral arm and outer regions do not exhibit large variations in their properties.

6.2.3. GMC masses in different environments

The masses of the GMCs are noticeably higher in the central region of M33. The median and minimum values indicate significantly higher masses compared to the other two regions. Apart from the exceptional case of NGC 604 in the spiral arm, the highest mass values are comparable to those in the central area, while the GMCs with the lowest masses have even lower values. The outer regions exhibit GMCs with similarly low masses as those in the spiral arms but lack GMCs with such high masses.

One hypothesis is that spiral arms, which contain a larger amount of material, increase the occurrence of cloud-cloud collisions, thereby supporting the creation of high-mass entities (Dobbs 2008). This would result in a tendency for the most massive clouds to be situated in spiral arms. However, the spiral arms exhibit lower densities. This is also true for the surface mass density compared to that in the central region. If larger GMCs gather more mass and thus support SF, then this should yield higher surface mass densities. Since the GMCs in spiral arms are merely larger without possessing higher column densities, this results in lower masses and surface mass densities, which correlate with SF, suggesting that SF should be lower. As discussed above, the impact of cloud-cloud collisions in the Milky Way have been investigated by Kobayashi et al. (2017) and Kobayashi et al. (2018), for which an effective impact has only been found for GMCs more massive than 10^6 $M_\odot$. Furthermore, while the most massive GMC (NGC 604) is located in the northern spiral arm, the other GMCs in these environments do not support this picture. Both the median and the 75th percentile values are lower than those of the center. Additionally, most outliers, except for NGC 604, have less mass compared to those in the center. This discrepancy may be due to the limited resolution of 75 pc, whereas Dobbs (2008) simulate molecular clouds with higher resolution. Corbelli et al. (2019) suggested that the formation of more massive clouds in the center may occur due to the rapid rotation of the disk relative to the spiral arm pattern, allowing the clouds to grow further as they traverse the arms.

6.2.4. GMC densities, surface mass densities, and radii in different environments

For GMC densities, the environments show minimal variation. The median values are similar across different regions. The main distinction is observed in the outliers at the outskirts, where the densities do not peak as high as those in the GMCs in other areas.

The surface mass densities demonstrate a pattern similar to that of the masses. The central region contains GMCs with the highest masses, whereas the median and the values at the lower ends of the spectrum decrease in the spiral arms and decrease even more in the outer regions. This finding aligns with the

---

[5] We focus hereafter on dust, since the results of dust and CO are very similar and we want to avoid to overcharge the paper.

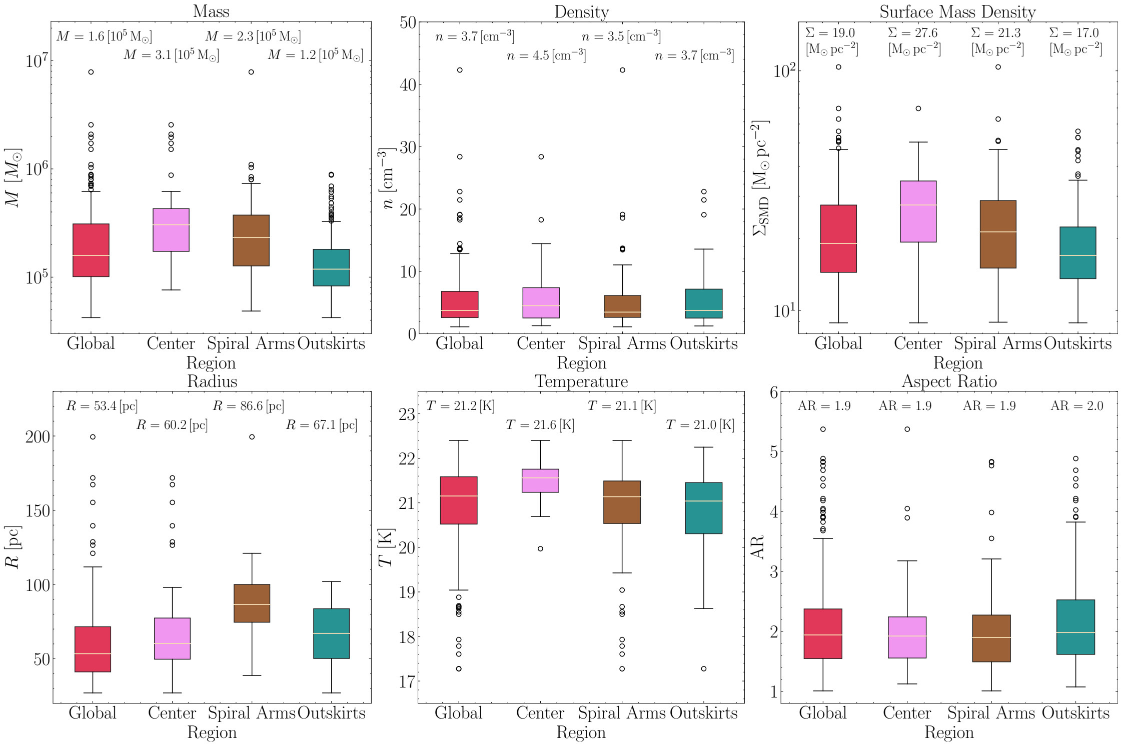

Fig. 10. Box plots of the determined dust-derived parameters categorized based on galactic environments. The lower and upper whiskers of the box plot represent the lowest and maximum values of the dataset, respectively. The colored box shows the distribution's interquartile spread, or the range from the 25th to the 75th percentile; the median is indicated by the solid beige line inside the box. The distributions' outliers are shown as circles.

radial trends that have been discussed in Sect. 6.1 and confirms Querejeta et al. (2021), reporting increased gas surface densities closer to the central regions of galaxies by analyzing the CO(2–1) data obtained from the PHANGS-ALMA survey (Leroy et al. 2021).

On the other hand, the GMC radii differ most significantly in the spiral arms, with NGC 604 as the outlier. The center and outskirts have smaller GMC radii. The median radius in the spiral arms is ~90 pc, while in the outskirts it is ~63 pc.

6.2.5. GMC elongations/aspect ratios and temperatures in different environments

The center has GMCs with the least elongation at the higher end of the spectrum, while the spiral arm and outskirts have slightly stronger elongated GMCs. It is not clear to which extent the GMCs with an AR larger than 3 represent GMFs that were found in the Milky Way (Ragan et al. 2014; Goodman et al. 2014; Zucker et al. 2015; Wang et al. 2020) and in external galaxies (Hughes et al. 2013; Leroy et al. 2016). These studies typically define GMFs as long filamentary structures with lengths exceeding 50 pc and masses above 10^5 $\mathrm{M}_\odot$ and suggest that they trace the denser spine region of the spiral arms and the midplane of the gravitational potential in the galaxy. We note that while some Galactic GMFs exhibit widths down to ~1 pc, a scale which remains indistinguishable from our current resolution, other GMFs possess notably larger widths (Zucker et al. 2018). In particular, Wang et al. (2020) presented dust and dense gas tracers of one filament in the Milky Way with an AR of about 3 and a length of 68 pc which would fit formally to some of the GMCs we detect. Figure 10 shows that there is only a very weak environmental dependency of the AR. However, the most elongated GMCs are found within the spiral arms and the outskirts and this could indicate (as discussed in Sect. E.5) a stretching effect due to shear forces on the massive GMCs (or molecular clouds) as they transition from the spiral arms to the inter-arm regions (Koda et al. 2009). It could also be the result of disruption caused by feedback from stars (Meidt et al. 2015; Chevance et al. 2020; Bonne et al. 2023). Duarte-Cabral & Dobbs (2016) discovered in a computational simulation of GMCs within a two-armed spiral galaxy that, while the average characteristics of the inter-arm and spiral arm GMCs are comparable in terms of their ARs, the extremely elongated GMCs in their dataset are predominantly associated with the inter-arm regions. Given that the outskirts exhibit highly elongated GMCs it is possible that stellar feedback contributes to the disruption of GMCs in both environments.

Hence, our proposition is that the shear forces in the center do not account for disrupting the GMCs, since the GMCs in the center exhibit the lowest median elongation. Additionally, the least elongated and most massive GMCs are located in the center (excluding NGC 604), indicating that the center is conducive to the formation of high-mass GMCs. As detailed in Sect. E.6, we argue that the strong galactic potential subjects GMCs to an isotropic pressure, which accounts for the observed distribution of GMC elongation. It is unlikely that stellar feedback plays a significant role in elongating GMCs in the center, as the feedback would be uniformly distributed throughout the center, resulting in disrupted GMCs across the region and dynamically altering GMC boundaries. After typical GMC lifetimes, any cloud detection algorithm would identify new segments of an original GMC as a new GMC, incorporating parts of previously disrupted GMCs. With this iterative process and the isotropic galactic potential, extreme elongation tendencies are expected to diminish, resulting in the non-increasing elongation

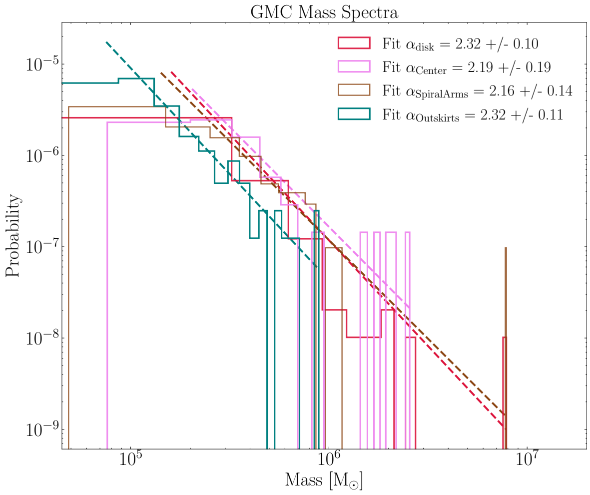

Fig. 11. Power-law mass spectra of GMCs in the dust-derived map for the three galactic environments. The power-law mass spectra is split into the three galactic environments center (pink), spiral arms (brown) and outskirts (turquoise). For comparison, the fit for the whole disk is shown again in red.

of GMCs, unless specific conditions, such as the presence of a bar, exist in the central area.

In summary, it is observed that while the overall dynamics on a large scale influences cloud properties, there is no clear indication that SFE is notably enhanced in any specific environment.

6.3. Power-law mass spectra with galactic environment

As pointed out in Sect. 6.2.3, there are noticeable differences in the masses of the GMCs between the center and the remaining disk of M33. We therefore also investigate the distribution of GMC masses within each large-scale environment by conducting power-law mass spectra.

Figure 11 illustrates the mass spectra of the GMCs in the different environments of M33. The central area and the spiral arms of M33 exhibit the highest abundance of high-mass clouds, with $\alpha_{\rm Center} = 2.19 \pm 0.19$ and $\alpha_{\rm SpiralArms} = 2.16 \pm 0.14$ having relatively shallow slopes. In contrast, there is a significant reduction in high-mass GMCs toward the outer regions, where GMCs have mainly lower to moderate masses with a steeper slope of $\alpha_{\rm SpiralArms} = 2.32 \pm 0.11$. Bigiel et al. (2010) observed smaller GMCs at larger galactocentric radii of M33, suggesting a steeper slope in the outskirts of M33, which is supported by the slope we determine. This higher slope suggests that high-mass objects in the outskirts may face challenges in their formation or are rapidly destroyed after formation. This aligns with the findings presented in Sect. 6.2.3 and with the results of Rosolowsky et al. (2021) in their examination of GMCs across spiral galaxies within the PHANGS dataset.

The spectra shown in Fig. 11 indicate that GMCs have higher masses in areas with lower galactocentric radii, closer to the center. In the outskirts, the most massive GMC reaches a mass of $\sim 1 \times 10^6$ $M_\odot$, the lowest of the three environments. This is consistent with having the steepest slope of all three. In the central region, GMCs that are only about three times more massive are found, while in the spiral arm, the most massive GMC (NGC 604) has a mass of $\sim 8 \times 10^6$ $M_\odot$. This observation indicates that cloud growth may be prevented or that large GMCs are being disrupted in the central area, at least to reach such high masses as observed in NGC 604. This phenomenon could be attributed to complex dynamics and shear forces or to the enhanced interstellar radiation field in the central region. In contrast, the mass distribution of GMCs in the spiral arms, excluding NGC 604, consists of less massive clouds than in the center. NGC 604 leads to a flattening of the slope in the spiral arms. Despite the predominance of low-mass objects in the spiral arms, the conditions in this region appear to be conducive to the growth of larger clouds, maybe due to the absence of a strong interstellar radiation field and/or shear forces disrupting the clouds. However, since the center hosts the GMCs with the highest masses, with the exception of NGC 604, this conclusion remains uncertain.

Dobbs et al. (2019) found a decrease in the power-law index after incorporating SF into their simulations. As clouds become dense, the index drops to values between $\alpha \approx 1.8$ and ≈ 2. Considering delayed SF results in an index that agrees better with observations. This suggests, in general, that SF occurs in later stages of GMC formation. These authors also divided the clouds into "star-forming" and "non-star-forming" clouds (SF clouds and non-SF clouds hereafter). While SF clouds inject energy into the clouds, heating them locally, this leads to a flattened slope of $\alpha = 1.8$, whereas non-SF clouds exhibit a slope of $\alpha = 2.68$. They identified that the non-SF clouds tend to reside at a larger galactocentric radius, indicating higher SF activity in the center. Increased surface mass densities are associated with this phenomenon and we also observe higher surface mass densities toward the center, in accordance with this. Additionally, a stronger galactic potential towards the center could account for this finding. Compared with our results, this suggests a higher SF activity in the center and spiral arms than in the outskirts. Dobbs et al. (2019) also provide reasons as to why larger clouds tend to host more SF: these larger clouds are statistically more inclined to have dense areas, thus increasing the likelihood of SF. These clouds probably accumulate more mass as they begin to form stars, suggesting that clouds not undergoing SF may just be in an earlier phase of their lifetime when they have lower masses.

This is consistent with what Braine et al. (2018) found by analyzing the IRAM 30 m CO data of M33. Detected GMCs (from the catalog of Corbelli et al. 2017) have been divided into three radial bins: $R_{\rm gal} < 2.2$ kpc, $2.2 < R_{\rm gal} < 3.7$ kpc and $R_{\rm gal} > 3.7$ kpc. The power-law indices for these bins are $\alpha = 1.36$, $\alpha = 1.68$ and $\alpha = 1.87$, respectively, showing an increase with radius. They also subdivided the GMCs into three SF classes – no obvious SF (A), embedded SF (B) and exposed SF (C) – based on Corbelli et al. (2017). More evolved GMCs accumulate more mass and show shallower slopes. Star-forming GMCs lie closer to the center than non-SF GMCs. However, A-class GMCs consistently show steep slopes regardless of their position, while C-type GMCs also have similar slopes regardless of their position, indicating that SF activity is more important than galactic environment.

As also discussed in Sect. 5.5, Fujita et al. (2023) found distinct power-law indices of $\alpha = 2.30 \pm 0.11$ and $\alpha = 2.51 \pm 0.14$ in the Milky Way within a galactocentric radius of <8.15 kpc and beyond <16.3 kpc, respectively. Taking the errors into account, this is also consistent with our data split into the environments, which represent distinct regions along the galactocentric radius.

7. Conclusion and summary

In Paper I, we presented a novel technique to use the H*erschel* flux maps and CO(2 − 1) data of M33 to produce $N_{\rm H_2}$ maps at 18.2″ (∼ 75 pc) resolution, resolving GMCs. A complete $X_{\rm CO}$ map was applied to the CO map to compute the $N_{\rm H_2}$ map with values in the range of $1.6-2\times10^{20}\,\mathrm{cm^{-2}/(K\,km\,s^{-1})}$. This X_{CO} factor is close to the Milky Way value and thus questions the usual approach of applying a single, adopted X_{CO} factor for the whole galaxy and simply using a two-times-higher value for M33 due to its lower metallicity.

We then employ the Dendrograms algorithm to identify GMCs from these maps, calculate the physical properties, and compare the results between dust and CO and with Milky Way data from the CO(1 − 0) Columbia survey presented in Nguyen-Luong et al. (2016). In addition, an investigation was conducted to explore the potential influences of the galactocentric radius and galactic environment on GMC properties.

1. We find that M33 lacks the more massive ($>10^6\,\mathrm{M_\odot}$) and denser GMCs that are present in the Milky Way. The mean GMC masses of M33 are about an order of magnitude lower than those of the Milky Way. A power-law fit to the mass spectrum gives values of $\alpha = 2.32 \pm 0.10$ for dust and $\alpha = 1.87 \pm 0.08$ for CO. These indices align with those found in other studies of M33, Milky Way values, and simulations, which all show a large spread.
2. There appears to be a limit to the sizes of GMCs of around 150 pc, as the distributions for the largest GMCs of M33 and Milky Way show similar shapes and a decline above ∼100 pc. We do not find the equivalent of GMFs in the Milky Way but note that there is an inter-cloud medium at column densities of around $10^{21}\,\mathrm{cm^{-2}}$ that contains a significant mass, in particular in the central region of M33. In the outskirts, the lower-column-density material encloses the GMCs, which is particularly evident in dust.
3. The surface mass densities for M33 are $22 \pm 5\,\mathrm{M_\odot\,pc^2}$ from dust and $16 \pm 6\,\mathrm{M_\odot\,pc^2}$ for CO, which are about an order of magnitude lower than the same values for the Milky Way. The increased surface mass density may suggest an increase in SFR. Finally, M33 shows similar patterns in some alternative characteristics to those observed in other nearby galaxies in the PHANGS survey.
4. We find no or only weak correlations between physical properties and galactocentric radius, but some results indicate a dependence on the larger-scale environment.
5. The central region of M33 displays slightly higher median values for parameters such as mass, average density, surface mass density, and dust temperature, but contains the GMCs with the smallest aspect ratios. The center hosts the most massive GMCs (except for NGC 604), which also exhibit the highest surface mass densities. However, as the center seems to be the region with the highest influence on star formation, the variations in physical parameters across the environments are predominantly minor in nature. The spiral arms mainly host the largest GMCs, while they contain most of the extreme outliers across different parameters, such as mass, surface mass density, size, and elongation. On the contrary, the outskirts generally feature the lowest median values, with the exception of average density and elongation. However, the majority of the GMCs, despite some outliers, do not seem to be significantly affected by the conditions of the galactic environment.
6. The power-law fits to the mass spectra derived from CO and dust vary with the galactic environment ($\alpha = 2.19 \pm 0.19$ for the center, $\alpha = 2.16 \pm 0.14$ for the spiral arms, and $\alpha = 2.32 \pm 0.11$ for the outskirts). These results are consistent with observations in the Milky Way, suggesting similar indices for both the inner and outer disk of our galaxy. However, the slope of the spiral arms decreases due to the high mass of GMC NGC 604. The remaining high-mass GMCs in the spiral arms have lower masses than those in the galaxy center. This complicates the identification of the physical mechanisms at work, as high interstellar radiation fields and shear forces are likely to disrupt more massive GMCs, whereas the absence of these mechanisms would enhance these parameters in the spiral arms.

Overall, we conclude that the center seems to have a slightly greater influence on GMC properties than the other environments, but that mechanisms operating at the cloud scale – notably stellar feedback – may have a similar or greater impact on GMCs than large-scale dynamics inherent to galactic environments.

Data availability

Full Tables 1 and 2 and the updated H_2 column density data are available at the CDS via anonymous ftp to `cdsarc.cds.unistra.fr` (`130.79.128.5`) or via `https://cdsarc.cds.unistra.fr/viz-bin/cat/J/A+A/692/A226`

Acknowledgements. E.K. and N.S. acknowledge support from the FEEDBACK-plus project of the BMWI via DLR, Project Number 50OR2217. E.K. acknowledges support by the BMWI via DLR, project number 50OK2101. S.K. acknowledges support from the Orion-Legacy project that is supported by the BMWI via DLR, project number 50OR2311. We gratefully acknowledge the Collaborative Research Center 1601 (SFB 1601 subprojects A6, B2 and B3) funded by the Deutsche Forschungsgemeinschaft (DFG, German Research Foundation) – 500700252. This research made use of astrodendro, a Python package to compute Dendrograms of Astronomical data (`http://www.dendrograms.org/`)

References

Bate, M. R., Bonnell, I. A., & Price, N. M. 1995, MNRAS, 277, 362
Berkhuijsen, E. M., Beck, R., & Tabatabaei, F. S. 2013, MNRAS, 435, 1598
Bigiel, F., Leroy, A., Walter, F., et al. 2008, AJ, 136, 2846
Bigiel, F., Bolatto, A. D., Leroy, A. K., et al. 2010, ApJ, 725, 1159
Blitz, L., & Rosolowsky, E. 2006, ApJ, 650, 933
Bolatto, A. D., Wolfire, M., & Leroy, A. K. 2013, ARA&A, 51, 207
Bonne, L., Kabanovic, S., Schneider, N., et al. 2023, A&A, 679, L5
Braine, J., Rosolowsky, E., Gratier, P., Corbelli, E., & Schuster, K. F. 2018, A&A, 612, A51
Carroll, B. W., & Ostlie, D. A. 2007, An Introduction to Modern Astrophysics (San Francisco: Addison-Wesley)
Casoli, F., & Combes, F. 1982, A&A, 110, 287
Chevance, M., Kruijssen, J. M. D., Hygate, A. P. S., et al. 2020, MNRAS, 493, 2872
Chevance, M., Kruijssen, J. M. D., Krumholz, M. R., et al. 2022, MNRAS, 509, 272
Chiang, I.-D., Sandstrom, K. M., Chastenet, J., et al. 2024, ApJ, 964, 18
Choi, W., Liu, L., Bureau, M., et al. 2023, MNRAS, 522, 4078
Clark, P. C., Glover, S. C. O., Ragan, S. E., & Duarte-Cabral, A. 2019, MNRAS, 486, 4622
Clark, C. J. R., Roman-Duval, J. C., Gordon, K. D., et al. 2023, ApJ, 946, 42
Cohen, R. S., Dame, T. M., & Thaddeus, P. 1986, ApJS, 60, 695
Colombo, D., Hughes, A., Schinnerer, E., et al. 2014, ApJ, 784, 3
Colombo, D., Duarte-Cabral, A., Pettitt, A. R., et al. 2022, A&A, 658, A54
Corbelli, E., Braine, J., Bandiera, R., et al. 2017, A&A, 601, A146
Corbelli, E., Elmegreen, B. G., Braine, J., & Thilker, D. 2018, A&A, 617, A125
Corbelli, E., Braine, J., & Giovanardi, C. 2019, A&A, 622, A171
Crockett, N. R., Garnett, D. R., Massey, P., & Jacoby, G. 2006, ApJ, 637, 741
Dame, T. M., Hartmann, D., & Thaddeus, P. 2001, ApJ, 547, 792
Dobbs, C. L. 2008, MNRAS, 391, 844
Dobbs, C. L., Burkert, A., & Pringle, J. E. 2011, MNRAS, 417, 1318
Dobbs, C. L., Krumholz, M. R., Ballesteros-Paredes, J., et al. 2014, in Protostars and Planets VI, eds. H. Beuther, R. S. Klessen, C. P. Dullemond, & T. Henning, 3
Dobbs, C. L., Pettitt, A. R., Corbelli, E., & Pringle, J. E. 2018, MNRAS, 478, 3793
Dobbs, C. L., Rosolowsky, E., Pettitt, A. R., et al. 2019, MNRAS, 485, 4997
Druard, C., Braine, J., Schuster, K. F., et al. 2014, A&A, 567, A118
Duarte-Cabral, A., & Dobbs, C. L. 2016, MNRAS, 458, 3667
Duarte-Cabral, A., & Dobbs, C. L. 2017, MNRAS, 470, 4261

Elmegreen, B. G. 1985, in Protostars and Planets II, eds. D. C. Black, & M. S. Matthews, 33
Elmegreen, B. G. 1990, ASP Conf. Ser., 12, 247
Elmegreen, B. G. 1996, IAU Symp, 169, 551
Elmegreen, B. G., & Elmegreen, D. M. 1986, ApJ, 311, 554
Fujimoto, M. 1968, ApJ, 152, 391
Fujita, S., Ito, A. M., Miyamoto, Y., et al. 2023, PASJ, 75, 279
Fukui, Y., Habe, A., Inoue, T., Enokiya, R., & Tachihara, K. 2021, PASJ, 73, S1
García, P., Bronfman, L., Nyman, L.-Å., Dame, T. M., & Luna, A. 2014, ApJS, 212, 2
Goicoechea, J. R., Pety, J., Cuadrado, S., et al. 2016, Nature, 537, 207
Goldsmith, P. F. 2001, ApJ, 557, 736
Goodman, A. A., Alves, J., Beaumont, C. N., et al. 2014, ApJ, 797, 53
Gratier, P., Braine, J., Rodriguez-Fernandez, N. J., et al. 2010, A&A, 522, A3
Gratier, P., Braine, J., Rodriguez-Fernandez, N. J., et al. 2012, A&A, 542, A108
Heitsch, F., Burkert, A., Hartmann, L. W., Slyz, A. D., & Devriendt, J. E. G. 2005, ApJ, 633, L113
Heitsch, F., Slyz, A. D., Devriendt, J. E. G., Hartmann, L. W., & Burkert, A. 2006, ApJ, 648, 1052
Henshaw, J. D., Ginsburg, A., Haworth, T. J., et al. 2019, MNRAS, 485, 2457
Heyer, M. H., Corbelli, E., Schneider, S. E., & Young, J. S. 2004, ApJ, 602, 723
Hughes, A., Meidt, S. E., Colombo, D., et al. 2013, ApJ, 779, 46
Jeffreson, S. M. R., & Kruijssen, J. M. D. 2018, MNRAS, 476, 3688
Karachentsev, I. D., Karachentseva, V. E., Huchtmeier, W. K., & Makarov, D. I. 2004, AJ, 127, 2031
Kasparova, A. V., & Zasov, A. V. 2008, Astron. Lett., 34, 152
Kauffmann, J., Bertoldi, F., Bourke, T. L., Evans, N. J. I., & Lee, C. W. 2008, A&A, 487, 993
Kauffmann, J., Pillai, T., Shetty, R., Myers, P. C., & Goodman, A. A. 2010, ApJ, 716, 433
Keilmann, E., Buchbender, C., Ossenkopf-Okada, V., et al. 2024, A&A, 688, A171
Kennicutt, R. C., & Evans, N. J. 2012, ARA&A, 50, 531
Kim, W.-T., & Ostriker, E. C. 2002, ApJ, 570, 132
Kobayashi, M. I. N., Inutsuka, S.-I., Kobayashi, H., & Hasegawa, K. 2017, ApJ, 836, 175
Kobayashi, M. I. N., Kobayashi, H., Inutsuka, S.-I., & Fukui, Y. 2018, PASJ, 70, S59
Kobayashi, M. I. N., Inoue, T., Inutsuka, S.-I., et al. 2020, ApJ, 905, 95
Kobayashi, M. I. N., Inoue, T., Tomida, K., Iwasaki, K., & Nakatsugawa, H. 2022, ApJ, 930, 76
Kobayashi, M. I. N., Iwasaki, K., Tomida, K., et al. 2023, ApJ, 954, 38
Koch, E. W., Rosolowsky, E. W., Lockman, F. J., et al. 2018, MNRAS, 479, 2505
Koch, E. W., Rosolowsky, E. W., Schruba, A., et al. 2019, MNRAS, 485, 2324
Koda, J., Scoville, N., Sawada, T., et al. 2009, ApJ, 700, L132
Kramer, C., Stutzki, J., Rohrig, R., & Corneliussen, U. 1998, A&A, 329, 249
Kramer, C., Buchbender, C., Quintana-Lacaci, G., et al. 2010, High. Astron., 15, 415
Kramer, C., Nikola, T., Anderl, S., et al. 2020, A&A, 639, A61
Krügel, E., & Siebenmorgen, R. 1994, A&A, 288, 929
Kruijssen, J. M. D., Schruba, A., Chevance, M., et al. 2019, Nature, 569, 519
Krumholz, M. R., McKee, C. F., & Tumlinson, J. 2008, ApJ, 689, 865
Krumholz, M. R., Burkhart, B., Forbes, J. C., & Crocker, R. M. 2018, MNRAS, 477, 2716
Larson, R. B. 1981, MNRAS, 194, 809
La Vigne, M. A., Vogel, S. N., & Ostriker, E. C. 2006, ApJ, 650, 818
Lehnert, M. D., van Driel, W., Le Tiran, L., Di Matteo, P., & Haywood, M. 2015, A&A, 577, A112
Leroy, A. K., Hughes, A., Schruba, A., et al. 2016, ApJ, 831, 16
Leroy, A. K., Schinnerer, E., Hughes, A., et al. 2021, ApJS, 257, 43
Li, C., Wang, H.-C., Wu, Y.-W., Ma, Y.-H., & Lin, L.-H. 2020, Res. Astron. Astrophys., 20, 031
Liu, L., Bureau, M., Li, G.-X., et al. 2022, MNRAS, 517, 632
Lombardi, M., Alves, J., & Lada, C. J. 2010, A&A, 519, L7
Lord, S. D., & Young, J. S. 1990, ApJ, 356, 135
Magrini, L., Stanghellini, L., Corbelli, E., Galli, D., & Villaver, E. 2010, A&A, 512, A63
Malhotra, S. 1995, ApJ, 448, 138
Marasco, A., Fraternali, F., van der Hulst, J. M., & Oosterloo, T. 2017, A&A, 607, A106
McKee, C. F., & Ostriker, E. C. 2007, ARA&A, 45, 565
Meidt, S. E., Hughes, A., Dobbs, C. L., et al. 2015, ApJ, 806, 72
Men'shchikov, A. 2021, A&A, 654, A78
Miura, R. E., Kohno, K., Tosaki, T., et al. 2014, ApJ, 788, 167
Miyamoto, Y., Nakai, N., & Kuno, N. 2014, PASJ, 66, 36
Moore, T. J. T., Urquhart, J. S., Morgan, L. K., & Thompson, M. A. 2012, MNRAS, 426, 701
Muraoka, K., Kondo, H., Tokuda, K., et al. 2020, ApJ, 903, 94
Muraoka, K., Konishi, A., Tokuda, K., et al. 2023, ApJ, 953, 164
Nguyen-Luong, Q., Nguyen, H. V. V., Motte, F., et al. 2016, ApJ, 833, 23
Offner, S. S. R., Bisbas, T. G., Bell, T. A., & Viti, S. 2014, MNRAS, 440, L81
Park, G., Currie, M. J., Thomas, H. S., et al. 2023, ApJS, 264, 16
Patel, E., Carlin, J. L., Tollerud, E. J., Collins, M. L. M., & Dooley, G. A. 2018, MNRAS, 480, 1883
Peltonen, J., Rosolowsky, E., Johnson, L. C., et al. 2023, MNRAS, 522, 6137
Pettitt, A. R., Dobbs, C. L., Baba, J., et al. 2020, MNRAS, 498, 1159
Phiri, S. P., Kirk, J. M., Ward-Thompson, D., Sansom, A. E., & Bendo, G. J. 2021, MNRAS, 504, 4511
Pineda, J. E., Arzoumanian, D., Andre, P., et al. 2023, ASP Conf. Ser., 534, 233
Poglitsch, A., Krabbe, A., Madden, S. C., et al. 1995, ApJ, 454, 293
Querejeta, M., Schinnerer, E., Meidt, S., et al. 2021, A&A, 656, A133
Querejeta, M., Leroy, A. K., Meidt, S. E., et al. 2024, A&A, 687, A293
Ragan, S. E., Henning, T., Tackenberg, J., et al. 2014, A&A, 568, A73
Ragan, S. E., Moore, T. J. T., Eden, D. J., et al. 2016, MNRAS, 462, 3123
Ramambason, L., Lebouteiller, V., Madden, S. C., et al. 2024, A&A, 681, A14
Regan, M. W., & Vogel, S. N. 1994, ApJ, 434, 536
Relaño, M., Verley, S., Pérez, I., et al. 2013, A&A, 552, A140
Renaud, F., Bournaud, F., Emsellem, E., et al. 2015, MNRAS, 454, 3299
Rey-Raposo, R., Dobbs, C., Agertz, O., & Alig, C. 2017, MNRAS, 464, 3536
Rice, W., Boulanger, F., Viallefond, F., Soifer, B. T., & Freedman, W. L. 1990, ApJ, 358, 418
Rice, T. S., Goodman, A. A., Bergin, E. A., Beaumont, C., & Dame, T. M. 2016, ApJ, 822, 52
Roberts, W. W. 1969, ApJ, 158, 123
Rohlfs, K., & Wilson, T. L. 1996, Tools of Radio Astronomy
Röllig, M., Ossenkopf, V., Jeyakumar, S., Stutzki, J., & Sternberg, A. 2006, A&A, 451, 917
Roman-Duval, J., Jackson, J. M., Heyer, M., Rathborne, J., & Simon, R. 2010, ApJ, 723, 492
Rosolowsky, E. 2005, PASP, 117, 1403
Rosolowsky, E., & Leroy, A. 2006, PASP, 118, 590
Rosolowsky, E., & Simon, J. D. 2008, ApJ, 675, 1213
Rosolowsky, E., Keto, E., Matsushita, S., & Willner, S. P. 2007, ApJ, 661, 830
Rosolowsky, E. W., Pineda, J. E., Kauffmann, J., & Goodman, A. A. 2008, ApJ, 679, 1338
Rosolowsky, E., Hughes, A., Leroy, A. K., et al. 2021, MNRAS, 502, 1218
Schinnerer, E., & Leroy, A. K. 2024, ARA&A, 62, 369
Schinnerer, E., Meidt, S. E., Pety, J., et al. 2013, ApJ, 779, 42
Schneider, N., & Brooks, K. 2004, PASA, 21, 290
Schneider, N., Bontemps, S., Simon, R., et al. 2011, A&A, 529, A1
Schneider, N., Bonne, L., Bontemps, S., et al. 2023, Nat. Astron., 7, 546
Shu, F. H., Milione, V., Gebel, W., et al. 1972, ApJ, 173, 557
Silva-Villa, E., & Larsen, S. S. 2012, A&A, 537, A145
SIMBAD 2024, SIMBAD Astronomical Database: Central Coordinates of M33 accessed: 2024-10-29
Simon, R., Jackson, J. M., Clemens, D. P., Bania, T. M., & Heyer, M. H. 2001, ApJ, 551, 747
Spilker, A., Kainulainen, J., & Orkisz, J. 2022, A&A, 667, A110
Stark, A. A., Bolatto, A. D., Chamberlin, R. A., et al. 1997, ApJ, 480, L59
Stutzki, J., & Guesten, R. 1990, ApJ, 356, 513
Su, Y., Yang, J., Zhang, S., et al. 2019, ApJS, 240, 9
Sun, J., Leroy, A. K., Schruba, A., et al. 2018, ApJ, 860, 172
Sun, J., Leroy, A. K., Ostriker, E. C., et al. 2020a, ApJ, 892, L48
Sun, J., Leroy, A. K., Schinnerer, E., et al. 2020b, ApJ, 901, L8
Sun, Y., Yang, J., Yan, Q.-Z., et al. 2021, ApJS, 256, 32
Tabatabaei, F. S., Braine, J., Xilouris, E. M., et al. 2014, A&A, 561, A95
Tamburro, D., Rix, H. W., Leroy, A. K., et al. 2009, AJ, 137, 4424
Urquhart, J. S., Figura, C., Cross, J. R., et al. 2021, MNRAS, 500, 3050
van der Marel, R. P., Fardal, M., Besla, G., et al. 2012, ApJ, 753, 8
Vazquez-Semadeni, E., Passot, T., & Pouquet, A. 1995, ApJ, 441, 702
Wadsley, J. W., Keller, B. W., & Quinn, T. R. 2017, MNRAS, 471, 2357
Wang, J., Koribalski, B. S., Jarrett, T. H., et al. 2017, MNRAS, 472, 3029
Wang, Y., Beuther, H., Schneider, N., et al. 2020, A&A, 641, A53
Williams, J. P., Blitz, L., & Stark, A. A. 1995, ApJ, 451, 252
Williams, T. G., Gear, W. K., & Smith, M. W. L. 2019, MNRAS, 483, 5135
Willner, S. P., & Nelson-Patel, K. 2002, ApJ, 568, 679
Wilson, C. D. 1997, ApJ, 487, L49
Wolfire, M. G., Hollenbach, D., & McKee, C. F. 2010, ApJ, 716, 1191
Yu, S.-Y., Ho, L. C., & Wang, J. 2021, ApJ, 917, 88
Zucker, C., Battersby, C., & Goodman, A. 2015, ApJ, 815, 23
Zucker, C., Battersby, C., & Goodman, A. 2018, ApJ, 864, 153

Appendix A: IRAM ^{12}CO$(2-1)$ line-integrated intensity map of M33

Figure A.1 shows the ^{12}CO$(2-1)$ map of M33 obtained with the IRAM 30m telescope (Gratier et al. 2010; Druard et al. 2014).

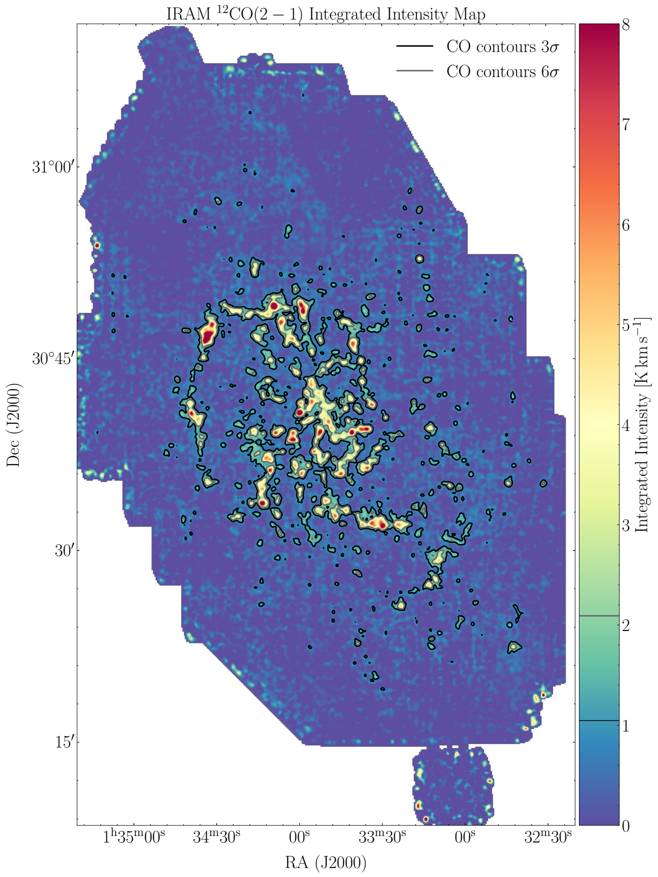

Fig. A.1. ^{12}CO$(2-1)$ line-integrated intensity map of M33 (Druard et al. 2014). The map has been smoothed to the resolution of 18.2″ and re-gridded to the coordinate grid of the SPIRE 250 μm map.

Appendix B: $X_{\rm CO}$ factor map of M33

Figure B.1 displays the $X_{\rm CO}$ factor map defined as the dust-derived $N_{\rm H_2}$ over CO line-integrated intensity at each position in M33 at 18.2″ and scaled with the CO$(\frac{2-1}{1-0})$ line ratio (Druard et al. 2014) to CO$(1-0)$ intensity. See Paper I for more details.

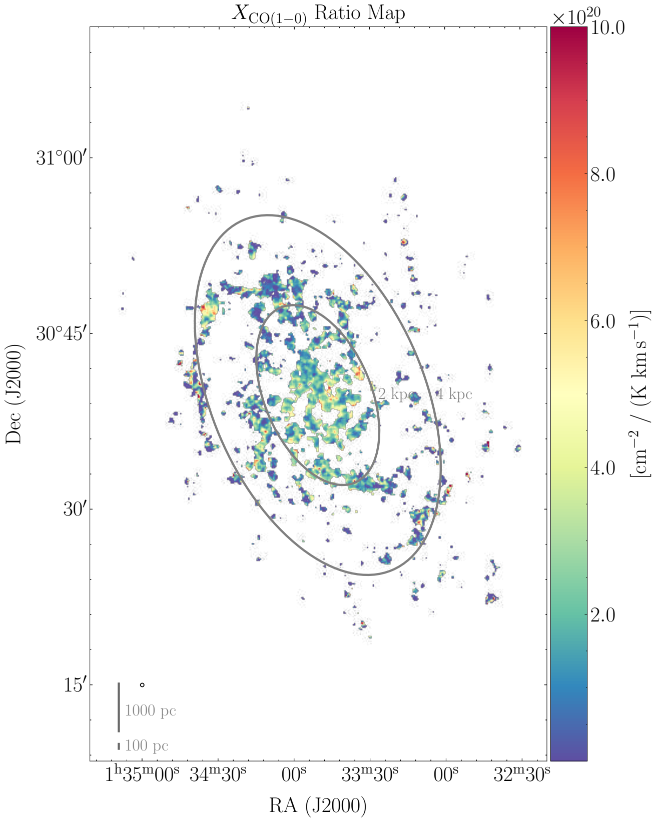

Fig. B.1. $X_{\rm CO}$ factor (ratio) map of Method I of Paper I. The two ellipses represent a circular radius equivalent to 2 and 4 kpc.

Appendix C: Influence of Dendrogram parameters on the GMC statistics

We conducted a Dendrograms parameter study by changing the `min_value` and the beam factor for cloud selection. Obviously, increasing these parameters results in the identification of larger and more massive GMCs, whereas changing `min_delta` practically does not alter the results. Nevertheless, the undetected residual emission became more substantial, while the results change non-significantly considering the uncertainties. Consequently, we conclude that the use of 3σ for `min_value` and a beam factor of 1.2 are the optimal settings for the Dendrogram analysis. Tables C.1 and C.2 list the mean values of the main properties of the dust- and CO-derived GMCs for a `min_value` of 5σ and a beam factor of 1.5. We further illustrate the results for a subset of the plots discussed above. Figure C.1 shows the distributions of the radii and surface mass densities for both varied parameters. The size is mainly unchanged, while a `min_value` of 5σ excludes the low-mass GMCs, leading to an overall shift towards higher values in mass and (surface mass) densities. However, the change is still low.

The effect on the galactocentric radius dependence as an example for the mass and density is marginally shifted to higher values. Furthermore, there is no notable trend with the galactocentric radius for any of the other properties, similar to the result found with a `min_value` of 3σ and a beam factor of 1.2.

For the power-law slopes, the increase in the slope for dust-derived data is insignificant. For CO, the slope rises from 1.87 to 2.03. However, considering the uncertainties, the change falls within the margin of error.

This analysis confirms that our selected Dendrogram parameters are robust and produce reliable results.

Appendix D: CO luminosity

For completeness and to enable comparison to other studies, we display in Fig. D.1 the ^{12}CO$(1-0)$ luminosity $L_{\rm CO}$ of M33, using the CO$(2-1)$/CO$(1-0)$ line ratio of 0.8 from Druard et al. (2014). The mean CO luminosity is $(9.2 \pm 2.0) \times 10^4$ K km s^{-1} pc^2, which is lower than the value of 3×10^5 K km s^{-1} pc^2 for the CO$(2-1)$ IRAM data at 12″, which corresponds to 3.75×10^5 K km s^{-1} pc^2 for CO$(1-0)$ applying the same line ratio of 0.8. Hughes et al. (2013) present M33 data from their observations of CO$(1-0)$, indicating values

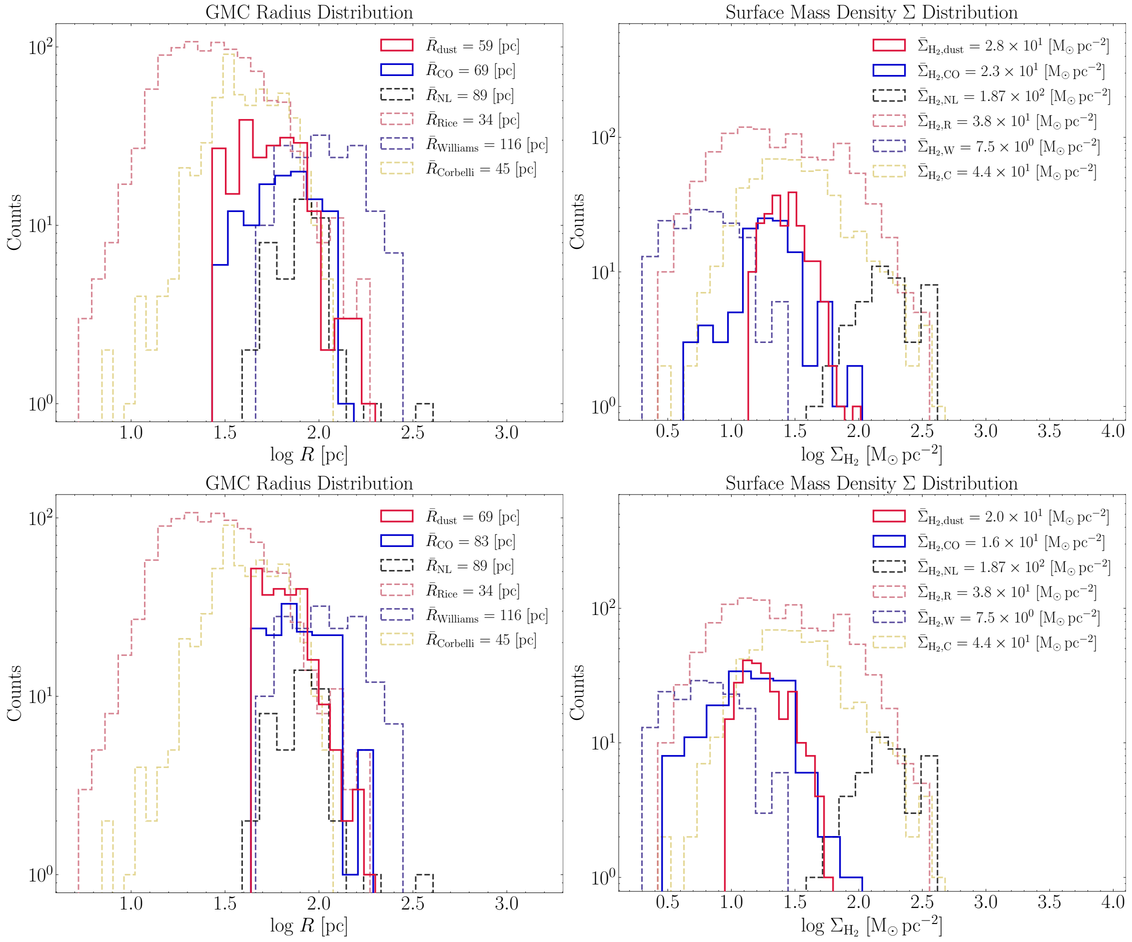

Fig. C.1. Distributions of GMC properties with varying Dendrogram parameters. The upper panels show histograms of radius and surface mass density with a `min_value` of 5σ. The lower panels display the same properties for a beam factor of 1.5.

Table C.1. Mean properties of dust-derived GMCs.

	`min_value` = 5σ	**beam factor = 1.5**
GMCs	214	242
M [×10^5 M$_\odot$]	3.5 ± 1.1	3.6 ± 1.1
n [cm^{-3}]	7 ± 3	3 ± 1
Σ [M$_\odot$ pc^{-2}]	28 ± 7	20 ± 5
R [pc]	59 ± 11	69 ± 12
$\kappa_{\rm Mass-Size}$	1.8 ± 0.1	2.0 ± 0.1
AR	1.9	1.9
α	2.38 ± 0.13	2.42 ± 0.12

Notes. The table shows the mean values for the parameters obtained with varying the Dendrogram parameters.

Table C.2. Mean properties of CO-derived GMCs.

	`min_value` = 5σ	**beam factor = 1.5**
GMCs	111	153
M [×10^5 M$_\odot$]	4.0 ± 2	3.8 ± 2
n [cm^{-3}]	4 ± 2	2 ± 1
Σ [M$_\odot$ pc^{-2}]	23 ± 9	16 ± 7
R [pc]	69 ± 15	83 ± 17
$\kappa_{\rm Mass-Size}$	2.0 ± 0.2	2.2 ± 0.2
AR	1.5	1.7
α	2.03 ± 0.12	2.13 ± 0.12
$L_{\rm CO}$	1.5 ± 0.1	1.8 ± 0.1

Notes. The table shows the mean values for the parameters obtained with varying the Dendrogram parameters.

around 1 × 10^5 K km s^{-1} pc^2. A slope of 1.5 indicates that the CO emission of smaller GMCs is faster saturated compared to larger GMCs. In other words, more CO emission per area can be accounted for in the outer regions of GMCs.

Appendix E: Trends with galactocentric radius of M33

It is evident across all parameters that the majority of GMCs do not exhibit a significant trend with the galactocentric radius. This observation is supported by Spearman correlation coefficients[6] ranging from |8.7 × 10^{-4}| to |0.4|, showing no or only low correlation at best (except for the temperature, which clearly shows

---

[6] The Spearman correlation coefficient is suitable for all types of monotonic relationships, whether linear or nonlinear, and does not require the data to follow a normal distribution. It ranges from −1 to 1, where −1 indicates a strong negative correlation, 0 no correlation and 1 a strong positive correlation. Given that the Spearman correlation coefficient is effective for both linear and nonlinear relationships, it does not differentiate between these types of correlations.

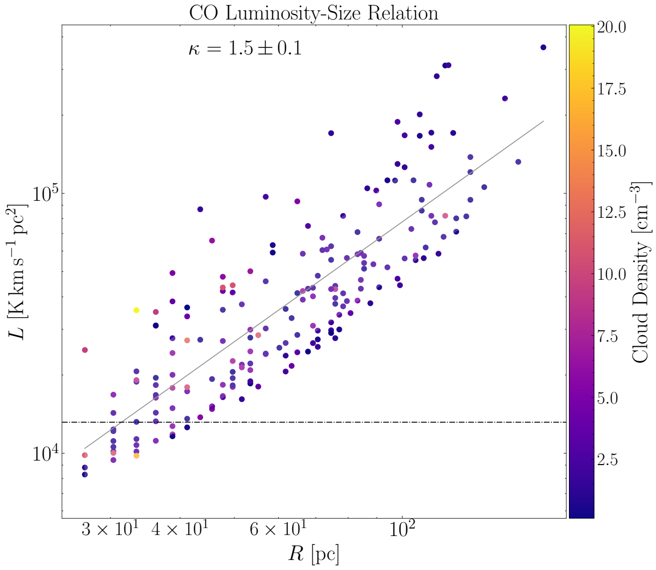

Fig. D.1. CO(1 − 0) luminosity-size relation of the structures identified in the CO data. The horizontal line represents the 2σ sensitivity limit.

a gradient; see Tabatabaei et al. 2014; Keilmann et al. 2024). Nonetheless, upon closer inspection of the GMCs at the extreme ends of the spectra, there is a subtle trend of mostly decreasing values with increasing galactocentric radius, especially for the surface mass density and average number density. Extreme GMCs, that is, GMCs at the tails of the distributions, enhanced in particular large-scale galactic environments, may suggest the presence of physical mechanisms directly enabling the development of particular cloud types in specific galactic regions, potentially influencing SF. We consider GMCs with surface mass densities above 40 $M_\odot$ pc^2 to account for an analysis of whether and how extreme clouds may depend on the galactocentric radius. The corresponding GMCs are depicted as thicker and darker pentagons in the following figures.

E.1. GMC masses with galactocentric radius

Specifically, for dust-traced masses, GMCs located within approximately 2 kpc demonstrate an increase toward the center for those with the lowest masses. This pattern is absent in CO-traced GMCs. This could be due to strong interstellar radiation fields, which photo-dissociate CO (Offner et al. 2014), leading to less CO emission in the center. The remaining GMCs beyond 2 kpc do not show a dependence on the galactocentric radius for both tracers. The Spearman correlation coefficients show practically no correlation with galactocentric radius over the whole data range. For the most massive GMCs observed with both tracers, their highest masses decrease with galactocentric radius, supporting Corbelli et al. (2017), who found a similar decrease beyond 4.5 kpc. The GMCs with the most extreme surface mass density values are not those with the highest masses; they appear to be arbitrarily distributed in terms of mass; see Fig. 7 (top left). The data point around 4 kpc is NGC 604. In the case of branches, the median mass is 2×10^5 $M_\odot$. Additionally, there are structures with increased masses within low galactocentric radii below 1 kpc. The remaining structures show a similar trend to the GMCs (leaves) with a slightly higher correlation coefficient of −0.5, which is still only a moderate correlation.

According to their simulation, Dobbs et al. (2019) report that the masses of GMCs are influenced by the distance from the center of M33. Their findings exhibit a resemblance to our results, particularly in the case of the most massive GMCs, showing a correlation with the galactocentric radius. Nevertheless, Dobbs et al. (2019) did not provide a quantitative assessment of this dependency, making direct comparisons difficult. Due to the similarity in the plots showing that the majority of the clouds do not seem to depend strongly on the galactocentric radius, it is possible that the actual dependency they state is similar in magnitude to what we quantify.

The lack of correlation between cloud mass and R_{gal} likely results from a balance between the more compact and therefore more luminous clouds at the galaxy center and the diffuse and hence more extended sources in the outskirts. Williams et al. (2019) identified a higher, yet still weak correlation between mass and galactocentric radius with a Kendall rank correlation coefficient[7] of 0.12.

E.2. GMC average densities with galactocentric radius

While, as in the case of masses, a subtle trend of the least dense GMCs is also noticeable in dust-traced GMCs in terms of average density, it is not observed in those traced by CO. In contrast, GMCs with the highest densities tend to be more concentrated toward the inner disk of M33, as indicated by dust-derived GMCs and to a lesser extent by the CO-derived GMCs. Almost all of these most dense GMCs are also those which have the highest surface mass densities. This is not surprising, as the number and the surface mass density are closely related. However, the overall correlation is absent, as in the case of the masses. The Spearman correlation coefficients practically do not quantify the correlation. Structures identified as branches show a median density of 1.1 cm^{-3} and exhibit a slightly higher correlation coefficient of 0.3, which is still only a weak correlation.

E.3. GMC surface mass densities with galactocentric radius

Since the masses are divided by the area of a GMC, the surface mass density is somewhat less dependent on the resolution, making it comparably easier to compare with other studies.

The surface mass density (Fig. 7, bottom left) exhibits a similar pattern as for the mass among dust-traced GMCs considering the GMCs with the lowest surface mass densities found within 2 kpc. For both tracers, GMCs located at the higher end of the spectrum demonstrate a slight tendency to exhibit a higher surface mass density as the galactocentric radius decreases.

The only strong connections to the other parameters are the radius (see Sect. E.4 and bottom right of Fig. 7) and the averaged number density (upper right of Fig. 7). The number density is related to the surface mass density in a natural way, which does not reveal new surprising insights.

The overall correlation for all data points in CO is practically absent, while for dust-derived GMCs a low correlation of −0.2 is determined. Thus, also the surface mass density seems to have no strong dependence on the galactocentric radius.

In the case of branches, the dependency is similar with a median value of 18 $M_\odot$ pc^{-2} and a doubled but still only lower moderate correlation coefficient of −0.4.

---

[7] The Kendall rank correlation coefficient measures non-parametrically how well a monotonic function describes the relationship between two variables without assuming their probability distributions. It indicates the similarity in rank orderings of data when sorted by each quantity. High Kendall correlation means similar ranks between variables (correlation of 1), while low means dissimilar ranks (correlation of −1).

E.4. GMC radii with galactocentric radius

Considering the radius, the data points suggest that there is no clear pattern with the galactocentric radius, which is further supported by the nearly nonexistent or very weak correlation of −0.3. However, there are also a small number of GMCs with the largest radii close to the center, which are not those with the highest surface mass densities. Instead, the GMCs with the highest surface mass density are preferably the smallest ones.

The branches show a median radii of 185 pc with very large structures within a galactocentric radius below 1 kpc. This mainly increases the correlation coefficient to a moderate value of −0.5.

E.5. GMC elongations with galactocentric radius

In terms of AR (Fig. 8, left), dust-derived GMCs that are most elongated tend to be situated farther away from the galaxy's center, typically beyond approximately 3 kpc, whereas the majority of GMCs do not show a clear trend, showing a weak correlation coefficient of 0.2. CO-derived GMCs exhibit a similar distribution with little to no correlation, with the most elongated GMCs to a low extent found in the mid-range between ∼ 2 kpc and ∼ 5 kpc of the galaxy. However, the most extreme GMCs do not follow a consistent pattern. For both tracers, there seems to be no distinct pattern regarding the GMCs with the highest surface mass densities. The overall elongation of CO-derived GMCs is less compared to dust-derived GMCs with a median of 1.6, which aligns with the contours of the CO-derived structures in Fig. 2.

An almost unchanged elongation is found for the branches with a median value of 2.1 and a reduced correlation coefficient of 0.1.

E.6. GMC temperatures with galactocentric radius

The data points for the temperature show a dependency with galactocentric radius to some extent (Fig. 8, right). However, some data points beyond roughly 2.5 kpc deviate distinctly from the remaining data points. This leads to the most significant correlation with the galactocentric radius among all the parameters analyzed, which is −0.4 and −0.6 for dust- and CO-derived GMCs, respectively. This is a weak to moderate correlation. Interestingly, Williams et al. (2019) find only a weak correlation of −0.26. In the case of branches, a similar trend is found with a slightly higher median temperature of 21.5 K and a correlation coefficient of −0.7. This is the strongest correlation found in this study. A natural explanation for the decreasing dust temperature is the overall decrease in intensity of the interstellar radiation field with increasing galactocentric radius (Rice et al. 1990).

A compelling relationship emerges when higher pressures appear to result in less elongated GMCs (indicated by higher densities and temperatures in the central region). Such a phenomenon could possibly be attributed to the pervasive pressure within the central region (Sun et al. 2020a,b) as a result of the stronger galactic potential, which acts uniformly, resulting in more isotropically shaped GMCs. In contrast, GMCs located in the outer regions appear to be influenced by pressure originating predominantly from a specific direction, causing forces that are not uniformly distributed across all GMCs. Those at mid-range distances (presumably located in the spiral arms) could be elongated when exiting the spiral arm and therefore its gravitational potential. It is also possible that stellar feedback causes those GMCs to elongate. Nevertheless, this phenomenon appears to be relevant solely to the GMCs lying at the tail of the spectra, specifically those with the greatest elongation.

Appendix F: Galactic environments of M33

We constructed an unsharp-masked image of the N_{H_2} map and identified the densest points along the spiral arms on our N_{H_2} map. This is different to Querejeta et al. (2021), who use stellar densities and a morphological decomposition based on Spitzer 3.6 µm. However, since we intend to define the spiral arms for GMCs, which are located in H_2 gas, we use our N_{H_2} map for this decomposition. The coordinates of the densest points were deprojected to the plane of the galaxy (using an inclination of 56° and a position angle of 23°). The fit was then performed in logarithmic polar coordinates. The log-spiral fit was projected back to the plane of the sky and is shown in Fig. F.1. It matches the areas of the spiral arms very well by eye-inspection. From this result, the asymmetry of both spiral arms becomes obvious. The northern spiral arm is wound stronger with a higher pitch angle starting from the center compared to the southern spiral arm. Overall, we distinguish three galactic environments: center, spiral arms and outskirts onto the dust-derived N_{H_2} map. We have chosen a circle of 1.3 kpc for the center to distinguish from the spiral arms and outskirts. This radius was selected since it encompasses the maximum column density distribution of the central region, while still maintaining reasonable borders for the fitted spiral arms.

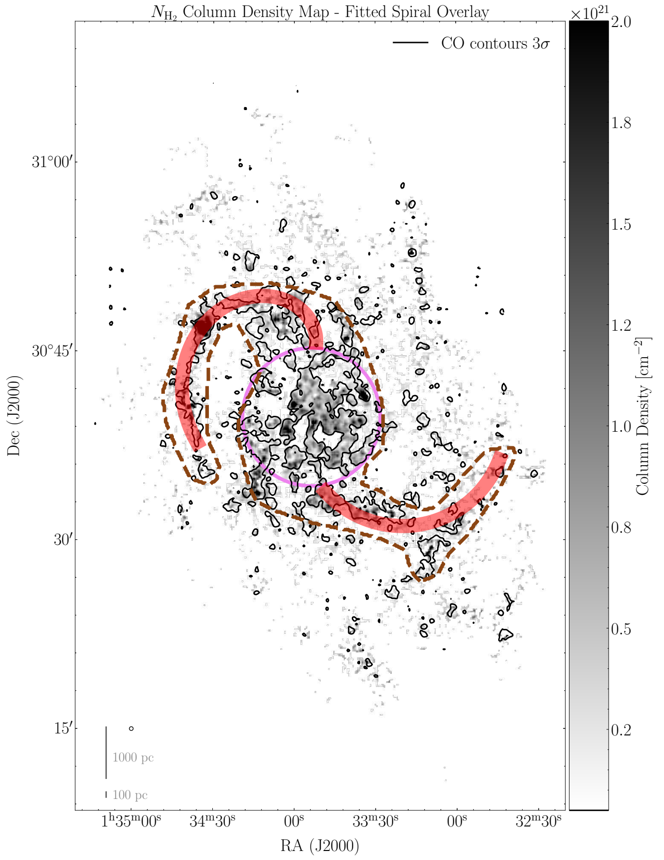

Fig. F.1. The dust-derived N_{H_2} map shows the boundaries of three galactic environments: the center (dashed pink lines), spiral arms (dashed brown lines) and outskirts (remaining area). Center coordinates are RA(2000) = $1^h33^m50^s$, Dec(2000) = 30°39′37″ (SIMBAD 2024). The result of the log-spiral fit is shown in red.

5.3 RCW79 (Keilmann et al., 2025)

Recent studies on stellar feedback, focusing on [C II] as an indicator of gas dynamics, have provided considerable insight into the formation and expansion of H II region bubbles within the ISM. The [C II] 158 μm fine-structure line has become an excellent tool for tracing the kinematics of ionized gas and the interfaces between molecular clouds and H II regions (Beuther et al., 2022), enabling the examination of bubble structures and feedback dynamics. Observations indicate that ionizing radiation and stellar winds shape H II regions by producing expanding shells in [C II] emission. These expanding bubbles, detected in various star-forming regions, are driven by strong stellar winds – beyond what thermal expansion alone can explain – and can also arise from a flattened molecular cloud breaking out of its natal cloud or during cloud dispersal (Pabst et al., 2020; Luisi et al., 2021; Beuther et al., 2022; Kabanovic et al., 2022; Bonne et al., 2023).

In the Letter to the Editor Keilmann et al. (2025), I perform a comprehensive analysis of the compact H II region within RCW79. An O7.5–9.5V/III star ionizes its local environment, leading to [C II] emissions. This emission creates a bubble within the larger RCW79 bubble (a bubble in a bubble), characterized by a low expansion velocity of approximately 2.6 km s^{-1}, which I have fitted with PV cuts. For the first time, a bubble "filled" with [C II] emission has been observed. This indicates an early evolutionary state that is consistent with the low expansion velocities, which lead to a short dynamical timescale. Position-velocity cuts and channel maps reveal that while the bubble is filled with [C II], there is yet a central emission dip. This dip is attributed in part to self-absorption and may be the cause of the so-called [C II]-deficit.

However, self-absorption of the [C II] line occurs only if the line is optically thick. I verify this condition using the optically thin ^{13}[C II] line, which consists of three hyperfine-structure (HFS) transitions. Since the [C II] line and its HFS lines lie close to each other in observed spectra, I was able to fit the radiative transfer equations for the [C II] HFS to the spectra wings that exhibit double-peaks due to self-absorption. I automatically detect two peaks in each spectrum and fit the [C II] HFS to the outer wings (after subtracting the blue- and red-shifted high-velocity gas from the superordinate RCW79 shell, see also Sect. 4.7.4). Additionally, I employ the two-layer multicomponent model to solve the radiative transfer equations, determine a lower limit for the excitation temperature, and further identify and quantify self-absorption effects. The spectra have been qualitatively modeled using SimLine, supporting self-absorption as one cause for the double-peaks (while the other cause is the low expansion velocity). I show that the observed [C II]-deficit in RCW79 can be explained by [C II] self-absorption effects. In addition, I have performed further calculations to ascertain the feedback processes that drive the bubble (Sect. 5.3.2).

My contributions to this Letter to the Editor are as follows. I took the lead in this study and produced all plots except for Figs. C.1 and C.2 in the Appendix C. I have reduced the APEX CO 6 → 5 data (along with not yet presented ^{13}CO 6 → 5 and C^{18}O 3 → 2 data) and tested all outcomes with data at different angular and spectral resolutions. I produced PV cuts and fitted ellipses to all of them to quantify the expansion velocity of the [C II]-filled bubble, resulting in $v_{\rm exp} \sim 2.6$ km s^{-1}.

I extensively analyzed the spectra in RCW79 to quantify the [C II] optical depth. Unfortunately, we did not detect [^{13}C II] at each position in RCW79. Thus, I analyzed the spectra, for example, for optical depth. I generated an optical depth map of [C II] based on Eq. 2.57 (which is not shown in the letter) that exhibits an average optical depth of the [C II] line of $\sim$4. I computed the average [C II] spectrum for a region identified with

Dendrograms, from which I additionally was able to derive the average optical depth of $\tau_{[\mathrm{C\,II}]} = 4.29$. This average spectrum then was the input data for the two-layer model, which I implemented and applied to these data (which was cross-checked by a co-author).

To analyze the [C II]-deficit, I developed a method to automatically detect signals and reconstruct missing fluxes (also see Sect. 4.7.4), and computed correction factors. From these spectra, I fitted Gaussian "background" components corresponding to the large-scale shell of RCW79 and subtracted these from the spectra. Next, I reconstructed the missing flux as a function of the excitation temperature T_{ex} and optical depth τ, from which I computed a "corrected" line-integrated intensity map and a corresponding correction factor map. I analyzed these maps alongside the FIR map produced via SED fits and also determined the correction factor's dependence on T_{ex}. For all data analysis, the Python code that I developed was transmitted to the FEEDBACK consortium and will be used for further studies on other sources. I have also cross-checked, reviewed, and redid the determination of the FIR maps. By utilizing what I had produced and analyzed, I was then able to evaluate the [C II]/FIR correlation to investigate the [C II]-deficit with both the measured [C II] map and the "corrected" version I generated. I also have produced all movies related to this study.

Initially, one of the original questions was regarding the driving mechanisms of the compact H II region in RCW79. Therefore, I also performed calculations related to stellar feedback. These include calculating the masses in the shells/bubble as well as the resulting energies and momenta. The results are not included in the letter, but parts of it are shown in Sect. 5.3.2.

I led all discussions about the progress and interpretation of the study, receiving many helpful suggestions (comments, feedback, ideas) from the co-authors.

Lastly, I basically wrote the entire main part of the letter. Additionally, I have written Appendix A, co-written Appendix B, and contributed in Appendix C. The co-authors also provided minor edits on the main part. However, once again I received many helpful comments and feedback from the co-authors, which strengthened the paper and enriched my understanding.

5.3.1 A Bubble in a Bubble - [C II]-deficit Caused by [C II] Self-Absorption in RCW79

A&A, 697, L2 (2025)
https://doi.org/10.1051/0004-6361/202453445

Astronomy & Astrophysics

LETTER TO THE EDITOR

[C II]-deficit caused by self-absorption in an ionized carbon-filled bubble in RCW79

E. Keilmann[1,⋆], S. Dannhauer[1], S. Kabanovic[1], N. Schneider[1], V. Ossenkopf-Okada[1], R. Simon[1], L. Bonne[2], P. F. Goldsmith[3], R. Güsten[4], A. Zavagno[5,6], J. Stutzki[1], D. Riechers[1], M. Röllig[7,1], J. L. Verbena[1], and A. G. G. M. Tielens[8,9]

[1] I. Physikalisches Institut, Universität zu Köln, Zülpicher Straße 77, 50937 Köln, Germany
[2] SOFIA Science Center, USRA, NASA Ames Research Center, Moffett Field, CA 94 045, USA
[3] Jet Propulsion Laboratory, California Institute of Technology, 4800 Oak Grove Drive, Pasadena, CA 91109-8099, USA
[4] Max-Planck Institut für Radioastronomie, Auf dem Hügel 69, 53121 Bonn, Germany
[5] Aix Marseille Univ., CNRS, CNES, LAM, Marseille, France
[6] Institut Universitaire de France, 1 Rue Descartes, Paris, France
[7] Physikalischer Verein, Gesellschaft für Bildung und Wissenschaft, Robert-Mayer-Str. 2, 60325 Frankfurt, Germany
[8] University of Maryland, Department of Astronomy, College Park, MD 20742-2421, USA
[9] Leiden Observatory, PO Box 9513, 2300 RA Leiden, The Netherlands

Received 13 December 2024 / Accepted 8 April 2025

ABSTRACT

Recent spectroscopic observations of the [C II] 158 μm fine-structure line of ionized carbon (C^+), using the Stratospheric Observatory for Infrared Astronomy (SOFIA), have revealed expanding [C II] shells in Galactic H II regions. We report the discovery of a bubble-shaped source (S144 in RCW79 in the GLIMPSE survey), associated with a compact H II region, excited by a single O7.5–9.5V/III star, which is consistent with a scenario that the bubble is still mostly "filled" with C^+. This indicates most likely a very early evolutionary state, in which the stellar wind has not yet blown material away as it has in more evolved H II regions. Using the SimLine non-local thermodynamic equilibrium radiative transfer code, the [C II] emission can be modeled to originate from three regions: first, a central H II region with little C^+ in the fully ionized phase, followed by two layers with a gas density around 2500 cm^{-3} of partially photodissociated gas. From these two layers, the second layer is a slowly expanding [C II] shell with an expansion velocity of ~2.6 km s^{-1} that corresponds approximately to a bright ring at 8 μm. The outermost layer exhibits a temperature and velocity gradient that produces the observed self-absorption features in the optically thick [C II] line ($\tau \sim 4$), leading to an apparent deficit in [C II] emission and a low ratio of [C II] to total far-infrared (FIR) emission. We developed a procedure to reconstruct the missing [C II] flux and find a linear correlation between [C II] and FIR without a [C II]-deficit after incorporating the missing [C II] flux. This example demonstrates that at least some of the [C II]-deficit found in Galactic H II bubbles can be attributed to self-absorption, although a broader sample of these objects needs to be studied to fully constrain the range of conditions in which [C II]-deficits can be explained by this process.

Key words. ISM: bubbles – evolution – HII regions – ISM: kinematics and dynamics – photon-dominated region (PDR) – infrared: ISM

1. Introduction

Recent spectroscopic studies of Galactic H II regions in the 158 μm line of ionized carbon ([C II]) have confirmed that this far-infrared (FIR) fine-structure line is a key tracer for the cooling processes and the dynamics of gas in photodissociation regions (PDRs). Exploratory observations have discovered expanding [C II] shells, e.g. in Orion (Pabst et al. 2019) and in FEEDBACK (Schneider et al. 2020) galactic H II region bubbles such as RCW120 (Luisi et al. 2021), using large maps of [C II] obtained with the Stratospheric Observatory for Infrared Astronomy (SOFIA). With velocities of up to 15 km s^{-1}, the shell expansion is mostly attributed to be driven by stellar winds of massive stars and not to the thermal expansion of the H II region.

These examples underline the potential of [C II] to trace the evolution of an H II region and its related molecular cloud. In this study, we report the detection of a C^+ bubble in a very early evolutionary phase, designated as S144, in the *Spitzer*/GLIMPSE survey (Churchwell et al. 2006). The 8 μm emission (Fig. 1) exhibits a bright infrared (IR) ring with an opening in the northeast (NE) and moderate emission inside the ring, except for a concentrated peak around the exciting O7.5–9.5V/III star. S144 is embedded in the southeastern (SE) PDR ring outside of the larger H II region RCW79. Figure 2 (top) presents the [C II] emission from the PDR ring of RCW79 and the associated molecular cloud fragments (Bonne et al. 2023). The bottom panel illustrates that the [C II] (as the 8 μm) emission from S144 does not exhibit a central void.

The diameter of S144 (Fig. 2) is about 1.5′, corresponding to 1.7 pc at a distance of 3.9 kpc (Bonne et al. 2023). S144 is

---

[⋆] Corresponding author: `keilmann@ph1.uni-koeln.de`

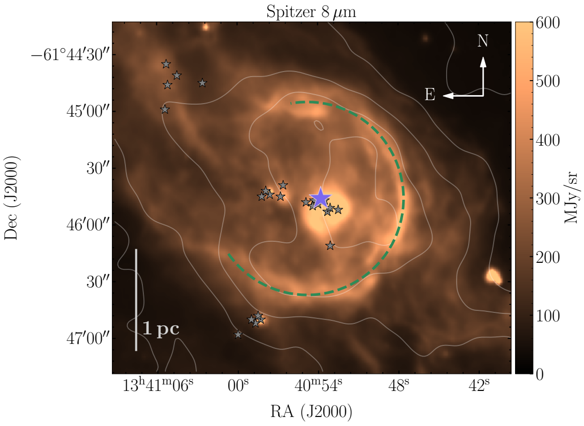

Fig. 1. *Spitzer* 8 µm image of the bubble at ∼2″ angular resolution from the GLIMPSE survey (Churchwell et al. 2006). The blue star is the O7.5–9.5V/III star and the small black stars are members of the associated IR clusters. The green circle is a by-eye approximation of the bright IR ring. The contour lines show [C II] emission from 50 to 250 K km s^{-1} in steps of 50 K km s^{-1}.

deeply embedded in a massive molecular clump (“condensation 2”, Zavagno et al. 2006) with a mass of ∼5000 M$_\odot$ (Liu et al. 2017), excited by an O7.5–9.5V/III star (Martins et al. 2010). The molecular gas bulk emission velocity ranges between −50 and −44 km s^{-1}. The region is undergoing massive star formation, witnessed by a small cluster of IR sources (Zavagno et al. 2006). The source is classified as a compact H II region (cH IIR) with a determined 5 GHz total flux of 1 Jy (Zavagno et al. 2006), corresponding to an ionizing flux of 1.9×10^{48} photons s^{-1}, typical of an O8 star. Assuming spherical symmetry for the cH IIR region, the authors calculated a dynamical age of 0.13 Myr.

We have studied the gas dynamics and excitation conditions of photodissociated gas in the S144 bubble to understand the evolution of H II regions and their molecular cloud. We show that the low observed ratio of [C II] to the total FIR luminosity, the so-called [C II]-deficit (Smith et al. 2017; Pabst et al. 2021), can be explained by [C II] self-absorption.

2. Observations

2.1. SOFIA

The [^{12}C II] line at 157.74 µm was mapped across RCW79 (∼470 arcmin^2) in the on-the-fly (OTF) mode, using the upgraded German REceiver for Astronomy at Terahertz frequencies (upGREAT; Risacher et al. 2018) on board SOFIA. A forward efficiency of $\eta_\mathrm{f} = 0.97$ and main beam efficiencies, η_mb, between 0.63 and 0.69 were applied to obtain main beam temperatures (for further observational information and details on the SOFIA legacy program FEEDBACK, see Schneider et al. 2020; Bonne et al. 2023). The generic angular resolution is 14.1″ and the velocity resolution was binned to 0.3 km s^{-1} wide channels.

2.2. APEX

The ^{12}CO and ^{13}CO 3 → 2 transitions at 345.80 GHz and 330.59 GHz were mapped in OTF mode with the LAsMA receiver on the APEX telescope and presented in Bonne et al. (2023). The data, in main beam temperature units using η_mb = 0.68 with a velocity resolution of 0.3 km s^{-1}, had a first-order baseline removed from the spectra at 18″ resolution. In May 2024, a 180″ × 180″ ^{12}CO 6 → 5 (ν = 691.47 GHz) map centered on S144 was observed in OTF mode with the SEPIA660 receiver (Belitsky et al. 2018). The data have an angular resolution of 9″ and a velocity resolution of 0.25 km s^{-1}, leading to a root-mean-square noise level of 0.59 K. Spectra were processed by removing a third-order spectral baseline and applying a main beam efficiency of η_mb = 0.6.

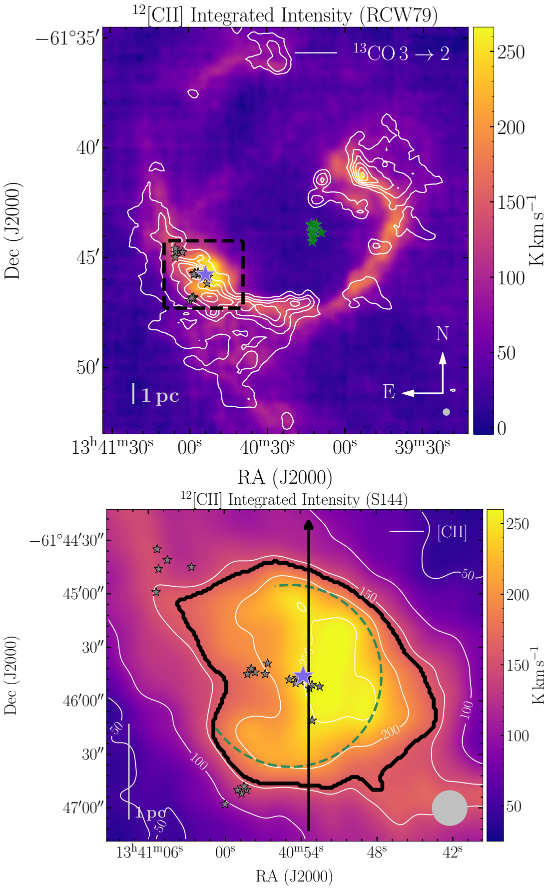

Fig. 2. Line-integrated (−70 to −20 km s^{-1}) [C II] intensity maps of RCW79 and S144. Top: RCW79 with an overlay of ^{13}CO 3 → 2 emission with contours from 7 to 52 K km s^{-1} in steps of 9 K km s^{-1} (∼5σ). The green stellar symbols indicate the central cluster of O-type stars (Martins et al. 2010), the blue stellar symbol the exciting O7.5–9.5V/III star of the cH IIR within S144 in the southeast, and the small black stellar symbols members of the IR clusters (Zavagno et al. 2006). The dashed black rectangle outlines the area shown in the bottom panel. Bottom: S144 with an overlay of ^{13}CO 3 → 2 at the same levels as in the upper panel. The dashed green circle (50″ radius) indicates the bright IR ring seen in the *Spitzer* 8 µm map (see Fig. 1). The region taken into account to compute the average [C II] spectrum is indicated by a black contour. The black line corresponds to the PV cut shown in Fig. 3. Both maps have an angular resolution of 20″, indicated by gray disks in the lower right corner of the panels.

3. Results

3.1. Spatial and kinematic distribution of [C II] emission

We observe centrally concentrated [C II] emission with a peak slightly to the west of the exciting O star; the bottom panel of Fig. 2 displays the [C II] line-integrated intensity in S144. The 8 µm image (Fig. 1) shows a more complex emission distribution with a small, circular emission peak just around the O star (radius ∼15″), followed by low-surface-brightness emission and a bright dust ring, which most likely represent a

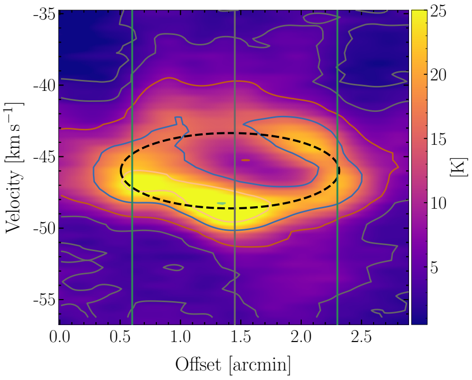

Fig. 3. Position-velocity cut in [C II] at 20″ angular resolution. The cut is outlined in the lower panel in Fig. 2. Offset 0 arcmin marks the lower declination. The dashed ellipse results from fitting the emission in various PV cuts. Movies are available online. In these PV diagrams, the dotted black line marks the cloud bulk velocity at −46.5 km s^{-1}, the vertical gray line the position of the O star, and the green lines the extent of the IR ring.

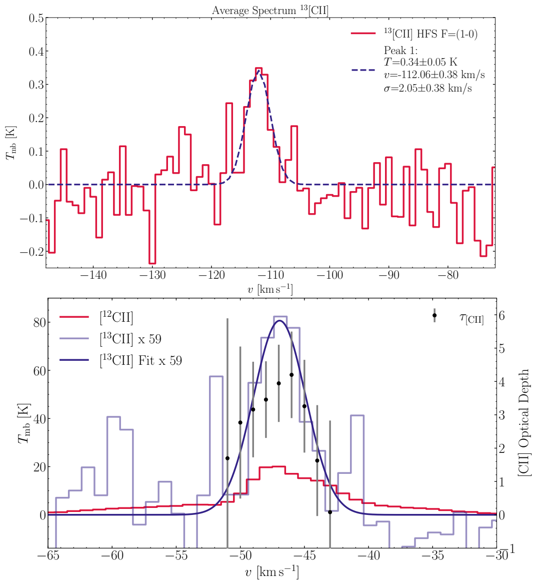

Fig. 4. Spatially averaged [^{12}C II] and [^{13}C II] spectra. Top: Averaged spectrum of the [^{13}C II] HFS $F = 1{-}0$ component. The spatial region over which the averaging was carried out is defined by the black dendrogram contour in Fig. 2. Gaussian fit parameters are included. Bottom: Averaged [^{12}C II] line (red) and the [^{13}C II] HFS $F = 1{-}0$ component (light blue histogram) with its Gaussian fit (dark blue curve), scaled by the ^{12}C/^{13}C ratio of 59 ± 10 (Milam et al. 2005) and considering the fractional weight (0.25) of the 1−0 HFS. Black dots indicate optical depth.

swept-up gas shell, as has been proposed for other H II regions (Deharveng et al. 2010). The 8 µm emission is dominated by the 7.7 and 8.6 µm features of polycyclic aromatic hydrocarbons (PAHs) that are easily destroyed by the hard radiation field of the central star or blown out by stellar winds (Churchwell et al. 2006). The absence of a central void in the 8 µm emission suggests that the cH IIR region is in an early evolutionary stage in which the gas dynamics are not yet dominated by stellar winds. Additionally, the UV radiation is attenuated by gas and dust, creating conditions that allow PAHs to survive.

Lastly, we have a scenario in which the central O star has created a cH IIR but no wind-blown cavity, and in which the star is enveloped by an extended PDR seen in the (F)IR and in [C II]. The whole region is embedded in a larger molecular cloud that extends mostly to the SE, containing a few dense clumps with ongoing star formation. Figure A.1 presents overlays of [C II] with several other tracers (*Herschel* 70 µm, 843 MHz continuum, etc.), a [C II] and ^{12}CO 3 → 2 channel map (Fig. A.2), and an overlay between [C II] and ^{12}CO 6 → 5 emission (Fig. A.3). The online material includes movies that further detail the bubble's characteristics.

Figure 3 presents a position-velocity (PV) cut of the [C II] emission showing the characteristic emission distribution of an expanding shell, with both blueshifted and redshifted parts. The latter is sometimes missing in other sources. The expansion speed is low, around 2.6 km s^{-1}, and was derived by fitting an ellipse to the emission distributions for all PV cuts and taking the overall average. The shell most likely corresponds to the bright IR ring (Fig. 1); whether it is driven by wind or thermal pressure will be discussed in another study. The central dip in the profiles may reflect the effects of absorption by a colder foreground gas. The emission within the dip reaches 10−15 K, which is above the 3σ noise (∼7.5 K in a 0.5 km s^{-1} channel), indicating significant [C II] emission at the center of the bubble. In the next section, we show that optical depth effects and self-absorption lead to the apparent depression in the emission line profile.

3.2. Self-absorption of the [^{12}C II] line

S144 has a complex spatial and velocity structure, which is also reflected in the spectra of [C II] and CO 6 → 5 emission (Fig. A.3). The [C II] and CO spectra often reveal two velocity components and a dip at ∼−46 km s^{-1}. In the SE region, the CO line consists of only one component at the bulk emission of −46.5 km s^{-1}. In the northwestern (NW) region, CO emission decreases, while the [C II] line is strong and shows two velocity components. In addition, the [C II] spectrum displays in all spectra high-velocity gas from the large expanding [C II] shell of RCW79 (Bonne et al. 2023), which is lacking in the CO line. There is also [C II] emission arising from the slowly expanding shell of the bubble and from the bulk emission of the PDR gas, in which the bubble is embedded.

To answer the main question – whether the [C II] intensity dip is due to the kinematics of the expanding [C II] shell of the bubble or due to self-absorption effects in an optically thick [C II] line, as is seen in other C$^+$ bubbles (Bonne et al. 2022; Kabanovic et al. 2022) – we need an observation of at least one hyperfine-structure (HFS) component of the optically thin [^{13}C II] line (Ossenkopf et al. 2013). For S144, we do not observe this line in individual spectra. We detect the [^{13}C II] $F = 1{-}0$ component[1] only in the averaged spectrum. Figure 4 shows the line together with the [C II] optical depth derived from the observed [^{12}C II]/[^{13}C II]-ratio in each velocity channel within the single-layer model using Eq. B.6 (Guevara et al. 2020; Kabanovic et al. 2022, and Appendix B). We find that the [^{13}C II] line, scaled by the local carbon abundance ratio, overshoots the [^{12}C II] line, resulting in a velocity-resolved optical depth between 1 and 5. The peak optical depth is shifted relative to the [C II] peak emission, which cannot be explained if the optical depth arises purely from a gas column with a single temperature. Thus, a more sophisticated calculation is needed to properly explain the observations, separating the gas into a warm emitting layer and a colder absorbing foreground gas. The two-layer model and its results are discussed in Appendix B. In

---

[1] The strongest [^{13}C II] $F = 2{-}1$ component is not accessible, as it is contaminated by the redshifted wing of the [C II] line.

the following, we assume that the [^{12}C II] line is optically thick throughout the map, which is a presumption because we do not have measurements of the [^{13}C II] line at each position. However, all observed [^{12}C II] lines show a dip or sometimes a flat-top profile (Fig. A.3) and considering the small extent of the region (diameter ~2 pc), we do not expect a large variation in the bulk emission of the gas, which would shift the [^{12}C II] dip and the [^{13}C II] line center position.

To verify our finding of partly self-absorbed [C II] profiles, we used the 1D non-local thermodynamic equilibrium radiative transfer code SimLine (Ossenkopf et al. 2001). This evaluation is not intended to provide a fully quantitative reproduction of the bubble parameters, as the angular resolution of the [C II] data imposes certain limitations.[2] Our goal is to demonstrate that even a simple model can satisfactorily reproduce the observations. The model consists of a central, fully ionized H II region (with a radius of $r = 0.5$ pc, electron density of $n_e = 100\,\mathrm{cm}^{-3}$, temperature of $T = 8000$ K), followed by a dense ($n = 2500\,\mathrm{cm}^{-3}$) PDR layer ($r = 0.95$ pc) with $T = 100$ K, surrounded by a layer in which the parameters drop to the environmental conditions reached at $r = 1.5$ pc using a power law with an exponent of −2. The PDR layer exhibits a radial velocity of 2.6 km s^{-1} and a turbulent velocity of 2.2 km s^{-1}, consistent with observational constraints. A detailed description of the model parameters and their values is provided in Appendix C.

The radius and width of the shells, the expansion velocity, and the steep outer temperature gradient are well constrained. Conversely, the local density and temperature are uncertain. A lower density can always be compensated for by a higher temperature and vice versa. The 8 µm ring likely traces a compressed shell that is somewhat thinner than the modeled PDR layer. This indicates that C$^+$ can be extended more than the PAHs in S144. However, these structural differences do not impact our key conclusion: the observed [C II] line can be self-absorbed due to temperature and velocity gradients. The exact amount of C$^+$ contained in the H II region remains currently unclear. Modeling the H II region with the assumed parameters from SimLine using the CLOUDY spectral synthesis code (Ferland et al. 2017) yields very small quantities of C$^+$ (less than 1%), although up to 20% of the observed [C II] can stem from the H II regions in other sources (RCW120, Luisi et al. 2021). Observations of carbon recombination lines could probably settle this issue and help investigate the dynamics of the expanding [C II] shell.

3.3. [C II]-deficit

The self-absorption seen in the [C II] line leads to a deficiency in the line-integrated emission. Thus, the ratio of [C II] to total FIR continuum is lower than the nominal value, assuming that the FIR emission is optically thin, an assumption that is reasonable given the density (a few 1000 cm^{-3}, Sect. 3.2) and the radiation field regime (up to a few 1000 G_0; Appendix A) present in S144 (Goldsmith et al. 2012).

To correct for the missing emission, we fit the [C II] line and the [^{13}C II] HFS to the outer wings of the double-peak spectra using radiative transfer equations, where the optical thickness, peak position, and width were free fit parameters. We first detected the peaks and then subtracted the blueshifted and redshifted components of the large shell of RCW79 that were fit with Gaussians. For each position, we calculated the area between the spectra and the fit line, denoted as the "correction factor"; we show an example spectrum in Fig. 5. We performed calculations for an excitation temperature, T_{ex}, between 54 to 80 K in steps of 1 K, but kept each T_{ex} fixed during the fitting process. As a lower limit, 54 K is derived from the two-layer model (Appendix B) and 80 K is an upper limit, since the mean correction factor becomes insensitive to $T_{\mathrm{ex}} \gtrsim 80$ K (see Fig. B.2). The correction factor is shown in Fig. B.3 and varies from ~1.1 to ~1.4.

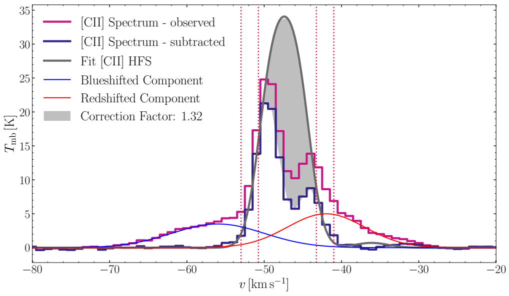

Fig. 5. Example of the fitting procedure for one spectrum toward the O star with fixed $T_{\mathrm{ex}} = 80$ K. Vertical dotted lines signify the outer wings of the double-peak spectrum. The gray area indicates the missing [C II] emission. The large blueshifted and redshifted expanding shell of RCW79 is fit and indicated.

Figure 6 compares the correlations of the [C II] intensity with the FIR intensity for both the "uncorrected" (top panel) and corrected [C II] values (bottom panel) reconstructed in the manner described above.[3] The total FIR intensity was determined from a spectral energy distribution fit to the *Herschel* fluxes (Appendix D). First, the distribution is bimodal for log(FIR) $\lesssim -0.9$ and log([C II]) $\lesssim -3.1$ due to environmental effects. The corresponding pixels originate from the map edges in the NW and SE, where PDR gas emits at similar [C II] levels but exhibits weaker FIR emission in the NW. Consequently, the [C II]/FIR ratio is higher in the NW, resulting in the observed bimodality.

Second, the upper panel shows that the highest [C II] intensities depend less than linearly on the FIR. This so-called [C II]-deficit is sometimes observed in Galactic and extragalactic star-forming regions. For ultraluminous IR galaxies, it is often a high dust optical depth, a high ionization parameter (when carbon can become doubly ionized to C^{2+} and higher states), metallicity variations, and very strong and hard radiation fields that can cause the [C II]-deficit (Lagache et al. 2018; Luhman et al. 2003, and references therein). In less extreme environments in Galactic PDRs, other processes are proposed. In very dense regions, an increased heating efficiency caused by dust grains and collisional de-excitation of [C II] can take place and in environments with high values of $G_0\,T^{0.5}/n_e$, photoelectric heating efficiency may drop, reducing overall gas cooling (Hollenbach & Tielens 1999; Goicoechea et al. 2015; Pabst et al. 2021). Saturation[4] of the [C II] line can occur under specific conditions, and [O I] cooling (Hollenbach & Tielens 1999) can dominate in very dense and warm PDRs. Self-absorption of the [C II] line is another viable mechanism for reducing the integrated [C II] line emission. This has not yet been discussed for [C II] in the literature;

---

[2] Note, however, that the angular resolution is handled fully self-consistently within SimLine.

[3] A linear relation, $\eta = \alpha + \beta\xi + \epsilon$, in log-log space was fit to the samples using Bayesian Interference with `linmix` (Kelly 2007). α and β correspond to the intercept and slope, while ϵ is the intrinsic scatter of the relation. The absolute values, however, are not relevant here and will be discussed in another study.

[4] The [C II] emissivity ceases to increase, even with a stronger radiation field. In this case, the fraction of ions in the upper excited state of the two-level system of the [C II] 158 µm line reaches a threshold.

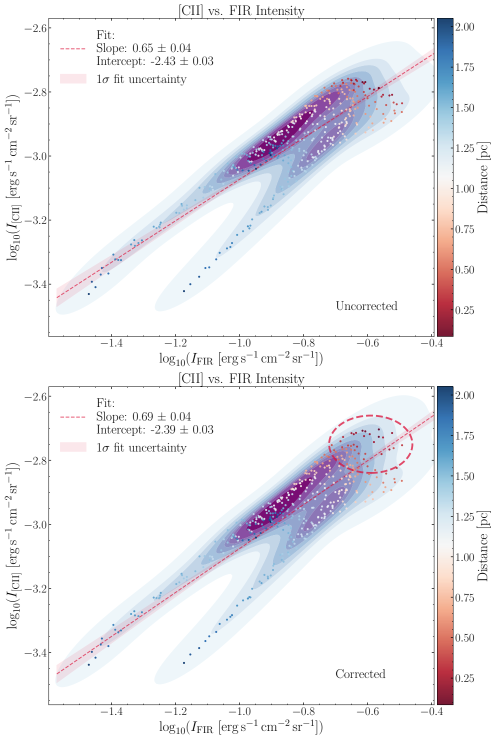

Fig. 6. [C II]/FIR correlation for both uncorrected (top) and corrected (bottom) [C II] emission. Pixels (derived from maps at 36″ resolution) are color-coded based on their proximity to the O star; their density is reflected in the shaded blue areas. A dashed red line represents a linear fit intended to guide the eye for a linear [C II]/FIR correlation. Corrected pixels near the O star with high [C II] and FIR values $\log(\mathrm{FIR}) > -0.6$ are shifted upward in the lower panel (indicated by a dashed red ellipse).

however, Goldsmith et al. (2021) propose this mechanism for a low [O I]/FIR ratio in W3.

For S144, we can exclude processes requiring extremely high density and UV radiation fields, as the conditions are moderate ($n \sim$ a few 1000 cm^{-3}, $G_0 \sim$ a few 1000). Saturation is also unlikely, as it typically becomes significant for dust temperatures exceeding 40 K (Fig. 16 of Ebagezio et al. 2024). However, the dust temperatures in S144 are below 30 K (Fig. 2a in Liu et al. 2017). A high ionization parameter is also not expected to be a significant issue. The [C II] emission predominantly originates in the PDR, where carbon remains in a C$^+$ state. While the C$^+$ to C^{2+} transition may occur within the H II region, Ebagezio et al. (2024) indicate that this process is more relevant for evolved H II regions, which is not the case for our cH IIR. Gerin et al. (2015) propose that the [C II]-deficit toward nuclear regions in luminous IR galaxies is caused by absorption on kiloparsec scales from diffuse gas in the foreground. This is not what we suggest, because in our case the absorption takes place very close to the source and is mostly due to a temperature and velocity gradient in the PDR.

Our straightforward approach of correcting for self-absorption shows that the [C II] to FIR correlation becomes linear again for high [C II] and FIR values, as shown in Fig. 6, in which the [C II] values shift upward. This finding does not exclude the possibility that other mechanisms are also at work, but demonstrates that in this PDR region with not-so-extreme radiation fields and densities the [C II]-deficit can indeed be mainly caused by self-absorption effects in the [C II] line. This view will be further investigated by studying the [C II]/FIR ratio and the [C II] line properties in other FEEDBACK sources and carrying out a comparison with simulations of H II regions including stellar winds and radiation.

Data availability

Movies associated to Figs. 3 and A.3 are available at https://www.aanda.org

Acknowledgements. This study was based on observations made with the NASA/DLR Stratospheric Observatory for Infrared Astronomy (SOFIA). SOFIA is jointly operated by the Universities Space Research Association Inc. (USRA), under NASA contract NNA17BF53C and the Deutsches SOFIA Institut (DSI), under DLR contract 50 OK 0901 to the University of Stuttgart. upGREAT is a development by the MPIfR and the KOSMA/University Cologne, in cooperation with the DLR Institut für Optische Sensorsysteme. This work was carried out in part at the JPL, California Institute of Technology, under contract with the National Aeronautics and Space Administration. Financial support for FEEDBACK at the University of Maryland was provided by NASA through award SOF070077 issued by USRA. The FEEDBACK project was supported by the BMWI via DLR, project number 50OR2217. S.D. acknowledges support from the IMPRS at the Universities of Bonn and Cologne. S.K. acknowledges support by the BMWI via DLR, project number 50OR2311. This work was supported by the CRC 1601 (SFB 1601 sub-projects B2, C1, C2, C3, C6) funded by the DFG – 500700252.

References

Belitsky, V., Lapkin, I., Fredrixon, M., et al. 2018, A&A, 612, A23
Bonne, L., Schneider, N., García, P., et al. 2022, ApJ, 935, 171
Bonne, L., Kabanovic, S., Schneider, N., et al. 2023, A&A, 679, L5
Churchwell, E., Povich, M. S., Allen, D., et al. 2006, ApJ, 649, 759
Cohen, M., Green, A. J., Parker, Q. A., Mader, S., & Cannon, R. D. 2002, MNRAS, 336, 736
Deharveng, L., Schuller, F., Anderson, L. D., et al. 2010, A&A, 523, A6
Ebagezio, S., Seifried, D., Walch, S., et al. 2023, MNRAS, 525, 5631
Ebagezio, S., Seifried, D., Walch, S., & Bisbas, T. G. 2024, A&A, 692, A58
Ferland, G. J., Chatzikos, M., Guzmán, F., et al. 2017, Rev. Mexicana Astron. Astrofis., 53, 385
Gerin, M., Ruaud, M., Goicoechea, J. R., et al. 2015, A&A, 573, A30
Goicoechea, J. R., Teyssier, D., Etxaluze, M., et al. 2015, ApJ, 812, 75
Goldsmith, P. F., Langer, W., Pineda, J., & Velusamy, T. 2012, ApJS, 203, 13
Goldsmith, P. F., Langer, W. D., Seo, Y., et al. 2021, ApJ, 916, 6
Guevara, C., Stutzki, J., Ossenkopf-Okada, V., et al. 2020, A&A, 636, A16
Hollenbach, D. J., & Tielens, A. G. G. M. 1999, Rev. Mod. Phys., 71, 173
Kabanovic, S., Schneider, N., Ossenkopf-Okada, V., et al. 2022, A&A, 659, A36
Kelly, B. C. 2007, ApJ, 665, 1489
Lagache, G., Cousin, M., & Chatzikos, M. 2018, A&A, 609, A130
Liu, H.-L., Figueira, M., Zavagno, A., et al. 2017, A&A, 602, A95
Luhman, M. L., Satyapal, S., Fischer, J., et al. 2003, ApJ, 594, 758
Luisi, M., Anderson, L. D., Schneider, N., et al. 2021, Sci. Adv., 7, eabe9511
Martins, F., Pomarès, M., Deharveng, L., Zavagno, A., & Bouret, J. C. 2010, A&A, 510, A32
Milam, S. N., Savage, C., Brewster, M. A., Ziurys, L. M., & Wyckoff, S. 2005, ApJ, 634, 1126
Motte, F., Zavagno, A., Bontemps, S., et al. 2010, A&A, 518, L77
Ossenkopf, V., Trojan, C., & Stutzki, J. 2001, A&A, 378, 608
Ossenkopf, V., Röllig, M., Neufeld, D. A., et al. 2013, A&A, 550, A57
Pabst, C., Higgins, R., Goicoechea, J. R., et al. 2019, Nature, 565, 618
Pabst, C. H. M., Hacar, A., Goicoechea, J. R., et al. 2021, A&A, 651, A111
Pabst, C. H. M., Goicoechea, J. R., Hacar, A., et al. 2022, A&A, 658, A98
Risacher, C., Güsten, R., Stutzki, J., et al. 2018, J. Astron. Instrum., 7, 1840014
Schneider, N., Ossenkopf, V., Csengeri, T., et al. 2015, A&A, 575, A79
Schneider, N., Simon, R., Guevara, C., et al. 2020, PASP, 132, 104301
Schneider, N., Ossenkopf-Okada, V., Clarke, S., et al. 2022, A&A, 666, A165
Schneider, N., Bonne, L., Bontemps, S., et al. 2023, Nat. Astron., 7, 546
Simón-Díaz, S., & Stasińska, G. 2011, A&A, 526, A48
Smith, J. D. T., Croxall, K., Draine, B., et al. 2017, ApJ, 834, 5
Zavagno, A., Deharveng, L., Comerón, F., et al. 2006, A&A, 446, 171

Appendix A: Multiwavelength plots and channel maps in [C II] and ^{12}CO 3 → 2 emission

Figure A.1 presents a *Herschel* 70 μm map, our computed UV field map, and a 843 MHz emission and *Herschel* column density map. The 843 MHz map outlines the approximate extent of the H II region, though it suffers from beam dilution due to its 45″ beam size. The dust ring, seen in both the *Herschel* 70 μm and the *Spitzer* 8 μm maps (Fig. 1), probably indicates compressed gas, predominantly to the west. The FUV map of the total RCW79 region was generated following the procedure outlined in Schneider et al. (2023), using the spectral classification of all O stars as detailed in Martins et al. (2010). The features in these maps partly motivated the modeling of the two outer shells using SimLine (Sect. C).

The *Herschel* dust column density map (Liu et al. 2017) illustrates the dense gas distribution, highlighting a SE region comprising multiple high-density clumps, one reaching up to 6×10^{22} cm^{-2} NE of the O star. Identified as a cluster-forming star-formation site (Zavagno et al. 2006), this molecular clump shields the H II region and PDR gas. The movie overlays with [C II] and CO alongside the column density nicely show the gas flow around this clump.

Figure A.2 displays a [C II] channel map with superimposed contours of ^{12}CO 3 → 2 emission. The purple areas represent [C II] emission of low surface brightness, primarily originating from the large expanding [C II] shells spanning the RCW79 region and the disorganized [C II] flows that are eroding the molecular cloud (Bonne et al. 2023). Within the velocity range of -54 km s^{-1} to -40 km s^{-1} (indicated in blue), we detect the shell/bubble of [C II] exclusively associated with the cH IIR. The "filled C$^+$ bubble" geometry is disturbed by the prominent CO clump, which becomes visible around -59 km s^{-1} to the west. Furthermore, near a velocity of ~ -47 km s^{-1}, a [C II]-deficit is detected due to self-absorption.

Figure A.3 displays a map of the line-integrated [C II] and ^{12}CO 6 → 5 emission, together with spectra overlays selected for two representative positions. The NW spectrum (left) is an example of a self-absorbed [C II] line, also showing prominent wings from the expanding [C II] shell. The right panel is a position from the SE where the PDR emission from the surface of the molecular clump dominates the [C II] and CO emission. The high-velocity [C II] wings are, however, well visible.

Appendix B: The two-layer radiative transfer model

The two-layer multicomponent model (Guevara et al. 2020; Kabanovic et al. 2022) solves the radiative transfer equation for multiple velocity components distributed between two layers with different excitation temperatures along the line-of-sight. While the model itself has no restriction on the excitation temperature, we choose the excitation temperature $T_{\rm ex,bg}$ of the background layer (bg) to be higher than the temperature $T_{\rm ex,fg}$ of the foreground layer (fg), considering the geometry of the region with the exciting O star in the center and cooler PDR shells around. Thus, we account for self-absorption due to a column of gas along the line-of-sight in a single layer (which results in flat top spectra for high optical depth τ) as well as the foreground absorption by a colder foreground layer (which produces absorption dips in the spectrum). The absorption can originate from a spatially separated, cold foreground cloud, which is located between the warm emitting gas and the observer, or from a temperature gradient along the line-of-sight of the same cloud. Following the model presented in Kabanovic et al. (2022), we solve the following equation:

$$T_{\rm mb}(v) = \left[\mathcal{J}_\nu(T_{\rm ex,bg})\left(1-{\rm e}^{-\sum_{i_{\rm bg}}\tau_{i_{\rm bg}}(v)}\right)\right]{\rm e}^{-\sum_{i_{\rm fg}}\tau_{i_{\rm fg}}(v)} + \mathcal{J}_\nu(T_{\rm ex,fg})\left(1-{\rm e}^{-\sum_{i_{\rm fg}}\tau_{i_{\rm fg}}(v)}\right). \quad \text{(B.1)}$$

The equivalent brightness temperature of a black body emission at a temperature $T_{\rm ex}$ is

$$\mathcal{J}_\nu(T_{{\rm ex},i}) = \frac{T_0}{{\rm e}^{T_0/T_{\rm ex}}-1}, \quad \text{(B.2)}$$

with the equivalent temperature of the transition $T_0 = h\nu/k_B$ and ν the transition frequency. The optical depth of each Gaussian component is given by

$$\tau(v) = \tau_0\,{\rm e}^{-4\ln 2\left(\frac{v-v_0}{w}\right)^2}, \quad \text{(B.3)}$$

with the central local standard of rest (LSR) velocity v_0 of each component. The line width w is expressed as the full width at half maximum (FWHM) of the component. For a simple two-level system, we can express the peak optical depth τ_0 of each Gaussian component as a function of the excitation temperature $T_{\rm ex}$ and column density N by

$$\tau_0 = N\frac{c^3}{8\pi\nu^3}\frac{g_u}{g_l}A_{ul}\frac{1-{\rm e}^{-T_0/T_{\rm ex}}}{1+\frac{g_u}{g_l}{\rm e}^{-T_0/T_{\rm ex}}}\frac{2\sqrt{2\ln 2}}{w\sqrt{2\pi}}. \quad \text{(B.4)}$$

For the [C II] fine-structure transition, the rest frequency is ν = 1900.5369 GHz, the Einstein coefficient for spontaneous emission $A_{ul} = 2.29\cdot10^{-6}$ s^{-1}, the equivalent temperature of the upper level $T_0 = h\nu/k_{\rm B} = 91.25$ K, and the statistical weights of the transition energy levels are $g_u = 4$ and $g_l = 2$.

Table B.1. Two-layer multicomponent model results.

	Model I: $T_{\rm ex,bg}$ = 54 K, $T_{\rm ex,fg}$ = 20 K			
Components	$N_{\rm [C\,II]}$ [10^{18} cm^{-2}]	τ_0	v_0 [km s^{-1}]	w [km s^{-1}]
Backg. Comp. 1	4.77	4.26	−47.06	4.48
Backg. Comp. 2	1.37	0.27	−48.88	20.02
Backg. Comp. 3	0.54	0.32	−44.29	6.67
Foreg. Comp. 1	0.17	0.28	−44.96	2.36
Foreg. Comp. 2	0.64	0.89	−50.88	2.90
	Model II: $T_{\rm ex,bg}$ = 80 K, $T_{\rm ex,fg}$ = 20 K			
Backg. Comp. 1	3.29	1.81	−46.81	5.07
Backg. Comp. 2	0.16	0.04	−59.13	10.50
Backg. Comp. 3	0.88	0.15	−46.26	15.95
Foreg. Comp. 1	1.28	0.81	−45.33	4.43
Foreg. Comp. 2	1.52	1.07	−50.69	3.95

The physical properties of the background layer can be derived from an optically thin line, which is not affected by self-absorption. In case of [C II], we can utilize the much weaker [^{13}C II] hyperfine transition lines, see Guevara et al. (2020) for a more detailed description. Model fit parameters such as LSR velocity, line width, and number of components can be simply derived from the observed line. However, the optical depth and the excitation temperature are not independent of each other. We therefore need to first derive the excitation temperature from the observed data, which leaves the optical depth as the free model fit parameter. Assuming that the warm emitting background can

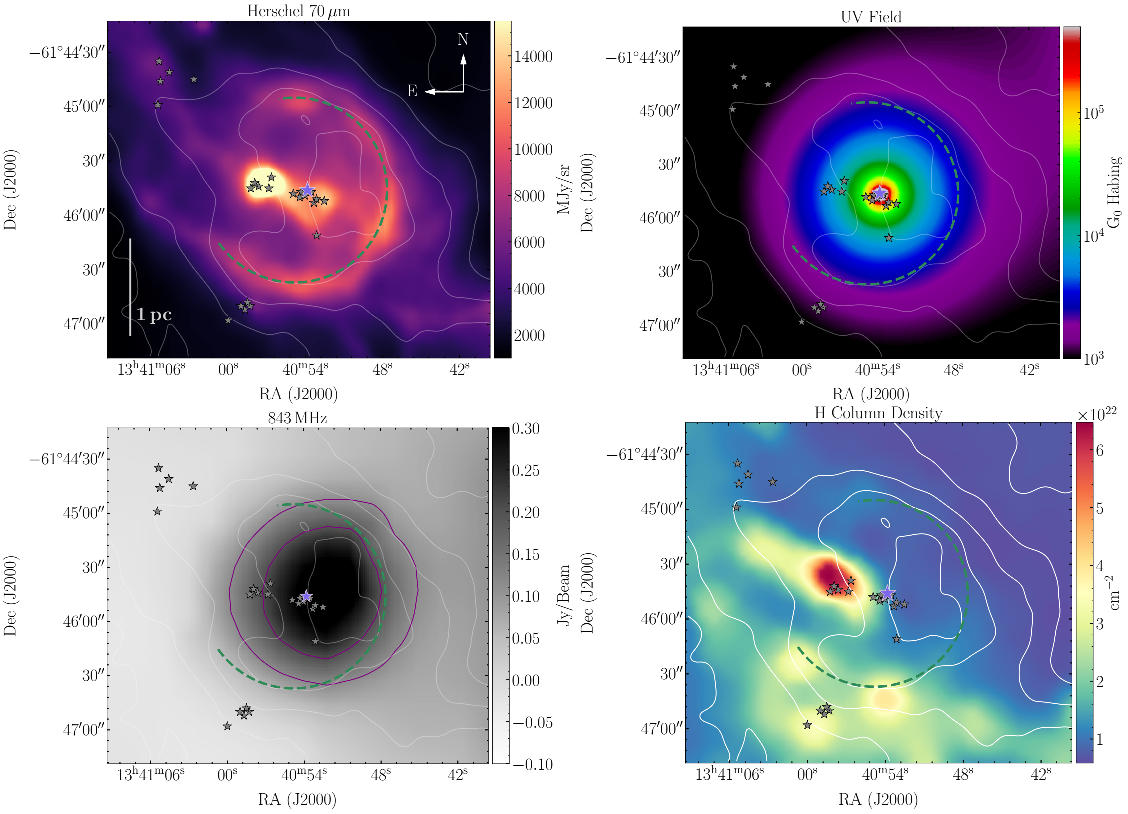

Fig. A.1. Complementary plots for the S144 C⁺ bubble in RCW79. The upper left panel illustrates the 70 μm emission from *Herschel* at ∼ 6″ resolution. This emission resembles the *Spitzer* 8 μm image (as seen in Fig. 1), though it highlights more clearly the NE clump containing the embedded IR cluster in the 70 μm map. The upper right panel presents the UV field, which is derived from the spectral type of the O star (indicated by a blue star) and the central O-cluster from RCW79, located farther to the west. The lower left panel displays the 843 MHz emission with a 45″ angular resolution, outlining the H II region (Cohen et al. 2002). In the lower right panel, the *Herschel* dust column density map (Liu et al. 2017) at 18″ angular resolution reveals the clumpy structure of condensation 2. Each panel includes [C II] contours in increments of 50 K km s^{-1} from 50 to 250 K km s^{-1}, while the 843 MHz map also depicts 843 MHz contours at 0.1 and 0.2 Jy/Beam in purple. The small black stars are members of the IR clusters.

partly shine through the cold absorbing layer (Kabanovic et al. 2022), we can determine the excitation temperature via

$$T_{\mathrm{ex}} = \frac{T_0}{\ln\left(\frac{T_0}{T_{[\mathrm{C\,II}],\mathrm{peak}}}\left(1-\mathrm{e}^{-\tau_{[\mathrm{C\,II}],\mathrm{peak}}}\right)+1\right)}. \tag{B.5}$$

The optical depth is then calculated from the observed [^{12}C II]/[^{13}C II] ratio at the peak of the [^{12}C II] emission

$$\frac{T_{[^{12}\mathrm{C\,II}]}(\upsilon)}{T_{[^{13}\mathrm{C\,II}]}(\upsilon)} = \frac{1-\mathrm{e}^{-\tau(\upsilon)}}{\tau(\upsilon)/\alpha} = \frac{1-\mathrm{e}^{\tau(\upsilon)}}{\tau(\upsilon)}\alpha, \tag{B.6}$$

with the local carbon abundance ratio α that we take as 59 ± 10 (Milam et al. 2005). The resulting velocity-resolved optical depth is shown in Fig. 4. For the calculation, only the second strongest [^{13}C II] F = 1 − 0 line is used, since the strongest F = 2 − 1 HFS line is covered by the redshifted [C II] wing and the weakest HFS F = 1 − 1 line is detected only marginally. The resulting lower limit for the [C II] excitation temperature is T_{ex} = 54 K. For the upper limit, we derive an excitation temperature of T_{ex} = 80 K, see Fig. B.2.

The resulting model fit of the two-layer model is shown in Fig. B.1 for a background excitation temperature of $T_{\mathrm{ex,bg}}$ = 80 K, which is the derived upper limit, indicating an optically thick [C II] line. However, the background (see Table B.1) derived from the [^{13}C II] line still overshoots the observed line, which requires additional cold foreground material. Although we do not have observational constraints on the excitation temperature in the foreground, multiple studies (Kabanovic et al. 2022; Schneider et al. 2023) have shown that a temperature of $T_{\mathrm{ex,bg}}$ = 20 K is reasonable for [C II]. We find that the observed foreground material is either blueshifted or redshifted from the systemic velocity. The blueshifted component can be explained due to the expanding bubble, which pushes the cold material in front of it toward the observer. However, the redshifted component cannot be attributed to the opposite hemisphere, since it is only visible in absorption. Decreasing the background excitation temperature results in a higher background column density and therefore higher optical depth; see Table B.1. Note, however, that we derived a temperature of ∼ 100 K from the SimLine modeling, so that low excitation temperatures are unlikely.

As a final note, we show in Fig. B.3 a map of the correction factor that was applied to the spectra showing self-absorption effects. Obviously, the spectra with the highest [C II] brightness are the most affected.

Appendix C: SimLine modeling of a C⁺ filled bubble

We use the 1D radiative transfer code SimLine (Ossenkopf et al. 2001) to model the observed [C II] emission from a symmetric spherical geometry. SimLine self-consistently solves the excitation problem of any species by taking into account the collisional excitation from the surrounding gas and the radiative

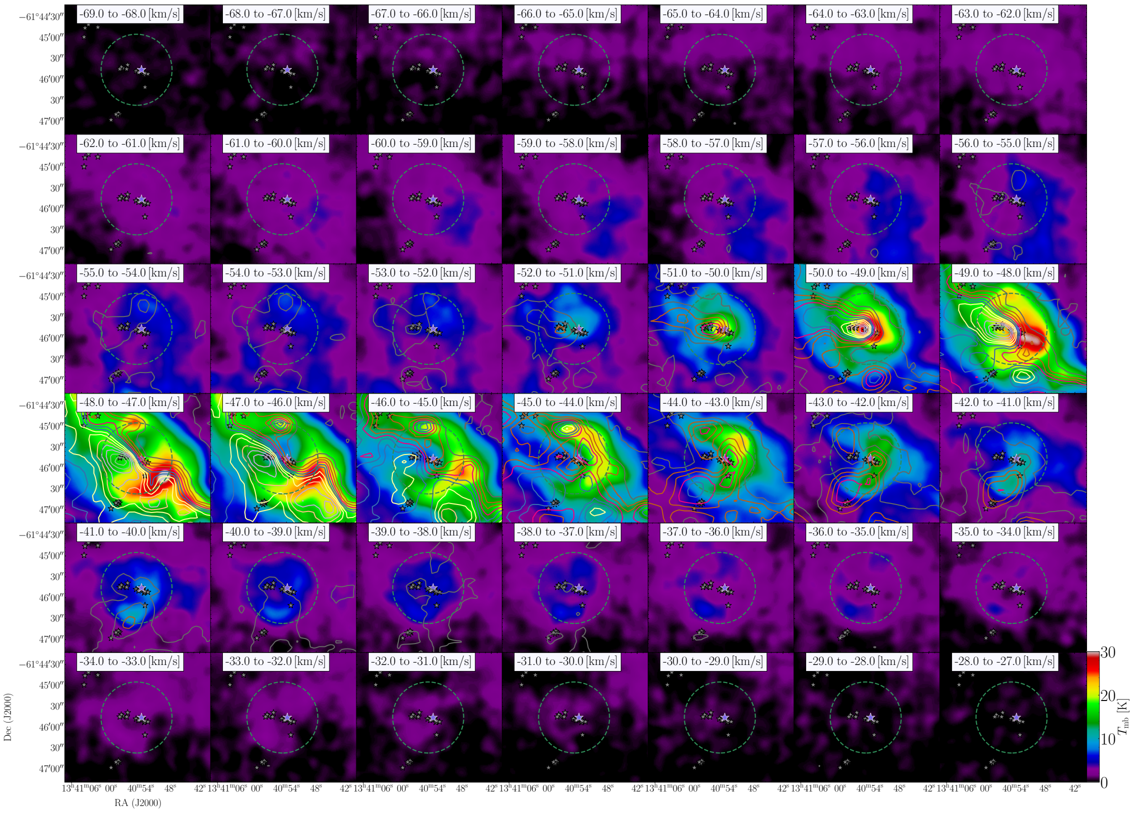

Fig. A.2. Channel map showing [C II] and ^{12}CO $3\rightarrow2$ emissions of the C$^+$ bubble. CO contours range from 0.67 to 32 K km s^{-1} in steps of 2.4 K km s^{-1}. The prominent blue star marks the position of the exciting O star, while smaller black stars denote IR cluster members. The green dotted circle indicates the approximate extent of the IR shell as observed in the *Spitzer* 8 μm image.

Table C.1. Parameters of SimLine modeling.

	shell 1	shell 2	shell 3
outer radius [pc]	0.5	0.95	1.5
density [cm^{-3}]	100	2500	2500
density profile (α_s)	-	-	−2
temperature [K]	8000	100	100
temperature profile (α_s)	-	-	−2
turbulent velocity [km s^{-1}]	3.7	2.2	2.2
turbulent velocity profile (α_s)	-	-	−1
radial velocity [km s^{-1}]	-	2.6	2.6
radial velocity profile (α_s)	-	-	−2
X([C II]) [10^{-4}]	1.2	1.2	1.2

interaction throughout the cloud. After solving the excitation problem through an accelerated Λ-iteration, the line profiles are computed at any desired velocity and spatial resolution. We simulate the properties of the observed [C II] data at 15″ resolution. Collisional excitation in the H II region is assumed to come from electrons in a fully ionized medium. In the outer shells, we assume that collisions are dominated by H$_2$, although a contribution of atomic hydrogen is also possible.

Due to the one-dimensional nature of the model, it can only reproduce angular-invariant properties, ignoring variations in different directions. Therefore, we ignore the SE direction which is heavily affected by the foreground molecular cloud and reproduce the observed radial profiles seen in the NW direction indicated by blue squares in Fig. C.1, which shows the general shell-setup of the model. We do not perform an accurate χ^2-fit to the data. This would fail due to the radial asymmetry given by the overabundance of foreground material from the molecular cloud at the peak position relative to the background material and the contribution of the high-velocity wing material that we ignored as discussed in Sect. 3.2. Instead, we performed a qualitative fit to all significant features by eye, ignoring the wings below −55 km s^{-1} and above −40 km s^{-1} and the blueshifted material close to the O star position.

The model consists of a central, fully ionized H II region, followed by a dense layer with high temperature and outer region providing a steep gradient in density, temperature, and expansion velocity ($\propto r^{-\alpha_s}$) to the surrounding ambient medium.

We estimated the approximate extent of the H II region using the 843 MHz emission map at 45″ angular resolution (lower left panel in Fig. A.1). First, the H II region must be smaller than the area enclosed by the 8 μm ring-like feature, represented by the green dashed circle with a radius of 50″. Second, the contour at 0.2 Jy/beam delineates the level, at which the emission drops to ~50% of its maximum value corresponding to an observed radius of approximately 34″. Using this value and a beam of 45″, we derive a de-convolved radius of the H II region of ~0.5 pc. We note that this is only an approximation, particularly as we see clear deviations from a circular symmetry. The H II region may be slightly smaller, suggested by the *Spitzer* 8 μm image, as a small circular feature is visible in Fig. 1, located directly around the exciting O star. Higher angular resolution cm observations are necessary to resolve this uncertainty. Beyond the H II region, the model assumes a PDR with a transition from atomic to molecular gas, where the outermost layer provides the transition to the gas from the surrounding ambient molecular cloud.

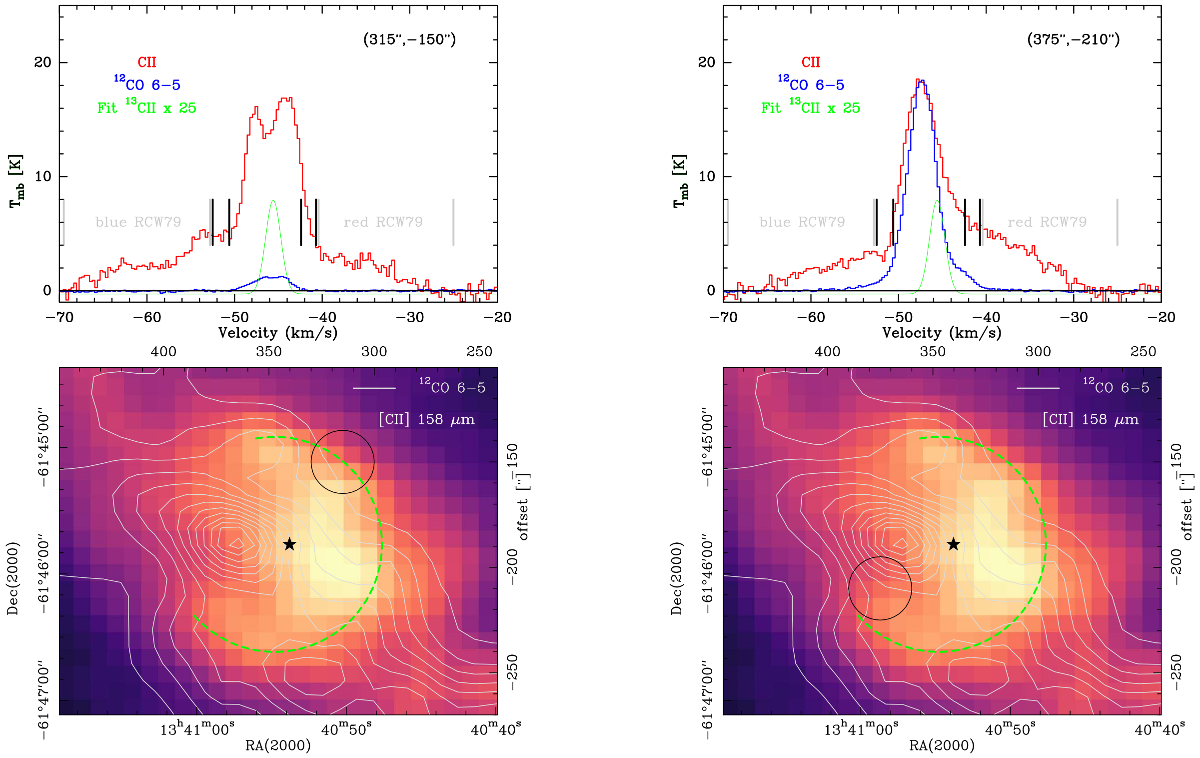

Fig. A.3. Example spectra of [^{12}C II] and ^{12}CO 6→5 lines with a fit to the HFS F = 1 − 0 component of the average [^{13}C II] line. The upper panels show the spectra/fit in a smoothed 30″ beam at the positions marked by a black circle in the lower panel of line-integrated [C II] emission and ^{12}CO 6→5 emission contours (10 to 130 by 10 K km s^{-1}). The two pairs of gray lines mark the blue and red velocity ranges of the large expanding [C II] shell over the whole RCW79 region (Bonne et al. 2023). The two pairs of black lines outline approximately the velocity range of the expanding [C II] shell. The black star in the lower panels indicates the position of the O-star and the green dashed circle the 8 μm ring. A movie showing all spectra is available online.

We setup the shells in the following way (all parameters are summarized in Table C.1): In the inner H II region (up to 0.5 pc), we assume that carbon is singly ionized. We cannot exclude that some of the C$^+$ is photo-ionized to C^{2+} caused by the stellar radiation (Ebagezio et al. 2023, 2024), but this effect should be more prominent in more evolved H II regions (Ebagezio et al. 2024). We take a typical temperature of 8000 K for the H II region. The density has no impact on the model result as long as it is below a few hundred cm^{-3}. We choose 100 cm^{-3} as a typical value.

The following two shells constitute the PDR, in which carbon collides with atomic and molecular hydrogen. For these shells, we adopt an abundance of X(C$^+$/H) = 1.2×10^{-4} (Simón-Díaz & Stasińska 2011). The first shell (up to 0.95 pc) has no velocity, density, or temperature gradient. It expands with the velocity of 2.6 km s^{-1} as determined in Sect. 3.1 and has a turbulent velocity dispersion of $v_{\rm turb}$ = 2.2 km s^{-1} to match the [C II] line width, a temperature of T = 100 K reflecting typical PDR conditions, in which the [C II] line cools efficiently, and a density of $n_{\rm H_2}$ = 2500 cm^{-3}.

This matches the density from the *Herschel* column density map at 18″ resolution from the HOBYS keyprogram (Motte et al. 2010) presented in Liu et al. (2017). The cutout for the bubble is shown in Fig. A.1. Since RCW79 is embedded in the Galactic plane, the column density is overestimated. Following the procedure presented in Schneider et al. (2015), that estimates the line-of-sight contamination directly from the *Herschel* maps, we derived a value of 4–6 × 10^{21} cm^{-2} for the contaminating column density. This is a typical value for massive star-forming regions (Schneider et al. 2022). After subtracting a value of 4×10^{21} cm^{-2}, we calculated densities between 2.3 and 2.9×10^3 cm^{-3} in an 18″ beam for the outermost points of shell 2 and 3, which fits our fit value of 2500 cm^{-3}.

The outer region (up to 1.5 pc), representing the transition to the pre-shock material in front of the expanding first shell, is simulated through a power-law decay of all parameters, with a steep exponent of $\alpha_s = 2$ for density, temperature, and expansion velocity; and a shallower exponent of $\alpha_s = 1$ for the turbulent velocity, reflecting the indirect driving of turbulence through the expansion. This description should roughly mimic the gas properties and condition in front of a C-shock, where the temperature and density rise steeply.

The result is shown in Fig. C.2 comparing the PV cut through the model and selected spectra with the correspondingly observed data at the same scale. Our SimLine setup with an absorbing layer, including temperature, radial, and turbulent velocity gradients, shows a good agreement to our observed spectra in terms of intensity and line profiles and PV cut. The most evident difference is the reversion of the blue and red peaks for positions Δr = 0 and 21. In an ideal bubble scenario including absorption, a higher redshifted line is expected since the blueshifted gas experiences more absorption along the sightline. However, the geometry of the C$^+$ bubble is more complex, as seen in Fig. C.1. The spherical symmetry of the H II region and the expanding C$^+$ bubble is disturbed by the molecular gas distribution located SE of the O star, which is slightly more blueshifted with respect to the [C II] emission. Therefore, the PDR surfaces of the molecular clumps emit [C II] efficiently and the increased gas density results in stronger [C II] emission.

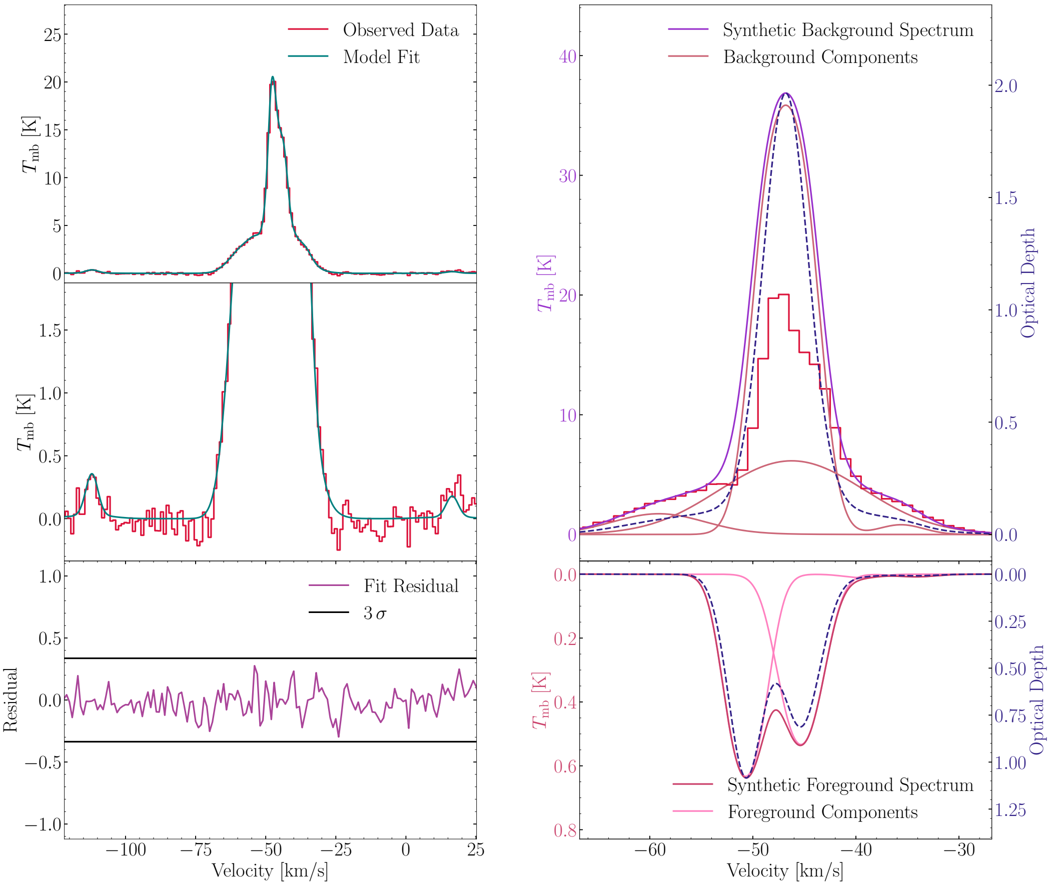

Fig. B.1. Two-layer model results for the average [C II] spectrum. The average spectrum corresponds to the area defined with dendrograms (refer to Fig. 2, right). The spectrum, shown in red, has a velocity resolution of 1 km s^{-1}. The model's background and foreground layer temperatures are $T_{\rm ex,bg}$ = 80 K and $T_{\rm ex,fg}$ = 20 K respectively. The upper left panel illustrates the observed spectrum in red beside its two-layer model fit in blue. The left central panel replicates the top panel's data but expands the intensity axis for clearer viewing of the three [^{13}C II] lines. The bottom left panel shows the residuals of the fit, with two horizontal black lines denoting the 3σ threshold. The top right panel focuses on individual background elements in red and the total background in violet. Meanwhile, the dashed blue curve represents velocity-resolved optical depth. The bottom right panel illustrates individual foreground elements in pink, alongside the overall foreground in red, again accompanying the dashed blue curve for optical depth representation.

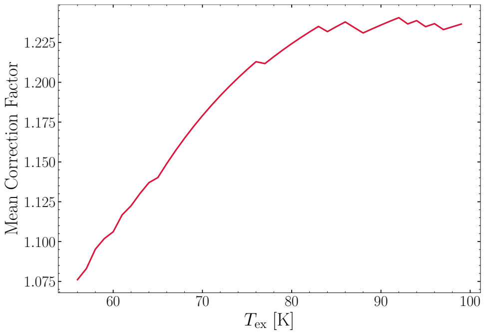

Fig. B.2. Mean correction factor versus $T_{\rm ex}$. The mean correction factor rises up to ~ 80 K, beyond which it becomes independent of $T_{\rm ex}$.

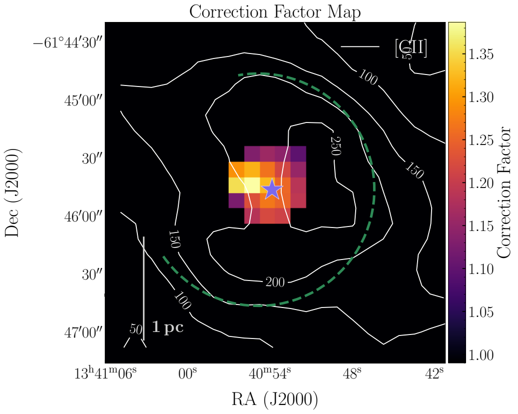

Fig. B.3. [C II] correction factor map (at an angular resolution of 36″ and 8″ grid) with fixed $T_{\rm ex}$ = 80 K.

Appendix D: Determination of the total far-infrared flux

In order to determine a total FIR flux, we create dust spectral energy distributions (SEDs) using the *Herschel* PACS 70 μm and 160 μm and SPIRE 250 to 500 μm bands. All maps are convolved and re-gridded to the largest common angular resolution of 36″ with an 8″ pixel size. Following Pabst et al. (2022), we fit a gray body given by

$$I_\lambda = B(\lambda, T_d)\left[1-\exp\left(-\tau_{160}\left(\frac{160\mu m}{\lambda}\right)^{\beta}\right)\right], \tag{D.1}$$

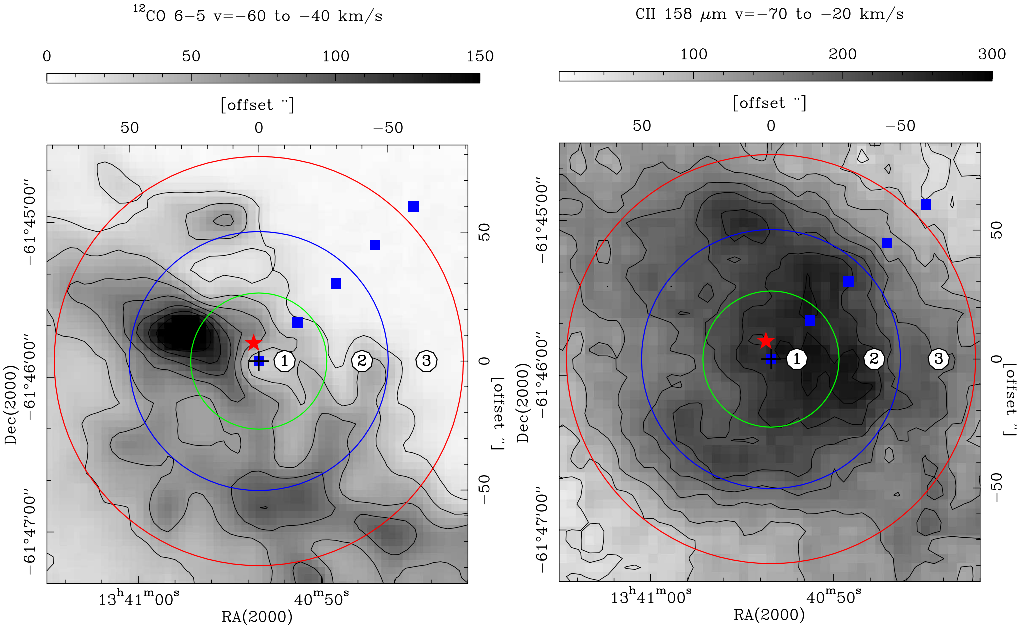

Fig. C.1. SimLine modeling setup of the C$^+$ bubble overlaid on the observed ^{12}CO $6 \rightarrow 5$ and [C II] intensities. The panels (^{12}CO $6 \rightarrow 5$ on the left and [C II] on the right) show a sketch of the setup for an ideal 3D bubble (note that the calculations are in 1D) in which the different shell regions are indicated. The positions of observed and modeled spectra, shown in Fig. C.2, are indicated by blue squares. The red star marks the exciting O star of the cH IIR.

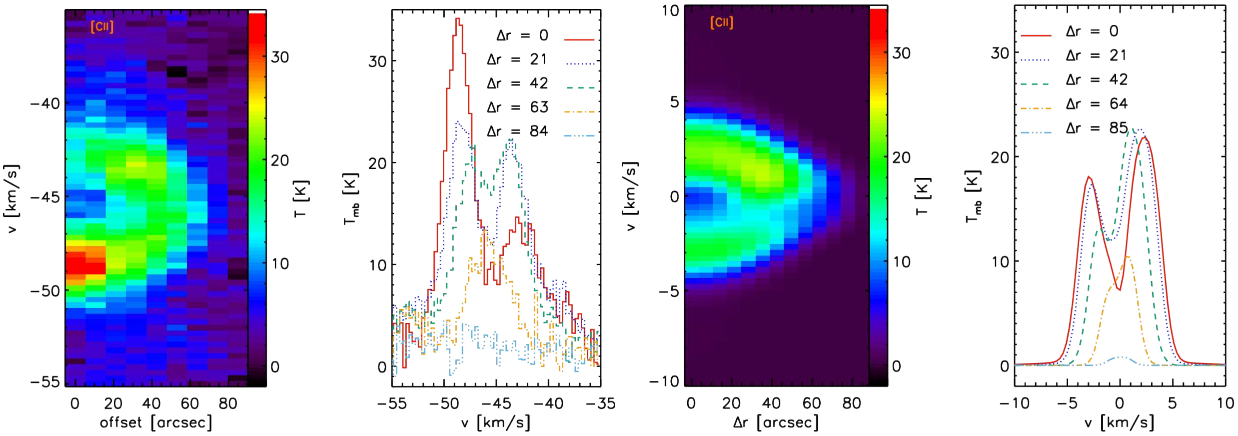

Fig. C.2. Observations versus results of the SimLine modeling. The left panel shows a PV cut from the center position along the positions of the observed and modeled spectra, indicated in Fig. C.1, together with the observed spectra. $\Delta r = 21$, etc. corresponds to an offset of (−15″, 15″) etc. The right panel displays the modeled PV cut and spectra from SimLine.

with a fixed emissivity index $\beta = 2$ and an optical depth specified at 160 μm. A total FIR flux is then determined by integration between 40 to 500 μm. The choice of fixing β biases the SED fit toward shorter wavelengths and warmer dust, but allows comparison with above mentioned studies. We note that the overall effect on the determined total FIR intensity is not strong, and the discussed correlations remain insensitive to this choice. The dominant error in the SED fit is the individual flux uncertainties in the *Herschel* PACS and SPIRE bands, which we assume to be 20% and 10%, respectively.

5.3.2 Prospectives: What drives the [C II] bubble in the compact H II region?

Understanding the mass and energy of the [C II] shell is essential to reveal the mechanisms driving its expansion within the compact H II region S144 in RCW79. Given the uncertainties in several parameters, the reported findings should be considered approximate estimates. I first present the results of the calculations and then subsequently the calculations later in this section.

Quantitative analysis of the [C II] emission provides key parameters of the expanding bubble. Fitting ellipses to the [C II] emission in the PV cuts (Fig. 3 in Keilmann et al. 2025) yields an expansion velocity of $\sim 2.6\,\mathrm{km\,s^{-1}}$, which, given the bubble's size, corresponds to a dynamical age of 0.35 Myrs. The kinetic energy of the expanding bubble shell is $E_{\mathrm{shell}} = 0.5 - 4.2 \times 10^{46}$ erg, with mass limits of $71\,\mathrm{M_\odot}$ and $605\,\mathrm{M_\odot}$. For shell 1 – as modeled with the radiative transfer code SimLine (Sect. 2.1.5) in the letter (Keilmann et al., 2025) – we derive a thermal pressure of $1.6 \times 10^6\,\mathrm{K\,cm^{-3}}$ and a thermal energy of 5.1×10^{45} erg (Lopez et al., 2011).

Stellar wind feedback further quantifies the system's dynamics. We obtain momentum and energy injection rates of $\dot{p}_{\mathrm{SW}} \approx 2.5 - 9.1 \times 10^{-4}\,\mathrm{M_\odot\,km\,s^{-1}\,yr^{-1}}$ and $\dot{E}_{\mathrm{SW}} \approx 0.6 - 1.2\,\mathrm{M_\odot\,km^2\,s^{-2}\,yr^{-1}}$, respectively.[1] Given the determined dynamical age, the stellar wind accumulates momentum of $p \approx 0.9 - 3.3 \times 10^7\,\mathrm{M_\odot\,km\,s^{-1}}$ and energy of $E \approx 3.9 - 8.7 \times 10^{48}$ erg.

Ionizing radiation exerts a dominant influence on the compact H II region. It injects a momentum of $\dot{p}_{\mathrm{ion,th}} = 1.7 \times 10^{-2}\,\mathrm{M_\odot\,km\,s^{-1}\,yr^{-1}}$ into the cloud, with an ionizing flux of $Q_i = 10^{48.79}\,\mathrm{s^{-1}}$ (Martins et al., 2010) and an ionization front of $r_{\mathrm{IF}} \approx 1$ pc (see Eq. 5.7). This momentum exceeds $\dot{p}_{\mathrm{SW}}$ by more than a factor of 15, and the total radiation energy emitted over the dynamical age is $E_{\mathrm{ion,th}} = 2 \times 10^{51}$ erg, suggesting the higher influence of the O star's radiation relative to its stellar wind – consistent with the early evolutionary state of the compact H II region.

Modeling of the bubble expansion using stellar wind parameters provides insights into its evolutionary stage. As stated in Sect. 4.2.2, the parameter set in Eqs. 4.13 and 4.14 is conducive to an early-stage bubble. Using the calculated dynamical age and the stellar parameters from Martins et al. (2010), we derive an expansion velocity of $v = 3.9\,\mathrm{km\,s^{-1}}$ and a bubble size of $R = 1.4$ pc. Although these predicted values exceed the observations by a factor of 1.4 to 1.5, they demonstrate rough consistency and progress in modeling stellar winds. Given the observational evidence of the significant impact of stellar winds on bubble mechanics, stellar winds should generally be included in simulations.

Energy calculations

Expanding shell energy Determining the hydrogen mass from the blue- and red-shifted [C II] emission is essential to calculate the kinetic energy of the expanding shell. The average spectrum (see Fig. 4 in Keilmann et al. 2025) yields the [C II] column density via Eq. 2.55 using a velocity range of $v_{\mathrm{blue}} \in (-54, -50.8)\,\mathrm{km\,s^{-1}}$ for the lower limit on blue-shifted emission and $v_{\mathrm{red}} \in (-43.5, -39.8)\,\mathrm{km\,s^{-1}}$ for red-shifted emission, which corresponds to the outer wings of the spectra. For an upper mass limit, the velocity

---

[1] The mass-ejection rates estimated based on Björklund et al. (2021) used for these calculations are unlikely to vary significantly (see Fig. 5 in Björklund et al. 2021), which justifies the numbers for the calculations.

extends to the bulk emission at $v \approx -47\,\mathrm{km\,s^{-1}}$, separating the blue- and red-shifted contributions. The conversion of the [C II] column density to hydrogen mass employs the C/H abundance ratio of 2.4×10^{-4} (Simón-Díaz and Stasińska, 2011) (as used in SimLine modeling), the proton mass, and the number of pixels in the compact H II region. This procedure yields a lower hydrogen mass limit of $71\,\mathrm{M_\odot}$ (with $21.5\,\mathrm{M_\odot}$ from blue-shifted and $49.5\,\mathrm{M_\odot}$ from red-shifted emission) and an upper limit of $605\,\mathrm{M_\odot}$ (with $333\,\mathrm{M_\odot}$ from blue-shifted and $272\,\mathrm{M_\odot}$ from red-shifted emission).

The kinetic energy is then simply calculated using

$$E_{\mathrm{shell}} = \frac{1}{2} M v^2 \ , \tag{5.1}$$

where M is the mass corresponding to the blue- and red-shifted emission and v the expansion velocity of the shell.

H II thermal expansion energy Using SimLine, we modeled an H II region with shell 1, characterized by a density of $n = 100\,\mathrm{cm^{-3}}$, a temperature of $T = 8000\,\mathrm{K}$ and a radius of $R = 0.5\,\mathrm{pc}$. With these numbers, the thermal pressure is calculated via

$$P_{\mathrm{th}} = n\,T \tag{5.2}$$

and the thermal energy with

$$E_{\mathrm{th}} = \frac{3}{2} k_{\mathrm{B}}\, P_{\mathrm{th}} V \ , \tag{5.3}$$

where k_{B} is the Boltzmann constant and V is the H II volume with radius R.

Stellar wind impact Detailed data on the O star within the compact H II region is limited, with only partial metrics reported by Martins et al. (2010), such as: an effective temperature of $T_{\mathrm{eff}} = 37500 \pm 2000\,\mathrm{K}$, an evolutionary mass of $M_{\mathrm{evol}} = 34.1 \pm 6.6\,\mathrm{M_\odot}$, a luminosity of $\log(L/L_\odot) = 5.25 \pm 0.22$, an ionizing flux of $\log(Q_i) = 48.79 \pm 0.23$, and an ionizing luminosity of $\log(L_0) = 38.26 \pm 0.23$. Yet, these parameters allow us to estimate mass-ejection rates and terminal wind velocities based on Björklund et al. (2021) (see their Table A.1).

With $\log(L/L_\odot) = 5.56$, a mass of $36\,\mathrm{M_\odot}$, and $T_{\mathrm{eff}} = 36673\,\mathrm{K}$, we estimate a mass ejection rate of 3.42×10^{-7} with a terminal wind velocity of $2672\,\mathrm{km\,s^{-1}}$. In contrast, with $\log(L/L_\odot) = 5.20$, a mass of $29\,\mathrm{M_\odot}$, and $T_{\mathrm{eff}} = 36826\,\mathrm{K}$, we estimate a mass ejection rate of 5.77×10^{-8} with a terminal wind velocity of $4389\,\mathrm{km\,s^{-1}}$. As stated in Björklund et al. (2021), the terminal wind velocities might be higher than those observed, suggesting that they could be overestimated.

The momentum injection rates are calculated with

$$\dot{p}_{\mathrm{sw}} = \dot{M} v_\infty \ , \tag{5.4}$$

where $\dot{M}$ is the mass-ejection rate and v_∞ the terminal wind velocity. The mechanical energy injection rate by the stellar wind is simply calculated using

$$\dot{E}_{\mathrm{sw}} = \frac{1}{2} \dot{M} v_\infty^2 = L_{\mathrm{sw}} \ . \tag{5.5}$$

The mechanical energy injection rate by stellar wind corresponds to the mechanical luminosity of the stellar wind, L_{sw}. Thus, Eq. 5.5 multiplied with the dynamical age t_{dyn} yields the energy injected by the stellar wind

$$E_{\mathrm{sw}} = L_{\mathrm{sw}}\, t_{\mathrm{dyn}} = \frac{1}{2} \dot{M} v_\infty^2\, t_{\mathrm{dyn}} \ . \tag{5.6}$$

Stellar radiation impact From observations and modeling of the O star, Martins et al. (2010) derived an ionizing flux of $Q_i = 10^{48.79}\,\mathrm{s^{-1}}$. To calculate how much ionizing radiation can inject total momentum into the cloud, we use

$$\dot{p}_{\mathrm{ion,th}} = 4k_{\mathrm{B}}\,T\sqrt{\frac{3\pi\,Q_i r_{\mathrm{IF}}}{\alpha_{\mathrm{B}}}}\ , \tag{5.7}$$

based on Strömgren (1939) (also see Sect. 4.1.1) and an escape fraction equal to zero. In this equation, k_{B} is the Boltzmann constant, $T = 8000\,\mathrm{K}$, r_{IF} the radius of the ionization front and $\alpha_{\mathrm{B}} = 2.5 \times 10^{-13}\,\mathrm{cm^3\,s^{-1}}$ the hydrogen recombination coefficient.

The total radiation energy is calculated from the ionizing luminosity L_0 determined by Martins et al. (2010) and the dynamical age

$$E_{\mathrm{ion,th}} = L_0\,t_{\mathrm{dyn}}\ . \tag{5.8}$$

Large shell of RCW79 We confront the driving forces in the compact H II region's [C II] bubble and the large expanding [C II] bubble in RCW79, which is ionized by twelve O stars. Martins et al. (2010) derived an ionizing flux of $Q_i = 10^{49.75}\,\mathrm{s^{-1}}$ and an upper limit for stellar wind momentum and energy. Assuming a terminal wind velocity of $v_{\mathrm{term}} = 2000\,\mathrm{km\,s^{-1}}$, we obtain $\dot{p}_{\mathrm{SW}} \leqslant 2.4\times10^{-3}\,\mathrm{M_\odot\,km\,s^{-1}\,yr^{-1}}$ and $\dot{E}_{\mathrm{SW}} \leqslant 2.4\,\mathrm{M_\odot\,km^2\,s^{-2}\,yr^{-1}}$. These values are higher by a factor of ~ 2 to ~ 10 compared to those for the small bubble in the compact H II region (S144), which are $\dot{p}_{\mathrm{SW}} \approx 2.5 - 9.1 \times 10^{-4}\,\mathrm{M_\odot\,km\,s^{-1}\,yr^{-1}}$ and $\dot{E}_{\mathrm{SW}} \approx 0.6 - 1.2\,\mathrm{M_\odot\,km^2\,s^{-2}\,yr^{-1}}$ (as given above). With Eq. 5.7 and a radius of $r_{\mathrm{IF}} = 7\,\mathrm{pc}$, the ionizing radiation injects a total momentum of $\dot{p}_{\mathrm{ion,th}} = 0.15\,\mathrm{M_\odot\,km\,s^{-1}\,yr^{-1}}$ into the cloud. This result is once again higher by a factor of ~ 10 compared to that of the small bubble, which is $\dot{p}_{\mathrm{ion,th}} = 1.7 \times 10^{-2}\,\mathrm{M_\odot\,km\,s^{-1}\,yr^{-1}}$ (as given above).

The ejected momentum and energy deduced with [C II] are $0.1 - 0.4\,\mathrm{M_\odot\,km\,s^{-1}\,yr^{-1}}$ and $1.3 - 5.3\,\mathrm{M_\odot\,km^2\,s^{-2}\,yr^{-1}}$, respectively. This indicates that the mass ejection can be momentum driven by ionizing radiation from the O stars. However, the conservative observed upper limit on the stellar wind energy of O stars still allows the observed expansion in [C II] to be driven by stellar winds if the mass ejection is adiabatic. Further observations that provide a deeper insight into the effect of ionizing radiation and stellar winds will thus be necessary to conclude which physical process drives the dispersal of the molecular cloud in RCW79.

5.3.3 Summary

The special morphology of RCW79 – featuring "a bubble in a bubble," i.e. a $\mathrm{C^+}$ bubble (source S144 from the GLIMPSE survey) embedded in the dust and gas ring around the larger H II region – offers an opportunity to study the properties and evolution of H II regions.

Using spectrally resolved [C II] 158 μm observations from the FEEDBACK legacy program on SOFIA, we identify an early-state H II region – a "$\mathrm{C^+}$ filled bubble" featuring an expanding [C II] shell ($v \sim 2.6\,\mathrm{km\,s^{-1}}$). This finding contrasts with all other $\mathrm{C^+}$ bubbles observed to date in this program, which are significantly larger, more evolved, and characterized by a clear central void in [C II] emission, caused by the evacuation of material by stellar winds.

We modeled the observed [C II] emission in S144 with the 1D model SimLine, which comprises three components: a fully ionized H II region (radius $\sim 0.5\,\mathrm{pc}$) surrounding the single exciting O7.5–O9.5V/III star, and two PDR shells with a temperature of 100 K and a density of $2500\,\mathrm{cm}^{-3}$. The outermost shell exhibits a temperature and velocity gradient. The model demonstrates that the optically thick ($\tau \sim 3 - 5$) [C II] line is self-absorbed, leading to a deficit in [C II] emission and thus to a lower ratio of [C II] to total FIR emission. However, this apparent [C II]-deficit disappears if we correct for the missing [C II] emission by fitting the wings of the [^{12}C II] line and the [^{13}C II] HFS.

We thus propose that self-absorption of the [C II] line can explain the [C II]-deficit observed in Galactic bubbles. This view will be further investigated by studying the [C II]/FIR ratio and the [C II] line properties in other FEEDBACK sources, and by comparing with simulations of H II regions that include stellar winds and radiation.

Chapter 6

Conclusions and Perspectives

Conclusions Recent studies on stellar feedback have revealed significant insights into the formation and expansion of bubbles in the ISM. These findings have important implications for our understanding of star formation and the evolution of molecular clouds. Recent [C II] observations in the Cygnus region have provided evidence that ionized carbon unveils dynamic interactions between cloud ensembles (Schneider et al., 2023). This process involves neither a head-on collision of fully molecular clouds nor a gentle merging of only atomic clouds, but rather an interaction between atomic and molecular gas over a wide range of velocities ($\sim 20\,\mathrm{km\,s^{-1}}$). Furthermore, the [C II] line has proven valuable in tracing the transition between warm, diffuse atomic gas and dense, cooler, partly molecular gas (Schneider et al., 2023). This transition is crucial for understanding the assembly of molecular clouds from the atomic hydrogen reservoir in galaxies.

In this regard, the study Schneider et al. (2024) on Draco, for which I am the third co-author, investigates [C II] emission and further helps to understand and address the question:

- What mechanisms lead to the formation of molecular clouds?

We found that the [C II] emission likely originates from shock excitation and reveals an early state of cloud formation in Draco and is also strongly governed by dynamic interaction between a partially atomic and partially molecular gas. The dynamics result from the fact that the Draco cloud descends with significant velocity onto the Galactic plane. A whole [C II] map would enlarge our view of this region and enable us to support our findings. An additional comparison with other similar clouds, but under different environmental conditions, would furthermore provide a valuable path to investigate and address the question of molecular cloud formation. In addition, comparing with simulations will help to better understand the processes underlying this formation. The follow-up paper (Schneider et al., in press), of which I am co-author, further investigates the H I-to-H_2 transition by also employing simulations.

In M33 (Keilmann et al., 2024a,b), I have addressed the following two main questions:

- How do cloud properties differ as a function of galactic environment, such as the central region or spiral arms?
- Do cloud properties systematically differ between the Milky Way and other galaxies, such as M33 with e.g. lower metallicity?

No clear trends of GMC properties with the galactocentric radius in M33 were found. Additionally, the vast majority of clouds appear to be independent of the galactic environments such as the central region or spiral arms of M33. There is only weak evidence in the data showing a vague trend for GMCs with the highest values of some cloud properties, such as the surface mass density or the size of GMCs. However, the center slightly tends to host more massive GMCs and GMCs with higher surface mass density, whereas the spiral arms host the largest GMCs. This challenges two commonly provided arguments in the literature, namely: First, spiral arms should be more conducive for star formation as larger conglomerates of gas should lead to increased star formation. And second, massive clouds or higher surface mass density correlate with higher star formation rates, which would hold true for the central region of M33. However, the overall trends as a function of galactic environment are weak. These are hints that the galactic environment does not play a crucial role in star formation, and probably small-scale mechanisms such as stellar feedback could have a greater influence on star formation.

Notably, some GMC properties between the Milky Way and M33 are similar, while others are different. These encompass, for instance, the size of the largest GMCs in both galaxies, although the size, mass, and evolutionary state (metallicity) differ in both galaxies significantly. These similar sizes of the largest GMCs in both galaxies hint at mechanisms that rely on, for example, the maximum size of supernovae remnants or the galactic scale height, which is similar in both galaxies. On the other hand, M33 lacks the high-mass clouds seen in the Milky Way, which could be attributed to the different density in both clouds.

However, other properties have not yet been analyzed, such as stellar feedback in more detail, or magnetic fields, turbulence, and the rotations of the GMCs. These can further provide deep insights into the properties of GMCs, and hence star formation. A study on investigating magnetic fields (for which I have data) and the rotations of the detected GMCs in M33 (using the IRAM 30m CO data) is already in preparation.

The [C II] 158 μm fine-structure line has emerged as an excellent tracer to study the kinematics of ionized gas and stellar feedback, primarily through ionizing radiation and stellar winds, which drive the dynamics of H II regions and lead to expanding shells visible in [C II] emission (e.g., Pabst et al., 2020; Beuther et al., 2022; Kabanovic et al., 2022). Hence, the [C II] line helps to address the questions I have studied, such as:

- What is the driving mechanism of stellar feedback? Which has a greater impact on the surrounding interstellar medium, stellar winds or radiation?
- What could be the potential time dependence of these processes and their final evolution?

The early evolutionary stage of the compact H II region S144 in RCW79 indeed shows that stellar winds are yet not dominant in affecting the surrounding medium. A comparison with a model suitable for early phases shows a reasonable prediction. However, although the results align with the picture that stellar winds become more important in later stages, further studies must unravel the contribution of stellar wind and radiation as a function of time. Different models of stellar winds need to be examined and simulations must be contrasted with observations, as well as studying stellar feedback in other (FEEDBACK) sources. Better understanding stellar feedback processes may also help in studying the stellar feedback contributions in M33.

In RCW79 Keilmann et al. (2025), I also analyzed the [C II]-deficit, which corresponds to different cooling pathways ([C II] and dust FIR) addressing the question:

- What influences the cooling pathways of different tracers in the ISM?

For the first time, the [C II]-deficit is explained by originating from [C II] self-absorption effects. The [C II]-deficit needs to be further examined in other (FEEDBACK) sources, which likely hold other mechanisms for the observed deficit, and hence a more complex picture of different cooling pathways in the ISM.

Finally, although stellar feedback is frequently claimed for “negatively” impacting the surrounding medium by dispersing clouds, its effect is rarely quantified or analyzed. In Bonne et al. (2023), where I was also involved, we demonstrated that the large shell of RCW79 is in a state of molecular cloud dispersal.

Perspectives The study of expanding bubbles and stellar feedback using [C II] observations is an active area of research. Future projects, such as NASA’s GUSTO[1] and ASTRHOS[2] balloon missions, will measure [C II] emission in the Milky Way and Magellanic Clouds, potentially revealing whether the observed interactions are common in other GMC regions. In conclusion, spectrally resolved [C II] observations have significantly advanced our understanding of stellar feedback processes, revealing the complex dynamics of expanding bubbles and their role in shaping the interstellar medium and influencing star formation.

Carbon ([C I]) in its neutral atomic form is a largely unexplored tracer of gas dynamics and excitation. The [C I] $1 \rightarrow 0$ and $2 \rightarrow 1$ transitions at 492 and 810 GHz, respectively, are predicted to arise in a region between the warm PDR, where [C II] serves as the primary cooling line, and the cold molecular cloud as traced by CO. However, the dynamics and excitation conditions of the [C I] emitting gas are yet unknown. The required extended mapping of these lines was not possible with previous facilities in the last decades. This limitation is set to improve with the upcoming Fred Young Submillimeter Telescope (FYST) of the CCAT[3] (Cerro Chajnantor Atacama Telescope) observatory. The FYST is a future submillimeter to millimeter wavelength observatory designed to address key questions in astrophysics, such as the nature of the cosmic microwave background, the evolution of galaxies, and the physics of star formation. The CCAT consortium consists of Cornell University, the University of Cologne, and other universities and institutions in Germany and Canada.

Featuring a 6-meter aperture with an off-axis crossed-Dragone optical design, the observatory minimizes blockage while providing a very large, unobstructed field of view, making it ideal for wide-area surveys. The observatory is located on Cerro Chajnantor in the Atacama Desert, northern Chile, at an altitude of around 5600 m, from which

---

[1] `https://science.nasa.gov/mission/gusto/`

[2] `https://www.jpl.nasa.gov/missions/asthros/`

[3] `https://www.ccatobservatory.org`

the observatory benefits from the combination of high altitude and extremely dry conditions, resulting in exceptional atmospheric transparency at submillimeter wavelengths (simply where the atmospheric conditions allow observations at high frequencies). The facility will be equipped with state-of-the-art instruments. These include the Prime-Cam, a large-format submillimeter camera, alongside the CCAT Heterodyne Array Instrument (CHAI), a spectroscopic heterodyne receiver. These devices will facilitate the comprehensive mapping of cosmic structures and the identification of faint, distant objects.

Various scientific objectives will be pursued, such as tracing the epoch of reionization with [C II] intensity mapping. However, most relevant to the work of this thesis is the **G**alactic **Eco**logy (GEco) project, which will map the [C I] lines as well as mid- to high-excitation CO lines (CO $4 \rightarrow 3$, CO $7 \rightarrow 6$, etc., and its isotopologues) as diagnostics of physical conditions and motions of interstellar clouds. CCAT will provide maps at $15'' \times \lambda/350\,\mu$m resolution over degree scales of the Milky Way including the Galactic center and Magellanic Clouds. This will allow us to study the mass budget of [C I], which traces the gas temperature and mass and is the complement cooling line in PDRs. The telescope will also help to study turbulent dissipation for which mid- to high-excitation CO and ^{13}CO lines will be used to study excitation conditions and shocked gas. It will also enable us to trace variable gas flow into cores and young stars.

While [C II] extends across all interstellar medium phases, [C I] is specific to CO-dark molecular gas, focusing on cloud edges or early molecular evolution (Clark et al., 2019). [C II] emission also primarily originates from atomic gas and not from CO-dark molecular gas (Franeck et al., 2018). Thus, integrating CO data with [C I] as a dark gas tracer provides a comprehensive understanding of molecular material, especially H_2 gas of low density. As these lines are narrow, they resolve distinct gas flows in velocity space. Furthermore, [C I] experiences less line-of-sight confusion compared to H I. Large-scale observations of the Galactic plane in [C I] and CO are essential to statistically compare models and data due to the randomness of turbulence. For further information, refer to the 2020 decadal review white paper Simon et al. (2019).

My research on M33, and particularly on FEEDBACK sources, is directly relevant to the GEco program. I have developed data reduction and analysis tools, such as N-PDFs, that are readily applicable to the scientific objectives of GEco. In particular, the comparative analysis of [C II], [C I], and CO will be of significant importance.

Appendices

Appendix A

[C I] APEX Observations in M33

Observations of dedicated atomic and molecular line tracers of individual GMCs in local galaxies address key questions in galaxy evolution. The six successfully observed positions of the atomic carbon line [C I] 1 → 0 along the cuts of the southern arm in M33 (Fig. A.1, APEX Proposal 109.23FN, with me as the PI via ESO[1] time) will be combined with existing [C II] and CO data, and thereby help to obtain information on the carbon budget and the fraction of CO-dark gas, which differs for GMCs in M33's lower metallicity environment relative to the Milky Way. Comparison of the spectral line shape of [C I] with existing CO and [C II] data may help determine the relative impact of stellar feedback and cloud–cloud collisions on gas dynamics. These combined observations provide important clues regarding the origin of various lines (molecular clouds versus intercloud-medium) and the line-of-sight structure (overlapping clouds).

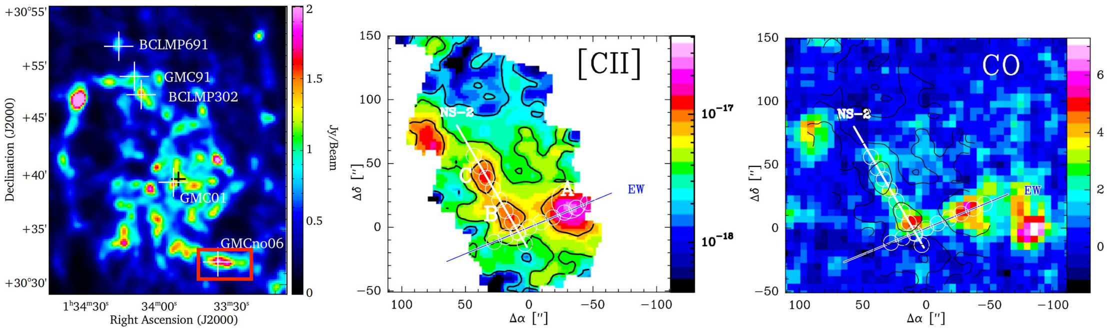

Figure A.1: Observed cuts of the southern arm in M33. Left: 350 μm SPIRE map (Xilouris et al., 2012) outlining the cuts in the southern arm with a red box (black cross marks the center at RA(J2000) = $01^h33^m51.02^s$, Dec(J2000) = $30°39'36.7''$). White crosses mark the positions of the [C I] observations. Middle: PACS [C II] map (Nikola et al., in prep.) of the southern arm region of M33 in proximity of GMCno06. Straight lines mark two on-the-fly HIFI [C II] cuts, while circles mark the 12″ beam and [C II] detections with HIFI (cf. Fig. A.2). Contours of [C II] fluxes are overlaid on all three maps with 8, 4, 2 levels in units of 10^{-18} W m^{-2}. Right: Integrated-intensity map of CO 2 → 1 of the same region.

M33 exhibits a particularly high star formation efficiency (Gardan et al., 2007) compared to the Milky Way, yet its underlying cause remains unclear. Observations at $\sim 10''$

---

[1] European Southern Observatory

(40.7 pc) resolution resolve individual large GMCs or GMAs. We plan to study the carbon budget and gas dynamics in the prominent inner southern, star-forming spiral arm of M33 (see Fig. A.1).

The [C II] line is primarily excited in the ionized and atomic phases of the PDR, while [C I] is expected to originate from the layer between the ionized gas and the molecular cloud. The [C I] ($^3P_1 \rightarrow {}^3P_0$) transition at 492.16 GHz is assumed to be mostly optically thin and has critical densities of $\sim 10^2 - 10^3\,\mathrm{cm}^{-3}$ for collisions with H I and H_2. PDR models and cloud-scale simulations predict that [C I] is an excellent tracer of H_2 over a wide range of densities and metallicities (Glover and Clark, 2016; Clark et al., 2019; Papadopoulos et al., 2018).

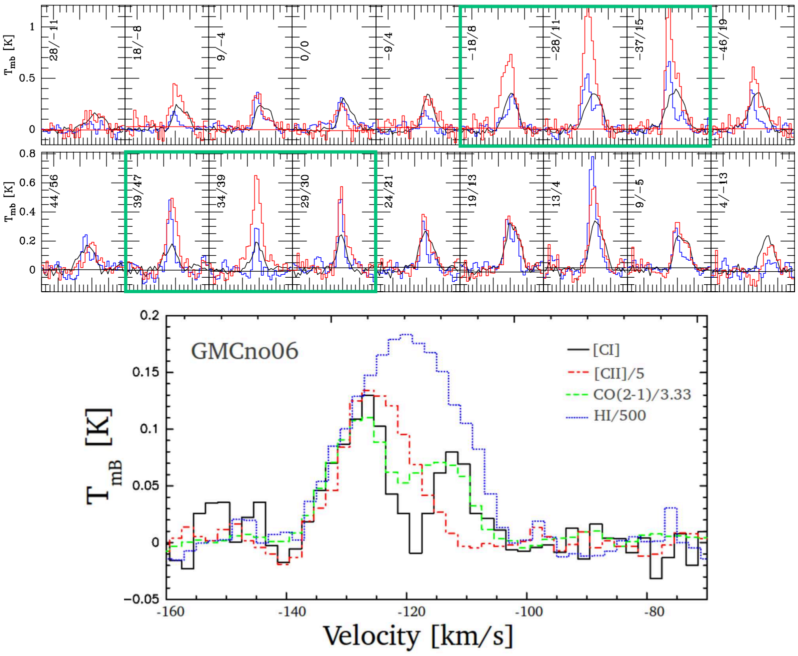

Figure A.2: Spectra of [C II] (red), CO(2 − 1) (blue), and H I (black) along the three cuts through the southern arm of M33 on a 10″ grid. Relative map positions are given in arcseconds. T_{mb} is shown versus v_{LSR} ranging from −180 to $-80\,\mathrm{km\,s^{-1}}$. The spectra have a common spectral resolution of $\Delta v = 2.6\,\mathrm{km\,s^{-1}}$. H I temperatures have been divided by 500. The green boxes correspond to the 6 observed positions.

Despite its potential, there is a lack of local galaxy observations that calibrate [C I] emissivity against parameters such as density or radiation field (e.g., Hitschfeld et al., 2008; Kramer et al., 2020). Moreover, most studies (e.g., Crocker et al., 2019; Jiao et al., 2017) focus on galaxy centers, and the variation of [C I] line strength across galaxies or its dependence on the local environment remains largely unexplored.

Studying nearby galaxies using all carbon tracers (CO, [C II], and [C I]) reveal galaxy-scale trends of the carbon cycle, particularly as a function of ISM conditions, dynamical environment, or large-scale phenomena (e.g., galactic outflows). From [C I] data, we can derive column densities, complementing existing observations of CO, [C II], and dust continuum data from Herschel (PACS and SPIRE) maps. Incorporating [C I] data will help identify the contributions of different ISM phases to [C II] emission and isolate PDR emission, thereby enabling a more accurate derivation of physical conditions via PDR models.

Appendix B

CO APEX Observations in RCW79

Recent observations of the [C II] line in Galactic H II region bubbles and low-density clouds reveal four major findings. First, [C II] was found to trace expanding shells driven mostly by stellar winds (e.g., Pabst et al., 2019; Luisi et al., 2021; Bonne et al., 2022; Beuther et al., 2022), although thermal expansion of the H II region may also contribute. Second, studies found large column densities of cold C^+ due to self-absorption features in the [C II] line (Guevara et al., 2020; Kabanovic et al., 2022); one explanation is that C^+ mixes with the atomic gas that envelops the molecular cloud. Investigations of [C II], CO, and H I self-absorption in RCW120 using the two-layer radiative transfer model support this conclusion. Third, Bonne et al. (2022) demonstrated that [C II] reveals the dispersal

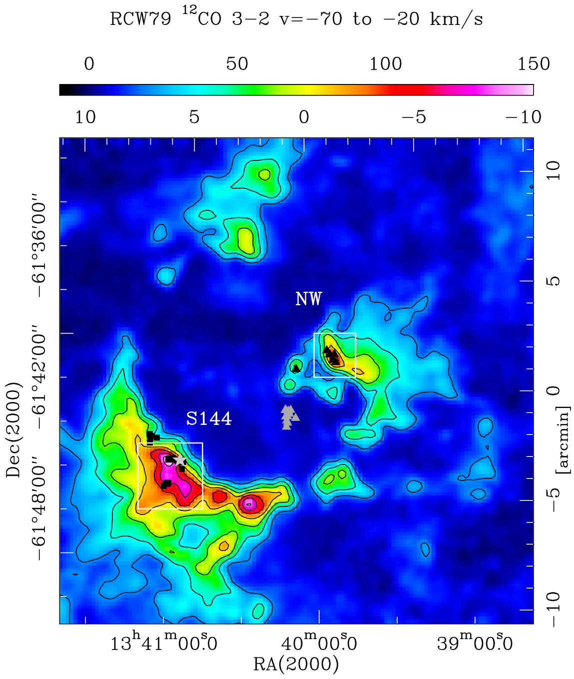

Figure B.1: Line-integrated $^{12}CO\,3\rightarrow2$ emission in RCW79. The proposed and successfully observed areas $C^{18}O\,3\rightarrow2$ and $^{12}CO\,6\rightarrow5$ are indicated with white boxes and comprise the compact H II region S144 in the southeast and a PDR region in the northwest (NW).

of molecular clouds in the H II bubble RCW79. Fourth, [C II] appears to trace shock dynamics (Schneider et al., 2024).

The APEX proposal (number M9502A_113 with me as the PI via Max-Planck time) has two objectives: First, to observe an optically thin CO line in RCW79 because existing CO data do not allow us to decide whether the observed line shapes result from self-absorption or independent velocity components (finding a situation similar to RCW120 would strongly support the argument that large columns of cold C^+ originate from extended H I envelopes around molecular clouds). Second, to perform comprehensive modeling of the physical conditions with radiative transfer and PDR modeling, which requires the higher excitation mid-J CO lines as proposed and successfully observed.

Figure B.1 displays the APEX line-integrated ^{12}CO $3 \rightarrow 2$ map (Bonne et al., 2023). The ring hosts young stellar objects, a compact H II region (S144) in the southeast, and an early site of high-mass star formation in the northwest. Channel maps of [C II] emission show that the H II region's border is traced by an expanding [C II] shell with $v \approx 15\,\mathrm{km\,s^{-1}}$ and that the small bubble is filled with [C II], marking a first detection of such a feature.

We proposed to map the ^{12}CO $6 \rightarrow 5$ line over the same area as the C^{18}O $3 \rightarrow 2$ observations (the two white boxes in Fig. B.1) and to obtain four positions in ^{13}CO $6 \rightarrow 5$ (at the O star, the CO peak emission in S144 and the [C II] peak emissions in S144 and in the northwestern region (NW), which is also the peak in CO emission in NW). This approach will help clarify the layering of gas components — hot gas near the O star and cooler gas in the molecular cloud. The main goal of the ^{12}CO and ^{13}CO $6 \rightarrow 5$ observations in S144 is to secure complementary data for modeling the emission of photodissociated gas and the cooler molecular cloud. Our existing dataset includes the key cooling lines for PDR and molecular cloud gas ([C II] 158 μm, [O I] 63 μm, [C I] $1 \rightarrow 0$, CO $11 \rightarrow 10$, $9 \rightarrow 8$ from SOFIA; ^{12}CO, ^{13}CO, C^{18}O $1 \rightarrow 0$ from Mopra; and ^{12}CO, ^{13}CO $3 \rightarrow 2$ from APEX). To precisely determine the density, gas mass, and UV field, we need mid-J CO lines, using the KOSMA-tau PDR model to develop a physical model with both clumpy and non-clumpy components. Our objective is to anatomize the compact H II region — with its complex layering of gas at varying temperatures and densities — and to gain insight into its evolutionary state, characterized by several [C II] bubbles. We will also perform RADEX calculations to compare with PDR modeling.

Among the high-mass star-forming regions examined in the SOFIA FEEDBACK project (e.g., RCW120, NGC7538, and RCW49), RCW79 stands out for its three distinct bubble-like structures at different evolutionary stages. The large-scale bubble shows clear signs of disruption by the central OB cluster, leaving a fragmented ring of PDRs, while the prominent southeast compact H II region contains an additional bubble. This configuration offers a unique opportunity to study the compact H II region in detail and to compare the properties of this potentially triggered star formation site with those in the remaining PDR ring. Therefore, we proposed to use the same observational setup to also observe the NW PDR — a high-mass star-forming site as indicated in Fig. B.1 — for a detailed comparison.

Appendix C

H I Data with Short-Spacing Corrections (Paper I, M33)

Keilmann et al. (2024a) (Paper I, M33) relies on H I data (Gratier et al., 2010) lacking short-spacing corrections, whereas the subsequent study (Keilmann et al., 2024b) (Paper II, M33) employs H I data from Koch et al. (2018), which includes those corrections. The discussion in this section focuses on how the results of Keilmann et al. (2024a) are impacted by using H I data with short-spacing corrections. Short-spacing corrections in interferometric data address a fundamental issue that arises due to the limited range of baselines (i.e., distances between pairs of antennas) in an interferometer telescope. Interferometers, such as ALMA or VLA, only sample specific spatial frequencies, which correspond to the baselines. The shortest baselines are responsible for capturing larger-scale structures, while the longer baselines capture the finer details of a source. Because interferometers lack baselines shorter than the minimum distance between the antennas, they miss information on the large angular scales of the emission. This is the "missing short spacings" problem, which leads to incomplete sampling of the Fourier transform of the sky brightness distribution, resulting in the loss of extended emission in the final image.

The H I map from Koch et al. (2018) incorporates short-spacing corrections, while that of Gratier et al. (2010) does not. The main difference between both lies in the diffuse, extended large-scale emission. This means that in the map of Gratier et al. (2010), the regions beyond our detected GMCs should be the most affected by short-spacing issues, whereas the denser regions should be fairly unaffected. We therefore, in general, can expect that the effect with or without short-spacing corrections should be small, since we are mainly interested in those regions, which are not diffuse. The GMCs that we detect are not located in diffuse H_2 gas (as can already be seen in Fig. 2 of the paper), nor are they located in regions of diffuse H I. Figure C.1 shows an overlay of the detected GMCs on the H I map of Koch et al. (2018).

In Fig. C.2 we show difference maps of both H I maps. The absolute difference is calculated by $\Delta_{\mathrm{abs}} = \mathrm{H\,I}_{\mathrm{Koch}} - \mathrm{H\,I}_{\mathrm{Gratier}}$, whereas the relative difference is determined via $\Delta_{\mathrm{rel}} = (\mathrm{H\,I}_{\mathrm{Koch}} - \mathrm{H\,I}_{\mathrm{Gratier}})/\mathrm{H\,I}_{\mathrm{Koch}}$. As can be seen, the difference is low in regions, where CO is above its 2σ level. The difference in these regions is of the order of 10 % or lower. In several other regions, the difference is also low. However, the deviation becomes more pronounced in large diffuse regions, in which we do not detect GMCs. Hence, the effect on our statistics is also low, which becomes obvious in the plots of the revised paper and

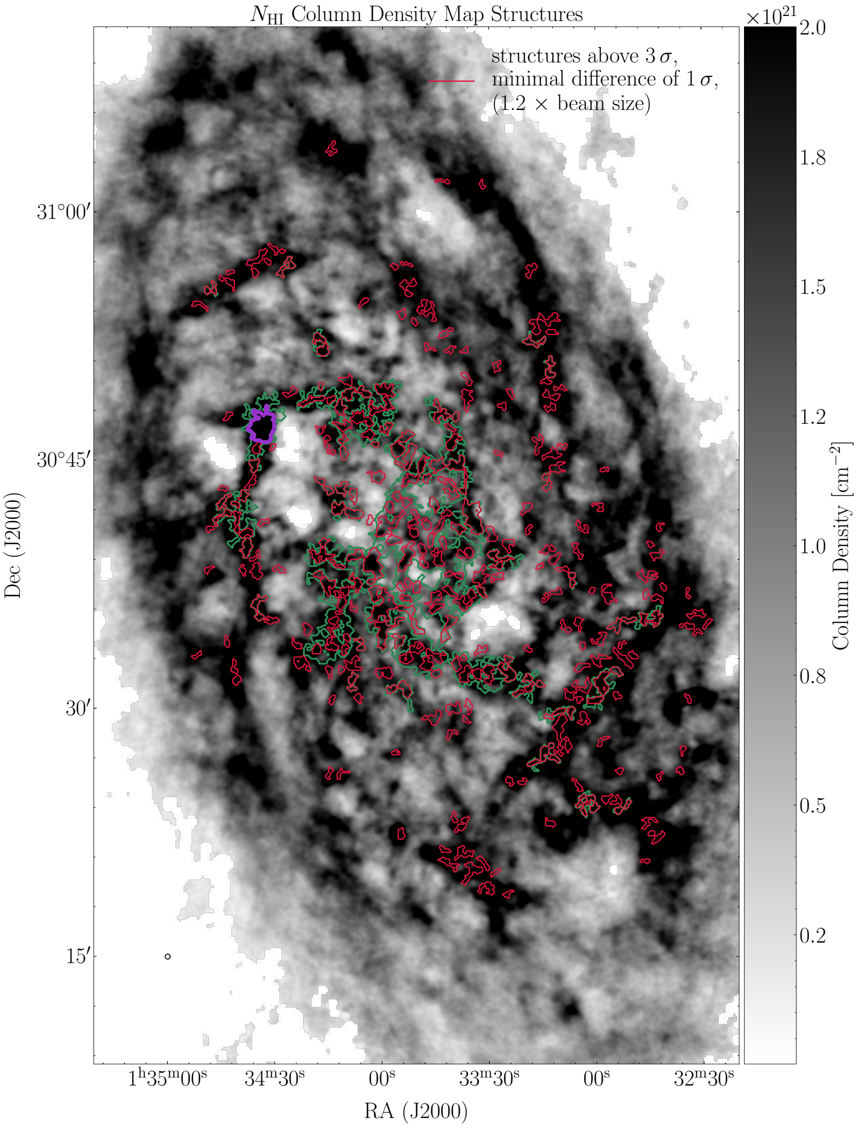

Figure C.1: Detected GMCs overlaid on the H I map of Koch et al. (2018).

the reported mean values.

The H I data is used in two steps in the production of the hydrogen column density map of Paper I. Now I describe briefly how I determine κ_0 and $N_{\rm H_2}$ in Paper I, because this illustrates why, in addition to the discussion above, the effect should be low to negligible. Equation 16 in Paper I is

$$\kappa_0 \approx \frac{I_{250\,\mu\rm m}}{\mu\, m_{\rm H}\, N_{\rm H\,I} B_\nu(T_d)} \;, \tag{C.1}$$

where $I_{250\,\mu m}$ is the SPIRE 250 μm map, μ the mean molecular weight, $N_{\rm H\,I}$ the H I column density and $B_\nu(T_d)$ the Planck function. Thus, due to the higher H I emission at some regions, κ_0 will become smaller in these regions. Equation 12 of Paper I uses this calibrated κ_0 in order to determine the total hydrogen column density map

$$N_{\rm H} = \frac{I_\nu}{\kappa_0(\lambda/250\,\mu\rm m)^{-\beta}\,\mu\, m_{\rm H}\, B_\nu(T_d)} \;, \tag{C.2}$$

where I_ν is again the Herschel map and β the emissivity index.

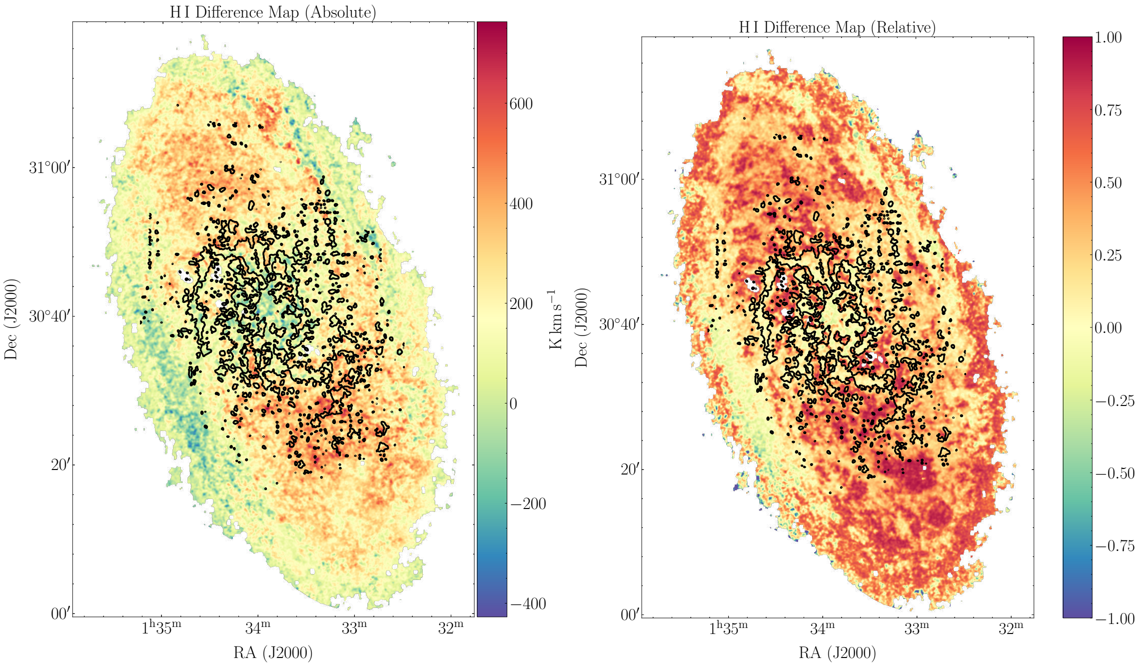

Figure C.2: H I difference maps of Koch et al. (2018) and Gratier et al. (2010). Left: Difference in absolute values ($\Delta_{\mathrm{abs}} = \mathrm{H\,I}_{\mathrm{Koch}} - \mathrm{H\,I}_{\mathrm{Gratier}}$). Right: Relative difference ($\Delta_{\mathrm{rel}} = (\mathrm{H\,I}_{\mathrm{Koch}} - \mathrm{H\,I}_{\mathrm{Gratier}})/\mathrm{H\,I}_{\mathrm{Koch}}$).

Since κ_0 is smaller in some regions, the total hydrogen will be higher. However, the effect is still low, because - in order to arrive at N_{H_2} - we subtract the H I map again. In the end, the increased H I in some regions leads to an increase in total hydrogen column density, but since we subtract again the increased H I column density, the overall difference is negligible.

Appendix D

Varying Dendrogram Parameters (Paper II, M33)

In the following, the impact of varying Dendrogram parameters on the results of follow-up Paper II (Keilmann et al., 2024b) is analyzed and discussed. The parameter `min_value` was chosen to vary from 3σ (as used in the paper) to 5σ, while the remaining parameters remain unchanged. In another subset, the beam factor has additionally been changed, which controls the minimum size of the structures to be identified. Kramer et al. (1998) investigated the effect of a beam factor of 1.1, 1.5 and 2 (see their Fig. 4). I show the change from 1.2 (as used in the paper) to 1.5. The remaining parameters are unchanged again. Finally, the study shows the individual effect that a parameter has on the results. Changing the parameter `min_delta`, which controls how much two local peaks must be apart to be considered as two separated structures, does practically not have an effect on the results. Therefore, I omit displaying the essentially identical plots. We denote the choice of parameters `min_value` $= 5\sigma$, `min_delta` $= 1\sigma$ and a beam factor of 1.2 as the "standard case" used in the paper.

D.1 `min_value` $= 5\sigma$

Figures D.1 and D.2 show the 214 detected GMCs and their distributions of the main parameters for a minimum threshold `min_value` set to 5σ, respectively. As expected, the mean values of mass and radius increase, whereas the density and surface mass density decrease. The mass-size relations presented in the paper for the standard case indicate that larger GMCs typically exhibit lower densities, thus explaining the decrease in (surface mass) density. To provide a comparison, I display the results of the additional studies referenced in the paper.

The slope of the mass-size relation (see Fig. D.3) for dust remains largely unchanged. For CO, the slope slightly decreases to 2.0. However, the mass-size relations for both tracers show marginal changes, taking into account the uncertainties. The CO luminosity also does not change significantly (see Fig. D.4). The fit remains at a slope of 1.5. The power-law slopes shown in Fig. D.5 increase for both tracers, as a result of excluding less massive GMCs. This means that the mass range is truncated at the lower end and shifts to higher values. This increase, however, is still low given the uncertainties.

Moreover, the dependence with the galactocentric radius R_{gal} exhibits a pattern com-

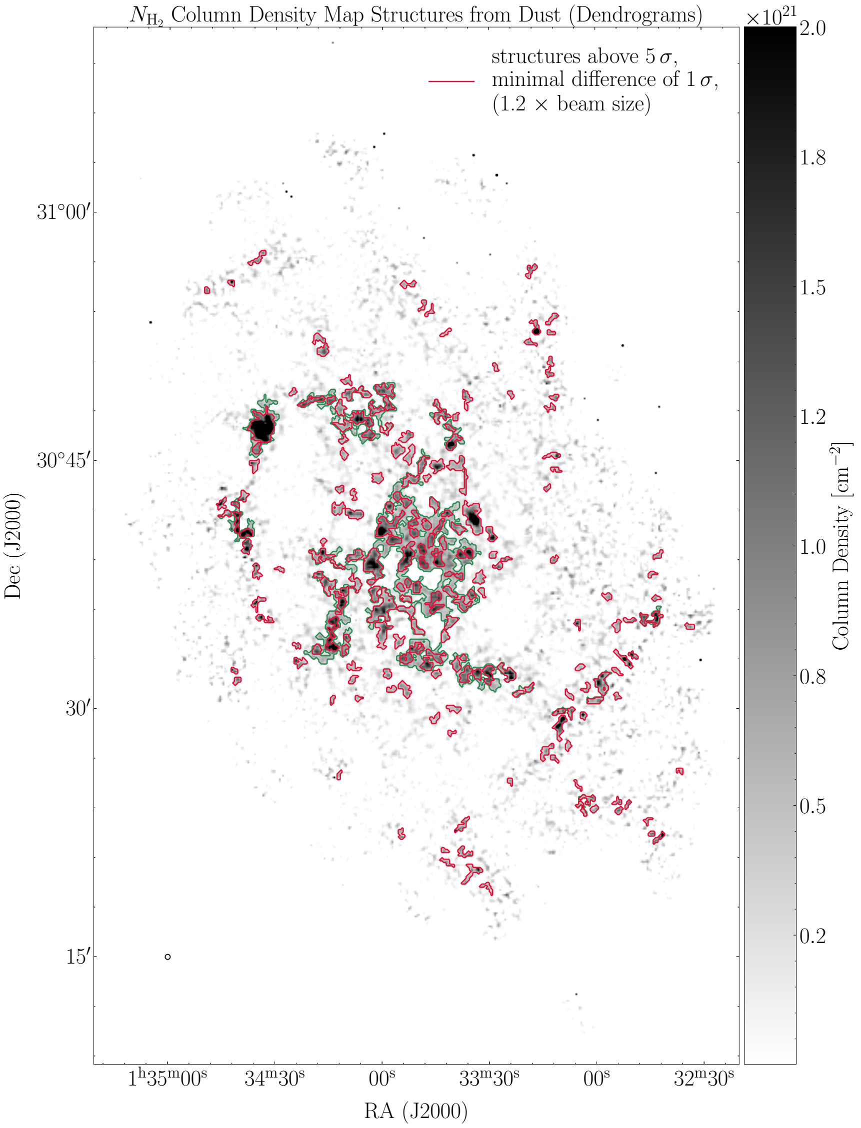

Figure D.1: Detected GMCs with a beam factor of 1.5.

parable to that shown in the paper and continues to lack significant trends (refer to Fig. D.6).

D.2 beam factor = 1.5

Additionally, the beam factor has been varied from 1.2 to 1.5. In Fig. D.7 the detected structures are overlaid on the N_{H_2} map. 242 GMCs have been detected, showing a similar distribution as in the standard case with a beam factor of 1.2.

Figure D.8 presents the distributions of the main parameters. As expected, the mean mass and radius values increase, while the density and surface mass density decrease. This reduction in density and surface mass density is inferred from the mass-size relation presented in the paper for the standard case, showing that larger GMCs generally tend to have lower densities. Here, I also present the results of other studies that I compare against in the main analysis.

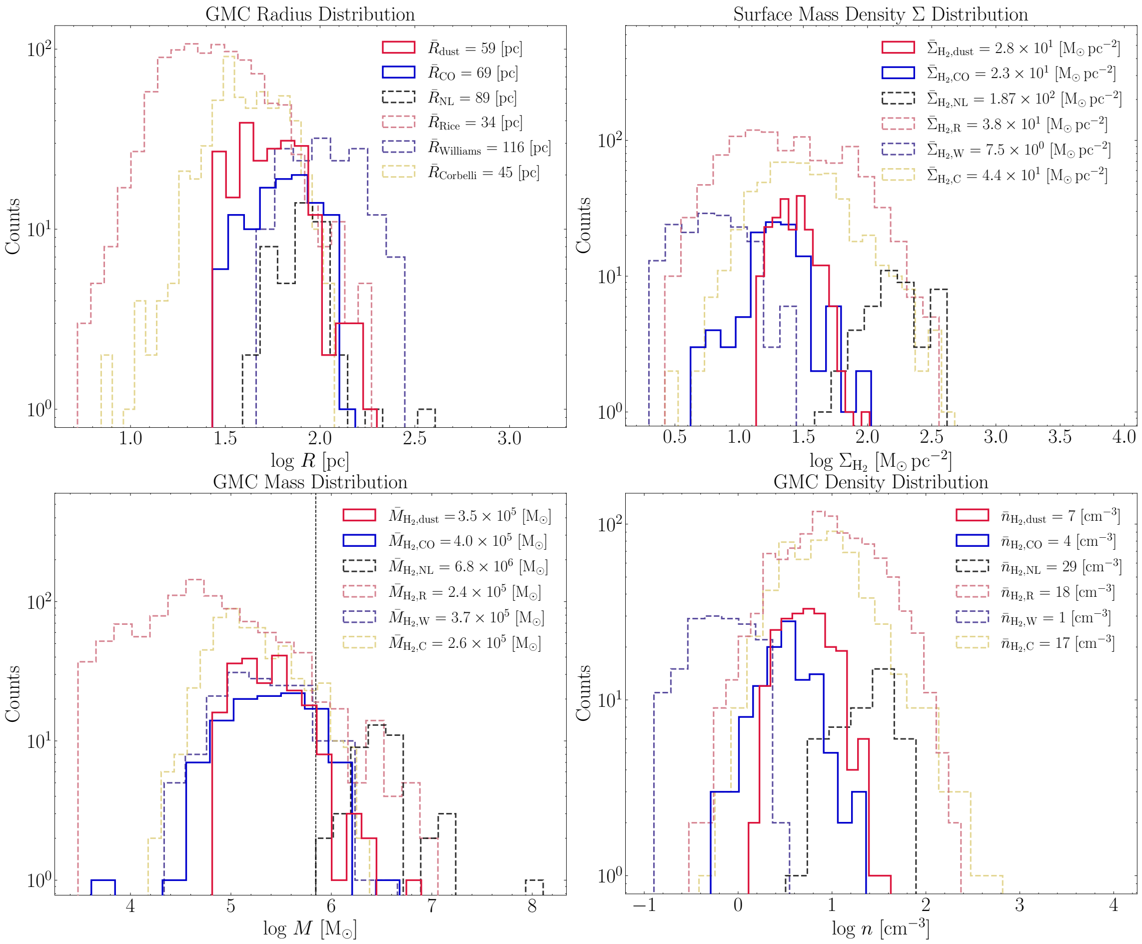

Figure D.2: Distributions of main GMC parameters with a `min_value` of 5σ.

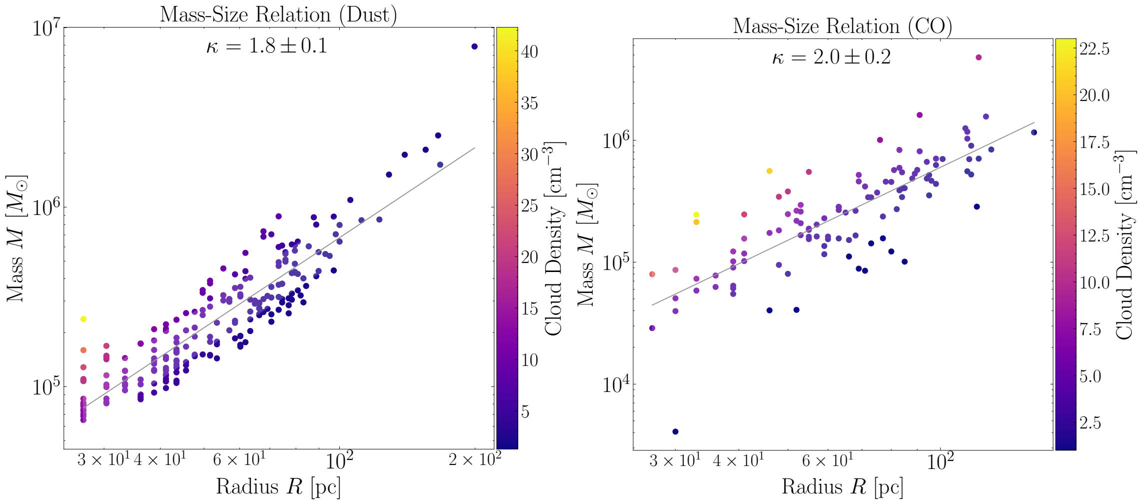

Figure D.3: Mass-size relation of GMCs detected with a `min_value` of 5σ.

The CO luminosity also does not change significantly (see Fig. D.9). The fit changes from 1.5 to 1.8, suggesting that this parameter choice leads to a larger number of pixels on the outskirts of a GMC, which show CO emission that is less saturated. This means

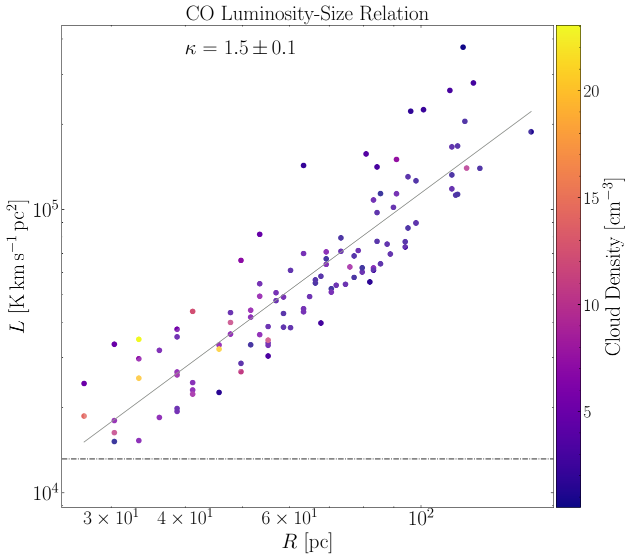

Figure D.4: CO luminosity of GMCs detected with a `min_value` of 5σ.

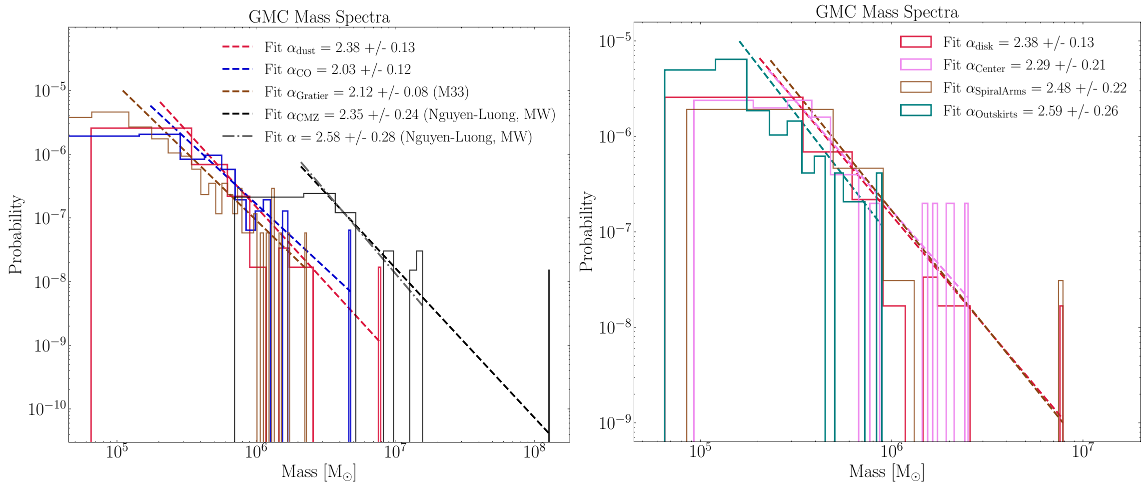

Figure D.5: Power-law mass spectra of GMC detected with a `min_value` of 5σ.

that the emission in the inner region of a GMC is even less able to show a CO emission level as at the edge of a GMC. In this manner, we increase the effect of the CO-dark H_2 gas. However, given the uncertainty, this increase is not significant.

The mass-size relations for both tracers also show no significant changes considering the given uncertainties. The power-law slopes increase in both cases, as a result of excluding smaller GMCs. This means that the mass range is truncated at the lower end and shifts to higher values. This increase, however, is still insignificant given the uncertainties. Also, the dependence with the galactocentric radius $R_{\rm gal}$ shows a similar characteristic and still does not show any significant trend (see Fig. D.12).

Overall, we conclude that our choice of parameters used in the paper is robust and varying the parameters does not significantly change the overall results and conclusions.

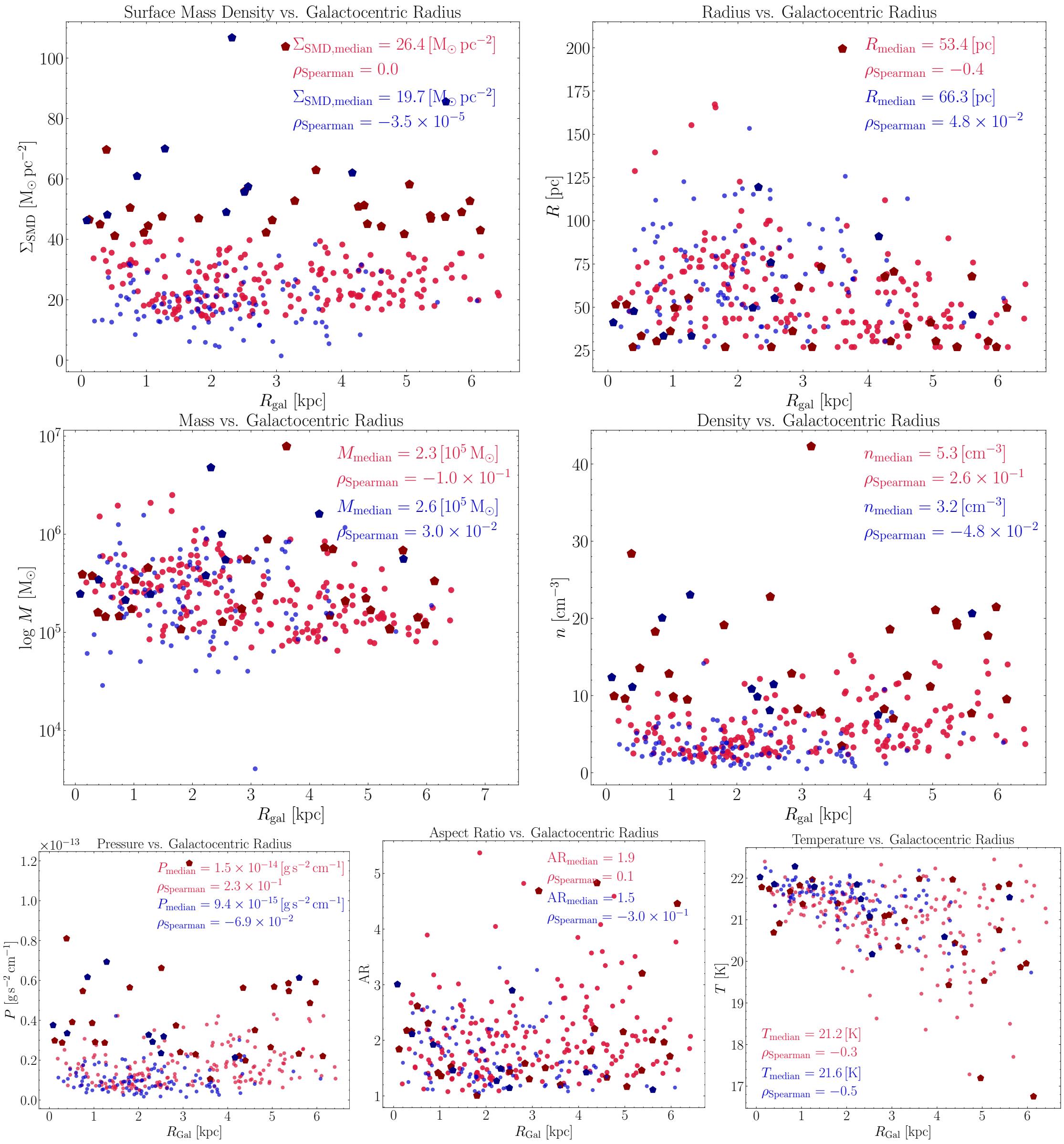

Figure D.6: Dependence with $R_{\rm gal}$ of main GMC parameters with a `min_value` of 5σ.

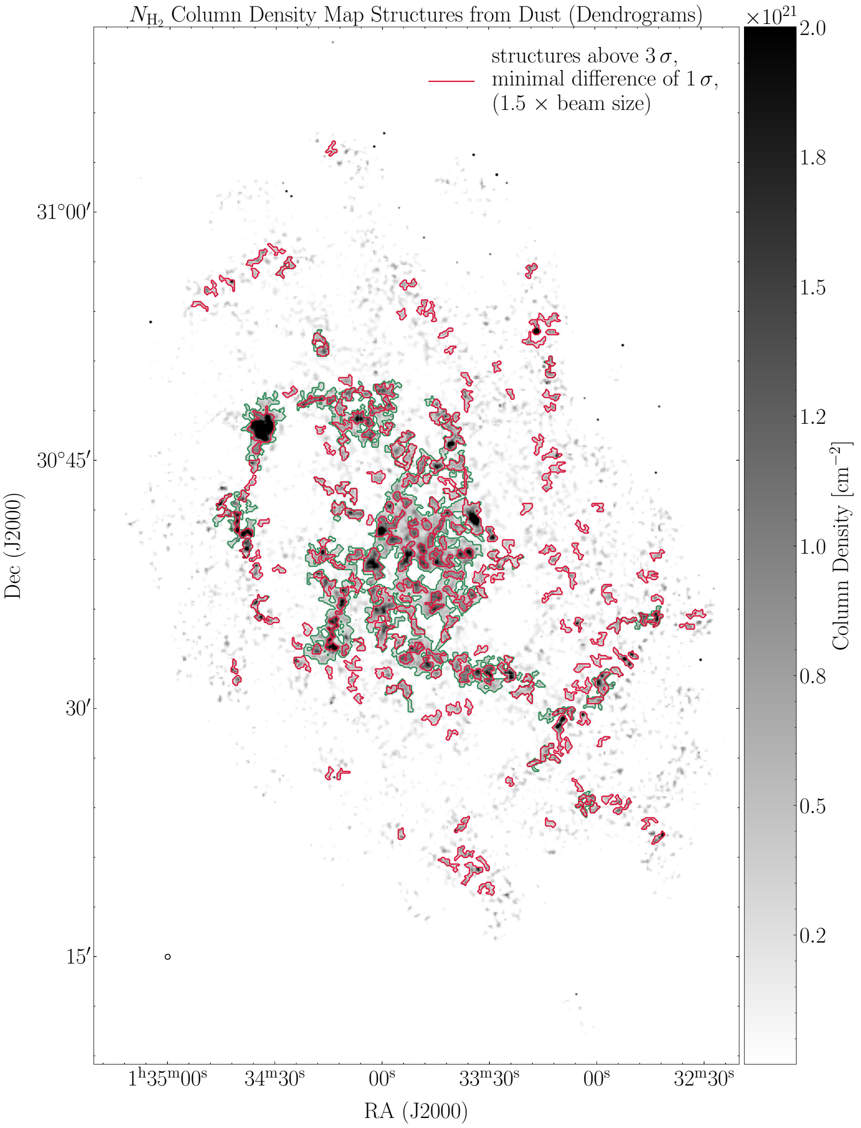

Figure D.7: Detected GMCs with a beam factor of 1.5.

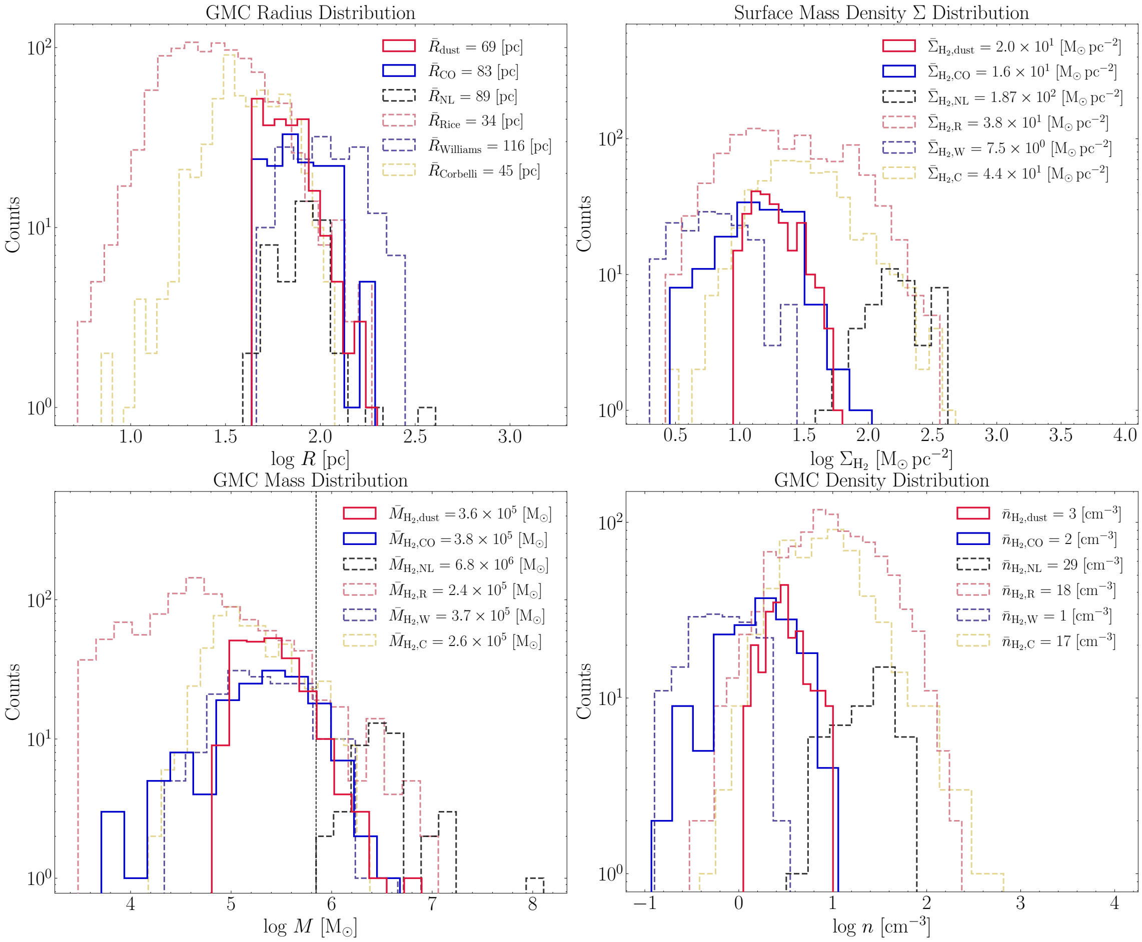

Figure D.8: Distributions of main GMC parameters with a beam factor of 1.5.

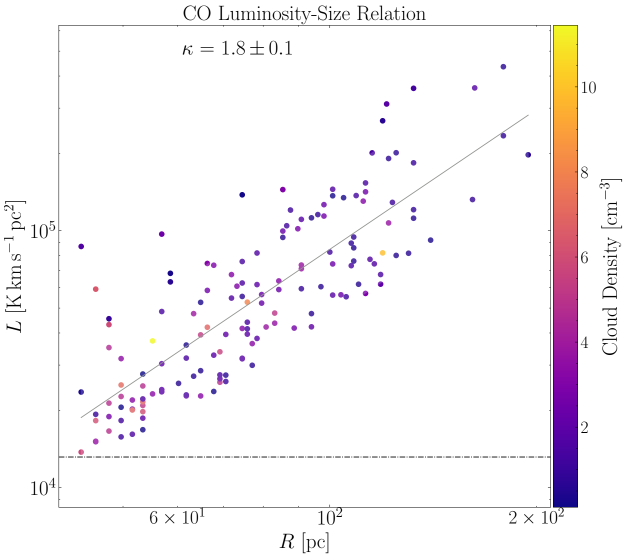

Figure D.9: CO luminosity of GMCs detected with a beam factor of 1.5.

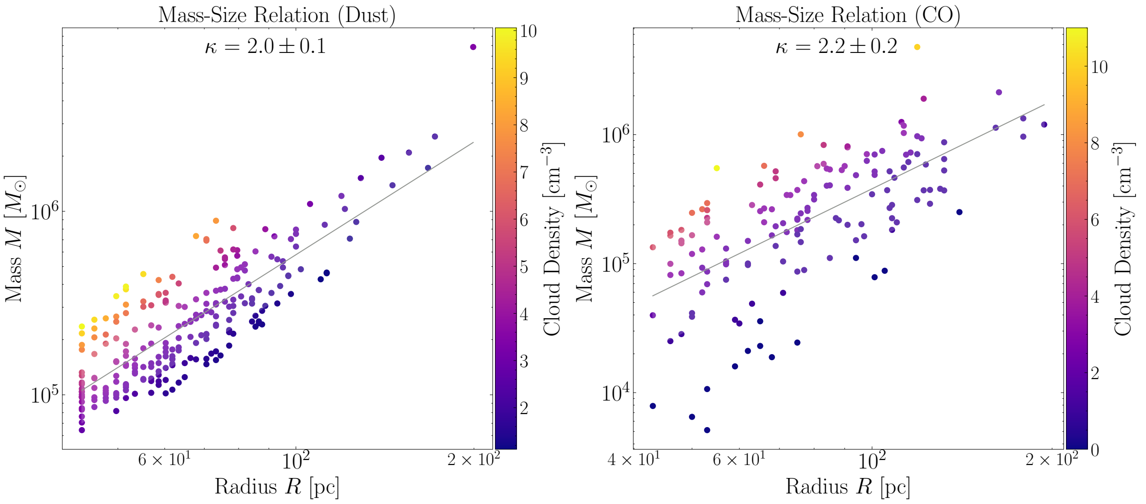

Figure D.10: Mass-size relation of GMCs detected with a beam factor of 1.5.

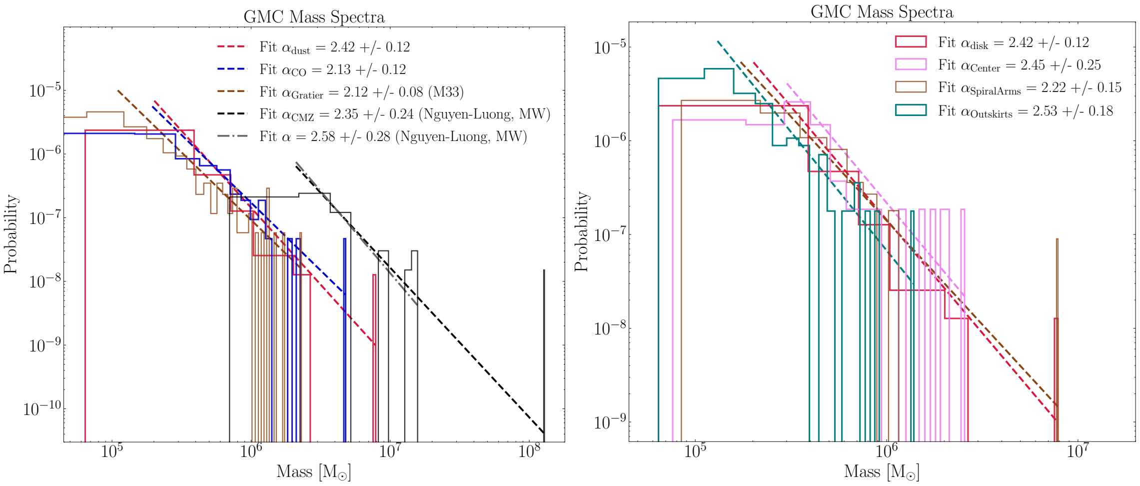

Figure D.11: Power-law mass spectra of GMCs detected with a beam factor of 1.5.

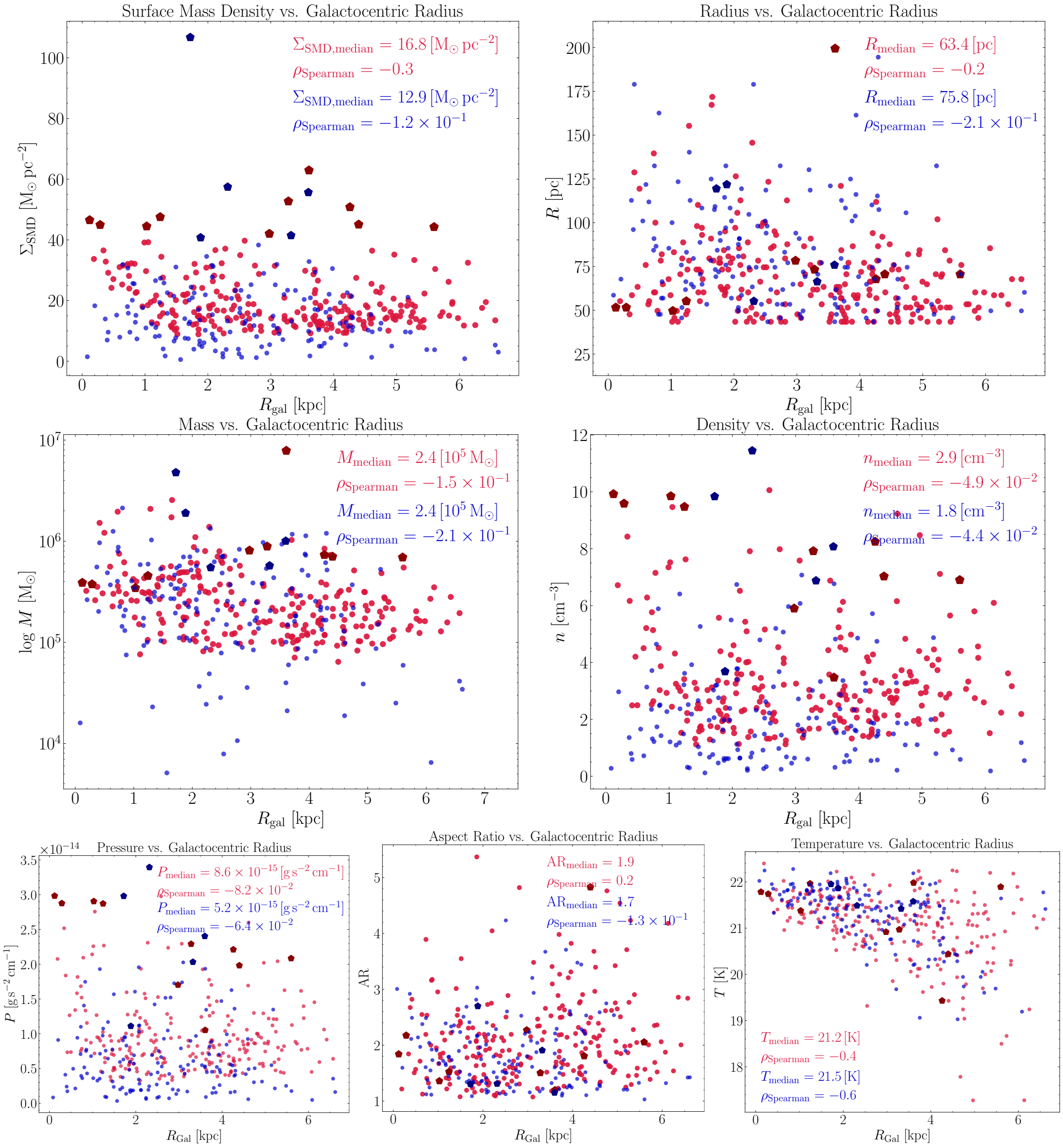

Figure D.12: Dependence with R_{gal} of main GMC parameters with a beam factor of 1.5.

Spiral Arm Definition in Paper II, M33

To demonstrate that the visually defined region employed in Paper II (Keilmann et al., 2024b) to differentiate between the two spiral arms and the outskirts of M33 is reliable and does not influence the statistics obtained or the conclusions drawn from them, I present a convolved version of the N_{H_2} map that highlights the large-scale structure of the spiral arms. I then define several thresholds for the column density and show that in each case the visually inferred spiral arm regions do not affect the final results and conclusions.

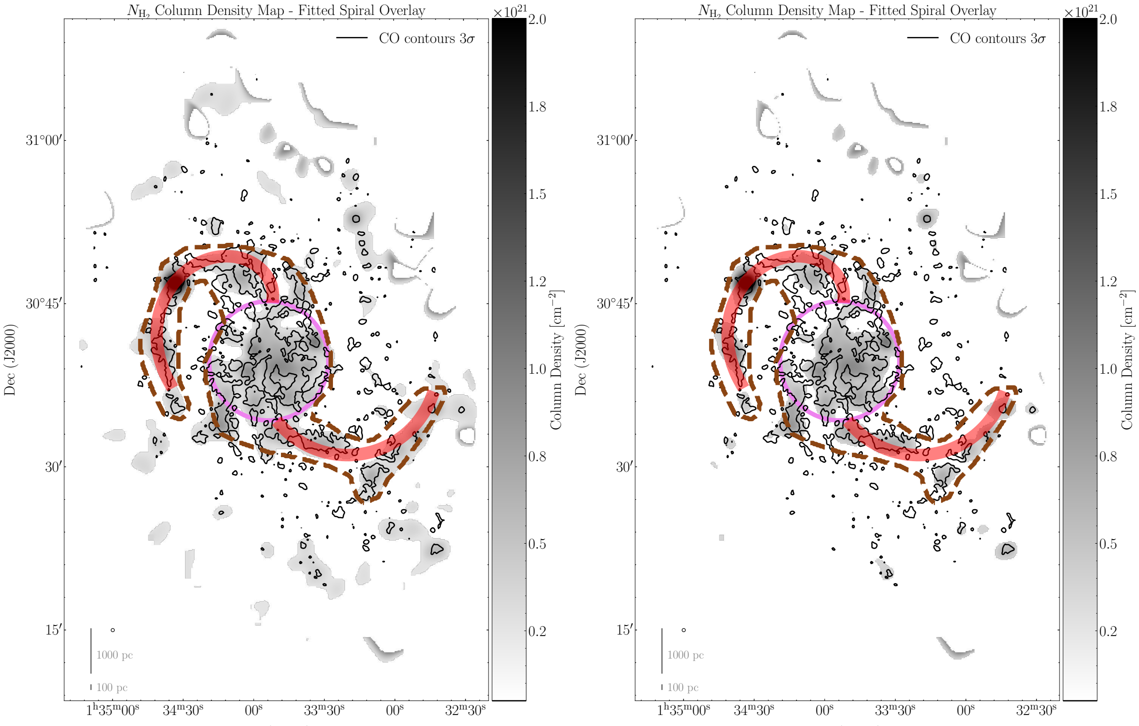

Figure E.1: Smoothed version of the original N_{H_2} map with different minimum thresholds. Left: Threshold of $2 \times 10^{20}\,\mathrm{cm}^{-2}$. Right: Threshold of $4 \times 10^{20}\,\mathrm{cm}^{-2}$. In both cases, the fitted log-spirals and the visually defined spiral arms as in the paper are shown for guidance.

Figure E.1 left shows a convoluted N_{H_2} map with an angular resolution (91″ angular resolution) five times larger than the original beam size. I establish a map threshold of $2 \times 10^{20}\,\mathrm{cm}^{-2}$, which effectively demonstrates the clear recovery of the spiral arms. For comparison, I show in brown the region I use in the paper. I run an analysis that applies this threshold to quantitatively define the borders of the spiral arms. The results of this re-analysis are shown in Fig. E.2. An additional analysis was conducted using a different threshold of $4 \times 10^{20}\,\mathrm{cm}^{-2}$ (Fig. E.1 right), and its results are presented in Fig. E.3.

In both cases, the results remain relatively close to the results presented in the paper. This clearly shows that my choice of the spiral arm region is not sensitive to the overall results. The main reason for that is the significant contrast between the H_2 gas within the spiral arms and that outside of them. Hence, a sharp border can already be easily defined by eye. Even if an alternate border results in some GMCs being classified as part of the spiral arms in one instance and as part of the outskirts in another, it will not affect the overall statistics or alter the conclusions we have drawn. Thus, I conclude that there is always some ambiguity and, whatever threshold I use, this does not provide a better criterion. Hence, determining a width in a more automatic, quantitative way does not improve our outcome.

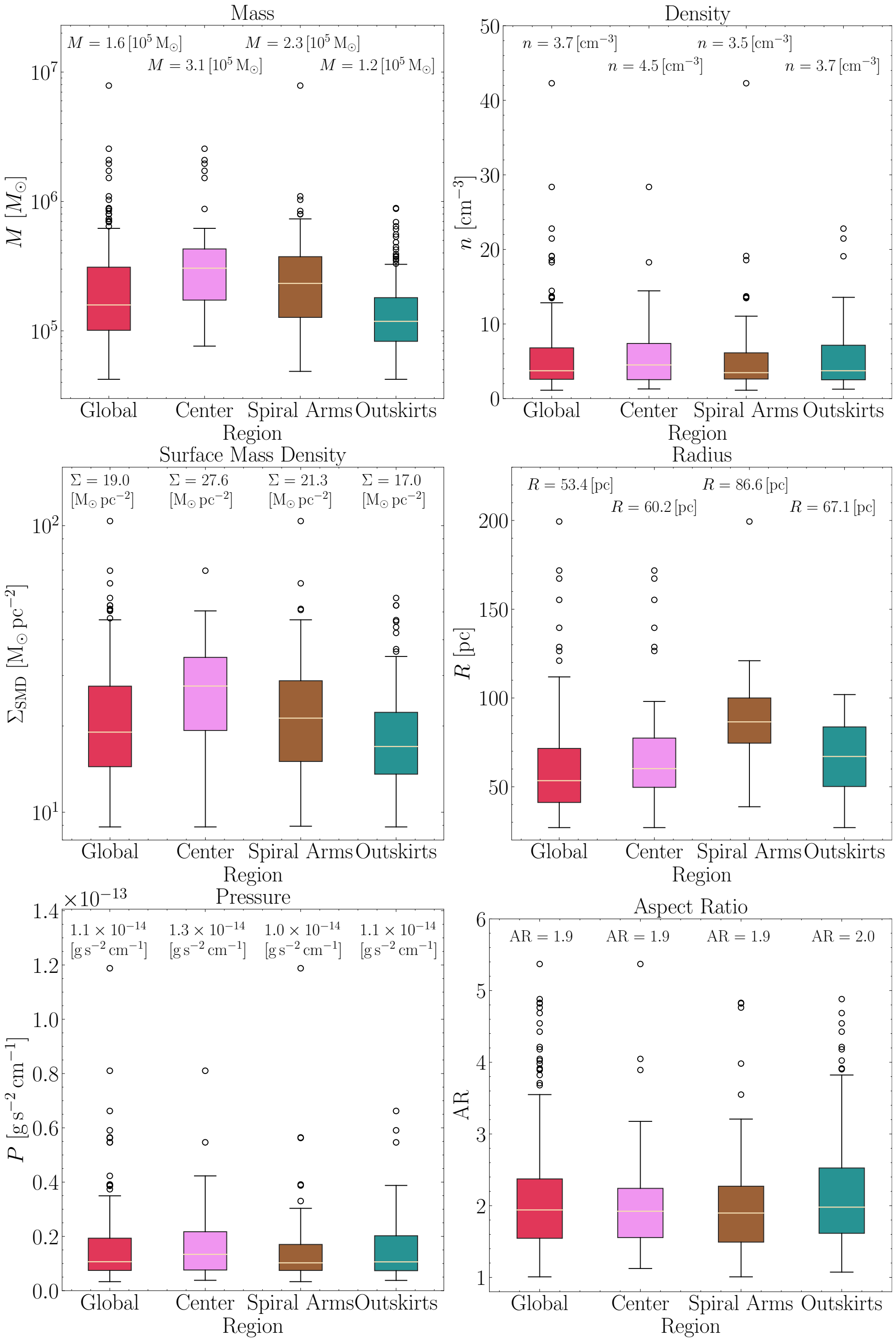

Figure E.2: Box plots of the determined dust-derived parameters categorized based on galactic environments. A threshold of $2 \times 10^{20}\,\mathrm{cm}^{-2}$ has been used. The lower and upper whiskers of the box plot represent the lowest and maximum values of the dataset, respectively. The colored box shows the distribution's interquartile spread, or the range from the 25th to the 75th percentile; the median is indicated by the solid beige line inside the box. The distributions' outliers are shown as circles.

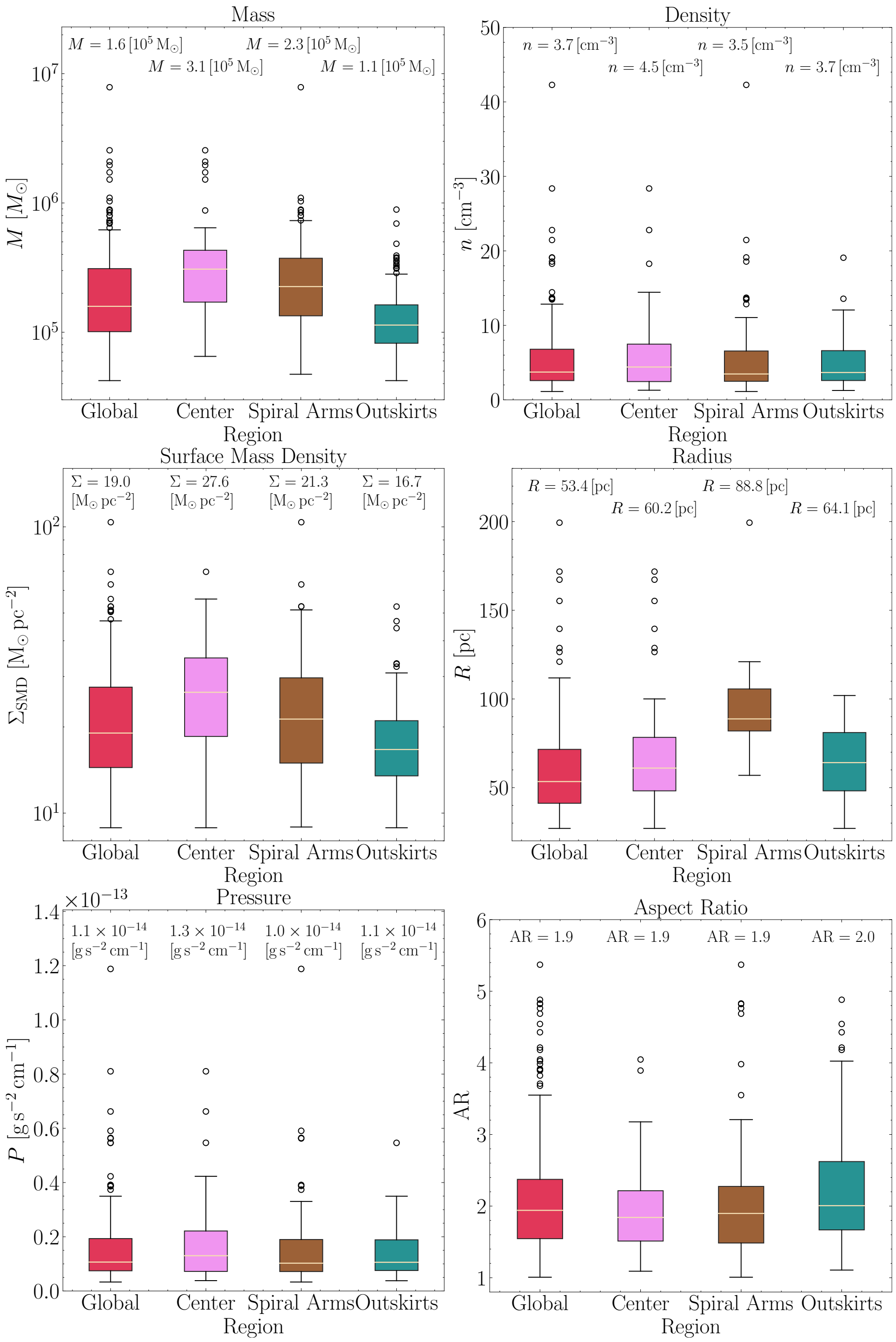

Figure E.3: Box plots of the determined dust-derived parameters categorized based on galactic environments. A threshold of $4 \times 10^{20}\,\mathrm{cm^{-2}}$ has been used.

Bibliography

Agertz, O., Kravtsov, A. V., Leitner, S. N., and Gnedin, N. Y. (2013). Toward a Complete Accounting of Energy and Momentum from Stellar Feedback in Galaxy Formation Simulations. *ApJ*, 770(1):25.

André, P., Men'shchikov, A., Bontemps, S., Könyves, V., Motte, F., Schneider, N., Didelon, P., Minier, V., Saraceno, P., Ward-Thompson, D., di Francesco, J., White, G., Molinari, S., Testi, L., Abergel, A., Griffin, M., Henning, T., Royer, P., Merín, B., Vavrek, R., Attard, M., Arzoumanian, D., Wilson, C. D., Ade, P., Aussel, H., Baluteau, J. P., Benedettini, M., Bernard, J. P., Blommaert, J. A. D. L., Cambrésy, L., Cox, P., di Giorgio, A., Hargrave, P., Hennemann, M., Huang, M., Kirk, J., Krause, O., Launhardt, R., Leeks, S., Le Pennec, J., Li, J. Z., Martin, P. G., Maury, A., Olofsson, G., Omont, A., Peretto, N., Pezzuto, S., Prusti, T., Roussel, H., Russeil, D., Sauvage, M., Sibthorpe, B., Sicilia-Aguilar, A., Spinoglio, L., Waelkens, C., Woodcraft, A., and Zavagno, A. (2010). From filamentary clouds to prestellar cores to the stellar IMF: Initial highlights from the Herschel Gould Belt Survey. *A&A*, 518:L102.

Avedisova, V. S. (1972). Formation of Nebulae by Wolf-Rayet Stars. *Soviet Ast.*, 15:708.

Balbus, S. A. (1988). Local Interstellar Gasdynamical Stability and Substructure in Spiral Arms. *ApJ*, 324:60.

Balbus, S. A. and Cowie, L. L. (1985). On the gravitational stability of the interstellar medium in spiral arms. *ApJ*, 297:61–75.

Bally, J. (2016). Protostellar Outflows. *ARA&A*, 54:491–528.

Barnes, A. T., Longmore, S. N., Battersby, C., Bally, J., Kruijssen, J. M. D., Henshaw, J. D., and Walker, D. L. (2017). Star formation rates and efficiencies in the Galactic Centre. *MNRAS*, 469(2):2263–2285.

Bates, D. R. and Spitzer, Jr., L. (1951). The Density of Molecules in Interstellar Space. *ApJ*, 113:441.

Betz, A. and Zmuidzinas, J. S. (1984). A 150 micron heterodyne spectrometer for airborne astronomy. In Thronson, Jr., H. A. and Erickson, E. F., editors, *Airborne Astronomy Symposium*, pages 320–329.

Beuther, H., Schneider, N., Simon, R., Suri, S., Ossenkopf-Okada, V., Kabanovic, S., Röllig, M., Guevara, C., Tielens, A. G. G. M., Sandell, G., Buchbender, C., Ricken, O., and Güsten, R. (2022). FEEDBACK from the NGC 7538 H II region. *A&A*, 659:A77.

Bialy, S., Burkhart, B., and Sternberg, A. (2017). The H I-to-H_2 Transition in a Turbulent Medium. *ApJ*, 843(2):92.

Bialy, S. and Sternberg, A. (2016). Analytic H I-to-H_2 Photodissociation Transition Profiles. *ApJ*, 822(2):83.

Bisbas, T. G., Tanaka, K. E. I., Tan, J. C., Wu, B., and Nakamura, F. (2017). GMC Collisions as Triggers of Star Formation. V. Observational Signatures. *ApJ*, 850(1):23.

Björklund, R., Sundqvist, J. O., Puls, J., and Najarro, F. (2021). New predictions for radiation-driven, steady-state mass-loss and wind-momentum from hot, massive stars. II. A grid of O-type stars in the Galaxy and the Magellanic Clouds. *A&A*, 648:A36.

Black, J. H. and Dalgarno, A. (1977). Models of interstellar clouds. I. The Zeta Ophiuchi cloud. *ApJS*, 34:405–423.

Bolatto, A. D., Wolfire, M., and Leroy, A. K. (2013). The CO-to-H_2 Conversion Factor. *ARA&A*, 51:207–268.

Bonne, L., Kabanovic, S., Schneider, N., Zavagno, A., Keilmann, E., Simon, R., Buchbender, C., Güsten, R., Jacob, A. M., Jacobs, K., Kavak, U., Polles, F. L., Tiwari, M., Wyrowski, F., and Tielens, A. G. G. M. (2023). The SOFIA FEEDBACK [CII] Legacy Survey: Rapid molecular cloud dispersal in RCW 79. *A&A*, 679:L5.

Bonne, L., Schneider, N., García, P., Bij, A., Broos, P., Fissel, L., Guesten, R., Jackson, J., Simon, R., Townsley, L., Zavagno, A., Aladro, R., Buchbender, C., Guevara, C., Higgins, R., Jacob, A. M., Kabanovic, S., Karim, R., Soam, A., Stutzki, J., Tiwari, M., Wyrowski, F., and Tielens, A. G. G. M. (2022). The SOFIA FEEDBACK Legacy Survey Dynamics and Mass Ejection in the Bipolar H II Region RCW 36. *ApJ*, 935(2):171.

Bonnell, I. A. and Bate, M. R. (2006). Star formation through gravitational collapse and competitive accretion. *MNRAS*, 370(1):488–494.

Boquien, M., Calzetti, D., Aalto, S., Boselli, A., Braine, J., Buat, V., Combes, F., Israel, F., Kramer, C., Lord, S., Relaño, M., Rosolowsky, E., Stacey, G., Tabatabaei, F., van der Tak, F., van der Werf, P., Verley, S., and Xilouris, M. (2015). Measuring star formation with resolved observations: the test case of M 33. *A&A*, 578:A8.

Boquien, M., Calzetti, D., Combes, F., Henkel, C., Israel, F., Kramer, C., Relaño, M., Verley, S., van der Werf, P., Xilouris, E. M., and HERM33ES Team (2011). Dust Heating Sources in Galaxies: The Case of M33 (HERM33ES). *AJ*, 142(4):111.

Boquien, M., Calzetti, D., Kramer, C., Xilouris, E. M., Bertoldi, F., Braine, J., Buchbender, C., Combes, F., Israel, F., Koribalski, B., Lord, S., Quintana-Lacaci, G., Relaño, M., Röllig, M., Stacey, G., Tabatabaei, F. S., Tilanus, R. P. J., van der Tak, F., van der Werf, P., and Verley, S. (2010). 100 μm and 160 μm emission as resolved star-formation rate estimators in M 33 (HERM33ES). *A&A*, 518:L70.

Boreiko, R. T., Betz, A. L., and Zmuidzinas, J. (1988). Heterodyne Spectroscopy of the 158 Micron C II Line in M42. *ApJ*, 325:L47.

Bradt, H. L. and Peters, B. (1950). Abundance of Lithium, Beryllium, Boron, and Other Light Nuclei in the Primary Cosmic Radiation and the Problem of Cosmic-Ray Origin. *Physical Review*, 80(6):943–953.

Braine, J., Gratier, P., Contreras, Y., Schuster, K. F., and Brouillet, N. (2012a). A detailed view of a molecular cloud in the far outer disk of M 33. Molecular cloud formation in M 33. *A&A*, 548:A52.

Braine, J., Gratier, P., Kramer, C., Israel, F. P., van der Tak, F., Mookerjea, B., Boquien, M., Tabatabaei, F., van der Werf, P., and Henkel, C. (2012b). Spectrally resolved C II emission in M 33 (HerM33es). Physical conditions and kinematics around BCLMP 691. *A&A*, 544:A55.

Braine, J., Gratier, P., Kramer, C., Schuster, K. F., Tabatabaei, F., and Gardan, E. (2010a). Molecular cloud formation and the star formation efficiency in M 33. Molecule and star formation in M 33. *A&A*, 520:A107.

Braine, J., Gratier, P., Kramer, C., Xilouris, E. M., Rosolowsky, E., Buchbender, C., Boquien, M., Calzetti, D., Quintana-Lacaci, G., Tabatabaei, F., Verley, S., Israel, F., van der Tak, F., Aalto, S., Combes, F., Garcia-Burillo, S., Gonzalez, M., Henkel, C., Koribalski, B., Mookerjea, B., Roellig, M., Schuster, K. F., Relaño, M., Bertoldi, F., van der Werf, P., and Wiedner, M. (2010b). Cool gas and dust in M 33: Results from the HERschel M 33 Extended Survey (HERM33ES). *A&A*, 518:L69.

Brunt, C. M. (2015). Power-law tails in probability density functions of molecular cloud column density. *MNRAS*, 449(4):4465–4475.

Buchbender, C., Kramer, C., Gonzalez-Garcia, M., Israel, F. P., García-Burillo, S., van der Werf, P., Braine, J., Rosolowsky, E., Mookerjea, B., Aalto, S., Boquien, M., Gratier, P., Henkel, C., Quintana-Lacaci, G., Verley, S., and van der Tak, F. (2013). Dense gas in M 33 (HerM33es). *A&A*, 549:A17.

Burbidge, E. M., Burbidge, G. R., Fowler, W. A., and Hoyle, F. (1957). Synthesis of the Elements in Stars. *Reviews of Modern Physics*, 29(4):547–650.

Burkhart, B., Collins, D. C., and Lazarian, A. (2015). Observational Diagnostics of Self-gravitating MHD Turbulence in Giant Molecular Clouds. *ApJ*, 808(1):48.

Burkhart, B. and Lazarian, A. (2012). The Column Density Variance-Ms Relationship. *ApJ*, 755(1):L19.

Burkhart, B. and Mocz, P. (2019). The Self-gravitating Gas Fraction and the Critical Density for Star Formation. *ApJ*, 879(2):129.

Capriotti, E. R. and Kozminski, J. F. (2001). Relative Effects of Ionizing Radiation and Winds from O-Type Stars on the Structure and Dynamics of H II Regions. *PASP*, 113(784):677–691.

Castor, J., McCray, R., and Weaver, R. (1975). Interstellar bubbles. *ApJ*, 200:L107–L110.

Chen, H. H.-H., Burkhart, B., Goodman, A., and Collins, D. C. (2018). The Anatomy of the Column Density Probability Distribution Function (N-PDF). *ApJ*, 859(2):162.

Chevance, M., Kruijssen, J. M. D., Hygate, A. P. S., Schruba, A., Longmore, S. N., Groves, B., Henshaw, J. D., Herrera, C. N., Hughes, A., Jeffreson, S. M. R., Lang, P., Leroy, A. K., Meidt, S. E., Pety, J., Razza, A., Rosolowsky, E., Schinnerer, E., Bigiel, F., Blanc, G. A., Emsellem, E., Faesi, C. M., Glover, S. C. O., Haydon, D. T., Ho,

I. T., Kreckel, K., Lee, J. C., Liu, D., Querejeta, M., Saito, T., Sun, J., Usero, A., and Utomo, D. (2020). The lifecycle of molecular clouds in nearby star-forming disc galaxies. *MNRAS*, 493(2):2872–2909.

Chevance, M., Kruijssen, J. M. D., Krumholz, M. R., Groves, B., Keller, B. W., Hughes, A., Glover, S. C. O., Henshaw, J. D., Herrera, C. N., Kim, J., Leroy, A. K., Pety, J., Razza, A., Rosolowsky, E., Schinnerer, E., Schruba, A., Barnes, A. T., Bigiel, F., Blanc, G. A., Dale, D. A., Emsellem, E., Faesi, C. M., Grasha, K., Klessen, R. S., Kreckel, K., Liu, D., Longmore, S. N., Meidt, S. E., Querejeta, M., Saito, T., Sun, J., and Usero, A. (2022). Pre-supernova feedback mechanisms drive the destruction of molecular clouds in nearby star-forming disc galaxies. *MNRAS*, 509(1):272–288.

Choi, W., Liu, L., Bureau, M., Cappellari, M., Davis, T. A., Gensior, J., Liang, F.-H., Lu, A., Williams, T. G., and Chung, A. (2023). WISDOM Project - XV. Giant molecular clouds in the central region of the barred spiral galaxy NGC 5806. *MNRAS*, 522(3):4078–4097.

Clark, P. C., Glover, S. C. O., Ragan, S. E., and Duarte-Cabral, A. (2019). Tracing the formation of molecular clouds via [C II], [C I], and CO emission. *MNRAS*, 486(4):4622–4637.

Colombo, D., Duarte-Cabral, A., Pettitt, A. R., Urquhart, J. S., Wyrowski, F., Csengeri, T., Neralwar, K. R., Schuller, F., Menten, K. M., Anderson, L., Barnes, P., Beuther, H., Bronfman, L., Eden, D., Ginsburg, A., Henning, T., König, C., Lee, M. Y., Mattern, M., Medina, S., Ragan, S. E., Rigby, A. J., Sánchez-Monge, Á., Traficante, A., Yang, A. Y., and Wienen, M. (2022). The SEDIGISM survey: The influence of spiral arms on the molecular gas distribution of the inner Milky Way. *A&A*, 658:A54.

Compiègne, M., Flagey, N., Noriega-Crespo, A., Martin, P. G., Bernard, J. P., Paladini, R., and Molinari, S. (2010). Dust in the Diffuse Emission of the Galactic Plane: The Herschel/Spitzer Spectral Energy Distribution Fitting. *ApJ*, 724(1):L44–L47.

Contursi, A., Poglitsch, A., Graciá Carpio, J., Veilleux, S., Sturm, E., Fischer, J., Verma, A., Hailey-Dunsheath, S., Lutz, D., Davies, R., González-Alfonso, E., Sternberg, A., Genzel, R., and Tacconi, L. (2013). Spectroscopic FIR mapping of the disk and galactic wind of M 82 with Herschel-PACS. *A&A*, 549:A118.

Cooksy, A. L., Blake, G. A., and Saykally, R. J. (1986). Direct measurement of the fine-structure interval and gJ factors of singly ionized atomic carbon by laser magnetic resonance. *ApJ*, 305:L89–L92.

Corbelli, E., Braine, J., Bandiera, R., Brouillet, N., Combes, F., Druard, C., Gratier, P., Mata, J., Schuster, K., Xilouris, M., and Palla, F. (2017). From molecules to young stellar clusters: the star formation cycle across the disk of M 33. *A&A*, 601:A146.

Corbelli, E., Braine, J., and Giovanardi, C. (2019). Rise and fall of molecular clouds across the M 33 disk. *A&A*, 622:A171.

Coupeaud, A., Demyk, K., Meny, C., Nayral, C., Delpech, F., Leroux, H., Depecker, C., Creff, G., Brubach, J. B., and Roy, P. (2011). Low-temperature FIR and submillimetre mass absorption coefficient of interstellar silicate dust analogues. *A&A*, 535:A124.

Crocker, A. F., Pellegrini, E., Smith, J. D. T., Draine, B. T., Wilson, C. D., Wolfire, M., Armus, L., Brinks, E., Dale, D. A., Groves, B., Herrera-Camus, R., Hunt, L. K., Kennicutt, R. C., Murphy, E. J., Sandstrom, K., Schinnerer, E., Rigopoulou, D., Rosolowsky, E., and van der Werf, P. (2019). [C I](1-0) and [C I](2-1) in Resolved Local Galaxies. *ApJ*, 887(1):105.

Csengeri, T., Leurini, S., Wyrowski, F., Urquhart, J. S., Menten, K. M., Walmsley, M., Bontemps, S., Wienen, M., Beuther, H., Motte, F., Nguyen-Luong, Q., Schilke, P., Schuller, F., Zavagno, A., and Sanna, C. (2016). ATLASGAL-selected massive clumps in the inner Galaxy. II. Characterisation of different evolutionary stages and their SiO emission. *A&A*, 586:A149.

Dale, J. E., Ercolano, B., and Bonnell, I. A. (2012). Ionizing feedback from massive stars in massive clusters - II. Disruption of bound clusters by photoionization. *MNRAS*, 424(1):377–392.

Dale, J. E., Ngoumou, J., Ercolano, B., and Bonnell, I. A. (2014). Before the first supernova: combined effects of H II regions and winds on molecular clouds. *MNRAS*, 442(1):694–712.

Dalgarno, A. and McCray, R. A. (1972). Heating and Ionization of HI Regions. *ARA&A*, 10:375.

de Jong, T., Boland, W., and Dalgarno, A. (1980). Hydrostatic models of molecular clouds. *A&A*, 91:68–84.

De Looze, I., Cormier, D., Lebouteiller, V., Madden, S., Baes, M., Bendo, G. J., Boquien, M., Boselli, A., Clements, D. L., Cortese, L., Cooray, A., Galametz, M., Galliano, F., Graciá-Carpio, J., Isaak, K., Karczewski, O. Ł., Parkin, T. J., Pellegrini, E. W., Rémy-Ruyer, A., Spinoglio, L., Smith, M. W. L., and Sturm, E. (2014). The applicability of far-infrared fine-structure lines as star formation rate tracers over wide ranges of metallicities and galaxy types. *A&A*, 568:A62.

de Villiers, D. I. L. (2016). Fast parametric modeling of radio astronomy reflector antenna noise temperature. *IEEE Transactions on Antennas and Propagation*, 64(6):2522–2526.

Decataldo, D., Lupi, A., Ferrara, A., Pallottini, A., and Fumagalli, M. (2020). Shaping the structure of a GMC with radiation and winds. *MNRAS*, 497(4):4718–4732.

Demyk, K., Meny, C., Lu, X. H., Papatheodorou, G., Toplis, M. J., Leroux, H., Depecker, C., Brubach, J. B., Roy, P., Nayral, C., Ojo, W. S., Delpech, F., Paradis, D., and Gromov, V. (2017). Low temperature MIR to submillimeter mass absorption coefficient of interstellar dust analogues. I. Mg-rich glassy silicates. *A&A*, 600:A123.

Dicke, R. H. (1946). The Measurement of Thermal Radiation at Microwave Frequencies. *Review of Scientific Instruments*, 17(7):268–275.

Dobbs, C. L., Burkert, A., and Pringle, J. E. (2011). The properties of the interstellar medium in disc galaxies with stellar feedback. *MNRAS*, 417(2):1318–1334.

Dobbs, C. L., Krumholz, M. R., Ballesteros-Paredes, J., Bolatto, A. D., Fukui, Y., Heyer, M., Low, M. M. M., Ostriker, E. C., and Vázquez-Semadeni, E. (2014). Formation of Molecular Clouds and Global Conditions for Star Formation. In Beuther, H., Klessen,

R. S., Dullemond, C. P., and Henning, T., editors, *Protostars and Planets VI*, pages 3–26.

Dobbs, C. L., Liow, K. Y., and Rieder, S. (2020). The formation of young massive clusters by colliding flows. *MNRAS*, 496(1):L1–L5.

Dobbs, C. L. and Pringle, J. E. (2013). The exciting lives of giant molecular clouds. *MNRAS*, 432(1):653–667.

Druard, C., Braine, J., Schuster, K. F., Schneider, N., Gratier, P., Bontemps, S., Boquien, M., Combes, F., Corbelli, E., Henkel, C., Herpin, F., Kramer, C., van der Tak, F., and van der Werf, P. (2014). The IRAM M 33 CO(2-1) survey. A complete census of molecular gas out to 7 kpc. *A&A*, 567:A118.

Duran, C. A., Gusten, R., Risacher, C., Gorlitz, A., Klein, B., Reyes, N., Ricken, O., Wunsch, H.-J., Graf, U. U., Jacobs, K., Honingh, C. E., Stutzki, J., de Lange, G., Delorme, Y., Krieg, J.-M., and Lis, D. C. (2021). 4GREAT—A Four-Color Receiver for High-Resolution Airborne Terahertz Spectroscopy. *IEEE Transactions on Terahertz Science and Technology*, 11(2):194–204.

Dyson, J. E., Williams, D. A., and Tayler, R. J. (1981). Book-Review - the Physics of the Interstellar Medium. *Nature*, 289:729.

Ebagezio, S., Seifried, D., Walch, S., and Bisbas, T. G. (2024). The origin and evolution of the [CII] deficit in HII regions and star-forming molecular clouds. *A&A*, 692:A58.

Einstein, A. (1916). Strahlungs-Emission und Absorption nach der Quantentheorie. *Deutsche Physikalische Gesellschaft*, 18:318–323.

Elia, D., Strafella, F., Dib, S., Schneider, N., Hennebelle, P., Pezzuto, S., Molinari, S., Schisano, E., and Jaffa, S. E. (2018). Multifractal analysis of the interstellar medium: first application to Hi-GAL observations. *MNRAS*, 481(1):509–532.

Elmegreen, B. G. (1979). Gravitational collapse in dust lanes and the appearance of spiral structure in galaxies. *ApJ*, 231:372–383.

Elmegreen, B. G. and Lada, C. J. (1977). Sequential formation of subgroups in OB associations. *ApJ*, 214:725–741.

Emerson, D. T. and Graeve, R. (1988). The reduction of scanning noise in raster scanned data. *A&A*, 190:353–358.

Evans, II, N. J., Dunham, M. M., Jørgensen, J. K., Enoch, M. L., Merín, B., van Dishoeck, E. F., Alcalá, J. M., Myers, P. C., Stapelfeldt, K. R., Huard, T. L., Allen, L. E., Harvey, P. M., van Kempen, T., Blake, G. A., Koerner, D. W., Mundy, L. G., Padgett, D. L., and Sargent, A. I. (2009). The Spitzer c2d Legacy Results: Star-Formation Rates and Efficiencies; Evolution and Lifetimes. *ApJS*, 181(2):321–350.

Federman, S. R., Glassgold, A. E., and Kwan, J. (1979). Atomic to molecular hydrogen transition in interstellar clouds. *ApJ*, 227:466–473.

Federrath, C. and Klessen, R. S. (2013). On the Star Formation Efficiency of Turbulent Magnetized Clouds. *ApJ*, 763(1):51.

Federrath, C., Klessen, R. S., and Schmidt, W. (2008). The Density Probability Distribution in Compressible Isothermal Turbulence: Solenoidal versus Compressive Forcing. *ApJ*, 688(2):L79.

Fielding, D. B., Ostriker, E. C., Bryan, G. L., and Jermyn, A. S. (2020). Multiphase Gas and the Fractal Nature of Radiative Turbulent Mixing Layers. *ApJ*, 894(2):L24.

Fierlinger, K. M., Burkert, A., Ntormousi, E., Fierlinger, P., Schartmann, M., Ballone, A., Krause, M. G. H., and Diehl, R. (2016). Stellar feedback efficiencies: supernovae versus stellar winds. *MNRAS*, 456(1):710–730.

Franeck, A., Walch, S., Seifried, D., Clarke, S. D., Ossenkopf-Okada, V., Glover, S. C. O., Klessen, R. S., Girichidis, P., Naab, T., Wünsch, R., Clark, P. C., Pellegrini, E., and Peters, T. (2018). Synthetic [C II] emission maps of a simulated molecular cloud in formation. *MNRAS*, 481(4):4277–4299.

Fujimoto, M. (1968). Motion of Gas and Spiral Structure. *ApJ*, 152:391.

Fukui, Y., Habe, A., Inoue, T., Enokiya, R., and Tachihara, K. (2021). Cloud-cloud collisions and triggered star formation. *PASJ*, 73:S1–S34.

Gallegos-Garcia, M., Burkhart, B., Rosen, A. L., Naiman, J. P., and Ramirez-Ruiz, E. (2020). Winds in Star Clusters Drive Kolmogorov Turbulence. *ApJ*, 899(2):L30.

Gardan, E., Braine, J., Schuster, K. F., Brouillet, N., and Sievers, A. (2007). Particularly efficient star formation in M 33. *A&A*, 473(1):91–104.

Garrod, R. T. (2013). A three-phase chemical model of hot cores: the formation of glycine. *The Astrophysical Journal*, 765(1):60.

Gatto, A., Walch, S., Naab, T., Girichidis, P., Wünsch, R., Glover, S. C. O., Klessen, R. S., Clark, P. C., Peters, T., Derigs, D., Baczynski, C., and Puls, J. (2017). The SILCC project - III. Regulation of star formation and outflows by stellar winds and supernovae. *MNRAS*, 466(2):1903–1924.

Geen, S., Bieri, R., Rosdahl, J., and de Koter, A. (2021). The geometry and dynamical role of stellar wind bubbles in photoionized H II regions. *MNRAS*, 501(1):1352–1369.

Geen, S. and de Koter, A. (2022). Bottling the champagne: dynamics and radiation trapping of wind-driven bubbles around massive stars. *MNRAS*, 509(3):4498–4514.

Geen, S., Hennebelle, P., Tremblin, P., and Rosdahl, J. (2015). Photoionization feedback in a self-gravitating, magnetized, turbulent cloud. *MNRAS*, 454(4):4484–4502.

Geen, S., Hennebelle, P., Tremblin, P., and Rosdahl, J. (2016). Feedback in Clouds II: UV photoionization and the first supernova in a massive cloud. *MNRAS*, 463(3):3129–3142.

Geen, S., Pellegrini, E., Bieri, R., and Klessen, R. (2020). When H II regions are complicated: considering perturbations from winds, radiation pressure, and other effects. *MNRAS*, 492(1):915–933.

Gerin, M., Phillips, T. G., Keene, J., Betz, A. L., and Boreiko, R. T. (1998). CO, C i, and C II Observations of NGC 7023. *ApJ*, 500(1):329–341.

Gierens, K. M., Stutzki, J., and Winnewisser, G. (1992). UV irradiated clumps in the Orion A molecular cloud : interpretation of low-J CO observations. *A&A*, 259:271.

Girichidis, P., Konstandin, L., Whitworth, A. P., and Klessen, R. S. (2014). On the Evolution of the Density Probability Density Function in Strongly Self-gravitating Systems. *ApJ*, 781(2):91.

Glassgold, A. E. and Langer, W. D. (1974). Model calculations for diffuse molecular clouds. *ApJ*, 193:73–91.

Glassgold, A. E. and Langer, W. D. (1975). The C^+-CO transition in interstellar clouds. *ApJ*, 197:347–350.

Glover, S. C. O. and Clark, P. C. (2016). Is atomic carbon a good tracer of molecular gas in metal-poor galaxies? *MNRAS*, 456(4):3596–3609.

Glover, S. C. O. and Mac Low, M.-M. (2007). Simulating the Formation of Molecular Clouds. II. Rapid Formation from Turbulent Initial Conditions. *ApJ*, 659(2):1317–1337.

Godard, B., Pineau des Forêts, G., Lesaffre, P., Lehmann, A., Gusdorf, A., and Falgarone, E. (2019). Models of irradiated molecular shocks. *A&A*, 622:A100.

Goicoechea, J. R., Pety, J., Cuadrado, S., Cernicharo, J., Chapillon, E., Fuente, A., Gerin, M., Joblin, C., Marcelino, N., and Pilleri, P. (2016). Compression and ablation of the photo-irradiated molecular cloud the Orion Bar. *Nature*, 537(7619):207–209.

Goicoechea, J. R., Teyssier, D., Etxaluze, M., Goldsmith, P. F., Ossenkopf, V., Gerin, M., Bergin, E. A., Black, J. H., Cernicharo, J., Cuadrado, S., Encrenaz, P., Falgarone, E., Fuente, A., Hacar, A., Lis, D. C., Marcelino, N., Melnick, G. J., Müller, H. S. P., Persson, C., Pety, J., Röllig, M., Schilke, P., Simon, R., Snell, R. L., and Stutzki, J. (2015). Velocity-resolved [CII] Emission and [CII]/FIR Mapping along Orion with Herschel. *ApJ*, 812(1):75.

Goldbaum, N. J., Krumholz, M. R., Matzner, C. D., and McKee, C. F. (2011). The Global Evolution of Giant Molecular Clouds. II. The Role of Accretion. *ApJ*, 738(1):101.

Goldsmith, P. F., Heyer, M., Narayanan, G., Snell, R., Li, D., and Brunt, C. (2008). Large-Scale Structure of the Molecular Gas in Taurus Revealed by High Linear Dynamic Range Spectral Line Mapping. *ApJ*, 680(1):428–445.

Goldsmith, P. F., Langer, W. D., Pineda, J. L., and Velusamy, T. (2012). Collisional Excitation of the [C II] Fine Structure Transition in Interstellar Clouds. *ApJS*, 203:13.

Goldsmith, P. F., Snell, R. L., Hasegawa, T., and Ukita, N. (1987). Small-Scale Structure and Chemical Differential in the Central Regions of the Sagittarius B2 Molecular Cloud. *ApJ*, 314:525.

Gordy, W. and Cook, R. (1984). *Microwave molecular spectra.* New York: Wiley.

Gratier, P., Braine, J., Rodriguez-Fernandez, N. J., Schuster, K. F., Kramer, C., Corbelli, E., Combes, F., Brouillet, N., van der Werf, P. P., and Röllig, M. (2012). Giant molecular clouds in the Local Group galaxy M 33⋆. *A&A*, 542:A108.

Gratier, P., Braine, J., Rodriguez-Fernandez, N. J., Schuster, K. F., Kramer, C., Xilouris, E. M., Tabatabaei, F. S., Henkel, C., Corbelli, E., Israel, F., van der Werf, P. P., Calzetti, D., Garcia-Burillo, S., Sievers, A., Combes, F., Wiklind, T., Brouillet, N., Herpin, F., Bontemps, S., Aalto, S., Koribalski, B., van der Tak, F., Wiedner, M. C., Röllig, M., and Mookerjea, B. (2010). Molecular and atomic gas in the Local Group galaxy M 33. *A&A*, 522:A3.

Grenier, I. A., Casandjian, J.-M., and Terrier, R. (2005). Unveiling Extensive Clouds of Dark Gas in the Solar Neighborhood. *Science*, 307(5713):1292–1295.

Griffiths, D. J. (2016). *Introduction to Quantum Mechanics*.

Groenewegen, M. A. T. and Lamers, H. J. G. L. M. (1989). The winds of O-stars. I. an analysis of the UV line profiles with theSEI method. *A&AS*, 79:359–383.

Grudić, M. Y., Guszejnov, D., Hopkins, P. F., Offner, S. S. R., and Faucher-Giguère, C.-A. (2021). STARFORGE: Towards a comprehensive numerical model of star cluster formation and feedback. *MNRAS*, 506(2):2199–2231.

Guélin, M. and Cernicharo, J. (2022). Organic Molecules in Interstellar Space: Latest Advances. *Frontiers in Astronomy and Space Sciences*, 9:787567.

Guevara, C., Stutzki, J., Ossenkopf-Okada, V., Simon, R., Pérez-Beaupuits, J. P., Beuther, H., Bihr, S., Higgins, R., Graf, U., and Güsten, R. (2020). [C II] 158 μm self-absorption and optical depth effects. *A&A*, 636:A16.

Gutcke, T. A., Pakmor, R., Naab, T., and Springel, V. (2021). LYRA - I. Simulating the multiphase ISM of a dwarf galaxy with variable energy supernovae from individual stars. *MNRAS*, 501(4):5597–5615.

Haid, S., Walch, S., Seifried, D., Wünsch, R., Dinnbier, F., and Naab, T. (2018). The relative impact of photoionizing radiation and stellar winds on different environments. *MNRAS*, 478(4):4799–4815.

Haworth, T. J., Tasker, E. J., Fukui, Y., Torii, K., Dale, J. E., Shima, K., Takahira, K., Habe, A., and Hasegawa, K. (2015). Isolating signatures of major cloud-cloud collisions using position-velocity diagrams. *MNRAS*, 450(1):10–20.

Heithausen, A., Bensch, F., Stutzki, J., Falgarone, E., and Panis, J. F. (1998). The IRAM key project: small-scale structure of pre-star forming regions. Combined mass spectra and scaling laws. *A&A*, 331:L65–L68.

Heitsch, F. and Hartmann, L. (2008). Rapid Molecular Cloud and Star Formation: Mechanisms and Movies. *ApJ*, 689(1):290–301.

Hennebelle, P. and Falgarone, E. (2012). Turbulent molecular clouds. *A&A Rev.*, 20:55.

Hennebelle, P. and Iffrig, O. (2014). Simulations of magnetized multiphase galactic disc regulated by supernovae explosions. *A&A*, 570:A81.

Heyer, M. H., Corbelli, E., Schneider, S. E., and Young, J. S. (2004). The Molecular Gas Distribution and Schmidt Law in M33. *ApJ*, 602(2):723–729.

Heyminck, S., Graf, U. U., Güsten, R., Stutzki, J., Hübers, H. W., and Hartogh, P. (2012). GREAT: the SOFIA high-frequency heterodyne instrument. *A&A*, 542:L1.

Hildebrand, R. H. (1983). The determination of cloud masses and dust characteristics from submillimetre thermal emission. *QJRAS*, 24:267–282.

Hitschfeld, M., Aravena, M., Kramer, C., Bertoldi, F., Stutzki, J., Bensch, F., Bronfman, L., Cubick, M., Fujishita, M., Fukui, Y., Graf, U. U., Honingh, N., Ito, S., Jakob, H., Jacobs, K., Klein, U., Koo, B. C., May, J., Miller, M., Miyamoto, Y., Mizuno, N., Onishi, T., Park, Y. S., Pineda, J. L., Rabanus, D., Röllig, M., Sasago, H., Schieder, R., Simon, R., Sun, K., Volgenau, N., Yamamoto, H., and Yonekura, Y. (2008). ^{12}CO 4-3 and [CI] 1-0 at the centers of NGC 4945 and Circinus. *A&A*, 479(1):75–82.

Hollenbach, D. J., Takahashi, T., and Tielens, A. G. G. M. (1991). Low-Density Photodissociation Regions. *ApJ*, 377:192.

Hopkins, P. F., Kereš, D., Murray, N., Quataert, E., and Hernquist, L. (2012). Stellar feedback and bulge formation in clumpy discs. *MNRAS*, 427(2):968–978.

Howarth, I. D., Siebert, K. W., Hussain, G. A. J., and Prinja, R. K. (1997). Cross-correlation characteristics of OB stars from IUE spectroscopy. *MNRAS*, 284(2):265–285.

Hughes, A., Meidt, S. E., Schinnerer, E., Colombo, D., Pety, J., Leroy, A. K., Dobbs, C. L., García-Burillo, S., Thompson, T. A., Dumas, G., Schuster, K. F., and Kramer, C. (2013). Probability Distribution Functions of ^{12}CO($J = 1 \rightarrow 0$) Brightness and Integrated Intensity in M51: The PAWS View. *ApJ*, 779(1):44.

Hunter, T. R. and Kimberk, R. (2015). Statistical Topics Concerning Radiometer Theory. *arXiv e-prints*, page arXiv:1507.04280.

Jeans, J. H. (1902). The Stability of a Spherical Nebula. *Philosophical Transactions of the Royal Society of London Series A*, 199:1–53.

Jiao, Q., Zhao, Y., Zhu, M., Lu, N., Gao, Y., and Zhang, Z.-Y. (2017). Neutral Carbon Emission in Luminous Infrared Galaxies: The [C I] Lines as Total Molecular Gas Tracers. *ApJ*, 840(2):L18.

Johnson, J. B. (1928). Thermal Agitation of Electricity in Conductors. *Physical Review*, 32(1):97–109.

Kabanovic, S., Schneider, N., Ossenkopf-Okada, V., Falasca, F., Güsten, R., Stutzki, J., Simon, R., Buchbender, C., Anderson, L., Bonne, L., Guevara, C., Higgins, R., Koribalski, B., Luisi, M., Mertens, M., Okada, Y., Röllig, M., Seifried, D., Tiwari, M., Wyrowski, F., Zavagno, A., and Tielens, A. G. G. M. (2022). Self-absorption in [C II], ^{12}CO, and H I in RCW120. Building up a geometrical and physical model of the region. *A&A*, 659:A36.

Kahn, F. (1954). *Design of the universe.*

Kainulainen, J., Beuther, H., Henning, T., and Plume, R. (2009). Probing the evolution of molecular cloud structure. From quiescence to birth. *A&A*, 508(3):L35–L38.

Karachentsev, I. D., Karachentseva, V. E., Huchtmeier, W. K., and Makarov, D. I. (2004). A Catalog of Neighboring Galaxies. *AJ*, 127(4):2031–2068.

Katz, N. (1992). Dissipational Galaxy Formation. II. Effects of Star Formation. *ApJ*, 391:502.

Kaufman, M. J., Wolfire, M. G., and Hollenbach, D. J. (2006). [Si II], [Fe II], [C II], and H_2 Emission from Massive Star-forming Regions. *ApJ*, 644:283–299.

Kaufman, M. J., Wolfire, M. G., Hollenbach, D. J., and Luhman, M. L. (1999). Far-infrared and submillimeter emission from galactic and extragalactic photodissociation regions. *The Astrophysical Journal*, 527(2):795.

Kawata, D. (2001). Effects of Type II and Type Ia Supernovae Feedback on the Chemodynamical Evolution of Elliptical Galaxies. *ApJ*, 558(2):598–614.

Keilmann, E., Buchbender, C., Ossenkopf-Okada, V., Schneider, N., Kabanovic, S., Stutzki, J., Simon, R., Riechers, D., Tabatabaei, F., and Bigiel, F. (2024a). Molecular cloud matching in CO and dust in M33: I. High-resolution hydrogen column density maps from Herschel. *A&A*, 688:A171.

Keilmann, E., Dannhauer, S., Kabanovic, S., Schneider, N., Ossenkopf-Okada, V., Simon, R., Bonne, L., Goldsmith, P. F., Güsten, R., Zavagno, A., Stutzki, J., Riechers, D., Röllig, M., Verbena, J. L., and Tielens, A. G. G. M. (2025). [C II]-deficit caused by self-absorption in an ionized carbon-filled bubble in RCW79. *A&A*, 697:L2.

Keilmann, E., Kabanovic, S., Schneider, N., Ossenkopf-Okada, V., Stutzki, J., Kobayashi, M. I. N., Simon, R., Buchbender, C., Riechers, D., Bigiel, F., and Tabatabaei, F. (2024b). Molecular cloud matching in CO and dust in M33: II. Physical properties of giant molecular clouds. *A&A*, 692:A226.

Keller, B. W. and Kruijssen, J. M. D. (2022). Uncertainties in supernova input rates drive qualitative differences in simulations of galaxy evolution. *MNRAS*, 512(1):199–215.

Kennicutt, Jr., R. C. (1998a). Star Formation in Galaxies Along the Hubble Sequence. *ARA&A*, 36:189–232.

Kennicutt, Jr., R. C. (1998b). The Global Schmidt Law in Star-forming Galaxies. *ApJ*, 498(2):541–552.

Kim, C.-G. and Ostriker, E. C. (2017). Three-phase Interstellar Medium in Galaxies Resolving Evolution with Star Formation and Supernova Feedback (TIGRESS): Algorithms, Fiducial Model, and Convergence. *ApJ*, 846(2):133.

Klessen, R. S., Heitsch, F., and Mac Low, M.-M. (2000). Gravitational Collapse in Turbulent Molecular Clouds. I. Gasdynamical Turbulence. *ApJ*, 535(2):887–906.

Kobayashi, M. I. N., Inutsuka, S.-i., Kobayashi, H., and Hasegawa, K. (2017). Evolutionary Description of Giant Molecular Cloud Mass Functions on Galactic Disks. *ApJ*, 836(2):175.

Kobayashi, M. I. N., Kobayashi, H., Inutsuka, S.-i., and Fukui, Y. (2018). Star formation induced by cloud-cloud collisions and galactic giant molecular cloud evolution. *PASJ*, 70:S59.

Koch, E. W. and Rosolowsky, E. W. (2015). Filament identification through mathematical morphology. *MNRAS*, 452:3435–3450.

Koch, E. W., Rosolowsky, E. W., Lockman, F. J., Kepley, A. A., Leroy, A., Schruba, A., Braine, J., Dalcanton, J., Johnson, M. C., and Stanimirović, S. (2018). Kinematics of the atomic ISM ifigun M33 on 80 pc scales. *MNRAS*, 479(2):2505–2533.

Koda, J., Scoville, N., and Heyer, M. (2016). Evolution of Molecular and Atomic Gas Phases in the Milky Way. *ApJ*, 823(2):76.

Kolmogorov, A. (1941). The Local Structure of Turbulence in Incompressible Viscous Fluid for Very Large Reynolds' Numbers. *Akademiia Nauk SSSR Doklady*, 30:301–305.

Kramer, C., Buchbender, C., Quintana-Lacaci, G., Braine, J., Gratier, P., and Rosolowsky, E. (2010). The interplay of dense gas and stars in M33. *Highlights of Astronomy*, 15:415–415.

Kramer, C., Nikola, T., Anderl, S., Bertoldi, F., Boquien, M., Braine, J., Buchbender, C., Combes, F., Henkel, C., Hermelo, I., Israel, F., Relaño, M., Röllig, M., Schuster, K., Tabatabaei, F., van der Tak, F., Verley, S., van der Werf, P., Wiedner, M., and Xilouris, E. M. (2020). Gas and dust cooling along the major axis of M 33 (HerM33es). Herschel/PACS [C II] and [O I] observations. *A&A*, 639:A61.

Kramer, C., Stutzki, J., Rohrig, R., and Corneliussen, U. (1998). Clump mass spectra of molecular clouds. *A&A*, 329:249–264.

Kruijssen, J. M. D. and Longmore, S. N. (2014). An uncertainty principle for star formation - I. Why galactic star formation relations break down below a certain spatial scale. *MNRAS*, 439(4):3239–3252.

Kruijssen, J. M. D., Schruba, A., Chevance, M., Longmore, S. N., Hygate, A. P. S., Haydon, D. T., McLeod, A. F., Dalcanton, J. J., Tacconi, L. J., and van Dishoeck, E. F. (2019). Fast and inefficient star formation due to short-lived molecular clouds and rapid feedback. *Nature*, 569(7757):519–522.

Krumholz, M. R. (2014). The big problems in star formation: The star formation rate, stellar clustering, and the initial mass function. *Phys. Rep.*, 539:49–134.

Krumholz, M. R. and McKee, C. F. (2005). A General Theory of Turbulence-regulated Star Formation, from Spirals to Ultraluminous Infrared Galaxies. *ApJ*, 630(1):250–268.

Krumholz, M. R., McKee, C. F., and Tumlinson, J. (2008). The Atomic-to-Molecular Transition in Galaxies. I. An Analytic Approximation for Photodissociation Fronts in Finite Clouds. *ApJ*, 689(2):865–882.

Krumholz, M. R. and Tan, J. C. (2007). Slow Star Formation in Dense Gas: Evidence and Implications. *ApJ*, 654(1):304–315.

Kutner, M. L. and Ulich, B. L. (1981). Recommendations for calibration of millimeter-wavelength spectral line data. *ApJ*, 250:341–348.

La Vigne, M. A., Vogel, S. N., and Ostriker, E. C. (2006). A Hubble Space Telescope Archival Survey of Feathers in Spiral Galaxies. *ApJ*, 650(2):818–834.

Lagache, G., Cousin, M., and Chatzikos, M. (2018). The [CII] 158 μm line emission in high-redshift galaxies. *A&A*, 609:A130.

Lamers, H. J. G. L. M. and Leitherer, C. (1993). What are the Mass-Loss Rates of O Stars? *ApJ*, 412:771.

Lancaster, L., Ostriker, E. C., Kim, J.-G., and Kim, C.-G. (2021a). Efficiently Cooled Stellar Wind Bubbles in Turbulent Clouds. I. Fractal Theory and Application to Star-forming Clouds. *ApJ*, 914(2):89.

Lancaster, L., Ostriker, E. C., Kim, J.-G., and Kim, C.-G. (2021b). Efficiently Cooled Stellar Wind Bubbles in Turbulent Clouds. II. Validation of Theory with Hydrodynamic Simulations. *ApJ*, 914(2):90.

Larson, R. B. (1974). Effects of supernovae on the early evolution of galaxies. *MNRAS*, 169:229–246.

Larson, R. B. (1981). Turbulence and star formation in molecular clouds. *MNRAS*, 194:809–826.

Larson, R. B. (2005). Thermal physics, cloud geometry and the stellar initial mass function. *MNRAS*, 359(1):211–222.

Lazarian, A., de Gouveia Dal Pino, E. M., and Melioli, C., editors (2015). *Magnetic Fields in Diffuse Media*, volume 407 of *Astrophysics and Space Science Library*.

Le Petit, F., Nehmé, C., Le Bourlot, J., and Roueff, E. (2006). A Model for Atomic and Molecular Interstellar Gas: The Meudon PDR Code. *ApJS*, 164(2):506–529.

Lee, Y.-N. and Hennebelle, P. (2018). Stellar mass spectrum within massive collapsing clumps. I. Influence of the initial conditions. *A&A*, 611:A88.

Leroy, A. K., Schinnerer, E., Hughes, A., Rosolowsky, E., Pety, J., Schruba, A., Usero, A., Blanc, G. A., Chevance, M., Emsellem, E., Faesi, C. M., Herrera, C. N., Liu, D., Meidt, S. E., Querejeta, M., Saito, T., Sandstrom, K. M., Sun, J., Williams, T. G., Anand, G. S., Barnes, A. T., Behrens, E. A., Belfiore, F., Benincasa, S. M., Bešlić, I., Bigiel, F., Bolatto, A. D., den Brok, J. S., Cao, Y., Chandar, R., Chastenet, J., Chiang, I.-D., Congiu, E., Dale, D. A., Deger, S., Eibensteiner, C., Egorov, O. V., García-Rodríguez, A., Glover, S. C. O., Grasha, K., Henshaw, J. D., Ho, I. T., Kepley, A. A., Kim, J., Klessen, R. S., Kreckel, K., Koch, E. W., Kruijssen, J. M. D., Larson, K. L., Lee, J. C., Lopez, L. A., Machado, J., Mayker, N., McElroy, R., Murphy, E. J., Ostriker, E. C., Pan, H.-A., Pessa, I., Puschnig, J., Razza, A., Sánchez-Blázquez, P., Santoro, F., Sardone, A., Scheuermann, F., Sliwa, K., Sormani, M. C., Stuber, S. K., Thilker, D. A., Turner, J. A., Utomo, D., Watkins, E. J., and Whitmore, B. (2021). PHANGS-ALMA: Arcsecond CO(2-1) Imaging of Nearby Star-forming Galaxies. *ApJS*, 257(2):43.

Leurini, S., Wyrowski, F., Wiesemeyer, H., Gusdorf, A., Güsten, R., Menten, K. M., Gerin, M., Levrier, F., Hübers, H. W., Jacobs, K., Ricken, O., and Richter, H. (2015). Spectroscopically resolved far-IR observations of the massive star-forming region G5.89-0.39. *A&A*, 584:A70.

Liu, L., Bureau, M., Li, G.-X., Davis, T. A., Nguyen, D. D., Liang, F.-H., Choi, W., Smith, M. R., and Iguchi, S. (2022). WISDOM Project - XII. Clump properties and turbulence regulated by clump-clump collisions in the dwarf galaxy NGC 404. *MNRAS*, 517(1):632–656.

Lombardi, M., Alves, J., and Lada, C. J. (2010). Larson's third law and the universality of molecular cloud structure. *A&A*, 519:L7.

Lopez, L. A., Krumholz, M. R., Bolatto, A. D., Prochaska, J. X., and Ramirez-Ruiz, E. (2011). What Drives the Expansion of Giant H II Regions?: A Study of Stellar Feedback in 30 Doradus. *ApJ*, 731(2):91.

Lord, S. D. and Young, J. S. (1990). Efficient Star Formation in the Spiral Arms of M51. *ApJ*, 356:135.

Loren, R. B. (1989). The Cobwebs of Ophiuchus. I. Strands of 13CO: The Mass Distribution. *ApJ*, 338:902.

Luhman, M. L., Satyapal, S., Fischer, J., Wolfire, M. G., Sturm, E., Dudley, C. C., Lutz, D., and Genzel, R. (2003). The [C II] 158 Micron Line Deficit in Ultraluminous Infrared Galaxies Revisited. *ApJ*, 594(2):758–775.

Luisi, M., Anderson, L. D., Schneider, N., Simon, R., Kabanovic, S., Güsten, R., Zavagno, A., Broos, P. S., Buchbender, C., Guevara, C., Jacobs, K., Justen, M., Klein, B., Linville, D., Röllig, M., Russeil, D., Stutzki, J., Tiwari, M., Townsley, L. K., and Tielens, A. G. G. M. (2021). Stellar feedback and triggered star formation in the prototypical bubble RCW 120. *Science Advances*, 7(15):eabe9511.

Mac Low, M.-M. and Glover, S. C. O. (2012). The Abundance of Molecular Hydrogen and Its Correlation with Midplane Pressure in Galaxies: Non-equilibrium, Turbulent, Chemical Models. *ApJ*, 746(2):135.

Mac Low, M.-M. and Klessen, R. S. (2004). Control of star formation by supersonic turbulence. *Reviews of Modern Physics*, 76(1):125–194.

Madden, S. C., Cormier, D., Hony, S., Lebouteiller, V., Abel, N., Galametz, M., De Looze, I., Chevance, M., Polles, F. L., Lee, M. Y., Galliano, F., Lambert-Huyghe, A., Hu, D., and Ramambason, L. (2020). Tracing the total molecular gas in galaxies: [CII] and the CO-dark gas. *A&A*, 643:A141.

Magrini, L., Stanghellini, L., Corbelli, E., Galli, D., and Villaver, E. (2010). Metal production in M 33: space and time variations. *A&A*, 512:A63.

Malhotra, S., Helou, G., Stacey, G., Hollenbach, D., Lord, S., Beichman, C. A., Dinerstein, H., Hunter, D. A., Lo, K. Y., Lu, N. Y., Rubin, R. H., Silbermann, N., Thronson, H. A., J., and Werner, M. W. (1997). Infrared Space Observatory Measurements of [C II] Line Variations in Galaxies. *ApJ*, 491(1):L27–L30.

Malhotra, S., Kaufman, M. J., Hollenbach, D., Helou, G., Rubin, R. H., Brauher, J., Dale, D., Lu, N. Y., Lord, S., Stacey, G., Contursi, A., Hunter, D. A., and Dinerstein, H. (2001). Far-Infrared Spectroscopy of Normal Galaxies: Physical Conditions in the Interstellar Medium. *ApJ*, 561:766–786.

Mangum, J. G. and Shirley, Y. L. (2015). How to Calculate Molecular Column Density. *PASP*, 127(949):266.

Marr, J., Snell, R., and Kurtz, S. (2020). *Fundamentals of Radio Astronomy: Observational Methods*. CRC Press.

Martins, F., Pomarès, M., Deharveng, L., Zavagno, A., and Bouret, J. C. (2010). Near-IR integral field spectroscopy of ionizing stars and young stellar objects on the borders of H II regions. *A&A*, 510:A32.

Massey, P., Puls, J., Pauldrach, A. W. A., Bresolin, F., Kudritzki, R. P., and Simon, T. (2005). The Physical Properties and Effective Temperature Scale of O-Type Stars as a Function of Metallicity. II. Analysis of 20 More Magellanic Cloud Stars and Results from the Complete Sample. *ApJ*, 627(1):477–519.

Mathews, W. G. and Baker, J. C. (1971). Galactic Winds. *ApJ*, 170:241.

Matzner, C. D. (2002). On the Role of Massive Stars in the Support and Destruction of Giant Molecular Clouds. *ApJ*, 566(1):302–314.

Matzner, C. D. and McKee, C. F. (2000). Efficiencies of Low-Mass Star and Star Cluster Formation. *ApJ*, 545(1):364–378.

McCray, R. and Kafatos, M. (1987). Supershells and propagating star formation. *ApJ*, 317:190–196.

McCray, R. and Snow, Jr., T. P. (1979). The violent interstellar medium. *ARA&A*, 17:213–240.

McKee, C. F. and Ostriker, E. C. (2007). Theory of Star Formation. *ARA&A*, 45(1):565–687.

McKee, C. F. and Ostriker, J. P. (1977). A theory of the interstellar medium: three components regulated by supernova explosions in an inhomogeneous substrate. *ApJ*, 218:148–169.

Meidt, S. E., Hughes, A., Dobbs, C. L., Pety, J., Thompson, T. A., García-Burillo, S., Leroy, A. K., Schinnerer, E., Colombo, D., Querejeta, M., Kramer, C., Schuster, K. F., and Dumas, G. (2015). Short GMC Lifetimes: An Observational Estimate with the PdBI Arcsecond Whirlpool Survey (PAWS). *ApJ*, 806(1):72.

Melnick, G., Gull, G. E., and Harwit, M. (1979). Observations of the 63 micron [O I] emission line in the Orion and Omega Nebulae. *ApJ*, 227:L29–L33.

Men'shchikov, A., André, P., Didelon, P., Motte, F., Hennemann, M., and Schneider, N. (2012). A multi-scale, multi-wavelength source extraction method: getsources. *A&A*, 542:A81.

Molina, F. Z., Glover, S. C. O., Federrath, C., and Klessen, R. S. (2012). The density variance-Mach number relation in supersonic turbulence - I. Isothermal, magnetized gas. *MNRAS*, 423(3):2680–2689.

Mookerjea, B., Kramer, C., Buchbender, C., Boquien, M., Verley, S., Relaño, M., Quintana-Lacaci, G., Aalto, S., Braine, J., Calzetti, D., Combes, F., Garcia-Burillo, S., Gratier, P., Henkel, C., Israel, F., Lord, S., Nikola, T., Röllig, M., Stacey, G., Tabatabaei, F. S., van der Tak, F., and van der Werf, P. (2011). The Herschel M 33 extended survey (HerM33es): PACS spectroscopy of the star-forming region BCLMP 302. *A&A*, 532:A152.

Muraoka, K., Konishi, A., Tokuda, K., Kondo, H., Miura, R. E., Tosaki, T., Onodera, S., Kuno, N., Kobayashi, M. I. N., Tsuge, K., Sano, H., Kitano, N., Fujita, S., Nishimura, A., Onishi, T., Saigo, K., Yamada, R. I., Demachi, F., Tachihara, K., Fukui, Y., Kawamura, A., and AAS Journals Data Editors (2023). ACA CO(J = 2-1) Mapping of the Nearest Spiral Galaxy M33. I. Initial Results and Identification of Molecular Clouds. *ApJ*, 953(2):164.

Murray, N. and Rahman, M. (2010). Star Formation in Massive Clusters Via the Wilkinson Microwave Anisotropy Probe and the Spitzer Glimpse Survey. *ApJ*, 709(1):424–435.

Naab, T. and Ostriker, J. P. (2017). Theoretical Challenges in Galaxy Formation. *ARA&A*, 55(1):59–109.

Neufeld, D. A. and Dalgarno, A. (1989). Fast Molecular Shocks. II. Emission from Fast Dissociative Shocks. *ApJ*, 344:251.

Nguyen-Luong, Q., Nguyen, H. V. V., Motte, F., Schneider, N., Fujii, M., Louvet, F., Hill, T., Sanhueza, P., Chibueze, J. O., and Didelon, P. (2016). The Scaling Relations and Star Formation Laws of Mini-starburst Complexes. *ApJ*, 833(1):23.

Offner, S. S. R. and Chaban, J. (2017). Impact of Protostellar Outflows on Turbulence and Star Formation Efficiency in Magnetized Dense Cores. *ApJ*, 847(2):104.

Oliver, B. M. (1965). Thermal and quantum noise. *IEEE Proceedings*, 53(5):436–454.

Oort, J. H. and Spitzer, Jr., L. (1955). Acceleration of Interstellar Clouds by O-Type Stars. *ApJ*, 121:6.

Ossenkopf, V., Röllig, M., Neufeld, D. A., Pilleri, P., Lis, D. C., Fuente, A., van der Tak, F. F. S., and Bergin, E. (2013). Herschel/HIFI observations of [C II] and [^{13}C II] in photon-dominated regions. *A&A*, 550:A57.

Ossenkopf, V., Trojan, C., and Stutzki, J. (2001). Massive core parameters from spatially unresolved multi-line observations. *A&A*, 378:608–626.

Osterbrock, D. E. and Ferland, G. J. (2006). *Astrophysics of gaseous nebulae and active galactic nuclei.*

Pabst, C., Higgins, R., Goicoechea, J. R., Teyssier, D., Berne, O., Chambers, E., Wolfire, M., Suri, S. T., Guesten, R., Stutzki, J., Graf, U. U., Risacher, C., and Tielens, A. G. G. M. (2019). Disruption of the Orion molecular core 1 by wind from the massive star θ^1 Orionis C. *Nature*, 565(7741):618–621.

Pabst, C. H. M., Goicoechea, J. R., Teyssier, D., Berné, O., Higgins, R. D., Chambers, E. T., Kabanovic, S., Güsten, R., Stutzki, J., and Tielens, A. G. G. M. (2020). Expanding bubbles in Orion A: [C II] observations of M 42, M 43, and NGC 1977. *A&A*, 639:A2.

Pabst, C. H. M., Hacar, A., Goicoechea, J. R., Teyssier, D., Berné, O., Wolfire, M. G., Higgins, R. D., Chambers, E. T., Kabanovic, S., Güsten, R., Stutzki, J., Kramer, C., and Tielens, A. G. G. M. (2021). [C II] 158 μm line emission from Orion A I. A template for extragalactic studies? *A&A*, 651:A111.

Padoan, P., Federrath, C., Chabrier, G., Evans, II, N. J., Johnstone, D., Jørgensen, J. K., McKee, C. F., and Nordlund, Å. (2014). The Star Formation Rate of Molecular Clouds. In Beuther, H., Klessen, R. S., Dullemond, C. P., and Henning, T., editors, *Protostars and Planets VI*, pages 77–100.

Padoan, P. and Nordlund, Å. (2011). The Star Formation Rate of Supersonic Magnetohydrodynamic Turbulence. *ApJ*, 730(1):40.

Palmeirim, P., André, P., Kirk, J., Ward-Thompson, D., Arzoumanian, D., Könyves, V., Didelon, P., Schneider, N., Benedettini, M., Bontemps, S., Di Francesco, J., Elia, D., Griffin, M., Hennemann, M., Hill, T., Martin, P. G., Men'shchikov, A., Molinari, S., Motte, F., Nguyen Luong, Q., Nutter, D., Peretto, N., Pezzuto, S., Roy, A., Rygl, K. L. J., Spinoglio, L., and White, G. L. (2013). Herschel view of the Taurus B211/3 filament and striations: evidence of filamentary growth? *A&A*, 550:A38.

Papadopoulos, P. P., Bisbas, T. G., and Zhang, Z.-Y. (2018). New places and phases of CO-poor/C I-rich molecular gas in the Universe. *MNRAS*, 478(2):1716–1725.

Parker, E. N. (1958). Dynamics of the Interplanetary Gas and Magnetic Fields. *ApJ*, 128:664.

Parker, E. N. (1960). The Hydrodynamic Theory of Solar Corpuscular Radiation and Stellar Winds. *ApJ*, 132:821.

Passot, T. and Vázquez-Semadeni, E. (1998). Density probability distribution in one-dimensional polytropic gas dynamics. *Phys. Rev. E*, 58(4):4501–4510.

Patel, E., Carlin, J. L., Tollerud, E. J., Collins, M. L. M., and Dooley, G. A. (2018). ΛCDM predictions for the satellite population of M33. *MNRAS*, 480(2):1883–1897.

Peltonen, J., Rosolowsky, E., Johnson, L. C., Seth, A. C., Dalcanton, J., Bell, E. F., Braine, J., Koch, E. W., Lazzarini, M., Leroy, A. K., Skillman, E. D., Smercina, A., Wainer, T., and Williams, B. F. (2023). Clusters, clouds, and correlations: relating young clusters to giant molecular clouds in M33 and M31. *MNRAS*, 522(4):6137–6149.

Peretto, N., Fuller, G. A., Duarte-Cabral, A., Avison, A., Hennebelle, P., Pineda, J. E., André, P., Bontemps, S., Motte, F., Schneider, N., and Molinari, S. (2013). Global collapse of molecular clouds as a formation mechanism for the most massive stars. *A&A*, 555:A112.

Pety, J., Guzmán, V. V., Orkisz, J. H., Liszt, H. S., Gerin, M., Bron, E., Bardeau, S., Goicoechea, J. R., Gratier, P., Le Petit, F., Levrier, F., Öberg, K. I., Roueff, E., and Sievers, A. (2017). The anatomy of the Orion B giant molecular cloud: A local template for studies of nearby galaxies. *A&A*, 599:A98.

Pineda, J. E., Arzoumanian, D., Andre, P., Friesen, R. K., Zavagno, A., Clarke, S. D., Inoue, T., Chen, C., Lee, Y., Soler, J. D., and Kuffmeier, M. (2023). From Bubbles and Filaments to Cores and Disks: Gas Gathering and Growth of Structure Leading to the Formation of Stellar Systems. In Inutsuka, S., Aikawa, Y., Muto, T., Tomida, K., and Tamura, M., editors, *Protostars and Planets VII*, volume 534 of *Astronomical Society of the Pacific Conference Series*, page 233.

Pineda, J. L., Stutzki, J., Buchbender, C., Koda, J., Fischer, C., Goldsmith, P. F., Glover, S. C. O., Klessen, R. S., Kramer, C., Mookerjea, B., Smith, R., Treß, R., and Ziebart, M. (2020). A SOFIA Survey of [C II] in the Galaxy M51. II. [C II] and CO Kinematics across the Spiral Arms. *ApJ*, 900(2):132.

Pittard, J. M. (2022). Momentum and energy injection by a wind-blown bubble into an inhomogeneous interstellar medium. *MNRAS*, 515(2):1815–1829.

Pittard, J. M., Wareing, C. J., and Kupilas, M. M. (2021). How to inflate a wind-blown bubble. *MNRAS*, 508(2):1768–1776.

Planck Collaboration, Ade, P. A. R., Aghanim, N., Alves, M. I. R., Arnaud, M., Ashdown, M., Atrio-Barandela, F., Aumont, J., Baccigalupi, C., Banday, A. J., Barreiro, R. B., Bartlett, J. G., Battaner, E., Benabed, K., Benoit-Lévy, A., Bernard, J. P., Bersanelli, M., Bielewicz, P., Bobin, J., Bonaldi, A., Bond, J. R., Borrill, J., Bouchet, F. R., Boulanger, F., Bucher, M., Burigana, C., Butler, R. C., Cardoso, J. F., Catalano, A., Chamballu, A., Chiang, H. C., Chiang, L. Y., Christensen, P. R., Clements, D. L., Colombi, S., Colombo, L. P. L., Couchot, F., Crill, B. P., Curto, A., Cuttaia, F., Danese, L., Davies, R. D., Davis, R. J., de Bernardis, P., de Rosa, A., de Zotti, G., Delabrouille, J., Dickinson, C., Diego, J. M., Dole, H., Donzelli, S., Doré, O., Douspis, M., Dupac, X., Enßlin, T. A., Eriksen, H. K., Falgarone, E., Finelli, F., Forni, O., Frailis, M., Franceschi, E., Galeotta, S., Ganga, K., Ghosh, T., Giard, M., Giardino, G., González-Nuevo, J., Górski, K. M., Gregorio, A., Gruppuso, A., Hansen, F. K., Harrison, D. L., Hernández-Monteagudo, C., Herranz, D., Hildebrandt, S. R., Hivon, E., Holmes, W. A., Hornstrup, A., Hovest, W., Jaffe, A. H., Jones, W. C., Juvela, M., Keihänen, E., Keskitalo, R., Kisner, T. S., Kneissl, R., Knoche, J., Kunz, M., Kurki-Suonio, H., Lagache, G., Lähteenmäki, A., Lamarre, J. M., Lasenby, A., Laureijs, R. J., Lawrence, C. R., Leonardi, R., Levrier, F., Liguori, M., Lilje, P. B., Linden-Vørnle, M., López-Caniego, M., Macías-Pérez, J. F., Maffei, B., Maino, D., Mandolesi, N., Maris, M., Marshall, D. J., Martin, P. G., Martínez-González, E., Masi, S., Matarrese, S., Mazzotta, P., Melchiorri, A., Mendes, L., Mennella, A., Migliaccio, M., Mitra, S., Miville-Deschênes, M. A., Moneti, A., Montier, L., Morgante, G., Mortlock, D., Munshi, D., Murphy, J. A., Naselsky, P., Nati, F., Natoli, P., Nørgaard-Nielsen, H. U., Noviello, F., Novikov, D., Novikov, I., Oxborrow, C. A., Pagano, L., Pajot, F., Paladini, R., Paoletti, D., Pasian, F., Patanchon, G., Peel, M., Perdereau, O., Perrotta, F., Piacentini, F., Piat, M., Pierpaoli, E., Pietrobon, D., Plaszczynski, S., Pointecouteau, E., Polenta, G., Ponthieu, N., Popa, L., Pratt, G. W., Prunet, S., Puget, J. L., Rachen, J. P., Reach, W. T., Rebolo, R., Reinecke, M., Remazeilles, M., Renault, C., Ricciardi, S., Riller, T., Ristorcelli, I., Rocha, G., Rosset, C., Rubiño-Martín, J. A., Rusholme, B., Sandri, M., Savini, G., Scott, D., Spencer, L. D., Starck, J. L., Stolyarov, V., Sureau, F., Sutton, D., Suur-Uski, A. S., Sygnet, J. F., Tauber, J. A., Tavagnacco, D., Terenzi, L., Toffolatti, L., Tomasi, M., Tristram, M., Tucci, M., Valenziano, L., Valiviita, J., Van Tent, B., Verstraete, L., Vielva, P., Villa, F., Vittorio, N., Wade, L. A., Wandelt, B. D., Yvon, D., Zacchei, A., and Zonca, A. (2014). Planck intermediate results. XIV. Dust emission at millimetre wavelengths in the Galactic plane. *A&A*, 564:A45.

Poglitsch, A., Krabbe, A., Madden, S. C., Nikola, T., Geis, N., Johansson, L. E. B., Stacey, G. J., and Sternberg, A. (1995). A Multiwavelength Study of 30 Doradus: The Interstellar Medium in a Low-Metallicity Galaxy. *ApJ*, 454:293.

Pound, M. W. and Wolfire, M. G. (2023). The PhotoDissociation Region Toolbox: Software and Models for Astrophysical Analysis. *AJ*, 165(1):25.

Ramambason, L., Lebouteiller, V., Madden, S. C., Galliano, F., Richardson, C. T., Saintonge, A., De Looze, I., Chevance, M., Abel, N. P., Hernandez, S., and Braine, J. (2024). Modeling the molecular gas content and CO-to-H_2 conversion factors in low-metallicity star-forming dwarf galaxies. *A&A*, 681:A14.

Regan, M. W. and Vogel, S. N. (1994). The near-infrared structure of M33. *ApJ*, 434:536–545.

Reina-Campos, M. and Kruijssen, J. M. D. (2017). A unified model for the maximum mass scales of molecular clouds, stellar clusters and high-redshift clumps. *MNRAS*, 469(2):1282–1298.

Relaño, M., De Looze, I., Kennicutt, R. C., Lisenfeld, U., Dariush, A., Verley, S., Braine, J., Tabatabaei, F., Kramer, C., Boquien, M., Xilouris, M., and Gratier, P. (2018). Spatially resolving the dust properties and submillimetre excess in M 33. *A&A*, 613:A43.

Relaño, M., Kennicutt, R., Lisenfeld, U., Verley, S., Hermelo, I., Boquien, M., Albrecht, M., Kramer, C., Braine, J., Pérez-Montero, E., De Looze, I., Xilouris, M., Kovács, A., and Staguhn, J. (2016). Dust properties in H II regions in M 33. *A&A*, 595:A43.

Relaño, M., Verley, S., Pérez, I., Kramer, C., Calzetti, D., Xilouris, E. M., Boquien, M., Abreu-Vicente, J., Combes, F., Israel, F., Tabatabaei, F. S., Braine, J., Buchbender, C., González, M., Gratier, P., Lord, S., Mookerjea, B., Quintana-Lacaci, G., and van der Werf, P. (2013). Spectral energy distributions of H ii regions in M 33 (HerM33es). *A&A*, 552:A140.

Renaud, F., Bournaud, F., Emsellem, E., Agertz, O., Athanassoula, E., Combes, F., Elmegreen, B., Kraljic, K., Motte, F., and Teyssier, R. (2015). Environmental regulation of cloud and star formation in galactic bars. *MNRAS*, 454(3):3299–3310.

Rey-Raposo, R., Dobbs, C., Agertz, O., and Alig, C. (2017). The roles of stellar feedback and galactic environment in star-forming molecular clouds. *MNRAS*, 464(3):3536–3551.

Rice, T. S., Goodman, A. A., Bergin, E. A., Beaumont, C., and Dame, T. M. (2016). A Uniform Catalog of Molecular Clouds in the Milky Way. *ApJ*, 822(1):52.

Risacher, C., Güsten, R., Stutzki, J., Hübers, H. W., Aladro, R., Bell, A., Buchbender, C., Büchel, D., Csengeri, T., Duran, C., Graf, U. U., Higgins, R. D., Honingh, C. E., Jacobs, K., Justen, M., Klein, B., Mertens, M., Okada, Y., Parikka, A., Pütz, P., Reyes, N., Richter, H., Ricken, O., Riquelme, D., Rothbart, N., Schneider, N., Simon, R., Wienold, M., Wiesemeyer, H., Ziebart, M., Fusco, P., Rosner, S., and Wohler, B. (2018). The upGREAT Dual Frequency Heterodyne Arrays for SOFIA. *Journal of Astronomical Instrumentation*, 7(4):1840014.

Risacher, C., Gusten, R., Stutzki, J., Hubers, H.-W., Buchel, D., Graf, U. U., Heyminck, S., Honingh, C. E., Jacobs, K., Klein, B., Klein, T., Leinz, C., Putz, P., Reyes, N., Ricken, O., Wunsch, H.-J., Fusco, P., and Rosner, S. (2016). First Supra-THz Heterodyne Array Receivers for Astronomy With the SOFIA Observatory. *IEEE Transactions on Terahertz Science and Technology*, 6(2):199–211.

Roberts, W. W. (1969). Large-Scale Shock Formation in Spiral Galaxies and its Implications on Star Formation. *ApJ*, 158:123.

Robitaille, J. F., Motte, F., Schneider, N., Elia, D., and Bontemps, S. (2019). Exposing the plural nature of molecular clouds. Extracting filaments and the cosmic infrared background against the true scale-free interstellar medium. *A&A*, 628:A33.

Rogers, H. and Pittard, J. M. (2013a). Feedback from winds and supernovae in massive stellar clusters - I. Hydrodynamics. *MNRAS*, 431(2):1337–1351.

Rogers, H. and Pittard, J. M. (2013b). Feedback from winds and supernovae in massive stellar clusters - I. Hydrodynamics. *MNRAS*, 431(2):1337–1351.

Rohlfs, K. and Wilson, T. L. (1996). *Tools of Radio Astronomy.*

Röllig, M. and Ossenkopf, V. (2013). Carbon fractionation in photo-dissociation regions. *A&A*, 550:A56.

Röllig, M., Ossenkopf, V., Jeyakumar, S., Stutzki, J., and Sternberg, A. (2006). [CII] 158 μm emission and metallicity in photon dominated regions. *A&A*, 451:917–924.

Röllig, M. and Ossenkopf-Okada, V. (2022). The KOSMA-τ PDR model. I. Recent updates to the numerical model of photo-dissociated regions. *A&A*, 664:A67.

Roman-Duval, J., Jackson, J. M., Heyer, M., Rathborne, J., and Simon, R. (2010). Physical Properties and Galactic Distribution of Molecular Clouds Identified in the Galactic Ring Survey. *ApJ*, 723(1):492–507.

Rosdahl, J., Schaye, J., Dubois, Y., Kimm, T., and Teyssier, R. (2017). Snap, crackle, pop: sub-grid supernova feedback in AMR simulations of disc galaxies. *MNRAS*, 466(1):11–33.

Rosolowsky, E., Engargiola, G., Plambeck, R., and Blitz, L. (2003). Giant Molecular Clouds in M33. II. High-Resolution Observations. *ApJ*, 599(1):258–274.

Rosolowsky, E. and Leroy, A. (2006). Bias-free Measurement of Giant Molecular Cloud Properties. *PASP*, 118(842):590–610.

Rosolowsky, E. W., Pineda, J. E., Kauffmann, J., and Goodman, A. A. (2008). Structural Analysis of Molecular Clouds: Dendrograms. *ApJ*, 679(2):1338–1351.

Russell, R. W., Melnick, G., Gull, G. E., and Harwit, M. (1980). Detection of the 157 micron /1910 GHz/ /C II/ emission line from the interstellar gas complexes NGC 2024 and M42. *ApJ*, 240:L99–L103.

Sawada, T., Koda, J., and Hasegawa, T. (2018). Internal Structures of Molecular Clouds in the LMC Revealed by ALMA. *ApJ*, 867(2):166.

Schaefer, H. F. and Klemm, R. A. (1970). Atomic Hyperfine Structure. IV Positive and Negative First-Row Ions. *Phys. Rev. A*, 1(4):1063–1069.

Schinnerer, E. and Leroy, A. K. (2024). Molecular Gas and the Star Formation Process on Cloud Scales in Nearby Galaxies. *arXiv e-prints*, page arXiv:2403.19843.

Schmidt, M. (1959). The Rate of Star Formation. *ApJ*, 129:243.

Schnee, S., Enoch, M., Noriega-Crespo, A., Sayers, J., Terebey, S., Caselli, P., Foster, J., Goodman, A., Kauffmann, J., Padgett, D., Rebull, L., Sargent, A., and Shetty, R. (2010). The Dust Emissivity Spectral Index in the Starless Core TMC-1C. *ApJ*, 708(1):127–136.

Schneider, N., André, P., Könyves, V., Bontemps, S., Motte, F., Federrath, C., Ward-Thompson, D., Arzoumanian, D., Benedettini, M., Bressert, E., Didelon, P., Di Francesco, J., Griffin, M., Hennemann, M., Hill, T., Palmeirim, P., Pezzuto, S., Peretto, N., Roy, A., Rygl, K. L. J., Spinoglio, L., and White, G. (2013). What Determines the Density Structure of Molecular Clouds? A Case Study of Orion B with Herschel. *ApJ*, 766(2):L17.

Schneider, N., Bonne, L., Bontemps, S., Kabanovic, S., Simon, R., Ossenkopf-Okada, V., Buchbender, C., Stutzki, J., Mertens, M., Ricken, O., Csengeri, T., and Tielens, A. G. G. M. (2023). Ionized carbon as a tracer of the assembly of interstellar clouds. *Nature Astronomy*, 7:546–556.

Schneider, N., Bontemps, S., Girichidis, P., Rayner, T., Motte, F., André, P., Russeil, D., Abergel, A., Anderson, L., Arzoumanian, D., Benedettini, M., Csengeri, T., Didelon, P., di, F. J., Griffin, M., Hill, T., Klessen, R. S., Ossenkopf, V., Pezzuto, S., Rivera-Ingraham, A., Spinoglio, L., Tremblin, P., and Zavagno, A. (2015a). Detection of two power-law tails in the probability distribution functions of massive GMCs. *MNRAS*, 453:L41–L45.

Schneider, N., Bontemps, S., Motte, F., Blazere, A., André, P., Anderson, L. D., Arzoumanian, D., Comerón, F., Didelon, P., Di Francesco, J., Duarte-Cabral, A., Guarcello, M. G., Hennemann, M., Hill, T., Könyves, V., Marston, A., Minier, V., Rygl, K. L. J., Röllig, M., Roy, A., Spinoglio, L., Tremblin, P., White, G. J., and Wright, N. J. (2016). Globules and pillars in Cygnus X. I. Herschel far-infrared imaging of the Cygnus OB2 environment. *A&A*, 591:A40.

Schneider, N., Bontemps, S., Simon, R., Ossenkopf, V., Federrath, C., Klessen, R. S., Motte, F., André, P., Stutzki, J., and Brunt, C. (2011). The link between molecular cloud structure and turbulence. *A&A*, 529:A1.

Schneider, N. and Brooks, K. (2004). The Bias of Molecular Clump Identification Programs: the Example of the Carina Molecular Clouds. *PASA*, 21(3):290–301.

Schneider, N., Csengeri, T., Bontemps, S., Motte, F., Simon, R., Hennebelle, P., Federrath, C., and Klessen, R. (2010). Dynamic star formation in the massive DR21 filament. *A&A*, 520:A49.

Schneider, N., Csengeri, T., Hennemann, M., Motte, F., Didelon, P., Federrath, C., Bontemps, S., Di Francesco, J., Arzoumanian, D., Minier, V., André, P., Hill, T., Zavagno, A., Nguyen-Luong, Q., Attard, M., Bernard, J. P., Elia, D., Fallscheer, C., Griffin, M., Kirk, J., Klessen, R., Könyves, V., Martin, P., Men'shchikov, A., Palmeirim, P., Peretto, N., Pestalozzi, M., Russeil, D., Sadavoy, S., Sousbie, T., Testi, L., Tremblin, P., Ward-Thompson, D., and White, G. (2012). Cluster-formation in the Rosette molecular cloud at the junctions of filaments. *A&A*, 540:L11.

Schneider, N., Ossenkopf, V., Csengeri, T., Klessen, R. S., Federrath, C., Tremblin, P., Girichidis, P., Bontemps, S., and André, P. (2015b). Understanding star formation in molecular clouds. I. Effects of line-of-sight contamination on the column density structure. *A&A*, 575:A79.

Schneider, N., Ossenkopf-Okada, V., Clarke, S., Klessen, R. S., Kabanovic, S., Veltchev, T., Bontemps, S., Dib, S., Csengeri, T., Federrath, C., Di Francesco, J., Motte, F., André, P., Arzoumanian, D., Beattie, J. R., Bonne, L., Didelon, P., Elia, D., Könyves, V., Kritsuk, A., Ladjelate, B., Myers, P., Pezzuto, S., Robitaille, J. F., Roy, A., Seifried, D., Simon, R., Soler, J., and Ward-Thompson, D. (2022). Understanding star formation in molecular clouds. IV. Column density PDFs from quiescent to massive molecular clouds. *A&A*, 666:A165.

Schneider, N., Ossenkopf-Okada, V., Keilmann, E., Röllig, M., Kabanovic, S., Bonne, L., Csengeri, T., Klein, B., Simon, R., and Comerón, F. (2024). First detection of the [CII] 158 µm line in the intermediate-velocity cloud Draco. *A&A*, 686:A109.

Schneider, N., Röllig, M., Simon, R., Wiesemeyer, H., Gusdorf, A., Stutzki, J., Güsten, R., Bontemps, S., Comerón, F., Csengeri, T., Adams, J. D., and Richter, H. (2018). Anatomy of the massive star-forming region S106. The [O I] 63 μm line observed with GREAT/SOFIA as a versatile diagnostic tool for the evolution of massive stars. *A&A*, 617:A45.

Schneider, N., Simon, R., Guevara, C., Buchbender, C., Higgins, R. D., Okada, Y., Stutzki, J., Güsten, R., Anderson, L. D., Bally, J., Beuther, H., Bonne, L., Bontemps, S., Chambers, E., Csengeri, T., Graf, U. U., Gusdorf, A., Jacobs, K., Justen, M., Kabanovic, S., Karim, R., Luisi, M., Menten, K., Mertens, M., Mookerjea, B., Ossenkopf-Okada, V., Pabst, C., Pound, M. W., Richter, H., Reyes, N., Ricken, O., Röllig, M., Russeil, D., Sánchez-Monge, Á., Sandell, G., Tiwari, M., Wiesemeyer, H., Wolfire, M., Wyrowski, F., Zavagno, A., and Tielens, A. G. G. M. (2020). FEEDBACK: a SOFIA Legacy Program to Study Stellar Feedback in Regions of Massive Star Formation. *PASP*, 132(1016):104301.

Schneider, N., Stutzki, J., Winnewisser, G. F., and Block, D. (1998). The rosette molecular complex i. co observations. *Astronomy and Astrophysics*, 335:1049–1069.

Seifried, D., Walch, S., Girichidis, P., Naab, T., Wünsch, R., Klessen, R. S., Glover, S. C. O., Peters, T., and Clark, P. (2017). SILCC-Zoom: the dynamic and chemical evolution of molecular clouds. *MNRAS*, 472(4):4797–4818.

Shetty, R. and Ostriker, E. C. (2008). Cloud and Star Formation in Disk Galaxy Models with Feedback. *ApJ*, 684(2):978–995.

Silva-Villa, E. and Larsen, S. S. (2012). The relation between surface star formation rate density and spiral arms in NGC 5236 (M 83). *A&A*, 537:A145.

Simon, R., Jackson, J. M., Clemens, D. P., Bania, T. M., and Heyer, M. H. (2001). The Structure of Four Molecular Cloud Complexes in the BU-FCRAO Milky Way Galactic Ring Survey. *ApJ*, 551(2):747–763.

Simon, R., Schneider, N., Bigiel, F., Ossenkopf-Okada, V., Okada, Y., Johnstone, D., Schilke, P., Stacey, G., Roellig, M., Sanchez-Monge, A., Seifried, D., Stutzki, J., Bertoldi, F., Buchbender, C., Fich, M., Herter, T., Higgins, R., and Nikola, T. (2019). The Cycling of Matter from the Interstellar Medium to Stars and back. *BAAS*, 51(3):367.

Simón-Díaz, S. and Stasińska, G. (2011). The chemical composition of the Orion star forming region. II. Stars, gas, and dust: the abundance discrepancy conundrum. *A&A*, 526:A48.

Somerville, R. S. and Davé, R. (2015). Physical Models of Galaxy Formation in a Cosmological Framework. *ARA&A*, 53:51–113.

Spilker, A., Kainulainen, J., and Orkisz, J. (2021). Bird's eye view of molecular clouds in the Milky Way. I. Column density and star formation from sub-parsec to kiloparsec scales. *A&A*, 653:A63.

Spitzer, L. (1978). *Physical processes in the interstellar medium.*

Stacey, G. J., Geis, N., Genzel, R., Lugten, J. B., Poglitsch, A., Sternberg, A., and Townes, C. H. (1991). The 158 micron C II line - A measure of global star formation activity in galaxies. *ApJ*, 373:423–444.

Stacey, G. J., Smyers, S. D., Kurtz, N. T., and Harwit, M. (1983). Observations of the 145.5 micron emission line in the Orion Nebula. *ApJ*, 265:L7–L11.

Starck, J. L., Aghanim, N., and Forni, O. (2004). Detection and discrimination of cosmological non-Gaussian signatures by multi-scale methods. *A&A*, 416:9–17.

Stark, A. A., Bolatto, A. D., Chamberlin, R. A., Lane, A. P., Bania, T. M., Jackson, J. M., and Lo, K.-Y. (1997). First Detection of 492 GHz [C I] Emission from the Large Magellanic Cloud. *ApJ*, 480:L59–L62.

Sternberg, A. (1988). The Infrared Response of Molecular Hydrogen Gas to Ultraviolet Radiation: A Scaling Law. *ApJ*, 332:400.

Sternberg, A. and Dalgarno, A. (1989). The infrared response of molecular hydrogen gas to ultraviolet radiation - High-density regions. *ApJ*, 338:197–233.

Sternberg, A. and Dalgarno, A. (1995). Chemistry in Dense Photon-dominated Regions. *ApJS*, 99:565.

Stoerzer, H., Stutzki, J., and Sternberg, A. (1996). FUV irradiated molecular clumps: spherical geometry and density gradients. *A&A*, 310:592–602.

Strömgren, B. (1939). The Physical State of Interstellar Hydrogen. *ApJ*, 89:526.

Stutz, A. M. and Kainulainen, J. (2015). Evolution of column density distributions within Orion A⋆. *A&A*, 577:L6.

Stutzki, J., Bensch, F., Heithausen, A., Ossenkopf, V., and Zielinsky, M. (1998). On the fractal structure of molecular clouds. *A&A*, 336:697–720.

Stutzki, J. and Guesten, R. (1990). High Spatial Resolution Isotopic CO and CS Observations of M17 SW: The Clumpy Structure of the Molecular Cloud Core. *ApJ*, 356:513.

Stutzki, J., Güsten, R., and Great Team (2023). Velocity resolved CII -Observations - a 40-year long story. In Ossenkopf-Okada, V., Schaaf, R., Breloy, I., and Stutzki, J., editors, *Physics and Chemistry of Star Formation: The Dynamical ISM Across Time and Spatial Scales*, page 133.

Stutzki, J., Stacey, G. J., Genzel, R., Harris, A. I., Jaffe, D. T., and Lugten, J. B. (1988). Submillimeter and Far-Infrared Line Observations of M17 SW: A Clumpy Molecular Cloud Penetrated by Ultraviolet Radiation. *ApJ*, 332:379.

Sun, J., Leroy, A. K., Ostriker, E. C., Hughes, A., Rosolowsky, E., Schruba, A., Schinnerer, E., Blanc, G. A., Faesi, C., Kruijssen, J. M. D., Meidt, S., Utomo, D., Bigiel, F., Bolatto, A. D., Chevance, M., Chiang, I.-D., Dale, D., Emsellem, E., Glover, S. C. O., Grasha, K., Henshaw, J., Herrera, C. N., Jimenez-Donaire, M. J., Lee, J. C., Pety, J., Querejeta, M., Saito, T., Sandstrom, K., and Usero, A. (2020). Dynamical Equilibrium in the Molecular ISM in 28 Nearby Star-forming Galaxies. *ApJ*, 892(2):148.

Syed, J., Wang, Y., Beuther, H., Soler, J. D., Rugel, M. R., Ott, J., Brunthaler, A., Kerp, J., Heyer, M., Klessen, R. S., Henning, T., Glover, S. C. O., Goldsmith, P. F., Linz, H., Urquhart, J. S., Ragan, S. E., Johnston, K. G., and Bigiel, F. (2020). Atomic and molecular gas properties during cloud formation. *A&A*, 642:A68.

Tabatabaei, F. S., Beck, R., Krause, M., Berkhuijsen, E. M., Gehrz, R., Gordon, K. D., Hinz, J. L., Humphreys, R., McQuinn, K., Polomski, E., Rieke, G. H., and Woodward, C. E. (2007). A multi-scale study of infrared and radio emission from Scd galaxy M 33. *A&A*, 466:509–519.

Tabatabaei, F. S., Braine, J., Xilouris, E. M., Kramer, C., Boquien, M., Combes, F., Henkel, C., Relano, M., Verley, S., Gratier, P., Israel, F., Wiedner, M. C., Röllig, M., Schuster, K. F., and van der Werf, P. (2014). Variation in the dust emissivity index across M 33 with Herschel and Spitzer (HerM 33es). *A&A*, 561:A95.

Tan, B., Oh, S. P., and Gronke, M. (2021). Radiative mixing layers: insights from turbulent combustion. *MNRAS*, 502(3):3179–3199.

Tanabe, K., Kinoshita, S., and Shiromizu, T. (2011). Asymptotic flatness at null infinity in arbitrary dimensions. *Phys. Rev. D*, 84:044055.

Tasker, E. J. and Tan, J. (2009). Formation and Evolution of Giant Molecular Clouds in Disk Galaxies. In *American Astronomical Society Meeting Abstracts #213*, volume 213 of *American Astronomical Society Meeting Abstracts*, page 347.05.

Tenorio-Tagle, G. (1979). The gas dynamics of H II regions. I. The champagne model. *A&A*, 71:59–65.

Thompson, A. R., Moran, J. M., and Swenson, Jr., G. W. (2017). *Interferometry and Synthesis in Radio Astronomy, 3rd Edition.*

Tielens, A. and Hagen, W. (1982). Model calculations of the molecular composition of interstellar grain mantles. *Astronomy and Astrophysics, vol. 114, no. 2, Oct. 1982, p. 245-260. Research supported by the Nederlandse Organisatie voor Zuiver-Wetenschappelijk Onderzoek.*, 114:245–260.

Tielens, A. G. G. M. and Hollenbach, D. (1985a). Photodissociation regions. I. Basic model. *ApJ*, 291:722–746.

Tielens, A. G. G. M. and Hollenbach, D. (1985b). Photodissociation regions. II. A model for the Orion photodissociation region. *ApJ*, 291:747–754.

Tiwari, M., Karim, R., Pound, M. W., Wolfire, M., Jacob, A., Buchbender, C., Güsten, R., Guevara, C., Higgins, R. D., Kabanovic, S., Pabst, C., Ricken, O., Schneider, N., Simon, R., Stutzki, J., and Tielens, A. G. G. M. (2021). SOFIA FEEDBACK Survey: Exploring the Dynamics of the Stellar Wind-Driven Shell of RCW 49. *ApJ*, 914(2):117.

Tremblin, P., Schneider, N., Minier, V., Didelon, P., Hill, T., Anderson, L. D., Motte, F., Zavagno, A., André, P., Arzoumanian, D., Audit, E., Benedettini, M., Bontemps, S., Csengeri, T., Di Francesco, J., Giannini, T., Hennemann, M., Nguyen Luong, Q., Marston, A. P., Peretto, N., Rivera-Ingraham, A., Russeil, D., Rygl, K. L. J., Spinoglio, L., and White, G. J. (2014). Ionization compression impact on dense gas distribution and star formation. Probability density functions around H II regions as seen by Herschel. *A&A*, 564:A106.

Tubbs, A. D. (1980). Galactic spiral shocks - Vertical structure, thermal phase effects, and self-gravity. *ApJ*, 239:882–892.

Utomo, D., Sun, J., Leroy, A. K., Kruijssen, J. M. D., Schinnerer, E., Schruba, A., Bigiel, F., Blanc, G. A., Chevance, M., Emsellem, E., Herrera, C., Hygate, A. P. S., Kreckel, K., Ostriker, E. C., Pety, J., Querejeta, M., Rosolowsky, E., Sandstrom, K. M., and Usero, A. (2018). Star Formation Efficiency per Free-fall Time in nearby Galaxies. *ApJ*, 861(2):L18.

Valdivia, V., Hennebelle, P., Gérin, M., and Lesaffre, P. (2016). H_2 distribution during the formation of multiphase molecular clouds. *A&A*, 587:A76.

van der Marel, R. P., Fardal, M., Besla, G., Beaton, R. L., Sohn, S. T., Anderson, J., Brown, T., and Guhathakurta, P. (2012). The M31 Velocity Vector. II. Radial Orbit toward the Milky Way and Implied Local Group Mass. *ApJ*, 753(1):8.

van der Tak, F. F. S., Black, J. H., Schöier, F. L., Jansen, D. J., and van Dishoeck, E. F. (2007). A computer program for fast non-LTE analysis of interstellar line spectra. With diagnostic plots to interpret observed line intensity ratios. *A&A*, 468(2):627–635.

Vázquez-Semadeni, E. and García, N. (2001). The Probability Distribution Function of Column Density in Molecular Clouds. *ApJ*, 557(2):727–735.

Vázquez-Semadeni, E., Palau, A., Ballesteros-Paredes, J., Gómez, G. C., and Zamora-Avilés, M. (2019). Global hierarchical collapse in molecular clouds. Towards a comprehensive scenario. *MNRAS*, 490(3):3061–3097.

Vázquez-Semadeni, E., Palau, A., Gómez, G. C., Arroyo-Chávez, G., Alig, C., Ballesteros-Paredes, J., Camacho, V., González-Samaniego, A., and Burkert, A. (2024). The GT and GHC models for molecular clouds compared. Differences, similarities, and myths. *arXiv e-prints*, page arXiv:2408.10406.

Vázquez-Semadeni, E., Ryu, D., Passot, T., González, R. F., and Gazol, A. (2006). Molecular Cloud Evolution. I. Molecular Cloud and Thin Cold Neutral Medium Sheet Formation. *ApJ*, 643(1):245–259.

Verley, S., Corbelli, E., Giovanardi, C., and Hunt, L. K. (2010a). Star formation in M 33: the radial and local relations with the gas. *A&A*, 510:A64.

Verley, S., Relaño, M., Kramer, C., Xilouris, E. M., Boquien, M., Calzetti, D., Combes, F., Buchbender, C., Braine, J., Quintana-Lacaci, G., Tabatabaei, F. S., Lord, S., Israel, F., Stacey, G., and van der Werf, P. (2010b). Properties of compact 250 μm emission and H II regions in M 33 (HERM33ES). *A&A*, 518:L68.

Wada, K., Spaans, M., and Kim, S. (2000). Formation of Cavities, Filaments, and Clumps by the Nonlinear Development of Thermal and Gravitational Instabilities in the Interstellar Medium under Stellar Feedback. *ApJ*, 540(2):797–807.

Walch, S., Girichidis, P., Naab, T., Gatto, A., Glover, S. C. O., Wünsch, R., Klessen, R. S., Clark, P. C., Peters, T., Derigs, D., and Baczynski, C. (2015). The SILCC (SImulating the LifeCycle of molecular Clouds) project - I. Chemical evolution of the supernova-driven ISM. *MNRAS*, 454(1):238–268.

Waldron, W. L. (1984). Recombination stellar wind model for the coronae of early-type stars. *ApJ*, 282:256–266.

Wall, J. E., Mac Low, M.-M., McMillan, S. L. W., Klessen, R. S., Portegies Zwart, S., and Pellegrino, A. (2020). Modeling of the Effects of Stellar Feedback during Star Cluster Formation Using a Hybrid Gas and N-Body Method. *ApJ*, 904(2):192.

Wall, J. E., McMillan, S., Mac Low, M.-M., Portegies Zwart, S., Klessen, R., and Pellegrino, A. (2019). A Dynamic Formation Channel for Binaries in Embedded Clusters. In *American Astronomical Society Meeting Abstracts #233*, volume 233 of *American Astronomical Society Meeting Abstracts*, page 208.04.

Weaver, R., McCray, R., Castor, J., Shapiro, P., and Moore, R. (1977). Interstellar bubbles. II. Structure and evolution. *ApJ*, 218:377–395.

White, R. L. and Long, K. S. (1991). Supernova Remnant Evolution in an Interstellar Medium with Evaporating Clouds. *ApJ*, 373:543.

Wiese, W. L. and Fuhr, J. R. (2007). Improved Critical Compilations of Selected Atomic Transition Probabilities for Neutral and Singly Ionized Carbon and Nitrogen. *Journal of Physical and Chemical Reference Data*, 36(4):1287–1345.

Williams, J. P., de Geus, E. J., and Blitz, L. (1994). Determining Structure in Molecular Clouds. *ApJ*, 428:693.

Wilson, C. D. (1997). Atomic Carbon Emission from Individual Molecular Clouds in M33. *ApJ*, 487:L49–L52.

Wilson, T. L., Rohlfs, K., and Hüttemeister, S. (2009). *Tools of Radio Astronomy*.

Wilson, T. L., Rohlfs, K., and Hüttemeister, S. (2013). *Tools of Radio Astronomy*.

Wolfire, M. G., Hollenbach, D., and McKee, C. F. (2010). The Dark Molecular Gas. *ApJ*, 716:1191–1207.

Wolfire, M. G., Vallini, L., and Chevance, M. (2022). Photodissociation and X-Ray-Dominated Regions. *ARA&A*, 60:247–318.

Xilouris, E. M., Tabatabaei, F. S., Boquien, M., Kramer, C., Buchbender, C., Bertoldi, F., Anderl, S., Braine, J., Verley, S., Relaño, M., Quintana-Lacaci, G., Akras, S., Beck, R., Calzetti, D., Combes, F., Gonzalez, M., Gratier, P., Henkel, C., Israel, F., Koribalski, B., Lord, S., Mookerjea, B., Rosolowsky, E., Stacey, G., Tilanus, R. P. J., van der Tak, F., and van der Werf, P. (2012). Cool and warm dust emission from M 33 (HerM33es). *A&A*, 543:A74.

Yahia, H., Schneider, N., Bontemps, S., Bonne, L., Attuel, G., Dib, S., Ossenkopf-Okada, V., Turiel, A., Zebadua, A., Elia, D., Kumar Maji, S., Schmitt, F. G., and Robitaille, J. F. (2021). Description of turbulent dynamics in the interstellar medium: multifractal-microcanonical analysis. I. Application to Herschel observations of the Musca filament. *A&A*, 649:A33.

Young, E. T., Becklin, E. E., Marcum, P. M., Roellig, T. L., De Buizer, J. M., Herter, T. L., Güsten, R., Dunham, E. W., Temi, P., Andersson, B. G., Backman, D., Burgdorf, M., Caroff, L. J., Casey, S. C., Davidson, J. A., Erickson, E. F., Gehrz, R. D., Harper, D. A., Harvey, P. M., Helton, L. A., Horner, S. D., Howard, C. D., Klein, R., Krabbe, A., McLean, I. S., Meyer, A. W., Miles, J. W., Morris, M. R., Reach, W. T., Rho, J., Richter, M. J., Roeser, H. P., Sandell, G., Sankrit, R., Savage, M. L., Smith, E. C., Shuping, R. Y., Vacca, W. D., Vaillancourt, J. E., Wolf, J., and Zinnecker, H. (2012). Early Science with SOFIA, the Stratospheric Observatory For Infrared Astronomy. *ApJ*, 749(2):L17.

Ysard, N., Koehler, M., Jimenez-Serra, I., Jones, A. P., and Verstraete, L. (2019). From grains to pebbles: the influence of size distribution and chemical composition on dust emission properties. *A&A*, 631:A88.

Yu, S.-Y., Ho, L. C., and Wang, J. (2021). Spiral Structure Boosts Star Formation in Disk Galaxies. *ApJ*, 917(2):88.

Acknowledgements

First of all, I wish to thank Professor Dr. Jürgen Stutzki for his trust in me and for giving me the opportunity to pursue my doctorate under his supervision. I would also like to thank Dr. Christof Buchbender, who assisted me with questions on basic topics, as I come from theoretical particle physics and was unable to attend any astrophysics lectures during my physics studies in Mainz. My sincere thanks go to Dr. Slawa Kabanovic for his contributions and engaging in discussions and answering many of the questions I had for him; and for all the fun and jokes he made. I am also grateful to Dr. Robert Simon, Dr. Volker Ossenkopf-Okada, and Simon M. Dannhauer for their contributions and many, very helpful feedback during my doctoral studies.

I want to express my gratitude to Prof. Dr. Andreas Schadschneider, my second thesis reviewer, and Prof. Dr. Susanne Crewell, the chair of my thesis defense committee. I appreciate that both agreed to be involved in the final phase of my Ph.D. journey.

Furthermore, a heartfelt and very special thanks goes to Dr. Nicola Schneider for her dedication, help, collaboration, valuable feedback, and for providing me with the opportunity to learn so much from her. Without her, the course of my doctoral studies would certainly have been very different. She encouraged me to think critically, and I learned from her vast experience the interpretation of various astrophysical processes. She also has given me the great opportunity to be part of the SOFIA Legacy Program FEEDBACK.

It was an incredible journey that I will never forget.

Finally, I would like to extend my special and heartfelt thanks to my family – to my parents, without whom my journey thus far would not have been possible; as well as to my wife Judith and my son Nicolas, who have continuously supported me, even though Nicolas and I would have loved to play together more often.